Development of scintillator detectors for measuring muons and air showers.

Von der Fakultät für Mathematik, Informatik und Naturwissenschaften der
RWTH Aachen University zur Erlangung des akademischen Grades eines Doktors der
Naturwissenschaften genehmigte Dissertation

vorgelegt von

Christine Peters, M.Sc. RWTH

aus Mönchengladbach

Berichter: Univ.-Prof. Dr. rer. nat. Thomas Hebbeker
Priv.-Doz. Dr. rer. nat. Oliver Pooth

Tag der mündlichen Prüfung 23.05.2019

Abstract

The number of muons contained in extensive air showers is an important quantity to study the chemical composition of ultra-high energy cosmic rays. For the measurement of the muonic component, a multi-channel scintillator detector prototype with silicon photomultipliers is developed in this thesis. The design of the detector is optimized based on detailed simulations. Furthermore, important simulated performance quantities are validated against measurements performed in the laboratory. Finally, the developed detector prototype is investigated by coincidence measurements with an external, small-scale detector array, demonstrating its ability to detect cosmic ray air showers.

Zusammenfassung

Die Anzahl von Myonen, die in ausgedehnten Luftschauern enthalten sind, ist eine wichtige Größe, um die chemische Zusammensetzung der kosmischen Strahlung höchster Energien zu untersuchen. Für die Vermessung der myonischen Komponente wird in dieser Arbeit ein mehrkanaliger Szintillator-Detektor-Prototyp mit Silizium-Photomultipliern entwickelt. Das Design des Detektors wird auf der Grundlage detaillierter Simulationen optimiert. Darüber hinaus werden wichtige simulierte Leistungsgrößen mit Messungen im Labor validiert. Schließlich wird der entwickelte Detektorprototyp mittels Koinzidenzmessungen mit einem externen Luftschauerdetektorarray untersucht, wobei seine Fähigkeit zur Erkennung von Luftschauern mit kosmischer Strahlung nachgewiesen wird.

Contents

Chapter 1

Introduction

The Earth's atmosphere is constantly hit by cosmic ray (CR) particles. When entering the atmosphere, the primary particle interacts with air molecules initiating a cascade of secondary particles. These extensive air showers are studied by measuring the secondary particles reaching the ground with surface detector arrays or by the light emission generated during the shower development. The arrival directions and energies of the primary particles as well as their particle types can be derived from these measurements. With regard to ultra-high energy cosmic rays (UHECRs), several important properties are not yet known. Their sources are difficult to identify since UHECRs comprise charged nuclei ranging from protons to iron nuclei. These are deflected by the magnetic fields as they travel through the universe, making it difficult to trace UHECRs back to their sources. Their flux as a function of energy depicts a suppression at the highest energy. Two main hypotheses aim to give a conclusive explanation for the suppression. They introduce different constraints on the characteristics of the sources and on the elemental abundances of cosmic rays. The origin of the suppression may thus be revealed by an excellent determination of the chemical composition of UHECRs. Important properties of UHECRs and extensive air showers are discussed in chapter 2. The largest observatory for measuring extensive air showers induced by UHECRs is the Pierre Auger Observatory in Argentina. The experiment is introduced in chapter 3. It allows for outstanding measurements by combining two detection techniques, a surface detector array and fluorescence telescopes capturing the light emission during the longitudinal shower development. Aiming to further improve its performance, especially in terms of reconstructing the mass of the arriving CRs, the Pierre Auger Observatory is undergoing a major upgrade, called AugerPrime. Among further improvements, the key element is the installation of a scintillator-based detector, called SSD, on top of each existing surface detector station. It enables the simultaneous examination of the same shower particles at ground with two complementary detection techniques. By analyzing the different responses of both detectors to the electromagnetic and muonic shower components, an improved reconstruction of the mass of the CR primary is achieved.
Starting as a proposal for this large-scale detector upgrade, a scintillator-based design with silicon photomultipliers (SiPMs) as photosensor has been designed in Aachen. The key element is one detector unit comprising a scintillator tile and a wavelength-shifting fibre that collects the scintillation light emitted during particle passages and directs it to a SiPM. An introduction to SiPMs is given in chapter 4. General characteristics of the further used materials and components within one detector unit are presented in chapter 5. The design, concept and readout electronics of a

detector unit is further described in chapter 6. The layout is originally based on detailed Monte Carlo (MC) simulations (cf. chapter 7). It has been optimized based on various tests of individual components and of prototype units. The performance of the final detector unit is studied in detail in chapter 8. A first demonstrator, known as MiniAMD, is realized (cf. chapter 9). While performing coincidence measurements with a small-scale detector array, it is confirmed that MiniAMD is not only well suited for the detection of individual atmospheric muons but allows also for the detection of cosmic ray showers. As an outlook, a simple analysis approach is used to study the response of an alternative large-scale detector to simulated air showers. This so-called Aachen Muon Detector comprises 64 detector units. The analysis concept follows studies performed for the SSD of the AugerPrime upgrade. It is presented in chapter 10 and indicates promising discrimination power between MC air showers with proton and iron primaries.

CHAPTER 2

Ultra-high energy cosmic rays

As for most of the research fields in modern particle physics the study of *cosmic rays* is highly influenced by the improvements regarding measurement techniques. Be it due to the development of technical equipment (detector components as light sensors, electronics etc.) or pioneering ideas such as a combination of complementary detection principles to study the same physical phenomenon. A historical review of the research field can be found e.g. in [1]. As high energy cosmic ray particles have small fluxes, their study is challenging. The energies of the highest energetic particles cannot be reached in the lab or at a particle accelerator, so that their interactions have to be studied in their natural environment. Experiments conducted by large (mostly international) groups of scientists supported by technical staff operating the detectors are needed.
Cosmic rays (CRs) are defined, in the scope of this thesis, as charged particles reaching the Earth's atmosphere coming from outer space. At the highest energies they are studied by means of *extensive air showers* developing in the atmosphere as natural detector medium. The processes taking place in the development of extensive air showers are described in section 2.1. As this thesis does not aim to give a conclusive overview of the research field of high energy CRs, the following discussion will concentrate only on few, popular explanations of their main characteristics. The description of both, extensive air showers and cosmic rays, is mainly based on a selection of a few reviews [2, 3, 4, 5, 6]. Additionally, to depict the recent status of the field, some of the important achievements by the *Pierre Auger Observatory* [7] are presented in this chapter. The experiment is designed for the study of cosmic rays of the highest energies and will be introduced in chapter 3.

2.1. Extensive air showers

In the ultra-high energy regime cosmic rays are studied via air showers produced in the atmosphere. While entering the Earth's atmosphere, the primary particle interacts with air molecules producing a cascade of secondaries. As such a particle cascade initiated by a vertical 10^{19} eV proton contains more than 10^{10} particles, which reach the ground at sea level and are distributed over a footprint of several kilometers [2], they are called *extensive air showers*. A schematic of an air shower development is depicted in figure 2.1. The particles contained travel by nearly speed of light towards ground and can be divided in three main components: the *muonic*, the *electromagnetic* and the *hadronic* component.
The hadronic component is composed of $\sim$ 90% (neutral and charged) pions and $\sim$ 10% of kaons

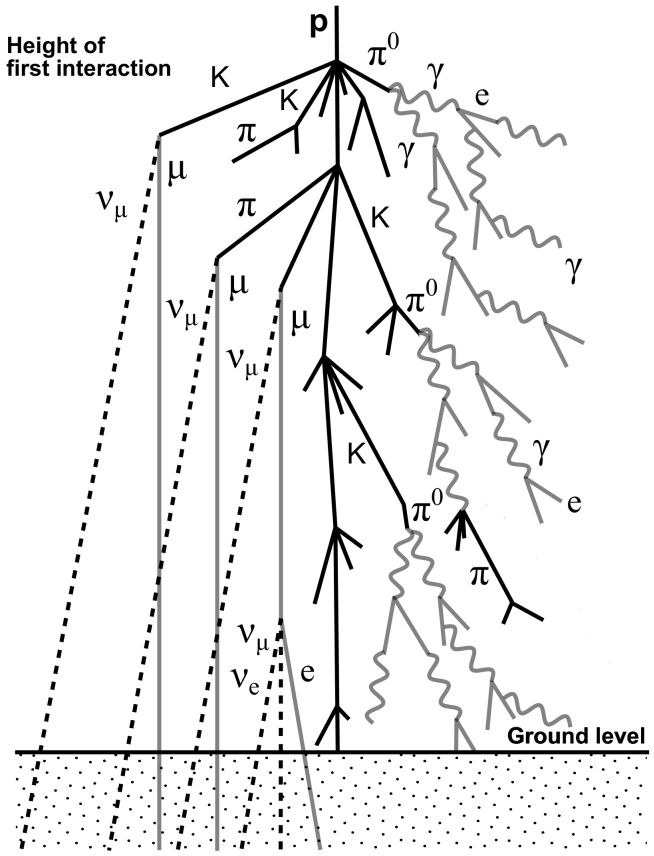

Figure 2.1.: Schematic view of an extensive air shower initiated by an energetic primary cosmic ray particle (here, a proton). During the evolution secondary particles are produced by interactions and decays. The hadronic cascade (mainly composed of pions and kaons) feeds constantly the electromagnetic cascade which in turn evokes the emission of fluorescence and Cherenkov light. Figure adapted from [9].

[8]. It is continuously feeding the electromagnetic component (composed of electrons, positrons and photons) due to their decay products. It also initiates the muonic component through pion and kaon decays. Once created, muons are unlikely to interact or decay on their way through the atmosphere. They are reaching in high quantity the ground containing still some information of their production. The air shower geometry and development depends on the arrival direction described by the zenith angle θ, the energy E_0 and the type or atomic number A of the primary particle.
Traditionally, extensive air showers are studied by ground-based arrays of detectors investigating all particles of the air shower or one explicit particle type that reaches the ground. They might be accompanied by telescopes observing photons produced by interactions of shower particles in the atmosphere. Two types of telescopes are commonly used. First, imaging telescopes studying fluorescence light isotropically emitted via de-excitation of molecules which have been excited by shower particles. Second, non-imaging telescopes measuring the beamed Cherenkov light in air.
It is common to use the quantity *atmospheric* or *slant depth* X to describe the longitudinal profile of air showers. The slant depth corresponds to the amount of matter an air shower has already traversed at a given point in its development.

For vertical showers, the slant depth can be calculated by integrating the density of air from the top of the atmosphere along the trajectory of the shower to height h in question

$$X(h) = \int_h^\infty \rho(h')\,\mathrm{d}h' = \int_h^\infty \rho_0\,\mathrm{e}^{-h'/h_0}\,\mathrm{d}h' \approx 1030\,\mathrm{g/cm^2}\,\mathrm{e}^{-h/h_0} \quad , \tag{2.1}$$

where $\rho_0 = 1.23\,\mathrm{kg\,m^{-3}}$ is the air density at sea level and $h_0 = 8.4\,\mathrm{km}$ is the scale height of the atmosphere [10].
Along this trajectory particles interact or decay. The slant depth of the atmosphere can be thus translated to the classical quantities *hadronic interaction length* and *electromagnetic radiation length* of particle physics in air [11]:

$$\begin{aligned} X(0) \equiv X_{\text{atmosphere}} &= 11 \cdot \lambda_\mathrm{i}^\mathrm{had} && \text{with hadronic interaction length } \lambda_\mathrm{i}^\mathrm{had} = 90.1\,\mathrm{g/cm^2} \\ &= 27 \cdot \lambda_\mathrm{r}^\mathrm{em} && \text{with electromagnetic radiation length } \lambda_\mathrm{r}^\mathrm{em} = 36.6\,\mathrm{g/cm^2}. \end{aligned}$$

For inclined showers with zenith angle θ the amount of matter traversed increases, following

$$X(h,\theta) \approx X(h) \cdot \frac{1}{\cos\theta} \quad . \tag{2.2}$$

Here, a flat atmosphere is assumed, so that this approximation is good up to 70 °. The evolution of an air shower is thereby a complex combination of electromagnetic cascades and hadronic interactions. For the nowadays best predictions detailed simulations are performed. As the center-of-mass energy of the first collisions in the atmosphere exceeds the energies achieved in recent Earth-based accelerators, the air shower models predicting the development of the particle cascade have to rely on an extrapolation of measurements and the predictions of the standard model of particle physics to higher energies. Several air shower models have been established. They are subject to large uncertainties, and predictions among models differ.
In the following a simple analytical model introduced by Heitler [12] will be considered to describe some important characteristics of the development of the electromagnetic cascade. Later, the concept will be extended to hadron-induced air showers according to [13].

2.1.1. Heitler model

The basic principle of the *Heitler model* for electromagnetic cascades is a binary tree with two processes involved: electrons and positrons above a critical energy lose energy due to bremsstrahlung via one photon and photons lose energy due to pair-production. Further interactions or energy losses are not taken into account like the generation of multiple photons in one bremsstrahlung process. The schematic view of the principle of the Heitler model is depicted in figure 2.2 on the left.
The average energy loss due to bremsstrahlung by an electron of energy E, in a thickness of matter $\mathrm{d}X$, is given by [14]

$$-\left.\frac{\mathrm{d}E}{\mathrm{d}X}\right|_\text{brems} = \frac{E}{\lambda_\mathrm{r}^\mathrm{em}} \quad , \tag{2.3}$$

whereby $\lambda_\mathrm{r}^\mathrm{em}$ is the radiation length corresponding to the characteristic amount of matter traversed. It refers to the average distance over which the energy of a high energetic electron/positron is reduced to $1/e$ of its initial energy due to bremsstrahlung processes as well as to the distance $\sim \frac{7}{9}$ of the mean free path for pair production by a high-energy photon [11].
For the Heitler model the step size $X_\text{step}^\mathrm{em}$ between two interactions corresponds to an equal distribution of the energy E_0 of the parent particle on two children particles. For the bremsstrahlung

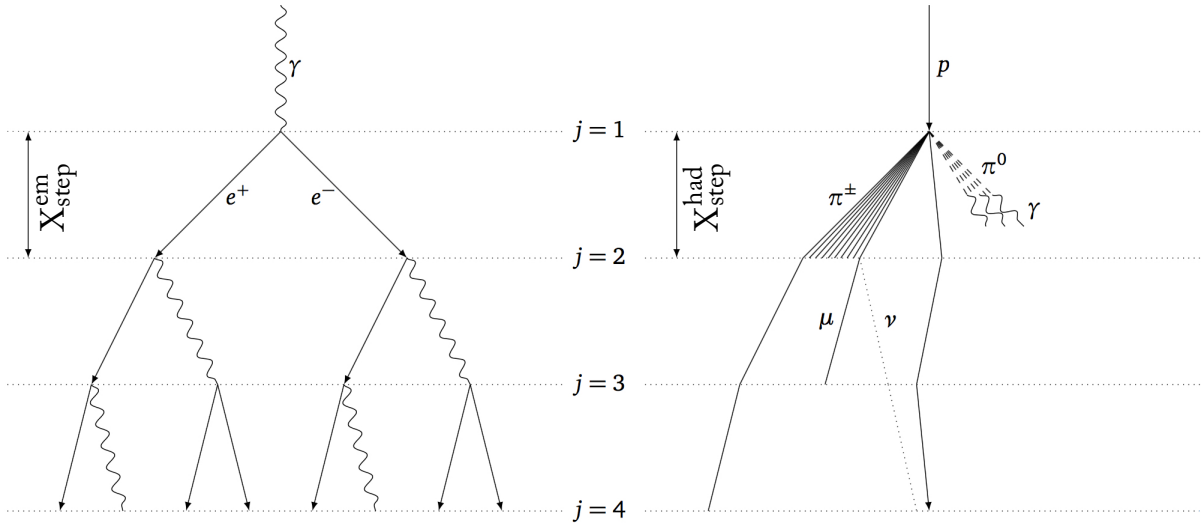

Figure 2.2.: Schematic view of an electromagnetic (left) and a hadronic cascade (right) of a hadron induced shower as described by the Heitler model. Both cascades evolve as a tree with j generations. At each step only two branches are proceeding. For an electromagnetic cascade at each node two particles are produced after a step length $X^{\mathrm{em}}_{\mathrm{step}}$. In the hadronic case, at each node after a step length $X^{\mathrm{had}}_{\mathrm{step}}$ groups of charged (solid lines) and neutral (dashed lines) pions are generated. Each decaying $\pi^\pm$ produces one muon and a neutrino. Modified, original from [6].

process, the electron will proceed with $E_0/2$ after emitting a photon carrying away the same energy. Integrating equation 2.3 with a thickness of traversed matter equalling one step length $X^{\mathrm{em}}_{\mathrm{step}}$ yields

$$E(X^{\mathrm{em}}_{\mathrm{step}})\Big|_{\mathrm{brems}} = E_0 \cdot e^{-X^{\mathrm{em}}_{\mathrm{step}}/\lambda^{\mathrm{em}}_{\mathrm{r}}} \stackrel{!}{=} \frac{E_0}{2} \tag{2.4}$$

$$\Rightarrow X^{\mathrm{em}}_{\mathrm{step}} = \ln(2) \cdot \lambda^{\mathrm{em}}_{\mathrm{r}} \quad . \tag{2.5}$$

Translated to the state of the cascade evolution after $j = X/X^{\mathrm{em}}_{\mathrm{step}}$ generations, the number of particles N contained in the electromagnetic cascade corresponds to $N(j) = 2^j$ whereby each particle carries an energy of $E(j) = E_0/2^j$. The slant depth traversed can be described as

$$X(j) = j \cdot X^{\mathrm{em}}_{\mathrm{step}} + X_0 \quad , \tag{2.6}$$

with X_0 being the depth of the starting point of the cascade.

The evolution of the binary tree comes to a stillstand at a critical energy $E^{\mathrm{em,\,air}}_{\mathrm{c}} \sim 86\,\mathrm{MeV}$ [2]. It is defined as the energy at which ionization processes start to dominate over radiative losses. At this point, the cascade has reached its maximum number of particles N_{max}, which corresponds to the step j_{max}.

As at each step all particles carry the same amount of energy, at the maximum each particle has an energy of $E_c^{\text{em, air}}$. Therefore, the initial energy E_0 can be described as

$$E_0 = E_c^{\text{em, air}} \cdot N_{\max} \tag{2.7}$$

$$\Rightarrow N_{\max}|_{j_{\max}}(E_0) = \frac{E_0}{E_c^{\text{em, air}}} = 2^{j_{\max}} \tag{2.8}$$

$$\propto E_0 \tag{2.9}$$

$$\Rightarrow j_{\max} = \frac{\ln\left(\frac{E_0}{E_c^{\text{em, air}}}\right)}{\ln(2)} \quad , \tag{2.10}$$

whereby $N_{\max}|_{j_{\max}}$ is the number of particles contained in the cascade at its maximum.

The *slant depth of the shower maximum* $X_{\max}^{\text{em}}$ can be calculated according to equations 2.6, 2.5 and 2.10 by

$$X_{\max}^{\text{em}}\big|_{j_{\max}} = j_{\max} \cdot X_{\text{step}}^{\text{em}} + X_0 \tag{2.11}$$

$$= j_{\max} \cdot \ln(2) \cdot \lambda_r^{\text{em}} + X_0 \tag{2.12}$$

$$\Rightarrow X_{\max}(E_0) = \ln\left(\frac{E_0}{E_c^{\text{em, air}}}\right) \cdot \lambda_r^{\text{em}} + X_0 \tag{2.13}$$

$$\propto \ln(E_0) \quad . \tag{2.14}$$

The increase of the maximum slant depth with the energy E_0 is defined as the *elongation rate* Λ^{em}. For an electromagnetic cascade, it can be expressed according to the Heitler model as

$$\Lambda^{\text{em}} = \frac{\mathrm{d}X_{\max}^{\text{em}}}{\mathrm{d}\log_{10} E_0} = \frac{\lambda_r^{\text{em}}}{\log_{10}(e)} = 2.3 \cdot \lambda_r^{\text{em}} \sim 85\,\mathrm{g/cm^2} \quad . \tag{2.15}$$

Although the Heitler model is limited in the prediction of the detailed evolution in an electromagnetic cascade, important relations can be described:

- The number of particles at the maximum $N_{\max}$ is proportional to the initial energy of the primary E_0.
- The depth of the shower maximum $X_{\max}^{\text{em}}$ depends logarithmically on the primary energy E_0.

Extension to hadronic cascades

The successful Heitler model for an electromagnetic cascade can be translated to the more complicated case of a cascade with a hadronic initiation [13, 15]. First, we study the case of a proton as primary. The proton of energy E_0 interacts after a step length $X_{\text{step}}^{\text{had}} = \ln(2) \cdot \lambda_i^{\text{had}}$, similar to the electromagnetic cascade model (cf. figure 2.2 (right)). The interaction generates n_{gen} new particles, each having an energy of E_0/n_{gen}. These particles consist by two thirds of charged pions $n_{\text{charged}} = \frac{2}{3} n_{\text{gen}}$ and by one third of neutral pions $n_{\text{neutral}} = \frac{1}{3} n_{\text{gen}} = \frac{1}{2} n_{\text{charged}}$. The neutral pions will decay immediately into two photons feeding the electromagnetic cascade. The charged pions might produce new particles by further interactions driving the evolution of the hadronic cascade. After j generations the energies contained by the hadronic cascade is E_{had} while the energy transferred to the electromagnetic cascade is E_{em}

$$E_{\text{had}} = \left(\frac{2}{3}\right)^j \cdot E_0 \qquad \text{and} \qquad E_{\text{em}} = \left[1 - \left(\frac{2}{3}\right)^j\right] \cdot E_0 \quad . \tag{2.16}$$

The evolution stops at its maximum (at step $j_{\max}$) when the particles contained in the cascade reach their critical energy $E_c^{\pi,\,\mathrm{air}}$ at which energy losses due to interactions, thus production of new hadrons, and due to decays are equal[1].
As the energy is shared equally by all generated particles, at the maximum each pion carries the same energy, $E_c^{\pi,\,\mathrm{air}}$,

$$E^{\pi}|_{j_{\max}} = \frac{E_0}{\left(n_{\mathrm{gen}}\right)^{j_{\max}}} = \frac{E_0}{\left(\frac{3}{2}n_{\mathrm{charged}}\right)^{j_{\max}}} \stackrel{!}{=} E_c^{\pi,\,\mathrm{air}} \tag{2.17}$$

$$\Rightarrow \ln\left(\frac{E_0}{E_c^{\pi,\,\mathrm{air}}}\right) = j_{\max}\cdot\ln\left(\frac{3}{2}n_{\mathrm{charged}}\right) \tag{2.18}$$

$$\Rightarrow \quad j_{\max} = \frac{\ln(E_0/E_c^{\pi,\,\mathrm{air}})}{\ln\left(\frac{3}{2}n_{\mathrm{charged}}\right)} \tag{2.19}$$

$$= \frac{\ln(n_{\mathrm{charged}})}{\ln\left(\frac{3}{2}n_{\mathrm{charged}}\right)}\cdot\frac{\ln(E_0/E_c^{\pi,\,\mathrm{air}})}{\ln\left(n_{\mathrm{charged}}\right)} \tag{2.20}$$

$$= \beta\cdot\frac{\ln(E_0/E_c^{\pi,\,\mathrm{air}})}{\ln\left(n_{\mathrm{charged}}\right)} \text{ with } \beta = \frac{\ln(n_{\mathrm{charged}})}{\ln\left(\frac{3}{2}n_{\mathrm{charged}}\right)} \approx 0.85 \text{ for } n_{\mathrm{charged}} \approx 10 \tag{2.21}$$

$$\approx 0.85\cdot\log_{10}\left(\frac{E_0}{E_c^{\pi,\,\mathrm{air}}}\right) \tag{2.22}$$

$$\approx 3\ldots6 \text{ for } E_c^{\pi,\,\mathrm{air}} = 20\,\mathrm{GeV}\,[13], \text{ with } E_c^{\pi,\,\mathrm{air}} \text{ slowly decreasing with increasing } E_0. \tag{2.23}$$

According to equation 2.16, at a maximum of 3 to 6 generations already 70% to 90% of the initial energy of a primary proton would be transferred to the electromagnetic component of an air shower. Therefore, the depth of the shower maximum of a hadronic cascade $X_{\max}^{\mathrm{had}}$ can be described, as an approximation, by terms of the depth of the shower maximum of an electromagnetic cascade $X_{\max}^{\mathrm{em}}$. To illustrate this principle, only the first generation of particles is assumed. After a step length $X_{\mathrm{step}}^{\mathrm{had}}$, the energy of each particle is E_0/n_{gen} whereby neutral pions transfer one third of the total energy to the electromagnetic cascade [13]

$$X_{\max}^{\mathrm{had}}(E_0) \sim X_{\mathrm{step}}^{\mathrm{had}} + \lambda_r^{\mathrm{em}}\cdot\ln\left(\frac{1}{3}\frac{E_0}{n_{\mathrm{gen}}}\frac{}{E_c^{\mathrm{em}}}\right) \quad . \tag{2.24}$$

Besides the feeding of the electromagnetic cascade also a muonic component is initiated in a hadron induced air shower. For a simple model, we assume that each charged pion will decay into one muon

[1] The decay length of a particle depends on the air density profile. As for a higher primary energy E_0 the particle is penetrating deeper in the atmosphere, the local air density is reduced at the point where the shower maximum occurs. Consequently, the critical energy $E_c^{\pi,\,\mathrm{air}}$ slightly decreases for increasing E_0. For the Heitler model an average value of 20 GeV is used [13].

(and one neutrino) if its energy is below its critical energy $E_c^{\pi,\,\mathrm{air}}$. Therefore, the *number of muons* N_μ equals the number of charged pions at the maximum of the hadronic cascade $n_{\mathrm{charged}}\big|_{j_{\max}}$

$$N_\mu = n_{\mathrm{charged}}\big|_{j_{\max}} = (n_{\mathrm{charged}})^{j_{\max}} \tag{2.25}$$

$$\Rightarrow \ln(N_\mu) = j_{\max} \cdot \ln(n_{\mathrm{charged}}) \tag{2.26}$$

$$= \frac{\ln(E_0/E_c^\pi)}{\ln(\frac{3}{2}\, n_{\mathrm{charged}})} \cdot \ln(n_{\mathrm{charged}}) \tag{2.27}$$

$$= \beta \cdot \ln(E_0/E_c^\pi) \tag{2.28}$$

$$\Rightarrow N_\mu = \left(\frac{E_0}{E_c^\pi}\right)^\beta \text{ with } \beta \approx 0.85 \quad . \tag{2.29}$$

The primary energy E_0 is shared between the charged pions-driven cascade and the initiated electromagnetic subshowers. The former is represented by N_μ muons, the latter by $N_{\max}$ electromagnetic particles. Similar to equation 2.8, the relative contribution of each particle type is scaled by its respective critical energy. Therefore, the total primary energy E_0 is described by

$$E_0 = E_c^{\pi,\,\mathrm{air}}\, N_\mu + E_c^{\mathrm{em},\,\mathrm{air}}\, N_{\max} \quad . \tag{2.30}$$

So far, the discussed hadron initiating a shower was a proton. A hadronic shower due to a heavier particle with mass number A can be described approximately as a superposition of A independent hadronic showers with $E_0^A = E_0/A$ as the binding energy of the nucleons is small compared to the energy of the primary hadron E_0.
The two important quantities, the number of muons N_μ^A and the depth of the shower maximum $X_{\max}^A$, are then evolving with mass number A

$$N_\mu^A = A \cdot \left(\frac{E_0/A}{E_c^\pi}\right)^\beta = A^{1-\beta} \cdot \left(\frac{E_0}{E_c^\pi}\right)^\beta = A^{1-\beta} \cdot N_\mu^{\mathrm{p}} \tag{2.31}$$

and

$$X_{\max}^A(E_0) \sim X_{\mathrm{step}}^{\mathrm{had}} + \lambda_{\mathrm{r}}^{\mathrm{em}} \cdot \ln\left(\frac{1}{3}\frac{E_0/A}{n_{\mathrm{gen}}}\, E_c^{\mathrm{em}}\right) \tag{2.32}$$

$$\sim X_{\mathrm{step}}^{\mathrm{had}} + \lambda_{\mathrm{r}}^{\mathrm{em}} \cdot \ln\left(\frac{1}{3}\frac{E_0}{n_{\mathrm{gen}}}\, E_c^{\mathrm{em}}\right) - \lambda_{\mathrm{r}}^{\mathrm{em}} \ln(A) \tag{2.33}$$

$$\sim X_{\max}^{\mathrm{had},\,\mathrm{p}} - \lambda_{\mathrm{r}}^{\mathrm{em}} \ln(A) \quad . \tag{2.34}$$

N_μ refers to the number of muons and $X_{\max}^{\mathrm{had},\,\mathrm{p}}$ refers to the depth of the shower maximum of a proton induced shower (cf. equation 2.24). According to this simple model, an iron induced air shower ($A = 56$) should have its shower maximum at about $150\,\mathrm{g\,cm^{-2}}$ higher altitude than the depth of the shower maximum for a proton induced air shower $X_{\max}^{\mathrm{had},\,\mathrm{p}}$. The iron shower is also expected to produce a 1.8 times higher number of muons assuming $N_\mu^{\mathrm{p}} \cdot A^{1-\beta}$ with $\beta \approx 0.85$.
Following the simple ansatz of the Heitler model and extending it to hadronic cascades allows us to describe several important characteristics of hadron induced air showers:

- The depth of the shower maximum of a hadronic cascade $X_{\max}^{\mathrm{had}}$ is mainly driven by the depth of the shower maximum of the electromagnetic cascade.
- For heavier particles the depth of the shower maximum is lowered proportional to $\ln(A)$ in respect to a proton induced air shower.
- The number of muons N_μ depends on the initial energy E_0 and the mass number A of the primary as well as on the particle multiplicity.

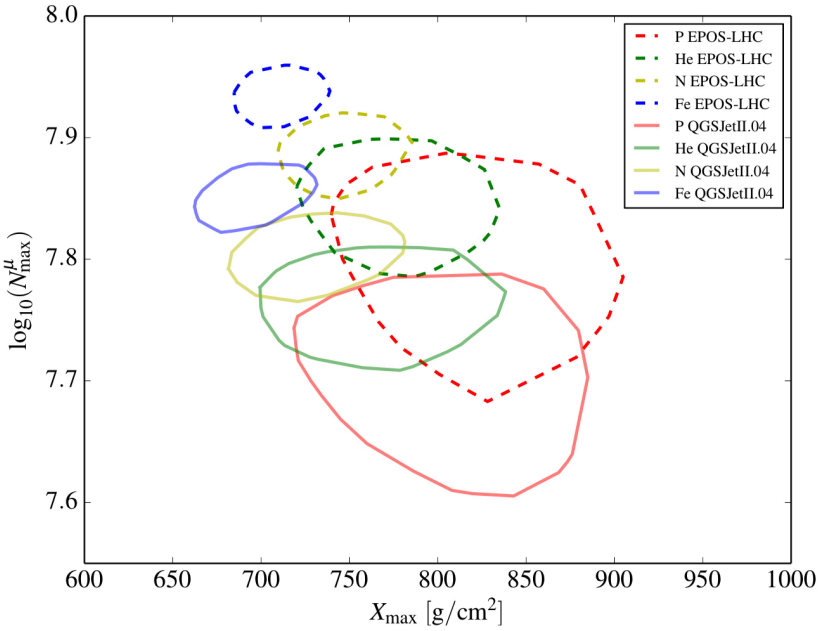

Figure 2.3.: Simulated 1σ contours of the number of muons at maximum of the shower development, $\log_{10} N^{\mu}_{\max}$, vs the depth of shower maximum, $X_{\max}$. The contours correspond to air shower simulations of different primaries, but with a fixed energy, $E = 10^{19}$ eV, and a fixed zenith angle, $\theta = 38°$. Depicted are two different hadronic interaction models EPOS-LHC and QGSJetII.04 (dashed and solid contours, respectively). Figure taken from [16].

Implications for the investigation of the chemical composition

By measuring the total energy E_0 of an air shower in combination with the depth of the shower maximum $X_{\max}$ or the number of muons N_μ as mass-sensitive observables, the atomic mass number A of the cosmic ray particle can be determined in principle. In a realistic experiment as the Pierre Auger Observatory the determination of the particle type is highly limited. As both observables are influenced by the fluctuations in the development of an air shower, the chemical composition studied by means of a single mass-sensitive observable can be only determined on a statistical basis. To emphasize the importance but also the limitations of both quantities, a more detailed view on their discrimination power of the particle type is depicted in figure 2.3. Shown are the predictions for the number of muons and the atmospheric depth of shower maximum based on air shower simulations for a certain energy $E = 10^{19}$ eV and zenith angle $\theta = 38°$ for different primaries and two hadronic interaction models. The predictions are represented by 1σ contours indicating the large fluctuations of the observables in a realistic scenario. Furthermore, the interpretation of the data becomes even more challenging due to the high impact by different hadronic interaction models. However, by a combination of measurements of both observables a determination of the particle type might be possible for a single event [16].
As an example how challenging the interpretation of data and how large the influence of hadronic interaction models might be, the measurement of the muon content of hadron induced air showers by the Pierre Auger Observatory is shown in figure 2.4. The parameter $\langle R_\mu \rangle$ is used as a measure of the muon content in inclined air showers (with zenith angles $\theta = 62° - 80°$) [17]. Comparing the parameter as a function of energy to predictions from air shower simulations hints at a higher muon number in the data, not compatible with predictions by the simulations. Large uncertainties on the hadronic interaction models, on the energy scale and on the determination of the number of muons

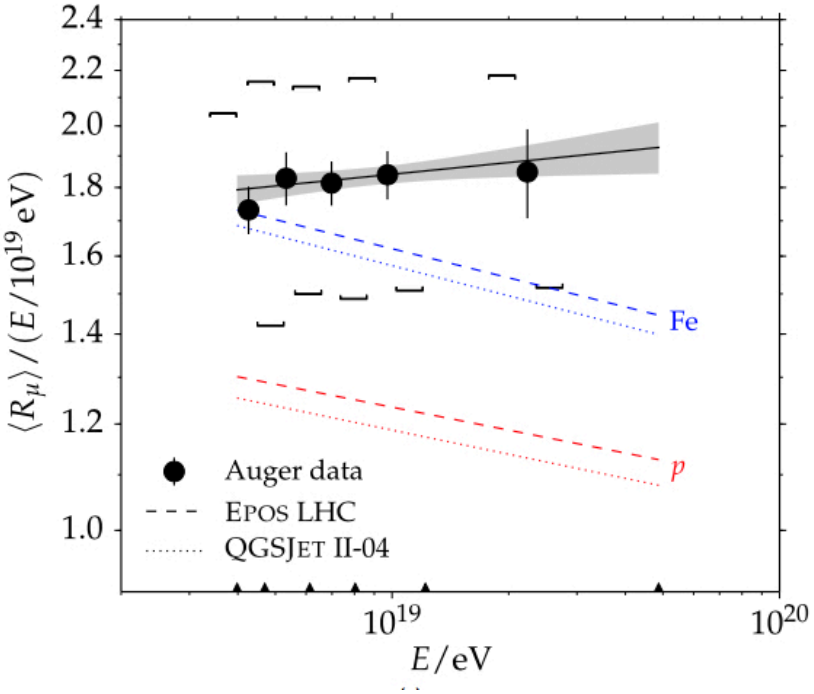

Figure 2.4.: Comparison of the measured average muon content $\langle R_\mu \rangle$ per shower energy E in units of 10^{19} eV as a function of the shower energy E for data of the Pierre Auger Observatory and predictions from air shower simulations. The data are shown with systematic uncertainties (brackets). These comprise the uncertainty on the energy scale of 14%. Predictions for two different hadronic interaction models for two benchmark primaries, proton and iron, are depicted by dashed lines. Figure from [17].

are limiting the significance of these measurements. Therefore, the discrepancy is subject of current studies and e.g. motivation for further improvements on the detection and analysis techniques at the Pierre Auger Observatory (cf. chapter 3.4).

2.2. Energy spectrum and chemical composition

Cosmic rays are covering a wide range of energy, flux and origin, and are therefore studied by many types of experiments. For the low energy range ($E < 10^{14}$ eV), CRs are considered to be of galactic origin and have a flux of several particles per square meter and second [18]. Therefore, balloon and satellite experiments are feasible to study CR particles directly regarding their particle type, energy and arrival direction. Those galactic CRs consist of 79% protons, while helium is building with 21% the dominant part of the remaining heavier particles [11].
Following an energy spectrum with a steep decrease of the flux as a function of energy, measurements with size limited detectors outside or at the edge of the atmosphere become challenging for primary energies $E_0 > 100\,\mathrm{TeV}$ [11]. For higher energy regimes thus ground-based experiments take over. They are based on the detection of secondaries produced while a CR primary particle is entering the Earth's atmosphere and interacts with the air molecules. By these interactions of the primary and those following by its secondary particles a large cascade of particles is developing in the atmosphere towards the ground. The experiments aim to investigate, by means of the detection of those *extensive air showers*, the chemical composition, the energy and the arrival directions of CRs of the highest energies to search for their sources and production mechanisms not known nowa-

days. They cover huge detection areas to compensate for the low fluxes in those energy regimes[2] but they are significantly less precise in the determination of the primary particle type, especially on an event-by-event basis. Therefore, the knowledge about the chemical composition of the CRs at highest energy is limited but is expected to consists of nuclei ranging from protons to iron nuclei [19].

Shown in figure 2.5 (top) is the all-particle spectrum. Depicted is the scaled differential flux $F(E)$ measured by ground-based detector and satellite/ballon-based experiments as a function of the energy per particle. The spectra are shown with statistical uncertainties only, systematics[3] are not included. The differential flux can be calculated by the energy E and the number N of cosmic rays observed by an experiment with a solid angle Ω, a sensitive area A and exposure time t. It follows a steep *broken power law*

$$F(E) = \frac{\mathrm{d}^4 N(E)}{\mathrm{d}E\ \mathrm{d}A\ \mathrm{d}\Omega\ \mathrm{d}t} \propto E^{-\gamma} \quad . \tag{2.35}$$

It decreases with energy with several features visible when a change in the spectral index γ occurs. To pronounce those features the energy spectrum is shown with the flux scaled by $E^{2.6}$ for energies larger than 10 TeV. For much lower energies the flux becomes modulated by solar winds, with a decreasing flux for periods with increasing solar activity [11, 20]. Also the all-particle spectrum measured by the Pierre Auger Observatory scaled by E^3 is shown (cf. figure 2.5 (bottom)). The data can be best described by a fit with a broken power law and a suppression setting in at the highest energies.
The prominent features of the energy spectrum are:

- $E_{\mathrm{knee}} = 10^{15} - 10^{16}\,\mathrm{eV}$: the *knee* with a change in the spectral index from $\gamma = 2.7$ to $\gamma \sim 3$.
- $E_{\mathrm{2nd\ knee}} = 8 \cdot 10^{16}\,\mathrm{eV}$: the KASCADE-Grande experiment measured an additional, less prominent feature, the *second knee*, with a second steeping to a spectral index of $\gamma \sim 3.2$ [21].
- $E_{\mathrm{ankle}} = 5 \cdot 10^{18}\,\mathrm{eV}$: flattening of the spectrum at the *ankle* with a change in the spectral index to $\gamma \sim 2.6$.
- $E_{1/2} = 2 \cdot 10^{19}\,\mathrm{eV}$: the *cutoff*. The energy $E_{1/2}$ indicates the energy where the flux has fallen to 50% compared to the flux expected without suppression (cf. figure 2.5 (bottom)).

Both knees are often explained by the natural end of the acceleration capabilities of the galactic sources (for an overview about recent theoretical models for the knee please refer to [23]). This popular explanation would result in an all-particle spectrum composed of a superposition of individual energy spectra of all arriving particle types. Each spectrum would follow the same power law with a common spectral index but would show an individual cutoff energy proportional to its charge Z as heavier particles can be accelerated to higher maximal energies.
The energy of the knee E_{knee} would correspond to the maximum achievable or cutoff energy for protons whereby the energy of the second knee $E_{\mathrm{2nd\ knee}}$ could correspond to the maximum energy for heavier primary particles[4].
Both knees have been studied in detail by the KASCADE-Grande experiment which was located

[2] At the highest energy, above $E \approx 70\,\mathrm{EeV}$, the flux is < 1 particle per km^2 per century.
[3] such as known differences in the energy scale of different experiments
[4] assuming $E_{\mathrm{2nd\ knee}} = Z \cdot E_{\mathrm{proton}} = Z \cdot E_{\mathrm{knee}}$ with Z up to ~ 25

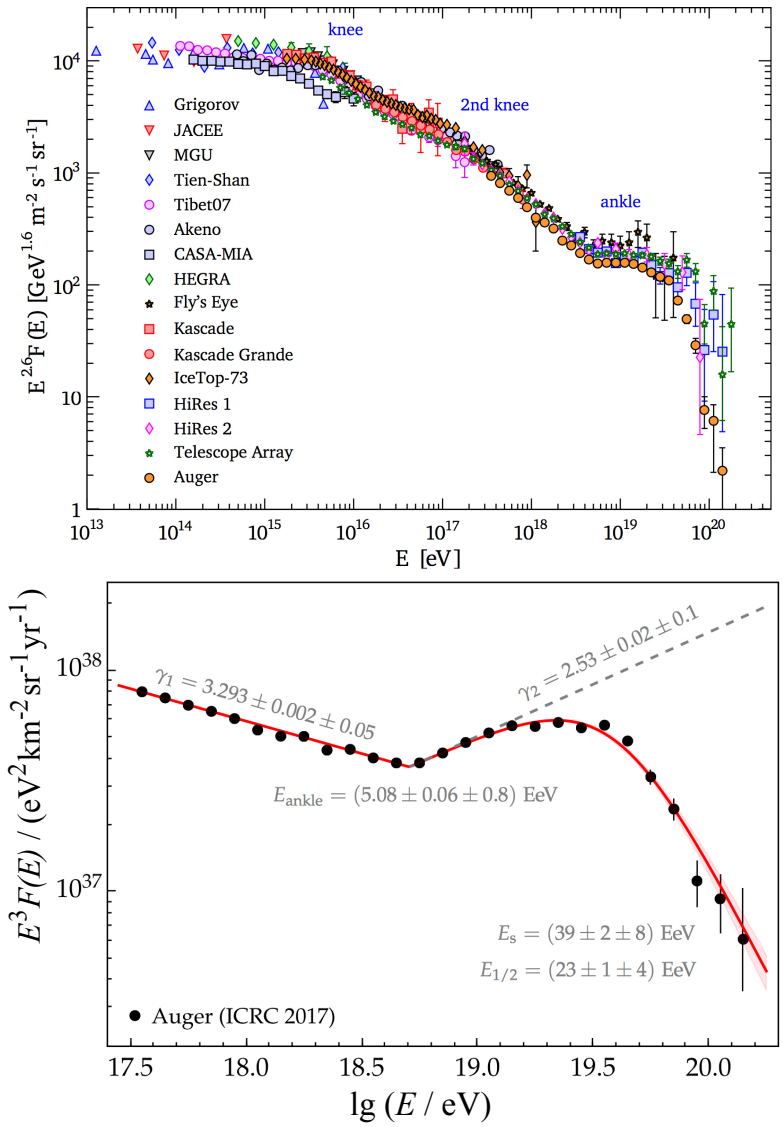

Figure 2.5.: Combined all particle energy spectrum obtained from indirect measurements of air showers. Spectrum is scaled by $E^{2.6}$ to pronounce breaks in the power law. Figure from [11] (top). Energy spectrum for the highest energy of the Pierre Auger Observatory scaled by E^3 (bottom). Figure from [22]. The data can be best described by a fit with a broken power law and a suppression. The dashed line extrapolates the broken power law function without suppression. The spectral indices and energies resulting from the fit for both features, the ankle and the suppression, are shown including their statistical and systematic uncertainties.

in Karlsruhe, Germany. It was explicitly designed to investigate the region between the knee and the ankle by studying the energy spectra of elemental groups (light - medium - heavy). The data support a fading of the light component around the knee and a knee-like feature in the heavy component around the second knee [21, 24, 25, 26].

If the galactic accelerators are fading out, most particles with energies larger than the energies of the knees have to be of extragalactic origin. Therefore, the ankle is often considered as transition region from galactic to extragalactic sources. The chemical composition of the ankle is indicated to be mixed as measured by the Pierre Auger Observatory (cf. figure 2.6 which will be discussed later).

The studies concluded a non-negligible contribution of medium or heavier particle masses (nuclei with $A > 4$), highly constraining theoretical source models [27]. After the ankle, a suppression of the cosmic ray flux at the highest energies has been reported by several experiments. However, the two largest experiments for UHECRs, the Pierre Auger Observatory and the Telescope Array [28] located at the southern and northern hemisphere, respectively, state different energies $E_{1/2}$.
There are two popular explanations for the suppression also constraining requirements on the characteristics of the sources (for a more detailed overview please refer to [5, 29, 30]). First, the maximum energy for the acceleration of cosmic rays by extragalactic sources is reached comparable to the expiration of the galactic sources in the region of the knee. Second, the suppression is the result of propagation effects along their way from source to Earth. Interactions of protons with photons of the cosmic microwave background (CMB), called the GZK effect [31, 32], predict a cutoff at $E_{\mathrm{GZK,\,p}} \sim 6 \cdot 10^{19}$ eV with the most likely interaction processes via the Δ^+-resonance:

$$\begin{aligned} p + \gamma_{\mathrm{CMB}} &\to \Delta^+ \to p + \pi^0 \\ &\qquad (\hookrightarrow \gamma + \gamma) \\ p + \gamma_{\mathrm{CMB}} &\to \Delta^+ \to n + \pi^+ \\ &\qquad (\hookrightarrow \mu^+ + \nu_\mu \to e^+ + \nu_e + \bar{\nu}_\mu) \\ &\qquad (\hookrightarrow p + e^- + \bar{\nu}_e) \qquad . \end{aligned}$$

As the protons lose energy due to these processes also reducing their average propagation length, the detection of protons with higher energies becomes unlikely. Detected protons with energies above $\sim 10^{20}$ eV have to be from nearby sources (within a radius $\lesssim 100$ Mpc).
Heavier cosmic ray nuclei show a similar energy loss behavior but lose energy via photo-disintegration

$$\text{example process} = X_A^Z + \gamma \to X_{A-1}^{Z-1} + p \tag{2.36}$$

also resulting in a maximum propagation distance for heavier nuclei with ultra-high energy.

Several implications arise from those propagation effects. The GZK effect of protons would be accompanied by a large number of high-energetic GZK photons and neutrinos which have not been found so far giving already constraints on the basic theoretical predictions [22]. Furthermore, a limited propagation distance would result in anisotropies in the arrival directions of cosmic rays as the distribution of matter is not isotropic in the nearby universe. Potential sources and acceleration mechanisms are discussed in the following section 2.3.

The origin of the suppression may be revealed by improving the determination of the chemical composition of cosmic rays at the highest energies. A model concerning photo-disintegration as the dominant mechanism e.g. would have a much larger fraction of light nuclei at the highest energies as those could be fragments of heavier particles [16].
Nowadays, ground-based arrays mostly study the important mass-sensitive observable X_{max} (which is the atmospheric depth at which an air shower contains the maximum number of particles, cf. equation 2.14) by fluorescence telescopes. They observe the full shower development in the atmosphere allowing a reconstruction of the type of primary. As the duty cycle of the fluorescence detector is limited and the flux at the highest energies is low, a mass-sensitive study is not possible in the region of interest ($E \geq 10^{19.4}$ eV) [16]. Also a determination of X_{max} by a surface detector array is possible but depends on a cross-calibration with a fluorescence detector. Furthermore, the development of hadronic air showers is subject to fluctuations, so that only the determination of an average quantity $\langle X_{\mathrm{max}} \rangle \propto \lg(E/A)$ for many events of the same shower energy is possible, but challenging to be interpreted.

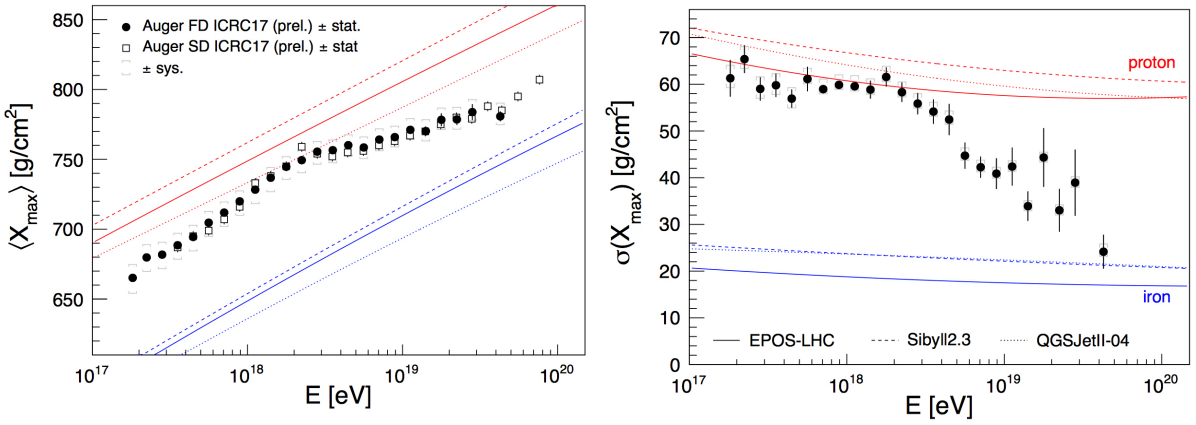

Figure 2.6.: Measurements of the Pierre Auger Observatory of $\langle X_{\mathrm{max}} \rangle$ (left) and $\sigma(X_{\mathrm{max}})$ (right) as a function of reconstructed energy. For comparison predictions of proton- and iron induced air shower simulations for three different hadronic interaction models are depicted. [22]

The Pierre Auger Observatory reported the average $\langle X_{\mathrm{max}} \rangle$ as a function of the reconstructed energy of the primary particle (cf. figure 2.6, left). The lines indicate predictions of air shower simulations for two benchmark scenarios, proton and iron as primaries, and for different hadronic interaction models having a high impact on the interpretation of the data. The evolution of data indicates first a transition to a lighter component up to a break around $10^{18.3}$ eV while after the break the composition shows a trend back to heavier nuclei. In addition, the standard deviation $\sigma(X_{\mathrm{max}})$ is shown (cf. figure 2.6, right). A large value of $\sigma(X_{\mathrm{max}})$, as seen in the lower energy regions, may indicate a dominant light component or a strongly mixed composition. For higher energies again a trend to a heavier component becomes visible.

However, as already stated, an improved determination of the chemical composition could severely constrain theoretical models of the suppression. Enhancements on the determination of the chemical composition are thus on-going at the Pierre Auger Observatory for example by using radio detector arrays (cf. the radio detector array AERA in chapter 3.3.1) or the investigation of the same showers by several detection techniques in one surface array aiming to disentangle the electromagnetic and muonic component of air showers (cf. the AugerPrime upgrade in chapter 3.4).

2.3. Acceleration mechanisms and potential sources

Cosmic rays are most likely to be accelerated in a non-thermal process, as indicated by the power law shape of the energy spectrum (cf. figure 2.5 (top)). One acceleration method in favor providing such an energy spectrum is the stochastic acceleration by scattering of confined particles in magnetized clouds or shocks. It allows a general idea about how particles can be accelerated. Furthermore, it introduces important requirements on possible sources, although the actual injection and acceleration processes remain unknown.
The method was first proposed by Enrico Fermi and is called, subsequently, Fermi acceleration [33]. Two models are derived from his ansatz. According to the *second order Fermi mechanism*, a particle can gain or lose energy by means of collisions with non-relativistic moving clouds depending on its orientation to the cloud. The processes, in which the particle gains energy, the 'head-on' interactions, occur more frequently leading to a slow but steady acceleration of the particle. Characteristics

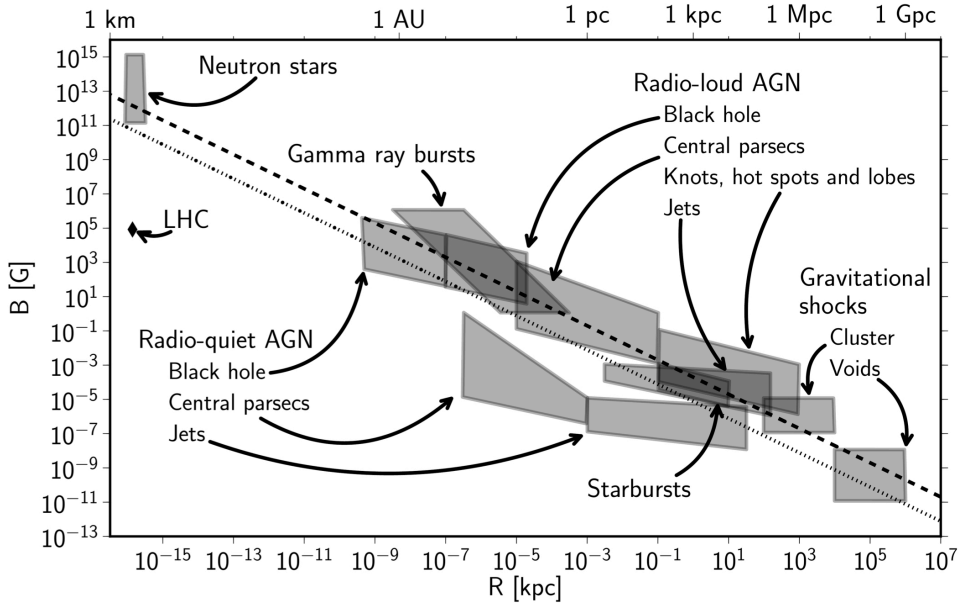

Figure 2.7.: Updated Hillas diagram. The parameter space of the magnetic field strength B and the size R of the acceleration region of potential UHECR sources are shown. The shaded areas indicate the uncertainties on these parameters for each source class. The dashed (dotted) line refers to the requirements for an acceleration of proton (iron) nuclei up to energies of 10^{20} eV (for $\beta = 1$). The Earth-based accelerator LHC at CERN is depicted as comparison. Figure from [34].

of the considered astrophysical scenario, here the speed of the cloud β_{cloud} in units of the speed of light c, defines thereby the average energy gain $\Delta E/E \propto \beta^2_{\text{cloud}}$ referring also to the 'efficiency' of the accelerator. However, this mechanism is not powerful enough to allow accelerations of cosmic rays to the highest energies because $\beta_{\text{cloud}} \ll 1$. The diffusive shock acceleration or *first order Fermi mechanism* allows a more efficient method to accelerate particles via shocks as e.g. observed in supernova remnants. A shock can be understood as a wave propagating through the surrounding plasma with velocity β_{shock} in units of c. If the wave has a velocity larger than the velocity of sound, information on the propagating wave is not transferred to the material in front of the shock until the wave has arrived. Therefore, two regions exist, a 'shocked' and an 'un-shocked' region forming a shock front in between. A particle crossing this shock front will be diffusely reflected by the present magnetic field inhomogeneities after each crossing. As the directions of the scattering centers is predominantly randomly distributed, the particle will see for all crossing orientations plasma moving towards it. So for each crossing the particle is accelerated and the average energy gain results in $\Delta E/E \propto \beta_{\text{shock}}$. At each cycle of crossings from shocked to un-shocked region and vice versa, the particle has a chance to escape the acceleration region. Particles remaining longer periods in the region will be the particles carrying the most energy. The need of a long confinement of the particles gives rise to several requirements on the condition of potential sources and results in a power law distribution of particle energies [35].
The maximum of the particle energy gained during the confinement in a source can be expressed by the *Hillas criterion*. It constraints important geometrical characteristics of the source regions and is in principle not only valid for stochastic acceleration models, but also for alternative hypotheses as the *one shot acceleration* not presented in this thesis (for more information on this method please refer to [35]). The Hillas criterion is defined as

$$\left(\frac{E_{\max}}{1\,\text{EeV}}\right) = 2 \cdot 1.08 \cdot Z \cdot \beta \left(\frac{B}{1\,\mu\text{G}}\right)\left(\frac{R}{1\,\text{kpc}}\right) \quad , \tag{2.37}$$

whereby β is a dimensionless factor and E_{max} is the maximum energy a particle with charge Z can reach if confined in a source with size R of the region the acceleration takes place and with a magnetic field strength B. For the stochastic acceleration mechanism, β corresponds to the velocity of the shock front β_{shock} in units of c. Given the Hillas criterion, the acceleration of cosmic rays is challenging as visualized in figure 2.7. Different potential source classes are depicted ranging over many magnitudes of magnetic field strength B and size of the accelerating region R. Also shown are the requirements for the acceleration of two particle types, proton and iron, as indicated by equation 2.37. They depict the lower limit for an accelerator producing a nucleus of an energy of 10^{20} eV with $\beta = 1$ corresponding to a highly efficient accelerator.
Two of the promising source candidates for UHECRs shown in the Hillas diagram are active galactic nuclei (AGN) and starburst galaxies. In reference [22], the Pierre Auger Observatory reported on directional correlations of high energy cosmic ray events with flux models based on source catalogues of gamma-ray AGNs detected by Fermi-LAT [36, 37] and of nearby starburst galaxies. The investigations yield mild indications of a possible correlation between data and both source candidates whereby the post-trial significance for a deviation from isotropy is enhanced for the studied starburst galaxies. For both analyses the position of the potential sources are smeared by an angle of 7° and 13° for the AGNs and the starburst galaxies, respectively. Also a scan of the energy has been performed. The signal is maximized at ~ 39 EeV for the studied starburst galaxies and ~ 60 EeV for the studied AGNs. In figure 2.8, skymaps of the event excess for both searches (left AGN, right starburst galaxies) in galactic coordinates are shown allowing a comparison of the observed data (top) and the source catalogues (bottom). Highlighted are important source candidates such as the strongest AGN source Centaurus A or the bright starburst galaxies NGC 4945 and M83. Also indicated is the corresponding smearing angle at the right bottom corner at each skymap. In addition to a directional search of correlation with candidate catalogues on a small angular scale, large-scale anisotropies are of particular interest to understand the origin of UHECRs. It combines two important quantities, the distribution of sources and propagation effects. For example, source candidates, which have too low fluxes to be studied by small angular directional searches, may be identified by their combined flux distribution. The Pierre Auger Observatory reported a significant large-scale anisotropy for cosmic ray events with energies $E \geq 8$ EeV [38, 39] indicating a dipole with a reconstructed position of

$$(\alpha, \delta) = ((95 \pm 13)^\circ, (-39 \pm 13)^\circ) \tag{2.38}$$

in declination δ and right-ascension α (cf. figure 2.9). The direction is about 125° from the Galactic Center hinting at an extragalactic origin. The large-scale anisotropy has been confirmed by several analysis methods. However, the origin of the dipole is still subject of speculations. For a further study, the knowledge about the chemical composition of the arriving particles on an event-by-event basis and about the magnetic fields seen by the particles along their way has to be improved. As charged, they are deflected in the extragalactic but also the galactic magnetic field. The extragalactic magnetic field is poorly understood, for the galactic field recent models[5] aim to describe its structure and strength. The understanding of the magnetic fields is thus strongly entangled with all open questions in the research field of UHECRs. For example, the chemical composition influences highly the deflection of the primary particles in the magnetic field obscuring the position of sources making the interpretation of the arrival directions challenging. This is also visible in figure 2.9. Aiming to bring the position of a dipole seen by a study of the matter distribution according to the 2MASS Redshift Survey (2MRS) catalogue and the position of the dipole seen by the study of UHECRs into agreement, a modification of the particle arrival directions according to the chemical composition of cosmic rays and to magnetic field models would have to be implemented.

[5] as the JF12 model [40]

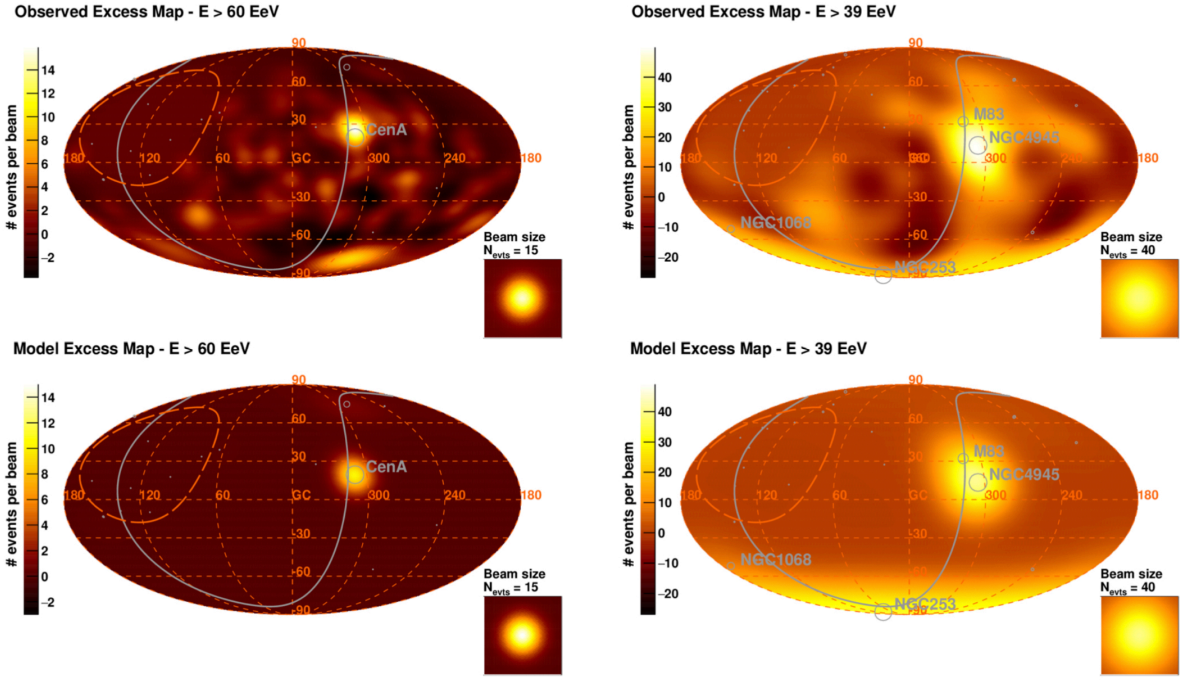

Figure 2.8.: Skymaps in galactic coordinates of the event excess with respect to isotropy for observed data of the Pierre Auger Observatory (top) and for flux models based on catalogues (bottom). Studied are two possible source class candidates, active galactic nuclei (left, including 17 bright nearby AGNs for the flux model) and starburst galaxies (right, including 23 bright, nearby starburst galaxies for the flux model). Indicated are the supergalactic plane as a grey, solid line and the limit of the field of view of the experiment as red, dashed line. The corresponding smearing angle can be estimated by the beam size on the lower, right side of each skymap for a particular number of events N_{evts}. Figure from [22].

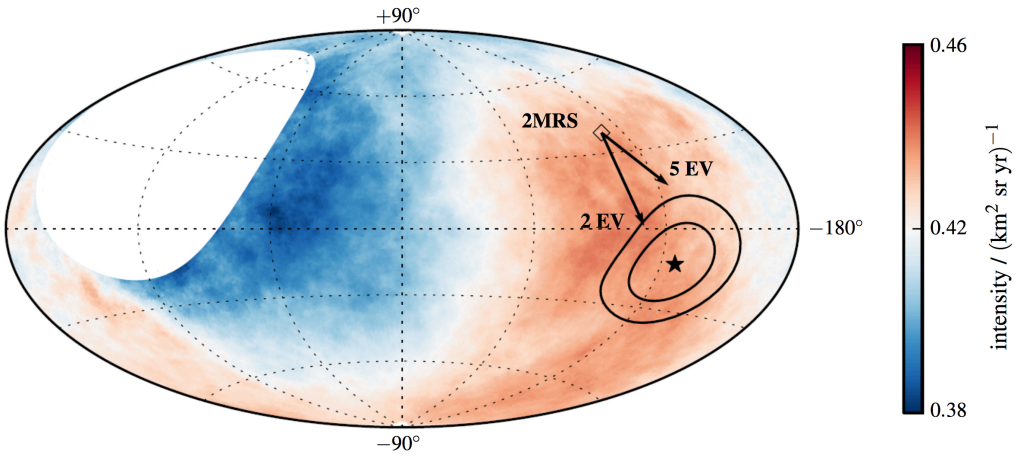

Figure 2.9.: Skymap in galactic coordinates of the intensity of events with an energy of $E \geq 8\,\text{EeV}$ detected at the Pierre Auger Observatory. The intensity map has been smoothed by 45°. It depicts a large-scale anisotropy preferentially explained by a dipole structure. The reconstructed position of the dipole is indicated by a star. The direction of another dipole indicated by the distribution of galaxies from the 2MRS catalogue is depicted by an open diamond. Arrows starting at the diamond indicate the change in the dipole position if deflections by magnetic fields for two exemplary rigidities (2 EV and 5 EV) are taking into account. Figure from [41].

CHAPTER 3

The Pierre Auger Observatory

The *Pierre Auger Observatory* [7] is a high precision experiment located in the flat semidesert area Pampa Amarilla, Argentina, nearby the city of Malargüe. It studies the properties of *ultra-high-energy cosmic rays* (UHECRs, $E \geq 10^{18}$ eV) by means of *extensive air showers* which UHECRs initiate while interacting with air molecules. As these cosmic ray particles are very rare, a huge area has to be equipped with detectors. The baseline design of the observatory consists of the *surface detector* (SD) array with ~ 1660 *water Cherenkov detector* (WCD) stations covering 3000 km^2 of the Pampa and of the *fluorescence detector* (FD) with 27 large reflecting telescopes at five sites located at the border of the array observing the atmosphere above the SD. A layout of the observatory is shown in figure 3.1. The fluorescence detector observes the longitudinal development of the air shower and is able to accurately determine the energy deposit. As the *fluorescence light* is faint with respect to the *night-sky background*[1], the operation of the telescopes is only possible in clear, moon- and cloudless nights inducing a duty cycle of approximately 15% [7]. The surface detector measures with a duty cycle of almost 100% the lateral development of the air shower, thus the density of secondary particles on the ground. It provides an excellent angular resolution of 1.6° for events recorded by more than three stations improving to 0.9° for events recorded by more than five stations [42]. The basic detection principle and event reconstruction of both detectors are explained in the following sections. An FD building and a WCD station are shown in figure 3.2.

Combining those two complementary detection techniques is the key element of the experiment. It allows an improved reconstruction of the air shower geometry, particle distribution and energy of the shower and thus to draw conclusions on characteristics of the primary particle of interest. An example event measured simultaneously by both detection methods is shown in figure 3.3.

The construction of the observatory started in 2004 and it became fully operational in 2008. The experiment is well calibrated and understood, which makes it a perfect facility to study further detection techniques using improved electronics or light sensors [43]. Few of those have been, or will be, installed as a large-scale upgrade of the standard design and are introduced in sections 3.3 and 3.4. The Argentinian Pampa was chosen as it offers a large plateau at an average height of 1400 m a.s.l. corresponding to an atmospheric overburden of 875 g/cm^2 for the location of the SD array. Furthermore, the weather conditions are suitable for the detection of the faint fluorescence

[1] as light from the moon and stars or artificial light sources

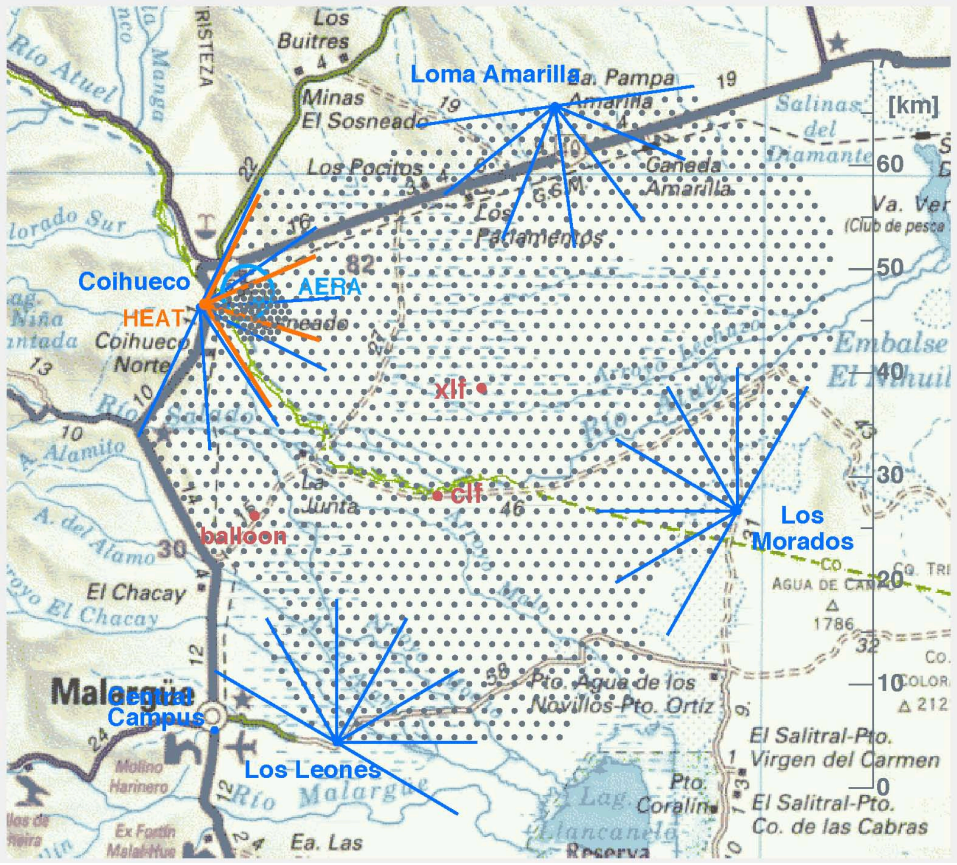

Figure 3.1.: Layout of the Pierre Auger Observatory located in the Pampa Amarilla near the city of Malargüe. Each dot represents a water Cherenkov station placed on a hexagonal grid with the spacing of 1.5 km. Straight lines denote the azimuthal field of view of the fluorescence telescopes overlooking the atmosphere over the surface detector array. The three telescopes of the low-energy extension HEAT, located near the standard site Coihueco, are denoted by the orange straight lines. The location of the two laser facilities (CLF [44] and XLF [45]) monitoring the aerosol content in the atmosphere are indicated with red dots. Additionally, further extensions of the experiment are shown: The Infill array and the radio detector AERA. The Infill array is nested in the standard SD array providing additional water Cherenkov stations with a smaller distances to each other. Both extensions are located in the field of view of the FD sites Coihueco and HEAT. Original courtesy of D. Veberič.

light. It rains rarely, the atmosphere is clear and the light pollution by civilization is manageable. However, the monitoring of the atmospheric conditions is crucial for the calorimetric measurement of the fluorescence technique [46, 47]. Therefore, several monitoring devices are installed in the array studying atmospheric parameters [48] as humidity, pressure or aerosol contamination [44, 45] and also cloud coverage [49, 50]. All these parameters change the mass traversed by an air shower, as well as the amount of emitted photons along the shower development [51].
One of those monitoring devises is a LIDAR located next to each FD telescope [52, 53]. It consists of a pulsed UV laser shooting regularly into the atmosphere above the telescope and in special cases also in the telescope field of view. By studying the structure of the back-scattered light, clouds and large amounts of aerosol can be identified.

(a) Fluorescence telescope building (Los Morados). Each building contains six telescopes and is accompanied by a tall communication antenna.

(b) A water Cherenkov station of the surface detector array with a communication antenna in the background.

Figure 3.2.: Overview photos of both detectors composing the baseline design of the Pierre Auger Observatory. Photo courtesy of S. Saffi.

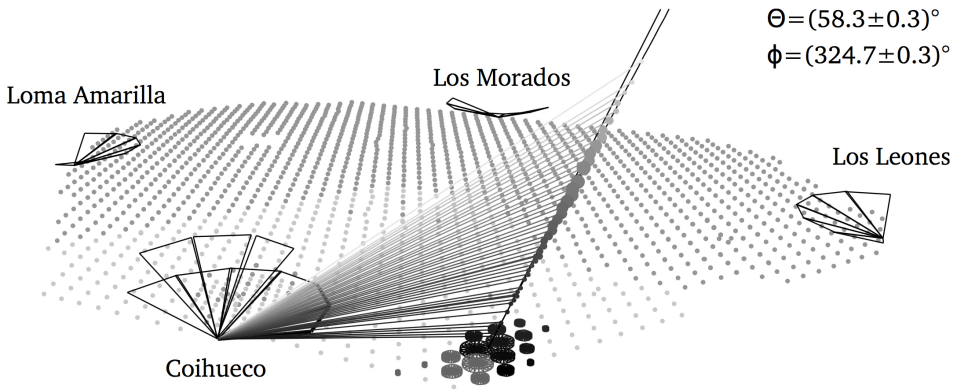

Figure 3.3.: Schematic of a reconstructed air shower event measured with the Pierre Auger Observatory. The event (Event 15346477) has been detected simultaneously with the SD array and a fluorescence telescope at Coihueco. The amount of signal seen by the WCD stations on the ground are denoted by the size of the marked stations in a logarithmic scale. The amount of signal during the shower development seen by the FD are marked as dots of different sizes in a logarithmic scale. The direction of the photons reaching the telescope is indicated by shaded lines with light lines denoting photons from the beginning of the shower and dark lines representing photons from a late state of the shower development. Both detector techniques reconstruct a shower axis seen as two downward-going solid lines. An energy of $E = (2.49 \pm 0.16) \cdot 10^{19}\,\mathrm{eV}$ has been reconstructed by the FD. Figure from [54], original from [19].

3.1. Surface detector

The surface detector array consists of $\sim$ 1660 water Cherenkov stations in a hexagonal grid [55]. The stations are separated from each other by 1500 m optimized for the energy range of interest. Each station is a light-tight cylinder with a surface area of 10 m^2, a height of 1.2 m and it is filled with 12 tons of highly purified water. The station is equipped with a solar panel and a battery allowing it to be operated autonomously. The data provided by the readout electronics are sent via a communication antenna which also handles trigger requests. Also a GPS receiver needed for the time synchronization of the stations is installed. An overview of the main components of a water Cherenkov station is depicted in figure 3.4. The lateral particle distribution, i.e. the footprint of the shower on the ground, is measured by the SD array. The full shower detection efficiency is reached for energies above $3 \cdot 10^{18}$ eV for zenith angles $\theta < 60^\circ$ [56] and above $4 \cdot 10^{18}$ eV for zenith angles $60^\circ < \theta < 80^\circ$.

If a charged, high energetic particle is traversing the water contained in a station, it produces Cherenkov light along its way. Due to its height, the station is also sensitive to photons if they convert to an electron-positron pair. The emitted light is reflected at the diffuse reflective surface of the sealed liner located in the interior of the station. The light is detected by three 9" inch PMTs located at the top of the liner looking downwards into the water through transparent windows. The PMTs are mounted at a distance of 1.2 m next to each other. The produced signal of the PMTs is then guided to the electronics. The electronics provide two amplifications, the high gain with an amplification of 32x of the last dynode signal and the low gain with the AC coupled anode signal. For both channels the analogue signal is filtered and digitized by two 10 bit 40 MHz semi-flash ADCs. The output is for both a trace of ADC count as a function of time. These signals in ADC count have to be translated into a universal signal unit valid for all detector station systems consisting of water Cherenkov station, PMTs and electronics. The chosen universal unit is VEM (Vertical-equivalent muon). It refers to the signal produced by a muon traversing the station with a vertical trajectory.

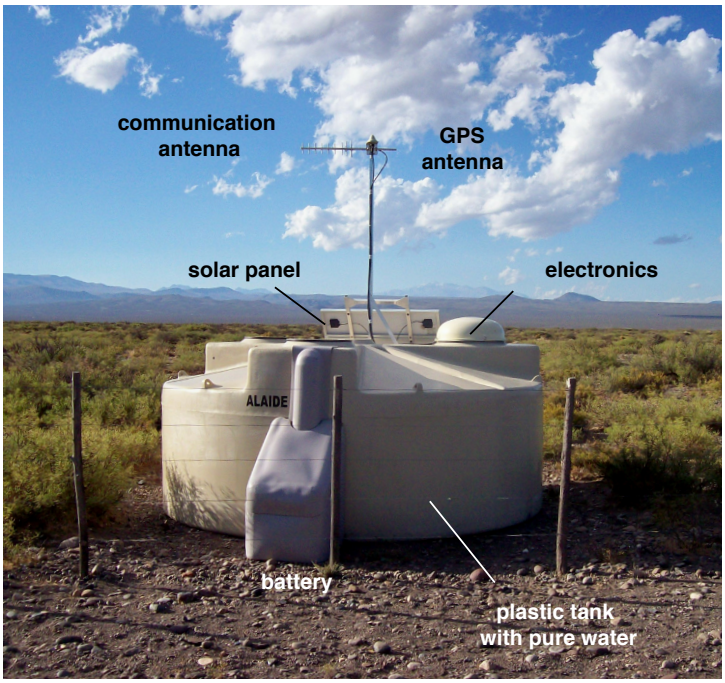

Figure 3.4.: A photo of the water Cherenkov station. Indicated are its main outside component. Inside, three PMTs are detecting the Cherenkov light produced by charged particles traversing the ultra-purified water contained in the station. Adapted from [55].

The trace is integrated, resulting into a signal S in VEM for each WCD station.
An air shower signal detected by the WCD stations ranges from few photoelectrons in stations very far from the shower core to hundreds of thousands photoelectrons in stations closer to the core. For the actual electronics the dynamic range is limited for stations close to the shower core as the Cherenkov signal produced by the air shower particles saturates the electronics. The dynamic range will improve with the on-going upgrade *AugerPrime* (cf. section 3.4 and [57]).

3.1.1. Event reconstruction

Several triggers are available and each of them is optimized for certain shower geometries and energies. For a detailed review about trigger modes, electronics and signal handling of the SD array please refer to [56] and [55]. A trigger on air showers requires a time and spatial coincidence of multiple SD stations, but also a trigger by the fluorescence detector can be received. All PMTs are read out for a triggered station. The signals as a function of time of multiple SD stations determine the arrival direction of the shower. The position of the region with highest particle density, the *core*, and the amount of energy, which can be measured by the SD stations, is highly influenced by the incident angle θ as the amount of traversed matter scales with $\sim 1/\cos\theta$. For high incident angles $\theta > 60^\circ$, so for *horizontal showers*, the electromagnetic component is strongly absorbed compared to the muonic component. The latter thus dominates the WCD signal in this angular range. Therefore, the reconstruction method for horizontal showers has to be adapted to compensate these influences. In this thesis only the reconstruction of vertical showers is introduced, for horizontal showers please refer to [58].

The lateral development of the shower can be modeled and fitted by an NKG-like *Lateral Distribution Function* (LDF) [59, 60]. The integrated signal S in VEM seen by stations at a distance r are given by

$$S(r) = S(r_{\text{opt}}) \cdot f_{\text{LDF}}(r) \tag{3.1}$$

$$= S(r_{\text{opt}}) \cdot \left(\frac{r}{r_{\text{opt}}}\right)^{\beta} \cdot \left(\frac{r + r_1}{r_{\text{opt}} + r_1}\right)^{\beta+\gamma} \tag{3.2}$$

with β and γ as free slope parameters. The distance r_1 allows for a more accurate description of stations far away from the shower core which is needed as different shower components dominate along the shower footprint. $S(r_{\text{opt}})$ is referring to the shower size and is determined for a characteristic distance r_{opt}. The accuracy of these LDF parameters is highly limited by experimental uncertainties. Therefore, it is necessary to define the optimum core distance r_{opt}, that depends solely on the detector array geometry. At this distance, the variation in the predicted signal as a function of the zenith angle, the shower energy and the form of LDF is minimized [61]. The predicted signal can be used as an energy estimator. For the standard SD array of the Pierre Auger Observatory this optimum distance is 1000 m defining the shower size parameter $S(r_{\text{opt}}) = S_{1000}$ [62, 63]. For r_1, 700 m has been found as the best description for the measured data.
The modified LDF for the regular SD array can be translated to

$$S(r) = S_{1000} \cdot \left(\frac{r}{1000\,\text{m}}\right)^{\beta} \cdot \left(\frac{r + 700\,\text{m}}{1700\,\text{m}}\right)^{\beta+\gamma} \quad . \tag{3.3}$$

An example LDF for the regular SD array is depicted in figure 3.5. The fit on the data includes also non-triggered stations (working stations with a signal below the threshold value) and saturated stations (stations whose signal is greater than the dynamic range of the FADC). The shower size parameter $S_{1000}(E, \theta)$ is still zenith-angle-dependent as the corresponding different amount

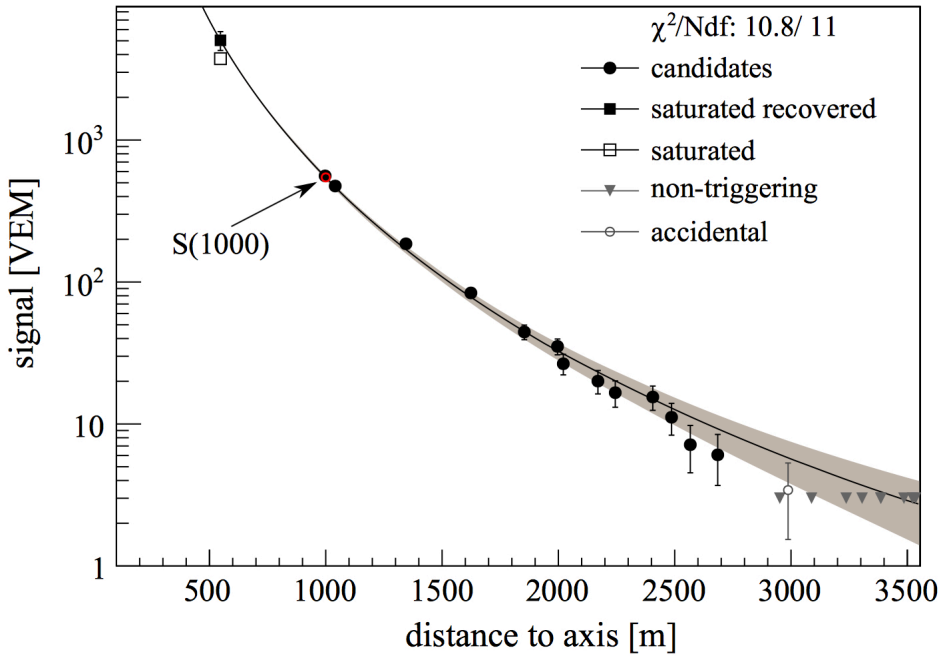

Figure 3.5.: Lateral distribution function. Shown is the dependence of the signal size in VEM on the distance to the shower core from an event detected by the regular surface detector array of the Pierre Auger Observatory. Included are triggered and non-triggered station. Also indicated is the energy estimator S_{1000}. Figure from [7].

of traversed matter influences the energy content measured by the SD array. For example, an air shower with zenith angle of 60 ° will traverse nearly twice the amount of the atmosphere as a vertical shower. It is therefore necessary to define a reference zenith angle to relate the measurement of $S_{1000}(E,\theta)$ to a zenith angle independent quantity. The median of the zenith angle distribution $\theta_{\text{ref}} \equiv 38\,^\circ$ is chosen as the reference angle. The energy estimator $S_{38}(E)$ is thus defined as the signal expected at 1000 m distant from the shower axis for a shower arriving with a zenith angle of 38 ° [64]

$$S_{38}(E) \equiv \frac{S_{1000}(E,\theta)}{\text{CIC}_{1000}(\theta)} \quad , \tag{3.4}$$

whereby the conversion function $\text{CIC}_{1000}(\theta)$ describes the attenuation of the air shower particles in the atmosphere. It is calculated via the CIC (Constant Intensity Cut) method [65, 66]. This mathematical approach is based on an isotropic distribution of arrival directions at the top of Earth's atmosphere. The method is assumed to be independent of the energy of the cosmic rays in the energy range of interest resulting in the following description of the attenuation curve for the SD array [7]

$$\begin{aligned} \text{CIC}_{1000}(\theta) &= 1 + a \cdot x + b \cdot x^2 + c \cdot x^3 \\ x &= \cos^2(\theta) - \cos^2(38\,^\circ) \\ a &= (0.980 \pm 0.004) \\ b &= (-1.68 \pm 0.01) \\ c &= (-1.30 \pm 0.45) \quad . \end{aligned}$$

The energy estimator S_{38} for the surface detector array can be calibrated by events measured simultaneously by the fluorescence detector. The FD provides the calorimetric energy of an air shower, E_{FD}. The relation between both observables can be described by a single power-law function, $E_{\mathrm{FD}} = A\, S_{38}^{B}$ with the fit results yielding $A \approx 1.90 \cdot 10^{17}$ eV and $B \approx 1.03$ [7, 67, 68]. The relation can be used as calibration of the SD measured energy by the energy of the fluorescence detector.

3.2. Fluorescence detector

The detection of fluorescence light is the most sensitive detection techniques to study the longitudinal profile of extensive air showers. The FD detector consists of 27 reflecting telescopes located at five sites at the border of the SD array [70]. The standard sites are Los Leones, Loma Amarilla, Los Morados and Coihueco with an additional site *HEAT* (High Elevation Auger Telescopes [69, 71]). At each standard site six telescopes are located in one building which provides clean, climate-controlled and light-tight rooms if the shutters are closed. The shutters are closed during daytime and are only opened if the ambient light flux is low enough to avoid any harm on the light sensors of the telescopes. Each telescope has a field of view (FoV) of $30^\circ \times 30^\circ$ in azimuth and elevation, so that six telescopes of one standard site observe 180° in azimuth. The standard fluorescence detector is designed to allow for each event, with energies above 10^{19} eV crossing the atmosphere above the SD array, a detection by at least one telescope [68]. The uncertainty on the energy scale is $\sim 12\%$ at 10^{19} eV increasing to 16% at an energy of 10^{18} eV [67]. The uncertainty is mostly driven by systematic uncertainties of the fluorescence light production, the FD telescope calibration and the shower profile reconstruction. For comparison the statistical FD energy resolution is $\sim 7.6\%$ [7]. The additional site HEAT has three telescopes. They are similar to the design of a standard telescope, but each has its own housing. The housing is tiltable upwards by 29° in elevation, which is used during data taking. As lower energy cosmic rays have a fainter light production and thus lower X_{max} in the atmosphere, an elevated FoV increases the efficiency for the corresponding energy regime. Thus, HEAT provides a low-energy extension of the standard fluorescence detectors. As HEAT is directly located at the standard site Coihueco, also a combined detection of air showers with a large FoV is possible. An example for an event measured by HEAT and Coihueco simultaneously is depicted in figure 3.6a, while in figure 3.6b a photo of the three housings tilted upwards is shown.

As already explained in chapter 2.1, electrons and positrons of an extensive air shower excite the nitrogen molecules[2] on their way through the atmosphere. De-excitation fluorescence light is isotropically emitted in the ultraviolet wavelength regime with peak wavelengths at $\lambda = 337\,\mathrm{nm}$ and 357 nm [73]. The amount of photons emitted is thereby, as a first approximation, proportional to the total energy deposit in the atmosphere [74], enabling the reconstruction of the longitudinal profile of the shower [72, 75, 76]. The photons reaching the aperture of the telescope will enter through a circular diaphragm with a diameter of 1.1 m. The diaphragm is covered by a UV pass-filter reducing photons with wavelengths not in the fluorescence wavelengths regime. The optical design of the reflective telescopes is based on a Schmidt optic [70]. A sketch of the complete setup is depicted in figure 3.7a, while a picture of an actual telescope at Coihueco is given in figure 3.7b. The incoming light is focused by a segmented $\sim 13\,\mathrm{m}^2$ spherical mirror onto the focal plane. The spherical aberrations introduced by the mirror are reduced by implementing a Schmidt corrector ring [77] in the aperture. This segmented corrector ring also eliminates coma aberration. The cam-

[2] The atmosphere consists mainly of nitrogen $\sim 78\%$, oxygen $\sim 21\%$ and argon $\sim 1\%$. As for oxygen, the transition for most of the excited stated to the ground state is strongly forbidden and furthermore most of the available emission lines have a wavelength larger than 395 nm, they do not contribute to the fluorescence light spectrum important for air shower experiments. [72]

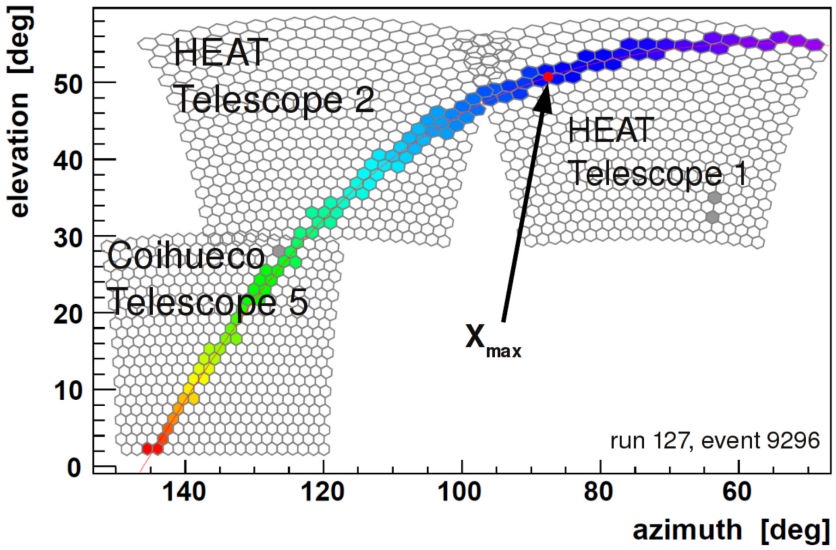

(a) Example of a low-energy event recorded in coincidence with two HEAT telescopes and one Coihueco telescope. The color indicates the time distribution of the signals in the filled pixels (purple = early, red = late).

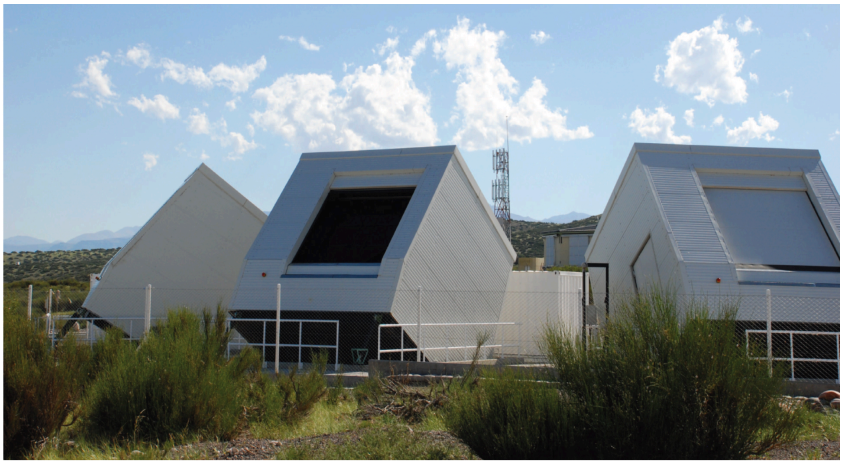

(b) Photo of the three HEAT telescopes in tilted mode. Each telescope has the same layout as the standard FD telescopes but has an own tiltable housing.

Figure 3.6.: The HEAT telescopes of the Pierre Auger Observatory. A low energy extension for the standard fluorescence detector sites, located near the standard site Coihueco. The shower depth maximum X_{max} is higher in the atmosphere for low energetic events and can be investigated by a combined FoV of HEAT and Coihueco. Photo and event from [69].

era is located in the focal plane and is instrumented by a grid of 440 PMTs or pixels. Each PMT has a hexagonal shape, a FoV of 1.5 ° x 1.5 ° and a maximal quantum efficiency of approximately 25% in the wavelength regime of interest [78]. To reduce dead area between PMTs, each PMT is complemented by a simplified version of a Winston cone, a so-called Mercedes star. A signal from a typical air shower developing in the atmosphere is contained approximately in one pixel during a single time bin. The whole shower forms a trace on the camera during the time period of microseconds, depending on its distance and geometry. A typical trace of an air shower event is depicted in figure 3.6a.

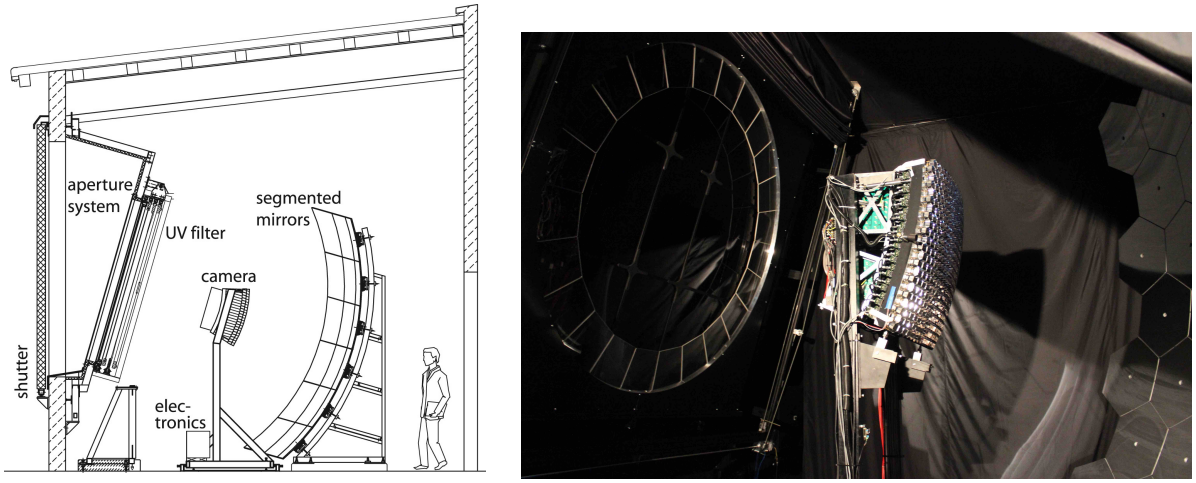

(a) Schematic view of the Schmidt-optic telescope and its main components [70].

(b) Photo of a fluorescence telescope at Coihueco.

Figure 3.7.: The fluorescence detector at the Pierre Auger Observatory. The light is entering through a diaphragm and a UV pass-filter and is focused by a spherical mirror onto the camera instrumented with 440 PMTs.

3.2.1. Event reconstruction

The reconstruction of air showers registered by the fluorescence detector is only shortly described in this section, for more details including the multi-stage trigger please refer to [70]. As a first step, after an air shower trigger occurs in one telescope [79, 80], the ADC traces of selected pixels in the camera are recorded and noise is subtracted. The cleaned ADC count will be converted to the number of impinging photons at the aperture according to a conversion function determined by the absolute and relative calibrations of the fluorescence telescopes. From the timing of triggered pixels the geometry of the air shower can be reconstructed. For a basic geometry of one telescope detecting an air shower, the *shower detector plane* (SDP) is an important auxiliary tool. The plane contains the shower axis and the observation point (cf. figure 3.8). The angle χ_0 is the angle inside the SDP between the shower axis and the ground. The shower distance R_p is perpendicular from the observing telescope to the shower axis. The distance is obtained by a fit of the recorded arrival time t_i of light in each pixel i having an elevation angle χ_i in the SDP in respect to the ground. The arrival time t_i is thereby defined as the time when the signal in pixel i reached its maximum

$$t_i(\chi_i) = t_0 + \frac{1}{c} R_p \tan\left(\frac{\chi_0 - \chi_i}{2}\right) \quad . \tag{3.5}$$

Reconstruction of the geometric parameters using the FD alone is susceptible to uncertainties, especially for events with a short track length within the camera. However, the additional information from only one WCD station improves the geometrical reconstruction significantly, particularly for χ_0.

The amount of light as a function of time can be converted into the amount of energy deposited along the shower axis. Other sources of light e.g. Cherenkov emission [81, 82] or nightsky-background as well as effects regarding light production efficiency or attenuation [83] must be taken into account. For this conversion, the knowledge of the atmospheric conditions is important. Therefore, the atmospheric conditions are continuously monitored throughout the data taking.

In figure 3.9, a shower profile of the light at the aperture as a function of time (left) and of the thereof calculated energy deposit in the atmosphere as a function of slant depth, X (right), is

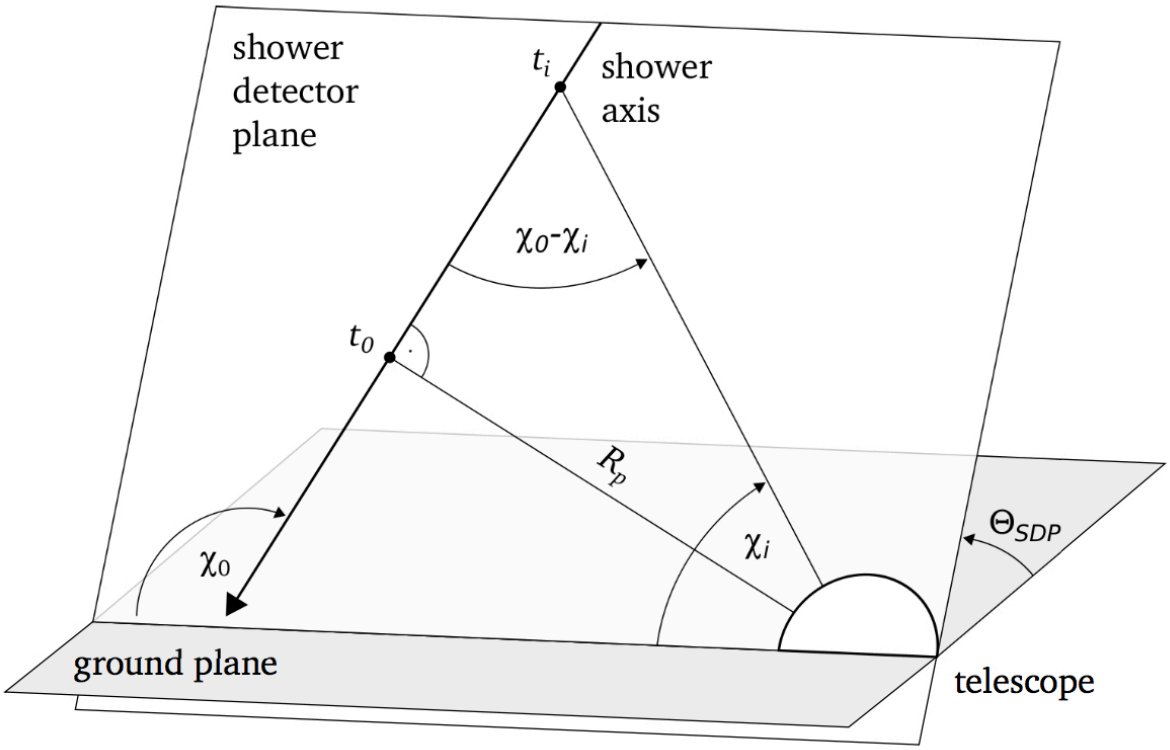

Figure 3.8.: Illustration of the geometrical shower reconstruction by a single telescope within the shower detector plane. The shower axis has an arrival direction of χ_0 in the shower plane. A PMT views the shower at time t_i under the angle χ_i in respect to the ground. The shower distance R_p is defined as the distance of the telescope to the shower, perpendicular to the shower axis at the reference time t_0. Adapted from [70].

shown for one event . For the reconstructed energy deposit the shower profile can be described by the Gaisser-Hillas function [7, 84]

$$f_{\mathrm{GH}}(X) = \left(\frac{\mathrm{d}E}{\mathrm{d}X}\right)_{\mathrm{max}} \left(\frac{X - X_0}{X_{\mathrm{max}} - X_0}\right)^{(X_{\mathrm{max}} - X_0)/\lambda} e^{(X_{\mathrm{max}} - X)/\lambda} \quad , \tag{3.6}$$

whereby X_0 and λ are shape parameters, X the slant depth, and X_{max} the depth of the shower maximum. A measurement of X_{max} performed at the Pierre Auger Observatory is presented in figure 2.6 (on page 23 in chapter 2.2). By integrating the shower profile, the shower energy carried by the electromagnetic component can be determined. The part of the energy not measured by the FD[3] is mainly carried by neutrinos and high-energy muons and can be determined by means of Monte Carlo simulations [85, 86] or measurements [87].

[3] often called *invisible energy*

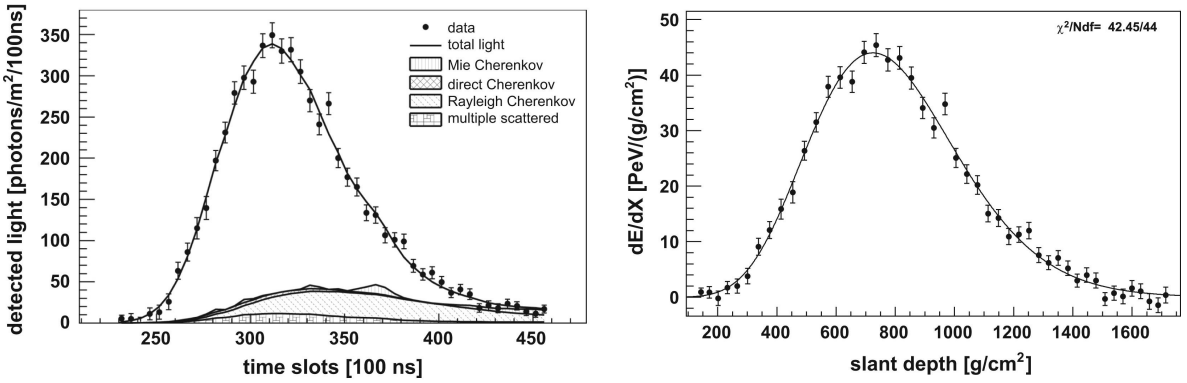

(a) Light at aperture of the telescope per 100 ns time bin. Denoted are further contributions to the photon flux besides fluorescence light.

(b) Thereof calculated energy deposit as a function of slant depth X. The line indicates a fit by the Gaisser-Hillas function to the data.

Figure 3.9.: Example of a reconstructed longitudinal shower profile recorded by the FD detector of the Pierre Auger Observatory [7].

3.3. Extensions of the standard design

The standard design of the Pierre Auger Observatory is based on the detection of fluorescence light and of the density of all charged secondaries reaching the ground having enough energy to produce Cherenkov light emission in the WCD stations. Besides those two techniques, further enhancements are realized in the array [43]. First, the investigation of air showers by the radio emission produced along the shower is shortly presented. Second, the *AMIGA* detector will be introduced. It comprises detector stations explicitly designed to study the muonic component of air showers.

3.3.1. The Auger Engineering Radio Array

The detection of radio emission in the MHz regime is a promising complementary method to observe air showers [88]. The dominant production process is found to be the geomagnetic emission. It arises from the deflection of electrons and positrons in the shower front in the Earth's magnetic field and is polarized along the direction of the Lorentz force. The emission enables an independent measurement of the shower depth maximum X_{max} and a highly accurate determination of the energy ($\mathcal{O}$(10%) [89, 90]) contained in the electromagnetic component of the shower. It achieves nearly 100% duty cycle while being independent of the atmospheric conditions and requiring lower investment. As its processes are only driven by the electromagnetic component of the air showers, they are well predictable and less dependent on shower-to-shower fluctuations compared to shower observables depending on hadronic interactions. By measuring air showers in coincidence with the surface and fluorescence detectors of the Pierre Auger Observatory, the *Auger Engineering Radio Array* (AERA [91]) started as a pathfinder radio detector. AERA has significantly contributed to the understanding of the radio technique and its emission processes and is now an important part of the experiment [22, 92]. It consists of an array of more than 150 autonomous stations. The stations are radio antennas of two different designs [93]. They cover an area of 17 km^2 combining several regions where the distances between stations differ. AERA is optimized for the detection of air showers up to zenith angles of 60° but allows also the reconstruction of inclined showers.

3.3.2. The Auger Muon and Infilled Ground Array

The AMIGA (Auger Muon and Infilled Ground Array [94, 95, 96]) enhancement is a joint system of water Cherenkov and buried scintillator detectors [97].

Infill

For the *Infill* ground array, additional WCD stations have been introduced in a small part of the regular SD array. The first hexagon started data taking at the end of 2007, while the complete Infill was deployed at the end of 2012. The Infill covers 23.5 km^2 and consists of 61 stations separated by the distance of 750 m referring to half of the distance between stations in the regular array. It is located nearby the FD site of Coihueco and HEAT. By reducing the distance between the stations the energy threshold of the surface detector array is lowered. The Infill reaches 100% efficiency at an energy of $3 \cdot 10^{17}$ eV for angles $\theta < 55\,^{\circ}$. Its measured energy spectrum is in good agreement with the energy spectrum of the regular array in the overlapping region of the energy [95].

Buried scintillators of AMIGA

Each station will be accompanied by a 30 m^2 scintillator detector with SiPM readout to study directly the muonic component of air showers. These detectors will be buried at a depth of 2.3 m to provide shielding against particles of the electromagnetic component. Each detector consists of three modules independently counting muons. It is triggered if the associated SD station registers an air shower candidate. Each module is built from 64 scintillation bars, each of dimensions 400 cm x 4 cm x 1 cm, and its total detection area is 10 m^2. Each bar has a 1.2 mm diameter wavelength-shifting (WLS) fiber glued to it, which transfers a signal to the photosensor. An Application Specific Integrated Circuit (ASIC), the Cherenkov Imaging Telescope Integrated Read Out Chip (CITIROC [98, 99]), is planned for the front-end readout of the detector providing 32 readout channels. AMIGA is designed to investigate the muonic content of air showers in the highly interesting transition region from galactic to extragalactic cosmic rays. Being located in the same region of the SD array as AERA and the FD sites Coihueco and HEAT, an unprecedented combined analysis of the same air showers by four detection methods becomes possible. The buried scintillators of AMIGA will also be important for a comparison with the AugerPrime detector upgrade presented in the following section [16].

3.4. AugerPrime upgrade

As a new stage of the Pierre Auger Observatory in the following years, the *AugerPrime* upgrade [16] will be installed in the SD array of the experiment. The upgrade comprises an improvement of the front-end and readout electronics of the SD array, an additional small PMT in each WCD station to increase its dynamic range and an extension of the AMIGA muon detector array. Furthermore, an extension of the duty cycle of the fluorescence detector is achieved. At times, at which a large fraction of the moon in the sky is illuminated, the telescopes will be operated by lowering the supplied high voltage. The new SD electronics provide an increased sampling frequency of 120 MHz with 12 bit ADCs compared to the recent 40 MHz with 10 bit ADCs. By a faster sampling of the ADC traces a better timing accuracy and a better reconstruction of the pulse shape becomes available. Also the dynamic range is increased and the electronics allows for more channels for the additional components of the upgrade. Most important, a new scintillator detector will be installed on top of

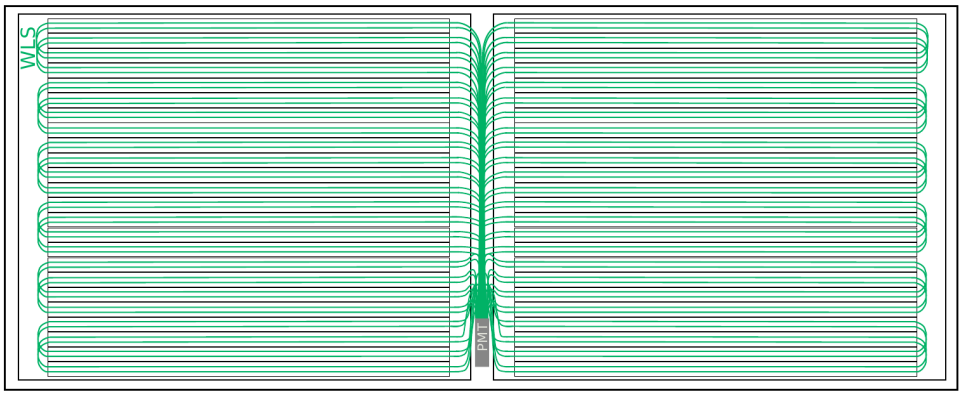

Figure 3.10.: Schematic of the SSD compartment mounted on top of the water Cherenkov detector station. It contains two modules with 24 scintillating bars each with two tunnels for the routing of wavelength shifting fibers. Each fiber has the same length in reality and is routed via two bars in a 'U'-shape. All fibres end at one single photosensor, a photomultiplier tube. Adapted from [22].

each SD station, which will be outlined below. It aims for an improved mass composition study by the ground-based array. In addition, each station will be equipped with a radio antenna which will allow for an improved mass composition sensitivity for inclined air showers.
The production and incorporation of all components of the upgrade is already on-going. With operation planned from 2018 until 2024, not only the event statistics will be doubled compared to the existing Auger data set, but the quality of data will be highly improved. A detailed review about the upgrade can be found in [16] and [22].

The principal motivation for the additional scintillator detector array (*Surface Scintillator Detector*, SSD) is an improved disentanglement of the electromagnetic and muonic components of air showers by analyzing data from two different detectors. Both detectors, WCD station and SSD station, will see the same showers but yield different responses. By a combination of both responses an estimate on the primary mass of the highest energy cosmic rays on a shower-by-shower basis will become possible with a duty cycle of $\approx 100\%$. The upgrade will allow to address important open questions in the research field of UHECRs:

- Is the origin of the flux suppression at the highest energies due to propagation effects or does the cosmic ray accelerators in the universe reach their maximum energy? Benchmark models predict different chemical compositions for both scenarios.
- How many protons contribute to the flux at highest energies? By identifying light primaries, e.g. improved anisotropy studies, photon and neutrino searches at the highest energies can be performed.
- Why does the Pierre Auger Observatory measure more muons than air shower simulations predict? Is there a change of hadronic interactions for the highest energies? By the upgrade a deeper study of the hadronic interactions of particles in the atmosphere and thereby improved hadronic interaction models, which highly influence air shower simulation predictions, are enabled. This could also allow re-analyses of already taken data.

Each scintillator detector station has a detection area of $3.8\,\mathrm{m}^2$ comprising two modules with 24 scintillator [100] bars each (cf. figure 3.10 for detector schematics, figure 3.11 for photo of a setup in the field). A bar is 1600 mm long, 50 mm wide and 10 mm thick. The bars are read out by

Figure 3.11.: Photo of a SSD compartment mounted on top of the water Cherenkov detector station at the Pierre Auger Observatory.

1 mm diameter WLS fibres. Each WLS fibre is routed via two bars in a 'U'-shape through a tunnel located in the medium height of a bar. All WLS fibres of both modules guide the light emitted by an energetic particle traversing the scintillator bars onto one single photosensor, a PMT. The SSD is designed to provide a high uniformity ($\approx 5\%$), a high signal yield per minimum ionizing particle and a large dynamic range, by relatively low costs and easy deployment. [16, 22]

Within the scope of the preparatory work of the AugerPrime upgrade, different detector proposals have been designed by several groups of the Pierre Auger collaboration. The main goal was to find the optimal layout in terms of detection performance, maintenance and installation effort, cost-efficiency, and compatibility with the SD readout electronics. As discussed, the SSD approach has been identified as best solution. An alternative scintillator-based design has been developed in Aachen, the Aachen Muon Detector (AMD). Its unique selling point is the use of silicon photomultipliers as photosensors (see chapter 4 for an introduction to these devices). The concept will be discussed in more detail in section 6.4. The strategy was to place a AMD detector underneath the standard WCD stations. While the WCD station is sensitive to all charged particles, a large fraction of the electromagnetic component will be absorbed within the water and will allow for the detection of muons in the AMD detector. The already existing SD array is thereby subject to only minor modifications. The alternative array would be easily backward compatible like for the chosen design of the SSD. A preliminary analyze based on air-shower simulations with the proposed detector is presented in chapter 10. The concept of the AMD detector for the Pierre Auger Observatory is not pursued further. However, the centerpiece of the detector, a detector unit (cf. chapter 6), allows not only for the detector suited for the investigation of cosmic rays at the Pierre Auger Observatory, but also for the development of multi-purpose detectors. The main focus of this work is therefore the optimization of the layout and of the performance of a detector unit, as well as the development of a software framework that describes the response of the detector unit to particle passages.

CHAPTER 4

Silicon Photomultipliers

As stated before, improvements in the research field of astroparticle physics go hand in hand with improvements regarding technological opportunities. For many applications, the choice of the ideal light sensor for the detection of photons produced, e.g. by traversing particles in the detector material, is crucial.
So far, most of the experiments have used *photomultiplier tubes* (PMTs) [101, 102] as they were the most sensitive sensors for small light fluxes. They consist of an evacuated glass tube with a photo sensitive photocathode at its entrance window followed by a multiple dynode structure to amplify the signal. They are based on the photoelectric effect [101]. So, if a photon hits the photocathode, there is a chance to release an electron[1]. The initial electron is then focused by an electrode and accelerated by an electric field produced by the following dynode structure towards the anode at the end of the tube. At each dynode there is the chance to produce secondary electrons. Typical multiplication factors are 3 (at $\sim$ 150 V accelerating voltage of the primary) to 6 (at $\sim$ 500 V accelerating voltage of the primary) for aluminum oxide as dynode material [103]. However, much larger multiplication factors up to 100 can be achieved for other materials [104]. As for each dynode an increment of the applied voltage has to be provided, a high operating voltage from 1000 to 1500 V has to be applied. The multiplication of the electrons will allow an amplified and therefore measurable signal compared to a signal produced by a single electron collected by the anode. PMTs offer a high quantum efficiency (up to 40% [105]) and an extended linear dynamic range if they are carefully characterized. They can cover large detection areas[2] as their entrance window is in the order of few to several hundreds cm^2. At the same time they require also a quite large volume due to the acceleration in the dynode structure, making them challenging for space-limited detectors. Also the usage of these sensors has to be prudent as they are damaged and age due to high light fluxes.
The rapid development of solid-state detectors has provided alternative candidates like *silicon photomultipliers* (SiPMs) as light sensors [108, 109] for many research fields [110]. They consist of an array of *avalanche photodiodes* (cells) operated in Geiger-mode. For an impinging photon, each cell gives a well-defined signal with a high amplification gain $\mathcal{O}(10^6)$ [111]. By connecting the cells in parallel, the number of cells refers, as a first approximation, to the number of impinging

[1] This is also possible by thermal excitation which is considered as intrinsic noise of a PMT.
[2] For examples of experiments exploiting the large size of PMTs please refer to the Super-Kamiokande [106] or the JUNO [107] experiment.

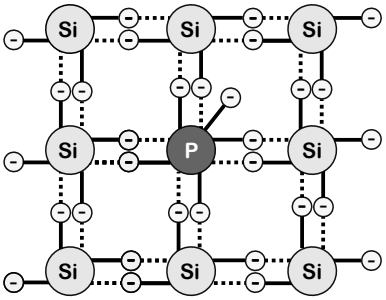

(a) Doping silicon with phosphor results in an n-type semiconductor. Free electrons contribute to carrier transport.

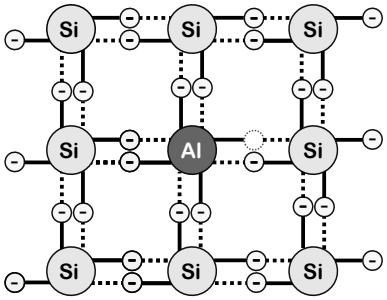

(b) Doping silicon with aluminum results in a p-type semiconductor. Holes contribute to carrier transport.

Figure 4.1.: Extrinsic semiconductors. Impurities are added to the neutral base material silicon.

photons. The dynamic range of a SiPM is therefore limited by the number of cells forming the device. Being thin ($\mathcal{O}(1\,\text{mm})$) and having small detection areas of $\mathcal{O}(\text{mm}^2)$ [105], they are easy to install in space-limited detectors. As being semiconductor devices, SiPMs are manufactured with great precision. Thus, the variation in the response of different cells and also between different SiPMs of the same type is small $\mathcal{O}(< 1\%)$ [112, 113]. Intense characterization as for PMTs is not mandatory. They only need a supply voltage of several ten volts which can be provided by dedicated electronics with a step-up conversion from power by a PC via 5 V-USB [114]. They are robust against mechanical stress, radiation [115, 116], regarding high light fluxes and they do not show significant aging [117]. However, the usage of SiPMs in some applications is limited by their dark count rate of $\mathcal{O}(100\ \text{kHz per mm}^2)$ [105, 111] and by their small size.

4.1. Introduction to semiconductor light sensors

The properties of the signal to be examined determine the choice of a device. Different kinds of silicon photodetectors exist. They focus on the determination of certain aspects as intensity, timing, or spacial resolution of the signal while losing precision for others. During this section several common devices are briefly described [118, 119].
All of those are based on two types of semiconductors: the intrinsic and the extrinsic. The intrinsic type has no dopants. The number of electrons in the conduction band equals the number of holes in the valence band. The extrinsic type refers to a doped semiconductor whereby the dopants mainly control the electrical properties (cf. figure 4.1). For an n-type ('negative') semiconductor ions with more valence electrons are added to the base material. The additional electrons are less bound. For a p-type ('positive') semiconductor an impurity with less valence electrons is added so that the hole concentration is increased with respect to the electron concentration. Holes correspond thereby to missing electrons / empty spaces in the valence band.

Pn junction diode

A *pn junction* is the simplest semiconductor device and consists of an n-type and a p-type semiconductor located directly next to each other (for the architecture of a pn junction cf. figure 4.2). At the boundary, electrons drift to the p-doped side recombining with the holes and vice versa leaving charged atoms behind. A narrow so-called *depletion zone* is formed with no mobile charge carriers available. The ions then produce an electric field counteracting this diffusion process until an

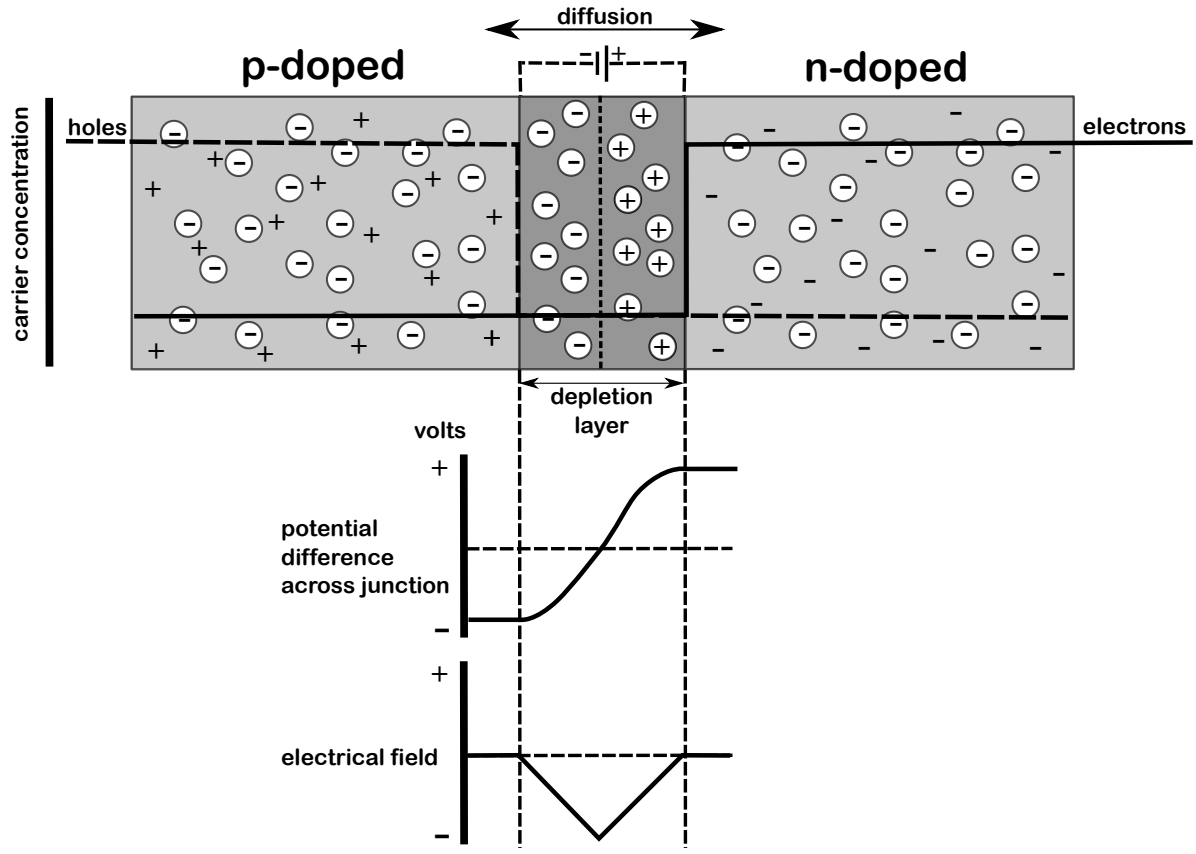

Figure 4.2.: Schematic of the architecture of a pn junction. At the boundary a depletion zone is formed with no mobile carriers available but containing ions. The ions cause a potential across the junction resulting in an electrical field.

equilibrium is reached. Charge carriers need additional energy to overcome the depletion zone which acts as a barrier. If a voltage V_{bias} is applied, an additional electric field is established. For the detection of photons the pn junction has to be operated reversely biased. A positive voltage is applied to the n-type region attracting electrons towards the positive electrode and away from the junction. The holes in the p-type end are also attracted away from the junction, towards the negative electrode. The depletion region and the internal electrical field are thereby increased. Practically no current flows through the junction diode.
If a photon with an energy E_γ larger than the band gap E_{gap} of a doped semiconductor reaches the pn junction, an electron-hole pair is created (for silicon at 300 K: $E_\gamma \geq E_{\text{gap}} = 1.12\,\text{eV}$). In general, these free charge carriers will likely recombine if they are not separated due to an electric field like introduced by the applied reverse bias voltage. If a separation occurs, the resulting recovery time is relatively large $\mathcal{O}(1\,\mu s)$ as the depletion zone is small. [118, 119]

Pin photodiodes

A *pin photodiode* allows a faster recovery process. It consists of a highly doped p^+n^+ junction with a quasi-intrinsic[3] region in between. The thickness of the intrinsic layer ranges between a few micrometers up to several hundred micrometers. Due to the low carrier concentration in the intrinsic layer only a small reverse bias voltage is required for a full depletion. A large region without

[3] A lightly doped, nearly intrinsic and usually p-type semiconductor.

mobile carriers is formed allowing a reduced capacitance compared to a pn junction diode [118]. The reduced capacitance enables faster signal and decay times. The depletion zone has thereby an almost constant width, mainly defined by the width of the intrinsic region, and only with small dependence on the reverse bias applied to the diode. Furthermore, an enlarged depletion layer improves the sensitivity for red and infrared photons[4] which penetrate deeply into the silicon before getting absorbed.
The detection principle is the same as for a pn junction. If a photon with enough energy traverses the depletion zone, again an electron-hole pair is created. Under the influence of the electric field the electron and the hole drift towards the n^+ and the p^+ regions, respectively. Reaching the connected electrodes they produce a measurable current. The amplification factor of a pin diode is still 1 and offers a large dynamic range with a linear response to the number of impinging photons. The output current is typically in a range from few 100 pA up to 1 nA. Limited by the noise of sensor and electronics, the pin photodiode is therefore not suitable for the detection of single photons.

Avalanche photodiodes

For an improved detection of low light fluxes, an *avalanche photodiode* (APD) can be used. An APD consists of a modified doping profile, a n-on-p structure. It is operated with a high reverse bias voltage in the proportional avalanche region to induce an internal charge amplification mechanism. Due to a higher electric field impinging photons produce not one electron-hole pair per photon but an avalanche of secondary charge carriers: As the energy gain by the electric field during the mean free path of the free charge carriers allows impact ionization, further electron-hole pairs are produced resulting in an intrinsic amplification. For an APD, only electrons reach this critical energy and the avalanche is developing towards the direction of the n-type region. The output signal is proportional to the number of primary electrons, referring to the deposited energy in the depletion region. Conventional avalanche photodiodes are designed to operate in this 'linear' mode of amplification and practical intrinsic amplification factors are in the range from 50 up to 200. [121]

Geiger-mode avalanche photodiodes

If the photodiode is operated in the Geiger-mode regime, an even higher gain can be achieved compared to an APD ($\mathcal{O}(100) \rightarrow \mathcal{O}(10^5 - 10^6)$, comparable to the gain of PMTs). With rising bias voltage the probability increases that an initial charge carrier pair, created by an absorption of a photon[5], will successfully initiate an avalanche breakdown of secondaries. Now also holes are strongly accelerated by the electric field reaching their critical energy to contribute to the avalanche process. The Geiger-mode is defined by a *bias voltage* V_{bias} larger than the avalanche *breakdown voltage* V_{break}. This allows the efficient detection of a single photon while losing the possibility to distinguish between several simultaneously impinging photons as each avalanche results in the same signal regardless of the deposited energy. Thus, each *Geiger-mode avalanche photodiode* (G-APD) is a binary device. The avalanche would be self-sustaining and would damage the diode. To avoid any harm to the device and to reduce large deadtimes, a quenching resistor $R_q \approx \mathcal{O}(100\,\text{k}\Omega)$ connected in series is needed. The voltage will drop along the resistor. If the voltage is below V_{break}, the avalanche will stop. After each trigger the diode needs time to recharge and to reach its initial state again. [121]

[4] Photons in the red wavelength regime have a larger absorption length of $\sim 4.2\,\mu$m (for $\lambda = 680$ nm) in silicon compared to the blue wavelength regime with an absorption length $\sim 0.3\,\mu$m (for $\lambda = 465$ nm) [120].
[5] to be precise: or due to thermal noise

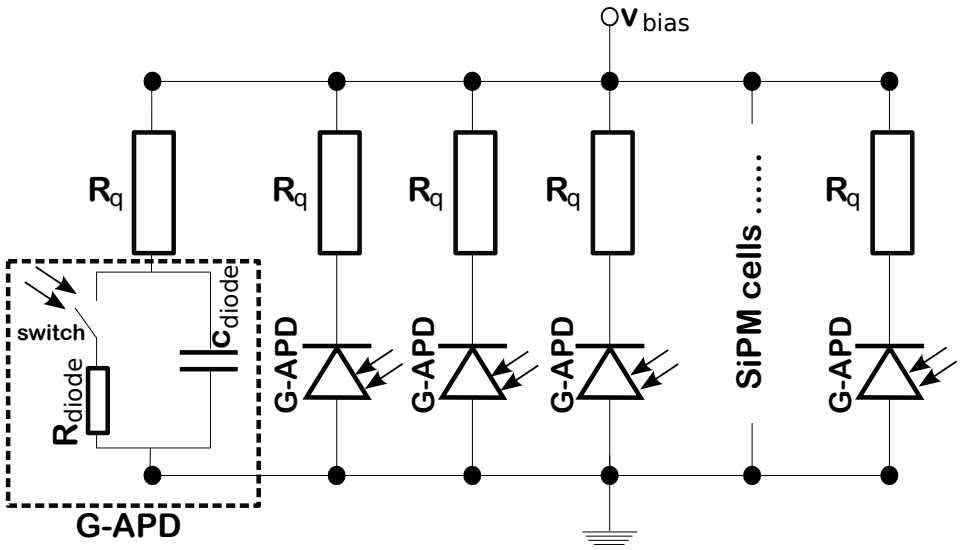

Figure 4.3.: Schematic of a SiPM. A SiPM consists of up to $\mathcal{O}(10000)$ cells connected in parallel. Each cell consists of a G-APD and a quenching resistor R_q connected in series. Also depicted is a proposal for an equivalent circuit of a G-APD on the left side of the figure. Here, an avalanche in a G-APD can be compared as a switch closing due to impinging photons initiating a capacitance c_{diode} to discharge over an internal resistance R_{diode}. For reasons of simplicity, further parasitic capacitances, resistances, and inductances are not shown. Please refer to [122] for an overview. Figure adapted from [121] and [123].

Silicon photomultipliers

Silicon photomultipliers combine a good timing resolution and the discrimination power in the range of single photons to larger number of simultaneously impinging photons. It consist of an array of cells connected in parallel whereby each cell corresponds to a G-APD with its mandatory quenching resistors in series. A schematic of the equivalent circuit of a SiPM is depicted in figure 4.3. If now a photon traverses one cell, it will produce a standardized signal S_i apart from small statistical fluctuations. Multiple photons triggering multiple cells will produce a signal corresponding to the sum of the signal of all cells $S_{\text{sipm}} = \sum_{i=1}^{N_{\text{cell}}} S_i$ offering a measure of the number of arriving photons[6]. According to the state of the art, SiPMs are available in small sizes of typically $1-100\,\text{mm}^2$ consisting of up to $\mathcal{O}(10000)$ cells. A magnified view of an example SiPM of Hamamatsu S12571-050P SMD type [105] is shown in figure 4.4.

[6] if the number of impinging photons is small and the photons are well distributed in time and over the complete area of the sensor.

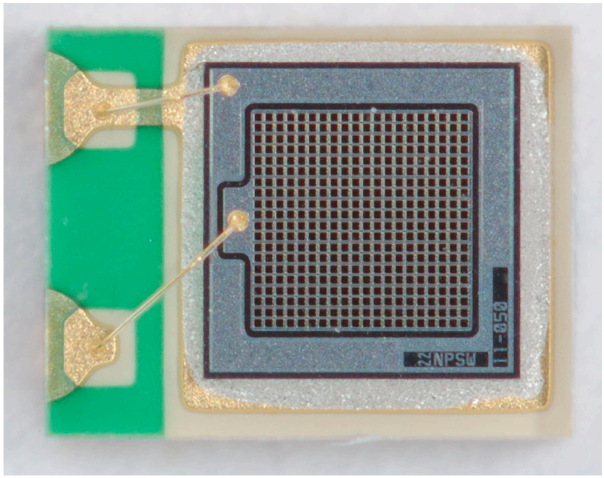

Figure 4.4.: Photo of a SiPM of Hamamatsu S12571-050P SMD type [105] used in this thesis. The active area of the presented device is 1 x 1 mm^2. It consists of 400 cells with a cell pitch of 50 μm. Photo courtesy of L. Middendorf.

4.2. Characteristics of silicon photomultipliers

The main parameter influencing the response of a given SiPM type is the *overvoltage* V_{ov}

$$V_{\text{ov}}(T) = V_{\text{bias}} - V_{\text{break}}(T) \quad . \tag{4.1}$$

It is defined as the difference between the reverse applied voltage V_{bias} and the minimal needed breakdown voltage for an avalanche process V_{break}. All further characteristics as the amplification factor and the *photon detection efficiency*, but also noise probabilities are influenced by this operating parameter.
Increased vibrations of the silicon lattice due to higher temperatures strongly reduce the mean free path length of the free charge carriers. Losing more energy on their way to the electrodes, a higher breakdown voltage is needed for the same response to photons. The dependence of the breakdown voltage V_{break} on the ambient temperature T can be described by

$$V_{\text{break}}(T) = V_{\text{break}}(T = 0\,^{\circ}\text{C}) + \beta \cdot (T - 0\,^{\circ}\text{C}) \quad , \tag{4.2}$$

whereby the coefficient β corresponds e.g. to $56 - 60\,\text{mV/K}$ for Hamamatsu devices [105, 124]. Depending on the breakdown voltage, also the overvoltage and all overvoltage-dependent characteristics are influenced by the ambient temperature.
As an example, the gain G is directly proportional to the overvoltage. At room temperature, the gain is $\mathcal{O}(10^6)$. Additionally, it depends on the capacitance c_{diode} of the diode and the elementary charge q_e [125]

$$G(T) = \frac{c_{\text{diode}} \cdot V_{\text{ov}}(T)}{q_e} \quad . \tag{4.3}$$

For the operation of a detector based on SiPMs, the gain should be kept stable for all temperatures to achieve a stable and predictable detector response. To achieve this, a compensation of the change of the breakdown voltage by adjusting the applied voltage is needed as defined by equation 4.2.

Photon detection efficiency

A high *photon detection efficiency* (PDE) is a prerequisite for SiPMs as a promising light detection device. The PDE denotes the overall probability for photon detection, taking into account the effi-

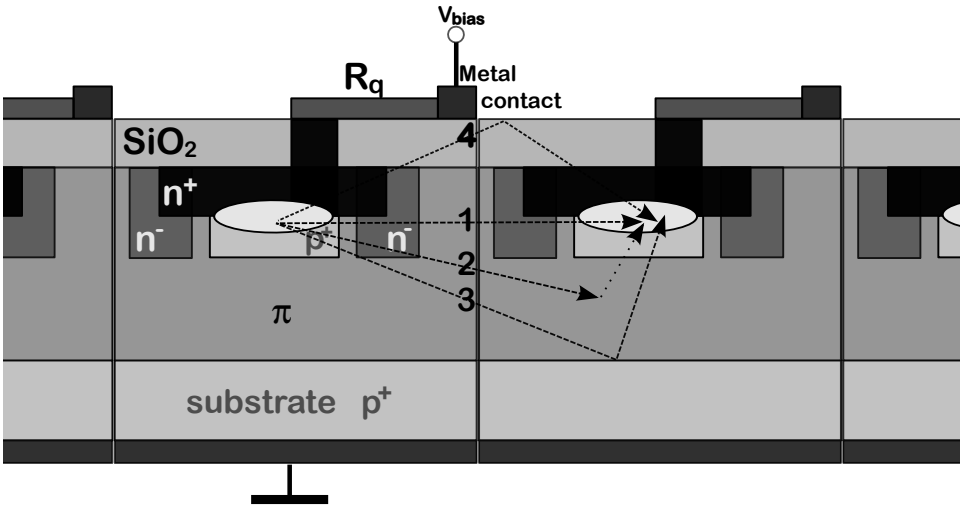

Figure 4.5.: Indicated in the schematic is the architecture of a Geiger-mode avalanche photodiode. The depletion zone is formed between the heavily doped n^+ and p^+ layers. Additionally, a lightly n-doped π-layer is included. Photons in the blue light wavelength regime are mainly detected in the depletion region while photons with larger wavelengths penetrate deeper in the material and are mainly detected in the thicker π-layer. In addition, different optical crosstalk processes are indicated: 1 - direct transmission; 2 - generation of charge carriers drifting into depletion zone and triggering a breakdown; 3 - reflection at boundaries; 4 - reflection at inner boundary of the coating layer. Adapted from [105].

ciencies of the individual detection stages. It is determined for SiPMs by four different effects (refer to equation 4.4) shortly described in the following. The photon detection efficiency can thus be expressed as

$$\mathrm{PDE}(\lambda, \theta, V_{\mathrm{ov}}) = \epsilon_{\mathrm{geom}} \cdot \mathrm{QE}(\lambda) \cdot p_{\mathrm{avalanche}}(V_{\mathrm{ov}}) \cdot \epsilon_{\mathrm{trans}}(\theta) \quad . \tag{4.4}$$

The geometrical fill factor ϵ_{geom} defines the fraction of the SiPM area which is sensitive to light. Dead space is caused by connection wires, the series quenching resistor or optical trenches to reduce noise. For common SiPM types the geometrical factor is about 80% [105]. The factor is depending on the cell pitch as more cells of a SiPM result in more dead space over the whole SiPM area.
The quantum efficiency $\mathrm{QE}(\lambda)$ describes the probability that a single photon reaching the active area of the SiPM generates an electron-hole pair. The probability of the absorption of a photon depends strongly on its wavelength λ and on material properties. The initial charge carrier pair may trigger an avalanche of further electron-hole pairs with a probability of $p_{\mathrm{avalanche}}(V_{\mathrm{ov}})$ [126]. The PDE is reduced depending on the incident angle θ of the photons on the entrance window as photons having an arrival direction other than vertical undergo multilayer Fresnel reflections at the optical boundaries from air to the entrance window and from the entrance window to the silicon chip. This is depicted by the transmission efficiency $\epsilon_{\mathrm{trans}}(\theta)$ (measurements [127, 128], analytical description [129]). For common devices the photon detection efficiency has its peak in the range of $20 - 50\%$ for its designated wavelength regime [105, 130]. Descriptions on how the photon detection efficiency can be measured can be found in [131, 132, 133, 134].

Noise phenomena

Noise phenomena of SiPMs include thermally generated noise as well as correlated noise and are highly dependent on the ambient temperature, the applied voltage and the number of cells.
Thermal noise is defined as a pair of charge carriers created in the depletion region by thermal

excitation. Thereby, an avalanche in the G-APD is triggered without the presence of an impinging photons. The avalanche results in the same response as for a photon and is not distinguishable from a signal trigger. The thermal noise rate is highly dependent on the temperature. An increase of 8 K results in a doubling of the rate as a rule of thumb [108]. Typical thermal noise rates are in the order of 30 kHz/mm^2 for recent Hamamatsu devices [105]. For a 1 mm x 1 mm SiPM with 100 cells, the thermal noise rate is $f \approx 30$ kHz. The probability to have two triggers in coincidence in a time gate $t_{\text{gate}} = 20$ ns is thus about $P_{2\cdot\text{th}} = 1 - e^{-t_{\text{gate}} \cdot f} \approx 0.06\%$. However, the rate may be considered as the main bottleneck for some applications even if it has been strongly reduced by continuous improvements in the manufacturing of SiPMs. The thermal noise rate is depending on the overvoltage V_{ov} and on the ambient temperature. So, even with a stable overvoltage the thermal noise rate will increase with increasing ambient temperature.

Optical crosstalk and *afterpulsing* are defined as *correlated noise*, so noise requiring a trigger due to a photon or thermal noise to be initiated.
During the avalanche breakdown free charge carriers can recombine emitting photons in the surroundings of the cell [135, 136, 137, 138]. Optical crosstalk is defined as those photons causing adjacent cells to be triggered. It results in an increased signal response. Different paths for crosstalk photons are depicted in figure 4.5. Avalanches can thus be caused by a photon directly transmitted and absorbed in a neighbouring cell or by a photon first crossing over in the n-doped layer of the adjacent cell. There an electron-hole pair may be generated which in turn drifts into the depletion zone and triggers an avalanche. Furthermore, a photon may get reflected onto a neighbouring cell at the inner boundaries of the cell or of the coating layer. If the number of additional firing cells would be constant, optical crosstalk would only cause an effective increase of the signal, and an earlier saturation behaviour. However, the number of additional cells triggering is subject to large fluctuations which deteriorates the achievable photon counting resolution. State of the art SiPMs therefore often use 'trenches' between individual cells to suppress the transition of photons to a neighboring cell whereby also the geometrical fill factor is affected as trenches introduce additional dead space between cells. The crosstalk probability has been strongly reduced in the last few years ($p_{\text{ct}} = 30\% \rightarrow < 10\%$ [105, 139]).
The crosstalk probability depends on the probability for each photon to trigger an avalanche, and also on the gain (cf. equation 4.3) as it influences the number of emitted photons possibly producing crosstalk. As both quantities are depending on the overvoltage, the crosstalk probability can be described roughly by a polynomial of second degree in V_{ov}.
Afterpulses are delayed triggers in the original triggered cell. They are initiated by the release of charge carriers trapped at material impurities during the avalanche process. The delay time has been found to follow an exponential distribution with two time constants $\tau_{\text{ap, fast}} = \mathcal{O}(10\,\text{ns})$ and $\tau_{\text{ap, slow}} = \mathcal{O}(100\,\text{ns})$. The afterpulse probability p_{ap} has been strongly reduced over the last years. It is nowadays the less dominant noise effects of recent devices ($\mathcal{O}(< 5\%)$).
Afterpulses is the only correlated noise component increasing the dark noise rate, so the rate of triggers occurring without any light signal. While crosstalk photons are producing a higher signal coincident with another trigger, an afterpulse event may introduce another trigger. Therefore, the dark noise rate is dependent on the thermal noise rate as well as on the afterpulse probability p_{ap} and can be approximated by [108]

$$f_{\text{dark}} = (1 + p_{\text{ap}}) f_{\text{th}} \quad . \tag{4.5}$$

To depict the influence of the noise phenomena, an example trigger queue and the corresponding trace is illustrated in figure 4.6. The trace is simulated by the SiPM simulation package *G4SiPM* [123] (cf. section 4.3). First, a thermal noise event occurs in one cell of a SiPM triggering not only an avalanche in this cell but also an optical crosstalk event in a neighboring cell. This is

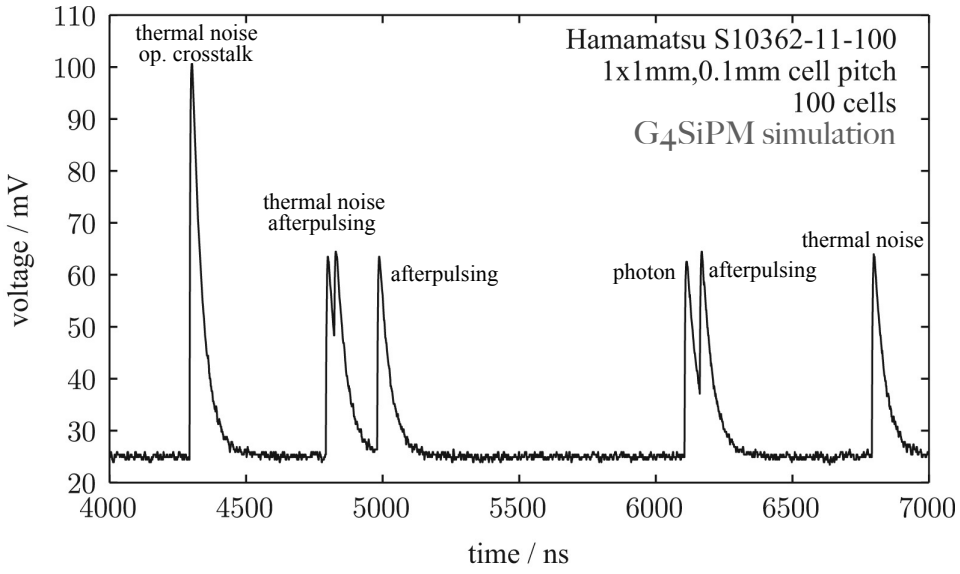

Figure 4.6.: Simulated voltage trace of a SiPM as it can be measured e.g. with an oscilloscope. Simulation is performed by a SiPM package for the software framework Geant4, called G4SiPM. Figure and caption adapted from [123].

followed by a second thermal noise event resulting in two delayed avalanches due to afterpulse events, one according to the fast, the other to the slow time constant. Later on, a single photon is reaching a third cell followed by an afterpulse event and again a thermal noise trigger. The corresponding voltage trace demonstrates the unique response of a SiPM. A thermal noise event is not distinguishable from a photon event. Therefore, a trigger is referred to as a *photon equivalent* (p.e.). A crosstalk event is producing an amplitude of twice the height of one avalanche in a single cell. Afterpulses are visible as delayed triggers, often resulting in a double peak structure.
By integrating such traces over time, a *charge spectrum*, more precisely the number of triggers as a function of the charge, can be produced. An example for a SiPM operated in darkness is shown in figure 4.7. Due to the standardized signal of the cell response, a peak-like structure is visible whereby each peak corresponds to a certain number of photon equivalents. The distance between two peaks thereby refers to the gain of the SiPM, the difference in amplitude for the first p.e. peaks is a measure of the crosstalk probability increasing the signal height. Simultaneous triggers due to thermal noise become unlikely for a high number of photon equivalents.
Containing information on the response of the SiPM, such spectra can be used as a monitoring system over the lifetime of an experiment. Changes in the SiPM, for example, in the gain would be directly visible. This also allows for the differentiation between changes in the detector itself and the light sensor, which is unique for SiPMs.

Dynamic range

The number of triggered cells of a SiPM is, as a first approximation, a direct measure of the number of impinging photons. This assumption can describe relatively small number of photons well distributed in time and spread over the whole area of the SiPM. For a larger number of photons, this linear response is not valid anymore as more and more photons are reaching one cell simultaneously, thus resulting in the same response as for a single photon trigger. Also correlated noise has a larger impact on the number of triggered cells, delaying or increasing the signal. However, the maximum number of detectable photons is fundamentally limited by the finite number of cells.

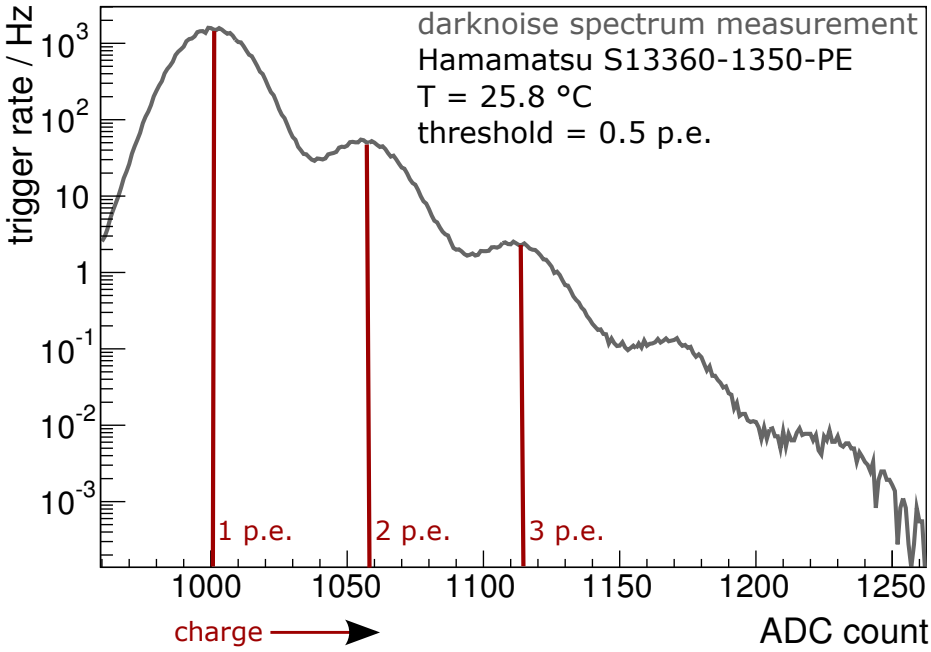

Figure 4.7.: Typical single photoelectron spectrum recorded with the electronics and the SiPM of Hamamatsu S13360-1350PE type [105] used in this thesis. The spectra for the SiPM in darkness is shown. The first peak corresponds to one cell trigger or one photon equivalent (1 p.e.), the next to 2 p.e. and so on. The individual peaks are well separated which indicates the good photon counting capabilities of a SiPM. The spectrum was measured with a trigger threshold of 0.5 p.e.

The optical signal range over which a SiPM delivers a useful output is defined as *dynamic range*.

For an ideal SiPM illuminated by a short light pulse, the response function to describe the SiPM non-linearity is

$$\frac{n_{\text{trig, cells}}(n_\gamma)}{\text{p.e.}} = n_{\text{tot, cells}}\left(1 - e^{-\text{PDE}^* \cdot n_\gamma / n_{\text{tot, cells}}}\right) \tag{4.6}$$

$$\overset{n_\gamma \to 0}{=} \text{PDE}^* \cdot n_\gamma \quad , \tag{4.7}$$

where $n_{\text{trig, cells}}$ refers to the number of fired cells of a SiPM due to n_γ impinging photons. The amount of triggered cells is thereby defined as the total signal charge divided by the gain G of a single cell, so that $n_{\text{trig, cells}}$ can be a decimal number. The quantity PDE* corresponds to the effective photon detection efficiency overestimating the probability for photon detection. This efficiency takes correlated noise effects into account in contrast to the regular PDE (cf. equation 4.4). $n_{\text{tot, cells}}$ is the total number of SiPM cells available.
The dynamic range is highly dependent on the actual noise rates, so on the ambient temperature and the chosen SiPM type, as well as on the time and spatial distribution of the impinging photons. For example, the fast recovery time of each cell allows a further trigger of the same cell during the recovery process. The corresponding avalanche will result in a smaller signal than for a completely charged cell but would still contribute to $n_{\text{trig, cells}}$. A study of the dynamic range for several types under the influence of the pulse time duration and the SiPM over-voltage is presented in [113]. The dynamic range can be also accurately described by means of Monte Carlo based simulation packages as G4SiPM [123] described in the following section 4.3.

4.3. G4SiPM - a Geant4 simulation package for SiPMs

G4SiPM [123] is a Monte Carlo (MC) based simulation package developed by T. Niggemann. The simulation package is supposed to be used in the scope of the *Geant4* (GEometry ANd Tracking) framework [140]. Geant4 is an open source toolkit widely used in the communities of high-energy, astroparticle, nuclear, accelerator physics and e.g. medical science related to physics. It was developed for the study of particles passages through matter using MC methods. The Geant4 software framework will be explained in detail in chapter 7.1.
G4SiPM follows the approach that the response of a SiPM on a single cell basis can be described over its complete dynamic range by means of a phenomenological model. This model is strongly based on measurements. The basic procedure of the simulation is the same for each SiPM type, but depends strongly on its characteristics. Therefore, the SiPM model of interest can be defined by the user in a properties file containing mandatory input parameters as number of cells, cell pitch, geometrical fill factor, thickness and refractive index of the entrance window, breakdown voltage, thermal noise rate, probability of crosstalk/afterpulsing and time constants of the afterpulsing, spectral and angular PDE or recovery time constants. Many of those properties are given in the datasheets of the manufacturer but mostly only for one working point. The dependence on the ambient temperature T or the applied voltage V_{ov} is accounted for in the simulation. For a correct prediction of the response, the user may define the actual environmental temperature and the used bias voltage in his personal setup. The SiPM may be exposed to light embedded in a Geant4 simulation framework, but also the simulation of pure dark noise is feasible.

The simulation schedule is described shortly in the following. Please refer for a detailed overview to [54, 123, 141].
A simulated SiPM is composed of geometric shapes and materials that correspond to the structure of a real device, whereby only the silicon of the SiPM is defined as the sensitive area. As in a real device, the successful detection of impinging photons is mainly depending on the photon detection efficiency of the device under study (according to equation 4.4).
Photons may now illuminate the entire area of the SiPM. Arriving at the entrance window under an incidence angle θ, photons may undergo multilayer Fresnel reflections at the optical boundaries at the coating and the silicon chip. These processes are implemented in the Geant4 framework itself. The probability for a photon to enter the sensitive area is thus automatically reduced comparable to the transmission efficiency $\epsilon_{\mathrm{trans}}(\theta)$ of photons included in the PDE. The photons arriving at the sensitive area may get rejected by the G4SiPM simulation if arriving at a dead space between cells of the SiPM (according to fill factor ϵ_{geom} included in the PDE). The surviving photon in turn may get considered as a hit (with a certain probability p_{hit}) or is rejected by the G4SiPM simulation. The probability for a hit is defined as $p_{\mathrm{hit}} = \frac{\mathrm{PDE}(\lambda)}{\epsilon_{\mathrm{geom}} \cdot \epsilon_{\mathrm{trans}}(\theta)}$. It depends thus as expected on the PDE. However, the PDE is divided by the two factors ϵ_{geom} and $\epsilon_{\mathrm{trans}}(\theta)$ as those have been already accounted for by the previous steps of the simulation[7].
The hit characteristics such as the time stamp or the creation process (signal hits - 'photons', later on for noise hits - 'thermal', 'crosstalk', 'afterpulsing') are stored. Also the cell id and the charge state of the cell at time of the hit are saved. After each avalanche in a cell, a recharge process sets in. Until the cell reaches its initial state again giving the known standardized pulse height, a further hit may trigger the cell. The corresponding avalanche won't yield the same signal as a fully recharged cell. For each hit, the recharge status of the cell is therefore accounted for by a weight $w = V_{\mathrm{out}}/V_{1\ \mathrm{p.e.}}$ whereby $w = 1$ corresponds to fully recharged cells.

[7] Please be aware of the fact that the PDE given in datasheets of manufacturers is determined by measurements of vertical photons.

The same calculation of the weight is used for the dark noise which is added for each individual cell after the photon tracking has come to an end. First, thermal noise is simulated according to the thermal noise rate of the chosen device. It is uniformly distributed in a time window reasonably larger than the time window of the signal. The cell identifier is distributed uniformly over the complete device. The hits by thermal noise are added to the signal hits queue in chronological order. As a next step, hits are processed chronologically regardless of its origin, and the probability for correlated noise is calculated. If a crosstalk hit occurs, a simultaneous hit may be assigned in a neighbouring cell. For an afterpulse hit a delayed hit is stored with a time difference according to the afterpulse time constants but in the same cell.
G4SiPM also allows a conversion from the hit queue to a more realistic response in form of a voltage trace. This conversion can be interpreted as an ADC conversion of the signal. For each hit a pulse

$$V_{\text{hit, i}} = w \cdot A_{1\text{ p.e.}} \left[1 - \exp\left(\frac{t - t_{\text{hit}}}{\tau_{\text{rise}}}\right)\right] \cdot \exp\left(-\frac{t - t_{\text{hit}}}{\tau_{\text{fall}}}\right) \tag{4.8}$$

is generated, where t_{hit} is the time of the hit, $A_{1\text{ p.e.}}$ the amplitude of a 1 p.e. pulse, w the weight according to the recharge status of the cell. The constants τ_{rise} and τ_{fall} correspond to the time constants of the rising and falling edge, respectively, and are characteristics of the readout electronics used. The response of a complete SiPM is then the sum of all pulses $V_{\text{trace}} = \sum_{i=1}^{N_{\text{hits}}} V_{\text{hit, i}} + V_0$. The additional component V_0 refers to the electronic noise of the setup used in the lab.

CHAPTER 5

Theoretical background of particle detection

The detection of charged particles utilizing photons is based on few components:

- a detector medium in which traversing particles may deposit energy which is converted into photons;
- a photosensor detecting the light and converting it into a measurable signal;
- electronics processing, preparing, and storing the signals for further analyses and providing monitoring and managing of the photosensor and data taking settings.

Aiming to design a device optimized for the measurement of charged particles (more precisely of muons contained in air showers) with silicon photomultipliers as photosensors and key elements, a scintillator-based detector has been designed within the scope of this thesis. It is studied by simulations as well as by detailed measurements of a prototype detector and substudies of its optical components.
Relevant physical processes for this thesis are discussed in this chapter.
The detection of particles is based on their interactions in the detector medium producing photons. Collection and transport efficiency of those photons depend on the optical characteristics of the detector components as for example the optical properties of their surfaces determining the manner and amount of reflection or refraction. Furthermore, basic characteristics of the chosen optical components for the particle detection, *plastic scintillators* as well as *wavelength shifting fibres* (WLS) and *optical waveguides*, are introduced.

5.1. Energy loss of charged particles in detector medium

When crossing matter, heavy charged particles (with masses $M \gg m_e$) interact with the shell electrons of the material. They can ionize or excite the atoms or molecules of the traversed medium. The resulting mean rate of continuous energy loss $\mathrm{d}E$ along the particle trajectory $\mathrm{d}x$ can be described by the Bethe-Bloch formula over many orders of magnitude of particle energy [11, 142, 143].
For most studies in high-energy physics, the average energy loss $\left\langle \frac{\mathrm{d}E}{\mathrm{d}x} \right\rangle$ in a given material can be described as a function of the particle velocity in units of speed of light, β, only.
An overview of the energy loss of a muon in copper is depicted in figure 5.1. The mass stopping

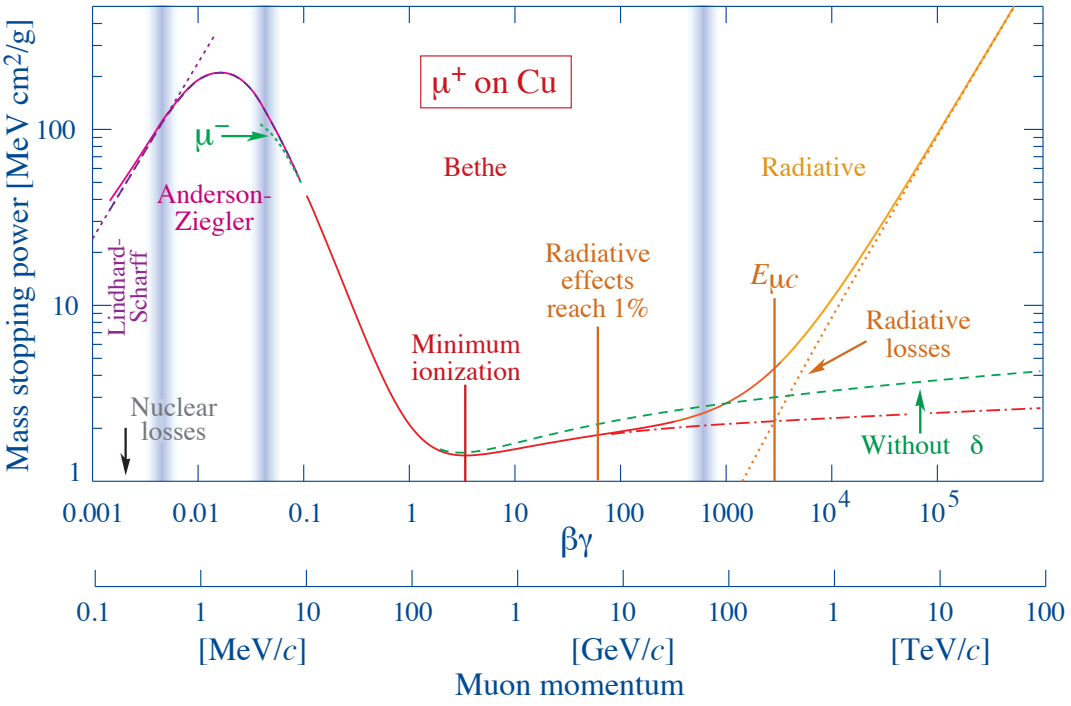

Figure 5.1.: Energy loss of a muon traversing copper as a function of the particle energy. The stopping power $-\left\langle \frac{dE}{dx} \right\rangle \frac{1}{\rho}$ for a medium energy range can be described by the Bethe-Bloch formula while for higher energies radiative effects dominate. Figure from [11].

power $-\left\langle \frac{dE}{dx} \right\rangle \frac{1}{\rho}$ is shown over a large range of particle energy as a function of $\beta\gamma = p/Mc$ whereby p and M are momentum and mass of the studied particle. ρ is the material density. For energies with $\beta\gamma > 0.05$, the energy loss can be described by the Bethe-Bloch formula until radiative losses become the most relevant process for $\beta\gamma \geq 1000$. An important quantity predicted by the Bethe-Bloch formula is the energy of a *minimum ionizing particle* (MIP). It is defined as the energy, at which the minimum energy loss for ionization processes occurs. In the region of the minimum with $\beta\gamma$ between approximately 2 and 100, the ionization losses of particles are only weakly dependent on their momentum. Most relativistic particles like muons in an air shower reaching the ground can be considered as MIP [11].

Due to its asymmetric shape with the extended tail towards high values, the mean energy deposition described by the Bethe-Bloch formula is not referring to the *most probable value* (MPV), μ_{mpv}, for the energy loss but states higher values.

The more adequate description for single particles crossing a moderate layer x of matter is therefore the Landau distribution (cf. figure 5.2) [11, 144]. It is expected, for example, that the number of photons, λ, emitted during a particle passage in a scintillator will follow the Landau distribution

$$p(\lambda) = \frac{1}{\pi} \int_0^\infty \mathrm{e}^{-t \log t - \lambda t} \sin(\pi t)\, \mathrm{d}t \quad . \tag{5.1}$$

The distribution is dominated by the fluctuations of the energy loss by particle ionization due to a small number of collisions. It is highly-skewed with a high energy tail theoretically extending to infinity. Thus, if the Landau distribution is integrated, the result is an infinite value. The degree of skewness increases with increased thickness of the material as well as the maximum of the distribution corresponding to the most probable value, μ_{mpv}.

Even if the Landau distribution should be able to describe the response of scintillator-based detec-

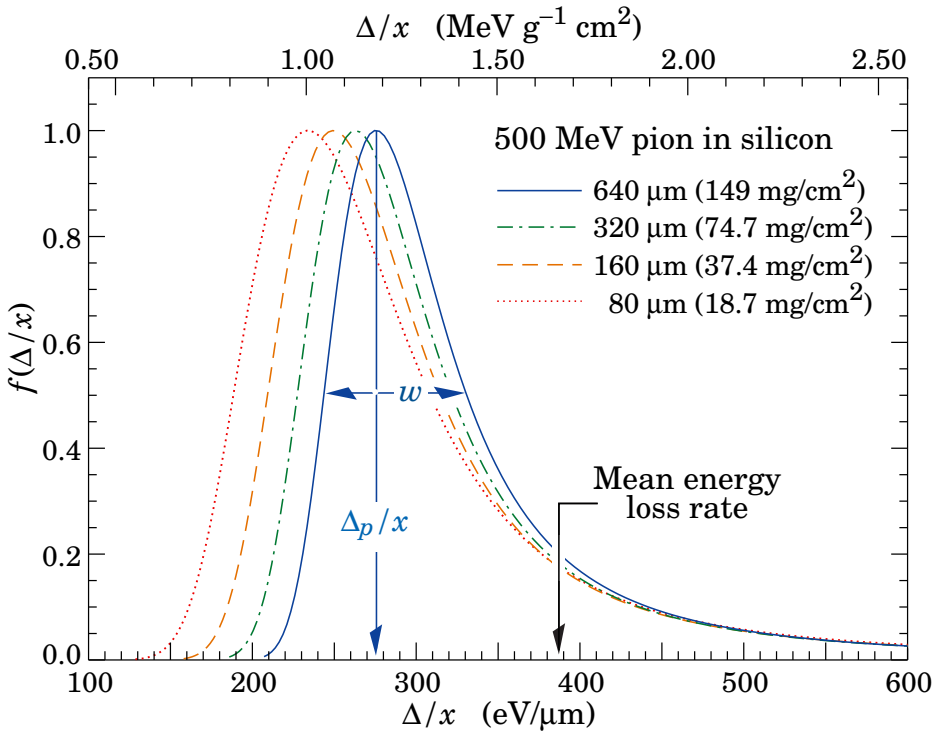

Figure 5.2.: Landau distribution describing the energy loss of a 500 MeV pion in silicon. Shown are several thicknesses of traversed matter x. The following important parameters are depicted for the distribution for a thickness of 640 μm, represented by a blue, solid line. The width w is the full width at half maximum. The left arrow marks the maximum energy loss Δ_p/x referring to the most probable value μ_{mpv} in the notation of this thesis, the right arrow marks the average energy loss described by the Bethe-Bloch formula. Figure from [11].

tors, often a convoluted Landau distribution with a Gaussian or Poisson distribution has to be used in a real experiment. Additional fluctuations by subsequent optical and detection components may conceal the pure Landau distribution.

5.2. Optical elements for particle detection

5.2.1. Scintillators

The sensitive volume of a scintillation detector is a luminescent material. Scintillators are widely used in various detector systems in the research fields of nuclear physics, high energy (astro-)particle physics, or nuclear medicine. The basic detection principle is the absorption of energy from traversing particles or radiation. The scintillation process is thus a special case of luminescence. A small part of the absorbed energy is then released by photons resulting is isotropic emitted light. Materials capable of scintillation are categorized into two basic groups, *organic and inorganic scintillators*, and can be in principle liquid, solid, and gaseous. As *plastic scintillators*, a subtype of organic scintillators, are subject of this thesis, only this type is discussed in the following. For a detailed overview of organic and inorganic scintillators please refer to [145, 146, 147].

Organic scintillators are characterized by extremely fast light signals of a few nanoseconds, allowing for pulse-shape discrimination. They are inexpensive and can be shaped as desired.

Due to their relatively low density in the order of 1.0 to 1.5 g/cm^3 [11], high energetic radiation and particles are usually not stopped in the material. The production of light in organic scintillators is based on the transitions in the energy level structure including vibrational sublevels of each molecule with delocalized π-electrons. The electron configuration allows singlet states S_j with spin 0 and triplet states T_j with spin 1. The ground state is referred to as $j = 0$ whereby triplet states have no ground state. Excited states are denoted by $j > 0$. When an ionizing particle (i.e. a muon) loses energy in the base material, a π-electron may get excited from the ground state S_0 to the first excited state S_1 or to higher modes. The additional energy is needed as an energy gap between two states is working as a barrier. The spacing between S_0 and S_1 is in the order of $3-4$ eV whereby the energy gap is strongly reduced for higher modes. The vibrational sublevels of each state differ by about 0.15 eV. As the average thermal energy at room temperature is already smaller than the energy gap between vibrational states, all molecules in the base material will populate the ground state. Following an excitation, a relaxation takes place over several energy levels, whereby transitions can take place without radiation. The energy is released by excitation of degrees of rotation or vibration of the molecule. A schematic overview of possible absorption and emission processes is shown in figure 5.3. Higher states as S_2, S_3, or vibrational sublevels de-excite quickly (in the order of picoseconds) to the S_1 state through radiationless transitions.
The emission of light is only initiated by a de-excitation or internal conversion of the S_1 state. Two possible mechanisms can be triggered. First, a de-excitation back into the ground state S_0 or to sublevels just above S_0 (cf. figure 5.3) takes place, which will emit fluorescence light ($\mathcal{O}$(ns)). This is the most prominent mechanism. Second, the conversion into a triplet state T_1 via an inter-system crossing occurs. The lifetime of the T_1 state is much longer than the lifetime of the S_1 state and can be in the order of $\mathcal{O}$(ms). A de-excitation from the excited T_1 state leads to the delayed emission of phosphorescence light. Also a thermally re-excitation from the T_1 state to S_1 is possible where again fluorescence light via a following de-excitation to the ground state would be emitted. As the energy difference of T_1 to S_0 is smaller than the energy difference of S_1 to S_0, the wavelength of the emitted phosphorescence photon is larger than the wavelength of the fluorescence light. The discrimination of phosphorescence from fluorescence light can thus be based on timing and wavelength.
The same principle allows organic scintillators to be almost transparent to their own fluorescence emission. All fluorescence emissions have a lower energy than the minimum required for further excitation. There is still some small overlap between emission and absorption spectra resulting in a shortened attenuation length. However, the emitted light mostly passes straight on through the scintillation medium. [148]
As a first approximation, for low radiation densities, the relation between light yield L and deposited energy E by a charged particle per unit length x would be linear with the scintillation efficiency ϵ_S of the studied material. With increasing density of traversing particles, the energy loss is regulated by recombination or quenching processes as e.g. non-radiative de-excitation processes. The intensity can then be described according to Birk's law [147]

$$\frac{\mathrm{d}L}{\mathrm{d}x} = \frac{\epsilon_S \cdot \frac{\mathrm{d}E}{\mathrm{d}x}}{1 + kB \cdot \frac{\mathrm{d}E}{\mathrm{d}x}} \quad , \tag{5.2}$$

whereby the influence by quenching is depicted by the Birk's constant kB. The constant is characteristic for the studied material and the traversing particle and has to be determined for each scintillator by measurement[1] [143]. All kind of ionizing particles from electrons up to heavier nuclei can be detected, even if not with the same efficiency. Deviations from the linearity due to

[1] whereby $B \cdot \frac{\mathrm{d}E}{\mathrm{d}x}$ depicts the density of excitation centers available in the medium along the trajectory of the particle and k is the quenching factor.

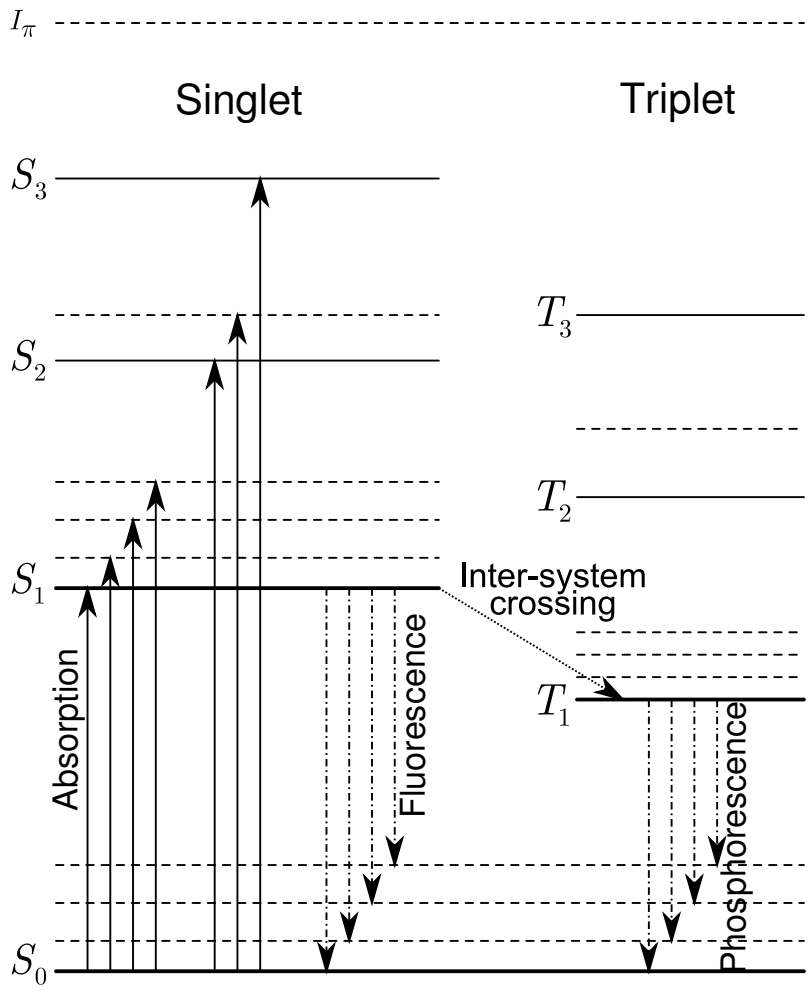

Figure 5.3.: Energy levels of a π-electron system of a single molecule in an organic scintillator. Dashed lines indicate vibrational sub-levels. The levels S_j denote singlet states, whereby S_0 indicates the singlet ground state and $j > 0$ are excited singlet states. De-excitation from the S_1 to the ground state S_0 results in fluorescence emission with a fast time constant. Triplet states T_j with $j > 0$ are populated via a non-radiative inter-system crossing from the excited singlet state S_1 as the direct transition is a spin-forbidden process. The de-excitation from a triplet to the singlet ground state results in phosphorescence emission. It has an enlarged time constant compared to the fluorescence emission. Modified, original figure from [147].

quenching effects e.g. are more pronounced for heavier and thus higher ionizing particles[2]. The performance of a scintillation device is mainly determined by its light output (i.e. the integration of equation (5.2) from the incoming-particle initial energy down to zero).

Plastic scintillators are a subcategory of solid organic scintillators. They consist of a plastic base material. In general, two different 'wavelength shifter' materials, commonly fluors, are added to the base material. A wavelength shifter is thereby characterized as a photofluorescent material that absorbs higher energy photons and emits lower energy photons. The base material of a plastic scintillator absorbs the energy of a traversing particle and emits typically fluorescence and phos-

[2]An increased ionization power will result in a higher density of excited molecules also increasing quenching effects. Thus, energy is carried away by interactions not resulting in luminescence.

phorescence photons in the ultra-violet (UV) wavelength regime with a short attenuation length $\mathcal{O}$(mm). First, a 'primary' fluor is dissolved into the base material. It allows for the absorption of the UV photons and the re-emission of photons with a wavelength shifting towards the visible spectrum regime and an increased attenuation length. By adding a second fluor, a shorter rise and decay time of the light output is achieved. Plastic scintillators allow for a reasonable cost per device and the use of complex scintillator shapes compared to e.g. inorganic scintillators. In return, a smaller light output and a higher probability of aging due to heat, UV light, or radiation damages are accepted. As a rule of thumb, the density of plastic scintillator material is about $1\,\mathrm{g/cm^3}$ and its photon yield about 1 photon per 100 eV deposited energy. Therefore, a 1 cm thick absorber yields about 2×10^4 photons if traversed by a MIP (e.g. a muon). Collection and transport efficiency of a complete detector system (from the scintillator to the photosensor) will reduce the light yield significantly.

When handling solid scintillator material, (cotton) gloves have to be worn all the time to avoid fingerprints on the surface as the body acid may cause the cracking of the plastic. These microcracks degrade the transmission of light by total internal reflection. Furthermore, performing, for example, a wrapping process in a clean room is highly advisable since the scintillators are electrostatically charged after removing their protective foil and therefore attract dust easily.

5.2.2. Reflective materials

Produced light in a scintillator will be contained to a high degree in the material due to total internal reflection at the border of the scintillator to the surrounding air. However, as detector parts (e.g. tiles or bars) made of scintillator have a large surface area, the loss of light at the edges and plain areas of those parts will occur, especially at contact areas with other material than air. To reduce theses losses and to prevent crosstalk between parts (if used in the same assembly), highly reflective materials are used to guide the light back into the detector medium. There are several reflectance materials common for *wrapping* or painting of scintillators. Diffuse reflector paint is provided by several manufacturers of scintillator like Saint Gobain (e.g. BC-620 [149]) or Eljen Technology (e.g EJ-510 [150]). It is composed of titanium dioxide pigments and a water soluble base building a bright white paint. Compared to painting, wrapping by hand of individual scintillator parts is both time consuming and difficult to do consistently, but is removable. It has to be performed in several layers to allow a full coverage of the surface and sufficient reflectance efficiency. As diffusive reflective wrapping material Polytetrafluorethylen (PFTE) or *Tyvek* can be used.
Tyvek is a synthetic material composed of high-density polyethylene fibres. It is provided as flexible but strong sheets. PTFE tape, also known under trademark *Teflon*, is available in various designs as threaded or plumbers tape and is normally used for sealing in gas and water systems. During studies presented in [151], no significant differences between the BC-642 PTFE reflector tape of Saint Gobain [152] and standard thread tape have been found. The wrapping with PTFE tape is more time consuming and challenging as for Tyvek sheets, as the tape is elastic. It stretches and due to its smooth surface it easily moves and creeps. It has to be wrapped with enough tension to avoid air inclusions between the scintillator and the tape if a reproducible wrapping procedure for detector parts is required.
Reflective foils provide specular reflectance. *Aluminum foil* or *reflective 'mirror' foil* with increased reflectance efficiency as the Enhanced Specular Reflector (ESR) films by 3M [153] are commonly used.
A study of the optical reflectance of several described reflectors has been performed in [154]. The angular distribution or relative light intensity as a function of the reflectance angle θ for Teflon and aluminum foil can be found as examples in figure 5.4 for different incidence angles. The

Reflector	relative reflection coefficient ± standard deviation
Teflon (4 layers)	1.000 ± 0.006
Teflon (3 layers)	0.992 ± 0.004
Tyvek paper	0.979 ± 0.004
Titanium dioxide paint	0.951 ± 0.003
ESR foil	0.944 ± 0.013
Aluminum foil	0.787 ± 0.014

Table 5.1.: Average reflection coefficients of commonly used optical reflectors for incident angles between 14° and 78°. Values are normalized to results of four layers of Teflon. Taken from [154].

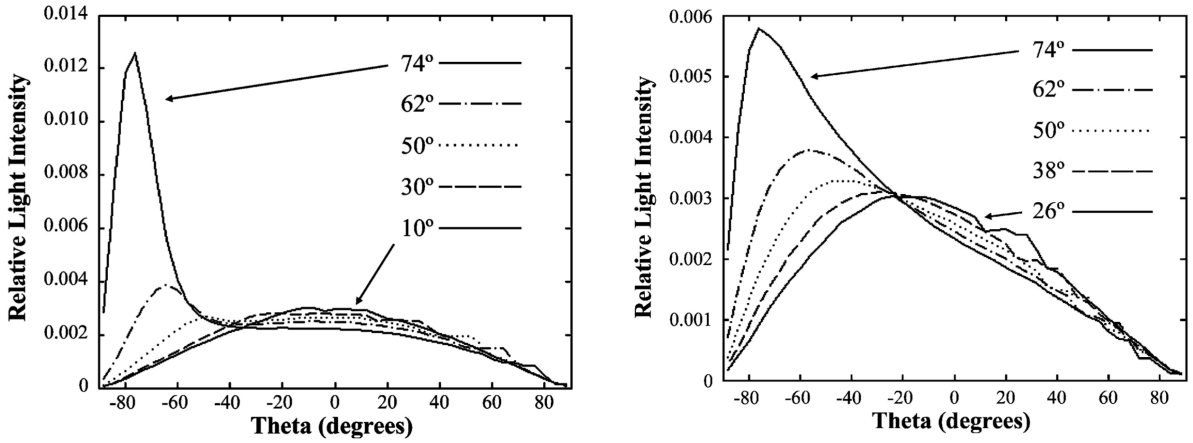

(a) Three layers of PTFE tape. Angular distribution refers to a diffuse reflector.

(b) Aluminum foil. Angular distribution refers to a specular reflector as the reflectance angle distribution corresponds to its corresponding incidence angle.

Figure 5.4.: Reflectance angular distribution profile. Shown are measurements of PTFE and aluminum foil for incidence angles of 10°, 30°, 50°, 62° and 74° for phi equal to 0°. Taken from [154].

different responses for material with dominating specular (aluminum foil) and diffusive (PTFE tape) reflections are visible. PTFE tape can be described as a pure Lambertian light distributor. Tyvek shows a complicated behaviour, neither fitting specular nor diffuse reflectors nor linear combination of both. Also the relative reflection coefficients were determined with respect to four layers of Teflon. A selection of materials is shown in table 5.1. All materials except aluminum foil show similar high reflection coefficients.

5.2.3. Optical fibres

Optical fibres can be used to collect light in optical detector elements. In physics three basic fibre types are commonly used: *Optical waveguides*, *wavelength shifting* and scintillation fibres. The first one provides only the guidance of light from the outside over long distances while the two latter include the emission of light in the fibre material. The basic components of all fibre types are a *core* and its *cladding(s)*. The cladding provides light guidance as having a lower refractive index than the core material. To reduce light losses, thus improving the light yield of the fibre, a further

cladding may be added with an even lower refractive index. Fibres with at least two claddings are referred to as multiclad fibres. Optical fibres used in physics have commonly diameters of $\mathcal{O}(1\,\mathrm{mm})$ whereby the thin cladding layers have a thickness of a few percent of the fibre diameters. Optical fibres are available with a round or a square cross-section. The core of an optical fibre is made of polystyrene (PS), while the claddings consist of polymethylmethacrylate (PMMA, inner cladding) and fluorinated polymer (FP, outer cladding) [155, 156]. As in this thesis only round fibres are studied, square fibres are not discussed here. For a general overview about fibre optics please refer to [155, 156].

As the photon wavelengths for optical fibres are in the visible spectrum, they are small compared to the dimensions of the fibre. The description of important optical processes as the guidance of the photons within fibres can be described by means of geometrical optics. Therefore, basic principles applied to fibres are introduced in the following. These principles are valid for all optical fibre types.

5.2.3.1. Total internal reflection

The transit or deflection of a photon at the border between two media can be described according to Snell's law

$$n_1 \cdot \sin(\theta_{\text{in}}) = n_2 \cdot \sin(\theta_{\text{out}}) \tag{5.3}$$

$$\Leftrightarrow \cos(\theta_{\text{out}}) = \sqrt{1 - \left(\frac{n_1}{n_2} \cdot \sin(\theta_{\text{in}})\right)} \tag{5.4}$$

$$\Leftrightarrow \theta_{\text{out}} = \arcsin\left(\frac{n_1}{n_2} \cdot \sin(\theta_{\text{in}})\right) \quad , \tag{5.5}$$

whereby n_1 and n_2 denote the refractive indices of the two media. θ_{in} and θ_{out} are the incidence and refraction angle, respectively. The angles are formed between the ray of light and the normal point of incidence or exit to the surface. The law describes three cases assuming $n_1 > n_2$. First, the ray is refracted inside the second medium. Second, the ray is deflected with a direction along the boundary. Third, the ray is reflected back and will stay in the first medium. The latter phenomena is called *total internal reflection* (TIR).
The critical angle for total internal reflection, α_{TIR}, is given by

$$n_1 \cdot \sin(\alpha_{\text{TIR}}) = n_2 \cdot \sin(90\,^\circ) \tag{5.6}$$

$$\alpha_{\text{TIR}} = \arcsin\left(\frac{n_1}{n_2}\right) \quad . \tag{5.7}$$

The angle is also defining the maximum acceptance angle α_{max} of a fibre. The full acceptance angle is defined as the maximum allowable input angle for each optical fibre and is directly related to the *numerical aperture* (*NA*) specification. The *NA* of a fibre is thus a number that defines its light gathering capability. A larger *NA* corresponds to a larger acceptance angle.
The *NA* of a *singleclad fibre* can be calculated from the index of refraction values for the fibre core (n_{core}), the fibre cladding (n_{cladding}) and the ambient material n_{ambient} whereby often $n_{\text{ambient}} \approx n_{\text{air}} = 1$

$$NA = n_{\text{ambient}} \sin(\alpha_{\text{max}}) \tag{5.8}$$

$$= n_{\text{core}} \sin(90\,^\circ - \alpha_{\text{TIR}}) = n_{\text{core}} \cos(\alpha_{\text{TIR}}) \tag{5.9}$$

$$= \sqrt{n_{\text{core}}^2 - n_{\text{cladding}}^2} \quad . \tag{5.10}$$

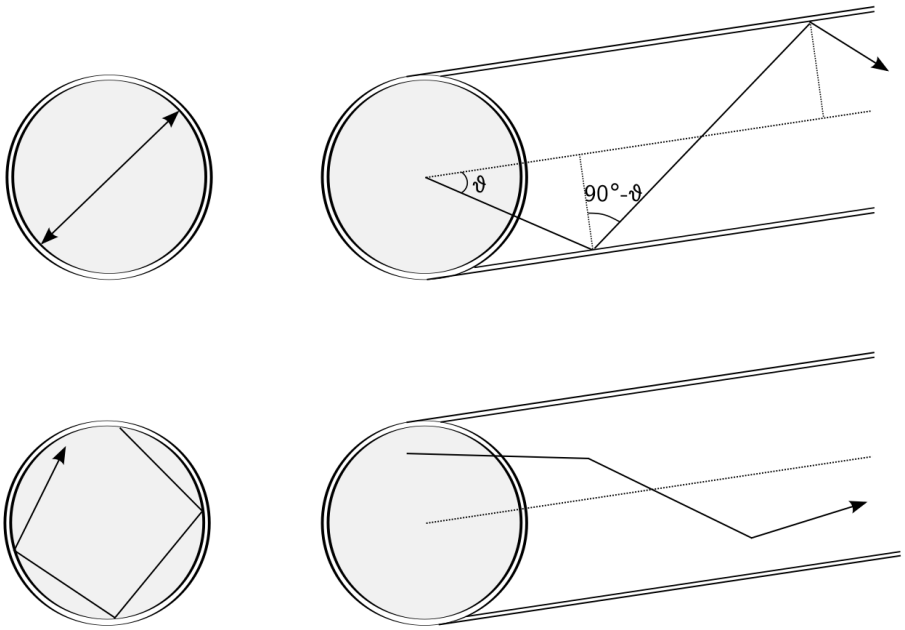

Figure 5.5.: Exemplary particle paths in a round multiclad fibre for meridional (top) and skew (bottom) light rays. Meridional rays propagate inside a constant plane crossing the fibre axis while skew rays spiral along the fibre axis but do not cross it. Figures adopted from [157].

The output beam of a fibre would also be scattered according to its numerical aperture. Thus, optical fibres do not produce beam-like outputs, but rather quickly diverging cones of illumination. However, due to symmetry principles in fibre optics, the output angle of a fibre is approximately the same as the input angle, even if the input angle is lower than the maximum acceptance angle. For a *multiclad fibre* an additional cladding is introduced influencing the ray paths within a fibre. The numerical aperture of a multiclad fibre is limited by the maximum angle captured by the second cladding. It is defined by

$$\sin(\alpha_{\text{max, multiclad}}) = \arcsin\left(\sqrt{n_{\text{core}}^2 - n_{\text{cladding2}}^2}\right) > \arcsin\left(\sqrt{n_{\text{core}}^2 - n_{\text{cladding1}}^2}\right) \quad . \tag{5.11}$$

The additional layer therefore increases the numerical aperture of a fibre and allows for larger input (and exiting) angles.
In general, in a real optical setup also larger angles are allowed. There are a specific number of ray paths that can efficiently propagate through a fibre. The ray paths can be grouped as *meridional* and *skew* rays (cf. figure 5.5). Meridional rays cross the fibre axis along their trajectory through the fibre. They will leave the fibre at any point of the end cross section. The numerical aperture calculation presented is valid for meridional paths.
Skew rays spiral along the fibre axis but do not cross it. They allow for larger exit angles than meridional rays. As traveling far away from the fibre axis, they strongly contribute to the distribution of exit angles towards the outer region of the fibre. Their spiral propagation prolongs the way needed for traversing the same distance in the fibre material compared to meridional rays. Due to attenuation effects, the fraction of skew rays may be strongly reduced for increased traversed fibre lengths.

5.2.3.2. Fresnel equations

Predictions of the behaviour of light when moving between media of differing refractive indices can be extended by the Fresnel equations.
The polarization of the light has a high impact on the fraction of light which is refracted given by the *transmission T* and which is reflected given by the *reflection coefficient R*. Two polarizations exist

1. s-polarized light, where the E-field is perpendicular to plane of incidence and
2. p-polarized light, where the E-field is parallel to plane of incidence.

Assuming unpolarized light[3], the combined reflection coefficient R can be calculated by

$$R = \frac{R_s + R_p}{2} \quad . \tag{5.12}$$

The reflection coefficients R_s for s-polarized light and R_p for p-polarized light at a boundary between two media with refractive index n_1 and n_2 are thereby given by

$$R_s(n_1, n_2, \theta_{\text{in}}) = \left| \frac{n_1 \cos(\theta_{\text{in}}) - n_2 \cos(\theta_{\text{out}})}{n_1 \cos(\theta_{\text{in}}) + n_2 \cos(\theta_{\text{out}})} \right|^2 = \left| \frac{n_1 \cos(\theta_{\text{in}}) - n_2 \sqrt{1 - \left(\frac{n_1}{n_2} \cdot \sin(\theta_{\text{in}})\right)}}{n_1 \cos(\theta_{\text{in}}) + n_2 \sqrt{1 - \left(\frac{n_1}{n_2} \cdot \sin(\theta_{\text{in}})\right)}} \right|^2 \tag{5.13}$$

and

$$R_p(n_1, n_2, \theta_{\text{in}}) = \left| \frac{n_1 \cos(\theta_{\text{out}}) - n_2 \cos(\theta_{\text{in}})}{n_1 \cos(\theta_{\text{out}}) + n_2 \cos(\theta_{\text{in}})} \right|^2 = \left| \frac{n_1 \sqrt{1 - \left(\frac{n_1}{n_2} \cdot \sin(\theta_{\text{in}})\right)} - n_2 \cos(\theta_{\text{in}})}{n_1 \sqrt{1 - \left(\frac{n_1}{n_2} \cdot \sin(\theta_{\text{in}})\right)} + n_2 \cos(\theta_{\text{in}})} \right|^2 \quad , \tag{5.14}$$

where θ_{in} and θ_{out} are the incidence and exiting angle.
As a consequence of the conservation of energy, the combined transmission can be calculated via

$$T = 1 - R \quad , \tag{5.15}$$

whereby the transmission coefficients are also defined by $T_{s,p} = 1 - R_{s,p}$.

For a real detector setup, which studies the light transmission from a WLS fibre to a light guide or from an optical fibre to a light sensor, often a small air gap between those components has to be considered. Therefore, the Fresnel equations have to be extended to a multilayer calculation depending on the refractive indices n_1, n_2, n_3 of the considered materials and on the incident angle θ_{in} on the exit surface of the fibre. The transmission coefficients T_{ij} refer to the transmission from material i to material j.
To first order, the transmission from the first to the third medium will be a product of the transmission of the considered materials

$$T_{13}^{\text{1st order}}(\theta_{\text{in}}) = T_{12}(\theta_{\text{in}}) T_{23}(\theta_{\text{out}}) \quad . \tag{5.16}$$

The angle θ_{out} corresponds to the angle after the transmission from the first to the second medium. As multiple layers are involved, higher orders of transmission processes are possible. A light ray may

[3] containing an equal mix of both polarizations

leave the first medium but will be reflected at the boundary from the second to the third medium. If the ray is reflected back again from the boundary from the second medium to the first medium, there is a chance to enter nevertheless the third medium. This leads to a next ordering process

$$T_{13}^{\text{2nd order}}(\theta_{\text{in}}) = T_{12}(\theta_{\text{in}})R_{23}(\theta_{\text{out}})R_{21}(\theta_{\text{out}})T_{23}(\theta_{\text{out}}) \quad . \tag{5.17}$$

Even higher orders of reflections back and forth between the boundaries are possible but become unlikely. The transmission including the inner-boundaries reflections can be described by means of an infinite geometric series and is given by

$$T_{13}^{\text{higher orders}}(\theta_{\text{in}}) = T_{12}(\theta_{\text{in}})\left[\sum_{i=0}^{\infty}(R_{23}(\theta_{\text{out}})R_{21}(\theta_{\text{out}}))^i\right]T_{23}(\theta_{\text{out}}) \tag{5.18}$$

$$= \frac{T_{12}(\theta_{\text{in}})T_{23}(\theta_{\text{out}})}{1-R_{23}(\theta_{\text{out}})R_{21}(\theta_{\text{out}})} \quad , \tag{5.19}$$

while neglecting light rays leaving the inner-boundary region at the fibre edges.
Therefore, air gaps between individual fibres result in transmission losses. Exemplary, a thin air gap introduced between the WLS fibre ($n_{\text{WLS}} = 1.60$) and an optical waveguide ($n_{\text{optical}} = 1.49$) results in the loss of half of the light if a uniform angular distribution is assumed. Mostly, as the maximum transmitted angle θ_{in} is reduced from 68° to 39°.

Attenuation

In an optical fibre, several more effects may cause a reduction of the light intensity along the fibre. For example, assuming a bending of the fibre in a detector setup, the change in orientation of the boundary seen by the ray paths may introduce light losses if the incident angle of light rays exceeds the critical angle of internal total reflection. In addition, mechanical damages to either the core or the cladding can be caused. Therefore, the bending radius of the fibre has to be carefully decided.

Furthermore, absorption losses may be caused by impurities in the fibre material and microscopic cracks in the claddings due to heat or freeze, or losses due to scattering may occur. The attenuation curve is commonly approximated by an exponential expression

$$I(x) = I_{\text{in}} \cdot \exp\left(-\frac{x}{d_{\text{att}}}\right) \quad , \tag{5.20}$$

with d_{att} being the attenuation length [155, 156]. The effective attenuation length provided by manufacturers are typically in the range of few meters for wavelength shifting fibres and is strongly increased for light guides. The effective attenuation length describes an average over all occurring light paths in the fibre. Additionally, transmission losses are wavelength dependent. This results in a change of the emission spectrum as a function of the fibre length. This change is characteristic for each specific fibre type and has to be determined by measurements.

Wavelength shifting fibres

Wavelength shifting fibres (WLS fibres) are a special case of optical fibres with a core serving as wavelength shifter. WLS fibres are a common technology in high-energy and astroparticle physics. For example, they are used as low-cost optical component in calorimeters and for the readout of scintillators. If a particle traverses the fibre core, it may get absorbed. The re-emitted photon is isotropically distributed and wavelength shifted. The standard wavelength shifting fibres are blue-to-green shifters. Due to the wavelength-shifting, the re-emitted photon may be trapped inside the

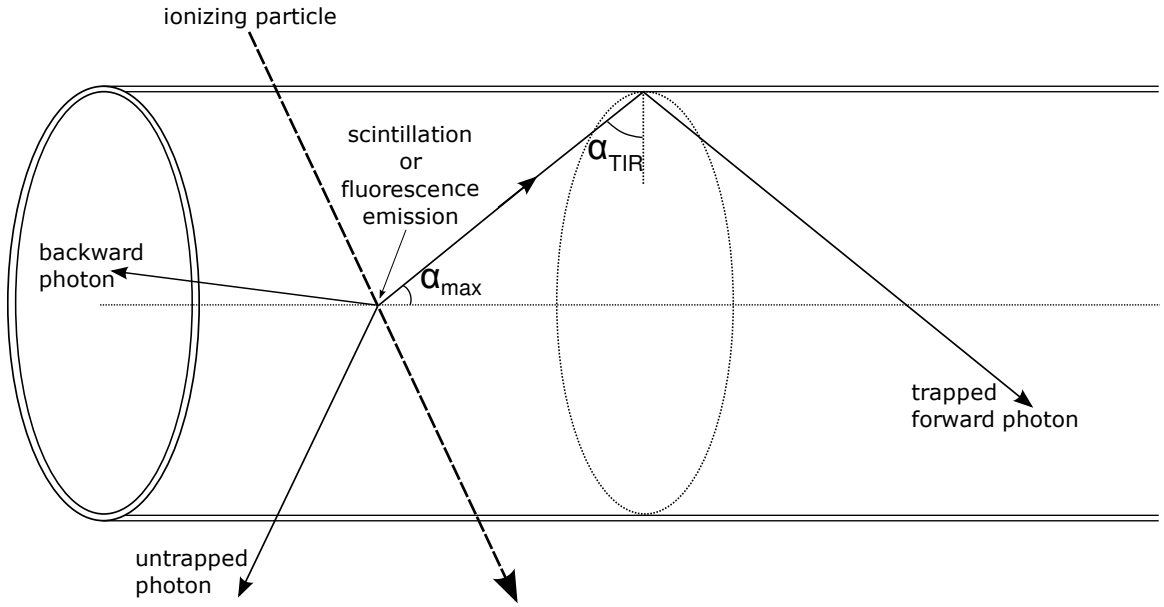

Figure 5.6.: Exemplary particle path in a multiclad fibre wavelength shifting fibre. A multiclad fibre is composed of a core and multiple claddings. Shown is in lateral view an exemplary path of a photon produced in the core region of the fibre by a traversing particle. The re-emitted photons may be contained in the fibre if having an angle $< \alpha_{\mathrm{TIR}}$ for the respective boundaries. Dimensions are not to scale.

fibre. Photons emitted in a direction smaller than the angle of total internal reflection α_{TIR} of the boundaries[4] will be captured and guided towards the fibre ends, where they can be detected. Figure 5.6 illustrates a particle crossing the fibre core, getting absorbed and re-emitting photons. The re-emitted, wavelength shifted photons may propagate within the fibre.
Additionally to the characteristics of optical fibres already discussed, the *trapping efficiency* is an important quantity of a WLS fibre. Besides the already mentioned losses due to attenuation or bending effects of captured photons, the *trapping efficiency* $\epsilon_{\mathrm{trap,axis}}$ describes the capability to capture created light in the WLS (or scintillation) fibre. It depends on the critical angle for total internal reflection at the boundary from the fibre core to the claddings. Assuming that all photons are emitted isotropically along the fibre axis and the boundaries have a perfectly smooth surface, the trapping efficiency can be described by

$$\epsilon_{\text{trap, meridional, forward}} = \frac{1-\cos(\alpha_{\max})}{2} = \frac{1}{2}\left(1-\frac{n_{\text{cladding}}}{n_{\text{core}}}\right) \approx \frac{\alpha_{\max}^2}{4} \tag{5.21}$$

with the maximum acceptance angle $\alpha_{\max} = 90^\circ - \alpha_{\mathrm{TIR}}$. Here, n_{core} and n_{cladding} are the refractive indices of the core and the (outer) cladding, respectively. In this calculation only photons on meridional ray paths emitted into one hemisphere, i.e. with angles $0^\circ < \theta < 90^\circ$ relative to the direction of the fibre axis, are taken into account [158].
In round fibres, the trapping efficiency also depends on the distance between the fibre axis and the event creating a WLS photon. Indeed, only an infinitesimal fraction of the light will be directly

[4] as from core to the inner cladding, the inner cladding to the outer cladding, or the outer cladding to the ambient material (often: air)

emitted along the fibre axis. It can be shown that the trapping efficiency of skew ray paths can be described by [158]

$$\epsilon_{\text{trap, skew, forward}} = \frac{(1-\cos(\alpha_{\text{max}}))\cos(\alpha_{\text{max}})}{2} \quad , \tag{5.22}$$

leading to a total trapping efficiency for forward propagating photons of [158]

$$\epsilon_{\text{trap, total, forward}} = \frac{1-\cos(\alpha_{\text{max}})^2}{2} = \frac{1}{2}\left(1-\left(\frac{n_{\text{cladding}}}{n_{\text{core}}}\right)^2\right) \approx \frac{\alpha_{\text{max}}^2}{2} \quad . \tag{5.23}$$

The trapping efficiency stated by manufacturers defines a minimum value achievable and is in the order of $3-5\%$ for common WLS fibres. The trapping efficiency of a complete detector setup may differ as the particle distribution traversing the WLS fibres has an impact. A more realistic efficiency has thereby to be studied by measurements or simulations.

Fibre preparation

The quality of the fibres is one of the factors which essentially determines their light yield. Optical fibres should be carefully handled to avoid microcrackings by mechanical damages or by body acid due to handling fibres with bare hands. A major challenge encountered while working with optical fibres is achieving a clean and undamaged fibre end surface. Several processes are available. Excellent results can be achieved by CO_2 laser cutting as it provides a smooth optical surface while avoiding damages of the fibre material. However, the procedure is cost-intensive and has to be performed by an external company. Other approaches are based on the polishing of the fibre end by mechanical polishing or by heat. These approaches may result in minor core and cladding damages but provide sufficient light yield for most of physical applications. The chosen procedure in this thesis is based on the cutting of the fibre with a sharp scalpel blade with subsequent polishing of the fibre end. The fibre is thereby fixated in an acrylic glass block. The block has four bores matching the diameter of the chosen fibres to allow the polishing of four fibres at the same time. The polishing procedure has three steps with emery paper in several degrees of fineness, and is demonstrated in figure 5.7.

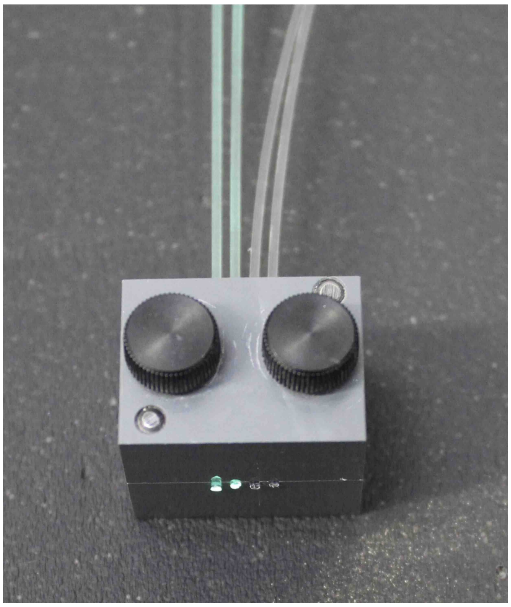

(a) The acrylic block holds two unpolished WLS fibres and two optical waveguides in place.

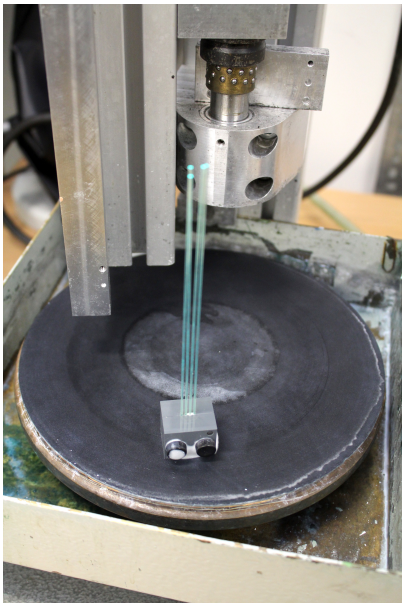

(b) The mechanical apparatus to polish fibre ends with wheels providing different states of granularities.

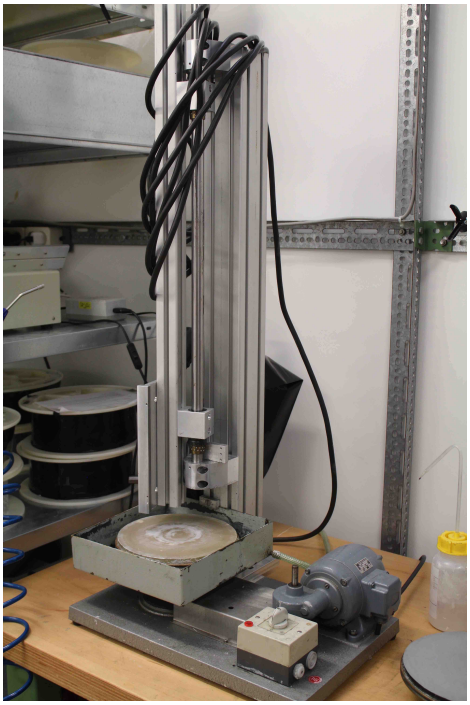

(c) The acrylic block is located on the polishing wheel with finest granularity.

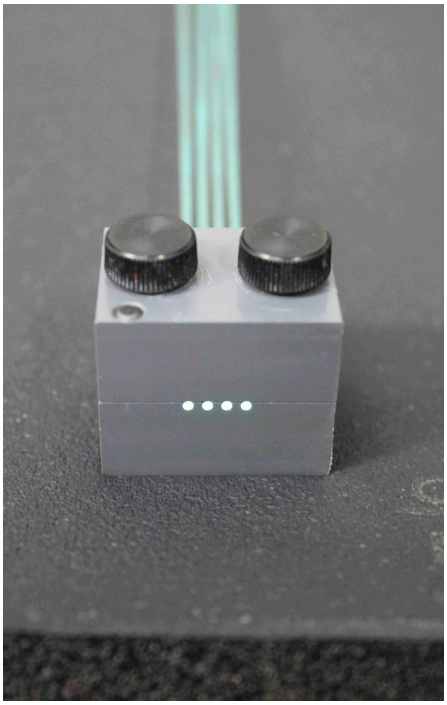

(d) The acrylic block contains four polished WLS fibres. A homogenous surface has been achieved. However, the outer cladding may be still damaged after polishing.

Figure 5.7.: Photos of the polishing procedure of WLS fibres and optical waveguides, as applied by the mechanical workshop of the Physics Institute III A of the RWTH Aachen University. An acrylic block allows a fixed position of up to four fibres while polishing. The fibre ends have been cut by a sharp scalpel blade. An apparatus uses polishing wheels with different granularities (used in steps from coarse to fine) to achieve a homogeneous and flat surface of the fibre ends.

CHAPTER 6

A scintillator-based particle detector unit with SiPM readout

The optical detector components presented in chapter 5 are commonly used in combination for the detection of ionizing particles. First, a traversing particle produces light in a *scintillator* along its trajectory. The light is emitted isotropically. While having finite scintillator dimensions, light has to be reflected back into the medium by reflective *wrapping* materials if leaving the scintillator. The light can be directly read out by a *light sensor*, but due to its isotropic distribution only a fraction of light will arrive at the sensitive area of the sensor. Therefore, *wavelength shifting fibres* (WLS fibres) are commonly used to collect the light and to guide it onto the light sensor. The capturing of light is allowed by the re-emission of photons with an increased wavelength[1] compared to the entering photon which has been absorbed in the inner core of the fibre[2]. The WLS fibre is embedded in the scintillator material. It covers the complete area of the scintillator tile which allows for a higher light yield and a more homogeneously distributed light collection efficiency than a direct coupling of a light sensor to the scintillator tile.
In this thesis, a scintillator-based detector with *silicon photomultipliers* (SiPMs, cf. chapter 4) as light sensors has been designed for the detection of atmospheric muons and of the muonic component of air showers initiated by ultra-high energy cosmic rays. The design of the detector is aiming to explicitly exploit the advantages of SiPMs like their high *photon detection efficiency* (PDE) but also their low cost per device, allowing a multi-channel detector.
The presented work in this thesis will be based on a detector comprising several scintillator tiles, each having a WLS fibre collecting the scintillation light. Each tile is connected to its own light sensor, a SiPM. One ***detector unit*** consists of these three optical components if referred to in the following. The design and response from a single unit to single particles will be studied in detail by Monte Carlo simulations and measurements in the first part of this thesis. The simulation and tracking of produced photons in all optical components, from scintillator tile to photosensor, allows to improve the understanding of the complex signal behavior in the detector (cf. chapter 7), while the effect of particular properties of these components can be estimated and cross-checked by measurements (cf. appendices I and J). The main design goal is thereby an excellent light yield

[1] commonly shifted from blue to green wavelength regime
[2] In the scope of this thesis, the wavelength-shifting process does not aim to improve the compatibility of the WLS fibre emission spectrum with the photon detection efficiency of the light sensor, but is only used for light collection purposes.

and signal-to-noise ratio. This allows for the determination of the number of impinging particles while no energy or time resolution is required. The materials and detector components studied are introduced in chapter 5.
After the optimization of the unit layout, the arrangement of several units in a complete detector setup will be studied. The chosen design is, due to its modular shape, highly flexible and easy to enlarge. During this thesis, a demonstrator, called ***MiniAMD***, has been assembled and tested, proving the capability of measuring air showers by this detection technique (cf. chapter 9). As the choice of a detector setup severely depends on the physical question posed, the response of a possible future large scale experiment, based on the studied single unit layout, will be further discussed by means of air shower simulations in the last part of this thesis (cf. chapter 10).
Besides the detector layout also the choice of the readout electronics depends on the intended purpose. The chosen electronics used in the course of this thesis is introduced in the last part of this chapter.

6.1. Unit baseline design

In the following, the applied materials of two realized unit layouts used for studies of the detection technique and used in demonstrators are introduced (cf. figure 6.1). Further configurations have been studied by means of simulations and will be subject of discussion in the following chapter 7.

The dimensions of the scintillator tile are 30 cm × 30 cm × 0.5 cm and have been chosen due to several reasons. First, previous studies within the RWTH Aachen University have proved similar tile dimensions [151] as excellent choice for particle detection supported by the simulation studies presented in this work. Secondly, the chosen readout electronics provide 32 channels, so that 32 units building one detector module would provide 2.88 m^2 as reasonable detection area for a station in an air shower experiment. However, a realistic module will be larger including also dead space between tiles needed for routing of cables. To cover, for example, the complete footprint of a water Cherenkov detector (WCD) station at the Pierre Auger Observatory, a detector size of around 10 m^2 would be needed. Two detector modules with 32 units each could be combined. This allows for a simultaneous detection of air showers in combination with the already installed WCD stations while covering a large part of the WCD station. As scintillator material, the EJ-212 plastic scintillator from Eljen Technology [159] has been chosen. Due to the relatively small thickness of the scintillator tile, the manufacturer recommended this material as it offers the best stability for large, but relatively thin tiles. Alternatively, the EJ-200 plastic scintillator from Eljen Technology [160] may be used for thicker tiles as the material is also commonly used for detectors based on scintillators and wavelength shifting fibres. The refractive index of EJ-212 is $n_{\mathrm{scint}} = 1.58$. The scintillation efficiency is stated as $\mathrm{d}N_{\gamma,\,\mathrm{scint}}/\mathrm{d}E \approx 10,000\,\mathrm{photons/1\,MeV}$ energy deposit by an electron per 1 cm path length. Its time response is relatively fast with rise and decay time constants of $\tau_{\mathrm{rise}} = 0.9\,\mathrm{ns}$ and $\tau_{\mathrm{decay}} = 2.4\,\mathrm{ns}$, respectively. The wavelength of maximum emission is 423 nm. For a detailed overview about important characteristics of the scintillator material please refer to appendix G.

To allow for a longer confinement of the light emitted in the scintillator and to provide a protection against crosstalk between units, a hand-made wrapping by two layers of Tyvek and two further layers of commercial aluminum foil is applied. Tyvek is a highly efficient Lambertian reflector. Aluminum foil offers a cost-effective additional, even if not highly efficient, specular reflection back of scintillation light into the tile and a protection against ambient light from the outside.

The scintillation light is collected by a wavelength shifting fibre embedded into a sigma-shaped

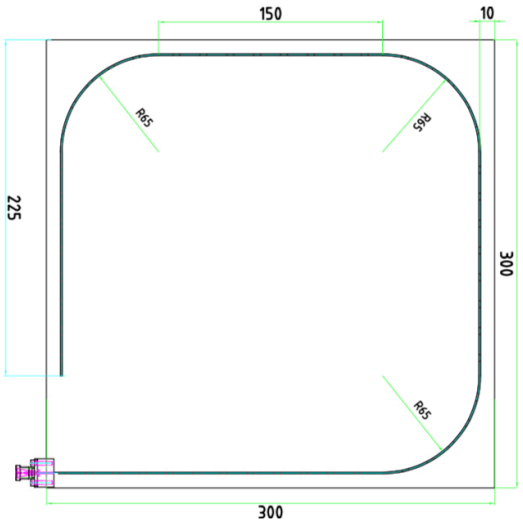

(a) Unit layout 1. Technical drawing including dimensions given in mm. The WLS fibre is located inside the tile in a sigma-shaped groove. The fibre is glued into the groove along its entire length. The Hamamatsu SiPM type S12571-050P with an active area of $1 \times 1\,\mathrm{mm}^2$ is used.

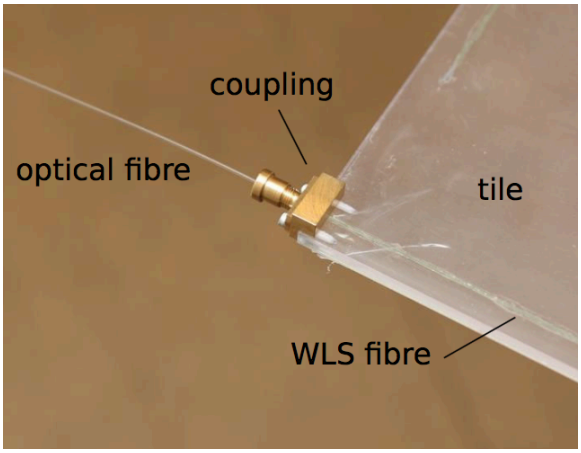

(b) Photo of the mechanical coupling of unit layout 1. The WLS fibre is coupled to an optical waveguide by a mechanical mounting structure. The clear waveguide transports the light to a SiPM located at a SiPM carrier board. The board is not connected to the tile but close to the readout electronics. Eight SiPMs are read out by one common board.

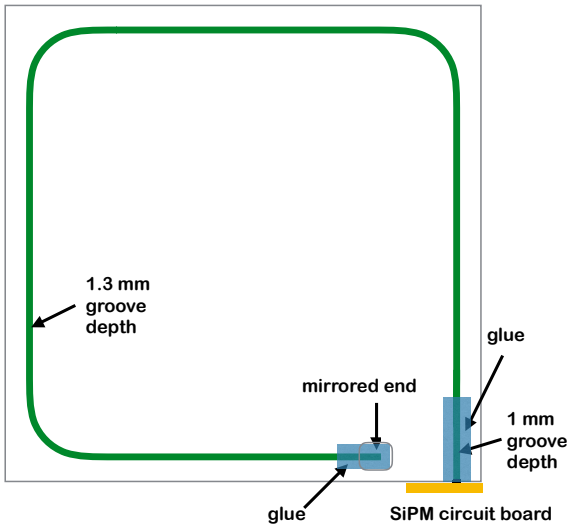

(c) Unit layout 2. The WLS fibre is directly coupled to the SiPM located at a carrier board screwed onto the tile. The carrier board provides also a temperature sensor. The analogue signal of each SiPM is guided by longer cables to the common readout electronics. The low noise Hamamatsu SiPM type S13360-1350PE with an active area of $1.3 \times 1.3\,\mathrm{mm}^2$ is used.

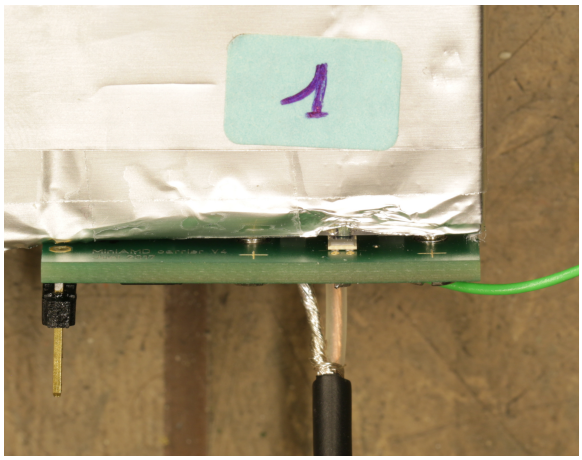

(d) Photo of the SiPM circuit board connected to the scintillator tile of unit layout 2. The WLS fibre is positioned within the active SiPM area. Two spacers, one located at each side of the SiPM, provide a stable and horizontal coupling between SiPM and scintillator tile edge. The circuit board is fixed to the tile by two screws. Three connectors are located on the circuit board.

Figure 6.1.: Sketches of two realized unit configurations. The scintillator tile of type EJ-212 comprises dimensions of $30\,\mathrm{cm} \times 30\,\mathrm{cm} \times 0.5\,\mathrm{cm}$. A wavelength shifting (WLS) fibre is embedded in a sigma-shaped, milled groove. The WLS fibre of type BCF-92 has a diameter of 1 mm, a distance to the tile edge of 10 mm and a bending radius of 65 mm at each corner. The surface of the fibre ending in the scintillator material is mirrored by a reflective material.

groove milled into the tile. Thus, one end of the fibre is located in the scintillator material while the other end is outside of the tile guiding the light onto the photosensor. The sigma-shaped design has been chosen to allow for a maximum fibre length in the material to collect as many photons as possible. Losses due to strong bending of the fibre and the needed SiPM sensor size are kept at a minimum. Using a small SiPM sensitive area allows for low noise and high PDE solutions which are preferred for this thesis. The typical diameter of fibres ranges between $1-2\,\mathrm{mm}$ which can be covered by a small, matching SiPM active area. If more than one fibre end is leaving the tile, multiple SiPMs or a larger SiPM size would be needed. Both alternatives would increase the noise rate but may also increase the light collection efficiency. Furthermore, multiple SiPMs would result in the need of more readout channels. For the chosen unit layout in this thesis, the solution of only one fibre end connected to one SiPM with an active area matching the diameter of the WLS fibre has been selected.
The WLS fibre applied is of type BCF-92, which is a fast blue-to-green shifter from Saint Gobain [161]. It has a a round shape with diameter of 1 mm. A multiclad fibre type has been chosen with a polystyrene core with refractive index of 1.60 and two claddings. The first cladding is made of Acrylic, has a thickness of 3% of the fibre radius and a refractive index of 1.49. The second cladding is made of Fluor-acrylic with a thickness of 1% of fibre diameter providing the lowest refractive index of 1.42. A detailed overview about important characteristics of the used WLS fibre type is given in appendix G. No minimal bending radius is given in the specifications of the fibre types of Saint Gobain but the manufacturer Kuraray proposes for similar WLS fibre types minimum bending radii of about $\gg 50\,\mathrm{mm}$ for long term usage [155] with an exponential increase of bending losses for smaller radii[3]. The position of the fibre inside the tile has been defined by means of simulations presented in chapter 7. The surface of both fibre ends are polished. The polishing procedure is crucial and is described in section 5.2.3.2. A homogenous and smooth surface allows for the best angular distribution and transmission efficiency. To improve the light collection in the WLS fibre, the surface ending in the scintillator material is mirrored by a reflective material.

The attenuation of WLS fibres is significantly increased compared to a clear optical waveguide [155]. Therefore, if transportation of photons within long fibres is needed, a coupling to an optical waveguide and the further guiding of the light by the latter may increase the light yield detected at the light sensor. The numerical aperture *NA* of the WLS fibre and the optical waveguide should be comparable to avoid light losses at the optical coupling. For several measurements, ESKA acrylic fibres produced by Mitsubishi and available by Edmund Optics are used as optical waveguides [162]. It offers a numerical aperture *NA* of 0.51 compared to a numerical aperture of 0.74 of the WLS fibre. An overview about important characteristics of the applied waveguides is given in appendix G.

The applied SiPMs have to provide sufficient gain, a good photon detection efficiency as well as a low noise rate to achieve an excellent signal-to-noise ratio. As a decent development and study of demonstrator modules take time and the research on SiPM resulted into heavily improved devices, two different SiPM types have been used during this work. Both types are Hamamatsu devices [105], offering a cell pitch of $50\,\mu\mathrm{m}$. Type S12571-050P is an older device type with an active area of $1\,\mathrm{mm} \times 1\,\mathrm{mm}$. Furthermore, a more current type S13360-1350PE has been used which has an enlarged active area of $1.3\,\mathrm{mm} \times 1.3\,\mathrm{mm}$, simplifying the optical coupling to the WLS fibre. The current SiPM type has a significantly reduced correlated noise rate and an improved photon detection efficiency (35% → 40% at peak wavelength). An overview about geometrical and operation parameters of both types is given in appendix G.

[3] By a long-term study of the light yield, the choice of the bending radius will be re-evaluated in the future.

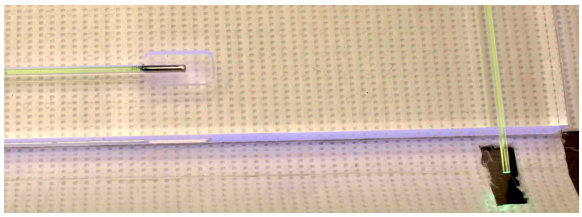

(a) Photo of chrome effect spray used in unit layout 1 to allow a backscattering of light rays at the polished surface of the WLS fibre. The drilled deepening as well as the complete groove, in which the end of the fibre is located, will be filled with optical cement of type EJ-500. This allows for a stable position of the WLS fibre in the tile.

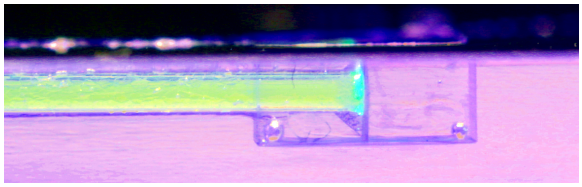

(b) Photo showing side view of the highly reflective foil glued to the polished surface of the WLS fibre of unit layout 2. The drilled deepening, in which the end of the fibre is located, is filled with the same optical cement of type EJ-500 to allow a stable position of the WLS fibre in the tile.

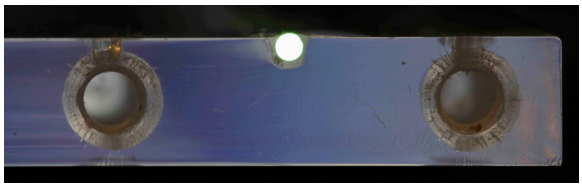

(c) Photo of a scintillator tile focussed on the drilled holes for the connection of the circuit board by two screws for unit layout 2. The wavelength shifting fibre is located between both drilling holes at the top of the tile. The position of the centre of both holes is adapted to the actual location of the WLS fibre.

Figure 6.2.: Photos of details of the unit layout 1 and 2.

Unit layout 1

A sketch of the layout of two realized units is shown in figure 6.1.
Unit layout 1 is designed for the transport of the light over long distances. An overview of the layout is presented in figure 6.1a. The achieved light yield is ≈ 8 p.e. for a traversing muon. The WLS fibre is glued into the groove along its entire length. The optical cement is of type EJ-500 by Eljen Technology [163]. It has a refractive index of 1.57 which is comparable to the refractive index of the scintillator material. The optical cement allows an improved connection to the WLS fibre and the scintillator tile such that photons enter more easily into the fibre but will also leave the fibre more likely along their path through the fibre. The groove has a width of 1.1 mm and a depth[4] of around 1.2 mm. The surface of the fibre end in the scintillator tile is covered by a high-glossy chrome effect spray of the brand DUPLI-COLOR as reflective material. It provides a maximum angle of reflectance of 60° according to DIN 67530, but with unknown reflectivity. The chrome effect spray was later found to be inefficient (cf. appendices I and J). The opposite end of the WLS fibre is sticking out of the tile by about 10 mm. A detailed photo of both fibre ends is presented in figure 6.2a. The WLS fibre is mechanically connected to a clear optical waveguide to reduce attenuation losses compared to light transport by a WLS fibre of the same length. A support structure offers stabilization. Therefore, the mechanical workshop of the Physics Institute III A of the RWTH Aachen University designed a mounting bracket visible in figure 6.1b and discussed in detail in [164]. The optical waveguide is connected to a SiPM located at a common SiPM carrier board for the use of up to eight detector units. The Hamamatsu SiPM type S12571-050P is used. The transport by optical fibres instead of WLS fibres has been preferred. The analogue signals of

[4]The depth may vary as the tile height is not uniform along the entire extent of the tile.

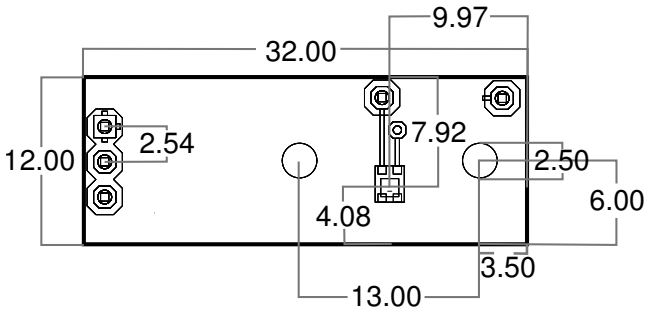

(a) Technical drawing of the SiPM circuit board.

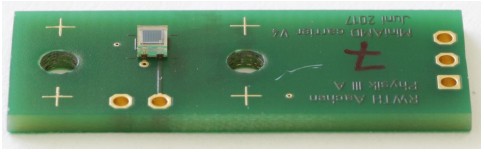

(b) Photo of the SiPM circuit board without additional components.

Figure 6.3.: The SiPM circuit board is designed to be directly connected to the wavelength shifting fibre at the scintillator tile edge of unit layout 2. In addition to the SiPM, it carries connectors for voltage supply and readout. The connectors are represented by octagons in the drawing. Additional components as the temperature sensor and spacers are not included in the drawing or the photo. The active area of the SiPM is $1.3 \times 1.3\,\mathrm{mm}^2$. The dimensions are given in mm.

SiPMs may be attenuated, or pulse shapes may be changed by dispersion if transported by long cables. In the thesis of Lukas Middendorf, this has been proven to be present for cables with length $l > 6\,\mathrm{m}$ (cf. [165]). However, detailed measurements have shown that the mechanical coupling introduces a larger light loss than expected. Ideally, the fibres are coupled with their ends perfectly aligned to each other so that no air exists between both surfaces. In a realistic scenario, non-planar orientation of the non-perfectly polished surfaces will introduce a small air gap and a rough surface of fibres reducing the light yield of the setup. The measurements will be discussed in appendices I and J.

Unit layout 2

Unit layout 2 is an improved unit version. An overview of the layout is presented in figure 6.1c. The achieved light yield is $\approx 25\,\mathrm{p.e.}$ for a traversing muon. The groove containing the WLS fibre has the same distance to the tile edge and bending radius. However, the groove width is slightly smaller to match the diameter of the WLS fibre. No glue is used along the WLS fibre but only at the two fibre ends. The WLS fibre is kept inside the groove by friction forces. The depth of the groove is 1 mm in the region around the fibre end in the direction of the photosensor while the rest of the groove has a depth of 1.3 mm to contain the complete WLS fibre inside the groove with a sloped transition region. A highly reflective foil of brand 3M [153] is glued onto the polished fibre end surface within the tile. Its reflectivity is stated as $> 98\%$. A close-up view of the reflective cover of the fibre end is presented in figure 6.2b. The opposite end of the WLS fibre ends flush with the scintillator edge. The WLS fibre is then directly connected to a SiPM located at an individual carrier board screwed onto the tile (cf. figure 6.2c). The Hamamatsu SiPM type S13360-1350PE is used providing a larger active area than the diameter of the WLS fibre. The connection to the circuit board is demonstrated in figure 6.1d. The circuit board carries beside the SiPM two spacers, one located at each side of the SiPM. They provide a stable and horizontal coupling between SiPM and scintillator tile edge. Furthermore, an individual temperature sensor is located on the carrier board. Therefore, the circuit board has several cables connected. On the left in figure 6.1d, a three-pin connector for the temperature sensor (voltage supply and readout) is shown. Furthermore, cables for the signal readout of the SiPM and for the voltage supply of the SiPM are connected (shown in the middle and on the left of the board, respectively, in figure 6.1d.)

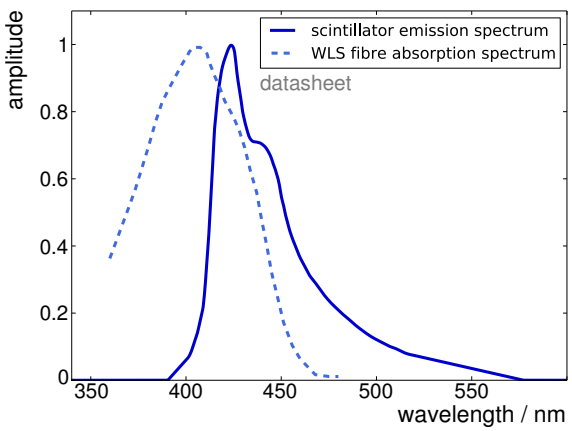

(a) Scintillator emission spectrum (EJ-212) and WLS absorption spectrum (BCF-92).

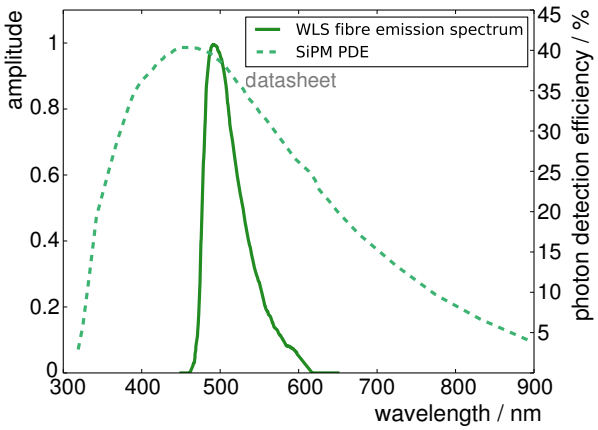

(b) WLS emission spectrum (BCF-92) and SiPM photon detection efficiency (PDE, S13360-1350PE). The PDE distribution covers the complete emission spectrum.

Figure 6.4.: Emission and absorption spectra of scintillator, WLS fibre and SiPMs. High overlaps guarantee a high light yield. Adapted from [105, 159, 161].

The positioning of the SiPM on the circuit board has been performed by a Hot Air SMD rework station by Finetech [166]. Its optics allow for sub-mm precision of the SiPM placement and the orientation in respect to the holes in the circuit board and consequently in respect to the WLS fibre. The positioning of the drilled holes for both screws in a tile has been optimized after the WLS fibre has been placed and glued into the groove. Thereby, deviations from the desired location of the WLS fibre in the groove can be compensated. For all produced units, the alignment of the WLS fibre and the active area of the SiPM has been successfully achieved within the intended precision of 0.15 mm in each direction. As already mentioned in chapter 4, the response of silicon photomultipliers (SiPMs) is temperature dependent. By adjusting the bias voltage by a SiPM-type specific temperature correction factor, the gain of the SiPM will be kept constant (cf. equation 4.2). Therefore, a temperature sensor has to be installed next to each SiPM. The technical drawing and a photo of the SiPM circuit board of unit layout 2 is shown in figure 6.3.

The optical materials used in both units are chosen such that their characteristics are best possible matching to each other. In figure 6.4a, the emission spectrum of the chosen EJ-212 plastic scintillator and the BCF-92 WLS fibre absorption spectrum are compared. Both are normalized to a maximum amplitude of 1. The absorption spectrum of the WLS fibre covers a large part of the scintillator spectrum. In figure 6.4b, the BCF-92 WLS fibre emission spectrum is compared to the photon detection efficiency of the Hamamatsu S13360-1350PE SiPM. The photon detection efficiency peaks near the maximum wavelength regime of the emission spectrum[5].

6.2. Electronics

The extraction of the signal may vary strongly among different techniques of particle detection. In principle, several general options are available. The *counting* of particle passages is preferred if the particle density is small and a distinction between signals of individual particles is feasible. For a larger amount of simultaneously arriving particles the *integration* of the signal of the light sensor

[5]The wavelength shifting process is mandatory for the capturing of photons in a WLS fibre. The shifting yields, in the scope of this thesis, no benefit for the matching to the SiPM PDE.

should be chosen. Here, the light sensor will detect the accumulated photons of coincident passages and no distinction can be made between individual particles. Only a timestamp of the event and one value per integration or counting of an event as a measure of the number of particles detected can be provided. Alternatively, the signal of the light sensor may be extracted as a *trace*, so the amount of signal as function of time, which allows also the study of pulse shapes or rise times.
In the scope of this thesis, commercially available SiPM readout electronics were combined with a *power supply unit* (PSU) and a SiPM electronic board designed in Aachen. As readout electronics the *Extended Analogue SI-pm ReadOut Chip* (EASIROC, [167, 168]) evaluation board has been chosen. It allows for the measurement of SiPM signals with both, the counting and integration method, but is not providing signal traces[6]. Each component of the readout chain will be explained in more detail in this section. A custom firmware for the operation of the evaluation board was developed in [165]. As all components have been carefully characterized in terms e.g. of functioning, noise effects and temperature dependence by Lukas Middendorf with the help by Rebecca Meißner, please refer for a detailed overview to their work presented in [164, 165]. It has been shown that for stable operation, the temperature has to be individually monitored for each SiPM, the EASIROC chip and the power supply unit on a regular time basis.

6.2.1. Power supply unit

The power for the DAQ is provided by a power supply unit (PSU). The PSU allows for a low power and stable conversion of an input voltage in the range of $9-32\,\mathrm{V}$ given by an external power source to the voltages needed by the DAQ. The wide range of the input voltage allows for example the use of different type of batteries at various states of charges for measurements outside of the lab[7]. The output of the PSU allows to operate the EASIROC evaluation board (need of $6.5\,\mathrm{V}$) and to apply the $< 70\,\mathrm{V}$ bias voltage for the SiPMs whereby a limitation of the SiPM supply current to $500\,\mu\mathrm{A}$ provides short-circuit protection. If needed, the PSU can also provide the power (up to $2.4\,\mathrm{A}$ at $5.1\,\mathrm{V}$) for the use of a single board computer.
The board has been designed and produced in the electronics workshop of the Physics Institute III A at the RWTH Aachen University. A photo of the PSU is presented in figure 6.5. The power consumption of the PSU is around $130\,\mathrm{mW}$ with no output and $165\,\mathrm{mW}$ with $70.5\,\mathrm{V}$ output voltage as presented in [165]. The board also features eight lines for communication between the FPGA on the EASIROC evaluation board and the PC. The temperature of the PSU is permanently monitored as its characteristics are slightly temperature dependent.

6.2.2. EASIROC - an ASIC for the readout of SiPMs

The EASIROC is an *application-specific integrated circuit* (ASIC) designed for the complex readout, signal processing and operation of silicon photomultipliers. It allows for the connection and use of up to 32 channels. It was developed by the Omega group[8] [167, 168]. The ASIC is the key element of the EASIROC evaluation board. Additionally, a *field programmable gate array* (FPGA) is located on the board, which provides the communication to the EASIROC and decides whether the trigger conditions requested are fulfilled. A slow control allows for different settings of the data taking which can be modified by the user via PC. Data are transferred via mini USB between PC and evaluation board.

[6] A continuous digitization of voltage traces of several SiPMs would require the use of one fast ADC per channel. The implementation would lead to high power consumptions and to a more complex electronics.
[7] Standard lead-acid batteries have nominal voltages of $12\,\mathrm{V}$ and $24\,\mathrm{V}$.
[8] formerly a microelectronics group of LAL in Orsay, France, became an independent lab (IN2P3/CNRS/Ecole-Polytechnique) located in Palaiseau, France.

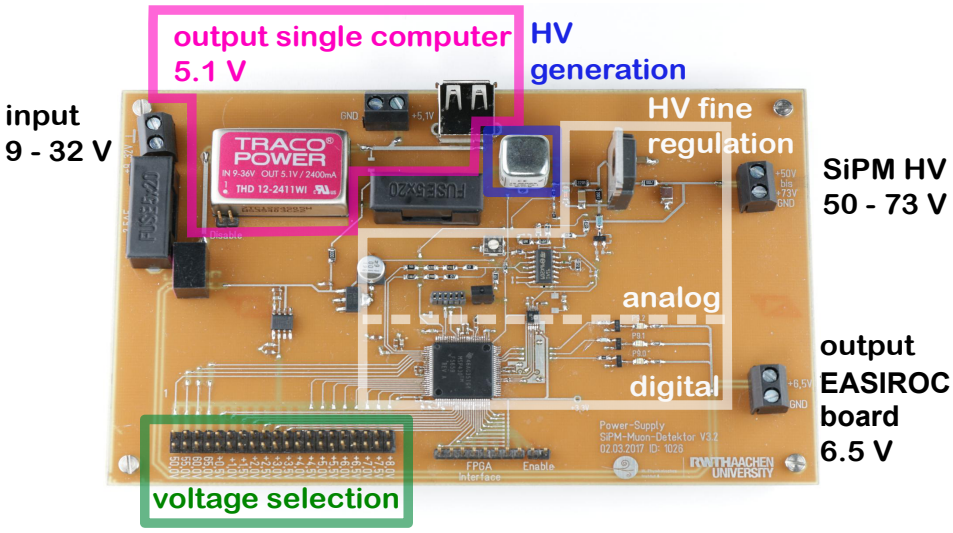

Figure 6.5.: The power supply unit designed and produced in the electronics workshop of the Physics Institute III A at the RWTH Aachen University. The input voltage ranges from 9 − 32 V. Three voltages are offered as output: the basic HV SiPM bias voltage, the supply voltage for the temperature sensors at the SiPM circuit boards and for a single board computer. The temperature of the PSU is monitored as its operational parameters are temperature dependent. Photo courtesy by Lukas Middendorf.

Important functionalities of the EASIROC evaluation board for this thesis are explained in the following. As the characterization of the EASIROC evaluation board as well as the programming of the FPGA and the custom firmware have been performed in [165], please refer for a detailed overview about the electronics to that work. A photo of the EASIROC evaluation board can be found in figure 6.6.

The regulation of the supply or bias voltage for each individual SiPM according to the temperature (cf. equation 4.2) is essential to allow for a stable gain operation.
The basic bias voltage is set by the self-designed power supply unit (cf. section 6.2.1) and is the same for all channels. The fine tuning of the bias voltage is performed by one 8-bit *digital to analogue converter* (DAC) per channel in the EASIROC and can be adjusted for each channel separately. The fine tuning ranges between 0 and 4.5 V which allows in principle for a temperature range of $4.5\,\mathrm{V}/(60\,\mathrm{mV}/\,^{\circ}\mathrm{C}) = 75\,^{\circ}\mathrm{C}$ (cf. equation 4.2). However, it would result in a rather coarse voltage setting as only a limited step number is available. Therefore, to reduce the step size and to cover a larger temperature range, the basic voltage provided by the PSU is also adapted according to temperature.

Besides the adjustment of the SiPM bias voltages, the EASIROC ASIC allows for several operations regarding the process of the incoming signal of SiPMs. Main operations are:

- preamplification of the analogue SiPM signal traces,
- shaping of the signal by a fast or a slow shaper,
- threshold discrimination per channel (essential for trigger conditions and for the counting of exceeded threshold over time),
- providing measure of integrated charge for each channel.

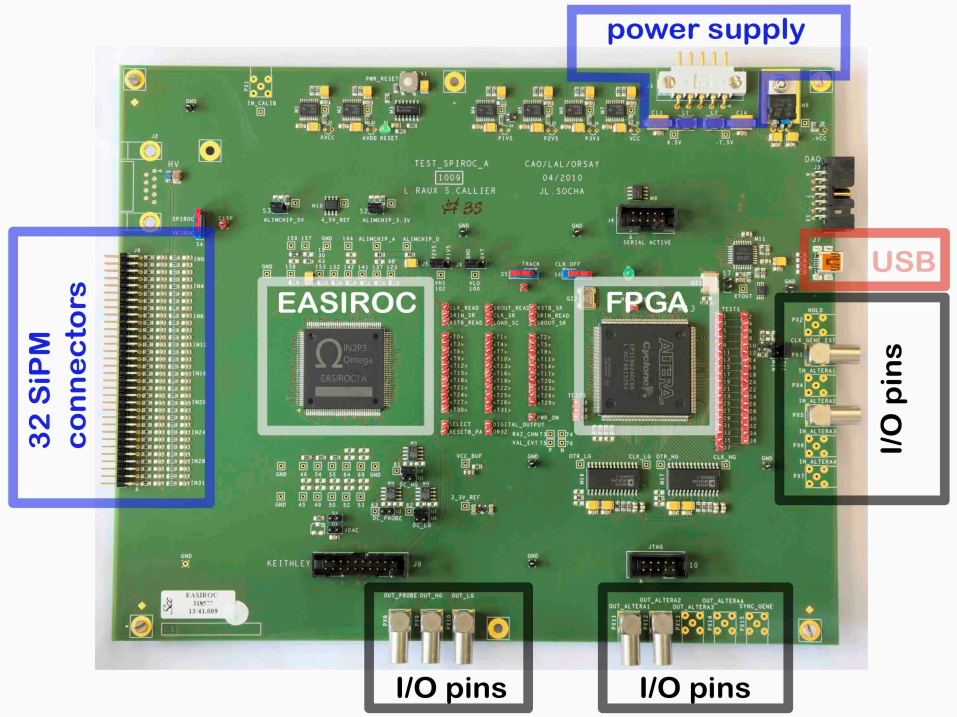

Figure 6.6.: The EASIROC evaluation board designed for detailed characterization studies of the EASIROC ASIC and the readout of up to 32 SiPMs. Depicted are I/O pins used in this thesis for coincidence trigger of and by external experiments. Indicated are the FPGA needed for the slow control as well as the readout and trigger process, the power supply connector linking to the PSU, and the miniUSB connector linking to the PC. Photo courtesy by Lukas Middendorf. Adapted from [168].

As a first step, the analogue signal of a SiPM is amplified. The SiPM signal is therefore passed on to two separate chains. There are two adjustable amplification settings available (*high* and *low gain*) to achieve a large dynamic range. It is important that both gains have an overlap-region to allow for a cross-calibration. Thereby, an analysis on the combined response is accessible.
For a correct conversion from the feedback value, selectable by the user, to the actual gain value, a dedicated measurement is needed and has been performed in [164, 165]. As a first approximation, the EASIROC is capable to measure a signal from a single photon (1 p.e. or 160 fC in charge for a 10^6 amplification factor of an SiPM) up to 2,000 photons (2,000 p.e. or 320 pC).

The EASIROC provides also two different trigger and readout mechanisms. In figure 6.7, an overview is given. Thereby, the shaping of the signal has a high impact. In principle, two shaping procedures per SiPM channel are available. One is the *fast shaper*, whereby the pulse form is reduced to 15 ns peaking time. The second is the *slow shaper* with increased peaking time. A common peaking time for all channels can be chosen between 25 – 175 ns. The peaking time can be approximated as the time between the start of the rising edge of the signal and the maximum of the submissive peak. One slow shaper is located in each gain chain while the fast shaper is only located in the high gain chain.
The fast shaper is used for the discrimination of the high gain signal. One discriminator for each channel is available with a common 10-bit DAC setting the threshold. As therefore the threshold setting is the same for all channels, the gain of all SiPMs has to be comparable and stable over temperature. The discriminator status of all channels at point of trigger is accessible. This allows

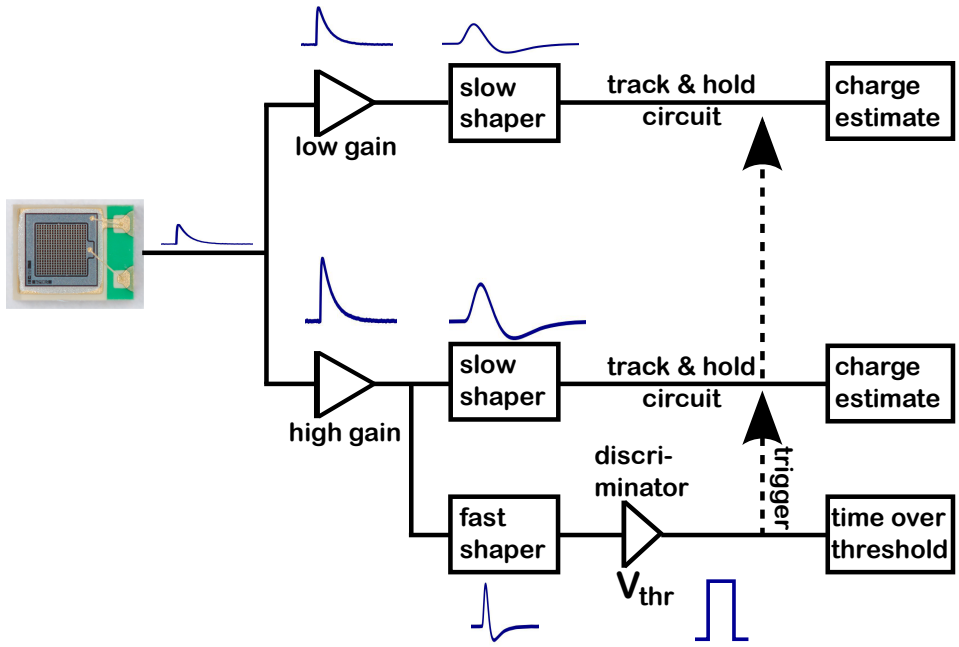

Figure 6.7.: Schematics of the signal readout by the EASIROC evaluation board. For each SiPM, two amplification chains are available (high and low gain). In the high gain chain, a fast shaper chain is used for the trigger decision. The signal is shaped with a short peaking time. A discriminator with adjustable threshold V_{thr} defines if an event is accounted as hit. For both amplification chains, the shaping of the signal by a slow shaper with a larger peaking time is followed by a track and hold circuit (see text for more information). The amplitude at a user-defined hold time after trigger is a measure of the integrated charge in an event.

for the implementation of trigger requirements as the selection of channels of interest. By the pure discriminator chain the *counting of traversing particles* is feasible. If the amount of simultaneous particles is small, the assumption of one discriminator trigger by each particle passage of interest can be used to analyze the number of particles traversing the detector in a certain time interval.

For a larger range in the number of arriving particles, the use of the two integration chains is favored. An integration chain is defined as a pre-amplifier (high / low gain), its slow shaper and an analogue memory in form of a *track and hold circuit*. The shaping corresponds to an integration of the signal. A measure of the integrated charge is provided by the value of the shaped pulse at a user-chosen *hold time* after trigger. This pickup time should be around the maximum of the signal. The capacitor after the slow shaper stores the voltage corresponding to the signal height. The determined amplitude of the integrated signal at hold is sampled by an external ADC on the evaluation board. At low peaking times, rough features of the original trace are still present in the shaped signal. For larger peaking times, structures are shrouded. Therefore, for the latter an air shower signal trace (several pulses in a short time window smaller than the peaking time) seen by a shaper results into one single pulse. This pulse is not distinguishable from a trace containing only a single pulse with the same integrated charge. To illustrate the influence of the shaping, please refer to figures 7.9 and 7.10, on page 95 and 96 in chapter 7. A readout of a complete event takes about 1 μs and has to be considered as dead time of the readout electronics.
Finally, the digitized signals are sent via miniUSB to a (mini-)computer.

Several configuration settings are stored in the *slow control* in the EASIROC on the evaluation board. These configurations include the information on the setting of the bias voltage for each individual SiPM as well as on the discriminator threshold and the disabling/enabling of EASIROC features. All needed features regarding trigger configurations, additional used measurement equipment or data to be stored are controlled via the custom firmware and the readout software (both developed in [165]).
The evaluation board was designed for test purposes of the EASIROC ASIC. Therefore, many I/O access points are available via LEMO plugs (cf. figure 6.6). The I/O pins used in this thesis are the trigger-out and trigger-in pins for coincident measurements with external detectors. The power consumption is quite high as the board consumes 2 W. However, as the EASIROC ASIC itself is designed for a low power consumption, this may be reduced by designing a board for the designated measurement setup not for a detailed measurement of all EASIROC characeristics in the lab. Furthermore, the installed electronics components are already out-of-date like the FPGA or the voltage regulators and could be replaced by current low power versions.

6.3. Expected light yield

The number, arrival time and wavelength of photons, that are reaching the SiPM, strongly affect the detector performance. For example, the photon detection efficiency is a function of wavelength and thus has to comply with the corresponding emission spectrum of the wavelength shifting fibre.

The number of expected photons in units of photon equivalents (p.e.), $\langle N_{\text{p.e.}} \rangle$, measured by the light sensor results from the conversion of deposited energy by a traversing particle into photons in the scintillator. The number of photons is reduced by the efficiencies of the further collection, transport and detection of these photons by the contributing optical components. As most of these parameters are also wavelength dependent, the convolution of all efficiencies has to be integrated over the wavelength spectrum. Two wavelength regimes have to be considered, the scintillator emission spectrum with wavelength λ_{em} and the shifted wavelength range λ_{s} introduced by the use of wavelength shifting fibre. However, it is assumed that most terms contributing are only weakly dependent on the wavelength and can be approximated as effective values[9]. The number of expected photons can be approximated according to

$$\langle N_{\text{p.e.}} \rangle \approx \int \mathrm{d}\lambda_{\text{s}} \int \mathrm{d}\lambda_{\text{em}} \frac{\mathrm{d}L_{\text{scint}}(\lambda_{\text{p}})}{\mathrm{d}\lambda_{\text{em}}} \times \epsilon_{\text{trap}} \times \frac{\mathrm{d}T_{\text{fibre}}(\lambda_{\text{em}}, \lambda_{\text{s}})}{\mathrm{d}\lambda_{\text{s}}} \times \text{PDE}_{\text{sipm}}(\lambda_{\text{s}}) \times T_{\text{sipm}}(\lambda_{\text{s}}) \tag{6.1}$$

$$\approx L_{\text{scint}} \times \epsilon_{\text{trap}} \times \widehat{T}_{\text{fibre}} \times \widehat{\text{PDE}}_{\text{sipm}} \times \widehat{T}_{\text{sipm}} \quad . \tag{6.2}$$

The various factors in this formula are explained in the following. The amount of scintillation photons emitted by a particle passage can be estimated according to Birk's law (cf. equation 5.2). As most of the air shower particles arriving at ground and being detected can be approximated as *minimum ionizing particles* (MIPs), the light yield L_{scint} can be estimated by

$$L_{\text{scint}}|_{\text{mip}} = E_{\text{deposited}}\Big|_{\text{mip}} S|_{\text{mip}} \tag{6.3}$$

$$= \frac{1}{\rho} \left.\frac{\mathrm{d}E}{\mathrm{d}x}\right|_{\text{mip}} \Delta x \left.\frac{\mathrm{d}N_{\gamma,\,\text{scint}}}{\mathrm{d}E}\right|_{\text{mip}} \quad . \tag{6.4}$$

From the literature the following values can be extracted for the energy deposit of a MIP in the plastic scintillator material $\mathrm{d}E/\mathrm{d}x|_{\text{mip}} = 1.956\,\text{MeV}\,\text{cm}^2/\text{g}$ [169], with a density of $\rho = 1.023\,\text{g/cm}^2$

[9] Those are indicated by a circumflex accent over the parameter.

and a scintillator yield of $\mathrm{d}N_{\gamma,\,\mathrm{scint}}/\mathrm{d}E\big|_{\mathrm{mip}} = 10,000\,\mathrm{photons/MeV}$ assuming a comparable energy deposition as by an electron in EJ-212. For a 0.5 cm thick scintillator, a MIP traversing the tile vertically would result in about 10,000 photons. The scintillation photon yield is strongly reduced according to the efficiencies of the following optical components up to the photosensor. Some photons emitted in a scintillator will be absorbed in the WLS fibre core followed by an isotropic emission of photons of longer wavelength. The trapping efficiency $\epsilon_{\mathrm{trap,\,forward}}$ (cf. section 5.2.3) is referring to the capability to capture those emitted photons. The efficiency is stated as $< 5\%$ by manufacturers. The photons will be guided by the fibre to the photosensor but will be attenuated along their way depicted by the average transmission efficiency of $\widehat{T}_{\mathrm{fibre}}$. It is assumed[10] to be in the order of 40%. It may be even more reduced due to an insufficient re-scattering of light rays which were emitted in the direction of the mirrored end of the fibre contained in the scintillator tile. If reaching the photosensor, the photons have to enter the sensitive area of the silicon photomultiplier. The probability to be detected is mainly determined by the effective photon detection efficiency ($\widehat{\mathrm{PDE}}$) of the chosen device and ranges in recent SiPM types between $30\%-40\%$ [105]. The PDE includes the transmission efficiency of the photons from air to the active area of the sensor (cf. equation 4.4). As now a direct transmission from the WLS fibre to the SiPM is studied, the relative change in the average transmission efficiency, over all incident angles from $0-90\,^{\circ}$, is calculated. It is referred to as $\widehat{T}_{\mathrm{sipm}}$. The calculation is based on a multilayer approach of the Fresnel equations (cf. equation 5.19). The refractive indices of air $n_{\mathrm{air}} \approx 1$, of the SiPM epoxy resin $n_{\mathrm{resin}} = 1.55$ [105], of the WLS fibre core $n_{\mathrm{WLS}} = 1.60$ [161], and of silicon[11] $n_{\mathrm{silicon}} = 4.35$ [170] are used. The relative change from a transmission from air - resin - silicon to a transmission from WLS fibre core - resin - silicon is $\widehat{T}_{\mathrm{sipm}} = 84\%$. Thus, from equation 6.2, around 50 photon equivalents may be registered by the SiPM.

However, each process is subject to statistical fluctuations and depends on the chosen detector setup. Also, further efficiencies have an impact on the light yield but are not included in the stated equation 6.2. They have to be estimated by simulations or measurements as they are highly depending on the studied detector setup. For example, the probability for a photon to cross the fibre core depends on the attenuation length and geometry of the scintillator and its embedded WLS fibre. The use of reflective wrapping material may increase the probability to interact with the fibre as increasing the duration of the containment of photons in the tile. Also, the transmission efficiency of the fibre system may change if the WLS fibre is connected to an optical waveguide for the further transport of the light to the photosensor. The use of an optical waveguide strongly reduces attenuation effects as having a longer attenuation length but will introduce an additional optical transition inducing light losses.

In the scope of this thesis, several of these quantities will be studied by simulations and measurements. However, this thesis does not aim at a precise determination of all stated quantities individually but at a prediction for the overall light yield of the optical setup.

6.4. The Aachen Muon Detector

The presented detector unit has been developed in the scope of the preparatory work for a large-scale detector concept. The detector is called *Aachen Muon Detector* (AMD) [171, 172, 173, 174]. It consists of 64 units. It has been developed in the context of the AugerPrime upgrade of the Pierre Auger Observatory (cf. chapter 3.4). The basic idea is a SiPM-based detector located underneath the existing water Cherenkov detector (WCD) stations (cf. chapter 3.1). By a simultaneous readout of the same cosmic ray air showers, an improved determination of the particle density on ground

[10] based on simulations performed in this thesis

[11] at the peak wavelength of the WLS fibre emission of 492 nm [161].

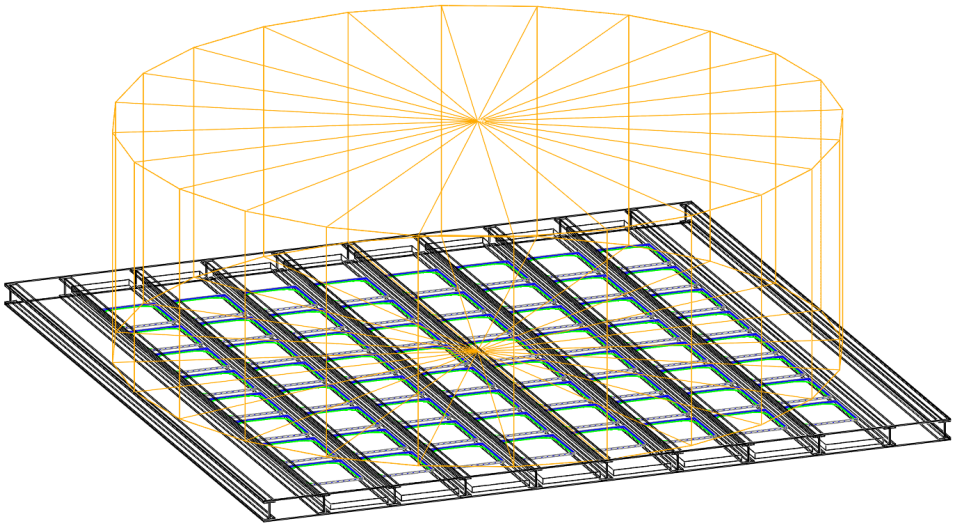

Figure 6.8.: Schematic view of the AMD detector simulation. In total, one AMD station consists of 64 units. They are located in a housing made of steel. A simplified sketch of a water Cherenkov detector (WCD) station of the surface detector of the Pierre Auger Observatory is also shown. The WCD station is placed on top of the housing. Additional steel I-beams are needed to carry the weight of the WCD station. By the struts, trays are formed. Eight trays are equipped, each with eight units. The outermost regions of the detector are left empty and can be used, for example, for the guiding of cables or the location of readout electronics.

and thus of the primary cosmic ray particle type is achieved. To allow for a stable placement of the WCD station, the units are located in a steel housing which is stabilized by inner steel I-beams. The height of the housing is 11 cm. Between two struts, groups of eight units are lined up on a 35 cm wide tray. They are located with a gap of 7.5 cm next to each other. A complete detector consists of eight equipped trays. Additionally, two empty, smaller compartments, carrying no units, can be used for infrastructure as cable routing or readout electronics. They are located at the outer edge of the detector. Each tray can be individually inserted or removed. To allow access, the endcaps of the trays are sealed with aluminum panels. Those can be fixated and sealed using black silicone. For technical reason, the steel housing composes of two individual parts with four equipped trays each. Each part covers an area of approximately $4 \times 1.8 \times 0.1\,\mathrm{m}^3$. The total instrumented area of the detector is 44%. A schematic view of the detector layout as implemented in the simulation is given in figure 6.8.

CHAPTER 7

Simulation of detector unit response to single particles

Detailed simulations are substantial to the development, understanding, and improvement of detectors. The aim is the prediction of the detector response for related physical scenarios. The framework developed in this thesis is embedded in the *Geant4* [140] simulation package. It is based on parts of a previous work by T. Niggemann, but has been extended and further improved. It enables the ray tracing of impinging (air shower) particles. It allows for a prediction of a detector response combining different optical components (cf. chapter 5) and for studying different detector layouts. First, the optimal layout of one individual, small-scale detector *unit* is investigated by means of the light yield achieved for atmospheric muons. The such defined layout is studied by means of detector prototypes (cf. appendices I and J). Several simulation parameters have been adapted to those measurements to allow for a realistic description of the chosen detector design. The new layout corresponds to the detector unit layout 2 presented in chapter 6. The corresponding modified *detector simulation framework* is used to derive expectations for important performance parameters. The results are presented in this chapter. These parameters are validated by measurements of prototype units of the corresponding layout in chapter 8. The simulation framework is further used in a chain of programs to investigate the response to extensive air showers. Therefore, multiple units are assembled to an extended detector station. The results of these simulation studies of a multi-channel detector are presented in chapter 10.

7.1. Geant4

Geant4 is an open source toolkit widely used in the communities of high-energy, astroparticle, nuclear, accelerated physics and e.g. medical science related to physics. It was developed for the study of particles passages through matter using *Monte Carlo* (MC) methods. It provides modules for handling of the detector geometry, material composition, and tracking of the particles or the interaction, they undergo. It allows for a storage of the detector response, of particle and geometry properties. Also useful tools as for the visualization of the geometry and the particle trajectories are provided. Its popularity is based on this described high modularity, the usage of the very common object-orientated programming language C++, and a wide range of interactions, fundamental particles or material characteristics feasible. Thereby, the toolkit allows the user to form flexible frameworks for the simulation of complete detector setups or only parts of those under study. Thus, it allows to investigate e.g. possible modifications of existing detector geometries or to predict the

response of future experiments.
The following description of the Geant4 concept is very limited. The user has a tremendous amount of possibilities to manipulate the detector geometry, the tracking of the particle through the setup and which information to store for further studies. Also a linking to own C++ modules outside of the standard Geant4 classes is easily possible. For a detailed overview about the Geant4 framework please refer to [175, 176, 177].
To study the detector configuration, a *run* of the framework is performed. Each run contains one or more *events*. If a run contains several events, each event starts with the same initial detector setup. Each event includes at least one *primary particle* defined by the user regarding the primary characteristics as type, energy or, if needed, polarization and geometrical settings. On its way through the predefined detector geometry, the particle interacts with the detector material. Thereby, an interaction depends on the particle type and its energy. The processes available can be controlled by the user [1]. By these interactions *secondary particles* may be produced undergoing further interactions. Each of these particles is tracked *step* by *step* through the detector. At each step in a Geant4 *track* the transient state of the particle like its time-of-flight spent in the step, energy loss, start and end point is calculated. An event stops if all particle tracks[2] are absorbed, left the defined detector geometry, disappeared due to decay, or are 'killed' by the user to avoid accidental trapping of a particle.
The detector geometry itself can be assembled via free scalable *solids*. These range from classical forms like spheres or boxes to complicated geometrical forms designed by the user. A solid and its corresponding material form a *logical volume*. The material can be a predefined material from the NIST database or a user-designed material also based on the NIST catalogue [178]. Here, the material has to be defined by a properties file. The location or orientation of a detector volume is defined by the *physical volume*. Hereby, the hierarchy of the volumes is important. A child volume has to be completely enclosed by its mother volume. The outermost mother volume is thereby often called 'world' defining the maximal dimension of the Geant4 detector setup. Overlaps in volumes result in an undefined region where neither the properties of the one nor of the other volume may be valid. Geant4 offers several possibilities to test for these overlaps. If a logical volume is defined as a *sensitive detector*, a particle reaching this region is considered as a *hit* and its properties of interest are stored in its own *hits collection*. This allows the user a readout of each sensitive detector hits collection at the end of a run or an event.
Furthermore, while defining properties in Geant4, the user has to assign values including a physical unit. The common unit system used is the CLHEP library. If no unit is assigned, an internal default unit will be chosen by Geant4. Values calculated by Geant4, like the energy of a particle after a step, are given without any uncertainties. These have to be introduced and studied by the user in the application itself or afterwards.

7.2. The GODDeSS package

For further studies, the *GODDeSS* ('Geant4 Objects for Detailed Detectors with Scintillators and SiPMs') simulation package [179, 180] was integrated in the developed framework. This package has been developed by E. Dietz-Laursonn [181]. It enables the detailed simulation of optical components as scintillators and optical fibers with a high variability in the modification of the setup characteristics. Many of those predicted characteristics of the simulations have been validated by measurements. As based on the Geant4 simulation package, it can be easily implemented in existing projects. It can be used only for the simulation of one explicit optical component while the other components are simulated according to the user's own framework. However, it provides in general

[1] This has the advantage that unnecessary processes can be omitted which reduces computing time.
[2] of the primary particle and all of its secondaries

a complete detector simulation on their own including an own physical list and data storage system. To implement the GODDeSS package in a framework, GODDeSS objects have to be invoked in the C++ code.
GODDeSS aims to simplify the study of a large range of scenarios in a small scale detector. It allows for complex geometrical layouts. Therefore, it concentrates rather on a high flexibility for the user than on a reasonable time- and resource-consuming performance. The simulation of a large scale detector with several scintillator tiles and readout channels is not the designated goal. Therefore, the GODDeSS package has been used to study and to improve the knowledge on details of interest in optical components and is not implemented in the final simulation framework for a multi-channel detector.

7.3. The detector simulation framework

The ray-tracing simulation of the muon detector unit comprises all optical components as presented in chapter 6. A single unit but also a detector consisting of multiple units can be studied. Photons are emitted by the energy deposit of particles traversing the *scintillator tile*. The type, energy, position, momentum, polarization, and amount of primaries can be chosen by the user. Fixed and randomly distributed quantities are available. The photons are collected by a *wavelength shifting* (WLS) fibre and guided onto the photosensor, a *silicon photomultiplier* (SiPM). The Geant4 based simulation package *G4SiPM* developed by T. Niggemann (cf. chapter 4.3) is used to predict the amount of photon equivalent (p.e.) detected for the studied scenario. Both applied SiPM types of Hamamatsu (S12571-050P and S13360-1350PE) have been introduced in the G4SiPM package by the author of this thesis. Optionally, the units can be embedded in a corresponding mechanical support structure[3] as presented for the MiniAMD demonstrator in chapter 9.
The simulation framework is written in the C++ programming language. The data storage is realized using the ROOT data analysis framework [182]. It was developed with Geant4 version 9.10 patch 2 and ROOT version 5.34 patch 11.
Important characteristics of the materials are given in properties files to be read in during the simulation. To study the response of the optical components for different layouts, flexible input parameters of interest are implemented in the C++ source code. These input parameters are handed over to the framework via a command line at the beginning of the simulation. Thereby, no change within the C++ code and re-compiling of this simulation package is needed.
First studies performed with the described detector simulation framework have been presented in [54, 172, 183, 184]. However, the simulations presented in the following have been performed by the author of this thesis.

7.3.1. Modification of individual optical components

The detector simulation framework allows for a large variety of materials and geometries to study. The goal is an optimal light yield achieved for traversing muons. Besides the amount of photons detected by the photosensor, the arrival time and spatial distribution of the photons at the sensor is a crucial indicator for the performance. Relevant modifications are presented in this section. A schematic overview of components under study is presented in figure 7.1. The performance of the modified unit is presented in relation to the performance of a *reference unit layout*. Thereby, only one parameter of one optical component is modified at once to lucidly study their influence. The reference unit has the following quantities:

[3] including materials of the padding or the box

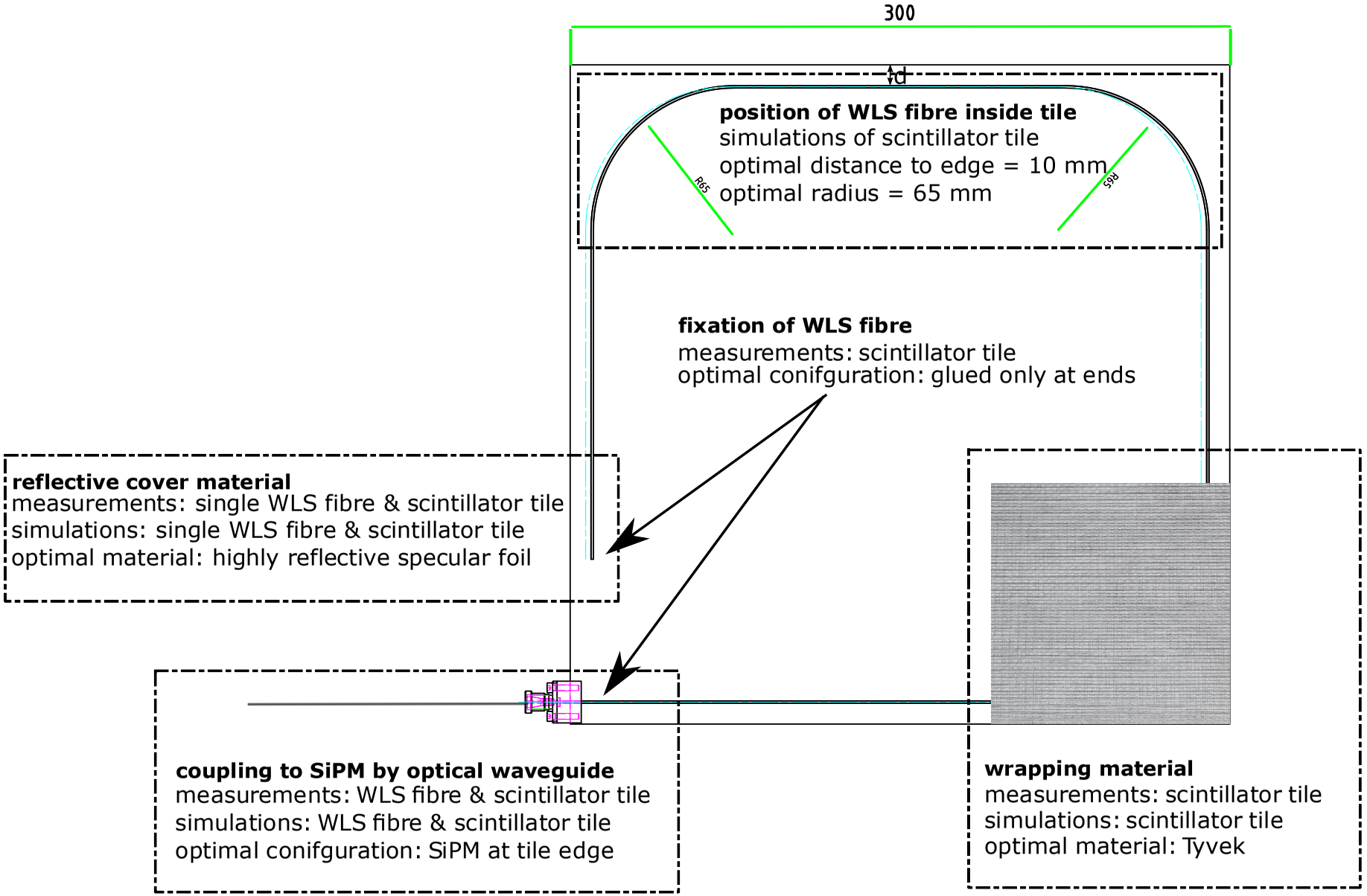

Figure 7.1.: Sketch of a unit. A unit is referring to a combination of a scintillator tile, a WLS fibre, an optional optical waveguide and a SiPM in this thesis. Dimensions and material of the tile has been chosen to $300 \times 300 \times 50\,\mathrm{mm}^2$ and EJ-212 from Eljen Technology. Shape and position of the WLS fibre within the tile have been studied by simulations. Depicted are several studies of optical components and of complete units which have been performed. They allow an evaluation of the optimal materials to achieve the largest light yield. The studies include both, measurements and simulations.

- A scintillator tile with dimensions of $300 \times 300 \times 5\,\mathrm{mm}^3$. The material refers to the EJ-212 by Eljen Technology [159]. The vertical energy loss of a *minimum ionizing particle* (MIP) in the plastic scintillator is roughly $2.3\,\mathrm{MeV/cm} = 1.15\,\mathrm{MeV}$.
- The tile is completely wrapped by a 1 mm thick Teflon sheet with an air gap of 0.1 mm. The constant thickness of the air gap is a limited representation of a real wrapping where deviations within the air gap thickness are expected.
- A WLS fibre is located in a sigma-shaped groove inside the tile. The groove has a width and depth of 1 mm corresponding to the diameter of the WLS fibre. The type of the fibre refers to a multiclad BCF-92 WLS fibre of Saint-Gobain [161]. The fibre is glued into the groove by an optical cement of type EJ-500 by Eljen Technology [163]. The chosen *radius of curvature* of the sigma-shape is $r = 65\,\mathrm{mm}$ and the *distance to the tile edge* is 10 mm.
- The WLS fibre end located inside the tile is covered by a reflective material corresponding to a highly specular reflective foil with $> 98\%$ reflectivity [153].
- An optical fibre is coupled to the WLS fibre. This transparent waveguide refers to the BCF-98 multiclad fibre of Saint-Gobain [185]. No air gap is assumed between both fibres, corresponding to a perfect coupling. The waveguide has a diameter of 1 mm and a length of 30 cm.
- A SiPM of type S133650-1350PE SiPM by Hamamatsu is placed at the optical fibre end. The dimensions of the active SiPM area are $1.3 \times 1.3\,\mathrm{mm}^2$ [105].

Here, the unit is studied surrounded only by air, neglecting materials corresponding for example to a mechanical support structure.
For each modification, 5,000 individual, vertical atmospheric muons have been uniformly distributed on the scintillator tile. Their energy range is corresponding to the energy of a MIP (cf. figure 5.1, Bethe-Bloch formula).

$$E_{\mathrm{MIP,\,range}} = \mathrm{e}^{[\ln(m_{\mathrm{MIP}})-1, \ln(m_{\mathrm{MIP}})+1]} \tag{7.1}$$

$$= [116.61, 861.62]\,\mathrm{MeV} \tag{7.2}$$

$$\text{with} \quad m_{\mathrm{MIP}} = 3 \times m_{\mu} = 316.98\,\mathrm{MeV} \quad . \tag{7.3}$$

For the investigation of the unit layout by simulations, only the number of detected photons at the SiPM is studied. Further influences by correlated noise or by the electronics are neglected. As the used SiPM type offers a low crosstalk (3%) and negligible afterpulsing (<1%) probability, these effects are of minor importance.
The expected energy deposit of a MIP in a scintillator can be described by a Landau distribution (cf. equation 5.1). Further processes as the collection or transportation of photons in the WLS fibre and the detection efficiency of photons at the SiPM can be assumed to be Gaussian distributed. Taking all processes into account, the photon distribution detected at the SiPM can be approximated by the convolution of a Landau and a Gaussian distribution. The most probable value (MPV, μ_{mpv}) of the Landau distribution defines the light yield.
The predictions by the simulations are compared to measurements with a *test unit* if possible. Details of the corresponding measurements are presented in appendices I and J.

Exemplary, the influence of the fibre cladding type is studied in more detail (cf. chapter 5.2.3). In general, optical fibres are available as *multiclad* or *singleclad* fibre. Multiclad types are highly preferred as the outermost cladding improves the containment of photons. Furthermore, multiclad fibres are expected to reduce light losses due to surface damages. Applying only multiclad types,

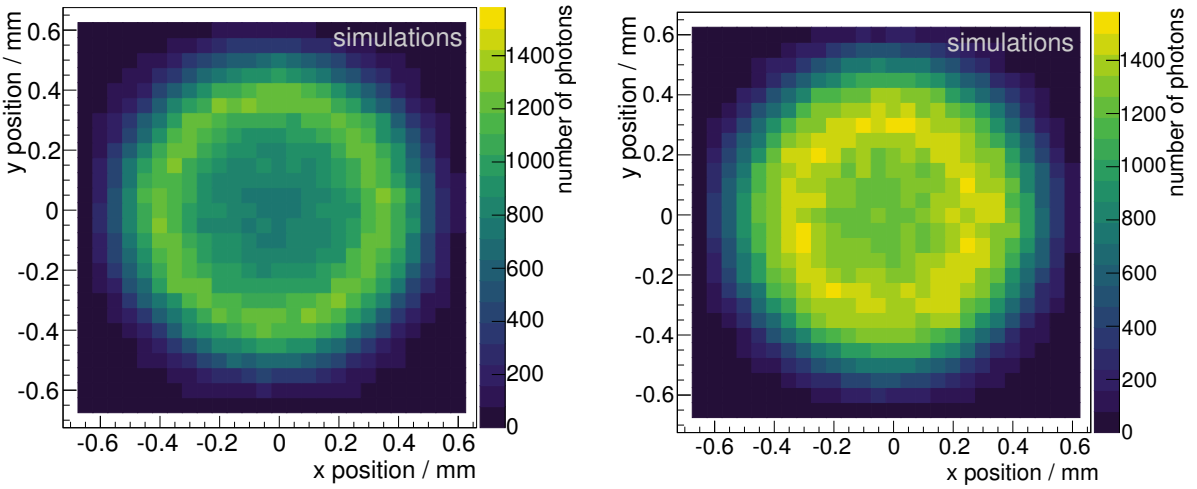

(a) Photon distribution of the singleclad types.

(b) Photon distribution of the multiclad types.

Figure 7.2.: Photon distribution on the $1.3 \times 1.3\,\mathrm{mm}^2$ SiPM surface of type S13360-1350PE for 5,000 individual vertical muon events. Compared are the arrival positions for a single- or multiclad WLS fibre coupled to a single- or multiclad optical waveguide. For each studied configuration, the simulated events are homogeneously distributed along the scintillator tile. The muons have energies corresponding to a MIP.

simulations predict an increase of up to 20% of the absolute light yield detected by the SiPM compared to their singleclad counterparts. Besides deviations in the achieved light yield, the photon distribution on the SiPM area is crucial. A homogenous distribution is strongly preferred to allow for an increased dynamic range of the photosensor. In figure 7.2, the photon spatial distribution on the SiPM surface of type S13360-1350PE is shown. In figure 7.2a, a combination of a singleclad WLS and a singleclad optical fibre is shown. A clear ring-like structure is visible as the majority of photons leaves the fibre at the outer part of the core, close to the core-cladding interface. Photons can enter the SiPM active area outside the fibre diameter of 1 mm due to the angular distribution of the photons leaving the WLS fibre. In figure 7.2b, a combination of a multiclad WLS and a multiclad optical fibre is presented. By adding a second cladding, the distribution becomes more homogenous. The distribution is also comparable for a combination of a multiclad WLS fibre and a singleclad optical waveguide. Thus, the multiclad option is chosen to achieve the best available absolute light yield detected by the SiPM and the most homogenous photon distribution on the SiPM surface.

Further studied options are shortly discussed in the following and are presented in table 7.1. For simulations, the light yield of the discussed reference layout is stated on top of the table as (36.36 ± 0.03) p.e. Then, individual components of the layout are studied. The corresponding change in the light yield compared to the light yield of the reference design is given. For the measurements, no absolute reference light yield can be stated. Each detector unit is a complex interaction of all optical components involved. Therefore, for each study of an optical component an individual reference light yield needs to be determined (cf. appendix I).

- The light yield of a unit significantly increases with the scintillator tile thickness as indicated by simulations. Thereby, the signal-to-noise ratio will also improve. However, as the light yield distribution becomes also broader, a clear allocation of a certain detected signal to the amount of particles traversing one unit becomes more complicated. For economical reasons,

Reference light yield in p.e. for simulations	36.36 ± 0.03		
Optical component	predicted change by simulation	measured change	remarks
thickness tile [0.5 cm]			
1 cm	1.65 ± 0.02	-	
1.5 cm	2.28 ± 0.04	-	
WLS fibre type [multiclad WLS fibre + multiclad optical fibre]			
Singleclad WLS fibre, singleclad optical fibre	0.80 ± 0.05	-	
Multiclad WLS fibre, singleclad optical fibre	0.99 ± 0.02	-	
use of glue in groove [WLS fibre is glued over its entire length in the groove]			
no glue	1.02 ± 0.05	1.04 ± 0.02	No significant deviations are found.
use of optical fibre [WLS fibre is coupled to an optical waveguide with a length of 30 cm]			
SiPM located at tile edge, no optical waveguide	1.15 ± 0.02	2.83 ± 0.04	A high light loss occurs at optical coupling between two fibres.
wrapping of scintillator tile [wrapping with Tyvek sheet]			
no wrapping	0.22 ± 0.02	0.43 ± 0.06	The general improvement by a wrapping is overestimated. The light yield without wrapping is well reproduced.
aluminum	0.71 ± 0.03	0.79 ± 0.07	The deviations are expected due to hand-wrapping.
Teflon sheet	1.25 ± 0.02	1.15 ± 0.05	The deviations are expected due to hand-wrapping.
reflective material at fibre end [cover with highly reflective foil]			
none	0.55 ± 0.01	0.86 ± 0.07	The use of highly reflective foil is less efficient than predicted, possibly due to imperfect coupling.
chrome spray	0.65 ± 0.01	0.87 ± 0.09	The use of chrome spray has no significant effect on the measured light yield. Incorrect assumptions implemented in simulations.

Table 7.1.: Summary of changes in the light yield by the modification of individual optical components in a unit. The default settings of the component under study are indicated in the brackets. The simulated light yield of a reference design (see text) is given for comparison. For each simulation, 5,000 vertical muons have been homogeneously distributed on the scintillator tile. The light yield is defined by the most probable value, μ_{MPV}, of a convoluted Landau-Gaussian distribution. For several components, simulations are compared to measurements presented in appendices I and J.

scintillator tiles with a thickness of 0.5 cm are used for detector units in the scope of this thesis.

- The use of glue in the WLS fibre groove has no impact on the light yield for both, simulations and measurements. As gluing of the WLS fibre along its entire length is time-consuming, the WLS fibre is only glued into the groove in the region of the both ends for detector units in the scope of this thesis.

- The coupling of a WLS fibre to an optical waveguide is a large source of light loss as indicated by measurements. Only $\approx$ 30% of photons are transmitted in the performed studies (cf. appendix I). A narrow air gap and a misalignment of fibres are reasonable factors, but further attenuation factors are necessary to explain the total light loss. The use of an optical fibre is not included in the final layout. The SiPM is directly located at the scintillator tile edge to allow for an easy and stable coupling.

- Both, simulations and measurements, confirm diffuse reflective materials to be optimal for the wrapping of the scintillator tile. The relations between the studied materials are comparable. However, the improvement in the light yield compared to a plain scintillator tile is overestimated by the simulations. The reflectivity of the applied material has to be adapted for a more realistic setup. A Tyvek wrapping is chosen for detector units in the scope of this thesis.

- Both, simulations and measurements, confirm specular reflective materials to be optimal for the cover of the WLS fibre end inside the scintillator tile. However, the improvement in the light yield compared to a WLS fibre without any additional cover is overestimated by the simulations. The reflectivity of the applied material has to be adapted for a more realistic setup. A cover by a highly reflective foil is chosen for detector units in the scope of this thesis.

As already indicated, three major sources of light losses have been identified: the efficiency of the wrapping, the efficiency of a reflective material at the fibre end and an optical coupling between two fibres[4]. The latter can be neglected, as a unit layout without any optical fibre is chosen. For the other two sources, the simulations were modified to allow for a more realistic description of the detector response. The reflectivity of both, the wrapping and the fibre cover material, has been reduced according to the measurements.
After these adaptions, important design parameters of the detector unit layout were revised, such as the position of the WLS fiber within the scintillator tile. For the WLS fibre a sigma-shaped layout inside the scintillator tile has been chosen. The WLS fibre is applied to achieve a homogenous and high detection efficiency over the complete area of the scintillator tile (cf. section 5). The fibre is located in a groove with a width of 1 mm matching the WLS fibre diameter. The geometry is thereby defined by two parameters, the distance to the tile edge d and the bending radius r. The latter refers to the radius of curvature of the fibre inside the tile. Various geometries have been studied, each by a vertical muon sample of 5,000 muons. In figure 7.3, the relative light yields achieved for the investigated layouts are shown. The distance to the tile edge proves to be optimal close to the tile edge. However, to allow for a stable milling of the groove a minimum distance of $d = 10$ mm is required. A large bending radius is preferred as less photons will be lost in the curves and the stress on the fibre material is minimal. On the other hand, the path length, that the photons have to travel within the WLS fiber, is increased. An optimal geometrical configuration is

[4] Additionally, the light loss along WLS fibres is bigger compared to simulations. However, as here only a qualitative estimation of the light loss is possible, the attenuation length of the fibre, as given by the manufacturer, has not been modified for the simulations.

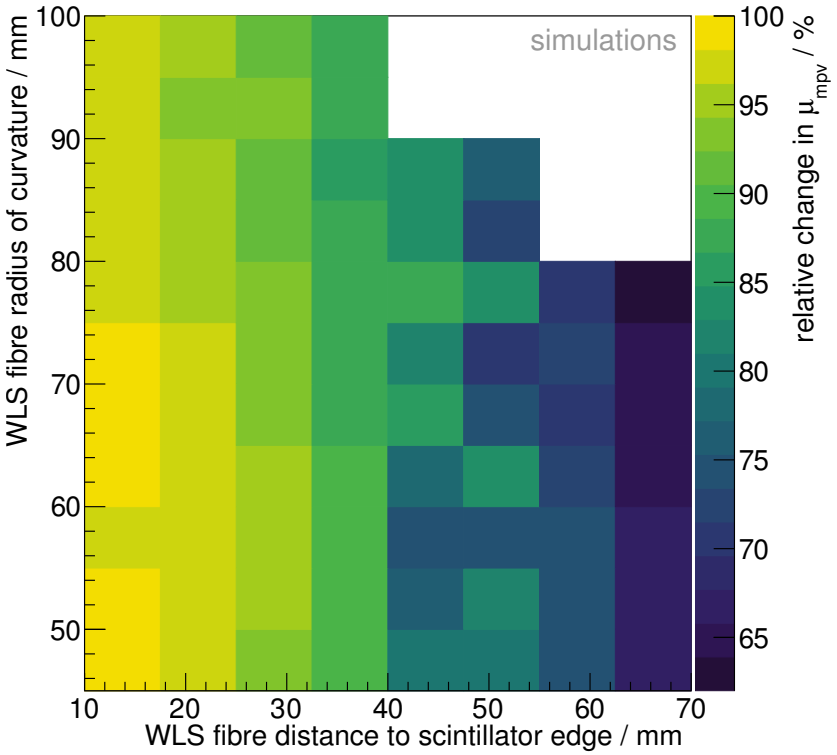

Figure 7.3.: Relative change in the light yield as a function of the distance of the WLS fibre to the tile edge and as a function of the WLS fibre radius of curvature. The relative light yield is thereby defined as $100\% \cdot \frac{\mu_{\text{mpv}}}{\mu_{\text{mpv, max}}}$. For each studied configuration, the simulations includes 5,000 vertical muon events homogeneously distributed along the scintillator tile. The muons have energies corresponding to a MIP.

found for $d = 10\,\text{mm}$ and $r = 60 - 70\,\text{mm}$ whereby 65 mm is chosen for the manufacturing of the unit prototypes. Besides the position of the WLS fibre, the length of the fibre may be interesting. The simulations predict no change in the light yield for a total fibre length of $(980 \pm 50)\,\text{mm}$. Two effects, an improved collection probability and a longer distance, compensate each other. After all modifications of the design and the adaptions of the simulation parameters, the detector simulation framework can successfully describe the response of a detector unit to particle passages. The layout corresponds thereby to a unit of layout 2 (cf. chapter 6). In figure 7.4, the light yield distribution for 10,000 individual vertical muons is shown. The simulated distribution can be described by a convoluted Landau-Gaussian distribution. The light yield is here defined by the most probable value, μ_{mpv}, of the Landau distribution. The simulated light yield of around $(29.9 \pm 0.1)\,\text{p.e.}$ can be assumed as the best case scenario for the studied unit. Compared to measurements of assembled units of layout 2, the unit with the highest light yield reaches $(28.3 \pm 0.1)\,\text{p.e.}$ for vertical traversing muons (cf. chapter 8). Thus, simulation and measurement are in acceptable agreement. All further units depict reduced light yields due to imperfections, for example, in the manufacturing process or in the material itself. An overview of the performance of all produced units can be found in table 8.2 on page 118.

7.3.2. Important performance quantities of the studied unit layouts

Based on the presented simulation framework, important performance characteristics of the chosen *final unit layout* can be predicted.

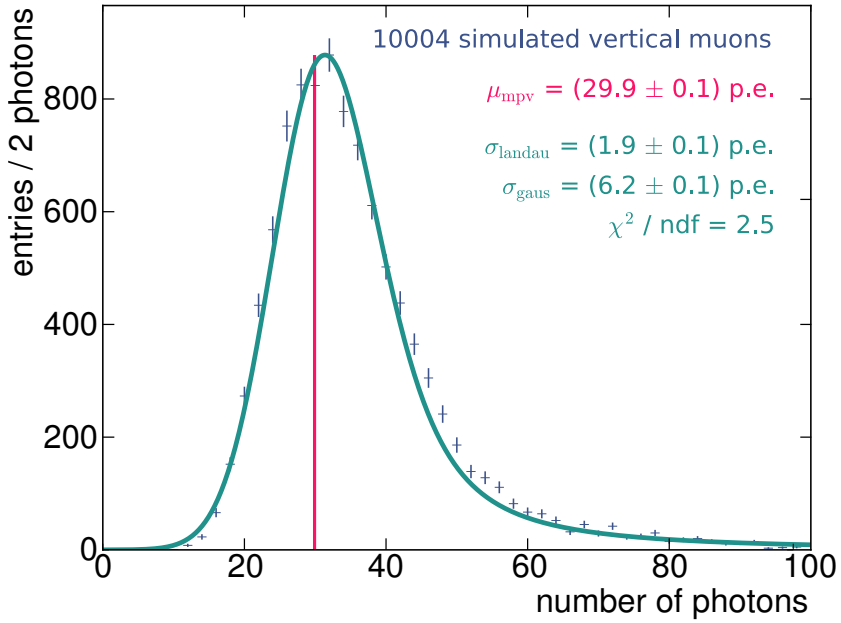

Figure 7.4.: Simulated light yield distribution of the final unit layout. Shown is the number of photons detected by the SiPM. The distribution contains 10,000 individual muon events with a kinetic energy corresponding to a MIP, $E_{\mathrm{MIP,\ range}}$ (cf. equation 7.3), and with an incident angle of $\theta = 0°$. A fit (green curve) by a convolution of a Landau and a Gaussian distribution can describe the simulated data. The reconstructed most probable value, μ_{mpv}, is denoted by a red, vertical line.

7.3.2.1. Indicator for an optimal threshold

A first indicator for an optimal *threshold* can be defined on the basis of the achieved *darknoise rejection* and the *muon detection efficiency*. The aim is to find a threshold, at which darknoise events are suppressed, but, ideally, signal events are not influenced.
First, darknoise traces are simulated. If the signal exceeds the chosen discriminator setting, an event is defined as triggered. The discriminator threshold refers thereby to a threshold in photon equivalent

$$n_{\gamma,\mathrm{thr}} = k + 0.5\,\mathrm{p.e.}\,, \quad k \in \mathbb{N}_0 \qquad . \tag{7.4}$$

Each trace covers a time interval of $t = 10\,\mu s$ referring to the average duration of a cosmic ray event. The darknoise rejection efficiency $\epsilon_{\mathrm{darknoise}}$ is defined by

$$\epsilon_{\mathrm{darknoise}} = 1 - \frac{N_{\mathrm{trigger}}(n_\gamma \geq n_{\gamma,\mathrm{thr}})}{N_{\mathrm{total}}} \qquad , \tag{7.5}$$

whereby $N_{\mathrm{trigger}}(n_\gamma \geq n_{\gamma,\mathrm{thr}})$ refers to the number of traces, in which at least one pulse exceeded the threshold. N_{total} refers to the total number of simulated traces. The rejection efficiency is shown as a function of discriminator threshold in photon equivalent in figure 7.5. Presented are darknoise simulation studies for both SiPM types used in this thesis. For both, only darknoise rejection efficiency points are presented for thresholds, at which at least one trace contained the corresponding amount of darknoise induced photons. The darknoise studies are statistics limited but indicate for the current SiPM type S13360-1350PE a sufficient threshold of ≥ 2.5 p.e. to suppress the darknoise component. The older SiPM type of S12571-050P has an increased thermal and correlated noise probability. The darknoise rejection efficiency is thus decreased. A higher trigger threshold would be needed to achieve the same suppression of darknoise events.

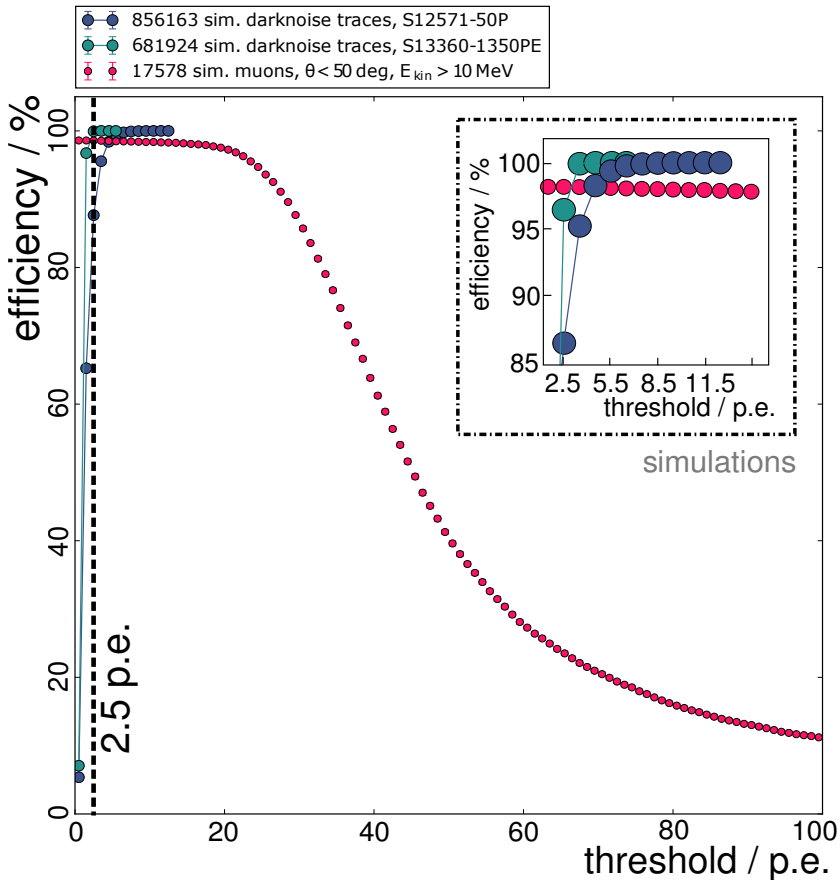

Figure 7.5.: Muon detection efficiency and darknoise rejection as a function of the discriminator threshold in p.e. For the current SiPM type S13360-1350PE, a significant suppression of darknoise is found for $n_{\gamma,\mathrm{thr}} \geq 2.5\,\mathrm{p.e.}$ The detection efficiency of muons is stable at $> 98\%$ for a threshold $n_{\gamma,\mathrm{thr}} \leq 20\,\mathrm{p.e.}$

For comparison, the muon detection efficiency is depicted as a function of the discriminator threshold. Around 17,000 single muon events are studied. The muons have kinetic energies of $10\,\mathrm{MeV} < E_{\mathrm{kin}} < 10^6\,\mathrm{MeV}$ and an incident angle of $\theta < 50\,^\circ$. They are uniformly distributed on a unit of layout 2. A muon detection efficiency of $> 98\%$ can be achieved up to a trigger threshold of 20 p.e. for simulations. This threshold is recommended for a future operation aiming to measure the muonic component in extensive air showers. A threshold of ≥ 2.5 p.e. allows for a reasonable suppression of 96% of the simulated darknoise events. This is also later confirmed by measurements (cf. figure 8.2). However, a slightly increased threshold of ≥ 3.5 p.e. allows for a suppression of nearly 100% of the simulated darknoise events. Therefore, this threshold is recommended for measurements that utilize the MIP peak for the calibration of a detector unit[5].

7.3.2.2. Simulated uniformity of a single unit

The *uniformity* of the light yield achieved by a unit is crucial to allow for a good estimator on the amount of particles traversing the detector material. The chosen shape of the WLS fibre inside the tile may introduce inhomogeneities. Furthermore, photons emitted close to the photosensor

[5] During the characterization and development of the detector units and MiniAMD, the MIP peak is of particular interest. Therefore, most measurements in the scope of this thesis will be performed with a threshold of 2.5 p.e. or 3.5 p.e.

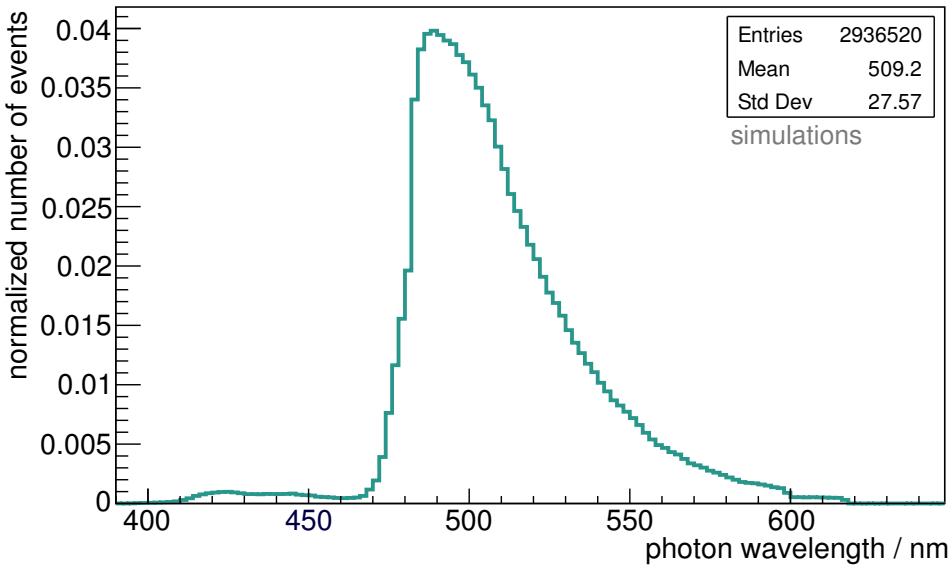

Figure 7.6.: Wavelength distribution of photons being detected by the $1.3 \times 1.3\,\mathrm{mm}^2$ SiPM of type S13360-1350PE. The total area of the histogram is normalized to 1. The SiPM is placed in front of the WLS fibre, directly located at the scintillator tile edge. The simulations includes 80,000 individual muon events homogeneously distributed over the scintillator tile. Their incident angles are homogeneously distributed on a sphere. The muons have energies corresponding to a MIP.

position may result in an increased signal yield. This is even more relevant for a photosensor located at the scintillator tile edge. Direct scintillation light might reach the SiPM surface as indicated in figure 7.6. Here, the simulated wavelength distribution for photons arriving at a SiPM located at the scintillator tile edge is presented. Two components can be identified. The majority of the spectrum corresponds to the scintillation emission spectrum, which has been wavelength-shifted by the WLS fibre. It depicts a peak wavelength of 490 nm. A smaller fraction corresponds to the unshifted scintillation spectrum in the UV-blue wavelength regime. For a SiPM located at an optical waveguide that is coupled to the WLS fibre, all direct light is shielded.
For both unit layouts, with and without optical waveguide, the uniformity is illustrated in figure 7.7. First, the mean light yield in p.e. is shown as a function of the point of incidence of single muons on the scintillator tile. For both layouts, the SiPM is located in the upper right corner. 80,000 individual muon events have been simulated for each layout. The sigma-shape of the WLS fibre is clearly visible. Scintillation photons are isotropically emitted while a particle traverses the scintillator material. If a muon position is located between the WLS fibre and the tile edge, the chance for photons to be collected by the WLS fibre is increased and the mean light yield is enhanced. Furthermore, muon positions next to the SiPM location depict even increased light yields. For the unit layout including an optical waveguide (corresponding to unit layout 1, cf. figure 7.7a), the increase results from shorter pathlengths of photons within the WLS fibre before entering the optical fibre. This is also true for the unit without any additional coupling (corresponding to unit layout 2, cf. figure 7.7b). However, the effect is strongly enhanced by direct scintillation light reaching the SiPM. Here in few bins next to the SiPM ($\approx$ 4% of total area), light yields up to 1.6 times the average light yield are found. As an estimate for the uniformity, the rms of the light yield distribution presented in figure 7.7a and in figure 7.7b is used. The expected uncertainty on the average light yield in each bin of the presented distributions comprises the intrinsic fluctuations in the light yield of a muon passage and fluctuations introduced by inhomogeneities. The former

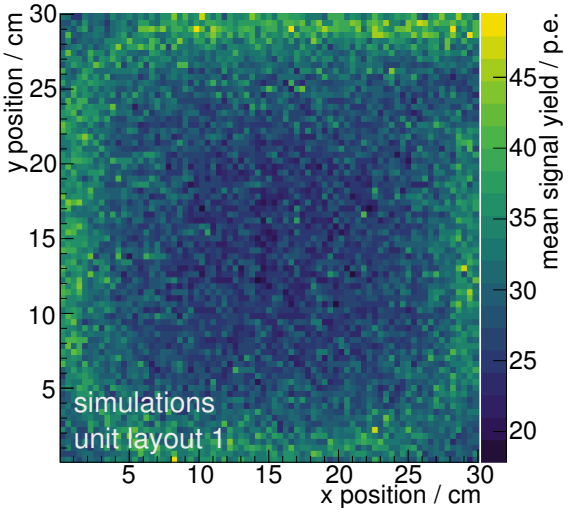

(a) Simulated light yield uniformity of unit including an optical waveguide to transport the photons to the photosensor. The photosensor is located 30 cm away from the scintillator tile.

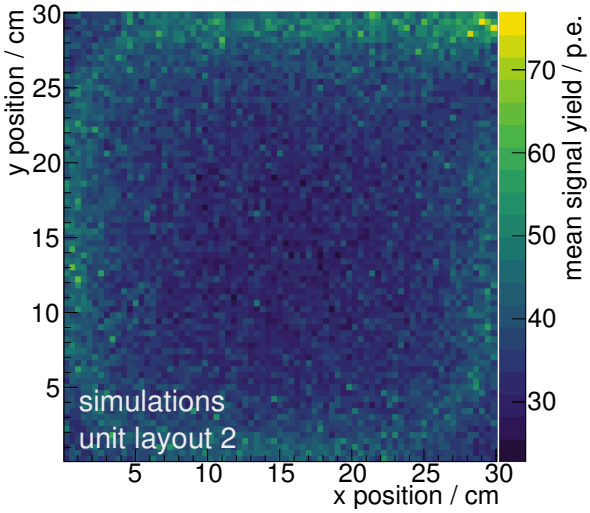

(b) Simulated light yield uniformity of a unit with the photosensor being located flush to the tile edge at the WLS fibre location.

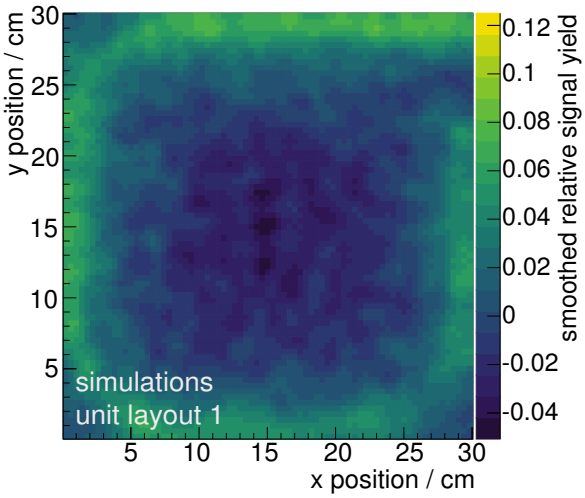

(c) Smoothed relative light yield distribution of a unit including an optical waveguide to transport the photons to the photosensor.

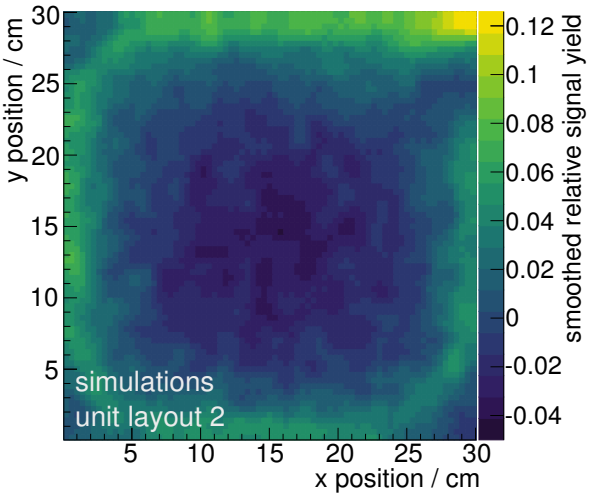

(d) Smoothed relative light yield distribution of a unit with the photosensor being located flush to the tile edge at the WLS fibre location.

Figure 7.7.: Simulated uniformity of two unit layouts. 80,000 individual muon events have been simulated for each layout. Their incident angles are homogeneously distributed on a sphere. Shown is the mean light yield as a function of the point of incident of a muon. The trigger threshold has been set to $n_{\gamma,\text{thr}} = 3.5\,\text{p.e.}$ The muons have energies corresponding to a MIP, $E_{\text{MIP, range}}$ (cf. equation 7.3). The photosensor type refers to the S133650-1350PE SiPM by Hamamatsu. Shown is also the smoothed relative light yield distribution. The bin contents of the resulting 2D-histogram are smoothed according to a kernel algorithm provided by the ROOT framework.

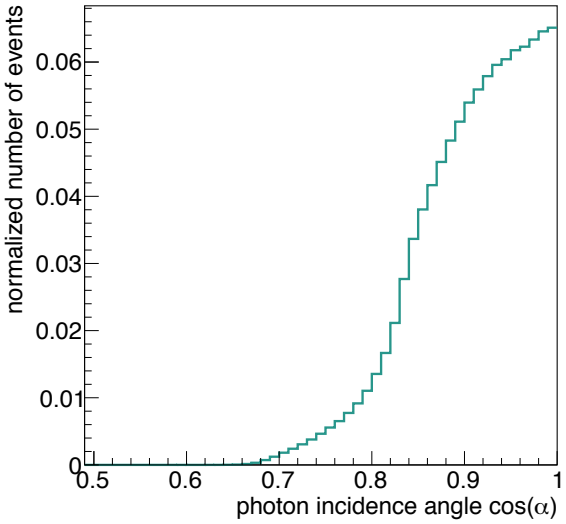

(a) Simulated photon incident angle distribution on the SiPM surface. The majority of the detected photons has an incident angle α smaller than 35° with 0° being normal to the SiPM surface.

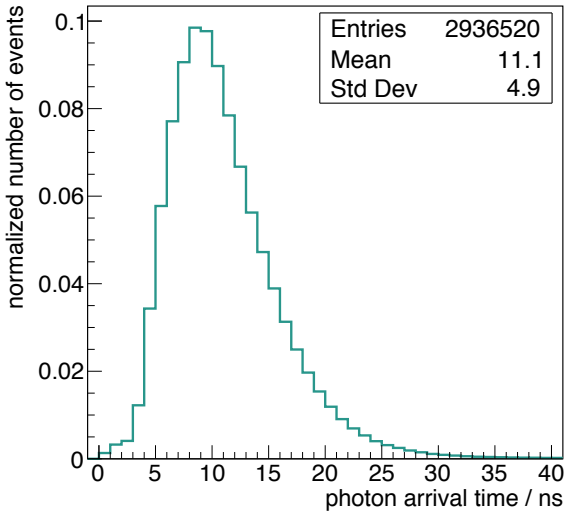

(b) Simulated photon arrival time at the SiPM. The majority of the photons arrives within a 10 ns window indicated by the width of the distribution.

Figure 7.8.: Simulated angular and photon arrival time distribution of photons being detected by the $1.3 \times 1.3\,\mathrm{mm}^2$ SiPM of type S13360-1350PE. The total area of both histograms is normalized to 1. The SiPM is placed in front of the WLS fibre, directly located at the scintillator tile edge. The setup corresponds to the unit layout 2. The Geant4 simulations include 80,000 individual muon events, homogeneously distributed over the scintillator tile. Their incident angles are homogeneously distributed on a sphere. The muons have energies corresponding to a MIP.

is (2.65 ± 0.06) p.e. for both layouts. The rms of the average light distribution of all bins for unit layout 1 is 4.22 p.e., for unit layout 2 it is 5.40 p.e. Thus, both layouts depict an increased light yield compared to the intrinsic fluctuations. Thus, a non-uniformity in the layouts is indicated, which is more present for the unit of layout 2. For an improved illustration, the relative light yield is presented in figure 7.7c and 7.7d for a unit with and without additional coupling to an optical waveguide, respectively. The relative light yield is defined as $s = \frac{s_{ij} - \bar{s}}{2 \cdot (s_{ij} + \bar{s})}$. Whereby $\bar{s}$ is the average light yield of all bins and s_{ij} is the signal in each bin. The simulated distribution is additionally smoothed by a kernel algorithm provided by the ROOT framework. Thereby, the underlying structure can be better elaborated. For unit layout 2, the non-uniformity is enhanced, but is accepted in favor of signal strength and stable coupling. The simulations discussed are confirmed by measurements in chapter 8.4 (cf. figure 8.25).

7.3.2.3. Photon angular and arrival time distribution

In figure 7.8a and 7.8b, the angular and the time distribution of photons arriving at the SiPM is shown. The simulated distributions contain 80,000 individual muon passages each. Their incident angles are homogeneously distributed on a sphere. The total area of both histograms is normalized to 1. The majority of the detected photons at the SiPM surface depicts incident angles α smaller than 35° while 0° corresponds to the SiPM surface normal. Larger angles are strongly reduced. They occur mainly in the less-populated outer cladding and are additionally suppressed by the transition of the fibre to the SiPM material (cf. section 5.2.3.2). The *photon arrival time* at the SiPM is influenced by the pathlengths of the photons inside all optical components. Key parameters

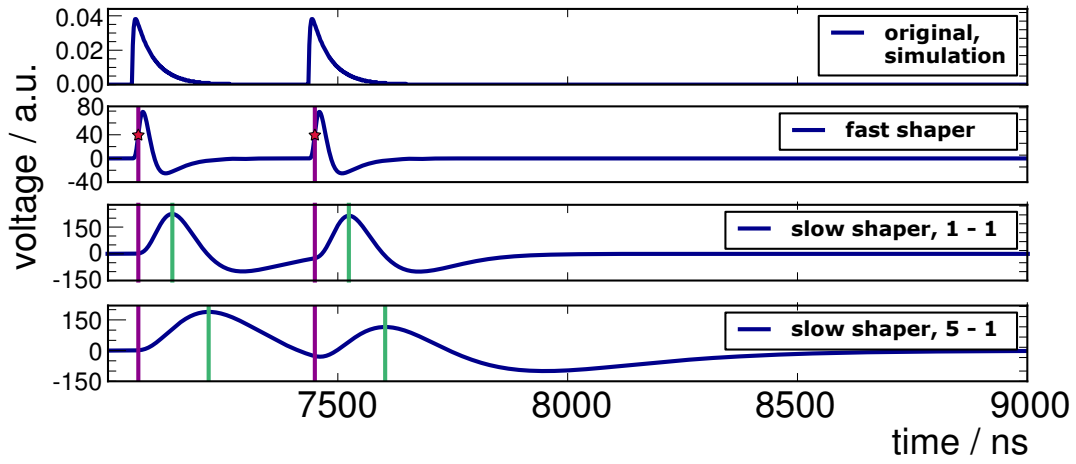

Figure 7.9.: Sketch of the electronics simulation. Shown is a simulated SiPM trace for different shaping procedures. The original trace contains two single p.e. pulses. The trace is shaped according to the electronics model introduced in [165]. The trigger decision is based on the signal modified by the fast shaper. If the signal exceeds a certain threshold (time of trigger = violet line, trigger threshold = red star), an event is registered. Additionally, two traces with different slow shaper configurations are depicted. The amplitude of the signal modified by the slow shaper at the hold time (green line) is a measure for the integrated charge contained in the event.

are the number of reflections inside the tile and the pathlength travelled inside the WLS fibre. As the photons are emitted isotropically, they depict highly individual paths until they are registered at the SiPM. Thus, an extended arrival distribution is expected. In figure 7.8b, the normalized number of simulated photons is presented as a function of the arrival time after the first photon of the event has been registered at the SiPM. On average, the majority of the photons arrives within a 10 ns time window and 10 ns after the first photon reached the SiPM. The simulated photon arrival time distribution is confirmed by measurements with units of layout 2 in chapter 8.2.

7.3.2.4. Shaper simulation

So far, the response of a unit is studied by means of the photons detected by the SiPM. For the prediction of the light yield, this is a valid assumption. The studies presented in [165] allow for a more complex description of the simulated detector response by introducing a simulation model of the readout electronics (cf. chapter 6.2.2).
By this model, simulated voltage traces are shaped according to a EASIROC fast and slow shaper. The model is originally based on detailed measurements of the slow shaper response. The fast shaper can not be studied directly. For an approximation of the fast shaper response, a slow shaper curve is compressed to account for the shorter peaking time of the fast shaper.
The trigger decision in simulation is sketched in figure 7.9. The incoming simulated SiPM signal is shaped by the fast shaper model. If the modified signal exceeds the chosen discriminator value, it is registered as event. In parallel, the signal is also shaped by the slow shaper model. The user can choose between different shaping and gain settings which are explained in detail in [165]. In figure 7.9, two shaper configurations are depicted. The first corresponds to a slow shaper time setting of 25 ns nominal peaking time and with highest possible gain (corresponds to shaping and feedback setting of 1). While the second corresponds to a slow shaper time setting of 125 ns nominal peaking time and with highest possible gain (corresponds to shaping setting of 5 and feedback setting of 1). The value registered for an event is the amplitude at the *hold time*. The hold time is a user-defined

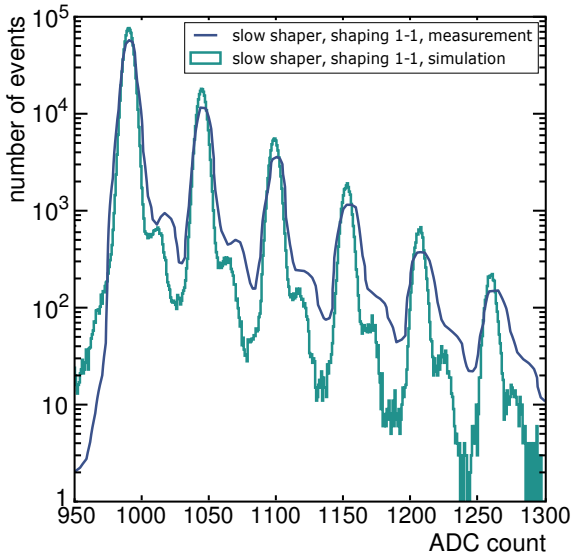

(a) Slow shaper time setting of 25 ns nominal peaking time and with highest possible gain (corresponds to shaping and feedback setting of 1).

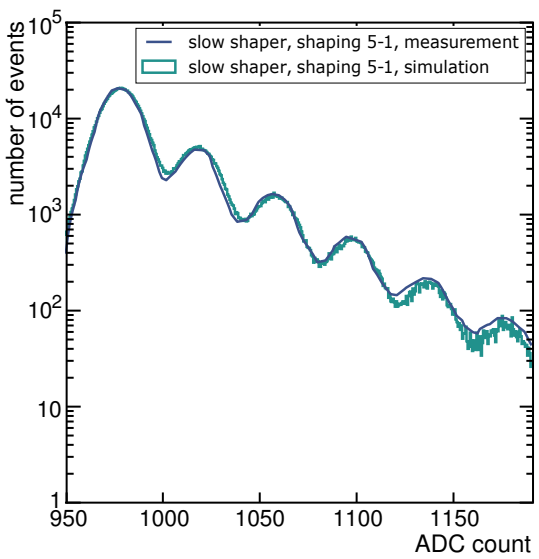

(b) Slow shaper time setting of 125 ns nominal peaking time and with highest possible gain (corresponds to shaping setting of 5 and feedback setting of 1).

Figure 7.10.: Measured and simulated darknoise spectra are shown as a function of ADC count. Measured darknoise spectra and slow shaper simulation are taken from [165]. The different slow shaper time settings influence the distance in ADC count between two consecutive peaks and the form of the spectrum.

time after the trigger signal which should be chosen close to maximum amplitude of the shaped signal. The amplitude is then a measure for the integrated charge contained in the triggered event. By the shaping procedure, the pulse form of the signal is strongly influenced and results in different signal responses. This is shortly illustrated in figure 7.10. Darknoise events of the same SiPM of type S12571-050P have been measured and simulated for two slow shaper configurations. The measurements are performed and presented in the scope of [165]. The simulations are performed by means of the G4SiPM framework by the author of this thesis. Over 1 million darknoise events are contained in each charge spectrum. For both configurations, the simulated and the measured spectra are compared. In figure 7.10a, the slow shaper configuration with shaping and feedback setting of 1 is presented. A clear peak-like structure is visible. The highest peak refers to the 1 p.e. peak, while peaks at higher ADC values correspond to crosstalk events. Interesting is a smaller second shoulder at the right side of each peak. These shoulders are caused by SiPM afterpulsing[6]. Their occurrence can be well described by the simulations. Furthermore, the simulations well describe the decline of the frequency for higher multiplicities, referring to the correlated noise probability. Crucial for a simulation is the correct description of the electronics noise influencing the baseline and the pulse shape. It is visible that the measurements depict a higher noise component than assumed for the simulation. Therefore, the peaks in the measured spectrum are broader and less pronounced. However, to illustrate the principle working of the shaper no more realistic description is necessary. In figure 7.10b, the slow shaper configuration with shaping setting of 5 and feedback setting of 1 is presented. Here, simulation and measurement are well in agreement. The larger shaping time is washing out the double peak structure visible in the former setting and

[6]The G4SiPM simulation allows to trace the source of each individual cell breakdown. Additionally, the effect is studied in detail in [114].

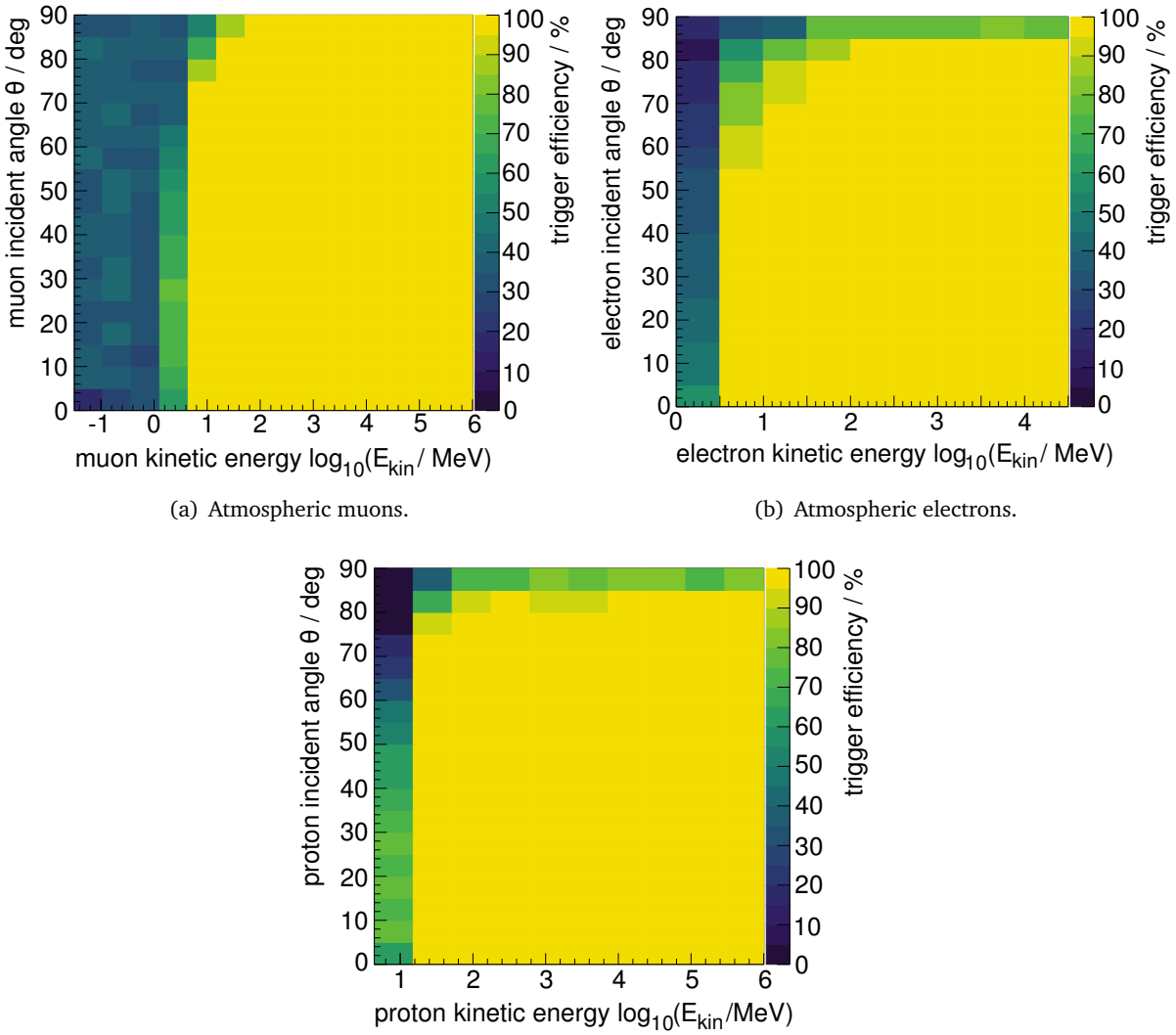

(a) Atmospheric muons.

(b) Atmospheric electrons.

(c) Atmospheric protons.

Figure 7.11.: Simulated trigger efficiency of a detector consisting of one unit. The incident angles θ of the simulated particles were homogeneously distributed on a sphere. They range from 0° to 90° while 0° is perpendicular to the tile area. The trigger threshold has been set to $n_{\gamma,\mathrm{thr}} = 3.5$ p.e. The photosensor type refers to the S133650-1350PE SiPM by Hamamatsu.

the peak shape can be described by a multi-gaussian. In summary, the electronics simulation is well functional.

7.3.2.5. Detection efficiency

The *detection efficiency* depends on the particle characteristics and the chosen discriminator threshold $n_{\gamma,\mathrm{thr}}$. In figure 7.11, the simulated trigger efficiency is shown as a function of the kinetic energy carried by the particle as well as its angle of incidence. The particle positions were homogeneously distributed over the scintillator tile. The incident angle $\theta = 0^\circ$ is perpendicular to the tile area. A trigger threshold of $n_{\gamma,\mathrm{thr}} = 3.5$ p.e. is applied. Presented are the detection efficiencies for the three most relevant particle species in atmospheric air showers: (Anti-)muons, (anti-)electron and (anti-)protons. For all types a high efficiency of nearly 95-100% is achieved for a large energy range. A

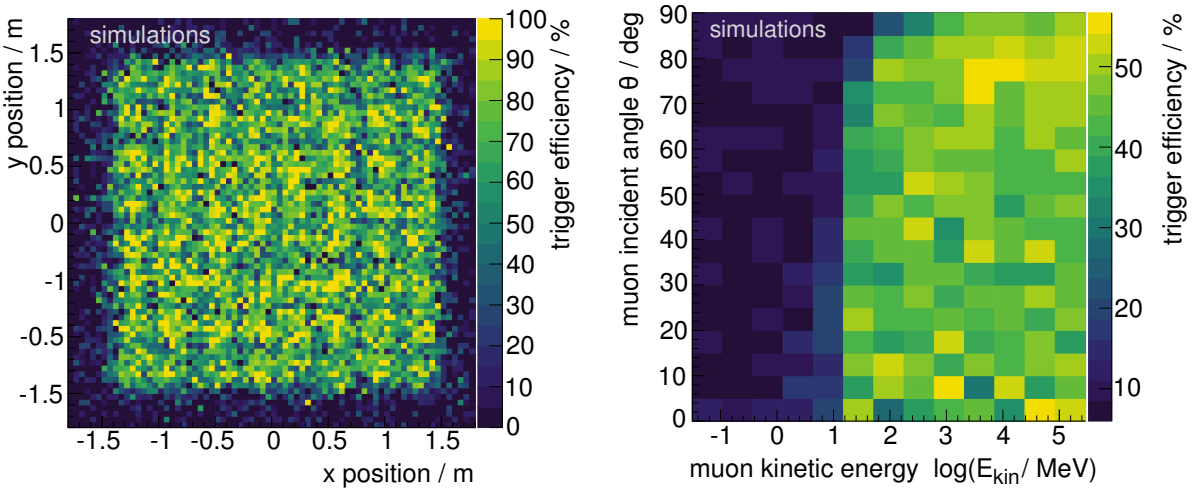

(a) Simulated trigger efficiency as a function of the point of incidence of a muon.

(b) Simulated trigger efficiency as a function of the kinetic energy and the angle of incidence of a muon.

Figure 7.12.: Simulated trigger efficiency of a detector consisting of 64 units. The incident angles θ of the simulated muons were homogeneously distributed on a sphere, ranging from 0° to 90°. The trigger threshold has been set to $n_{\gamma,\mathrm{thr}} = 3.5$ p.e.

decrease of the detection efficiency for larger angles results from clipping muons, which only partly traverse the scintillator tile. For a more realistic setup, the trigger efficiency of the Aachen Muon Detector (AMD) as a large-scale detector is studied. The detector concept is presented in section 6.4. A schematic view of the detector layout as implemented in the simulation is given in figure 6.8 in chapter 6 on page 67. The total instrumented area of the detector is 44%. In figure 7.12, the simulated trigger efficiency for the AMD detector is shown as a function of the incident angle, position and kinetic energy of the traversing muons. The distributions contain 80,000 individual muon events each.
A high detection efficiency is found at the positions of the units, with a grid with reduced efficiency identifying the gaps between individual trays and units. The outer region of the detector is not equipped. The detection efficiency for all incident angles is on average 40-50% for kinetic energies above 30 MeV. This is well compatible with the determined detection efficiency $> 95\%$ for a single unit. While taking the fill factor of the detector into account, a detection efficiency of $95\% \times 44\% \rightarrow 42\%$ is expected.

7.3.3. The MIP spectrum

So far, the light yield distribution was studied by means of simulations of atmospheric muon passages having an energy of a minimum ionizing particle. In this section, a first comparison of the simulated signal spectrum to measurements is discussed to illustrate the performance of the presented detector simulation framework. More detailed measurements of unit prototypes are presented in the following chapter 8. In a real setup, not only MIPs will traverse the scintillator tile but all different kinds of particles having a wide range of energy and angles. The majority of these particles will originate from low energetic cosmic ray air showers. Only few particles of these showers will arrive at Earth's ground for a detector located at sea level. They are mainly composed of electrons / positrons, (anti-)muons and photons. To investigate the expected signal spectrum measured by the presented unit, cosmic ray air showers are simulated by CORSIKA [186]. They are propagated to the height of Aachen, 282 m above sea level. The following simulation parameters are applied. Only

protons are used as primary particles. GHEISHA and QGSJet II-04 are used as low and high energy hadronic interaction model, respectively. The energy of the showers follows an energy spectrum of $E^{-2.7}$ starting from 10 GeV (cf. chapter 2.2). The shower directions are uniformly distributed in azimuth and range from 0 ° to 65 ° in zenith assuming an isotropic distribution. This corresponds to a simulated solid angle of $\Omega_{\text{sim}} = 2\pi(1-\cos(65\,^\circ))\,\text{sr}$. The magnetic field corresponding to central Europe is applied as well as the default US-standard atmosphere. Thinning is not active and all energy cuts are set to their minimum value. The remaining cut on the minimal kinetic energy for each particle type is apparent in figure 7.13 in the low-energy region of the corresponding absolute kinetic energy distribution.
For a reasonable statistics also for high air shower energies, the CORSIKA events are simulated in four energy ranges E_i: $E_1 = 10-100\,\text{GeV}$, $E_2 = 100-3{,}000\,\text{GeV}$, $E_3 = 3{,}000-10{,}000\,\text{GeV}$ and $E_4 > 10{,}000\,\text{GeV}$. For each energy range, $N = 20{,}000$ CORSIKA showers are simulated. To achieve a steady falling energy spectrum, an energy-weight e_i is introduced. This weight is based on the number of events, which would be actually needed to be simulated. The energy-weight e_1, corresponding to the lowest energy bin E_1, is set to 1. All further energy-weights are smaller than 1. The simulated shower cores are homogeneously distributed on a circle with an area of $A_{\text{sim}} = 5\,\pi\,\text{km}^2$. Each shower is reused several times. The amount of reuse decreases with shower energy as more computing resources are needed. Thus additionally to the energy-weight, a reuse-weight r_i is introduced for each energy bin. The reuse-weight r_1, corresponding to the lowest energy bin E_1, is set to 1. All further reuse-weights are larger than 1.
The estimated amount of simulated air showers is then given by

$$N_{\text{sim, shower}} = \sum_i e_i \cdot r_i \cdot N \quad \text{with } e_1 = r_1 = 1; \quad e_{i>1} < 1; r_{i>1} > 1 \qquad . \tag{7.6}$$

This number is much larger than the actual performed simulations ($80{,}000 \rightarrow 1.5 \times 10^{14}$). In the centre of the circle, eight detector units are placed next to each other. All particles crossing the detector units are registered. The absolute kinetic energy distributions for the different particle species are presented in figure 7.13. They cover a large energy range from $10^{-4.5}$ to $10^{4.5}\,\text{GeV}$. The highest energies are carried by muons. The majority of the particles arriving at the surface are photons, followed by muons and electrons. These atmospheric particles are further processed by terms of the presented detector simulation framework. In the scope of this framework, the particles are homogeneously distributed on a single detector unit with a starting point few cm above the scintillator tile. Their resulting light yield distribution is presented in figure 7.14. Only 5% of the photons are depositing enough energy to be registered at the SiPM. Their signal distribution follows an exponential decrease and has its highest contribution in the low signal region. The energy deposit of atmospheric muons corresponds to the MIP peak spectrum (cf. chapter 8.1.3). The light yield is given in physical units of MIPs. The position of the peak maximum is thereby assumed as most probable value for a single MIP passage and is scaled to 1 MIP. All muons produce a detectable light yield while for electrons and protons only 70% of the particle passages are registered by the SiPM. The electron light yield depicts a comparable peak like structure as muons but with a broader distribution and an even more asymmetrical tail to larger signals. They are responsible for a change in the slope of the overall light yield distribution for all particles at higher signals.

To enable a comparison to measurements, the absolute simulated distribution of counts must be translated into a distribution of the event rate. Therefore, a measurement time t is estimated for the simulated number of events $N_{\text{sim, shower}}$ using the literature value of the cosmic ray flux. For an energy range from several GeV up to 100 TeV, the differential flux it is given approximately as

$$F(E) = k \cdot \left(\frac{E}{1\,\text{GeV}}\right)^{-\gamma} \approx 1.8 \times 10^4 \frac{1}{\text{m}^2\ \text{s sr GeV}} \left(\frac{E}{1\,\text{GeV}}\right)^{-\gamma} \qquad , \tag{7.7}$$

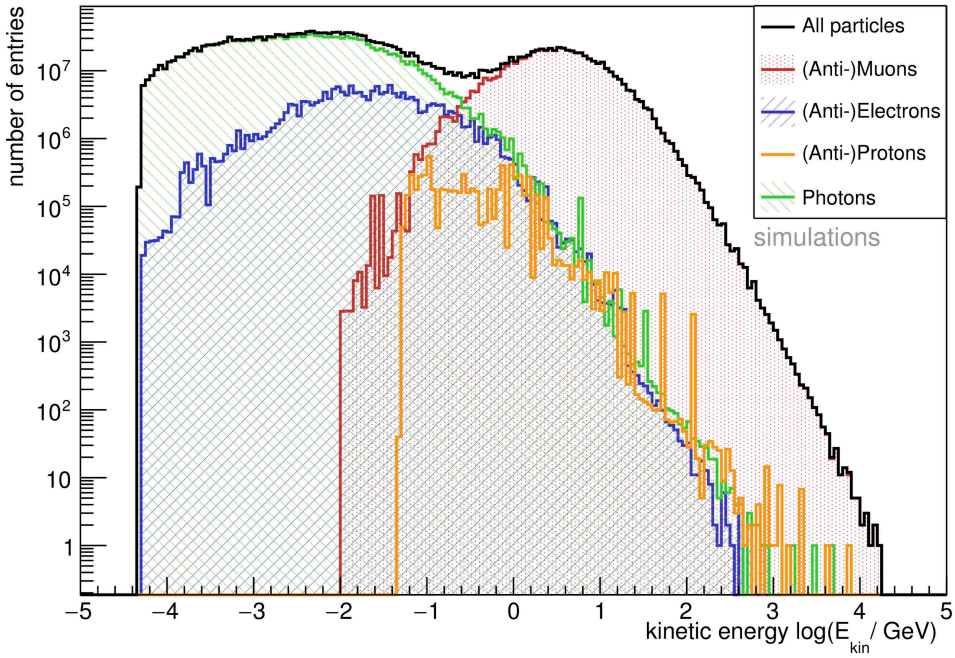

Figure 7.13.: Absolute simulated kinetic energy distribution of atmospheric particles. The distribution contains information of 80,000 CORSIKA showers. Most of the particles arriving are photons, followed by muons and electrons. The low-energy cut-off of each distribution results from the minimum kinetic energy cut that CORSIKA applies individually to each particle type.

whereby $\gamma = 2.7$ is the spectral index in the corresponding energy range and E the energy-per-nucleon [11].
A measurement includes all kinds of possible energies and the integrated flux F_I is the observable of interest. It can be determined by integrating the differential flux

$$F_I(E > E_{\text{min}}) = \left(\int_{E_{\text{min}}}^{\infty} F(E)\, \mathrm{d}E \right) \stackrel{!}{=} \int_{E_{\text{min}}}^{\infty} \frac{\mathrm{d}^4 N(E)}{\mathrm{d}E\, \mathrm{d}A\, \mathrm{d}\Omega\, \mathrm{d}t} \mathrm{d}E \tag{7.8}$$

$$\Rightarrow \left[\frac{k}{1-\gamma} \left(\frac{E}{1\,\text{GeV}} \right)^{1-\gamma} \right]_{E_{\text{min}}}^{\infty} = \frac{N_{\text{sim, shower}}}{A_{\text{sim}} \cdot \Omega_{\text{sim}} \cdot t} \tag{7.9}$$

$$\Rightarrow t = \frac{N_{\text{sim, shower}}}{A_{\text{sim}} \cdot \Omega_{\text{sim}} \left(\frac{E_{\text{min}}}{1\,\text{GeV}} \right)^{1-\gamma}} \frac{\gamma - 1}{k} \quad . \tag{7.10}$$

Thereby, the simulations are assumed to describe well the ratios between the individual particle species but the information of the absolute event rate is limited.
The simulated distributions are compared to three measurement setups. Two setups are located in a laboratory. The surrounding walls are assumed to shield part of the particles, mainly photons and electrons. More details on these measurements can be found in chapter 8. One setup is located outdoors (cf. chapter 9). First, the particles of interest are studied. The simulated muon spectrum is compared to the MIP spectrum measured for a unit operated in a stack of eight units in the laboratory (cf. figure 7.15a). A six-fold coincidence including the unit under study is required in the measurements to suppress all background events. By the geometrical configuration of the stack, the incident angle of muons is strongly limited to a maximum angle of 15 °. This limited geometrical acceptance is used for the calculation of the arriving particle flux at the detector units

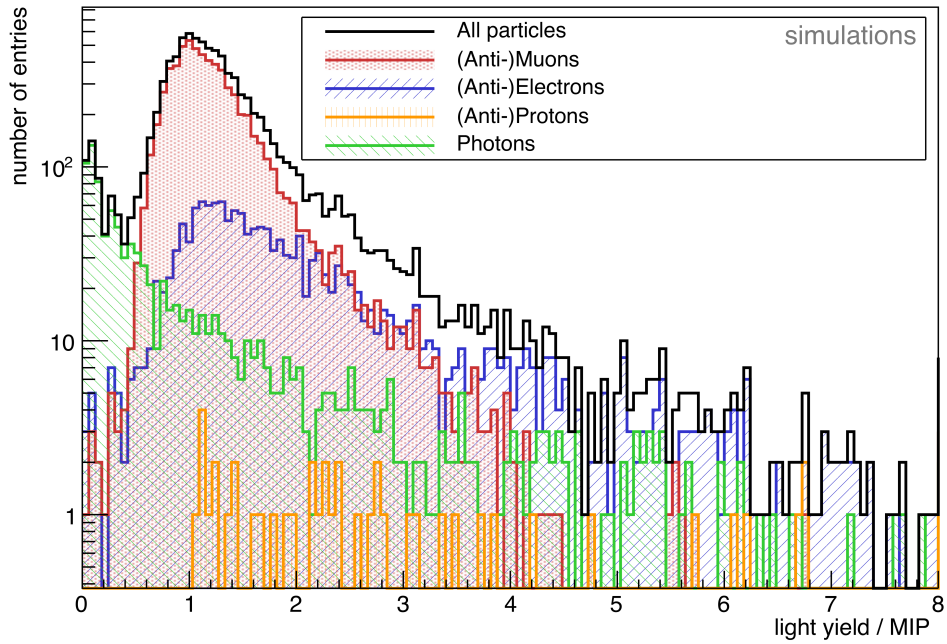

Figure 7.14.: Absolute simulated light yield distribution of passages of atmospheric particles. The distribution contains information of 80,000 CORSIKA showers.

in the simulations. Both distributions, measured and simulated, are presented as a function of the light yield given in physical units of MIPs. The position of the peak maximum is thereby assumed as most probable value for a single MIP passage and is scaled to 1 MIP for simulation and measurement. Both distributions are in excellent agreement with each other. As next step, the all-particle light yield distribution is compared to the measured MIP spectrum requiring only a two-fold coincidence including the unit under study. During this measurement, MiniAMD is located outdoors. By the geometrical configuration of the stack, the incident angle of muons is limited to a maximum angle of 70°. This limited geometrical acceptance is used for the calculation of the arriving particle flux in the simulations. The comparison is presented in figure 7.15b. The less strict requirement allows other particles than muons to be detected. The resulting detected distribution is broader than a pure muon spectrum, as expected, and describes well most part of the spectrum. Only the highest energy tail can not be reproduced. The measurements depict a lower event rate for light yields larger than 3 MIP. A possible reason may be the required two-fold coincidence in measurements. For example, electrons can be stopped in the upper unit, resulting in a high light yield, but those particles won't reach the second unit. The last measurement is presented in figure 7.15c and is performed in the laboratory. The overall particle spectrum is compared to a unit operated in self-triggering mode. Additionally, the measured darknoise spectrum is depicted. Below 5 p.e., the spectrum is dominated by darknoise. The simulated spectrum includes again all particle species, but now allows all possible arrival directions. For this setup, the simulated spectrum can not reproduce the measurements. Again a more pronounced highest energy tail is present in the simulations. Additionally, a smaller absolute event rate is measured. A possible reason may be the energy loss of the electrons in the material they pass through until they reach the laboratory. Furthermore, the simulations predict a significant larger peak-to-valley ratio between the minimum before the MIP peak and the height at the MIP peak maximum. In the measured self-triggered spectrum, no valley can be observed. An additional component is needed to explain the data. Radioactive isotopes as present in the air may be possible sources as indicated by measurements presented in chapter 8.3.

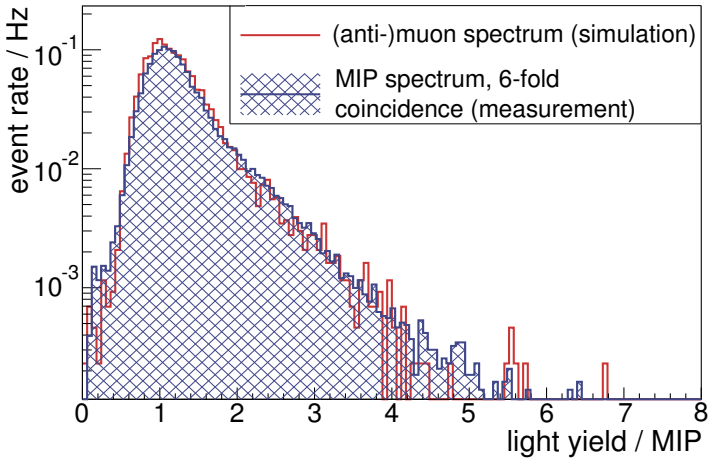

(a) Comparison of the simulated and measured MIP spectrum. For the measurement in the lab, a six-fold coincidence of units in a stack is required to detect mainly muons.

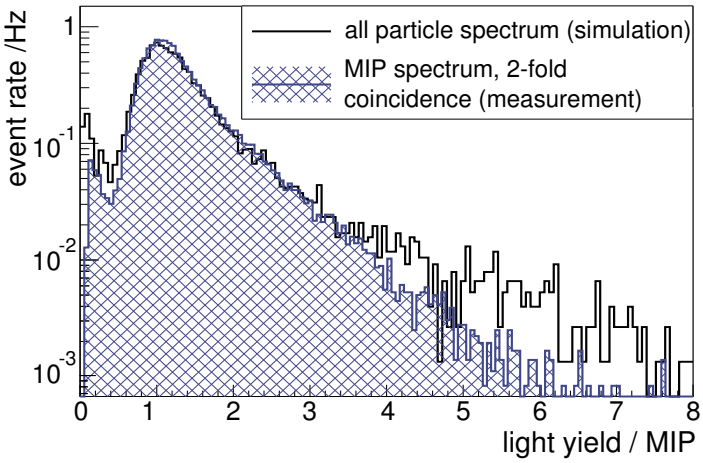

(b) Comparison of the simulated all particle spectrum and a measured particle spectrum. For the measurement in the lab, a two-fold coincidence of units in a stack is required.

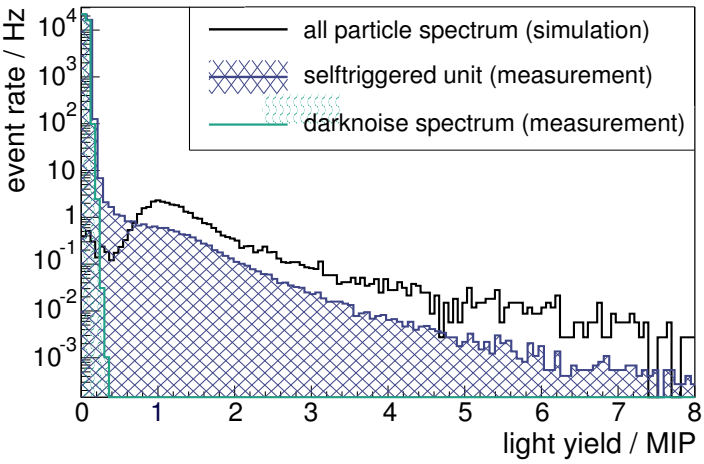

(c) Comparison of the simulated and measured particle spectrum. For the measurement in the lab, a unit is operated in self-triggering mode. Additionally, the measured darknoise spectrum is shown in green.

Figure 7.15.: Comparison of simulated light yield distribution of atmospheric particles compared to measured distributions by the units presented in chapter 6. The light yield is given in physical units of MIPs. The position of the peak maximum is thereby assumed as most probable value for a single MIP passage and is scaled to 1 MIP for simulation and measurement. The event rate distributions are presented. The all particle spectrum comprises muons, electrons/positrons, photons and protons. The limited geometrical acceptance of each setup is used for the calculation of the trigger rate of the detector units in the simulations. See text for discussion.

CHAPTER 8

Performance measurements of unit prototypes

This chapter addresses the performance of the actual manufactured units of layout 2, first introduced in chapter 6. Based on the extensive knowledge gained by simulations and measurements presented in chapter 7 and in appendix I and J, respectively, the best possible unit layout has been chosen. A *unit* comprises a scintillator tile with a sigma-shaped WLS fibre directly connected to a silicon photomultiplier (SiPM, cf. chapter 4) without an additional optical waveguide in between. A highly reflective foil is glued onto the fibre end located inside the tile. As wrapping a combination of a Tyvek sheet and two layers of aluminum foil is applied. As photosensor the SiPM type S13360-1350PE by Hamamatsu [105] is applied, always operated with a default bias voltage 3 V above breakdown.
16 units of this type are produced in the mechanical workshop of the Physics Institute III A of the RWTH Aachen University. These are later assembled to two modules building a so-called *MiniAMD* detector (cf. chapter 9). The detector serves as a demonstrator to study the ability to detect cosmic ray air showers. Several important characteristics are investigated by the response of the 16 units to a constant flux of atmospheric muons. The studies are performed by units operated in self-triggering mode and by coincident measurements within a stack of units or with an external muon tomograph providing spatial resolution. All investigations confirm an excellent performance achieved by the units. First, main operation parameters as the *darknoise rate* or the *light yield* of these units are determined. Furthermore, investigations of the *detection efficiencies* for single atmospheric muons depending on the *discriminator threshold* are discussed.
All measurements are performed by the readout electronics presented in chapter 6. For the EASIROC slow shaper, the following settings are used, a shaping parameter of 125 ns nominal peaking time[1] and the highest possible gain[2]. While main operation parameters, e.g. the discriminator threshold or the baseline of the EASIROC, are temperature dependent, the temperature, at which the measurements are performed, is indicated. The temperature is mostly stable within 1.5 °C for each individual measurement procedure. For all measurements the temperature ranges within 23 − 29 °C. To allow for a stable gain of the SiPMs, a temperature compensation by means of a fine adjustment of the bias voltage is applied (cf. equation 4.2) during all measurements. All tiles and SiPMs are numbered according to their respective EASIROC channel number.
The configuration scripts and measurement programs are modified but are based on programs de-

[1] corresponding to a shaping setting of 5
[2] corresponding to a feedback setting of 1

veloped by L. Middendorf [165]. Basic principles of several measurements discussed in this thesis have already been presented in [164, 165]. However, unless stated otherwise all measurements are performed by the author of this thesis.

8.1. Darknoise quantification and optimal threshold estimate

For the operation of the presented units, the knowledge of its basic characteristics as the light yield for crossing minimum ionizing particles (MIPs) or the expected influence by background or darknoise events is mandatory. They are further needed to find a first estimate for an optimal trigger threshold which is based on a trade-off between darknoise suppression and the loss of signal by muons. All units are studied in two scenarios. First, the SiPMs are measured in darkness without any connection to a scintillator tile. Second, the SiPMs are connected to one tile each. The performance of these units, arranged in a stack, are investigated regarding their response to atmospheric muons. For both scenarios, a rate scan as a function of the trigger threshold and a charge spectrum measurement are performed. These presentations are followed by a brief comparison to expectations of key parameters such as the darknoise and the atmospheric muon rate. Furthermore, a determination of the trigger efficiency for single muon events is aspired. All presented performance characteristics are compared to those determined for units of layout 1 as presented in [165].

8.1.1. Rate scan as a function of the trigger threshold

The readout electronics allows for a fine setting[3] of the discriminator threshold of the EASIROC fast shaper chain (cf. chapter 6.2.2, [165, 167, 168]). The discriminator value given in DAC count is common for all channels. It is important that the common threshold in DAC count will also allow for a common threshold in photon equivalent (p.e.) for all SiPMs of type S13360-1350PE if they have comparable gains.
A *rate scan* as a function of the trigger threshold is performed for two scenarios, first of SiPMs operated in darkness, second of SiPMs connected to a scintillator tile and thus detecting light produced by traversing MIPs. All rate scans are performed at an average ambient temperature of $(26.85 \pm 0.18)\,^{\circ}\mathrm{C}$ with temperatures ranging from 26.5 °C to 27.5 °C .
Each rate scan is performed as the following: For each presented data point in figure 8.1 and 8.2, $n_{\mathrm{run}} = 40$ number of runs are performed. For each run, the FPGA counts all discriminator events within a measurement time t which have exceeded the imposed hardware threshold in DAC count. A new hit is registered if the discriminator becomes active after being inactive for $\approx 10\,\mathrm{ns}$.
Therefore, the rate R corresponding to each data point is calculated by

$$R = \frac{\sum_{i=0}^{n_{\mathrm{run}}} n_i}{t \cdot n_{\mathrm{run}}} \quad . \tag{8.1}$$

The dark count rate scan

In figure 8.1, *dark count rate scans* for 16 SiPMs are presented as a function of the discriminator threshold of the fast shaper for three different scales. A step-like structure is visible for all SiPMs. Each step corresponds to a photon equivalent. Small deviations in the positions of the steps are expected due to deviations in the gain but still allow for a common threshold in p.e. for all SiPMs as desired.
The baseline is apparent at an effective threshold of 0 V. At a threshold of 0.5 p.e. an average

[3] The step size is $< 2\,\mathrm{mV}$.

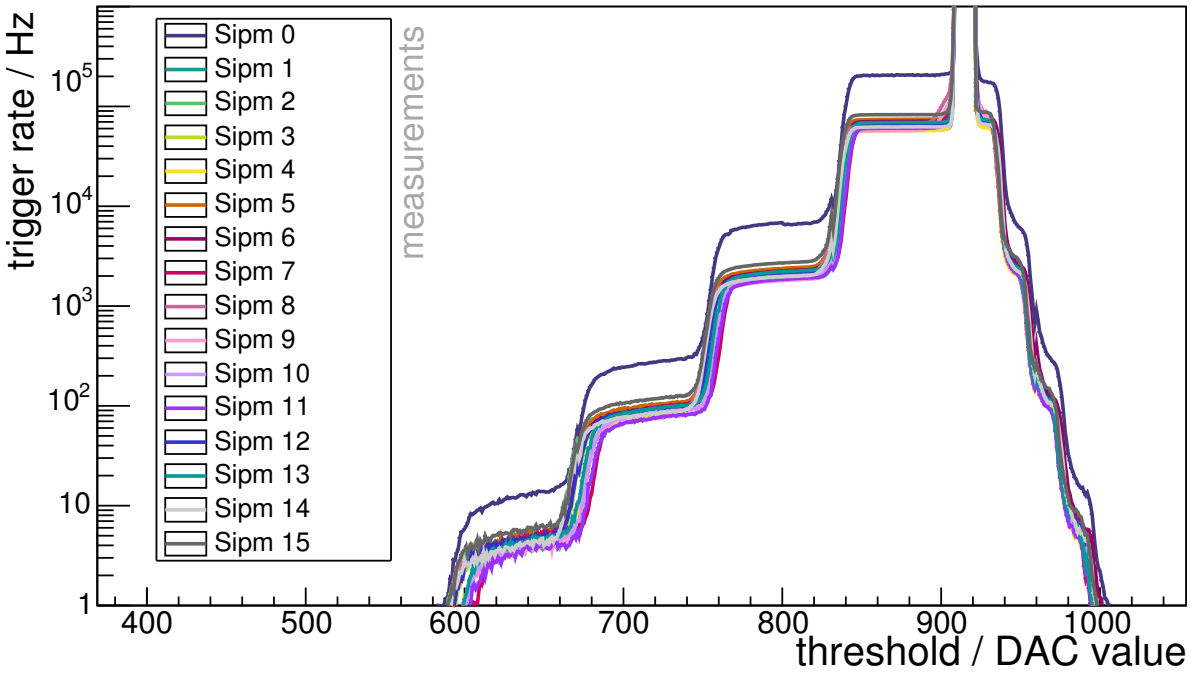

(a) Darknoise rate scan as a function of the hardware threshold in DAC count.

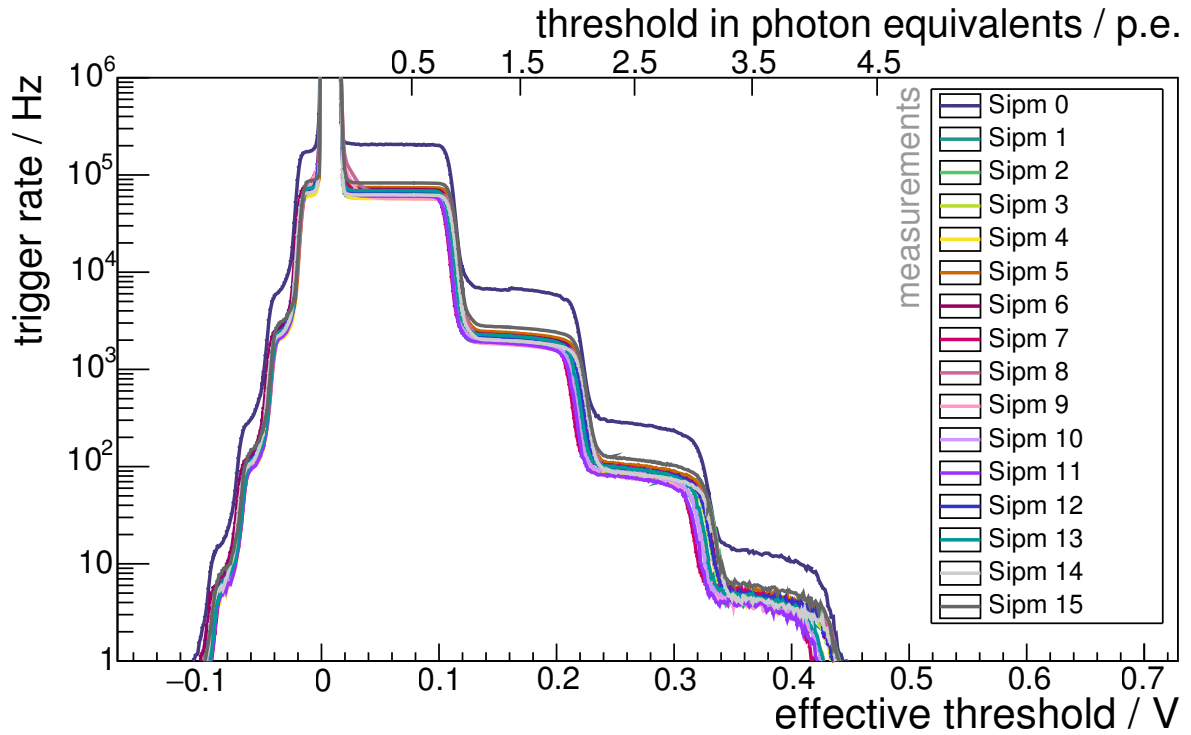

(b) Darknoise rate scan as a function of the effective threshold in V.

Figure 8.1.: Dark count rate scan for 16 SiPMs as a function of the trigger threshold with three different scales. The hardware threshold in DAC count and the effective threshold in V are common for all SiPMs. A lower DAC count corresponds to a higher threshold voltage. A third scale represents a conversion in photon equivalent for SiPM 1. The baseline is apparent at an effective threshold of 0 V. For the increased rate of SiPM 0, please refer to the text.

Threshold		
hardware in DAC count	**effective in volts**	**device in p.e.**
860	0.08	0.5
790	0.17	1.5
720	0.26	2.5
640	0.36	3.5

Table 8.1.: Approximate conversion between the three different scales of the discriminator threshold based on the dark count rate scan performed for SiPMs of type S13360-1350PE at a temperature of $26-27\,^{\circ}\mathrm{C}$.

darknoise rate of $60-85\,\mathrm{kHz}$ is detected. The darknoise rate is reduced to an average darknoise rate of $< 10\,\mathrm{Hz}$ at a threshold of 3.5 p.e. One SiPM (channel 0) depicts a higher thermal trigger rate of around $110\,\mathrm{kHz}$ at a threshold of 0.5 p.e. while its crosstalk probability and gain are comparable to the other SiPMs. This behavior can be reproduced while connecting the same SiPM to a different channel of the EASIROC and is thus a SiPM defect. However, the increased darknoise rate does not influence the performance of the SiPM for the signal region as will be investigated in the following.

The trigger threshold scales

As a short digression, the three presented scales are discussed in more detail.

- The *hardware threshold in DAC count* is important for the user of the readout electronics. While the setting of the threshold in the EASIROC is performed by a 10-bit DAC, the imposed trigger threshold is given in DAC count by the user. The value is independent of all ambient effects as temperature or SiPM characteristics, but is counterintuitive as a larger value in DAC count corresponds to a smaller imposed trigger threshold. It has to be converted to other units to provide a physical meaning.

- The *effective threshold in volts* is the conversion of DAC count in the corresponding voltage output. Its value increases as expected with a larger trigger threshold. A DAC count of 0 represents the state at which all bits are switched off and the maximal output voltage of $4.5\,\mathrm{V}$ is reached [164]. Each additional DAC count or step corresponds to a voltage decrease of approximately $2\,\mathrm{mV}$. The output voltage depends on the ambient temperature and the chosen EASIROC configurations. It has been carefully characterized in [164, 165]. The applied conversion in this thesis is based on these studies.

- The *device threshold in p.e.* provides a scale with physical meaning but is only valid for an individual SiPM. As indicated by the step-like pattern of the trigger rate as a function of the trigger threshold, each step in the rate corresponds to a step in the threshold in p.e. Providing a binary signal for each triggered cell, this structure is rather sharp, but depends on the gain and response of each SiPM.

A conversion between all three scales is possible as the dark count rate scan proves the ability to set a common threshold in p.e. for all studied SiPMs for a stable temperature regime. However, the conversion presented in table 8.1 is not valid in general.

The signal rate scan

In figure 8.2, *signal rate scans* are presented as a function of the effective threshold. First, in figure 8.2a the first eight SiPMs are connected to a tile while the second eight SiPMs are operated in darkness. A step-like structure is visible for all SiPMs. Again, each step corresponds to a photon equivalent. The baseline is apparent at an effective threshold of 0 V. At an effective threshold of 0.26 V or 2.5 p.e., the contribution by darknoise events and by particle passage induced events in the scintillator tile are equal, indicating a first measure for an optimal threshold. Secondly, the rate scans, while all 16 SiPMs are connected to a tile, are presented in figures 8.2b and 8.2c. For each SiPM a plateau arises with a trigger rate of 60 Hz at an effective threshold of 0.35 V. The plateau is slowly decreasing to 30 Hz at an effective threshold of 0.7 V. This behavior indicates a constant flux of atmospheric muons superimposed by background events. *Background* is defined, in context of this thesis, as events originating from radioactive decays in the air around the experiment or originating from other particles than muons like the electromagnetic component of air showers. *Noise* indicates darknoise or electronic noise events always present during SiPM measurements.

Discussion

Significantly reduced trigger rates, compared to the expectations for atmospheric muons, may indicate shielding of muons as by thick walls surrounding a lab or reduced detection efficiency of the units. A strong increase would indicate the presence of background or noise events. The atmospheric muon rate can be estimated by a simple calculation based on the integral intensity of vertical muons with a momentum $> 1\,\mathrm{GeV/c}$ at sea level [11]

$$\frac{\mathrm{d}^3N}{\mathrm{d}A\,\mathrm{d}t\,\mathrm{d}\Omega} = \Phi_\perp = 70\,\mathrm{m}^{-2}\mathrm{s}^{-1}\mathrm{sr}^{-1} \quad , \tag{8.2}$$

with N the number of muons, A the detection area, t the measurement time, and Ω the solid angle. A flat, circular detector with radius R is considered. Its acceptance Γ is weighted by the angular distribution of the atmospheric muon flux $\frac{\mathrm{d}N}{\mathrm{d}\cos(\theta)} \propto \cos(\theta)^n$

$$\Gamma = \int_A \sin(\theta')\mathrm{d}A' \int_\Omega \cos(\theta')^n \mathrm{d}\Omega' \tag{8.3}$$

$$= A \int_0^{2\pi} \mathrm{d}\phi' \int_{\theta_1}^{\theta_2} \sin(\theta')\cos(\theta')^n \mathrm{d}\theta' \tag{8.4}$$

$$= 2\pi A \int_{\cos(\theta_2)}^{\cos(\theta_1)} \cos(\theta')^{n+1} \mathrm{d}\cos(\theta') \tag{8.5}$$

with $A = \pi R^2$ being the active area of a unit and θ being the muon incident angle.
Assuming a solid angle of 2π, its acceptance is

$$\Gamma = \pi R^2 \frac{2\pi}{n+2} \quad . \tag{8.6}$$

The expected rate of one unit can be approximated as

$$f_\perp = \Phi_\perp \cdot \Gamma = 70\,\mathrm{m}^{-2}\mathrm{s}^{-1}\mathrm{sr}^{-1}\ \pi R^2 \frac{2\pi}{n+2} \approx 10\,\mathrm{Hz} \tag{8.7}$$

with $R = 0.17\,\mathrm{m}$ (approximated by scintillator unit area $0.09\,\mathrm{m}^2$) and $n \approx 2$. As the signal rate scan of unit layout 2 depicts even at high thresholds a larger trigger rate than expected, a non-negligible

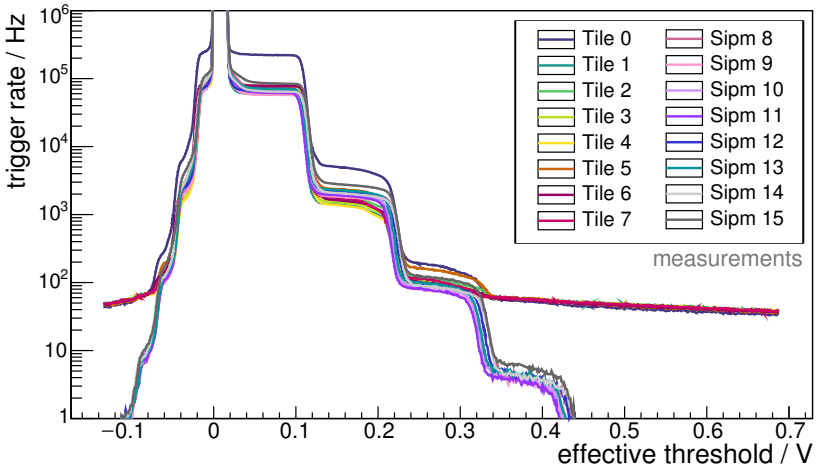

(a) Rate scan as a function of the effective threshold in V for SiPMs operated in darkness compared to rate scan for SiPMs connected to a tile.

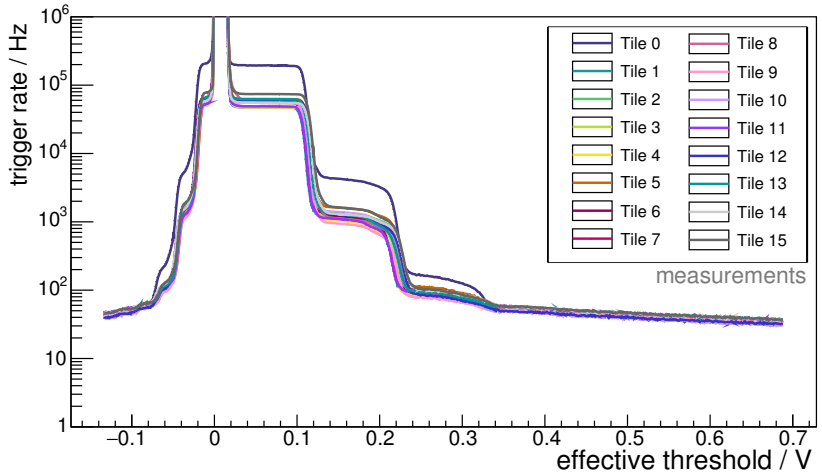

(b) Signal rate scan as a function of the effective threshold in V.

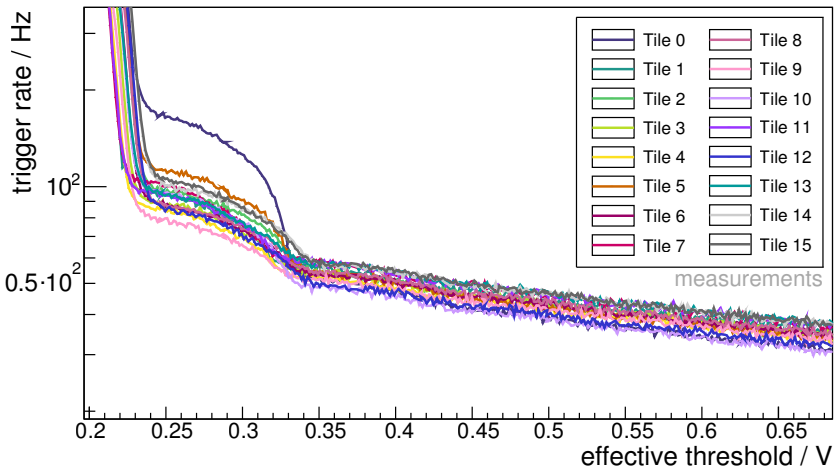

(c) Zoom on the plateau of figure 8.2b.

Figure 8.2.: Signal rate scan for SiPMs connected to unit layout 2 as a function of the effective threshold. A step-like structure is visible for all SiPMs up to an effective threshold of 0.36 V or 3.5 p.e. Each step corresponds to a photon equivalent. The baseline is apparent at an effective threshold of 0 V.

contribution of background events has to be present.

For further comparisons, also rate scans including the former unit layout 1 are investigated. Here the WLS fibre is connected to the SiPM via an optical fibre of length 50 cm. Only SiPM 1, layout 2, is of type Hamamatsu S13360-1350PE. All further SiPMs are of type Hamamatsu S12571-050P (corresponding to layout 1). The measurements are performed with the same EASIROC evaluation board, but with the corresponding SiPM carrier board and power supply unit for each SiPM type. The default bias voltages stated in the datasheets [111] are applied. The average temperature at the SiPMs is (26.82 ± 0.42) °C. In figure 8.3a, all SiPMs are operated in darkness. Both SiPM types demonstrate a step-like pattern but with reduced thermal noise and crosstalk probability of SiPM type S13360-1350PE in comparison to S12571-050P [105].
The darknoise rate at an effective threshold of 0.08 V is around 85 kHz for SiPM 1, layout 2, while all SiPMs of the older type depict an average rate of 135 kHz. A darknoise rate of 30 kHz/mm^2 at 21 °C and an increase by a factor of two per 8 K for current SiPM types can be assumed [114]. The SiPM 1, layout 2, has an effective area of $1.3 \times 1.3\,\text{mm}^2$ and is measured at a temperature increased by 5.8 ° compared to the reference value. Therefore, an average darknoise rate of 84 kHz is expected which is well compatible with the determined value. For the older SiPM types a darknoise rate of 100 kHz/mm^2 at 25 °C is stated. Thus, at the corresponding temperature a darknoise rate of 127 kHz is expected, also well compatible with the detected darknoise rate.
For an effective threshold of 0.45 V, SiPM 1, layout 2, demonstrates already a negligible darknoise rate compared to all further SiPMs which have a strong darknoise contribution up to 9.5 p.e. In figure 8.3b, SiPM 1, layout 2, is connected to a unit of layout 2, while SiPMs 3 and 5 are connected to units of layout 1. All further SiPMs are operated in darkness without being connected to a tile. Compared to its darknoise rate scan, SiPM 1, layout 2, depicts a plateau for an effective threshold larger than 0.35 V representing the atmospheric muon flux. The sharp cut-off around 1.1 V refers to a saturation of the preamplifier or the fast shaper and limits the maximum achievable threshold. The atmospheric muon flux is less prominent for the connected SiPMs 4 and 6. The SiPM type S12571-050P has not only a larger darknoise component but also the unit layout 1 has a reduced light yield by a factor of 3 compared to unit layout 2. The darknoise rate scan and the rate scan containing signal are thus only distinguishable at the largest effective thresholds > 0.8 V. Even at these thresholds the trigger rate for atmospheric muons is only 8 Hz compared to 20 Hz for units of layout 2 and 10 Hz expected for atmospheric muons. This indicates a reduced trigger efficiency for units of layout 1 and an additional background component detected by units of layout 2.

Besides an indication for the best common trigger threshold, rate scans are an important monitoring tool for measurement setups and should be recorded on a regular basis. Potential electronic noise effects may be apparent in the low p.e. regime of a rate scan and would indicate the need to increase the threshold.

As now an approximate conversion of the hardware discriminator threshold in DAC count to a threshold in units of photon equivalent is known, the signal determined by the slow shaper output can be studied.

8.1.2. SiPM darknoise spectrum

The SiPM *darknoise spectrum* is defined as the charge spectrum of SiPMs which are operated in darkness and are not connected to a scintillator tile. Exemplary darknoise spectra of SiPMs are compared in figure 8.4. They are measured at an average ambient temperature of (25.82 ± 0.18) °C. A trigger threshold corresponding to 0.5 p.e. is imposed. The spectra include data taken within

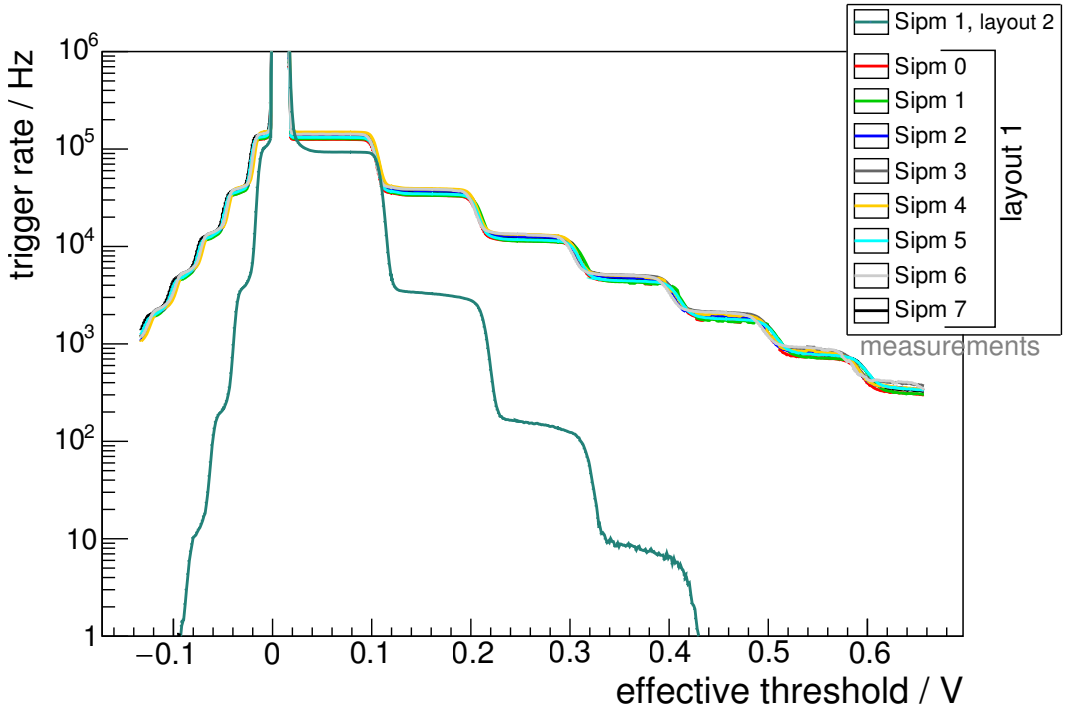

(a) Darknoise rate scan. Both SiPM types demonstrate a step-like pattern but with reduced thermal noise and crosstalk probability of SiPM type S13360-1350PE in comparison to S12571-050P [105].

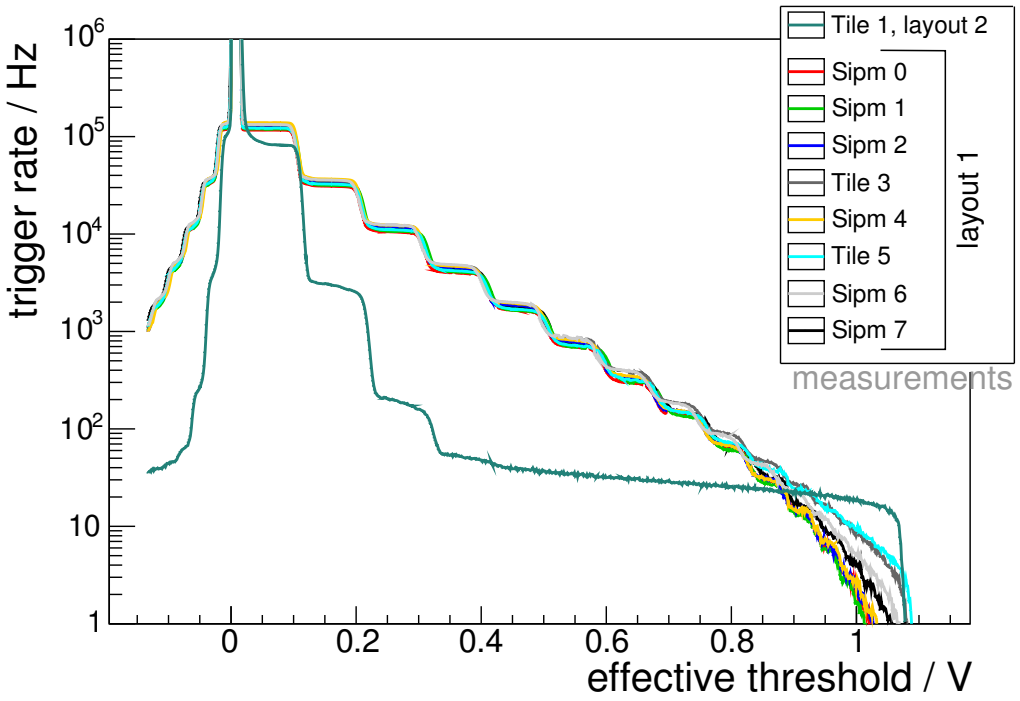

(b) SiPM 1, layout 2, is connected for the signal rate scan to a unit of layout 2. SiPM 3 and 5 are connected to units of layout 1. All further SiPMs are operated in darkness and are not connected to a tile. For SiPM 1, layout 2, a plateau representing the stable atmospheric muon flux is arising for an effective threshold $> 0.35\,\mathrm{V}$.

Figure 8.3.: Rate scan for eight SiPMs as a function of the effective threshold. SiPM types used in unit layout 1 and unit layout 2 are compared. SiPM 1, layout 2, is of type Hamamatsu S13360-1350PE. All further SiPMs are of type Hamamatsu S12571-050P.

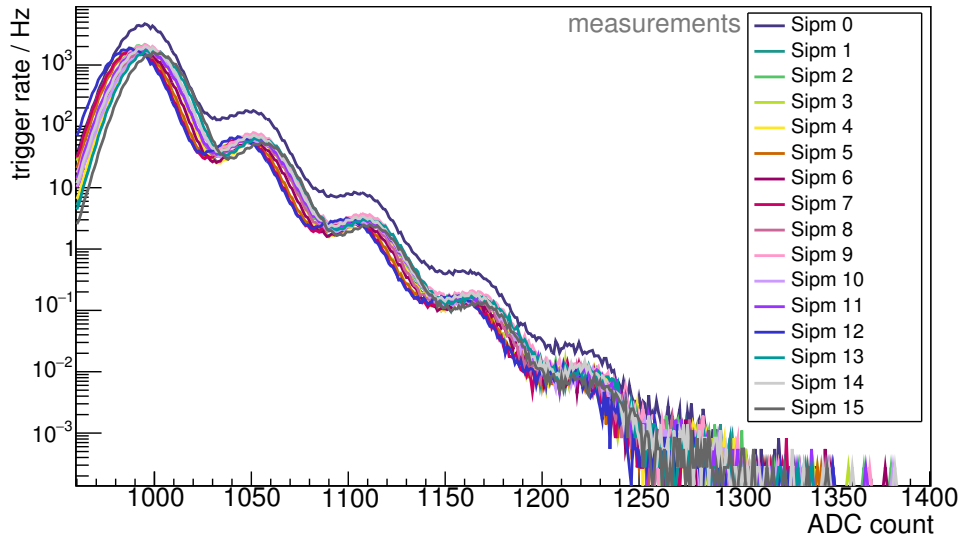

Figure 8.4.: Charge spectra of SiPMs of type S13360-1350PE in darkness as a function of ADC count. The spectra include data taken within one hour. A trigger threshold of 0.5 p.e. is imposed. Peaks up to 5 p.e. are visible. For the increased rate of SiPM 0, please refer to the text.

a measurement time of one hour. The trigger rate is given in units of ADC count. The peaks corresponding to the number of cell breakthroughs are visible up to 5 p.e. Deviations in the positions of the peaks correspond to small deviations in the gain and in a small shift in the baseline for each SiPM. An average trigger rate of 100 kHz is determined as expected according to datasheet values given by Hamamatsu. Again, for SiPM 0 an increased trigger rate is apparent while no difference in the gain or the crosstalk probability can be identified.
So far in the research field of astroparticle physics, the most prominent experiment based on light detection by SiPMs is the FACT (the First G-APD Cherenkov Telescope) telescope in La Palma [187]. It has not only proven the stability of SiPM performance over several years [188] but has also shown the capability to extract important characteristics of SiPMs from their dark count spectrum [189]. Therefore, on the presented darknoise spectra in figure 8.4 an analysis is performed which follows the approach presented by the FACT collaboration. It is based on the assumption that each charge spectrum of a SiPM can be described as a sum of normal distributions weighted with a modified Erlang distribution P_n [189]. The approach has been already successfully applied to the darknoise spectra measured by units of layout 1 as presented in [165].
The modified Erlang distribution

$$P_n = c \cdot \frac{(n\,q)^{n-1}}{[(n-1)!]^{\nu}} \qquad \text{with} \quad q = p \cdot e^{-p} \tag{8.8}$$

depicts the probability that a single cell breakthrough due to thermal noise triggers a chain of correlated noise events resulting in various cell breakthroughs n. It is based on the Erlang exponent ν, the probability p and a normalization parameter c chosen such that

$$\sum_{n=1}^{\infty} P_n = 1 \quad . \tag{8.9}$$

The normal distribution of each number of cells triggered, n, is defined by

$$f_n(x) = \frac{\exp\left(-\frac{1}{2}\left[\frac{x-x_n}{\sigma_n}\right]^2\right)}{\sqrt{2\pi\,\sigma_n^2}} \quad , \tag{8.10}$$

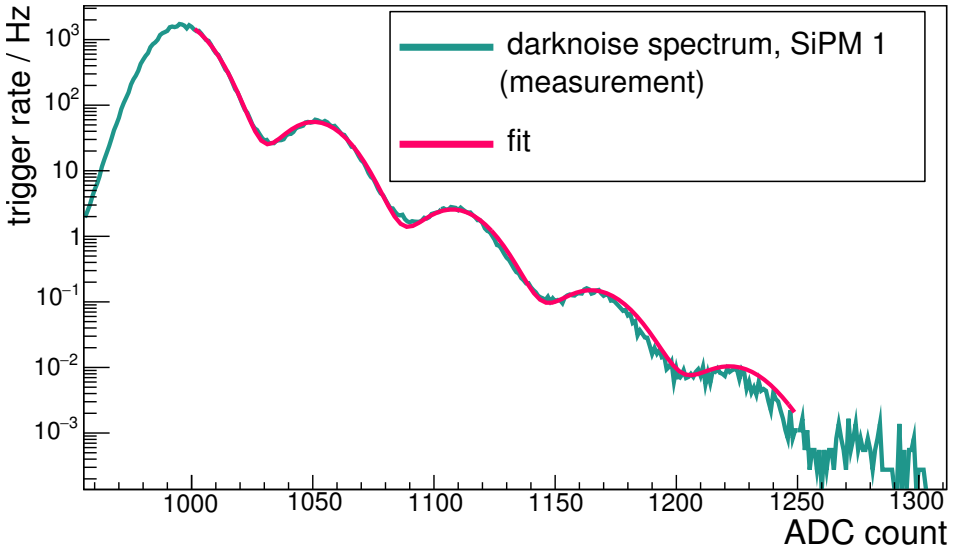

Figure 8.5.: Charge spectrum of SiPM 1 of type S13360-1350PE in darkness as a function of ADC count. The spectra includes data taken within one hour. A trigger threshold of 0.5 p.e. is imposed. Peaks up to 5 p.e. are visible. By a fit of a sum of normal distributions weighted with a modified Erlang distribution important quantities of the SiPM can be determined as the gain or the crosstalk probability of only 3%.

whereby

$$x_n = x_0 + n \cdot G \quad \text{and} \quad \sigma_n = \sqrt{n\,\sigma_{\text{pe}}^2 + \sigma_{\text{el}}^2} \quad . \tag{8.11}$$

The position of the peaks x_n in ADC count is determined with respect to the baseline or pedestal peak position x_0 and increases linearly with gain G. The width of the normal distribution σ_n takes additional noise components as the electronics noise σ_{el} and small deviations of the charge released at each cell breakthrough σ_{pe} into account. Both components are assumed to be Gaussian distributed and result in a broadened peak for each photon equivalent. While the electronics noise is the same for each photon equivalent, the fluctuations on the charge increase linearly with the number of cells triggered, n. The amplitude of each peak is decreasing, with $A_{1\text{ p.e.}}$ being the amplitude of the first p.e. peak.

By a fit of the combined function $f(x) = A_{1\text{ p.e.}} \sum_{n=1}^{\infty} P_n \cdot f_n(x)$ several important characteristics of the SiPM can be studied:

- the multiplicity N corresponding to the average number of cells triggered $N = \sum_{n=1}^{\infty} n \cdot P_n$,
- the gain G depending on the corresponding SiPM type and on its state given by the ambient temperature and the applied overvoltage,
- the crosstalk probability $p_{\text{cross}} = 1 - P_1$,
- the conversion of ADC count into the unit of photon equivalent based on the baseline shift x_0 and the determined position of each peak x_n.

The second correlated noise effect of SiPMs, the afterpulsing, cannot be separately identified by the model. As nowadays SiPM types have an afterpulse probability of $\leq 1\%$, it is of minor importance but will result into an additional broadening of the peaks. The effect will thus be included in the determined σ_n.

An example of a performed fit to a darknoise spectrum is depicted for SiPM 1 in figure 8.5 in red with parameters $p = 0.02$, $\nu = 0.55$, $A_{1\,\mathrm{p.e.}} = 1.86 \cdot 10^3$ and $\sigma_{\mathrm{pe}} = 0.08$, $\sigma_{\mathrm{el}} = 10.74$. The following quantities of the SiPM are derived by the fit: the crosstalk probability $p_{\mathrm{cross}} \approx 3\%$, the average number of triggered cells $N = 1.03$ and a gain of $G = 57.25\,\mathrm{ADC\ count}$. Compared to the SiPM type S12571-050P used in units of layout 1 as presented in [165], a strongly reduced crosstalk probability ($p_{\mathrm{cross}} \approx 28.7\% \rightarrow 3\%$) can be confirmed as already stated in the datasheet of Hamamatsu. Likewise, the average number of triggered cells is reduced ($N = 1.46 \rightarrow 1.03$) as less neighbors are triggered during the avalanche breakdown of a single cell.

8.1.3. Signal spectrum of minimum ionizing particles

The *signal charge spectrum* of SiPMs connected to a tile is a convolution of noise or background events, events of single atmospheric muons, and air shower candidates (several particles traverse one unit simultaneously). While at small charges the darknoise of SiPMs is dominating, at medium charges the signal of atmospheric muons corresponding to the signal of MIPs will strongly contribute.

Before presenting the investigations of the MIP charge spectra of all 16 units, important general information about the representation of this data is discussed.

High gain - Low gain cross calibration

The readout electronics provide a measure for the integrated signal per detector unit and event. The charge is registered for two different gain settings corresponding to high and low gain of the EASIROC slow shapers. These signals are given in units of ADC count. A calibration between both scales is needed to allow for a detection over the complete desired dynamic range of the signal ranging from one up to hundreds of MIPs. The high gain regime is dedicated to measurements of the charge spectrum containing the MIP peak as monitoring device for the detector response. By this spectrum also a continuous monitoring of the gain is possible if the individual p.e. peaks are apparent. The low gain regime is important for the detection of extensive air showers and no single p.e. resolution is necessary. A calibration method has been developed by L. Middendorf [165]. It allows for a conversion of the low gain signals into the corresponding high gain signal scale. If a scale is given in ADC count without an additional specification of the gain regime (HG - high gain, LG - low gain), the described interpolation is used for the corresponding data.

The importance of the MIP peak

The position of the maximum of the atmospheric muon spectrum, called the *MIP peak* is referring to the most probable value for the signal for one MIP traversing the unit.
The width of the peak is defined by deviations in the signal of single MIPs traversing the unit. Possible reasons are deviations in the energy deposit due to different paths of MIPs inside the tile (vertical or inclined) and due to inhomogeneities in the scintillator tile as well as deviations in the detection and collection efficiency of the further optical components. For example, inclined muons may be edge-clipping. These muons are not traversing the complete thickness of the unit and deposit less energy in the material. If the track of an inclined muon is completely contained,

the particle deposits more energy in the material compared to a vertical muon due to its increased path in the unit. The increased track length l is given by

$$l = \frac{d_{\text{unit}}}{\cos(\theta)} \tag{8.12}$$

$$\Rightarrow S_{\text{adc, max}_\perp} = \frac{S_{\text{adc, max}}}{\cos(\theta)} \quad , \tag{8.13}$$

whereby the thickness of the unit $d_{\text{unit}} = 0.5\,\text{mm}$ is the track length of a vertical muon in the presented tile and θ is the incident angle with respect to the unit normal. The signal yield of a scintillator tile achieved by a crossing muon is $\propto l$. Thus, this can be translated to the deposited signal of a vertical MIP $S_{\text{adc, max}_\perp}$ compared to the signal $S_{\text{adc, max}}$ for an inclined muon. Both scenarios lead to a broadened MIP spectrum. A broadened distribution may thus indicate an increased ratio of inclined to vertical muons.
Furthermore, the peak-to-valley ratio between the minimum before the MIP peak and the height at the MIP peak maximum contains information about deviations from the energy deposit by vertical muons. For a pure muon sample, a clear minimum is expected. For an increased background or noise rate the height of the minimum will increase and the ratio will be strongly reduced.
The latter is less present in the performed measurements as would be expected for example in an alternative setup located in the Argentinian Pampa at the Pierre Auger Observatory. Aachen is located at an altitude of 173 m, therefore a large fraction of the electromagnetic component in an air shower will be already absorbed by the atmosphere. If units are measured in a building, the material surrounding the detector absorbs further amounts of the electromagnetic particles but also the muon rate will be reduced. The lab, in which the measurements are performed, is located in the first floor of the physics department with four levels above and several walls between the lab and the outside of the building to each side. Therefore, only a minimal impact by electromagnetic component of air showers is expected for those studies.

Interpretation of the signal scale

The amount of ADC count for the integrated signal per detector unit has to be translated to a common scale for all units. Thereby, comparisons between different measurement setups of the same detector but also between different experiments are enabled. The detector studied in this thesis is designed for the determination of the number of muons in air showers. As these particles provide a unique response while traversing the detector, the intended scale is the response of the detector to a single MIP unbiased by the actual unit traversed. Therefore, all characteristics of the individual detector components have to be included. First, the measured signal given in unit of ADC count, S_{adc}, is translated to a signal given in units of photon equivalent, $S_{\text{p.e.}}$ The conversion factor is the gain G of the SiPM under study. The resulting scale includes thus different characteristics of each SiPM installed and can be calculated according to

$$S_{\text{p.e.}}(T) = \frac{(S_{\text{adc}} - S_{\text{adc, pedestal}}(T))}{G(T)} \quad . \tag{8.14}$$

Therefore, the actual gain G and the pedestal position $S_{\text{adc, pedestal}}$ have to be determined with the help of the peak structure of the charge spectrum. As these quantities may be temperature dependent, the ambient temperature T has to be taken into account to allow for a universal conversion. In the scope of the MiniAMD demonstrator, a detailed investigation of the temperature dependence of the signal is performed (cf. chapter 9). As a further step, the scale should compensate for deviations in the characteristics of the individual scintillator tile and of the wavelength shifting fibre.

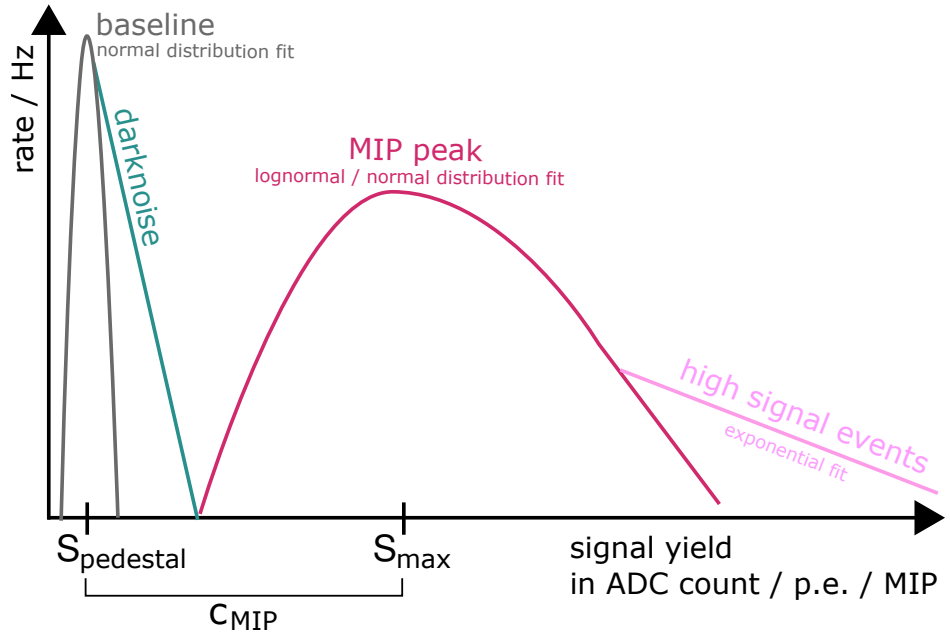

Figure 8.6.: The charge spectrum comprises several components. In the low signal regime, the baseline contribution or pedestal, $S_{\text{adc, pedestal}}(T)$, dominates. The position of the peak defines the zero position of the scales in units of p.e. and MIP. The pedestal is followed by the SiPM darknoise component. Ideally, for medium signals the MIP peak dominates. The position of the maximum, $S_{\text{adc, max}}(T)$, refers to the most probable value of the signal yield for a MIP particle passage. The MIP peak can be concealed by background events which are not presented in this sketch. However, it depicts an asymmetric tail to higher signals. A change in the slope of this tail indicates an additional component of high signal events as e.g. multiple particles traversing per event.

The corresponding scale allows for a description of the signal in units of MIP, S_{MIP}. Therefore, the MIP charge spectrum of each unit is determined. By fitting a function to the measured charge spectrum, the position of the maximum of the MIP peak $S_{\text{adc, max}}$ is determined. The conversion factor is referred to as c_{MIP} in the scope of this thesis. A sketch of the different components included in a signal charge spectrum is presented in figure 8.6.

$$S_{\text{MIP}} = \frac{S_{\text{adc}} - S_{\text{adc, pedestal}}(T)}{c_{\text{MIP}}(T)} \tag{8.15}$$

whereby (8.16)

$$c_{\text{MIP}}(T) \equiv S_{\text{adc, max}}(T) - S_{\text{adc, pedestal}}(T) \quad . \tag{8.17}$$

A pure muon sample should be chosen to determine the signal response of each unit to muons. As achieving a pure sample is challenging for a single unit, coincident measurements of stacks of detector units are preferred for studying the MIP peak. An aluminum support structure for the vertical stacking of up to eight units has been designed by the mechanical workshop of the institute. This *shelf* allows for studies, e.g., of the detection efficiency. The vertical distance between two units is 15 cm. The shelf has been mainly used for further measurements of the units of layout 1, please refer for more details to [165]. A photo of the shelf is shown in figure 8.7.

A stack of units measured in coincidence allows for the determination of the average light yield

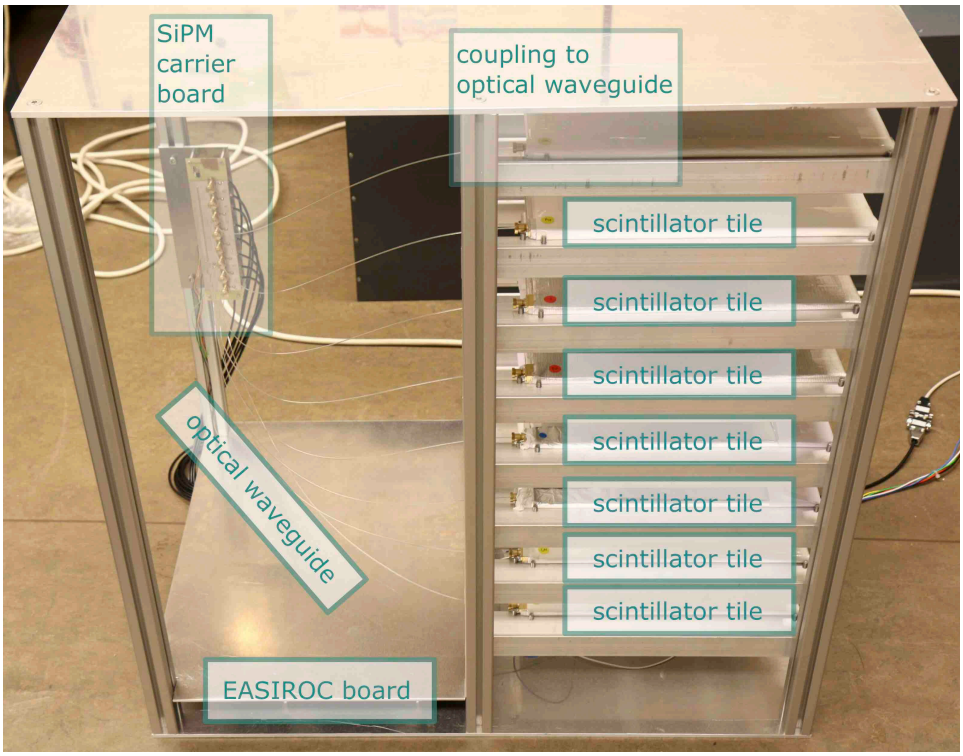

Figure 8.7.: The *shelf* allows for a vertical arrangement of up to eight units. Shown in the photo are units of layout 1. Each scintillator tile is read out by an optical waveguide ending at a common SiPM carrier board. The DAQ electronics is hidden below a protective aluminum board at the bottom.

of individual units. For the study of the distribution of the light yield along the scintillator tile, measurements of the detector embedded in a muon tomograph are performed. It provides spatial resolution. The results are presented in section 8.4.

Light yield of the scintillator units measured in coincidence

The average light yield of detector units is first measured in the lab, expecting only a minor impact by the electromagnetic component of air showers. The detection of such background events is strongly reduced by measuring with several units in coincidence. Therefore, the 16 units are studied in packages of eight units in the shelf.
The ambient temperature of the measurements presented for units 0-7 is (26.86 ± 0.15) °C, while for units 8-15 the average temperature is (27.05 ± 0.40) °C. For both measurements, only minor fluctuations in the spectrum quantities due to temperature are assumed. An exemplary charge spectrum of unit 13 is shown in figure 8.8. The spectrum includes events at which four random units (also possibly including the unit of interest) out of the eight units in the shelf are above the discriminator threshold of 0.26 V or 2.5 p.e. Unit 13 is read out regardless of its own trigger condition. Noise events are apparent in the low signal region, whereby the first peak corresponds to electronic noise. The position of this peak is determined by a fit of a Gaussian distribution and defines the zero position of the scales in units of p.e. and MIP. The imposed discriminator threshold introduces a sharp dip after the pedestal. The single p.e. peaks, arising after this minimum, are fitted by a sum of normal distributions with correlated distance between individual peaks corresponding to the gain. The peak-to-valley ratio is 2. The MIP peak is fitted for comparison by a log-normal distribution as

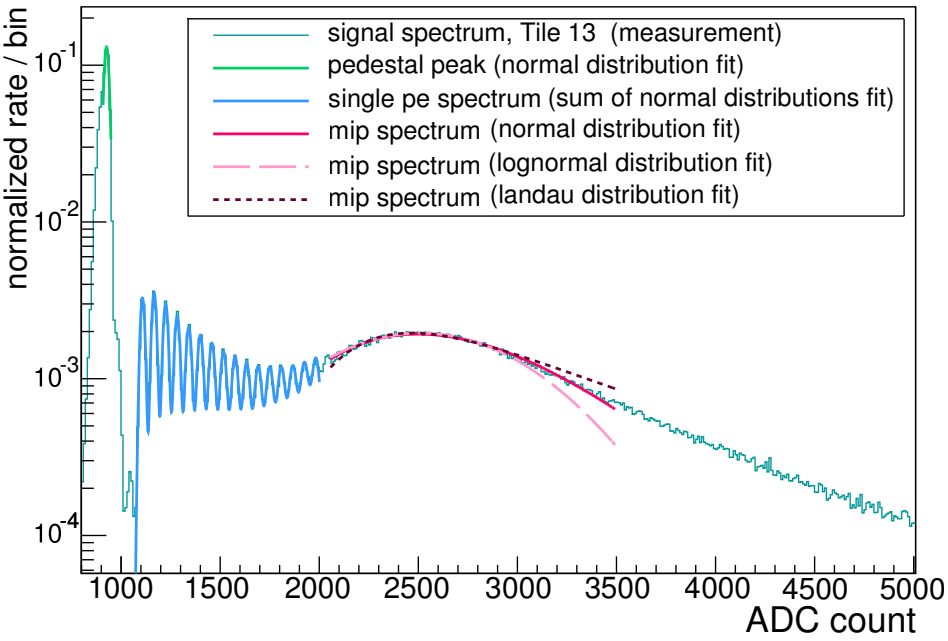

Figure 8.8.: Normalized charge spectrum as a function of ADC count and as a function of the signal in MIP for unit 13 (layout 2, SiPM type S13360-1350PE). The spectrum includes events where at least four random units in a stack of the eight units are above the trigger threshold of 0.26 V or 2.5 p.e. with a measurement time of 12 hours. Therefore, the charge spectrum contains events at which the unit is above threshold as well as randomly read out signals while other units registered an event. Five individual fits are depicted, the pedestal peak (green), the single p.e. fit (blue) and a MIP peak fit by a log-normal (red), Gaussian (rose) and a Landau distribution (dark red). For more information, please see text.

well as by a Landau (cf. equation 5.1), and by a Gaussian distribution limited around the maximum determined by the log-normal fit. The *log-normal distribution* describes thereby a random variable X if the logarithm $\log X$ of the variable is normally distributed.
The p.d.f. of the asymmetric distribution is given by

$$f(x|m,s) = \frac{1}{xs\sqrt{2\pi}} \exp\left(-\frac{(\ln x - m)^2}{2s^2}\right) \quad , x > 0 \tag{8.18}$$

with $m \in \mathbb{R}$ and $s > 0$.
The maximum of the MIP peak is defined by the mode e^{m-s^2} of the log-normal distribution

$$S_{\text{adc, max}} = e^{m-s^2} \quad . \tag{8.19}$$

This maximum (cf. equation 8.19) is comparable to the mean of the Gaussian fit, but the lognormal-distribution provides in general a better description of the skewed peak and is therefore preferred. However, the sigma of the distribution (indicating the width) is additionally given for the Gaussian fit. The physically motivated Landau fit has a systematic tendency to lower peak positions. It results in too large predicted values for the tail on the right side of the peak, while both Gaussian and log-normal distribution predict smaller values than the measured spectrum. A summary of all determined spectrum parameters of the studied detector units is given in table 8.2. The light yields are ranging from 18.75 to 28.30 p.e. per MIP with an average light yield of (23.67 ± 2.47) p.e. per MIP and a maximum deviation of 34% from the average light yield. The large range can be explained by deviations in each component of the handmade units. The polishing, the mirroring,

Unit number	gain G in ADC count / p.e.	pedestal position $S_{\text{adc, pedestal}}$ in ADC count	light yield in p.e.	log-normal $\sqrt{\text{variance}}$ in MIP	gaussian sigma in MIP
0	57.52 ± 0.05	925.30 ± 0.05	18.75± 0.05	0.446 ± 0.003	0.382± 0.006
1	57.29 ± 0.03	927.27 ± 0. 05	25.77± 0.08	0.403 ± 0.004	0.359± 0.009
2	58.07 ± 0.03	924.82 ± 0.05	24.50± 0.09	0.420 ± 0.004	0.377± 0.010
3	57.33 ± 0.03	919.39 ± 0.04	25.19± 0.09	0.413 ± 0.004	0.371± 0.009
4	58.00 ± 0.03	925.52± 0.05	23.90± 0.09	0.442 ± 0.005	0.393± 0.010
5	57.44 ± 0.03	922.73 ± 0.05	22.76± 0.07	0.437 ± 0.004	0.371± 0.008
6	58.64 ± 0.03	925.21 ± 0.05	23.18± 0.08	0.431 ± 0.004	0.380± 0.009
7	57.51 ± 0.04	922.71 ± 0.05	25.90± 0.08	0.376 ± 0.004	0.350± 0.010
8	57.82 ± 0.02	930.01± 0.03	22.35± 0.03	0.439 ± 0.002	0.382± 0.004
9	57.81 ± 0.02	925.76 ± 0.03	21.78± 0.03	0.447 ± 0.002	0.390± 0.004
10	58.54 ± 0.02	928.53 ± 0.03	20.27± 0.03	0.406 ± 0.002	0.394± 0.004
11	57.30 ± 0.02	917.90 ± 0.02	28.30± 0.05	0.364 ± 0.002	0.306± 0.004
12	59.27 ± 0.03	924.22 ± 0.02	20.47± 0.03	0.418 ± 0.002	0.307± 0.003
13	58.37 ± 0.02	926.57 ± 0.03	26.92± 0.05	0.393 ± 0.002	0.364± 0.005
14	59.01 ± 0.02	924.62± 0.03	24.66± 0.04	0.418 ± 0.002	0.344± 0.005
15	58.15 ± 0.02	924.71± 0.03	23.83± 0.04	0.428 ± 0.002	0.362± 0.004
all	58.03 ± 0.60	924.71± 2.95	23.67± 2.47	0.400 ± 0.076	0.368± 0.021

Table 8.2.: Summary of important charge spectrum quantities determined by fits at the spectrum of all studied units of layout 2. Uncertainties given for each individual unit are the fit uncertainties provided by ROOT. As average quantities the mean and standard deviation are given.

and the overall status of the WLS fibres have a large impact as shown by measurements presented in appendices I and J. Also the wrapping of the tiles or the placement of the SiPM at the tile edge may deviate. As discussed, the average light yield is shifted according to the actual acceptance angle for muons (cf. equation 8.13). Taking four units into account limits the zenith angle, so that the determined signal yield is comparable to a vertical MIP scenario. This is confirmed by the measurements with an external muon tomograph presented in section 8.4. If the four-fold coincidence is required to include the unit under investigation, all noise events in the spectrum are eliminated. Only the MIP peak is apparent. The normalized MIP charge spectra for all units are compared in figure 8.9. For the first eight units, a measurement time of three hours is accumulated. For the second eight units, 12 hours measurement time is included. The enhancement of the statistics is visible by the improved delimitation between the individual p.e. peaks up to 20 p.e. All spectra are comparable except of the average light yield. SiPM 0, which depicted an increased darknoise rate, has a comparable distribution of the charge. As this SiPM depicts the smallest light yield of all units, a different SiPM is connected to the tile as a crosscheck providing a comparable small light yield (5% uncertainty on light yield in both directions). All spectra depict beside the MIP peak a

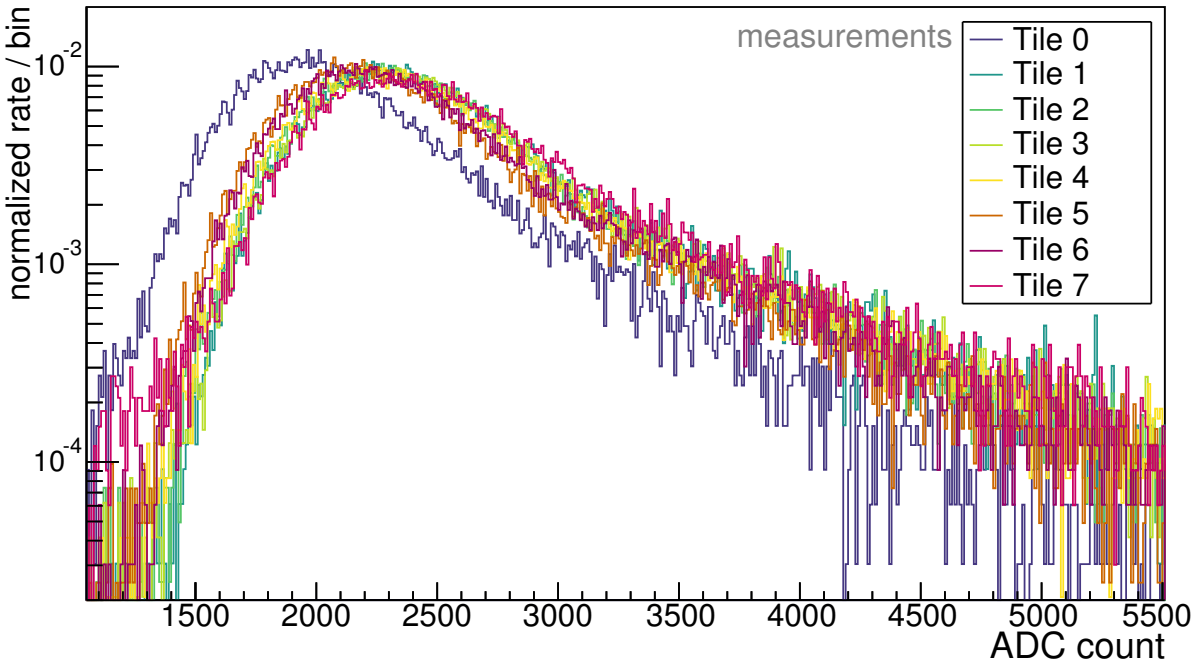

(a) First stack of units. The spectra include data taken within 3 hours.

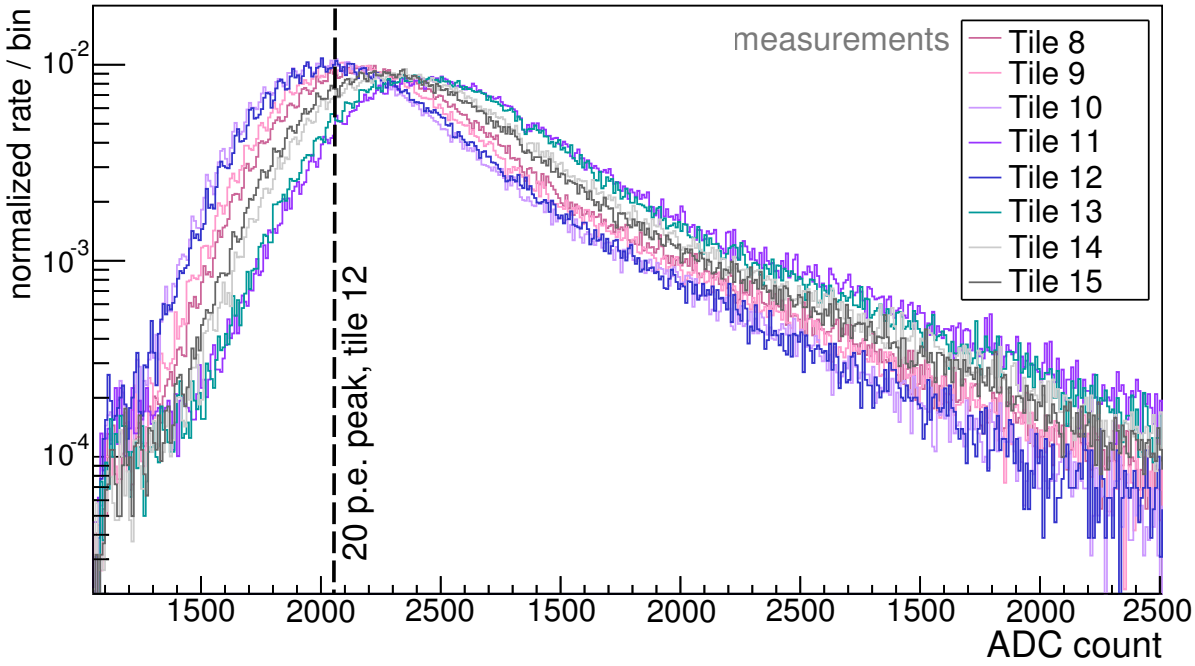

(b) Second stack of units. The spectra include data taken within 12 hours.

Figure 8.9.: Signal charge spectra as a function of ADC count for SiPMs of type S13360-1350PE each connected to an individual scintillator tile. Only events are included where at least four units in a stack of eight units including the unit of interest have seen a signal within $\approx 70\,\text{ns}$. An effective trigger threshold of 0.26 V or 2.5 p.e. is imposed. Spectra are normalized to allow for a comparisons between different measurement times. Peaks up to 20 p.e. are visible for most of the units. Exemplary for tile 12, the position of the 20 p.e. peak is depicted by a black dashed line. Deviations in the MIP peak positions result from different light yields of the units. The expected small deviations in the gain and small shift in the baseline for each SiPM are of minor impact. A conversion to a common scale in units of MIP is possible by equation 8.17 and table 8.2.

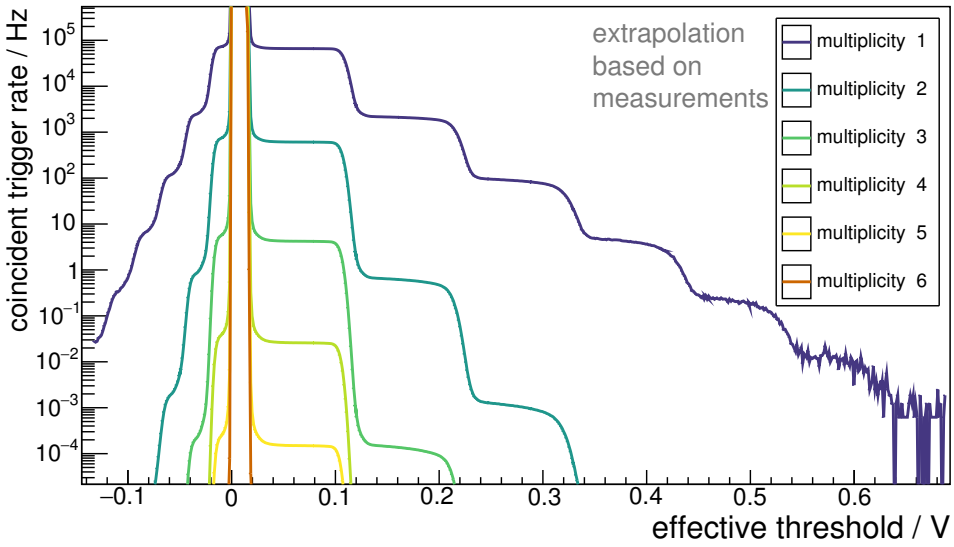

Figure 8.10.: Estimated coincident rate for false triggers by pure darknoise events in a coincident time window of 70 ns as a function of effective threshold in V. Different multiplicities m of coincident SiPMs are shown. Calculations are based on the performed rate scans for SiPMs in darkness, presented in figure 8.1.

tail to higher values with a different slope than the peak itself. The tail is part of the fluctuations in the energy deposit of the MIP, but contains also multiple muons traversing a unit, highly energetic single muons, which are subject to radiative losses, and electrons (cf. chapter 7.3.3).

8.1.4. Average detection efficiency for single atmospheric muons

An important design goal of the unit is a large *trigger efficiency* for crossing atmospheric muons while keeping the purity of the sample at an acceptable level. Only darknoise is assumed as source of false trigger events. The trigger threshold should be chosen such that the trigger rates for atmospheric muons is smaller or comparable to the darknoise rate. Taking the threshold scans for the darknoise measurements into account (cf. figure 8.1), the amount of darknoise expected per channel as a function of the chosen trigger threshold can be extracted. The rate of random coincident triggers in a gate width w detected by m SiPMs, which measure darknoise with a rate of r_i each, can be roughly estimated according to

$$R_m = m \cdot w^{m-1} \prod_{i=1}^{m} r_i \quad . \tag{8.20}$$

The formula corresponds to the special case of the number of detector units under study being equal to the multiplicity imposed. In figure 8.10, the estimated rate of random coincident triggers for different imposed *multiplicities* m of SiPMs is shown. The rate used for the calculation is based on the average rate and on its deviation which are determined by the rate scans of all studied SiPMs[4] as presented in figure 8.1. The gate width w is in the order of 70 ns [165]. For a multiplicity of three SiPMs, the darknoise component becomes comparable to the signal trigger rate of 10 Hz for an effective threshold of 0.08 V. This is only valid in the studied temperature regime, as the darknoise rate is increasing with temperature. For the determination of the detection efficiencies for signal, two groups of eight detector units of layout 2 are studied in the *shelf*[5]. The basic idea is again to

[4] except of channel 0 as it shows a much larger darknoise rate than the other SiPMs
[5] These units will be part of the MiniAMD modules discussed in the following chapter 9.

use the stacked units as coincident measurement system without the need of an external detector. For each individual unit, the further units of the stack can be used to decide if a muon has crossed the unit of interest. The trigger efficiency is then determined by the ratio of the events where the unit has exceeded a required trigger threshold to all events in which a muon should have passed the unit. The method has been successfully applied to the units of layout 1 as presented in [165].
While performing a threshold scan with a discriminator threshold common for all SiPMs, the number of units included in the multiplicity trigger must be adapted. As for low effective thresholds the darknoise will dominate the trigger rate for a too weak multiplicity trigger criterion (cf. figure 8.10), the efficiency may be altered by falsely detected darknoise events. Therefore, a stricter hardware multiplicity trigger has to be chosen in this discriminator threshold regime.
Besides the hardware trigger requirements, additional criteria have to be fulfilled for the associated analysis:

- To allow for the study of the trigger efficiency of a unit, the trigger decision is not allowed to be based on the unit in question. This imposes that for a hardware multiplicity trigger m and a trigger in the unit in question, at least $m+1$ units have to exceed the threshold in the analysis.

- To select mainly muons for the sample, at least one unit above and one unit below the studied unit have to exceed the threshold. As this requirement cannot be fulfilled by the uppermost and lowermost units, the order of the units is shuffled to allow for the study of all units.

- A more strict cut on the multiplicity as required for the hardware decision may be needed for the analysis to achieve a pure muon sample. If darknoise events are still present, the apparent trigger efficiency is reduced. The random coincidences in the trigger units provide an overestimated number of muons which should have been detected by the unit under observation. Darknoise influenced events can be events with only darknoise triggers in coincidence. Also muons which traversed several units but are accompanied with darknoise events in further units of the stack can be present. Alternatively, darknoise events may result in a slight overestimation of the detection efficiency. They artificially enhance the signal yield if a random coincidence with a passing muon occurs. However, as the tile under study is read out regardless of its own trigger condition and the EASIROC provides the integrated signal, this darknoise effect is assumed to be of minor importance.

The temperature at the SiPMs during the measurements is stable between 26 and 27 °C.
The trigger threshold is varied between $[890, 150]$ DAC count with steps of 20 DAC count or expressed as effective threshold between $[0.04, 1.17]$ V. The hardware multiplicity trigger is chosen as four-fold coincidence between $[0.04, 0.12]$ V, as three-fold coincidence for an effective threshold of 0.14 V and is relaxed to a two-fold coincidence for all larger values. For each threshold, an event sample is collected with a measurement time of one hour per data point. In figure 8.11a, the trigger efficiency according to the hardware multiplicity trigger and the additional requirement of a triggered unit above and below the unit under investigation is shown. Clear jumps are visible in the trigger efficiency scan at each relaxing of the multiplicity hardware trigger criterion. They are introduced by darknoise events passing this trigger. They reduce the apparent trigger efficiency by up to 40% in the most extreme case in the low threshold regime. Events are less influenced for larger thresholds as the darknoise spectrum is steeply falling with the threshold. This structure is also apparent in the number of events detected for different trigger thresholds (cf. figure 8.12a). A smooth transition is expected for a pure data sample, slowly decreasing with increasing threshold. To remove the bias by the darknoise events on the trigger efficiency of the units for atmospheric muons, the multiplicity trigger is tightened for the analysis to a five-fold coincidence. Shown in

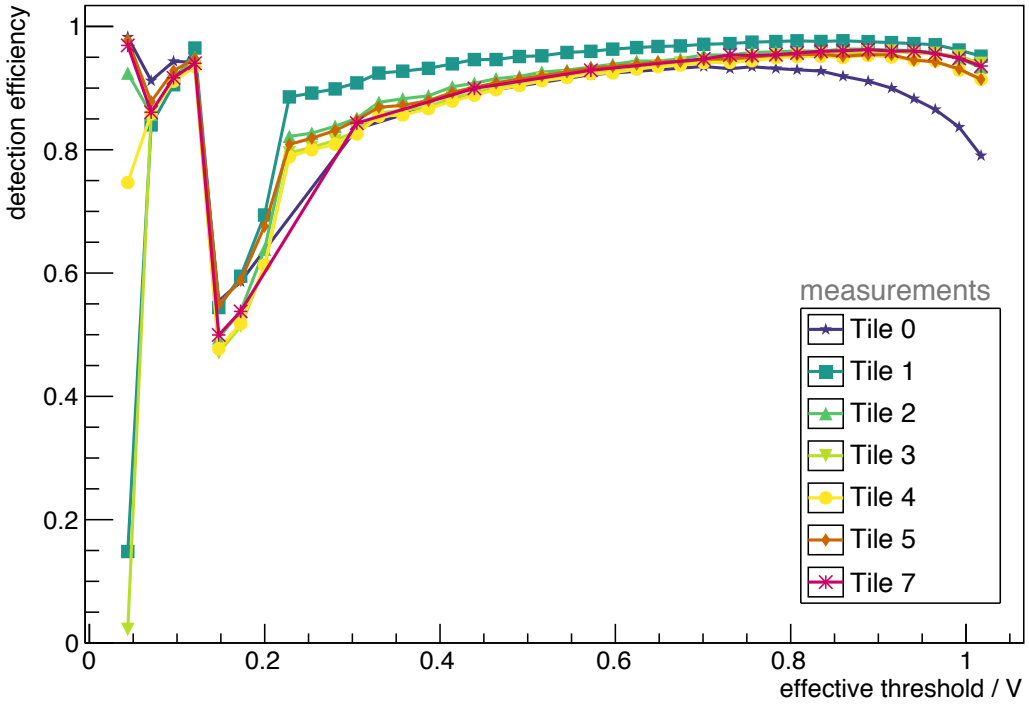

(a) The hardware multiplicity trigger is adapted to the imposed trigger threshold to suppress most of the random coincidence triggers introduced by darknoise events. For low thresholds up to 0.12 V, a four-fold coincidence is required. For 0.14 V, a three-fold coincidence is chosen, which is relaxed to a two-fold coincidence for all larger thresholds.

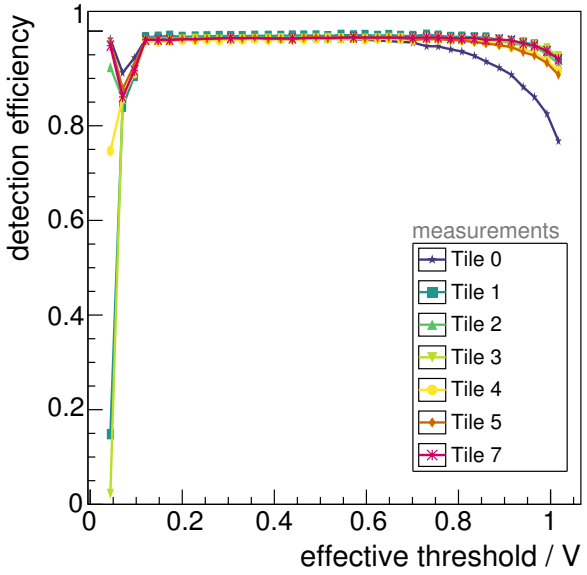

(b) A five-fold coincidence is required for all thresholds. Tiles 0 - 7 are shown.

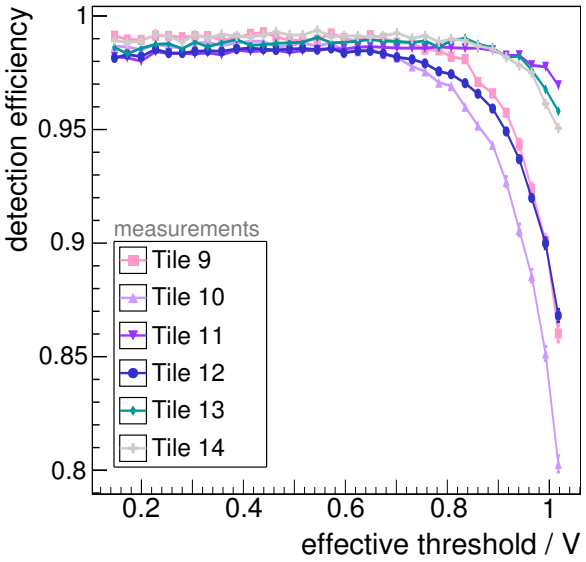

(c) A five-fold coincidence is required for all thresholds. Tiles 9 - 14 are shown.

Figure 8.11.: Trigger efficiency for units of layout type 2 as a function of the effective threshold in V. Each data point represents a data sample with a measurement time of one hour. For the event selection eight units are combined in a stack. The unit under study is not included in the trigger decision. See text for discussion.

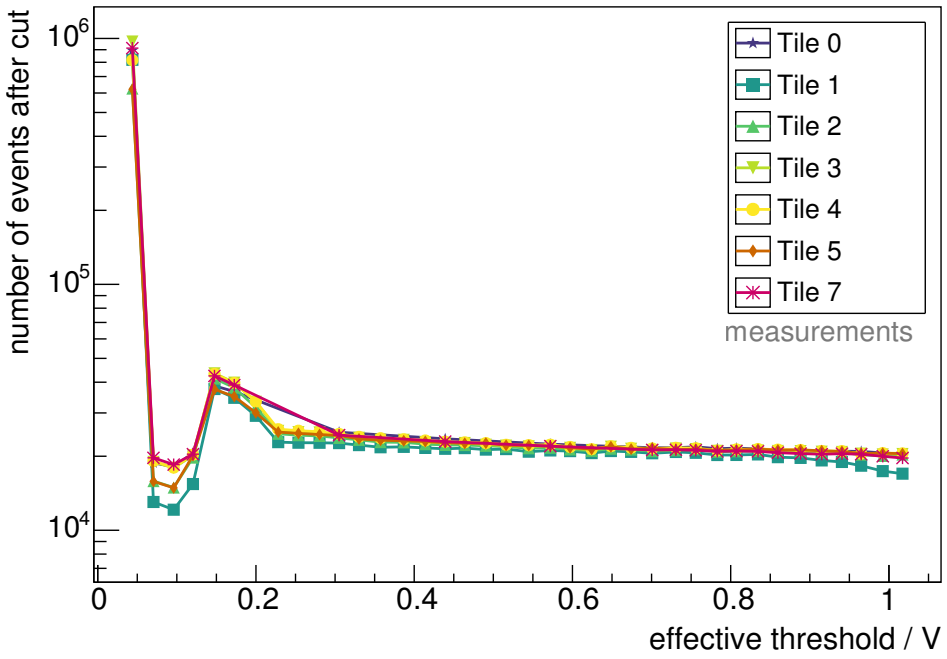

(a) A four-fold coincidence of the other units is used for event selection for low threshold values ($< 0.12\,\mathrm{V}$), a three-fold coincidence for a medium threshold ($0.14\,\mathrm{V}$) and a two-fold coincidence for all higher effective thresholds. The thresholds, at which the multiplicity condition is relaxed, are clearly visible as a step in the event count.

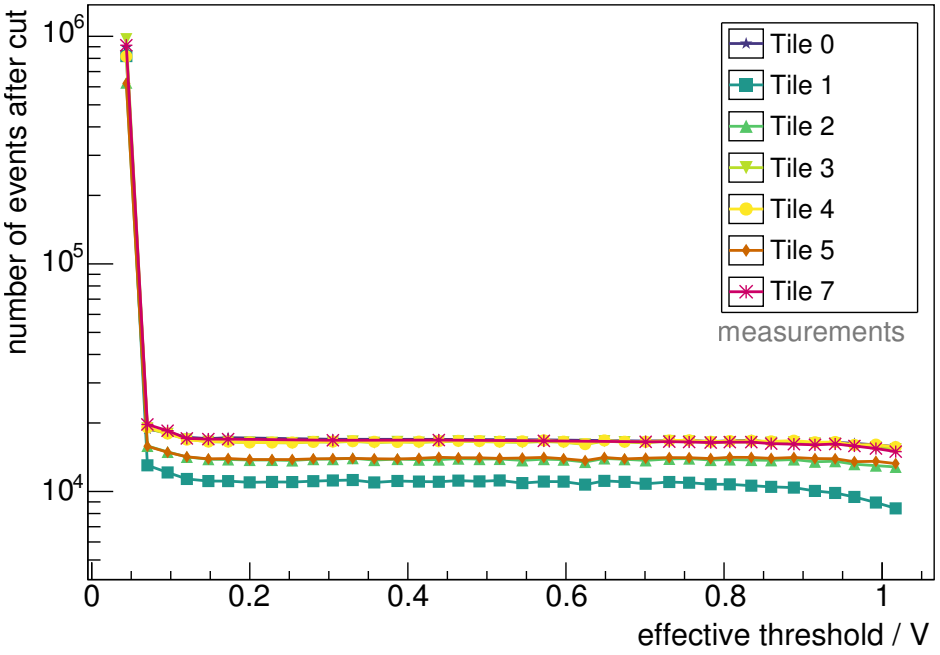

(b) A five-fold coincidence is required for all thresholds. The event rate is flat for thresholds above $0.1\,\mathrm{V}$ but with deviations between different units by a factor up to 1.5.

Figure 8.12.: Number of events detected by the first eight units of layout type 2 as a function of effective threshold. The unit under study is not included in the trigger decision. Each data point represents a data sample with a measurement time of one hour. See text for discussion.

figures 8.11b, 8.11c and 8.12b are the now smooth trigger efficiency and number of events passing the cut as a function of the trigger threshold.
A stable, average trigger efficiency of around $98-99\%$ is visible in the main regime of effective threshold for all units. For small effective thresholds, still a decrease of the trigger efficiency of all units due to darknoise events is apparent.
For large effective threshold values ($> 0.7\,\mathrm{V}$) a suppression of the signal sets in. Thereby, a deviation in the onset of the suppression is determined. Units with a reduced light yield provide a worse signal-to-noise ratio and are earlier affected.
The number of events is, as expected, slowly decreasing with increasing threshold for $> 0.1\,\mathrm{V}$.
Poisson statistics is used to determine the uncertainty on the number of events triggered by a unit under investigation. The uncertainty on the detection efficiency is derived using the Clopper-Pearson interval, obtained by ROOT, and represents the 68% confidence level.
Small deviations in the relative placement of detector units may influence the trigger efficiency. The area and the angular acceptance allowed for muons change for units, which are not correctly aligned to each other. These deviations can be studied by an intentional misplacement of units.
Therefore, unit 4 is shifted by 1 cm in x- and y-direction with respect to the optimal position in the stack. The trigger efficiency is reduced by 6% for unit 4. The shifted position influenced also the neighboring units, 3 and 5, as the requirement of a unit triggered above and below is harder to fulfill. Their efficiency is reduced by 2.5%.
The measurement setup is subject to further systematic uncertainties as events may be included which are introduced by multiple, simultaneously arriving muons or by random noise triggers as radioactivity in the surrounding air. A study by an external detector with spatial resolution in coincidence would allow to improve the determination of the trigger efficiency as events with single atmospheric muons can be selected. Therefore, a further measurement setup at a muon tomograph is used to study the trigger efficiency of all 16 units (cf. section 8.4).
All 16 units demonstrate within the scope of this measurement a trigger efficiency better than 98% for atmospheric muons over a large range of discriminator thresholds. This indicates also an excellent application as a detector of cosmic ray induced extensive air showers and as an external detector for characterization studies of other detector setups.

8.2. Study of the photon arrival time distribution

A further important quantity predicted by simulations is the extended photon arrival time for a passage of a single muon. It is presented in figure 7.8b on page 94 in chapter 7.3.2.3. A Monte Carlo (MC) simulation, based on measurements, is now used to verify the predicted width of the simulated arrival time distribution of $\approx 10\,\mathrm{ns}$. In the first instance, the basic principle of the approach is explained, followed by the presentation of the measurements and the MC study. First, the 1 p.e. pulse shape is determined. It will be used as a template for the response of the SiPM to a single photon. Based on this template, the response for multiple photons arriving at the SiPM can be approximated. Therefore, the responses of each photon will be added up to a trace. The photon arrival time follows the simulated arrival time distribution presented in chapter 7.3.2.3. In addition, a trace is simulated where the arrival time of each photon is the same, corresponding to a delta distribution. Those traces are compared to measured traces of muon passages containing the same number of photons as in the simulations.
To extract the 1 p.e. pulse shape, an oscilloscope is used to study the pure SiPM voltage traces[6]. In figure 8.13a, a screenshot from the oscilloscope for the SiPM of type S133650-1350PE connected to a unit of layout 2 is presented. The trigger is set to be below 1 p.e. The color of the measured traces

[6]The default readout electronics provide only an integrated value of the charge (cf. chapter 6.2.2).

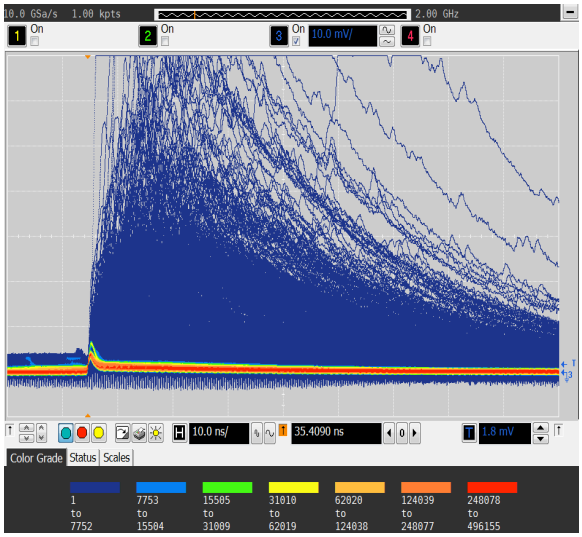

(a) Oscilloscope view of the measured SiPM signal. Each grid cell corresponds to a time of 10 ns and a voltage of 10 mV. The color refers to the amount of traces triggered. The pulse shape in red corresponds to the 1 p.e. and the pulse shape in green to the 2 p.e. pulse. For higher amount of photons, a continuum of traces is visible.

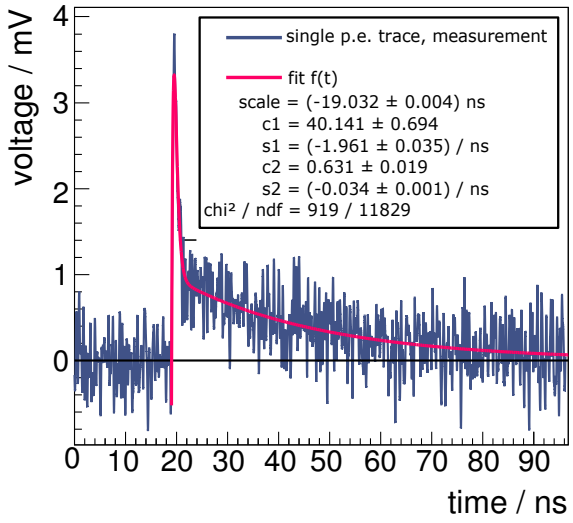

(b) A measured single p.e. pulse is fitted by a function $f(t)$, which comprises a sum of two exponentials with a fast and a slow component (cf. equation 8.21). The rising edge is shaped by a hyperbolic tangent. The pulse shape is used as base of the Monte Carlo simulation for particle passages.

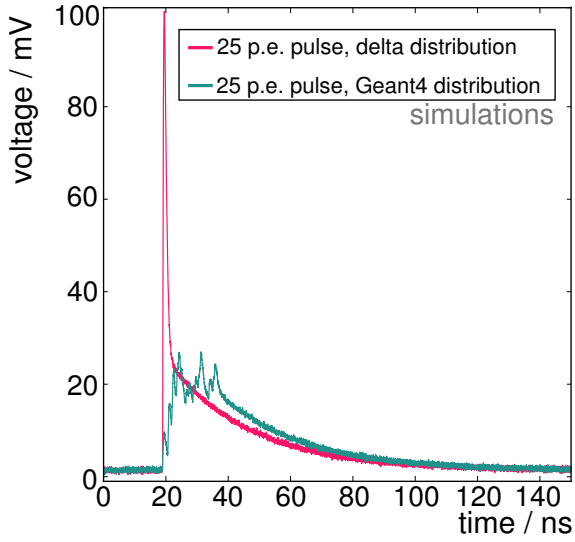

(c) Comparison of two different SiPM traces. In pink, the simulated 25 p.e. distribution is presented assuming all photons to arrive simultaneously. In green, an exemplary simulated 25 p.e. distribution is presented assuming the photons to arrive according to the simulated photon arrival time distribution shown in figure 7.8. For both simulations, the response of each photon hit is described by the measured single p.e. pulse (cf. figure 8.13b).

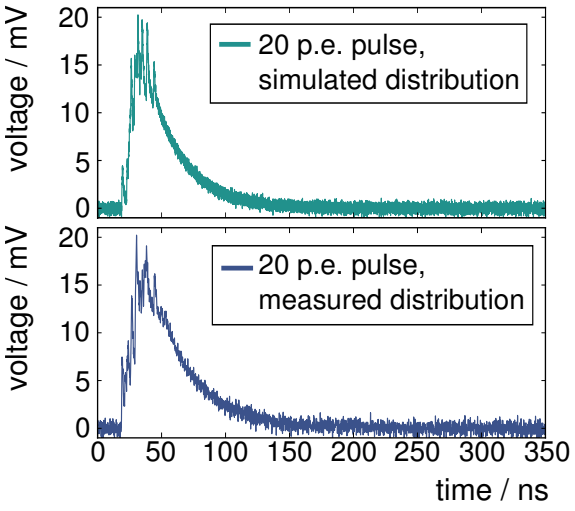

(d) Comparison of two different SiPM traces. In blue, a measured 20 p.e. distribution is presented. In green, an exemplary simulated 20 p.e. distribution is presented assuming the photons to arrive according to the simulated photon arrival time distribution shown in figure 7.8.

Figure 8.13.: Measured and simulated SiPM traces are shown as a function of time in ns.

refers to the amount of traces triggered (red → blue corresponds to high → low trigger rates). The 1 p.e. pulse is depicted in red, corresponding to thermal noise events. The 2 p.e. pulse is visible in green, corresponding to crosstalk events. For higher p.e. values a continuum of traces is apparent with individual distributions and signal yields, corresponding to the passage of particles. In figure 8.13b, an exemplary measured trace of a 1 p.e. pulse is shown as a function of time in ns. To extract the pulse shape, a function of the form

$$f(t) = \tanh(t + \text{scale}) \cdot \left(e^{c_1 + s_1 \cdot t} + e^{c_2 + s_2 \cdot t}\right) \tag{8.21}$$

is fitted onto the data. The sum of exponentials describes the decay with a fast and a slow time constant, s_1 and s_2, respectively. Two constants c_1 and c_2 allow for a smooth transition between both exponentials. The hyperbolic tangent modulates the steep increase up to the maximum peak corresponding to the fit parameter scale. Based on the knowledge of the SiPM response to an individual photon, the response to muon passages is approximated. In figure 8.13c, two simulated 25 p.e. SiPM signals are presented. First, the signal is simulated by assuming that all photons arrive simultaneously (delta distribution) and by adding up all individual pulses. As expected, the resulting shape can be described as a scaled version of the single p.e. pulse and depicts a steep rising edge. For comparison, the simulated photon arrival time distribution (cf. figure 7.8b) is used to simulate the multi-photon response. The signal is reminiscent of a mountain. Due to the individual arrival times, the shape is broadened and the maximum reached voltage amplitude is strongly reduced. This shape is well in agreement with measured traces containing about the same amount of photons. One example of a measured and a simulated SiPM trace, both including 20 p.e. in the event, is shown as a function of time in ns in figure 8.13d. Under the assumption of an extended time distribution, the simulated measurement curve fits the measurements very well. This is an important indication that the simulation well describes the response of the unit to particle passages. In any case, the alternative hypothesis that photons simultaneously reach SiPM can be excluded.

8.3. Self-triggered scintillator unit

The determination of the MIP peak of a single unit without requiring coincidence events with an external detector or with other units in a stack would allow for its autonomous monitoring and characterization but is challenging due to darknoise and background events. To investigate sources of background, several setups are studied:

1. SiPM in darkness with a discriminator threshold of 0.08 V or 0.5 p.e.
2. Single unit with a discriminator threshold of 0.08 V or 0.5 p.e.
3. Single unit with a discriminator threshold of 0.08 V or 0.5 p.e. but with a vertical orientation. Additionally to events by atmospheric muons or darknoise, artificial events induced by energy deposit of radioactive sources ^{60}Co and ^{22}Na are investigated.
4. Stack of three units. The middle unit is equivalent to layout 2 and is the first detector unit assembled for test measurements. Therefore, no further unit of this type was available at this time and the other units in the stack are of layout 1. All units are read out by a common EASIROC evaluation board, but with the corresponding SiPM carrier board and power supply unit for each layout. Therefore, all units are operated with a discriminator threshold of 0.26 V corresponding for both setups to 2.5 p.e. Various combinations of those units are used for coincident measurements and as veto:

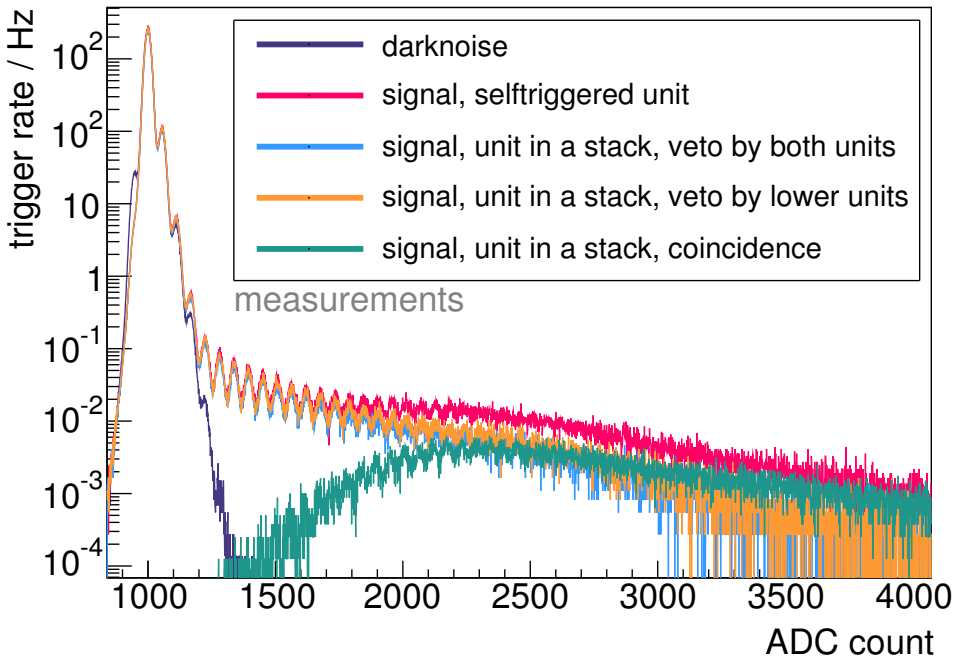

Figure 8.14.: Comparison of charge spectra as a function of ADC count for a SiPM in darkness and the same SiPM connected to a scintillator unit of layout 2 for different setups. First, the unit is studied in self-triggering mode. Secondly, the unit is operated in a stack with two units of layout 1, directly located above and below the unit under investigation. Third, the top and bottom units are used as veto. A trigger threshold of 0.5 p.e. is imposed for the unit in self-triggering mode and operated in the veto setup. A trigger threshold of 2.5 p.e. is imposed for the unit operated in the coincidence setup.

- The upper and the lower units are used for coincidence measurements, where the middle unit is of interest.
- The upper and the lower units are used as veto of events registered in the middle unit being subject of interest.
- Only either the upper or the lower unit is used as veto of events registered in the middle unit being subject of interest.

In figure 8.14, the charge spectra of all discussed setups except of the vertically orientated unit (point 3) are presented as a function of ADC count. As the deviation in the trigger rate is large between the different spectra, their absolute scales are difficult to compare. Nevertheless, all spectra shown are normalized to the same measurement time. First, the unit is studied in self-triggering mode. The MIP peak is hardly visible as the peak-to-valley ratio is small. Compared to the darknoise spectrum of the same SiPM, it is apparent that the rate blanketing the MIP peak is not a SiPM noise effect but originates from an additional source. Electronic noise can be excluded as source, as these events would be also apparent in a darknoise measurement performed with the same electronics settings and cables. Secondly, the unit is operated in a stack with two units of layout 1, directly located above and below the unit under investigation. The MIP peak becomes clearly visible in the coincidence measurements, but is slightly reduced compared to the spectrum of the unit in self-triggering mode. The total trigger rate of the MIP peak is around 7 Hz. This is slightly reduced compared to the expectation of 10 Hz (cf. equation 8.7), but results mainly from the requested coincidence. The self-triggered unit depicts for a signal above 1800 ADC count a total trigger rate of 16 Hz. Using the top and bottom units as veto, the signal in the region of the MIP peak is reduced but

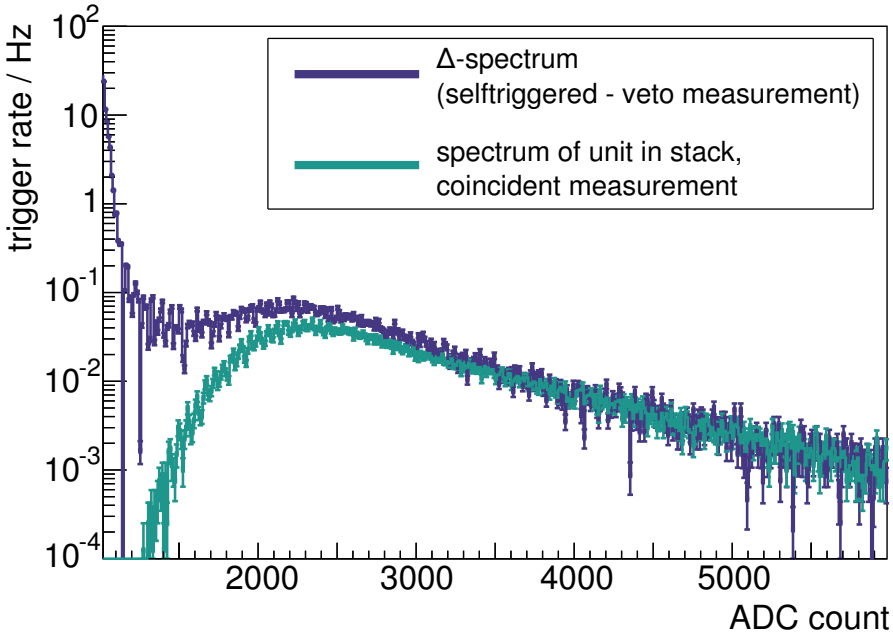

Figure 8.15.: Comparison of charge spectra as a function of ADC count for a detector unit of layout 2. The unit is located in a stack with two detector units of layout 1, directly located above and below the unit under investigation. First, the spectrum measured in coincidence with the other units is shown. Secondly, the difference between the spectrum measured in self-triggering mode and the spectrum measured using the other units as a veto is presented. A trigger threshold of 0.5 p.e. is imposed for the unit in self-triggering mode and operated in the veto setup. A trigger threshold of 2.5 p.e. is imposed for the unit operated in the coincidence setup.

does not vanish while the background rate is unchanged. Thereby, no significant deviation between a veto comprising both units and comprising only one, top or bottom, unit can be identified. By the veto, each particle traversing more than one unit is excluded. Such particles would include muons and other high energetic particles. Furthermore, coincident triggers by a darknoise event and a muon event are eliminated. As all detector units have the same dimensions, only highly inclined particles will pass this veto criterion. Candidates for these inclined particles are the products of radioactive decay in air.
The subtraction of the spectrum, measured using a unit above and below the unit of interest as veto, from the self-triggered spectrum is compared to the MIP spectrum determined by units operated in coincidence. The comparison is presented in figure 8.15. While darknoise events are eliminated by the subtraction, a large part of the background events is still apparent, resulting in a peak-to-valley ratio of only 1.5. This ratio is slightly worse but comparable to the charge spectrum presented in figure 8.8. In the region of the MIP peak, a comparable trigger rate as for the MIP spectrum measured in coincidence is determined. The high signal tail can be well reproduced by the subtracted Δ-spectrum. However, no strict statement is possible as the different trigger criteria are biasing the rate. The spectrum measured in coincidence will contain muon events with a higher energy threshold and a smaller acceptance angle compared to a detector unit in self-triggering mode.

Energy deposit by radioactive sources

Radioactive sources can be used to investigate the response of scintillator tiles to natural radioactive decays in air, as particles are produced in large quantity and with constant flux. There are

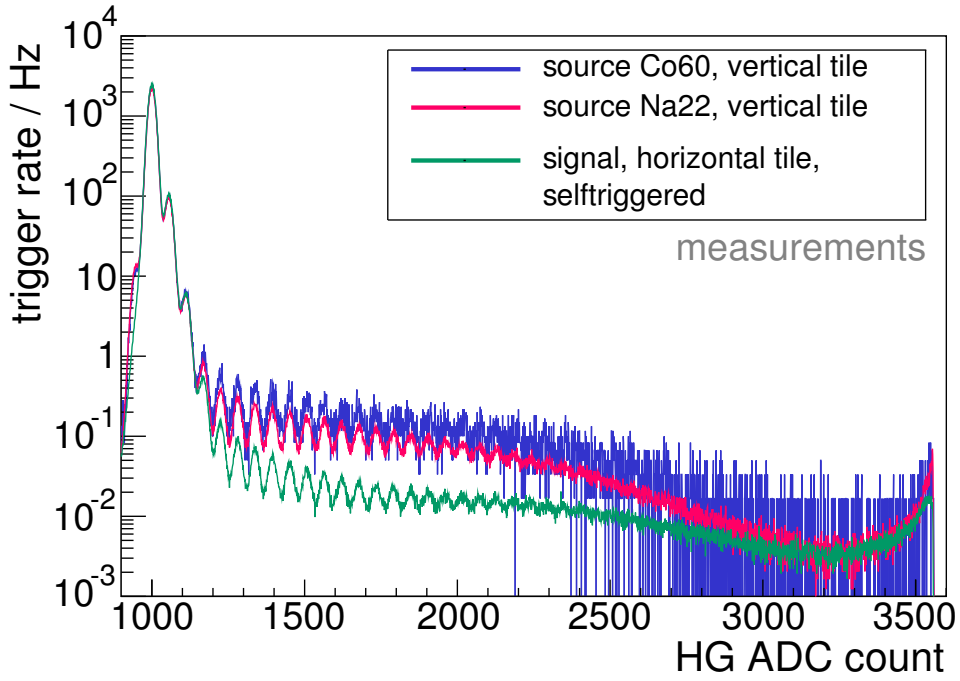

Figure 8.16.: Comparison of the trigger rate in Hz as a function of HG ADC count for a detector unit of layout 2 operated in self-triggering mode. Two different radioactive sources, ^{60}Co and ^{22}Na, are placed next to a vertically orientated tile. The spectra are compared to the spectrum of the same tile with horizontal orientation. A trigger threshold of 0.5 p.e. is imposed.

several groups of natural radioactive isotopes. The major radionuclides of concern are potassium (^{40}K undergoing beta decay with a maximum electron energy of 1.3 MeV or gamma decay with a maximum energy of 1.5 MeV), uranium (^{235}U, ^{238}U emitting an α-particle), thorium (^{232}Th emitting an α-particle) and their decay products like radon (^{222}Rn emitting an α-particle). Furthermore, isotopes are produced continuously via nuclear reactions of the particles in cosmic ray induced air showers with nuclei in the atmosphere. One of the most important radioactive isotope is thereby radiocarbon, ^{14}C, which undergoes beta decay with a maximum electron energy of 0.16 MeV. [190] For an estimate of the expected trigger rate, a back-on-the-envelope calculation is performed. The γ-local dose rate in Aachen is stated as $D_\gamma = 0.088\,\mu$Sv/h [191]. The expected trigger rate r_γ in the scintillator tile is

$$r_\gamma = \epsilon_{\text{trigger}} \cdot \frac{D_\gamma}{\langle E_\gamma \rangle} \cdot m_{\text{scint}} \approx 3.5\,\text{Hz} \quad . \tag{8.22}$$

Thereby, $m_{\text{scint}} = 460.35\,$g is the weight of a scintillator tile, $\langle E_\gamma \rangle = 1\,$MeV is the average kinetic energy and $\epsilon_{\text{trigger}} = 5\%$ is the expected trigger efficiency of gammas (cf. section 7.3.3). This estimate indicates a non-negligible contribution of radioactive decay products to the background rate of a self-triggered detector unit.

As the possible natural radioactive background may be a mixture of gamma and beta radiation[7], two radioactive sources having a signature of both radiations are studied. ^{60}Co produces two gammas with energies of 1.17 MeV and 1.33 MeV, as well as an electron with end point decay energy of 0.31 MeV. It has a half-life of 5.25 years. ^{22}Na has a half-life of 2.6 years and produces during the decay a gamma with an energy of 1.27 MeV and a positron via β^+ decay with an end point energy of 0.543 MeV. The activities are stated as 29.8 kBq and 11.8 kBq for the ^{60}Co and ^{22}Na source, re-

[7] α-particles will not enter the scintillator material through the wrapping

spectively. The trigger rate introduced by a radioactive source placed next to a scintillator material will dominate the corresponding signal spectrum while atmospheric muons will have a negligible impact.
For the test setup, the unit of layout 2 is used in a vertical orientation to reduce muon background. Placing now radioactive sources in front of a vertically oriented unit, the resulting charge spectra are compared to the spectrum measured by the horizontally orientated unit without artificial source. The spectra are presented in figure 8.16. The response of the scintillator tile to the radioactive source is covering the complete charge region from the darknoise region up to the decline of the MIP peak. These measurements hint, that radioactive decays in the air and the surrounding material may be possible sources of the background events apparent in the charge spectrum of a self-triggered unit. This additional component leads to an increased trigger rate with respect to theoretical muon rate predictions. This is already indicated by the signal rate scans (cf. figure 8.2). Therefore, the characterization of the light yield of a single unit is not possible, while important SiPM characteristics can be still investigated. For a sufficient study of the MIP peak at least a stack of two units is needed as will be available in the demonstrator detector MiniAMD introduced in the next chapter 9.

8.4. Position-resolving measurements of performance

Coincident measurements with a position-resolving external detector at KIT, referred to as a *muon tomograph* in the scope of this thesis, allow for the study of the performance of both unit layouts for single impinging atmospheric muons.
While being a part of the former KASCADE-Grande experiment [25], the tomograph allows to measure the direction of high-energetic charged particles with a high accuracy of 0.3 ° [192]. Detailed information on the muon tomograph as part of the KASCADE-Grande can be found in [193] while a general description of the actual setup at KIT is given in [194]. The detector comprises three identical horizontal levels with a sensitive area of $2 \times 4\,\mathrm{m}^2$. Each registers muons with an energy $\gtrsim 800\,\mathrm{MeV}$ by streamer tube detectors. Due to their spatial resolution, the three levels can be used to study the units of layout 1 and 2. The main goal is thereby to determine their response homogeneity and detection efficiency. Requesting a coincidence trigger in all levels of the muon tomograph results in a definition of a single particle track. This track is defined by its coordinates in a given z-layer (with a positional resolution of 1 cm) and its direction. If now a unit is placed between two detector levels and a readout system combining the responses of the muon tomograph and of the unit is implemented, it can be checked if a muon has traversed the sensitive area of the unit and whether the unit has seen a signal in coincidence.
To test the influence of the chosen unit configuration for the light collection, a measurement of both unit layouts is performed. First, one unit of layout 1 is studied. The unit is located in a light-tight box (the *AMD unit container* as presented in [165]) and the WLS fibre is connected to a SiPM by a short optical fibre with a length of around 1 cm. The SiPM is of the through-hole type S12571-050C instead of the surface mounted devices in the standard unit layout. To allow for the matching of events registered by the tomograph and the unit, both have to be read out simultaneously. The signal of the tomograph is thereby determined via a PicoScope[8]. As an implementation of the detector unit response within this already existing readout chain is easier with analog signals, an alternative DAQ is used to study the unit layout 1. This DAQ provided traces of the SiPM which are integrated to determine the detected charge.
For the measurement of unit layout 2, 16 units are studied simultaneously. Thereby, a group of eight units each is located in one module of the detector prototype MiniAMD presented in chapter

[8] Used is a PicoScope type 6403 which is a mixed-signal oscilloscope [195].

Figure 8.17.: Photo of the setup at the muon tomograph at KIT, Karlsruhe. Shown are the three layers of the tomograph. Between the two lower layers, two MiniAMD modules are located. They comprise in total 16 units of layout 2. Here, both modules are stacked. For the measurements presented, both modules are placed next to each other at the same level.

9. The designated and presented readout system (EASIROC and power supply unit in chapter 6) is used. This DAQ provides only a digital data stream. All units are in self-triggering mode requiring a signal larger than 3.5 p.e. threshold for a single unit. The self-triggering rate is 200 Hz. However, the readout of the buffer is only started if a hardware 'confirm' trigger from the muon tomograph was received in a time window of up to 1 μs length. Otherwise no ADC event is registered for the units under study. This allows for a synchronization of both detector setups whereby the readout is independent on the status of the MiniAMD detector. The confirm trigger is a LV TTL pulse registered by the FPGA of the EASIROC evaluation board. The trigger is sent by the tomograph if it has registered a valid muon candidate. The event is valid if it fulfills the requirements of only one hit in each of the three layers in the tomograph and allows for a reasonable reconstruction of a track. The setup, here, with both modules of the detector stacked, is shown in figure 8.17. In the measurements presented both modules are located next to each other.

Position-resolving detection efficiency for single atmospheric muons

The detection efficiency of both unit layouts is expected to be almost independent of the position at which the unit is traversed by a muon for the chosen trigger conditions. This expectation is based on Geant4 simulations performed for each setup assuming atmospheric muons presented in chapter 7. The measurements at KIT support these simulations.
In figure 8.18, the efficiency for all 16 units of layout 2 is shown (right). It is defined by the number of the particle hits detected by the units (middle) divided by the total number of particles which trigger the muon tomograph (left). All units show a comparable and flat detection efficiency well above 95% with a steep decrease at the edges. The edges of the units are subject to the position

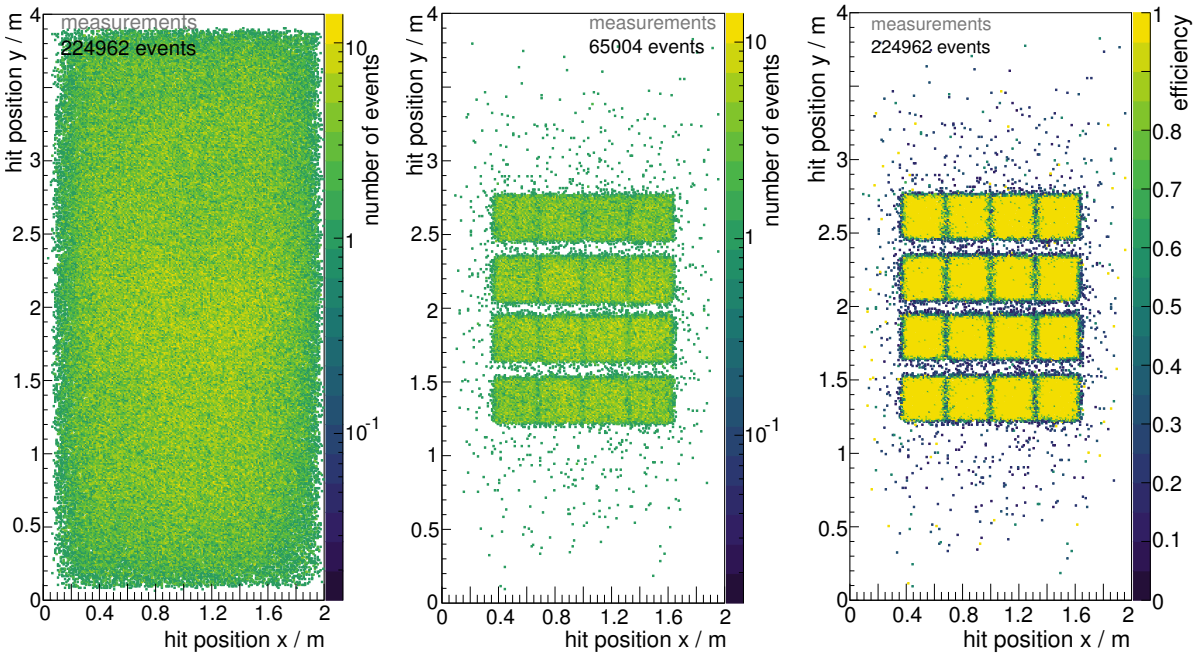

(a) Total number of particles which triggered the muon tomograph.

(b) Number of particle hits detected by the 16 units.

(c) Detection efficiency defined by the number of hits in the detector units divided by the total number of triggered particles by the tomograph.

Figure 8.18.: Particle distribution and detection efficiency at the z-level corresponding to the position of the scintillator units of layout 2. The 16 units can be clearly identified. All units demonstrate a detection efficiency above 95% with a steep decrease towards the edges. No dependency on the particle position is apparent. A trigger threshold of 3.5 p.e. is imposed.

uncertainty of the muon tomograph.
To increase the statistics, also an analysis on superimposed data of all units is performed assuming that all units have a comparable response distribution. Therefore, each unit is subdivided in a grid of 30 times 30 bins corresponding to a unit size of $30 \times 30\,\mathrm{cm}^2$ and a spatial resolution of 1 cm. As the units have different orientation in a module (cf. figure 9.1 on page 142), the grid for each unit is rotated such that the position of the SiPM is always located in the same bin (right bottom corner). While this method allows for an evaluation of the average unit response, influences of position uncertainties or of clipping muons dominate the outer region of the unit as apparent in figure 8.19a. Thereby, the response in the two outermost bin rows in each direction can be only interpreted to a limited extent. While excluding these two outermost rows along each edge, the fraction of bins with a detection efficiency being greater than 95% is 80% (cf. figure 8.19b). The uncertainty on the detection efficiency of each bin is determined using the Clopper-Pearson interval, while a 95% confidence level is imposed. The uncertainty is obtained by ROOT. This uncertainty is further propagated by a toy MC simulation to the cumulative distribution presented in figure 8.19b. If only the outermost row is excluded, the fraction of bins with a detection efficiency being greater than 95% is decreased to 70%, while for all rows taken into account, the fraction is further decreased to 60%. However, an excellent trigger efficiency for the units can be confirmed as stated by simulations (cf. figure 7.5) and measurements of the detector units in a stack (cf. figure 8.11).

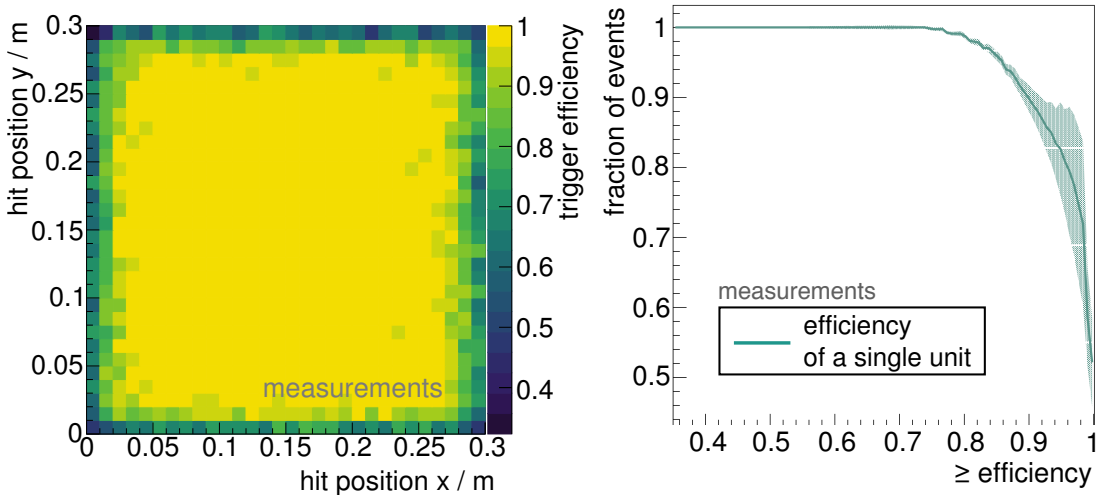

(a) Detection efficiency distribution. The distribution is flat in the main region of the unit but demonstrates a steep decrease towards the edges.

(b) Fraction of bins with a value being greater than the imposed detection efficiency. The two outermost rows along each edge are not taken into account. The uncertainty on the detection efficiency is derived using the Clopper-Pearson interval, obtained by ROOT, and represents the 95% confidence level.

Figure 8.19.: Detection efficiency determined by the superposition of all 16 units. Each unit is divided in a grid of 30×30 bins and is rotated such that the SiPM is located in the same bin in the right bottom corner. While excluding the two outermost rows along each edge 80% of all bins provides a detection efficiency better than 95%.

Detection efficiency of both modules

The same measurement setup is used to study the detection efficiency of the later presented MiniAMD demonstrator (cf. chapter 9). Here both modules are located on top of each other as presented in figure 8.17. A unit in the upper module in combination with the unit at the same location in the lower module is defined as a *stack*. A coincident trigger of the muon tomograph and of one MiniAMD stack is required. A MiniAMD stack is triggered if the signal in both units in the stack exceeds a trigger threshold of 3.5 p.e. Each unit is subdivided in a grid of 30 times 30 bins. The detection efficiency is determined for each bin individually. The two outermost rows along each edge of each unit are not taken into account. Two scenarios are studied. For both, a trigger of the entire stack of the MiniAMD detector is requested. First, only events are considered in which a muon traversed both units in a stack. Secondly, all events are considered in which a muon traversed the lower unit in a stack. For the latter, the resulting detection efficiency includes the lowered geometrical acceptance due to the requested trigger in a stack and the corresponding limitation of the maximum incidence angle. Both scenarios are presented in figure 8.20. Presented is the cumulative distribution of the fraction of bins of a unit in a stack with a value being greater than a requested detection efficiency. The uncertainty on the detection efficiency of each bin is determined using the Clopper-Pearson interval, while a 95% confidence level is requested. The uncertainty is obtained by ROOT. This uncertainty is further propagated by a toy MC simulation to the cumulative distribution. For comparison, the average detection efficiency of a single unit is determined to 0.95 ± 0.10 (cf. figure 8.19b), of a stack to 0.90 ± 0.16 (cf. figure 8.20) and of the lower unit in a stack to 0.82 ± 0.19 (cf. figure 8.20).

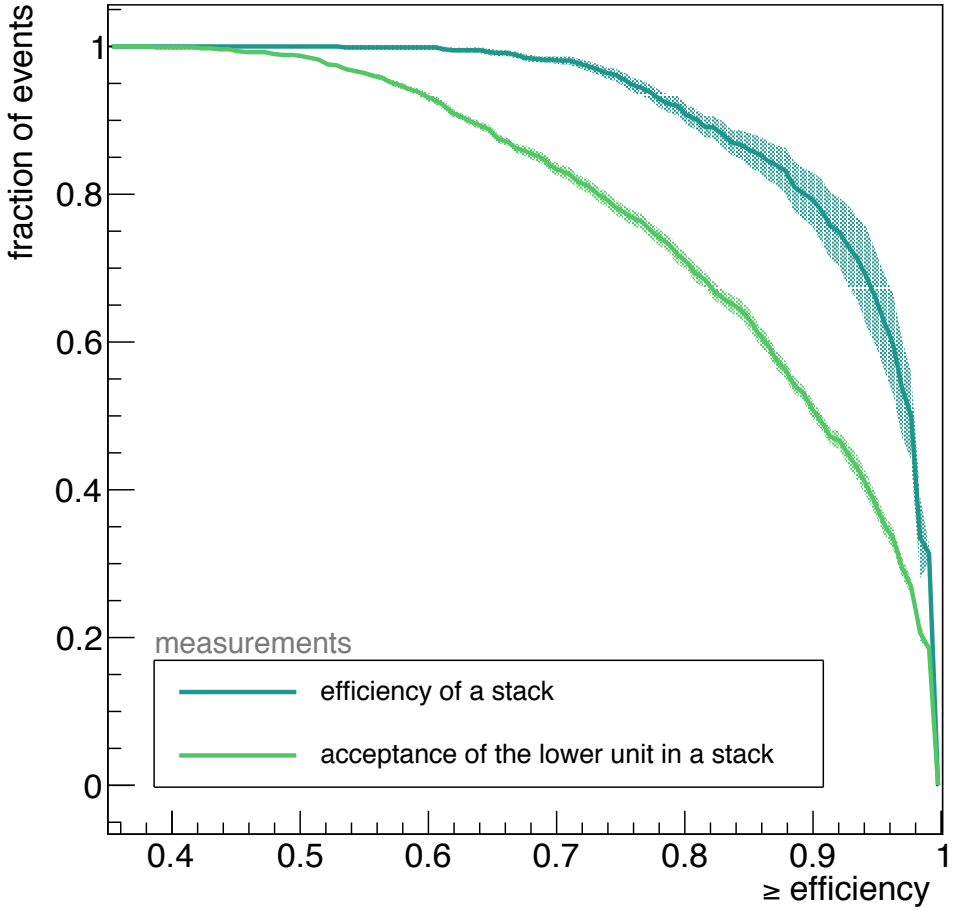

Figure 8.20.: Detection efficiency of a MiniAMD stack determined by the muon tomograph. Presented is the fraction of bins with a value greater than the requested detection efficiency. Two scenarios are compared, see text for discussion. Each unit is divided in a grid of 30×30 bins. The events of all units are stacked. The two outermost rows along each edge of a unit are not taken into account. The uncertainty on the detection efficiency of each bin is determined using the Clopper-Pearson interval, while a 95% confidence level is requested. The uncertainty is obtained by ROOT. This uncertainty is further propagated by a toy MC simulation to the cumulative distribution. A trigger threshold of 3.5 p.e. per unit in a stack is imposed.

Vertical MIP determination

Each detector unit depicts an individual light yield for a traversing muon. To allow for a comparison, the response of each detector unit in ADC count has to be converted into a common scale in MIP. Therefore, for each detector unit the charge spectrum as a function of ADC count is investigated. Exemplary, spectra for unit channel 3 are presented in figure 8.21. In figure 8.21a, the spectrum including all events regardless of the unit trigger status is shown. Electronic noise events are apparent in the first peak, the pedestal. In figure 8.21b, the spectrum, which includes only events exceeding the imposed discriminator threshold of 3.5 p.e., is presented. The MIP peak is dominant. The conversion into the common scale in MIP is performed according to equation 8.17. A Gaussian distribution[9] is fitted to the spectrum. A mean of (1.01 ± 0.02) MIP and a width of (0.32 ± 0.02) MIP is determined. Additionally, a log-normal fit (cf. equation 8.18) is performed. With a maximum of (0.98 ± 0.04) MIP, the result is well compatible to the fit of a Gaussian dis-

[9] limited in a range of (1.0 ± 0.3) MIP

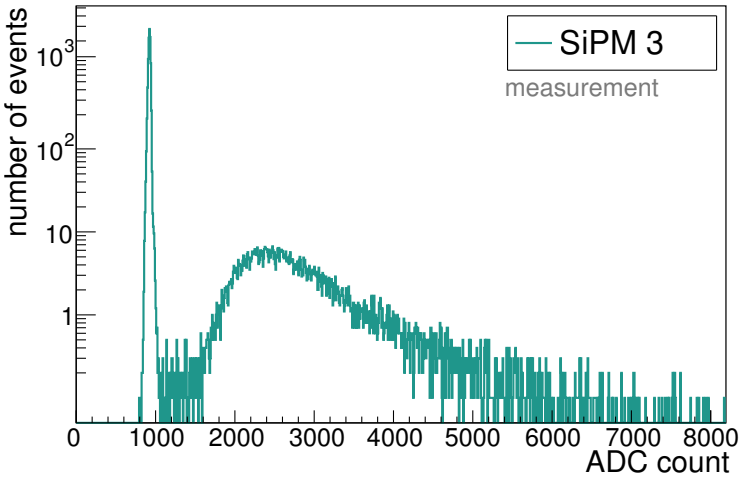

(a) Signal spectrum as a function of the signal in ADC count for all events. The pedestal peak describing electronic noise is apparent.

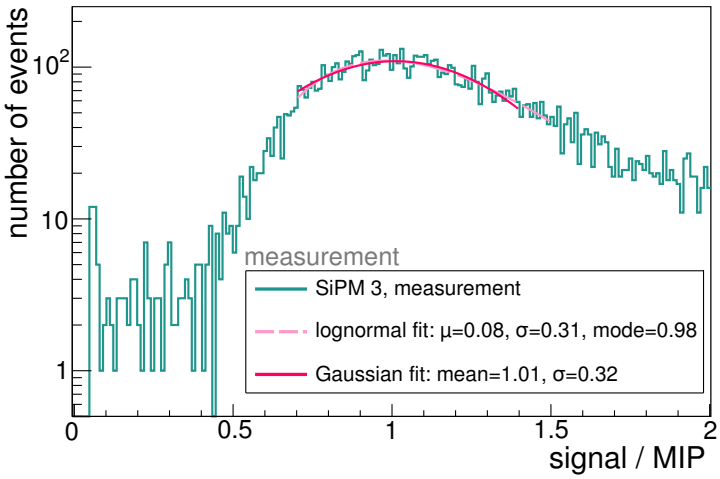

(b) Signal spectrum as a function of the signal in the common unit of MIP. The MIP peak is shown with a width of (0.32 ± 0.02) MIP determined by a fit of a Gaussian distribution. A trigger threshold of 3.5 p.e. is imposed.

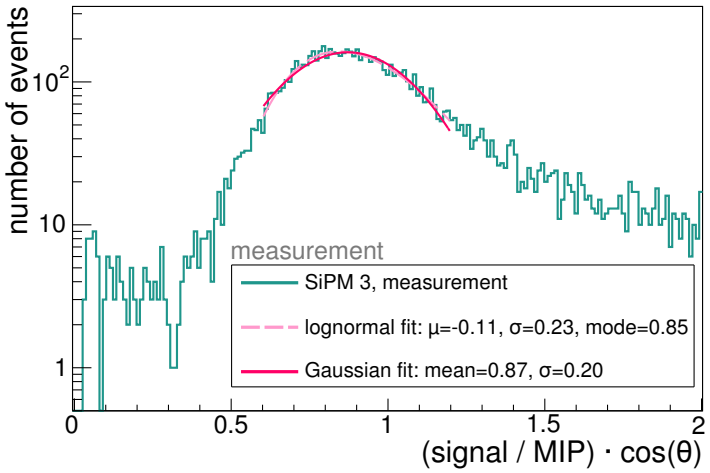

(c) Signal spectrum as a function of the signal in vertical MIP. The peak has a maximum at (0.87 ± 0.01) MIP and a width of (0.20 ± 0.01) MIP. A trigger threshold of 3.5 p.e. is imposed.

Figure 8.21.: Absolute signal spectra, exemplary for unit channel 3. Shown is the number of events as a function of the signal height.

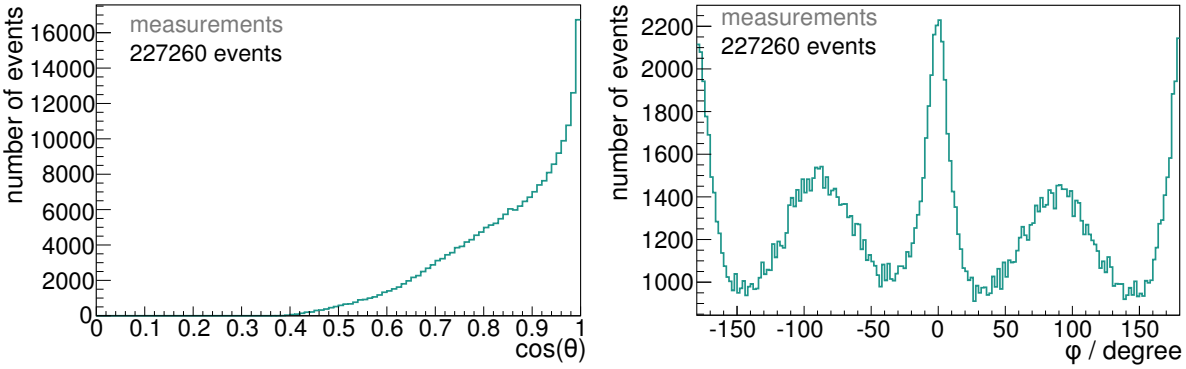

(a) The zenith distribution peaks at $\cos\theta = 1$.

(b) The azimuth distribution peaks at $0^\circ, \pm 90^\circ$ and $\pm 180^\circ$.

Figure 8.22.: Angular distribution of events detected by the muon tomograph. Shown is the number of events as a function of the azimuth angle ϕ in degrees and as a function of $\cos\theta$ with zenith angle θ.

tribution. As the muon tomograph allows for the reconstruction of the muon track, not only the position but also the direction of the muon can be determined. The angular distributions of zenith, $\cos\theta$, and azimuth, ϕ, of all events detected by the muon tomograph are shown in figure 8.22. In the azimuth distribution four preferred directions can be identified at $\phi = 0^\circ, \pm 90^\circ$ and 180°. They result from the geometry of the muon tomograph. The zenith distribution peaks at $\cos\theta = 1$. A vertically equivalent MIP signal, $\text{MIP}_\perp$, can be calculated by multiplying the signal in MIP with $\cos\theta$ of the reconstructed track shown in figure 8.21c. The vertical MIP peak has its maximum at $S_{\text{adc, max}_\perp} = (0.87 \pm 0.01) \cdot S_{\text{adc, max}}$ and a width of (0.20 ± 0.01) MIP. The value allows for a simple comparison of the presented detector with other detector layouts, since it is not influenced by the acceptance angle of individual detector configurations. Alternatively, the MIP spectra for different zenith angle bins can be studied. The signals detected by each individual detector unit are converted into the common MIP scale. These signals are accumulated in one common MIP spectrum for all detector units per zenith angle bin. The light yield $S_{\text{adc, max}}$ is determined by a fit to the corresponding MIP peak of each spectrum. The position of the maximum is expected to decrease with increasing $\cos(\theta)$ as muons have a longer pathlength inside the scintillator tile for larger angles (cf. equation 8.13). In figure 8.23, the light yield $S_{\text{adc, max}}$ for eight zenith angle bins ranging from $\cos(\theta) = 0.65$ to 1 is shown. The error bars refer to the uncertainties given by the fit on the value of the maximum. A linear fit determines a decrease following $f(\cos(\theta)) = 2.10 - 1.21 \cdot \cos(\theta)$ for all data points. The slope of (-1.21 ± 0.02) is thus slightly larger than expected. The corresponding uncertainties on the fit of the maximum per angle seem to be underestimated. Fitting only the largest $\cos(\theta)$ bins, the linear fit determines a slope of (-0.948 ± 0.003) which is more compatible with the expectation of -1.

Position-resolving signal uniformity

For the detection efficiency, no evidence is found that any part of the unit is preferred for the chosen threshold. However, the signal height itself may be enhanced in certain regions due to geometrical aspects or be reduced due to imperfections in the manufacturing process.
As indicated by simulations and presented in figure 7.7, photons produced next to the WLS fibre have to traverse a minimal distance to be collected by the fibre. This reduces the probability of photons being absorbed due to attenuation effects in the scintillator. In the region between fibre and the scintillator edges, the collection efficiency may be improved even more. Photons isotropically

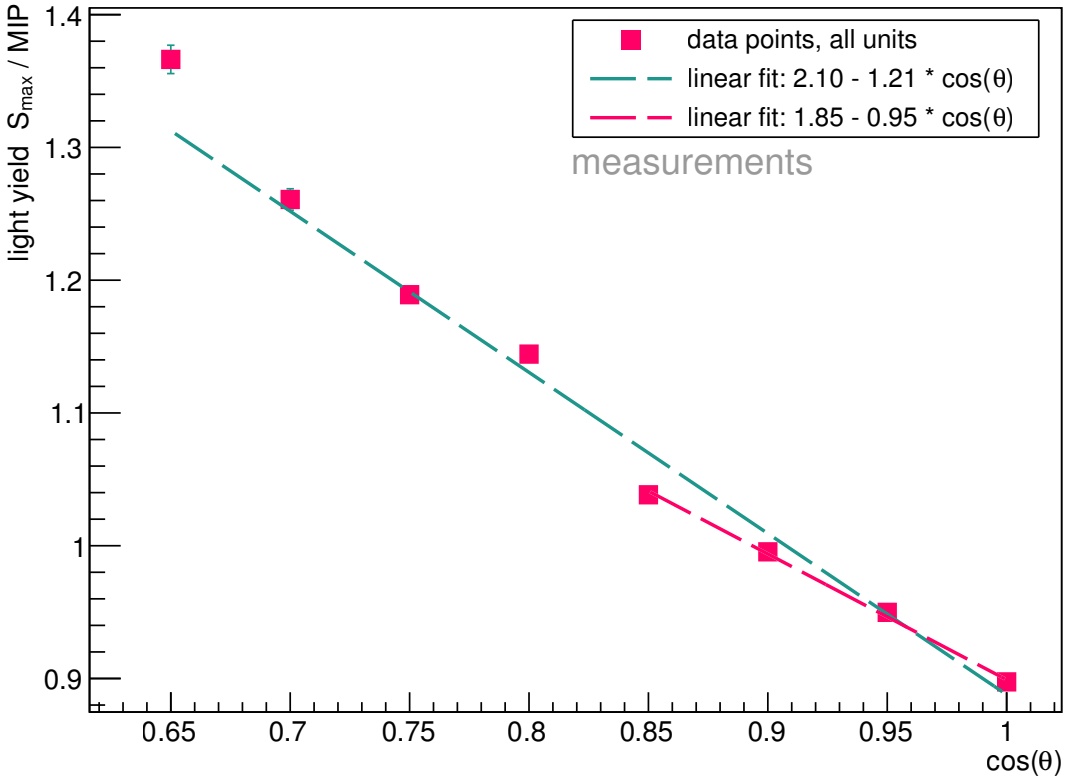

Figure 8.23.: Signal yield $S_{\text{adc, max}}$ determined by the combined MIP spectrum of all units for eight zenith angle bins of $\cos\theta$. A linear fit to all data points is performed. Additionally, a linear fit to the data points of the largest $\cos(\theta)$ bins is depicted. For the latter, a slope of (-0.948 ± 0.003) as a function of $\cos\theta$ is well compatible to the slope expectation of -1.

emitted in this region can either be captured directly in the fibre, or they are first reflected at the scintillator edge or at the wrapping and then collected in the fibre. Next to the SiPM carrier board, three effects may occur:

1. A short distance between photon emission point and WLS fibre reduces attenuation effects.

2. Photons have to travel only a short path length inside the WLS fibre before leaving the fibre for an optical waveguide or the SiPM, so that several photons may not undergo the wavelength shifting procedure. These photons are in the UV-blue wavelength regime offering a slightly improved photon detection efficiency (up to 10%) of the SiPM.

3. Direct scintillation light may reach the photosensor. This is more present for unit layout 2 as for layout 1 the mechanical coupling strongly reduces the aperture for direct scintillation light.

Figure 8.24 presents the average charge distribution of unit layout 1 in log scale, while the number of hits and the detection efficiency are shown in linear scale. The signal distribution of unit layout 1 is flat. Also the detection efficiency depicts no inhomogeneities and a high efficiency $> 95\%$. However, the mechanical coupling to an optical waveguide in unit layout 1 is a large source for light losses. Layout-induced fluctuations in light yield are thus challenging to identify. In figures 8.25a and 8.25b, measurements performed with units of layout 2 are shown. Again each detector unit is subdivided into a grid with 1 cm spacing which is rotated so that the position of the SiPM is

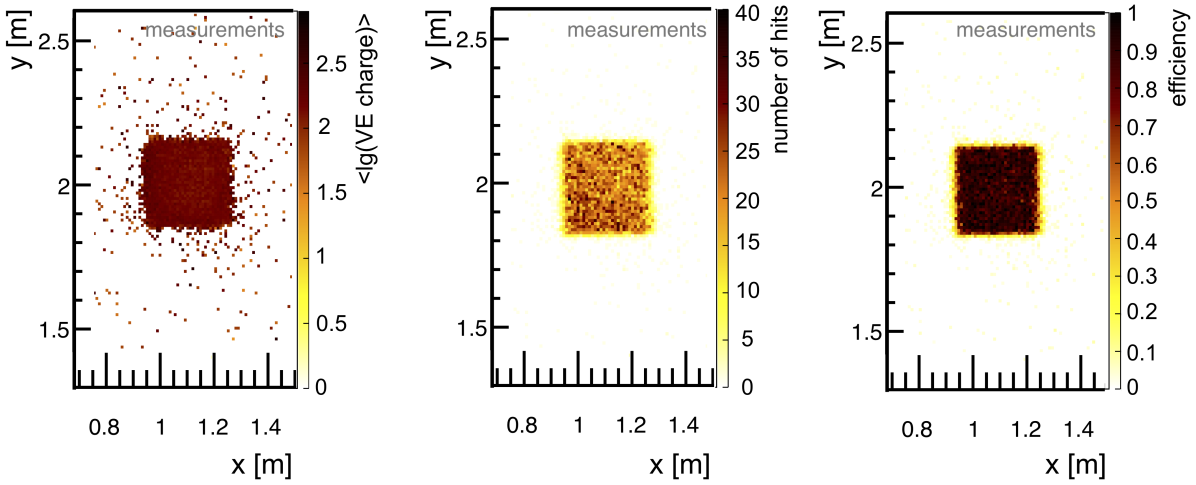

Figure 8.24.: Measurement performed with the unit of layout 1. Shown is the average signal. The signal of each event is determined by an integration of the analog trace of the SiPM detected by a PicoScope. It is given in VE (vertical equivalent) charge corresponding to the detected signal for a vertically traversing MIP. The detected charge distribution is flat.

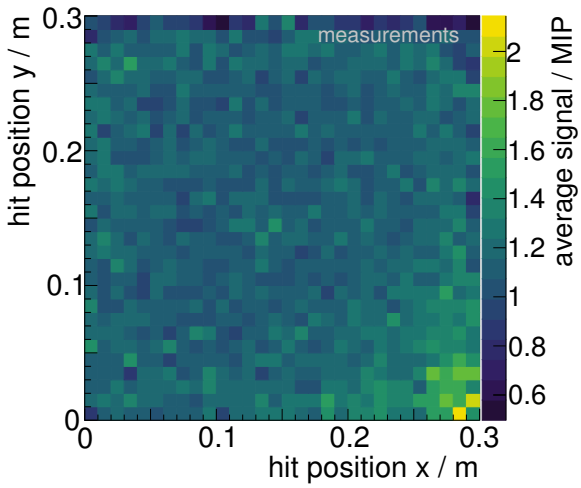

(a) Average signal distribution achieved with units of layout 2 in units of MIP. The average signal is $\bar{s} = 1.14\,\mathrm{MIP}$. An increase (up to twice of the average signal) is identified in the right bottom corner, where the SiPM is located.

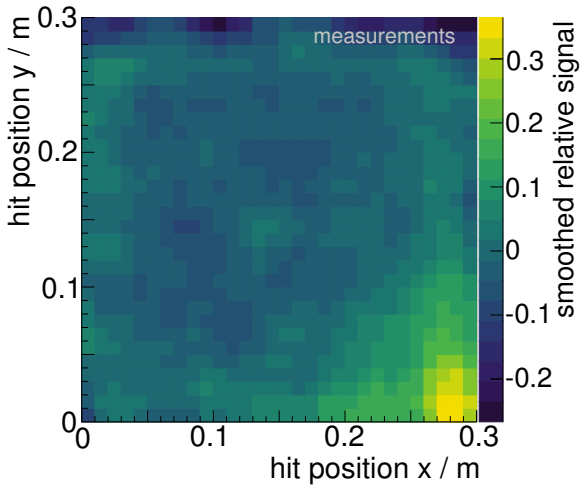

(b) Smoothed relative signal distribution of units of layout 2. The relative signal is defined as $s = \frac{s_{ij}-\bar{s}}{2\cdot(s_{ij}+\bar{s})}$. Whereby $\bar{s}$ is the average signal height of all bins and s_{ij} is the signal in each bin. The bin contents of the resulting 2D-histogram are smoothed according to kernel algorithms provided by the ROOT framework.

Figure 8.25.: Uniformity of the average signal of scintillator units in coincidence with the muon tomograph for charged particles crossing the units at different positions. The bin size of $1 \times 1\,\mathrm{cm}^2$ corresponds to the positional resolution of the tomograph. The signal distribution for units of layout 2 is determined by the average of all units whereby each unit is divided in a grid of 30×30 bins and rotated such that the SiPM is located in the same bin in the right bottom corner. See text for discussion.

always located in the same bin (right bottom corner). The average uniformity is determined for all 16 units. Several regions depict an increased signal yield compared to the average signal registered per muon passage. A significant increase of up to twice the average signal is apparent in the region of the SiPM carrier board. A smaller increase is apparent in the region between the scintillator edge and the WLS fibre located 1 cm from the edge. As discussed, the first inhomogeneities are expected to be mainly introduced by the installation of the SiPM at the edge of the scintillator tile. This results in direct scintillation light entering the SiPM detection area. The measurements depict an even higher increase of the relative signal as predicted by the simulations. The same smoothing algorithm is applied to both, simulations and measurements. The applied optical coupling is chosen as being very efficient in cost, production time and photon detection. It allows for a simple and above all stable coupling. The units are such designed, that an alternative, future coupling can be installed without the need of a reproduction of the scintillator tiles.

8.5. Conclusions

The most important performance parameters of the prototype units of layout 2 are summarized in the following. It is confirmed that the presented detector units allow an excellent detection of charged particles.

- The applied SiPM type S13360-1350PE depicts a reduced thermal noise and crosstalk probability in comparison to S12571-050P used for units of layout 1. The darknoise rate at an effective threshold of 0.08 V is around 85 kHz for the SiPM type S13360-1350PE, while the older type depicts an average rate of 135 kHz. The crosstalk probability is reduced from $\approx 28.7\%$ to 3%. Therefore, the currently applied SiPM type allows for a good signal-to-noise ratio.

- The response of the self-triggered unit does not allow for the investigation of the MIP peak. The charge spectrum by additional events as electrons or, possibly, products of radioactive decays in air superimposes the MIP peak.

- The measurement of units in coincidence allows for the investigation of the MIP peak. The light yields of 16 studied units are ranging from 18.75 to 28.30 p.e. per MIP with an average light yield of (23.67 ± 2.47) p.e. per MIP and a maximum deviation of 34% from the average light yield. The achieved light yield is well suitable for the identification of passages of charged particles.

- An extended photon arrival time distribution at the SiPM per muon passage as predicted by simulations can be confirmed (cf. chapter 7). Photons are expected to arrive within 10 ns.

- An increased signal yield in the region around the SiPM location, which has been already identified by simulations (cf. chapter 7), can be confirmed. This results in a broadened MIP peak. However, the overall detection efficiency is not influenced.

- The detection efficiency of a single unit for muon passages is determined by the coincident measurement of eight units in a stack and by a coincident measurement of units with a position-resolving external muon tomograph. The former identifies a detection efficiency of $98 - 99\%$. The latter determines a detection efficiency of above 95% at a threshold of 3.5 p.e. over the complete extent of the unit (except the scintillator tile edges). The detection efficiency is in good agreement with the predictions of simulations (cf. chapter 7).

CHAPTER 9

MiniAMD - a small and mobile universal muon detector

The combined assembly (scintillator - wavelength shifting fibre - silicon photomultiplier), referred to as *unit* in this thesis, provides an excellent detection of atmospheric muons. The layout of the unit is described in chapter 6. Studies of the unit performance by its response on single particle passages are described in detail in chapter 8. As a further step, the detection of extensive air showers initiated by cosmic rays is targeted. These showers result in several particles (like electrons / positrons, muons or photons) arriving within a short time window of several 100 ns at ground. A detector consisting of several of the presented units allows for the investigation of those particles. As a proof of principle, a demonstrator is designed, assembled, and tested.
The chapter is structured as followed. First, the baseline design of the demonstrator, called ***MiniAMD***, is presented. Its performance is studied while the demonstrator is outdoors on the roof of the physics department in Aachen. Thereby, not only its response to atmospheric muons but also the ability to monitor important detector characteristics is studied. For example, the stability of the gain of the silicon photomultipliers (SiPMs, cf. chapter 4) as a function of temperature is of major importance. Secondly, coincidence measurements with a small air shower array based on liquid scintillator as detector medium and SiPMs as light sensors are performed. The characteristics of this experiment are shortly explained and studied. The performed coincidence measurements are analyzed and compared to standalone measurements. Those measurements confirm that MiniAMD is not only well suited for the detection of (atmospheric) muons but allows also for the detection of cosmic ray candidates.

9.1. MiniAMD baseline design

The MiniAMD demonstrator comprises two identical detector modules consisting of eight units each. The modules are located on top of each other for background suppression. *Background* is defined, in context of this thesis, as events originating from radioactive decays in the air around the experiment or originating from other particles than muons like the electromagnetic component of air showers. However, each module may be used individually. The units are arranged in a matrix of 2×4 units. Each unit complies with layout 2 presented in chapter 6 and figure 6.1. In figure 9.1, a sketch of one MiniAMD module with indicated dimensions is presented. The units are located in a frame with outer dimensions of 820 mm × 1430 mm × 65 mm which is based on hollow profiles

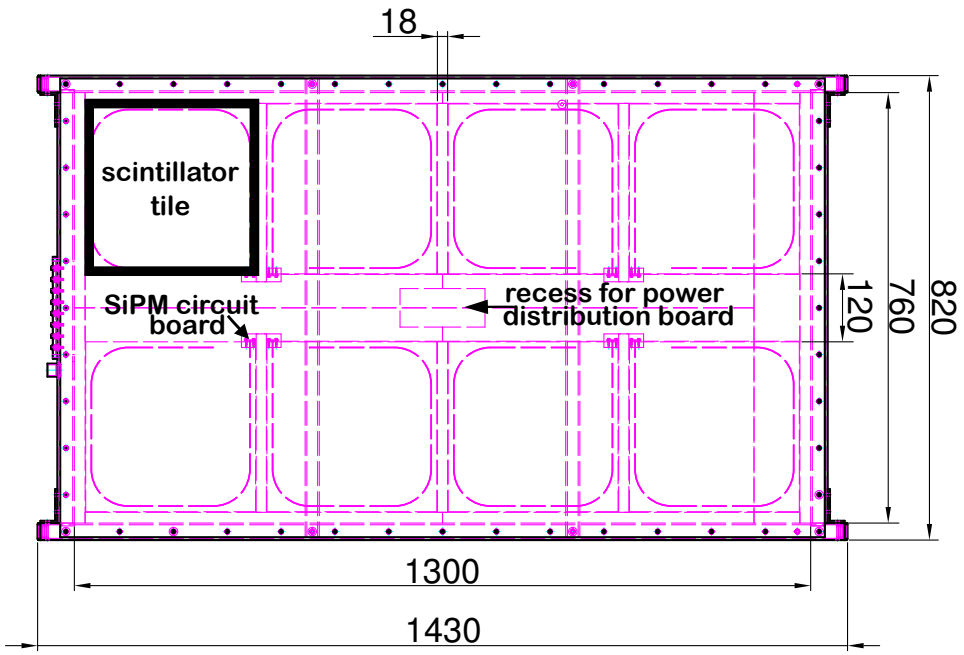

Figure 9.1.: Sketch of a MiniAMD module. All dimensions are given in units of mm. Each module consists out of eight units located in a 2×4 configuration. The SiPM is directly connected to the wavelength shifting fibre end and is located at the scintillator tile edge. The MiniAMD demonstrator combines two modules identical in construction located on top of each other.

made of aluminum[1]. The top and bottom of the frame is covered by a thin aluminum sheet with a thickness of 5 mm. While the top sheet is screwed to the profiles to allow for an easy access to the units, the bottom sheet is riveted. The boxes are designed to be water- and light-tight as well as lightweight. Each equipped module has a weight of roughly 30 kg and can be easily handled by two persons.

In figure 9.2, an overview about the assembly of one MiniAMD module is presented via detailed photos. They depict the routing of cables through connectors to the outside, the distributor circuit board for the bias voltages and the cabling for the temperature sensors. The front profile includes several water-tight connectors allowing for the powering of and the communication with the electronics located in the module. The other three profiles have no connection to the inner part. Each module contains three layers of extruded polystyrene rigid foam as padding material, known under the brand mark Styrodur®. The padding also allows for the separation between different units and for a support structure for their placement. The distance between two units in a row is 18 mm. The fill factor of each module is defined as the ratio of active area comprising of scintillator tiles and the padding material and is 0.7. Both rows are separated by a distance of 120 mm to allow for the routing of the cables[2]. Several cables per SiPM circuit board are needed to provide power supply and readout of the temperature sensor and of the photosensor. The allocation of the bias voltage of each SiPM is defined by its identification number and is independent of the cable connected. For the temperature sensor, three individual wires are connected to the circuit board by a three-pin connector. The wires provide ground, supply voltage and a data line for the monitoring of the temperature at each SiPM over time.

[1] The frame has been designed and assembled by the mechanical workshop of the Physics Institute III A of the RWTH Aachen University.

[2] An alternative arrangement of the units would comprise the reduction of dead space between both rows and an alternative routing of the cables between each row and the corresponding edge of the module.

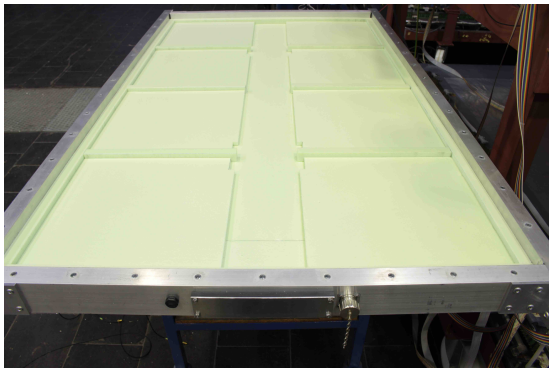

(a) First, a styrodur layer with a thickness of 20 mm is used as padding. A further layer provides also a support structure for the location of the eight detector units.

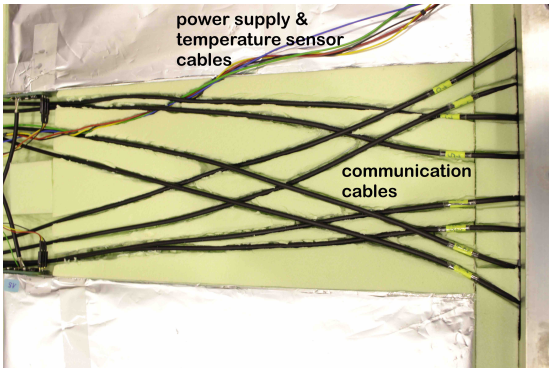

(b) Shown is the routing of eight SiPM communication cables. The colored cables provide power supply of the SiPMs and temperature sensors, as well as communication with the latters.

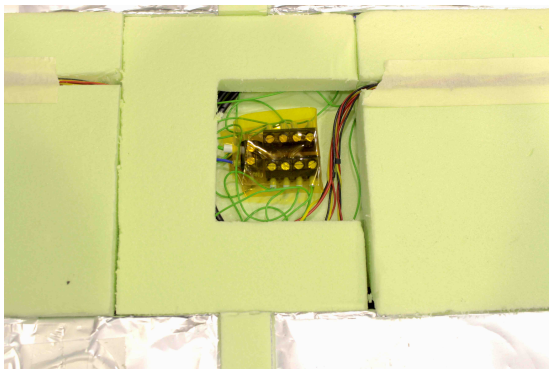

(c) Photo of a circuit board distributing the power supply voltage for the eight SiPMs located in each MiniAMD module. The board is placed in the recess indicated in figure 9.1. For each SiPM an individual power supply is provided. The SiPM id is registered at the corresponding circuit board located at the scintillator tile.

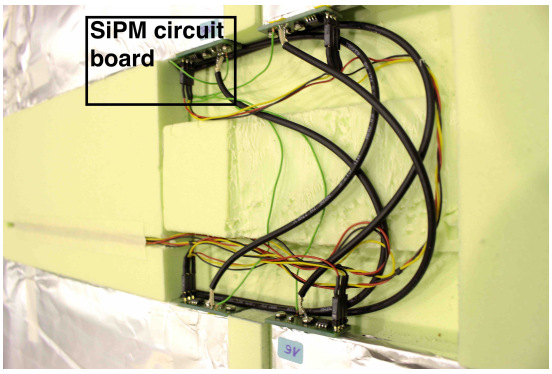

(d) Photo of the cable routing and connection of four SiPM circuit boards to its corresponding scintillator tile. Three connectors are located at each circuit board. One connector for three cables provide power supply and communication with the temperature sensor. Power and communication for the SiPM have two separate connections.

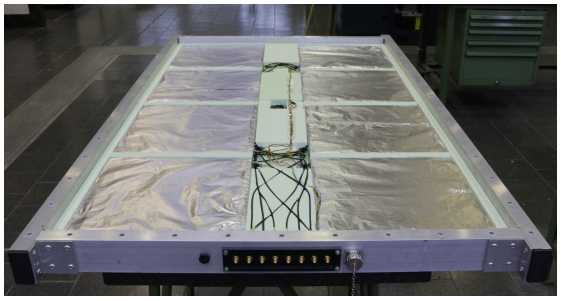

(e) Photo of an equipped MiniAMD module. Shown are eight units located in a 2×4 matrix. The region between both rows is used for the routing of the cables. Layers of styrodur are used as padding material and for the stabilization of the tiles.

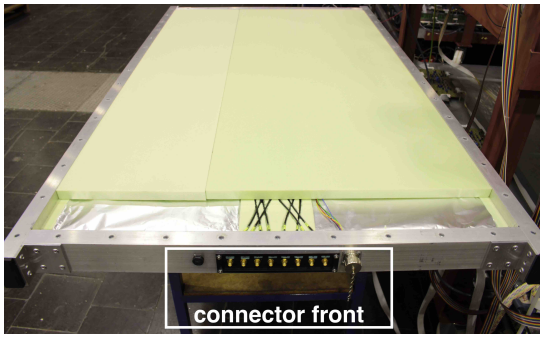

(f) A further styrodur layer with a thickness of 20 mm is used as padding. In front from left to right, an air pressure equalization vent, eight connectors for the communication with the SiPMs and a connector guiding all further cables to the electronics box are located.

Figure 9.2.: Photos of the assembly of a MiniAMD module.

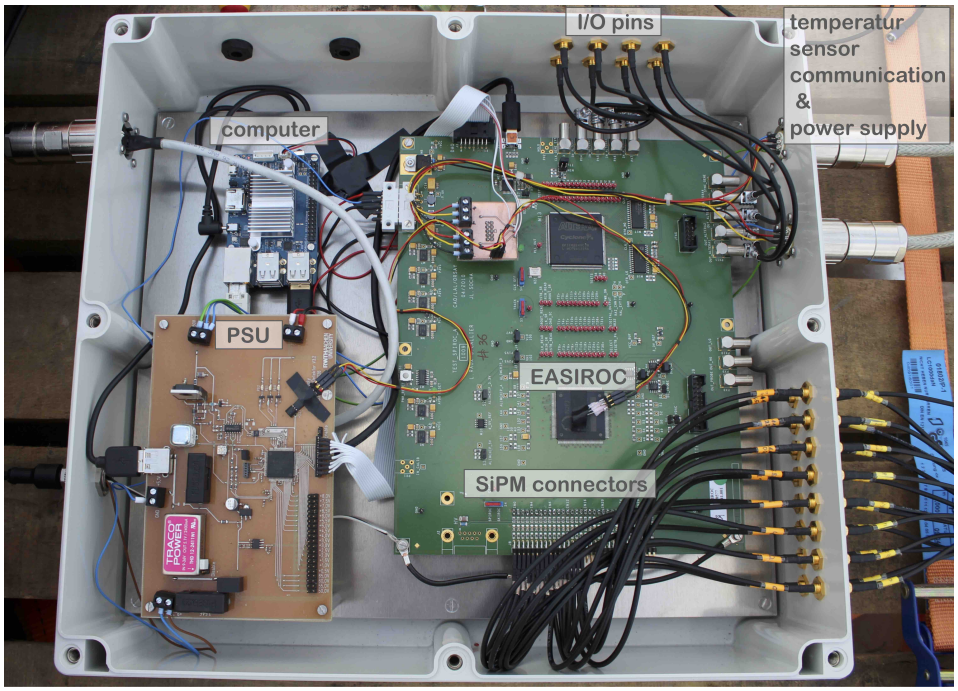

Figure 9.3.: Photo of the water-tight box containing the readout and supply voltage electronics for measurements with the MiniAMD demonstrator. On the left side, the power supply unit (PSU) and a single-board computer are located. The EASIROC evaluation board (shown on the right side of the box) provides the usage of up to 32 SiPMs. The cables for the communication with the SiPMs are shown in the lower right edge of the box. Furthermore, I/O pins for the communication with the FPGA are connected to the outside of the box in the upper right corner of the box, seen from top. For the power supply and the communications with the temperature sensors at the SiPMs inside the modules, two cables with several wires are connected to the electronics box in the upper right corner, seen from the side.

Both modules are identical in construction but the light yields of the individual units vary by up to ±20%. Module 1 contains units with id [0-7] while module 2 contains units with id [8-15]. A summary table of individual performance parameters of all units can be found in table 8.2 on page 118. If not otherwise stated, module 1 is located on top of module 2 for measurements with both modules.

A separate water- and light-tight electronics box is equipped with the described readout, communication and power supply electronics for both modules (cf. chapter 6.2). The box is shown in figure 9.3. The box contains the power supply unit (PSU), a single-board computer and the EASIROC evaluation board. The board provides the usage of up to 32 SiPMs while 16 SiPMs are currently connected for the MiniAMD demonstrator (eight SiPMs in each module). Furthermore, I/O pins for the communication with the FPGA on the evaluation board allows for the usage of MiniAMD as trigger for other experiments or allows for MiniAMD to receive triggers by an external experiment. The I/O pins are connected to the outside of the box in the upper right corner of the box. Two temperature sensors are available in the box, one for the EASIROC and one for the PSU. The connectors for the cables from the SiPMs to the EASIROC are additionally grounded at the EASIROC to reduce electronics noise. The SiPM cables are connected via SMA sockets. The SMA cables for the readout have a length of 20 cm inside the electronics box, a length of 120 cm from the electronics box to the MiniAMD modules and a length of 120 cm inside the module. Therefore, the analogue signals of the SiPMs are transported each by a cable length of 260 cm. This is well below the critical length

of 6 m at which the SiPM signal is distorted and attenuated due to long cables [165]. However, the cables routed outside of the detector modules may be subject to pick up noise.

9.2. MiniAMD performance characteristics

In this section, first the ability of the MiniAMD demonstrator to provide a constant *monitoring* of important detector performance characteristics is presented. The monitoring is performed by the measurement of single atmospheric muons. The characteristics of interest are the expected signal for a minimum ionizing particle (MIP) in photon equivalents (p.e.) or in ADC count, the gain of the individual SiPMs and the expected signal rate as a function of the preset trigger threshold. Thereby, a translation from the signal of each individual unit in ADC count to a signal in MIP for the complete demonstrator can be achieved.
In normal operation of the MiniAMD detector, both modules are located on top of each other. A unit in the upper module in combination with the unit at the same location in the lower module is defined as a *stack*. These stacks allow for comparable studies of the charge spectrum as presented in chapter 8, but are expected to be more influenced by background events and provide a larger angular acceptance.

9.2.1. Monitoring of the MiniAMD modules

The *MIP peak* is regularly measured by MiniAMD operated in *self-triggering mode*. The default hardware trigger criterion is at least one stack where the signal in both units of the stack exceeds a 2.5 p.e.-threshold. Additionally, a *trigger rate scan* is performed after each MIP peak measurement. Presented is data which is taken every five hours over several weeks with changing temperature over time. The goal is a stable conversion of the signal registered by each individual unit from ADC count to the common scale in MIP.
Each charge spectrum includes data of one hour measurement time. The spectrum includes also noise events enabling the investigation of a baseline shift with temperature. As presented in section 8.1.3 and in figure 8.8 on page 117, three fits are performed to the spectrum to determine the pedestal peak and the MIP peak position as well as the gain of the individual SiPMs. A gaussian distribution is fitted to the pedestal peak. A multi-gaussian distribution is fitted to the the rising edge of the MIP peak where the peak structure is apparent. The gain corresponds to the distance between two peaks. Both, a log-normal (cf. equation 8.18) and a Gaussian distribution, are fitted to the MIP peak.

Gain stability

As a reminder, the gain is depending on the overvoltage V_{ov} (cf. chapter 4, equation 4.2).
The breakdown voltage V_{break} is increasing with temperature by a factor $\beta = 60\,\mathrm{mV/K}$ according to the datasheet of the manufacturer for the applied SiPM type [105]. By compensating the change in the breakdown voltage by a corresponding change in the applied bias voltage $V_{\mathrm{bias}}(T)$, a constant overvoltage V_{ov} and thus a stable gain G over temperature T can be achieved. This is important as main characteristics of the SiPM, such as the photon detection efficiency, depend on the gain (cf. chapter 4).
For all presented measurements, the voltage regulation according to temperature is implemented in the electronics. An investigation of the achieved gain stability over a large temperature regime is presented in the following.
First, the gain G as a function of temperature is presented for unit channel 2 in figure 9.4. The

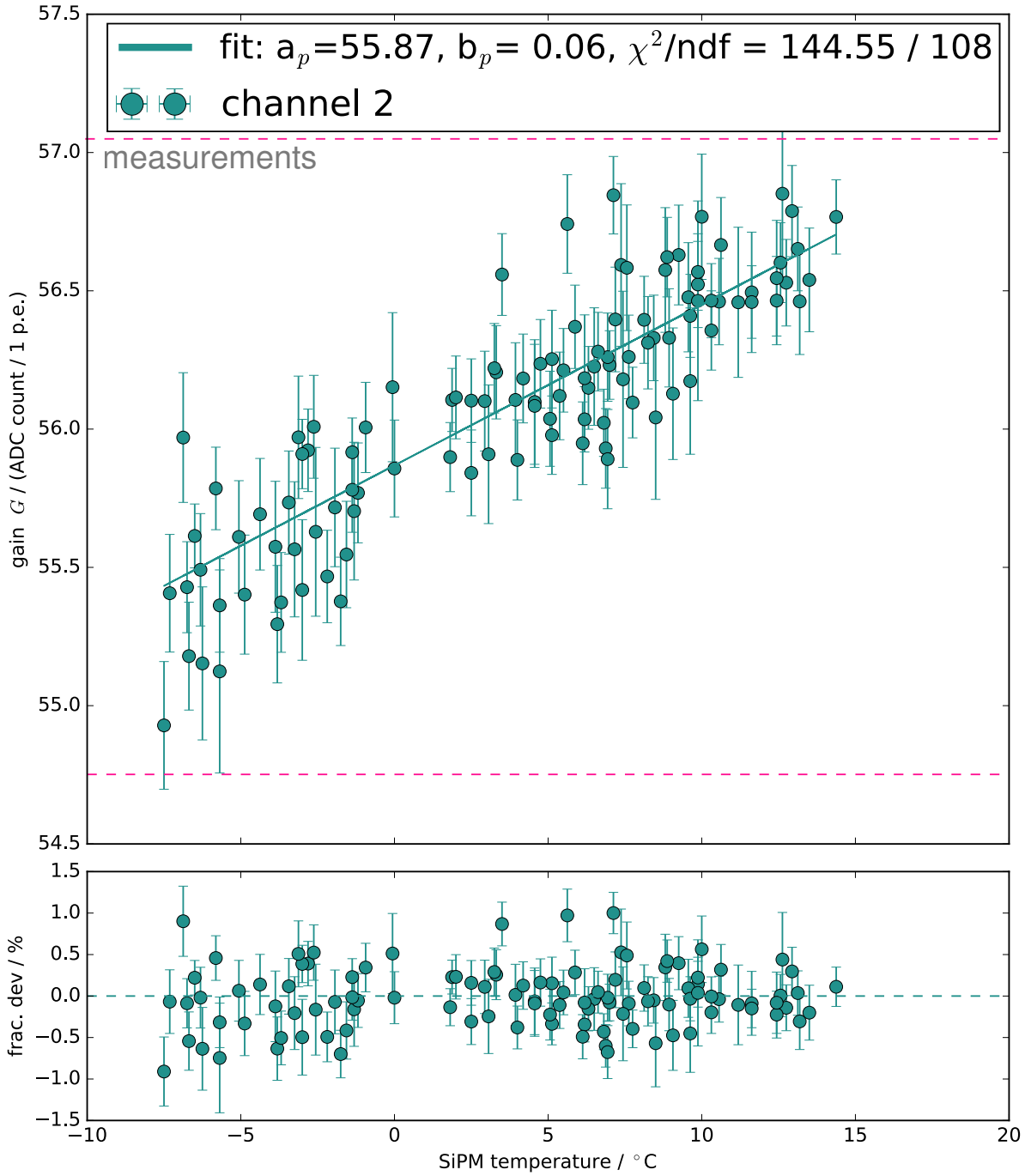

Figure 9.4.: Gain as a function of the SiPM temperature for unit channel 2 after temperature compensation. The gain is determined by a fit of a multi-gaussian function to the MIP spectrum. The uncertainty of each data point refers to the uncertainty on the fit provided by ROOT [182]. For each data point, the MIP spectrum includes events measured over one hour. The hardware trigger criterion is at least one stack where the signal in both units of the stack exceeds a 2.5 p.e.-threshold. By the two vertical dashed lines, a deviation by ±2% over a temperature range of (0 ± 20) °C is indicated.

uncertainty of each data point refers to the uncertainty on the multi-gaussian fit. Even if the temperature compensation is implemented, a temperature dependency is apparent. A linear function is fitted to the data points which allows for a good description of the increase. This is also indicated by the $\chi^2 = 144.55$. With a ndf of 108, the result corresponds to a deviation by 2.5σ from the expected value. The gain $G(T)$ in ADC count / p.e. changes according to

$$G(T) = a_g(T_{\text{SiPM}} = 0\,^\circ C) + b_g T_{\text{SiPM}} \tag{9.1}$$

$$= (55.88 \pm 0.05) + (0.06 \pm 0.01) \cdot T_{\text{SiPM}} / \,^\circ\text{C} \quad . \tag{9.2}$$

Also indicated in the plot by two horizontal lines is the deviation by ±2% over a temperature range (0 ± 20) °C. This small deviation is already a very good result achieved by the applied temperature compensation. However, as the gain G seems to be overcorrected, a slightly reduced compensation factor β is recommended. Taking the relative gain change $\frac{\Delta G}{\Delta T} = 1\%/10\,\text{K}$ into account, a β factor of 57 mV/K can be calculated

$$\beta = 60\frac{\text{mV}}{\text{K}} - V_{\text{ov}}\frac{\Delta G}{\Delta T} \tag{9.3}$$

$$= 60\ \frac{\text{mV}}{\text{K}} - 3\,\text{V}\frac{0.01}{10\,\text{K}} = 57\frac{\text{mV}}{\text{K}} \quad . \tag{9.4}$$

For a crosscheck, all further channels can be taken into account. Their gain measurements show a comparable increase with temperature and are presented in appendix A. Calculating the average and the standard deviation of all 16 units, a similar factor of $\beta = (56.97 \pm 0.28)\,\text{mV/K}$ is determined. The value is well compatible with the compensation factor presented in [196] for the same SiPM type but with different readout electronics. The improved factor of 57 mV/K is implemented in the MiniAMD demonstrator and has to be verified in further studies. However, for all further measurements presented in this chapter, the correction factor of $\beta = 60\,\text{mV/K}$ was still applied and allowed for a reasonable data taking and analysis.

MIP peak stability

As discussed in section 8.1.3, the signal given in ADC count is strongly influenced by the individual light yield achieved by each unit. A conversion based on the characteristics of the signal spectrum is based on the pedestal peak as well as the MIP peak position. The latter is increasing with the temperature at the SiPM as the gain is not completely stable over a large temperature range. The former depends on the temperature at the EASIROC as most temperature sensitive part of the readout electronics. The goal is to define a conversion from the individual unit signal to a signal in MIP for all temperatures. Therefore, for each unit the pedestal and MIP peak position as a function of temperature is determined and a linear function is fitted to the corresponding data. In figure 9.5, the change of the pedestal peak position is shown as a function of temperature. The peak position is determined by a fit of a Gaussian function to the signal spectrum. The uncertainty of each data point refers to the uncertainty on the fit. A linear fit $S_{\text{adc, pedestal}}(T_{\text{EASIROC}}) = a_p(T_{\text{EASIROC}} = 0\ ^\circ\text{C}) + b_p \cdot T_{\text{EASIROC}}$ can describe the data except of the lowest temperature regime for $T_{\text{EASIROC}} < 0\ ^\circ\text{C}$. Here, a small systematic shift to larger values ($\mathcal{O}(0.1\%)$) than predicted by the fit is apparent. However, this shift is negligible for the presented measurements. The $\chi^2 = 318.73$ and the residuals indicate that the uncertainty on the pedestal value are underestimated. With ndf = 117, the fit depicts a deviation by 13σ from the expected value. An overall decrease by a factor of 1%/20 K can be determined. All further units depict a comparable behavior and are presented in appendix A. The MIP peak position in ADC count is presented in figure 9.6. It is determined by a fit of a log-normal distribution in the region of the MIP peak. A fit by a Gaussian predicts a comparable result for the peak position. A

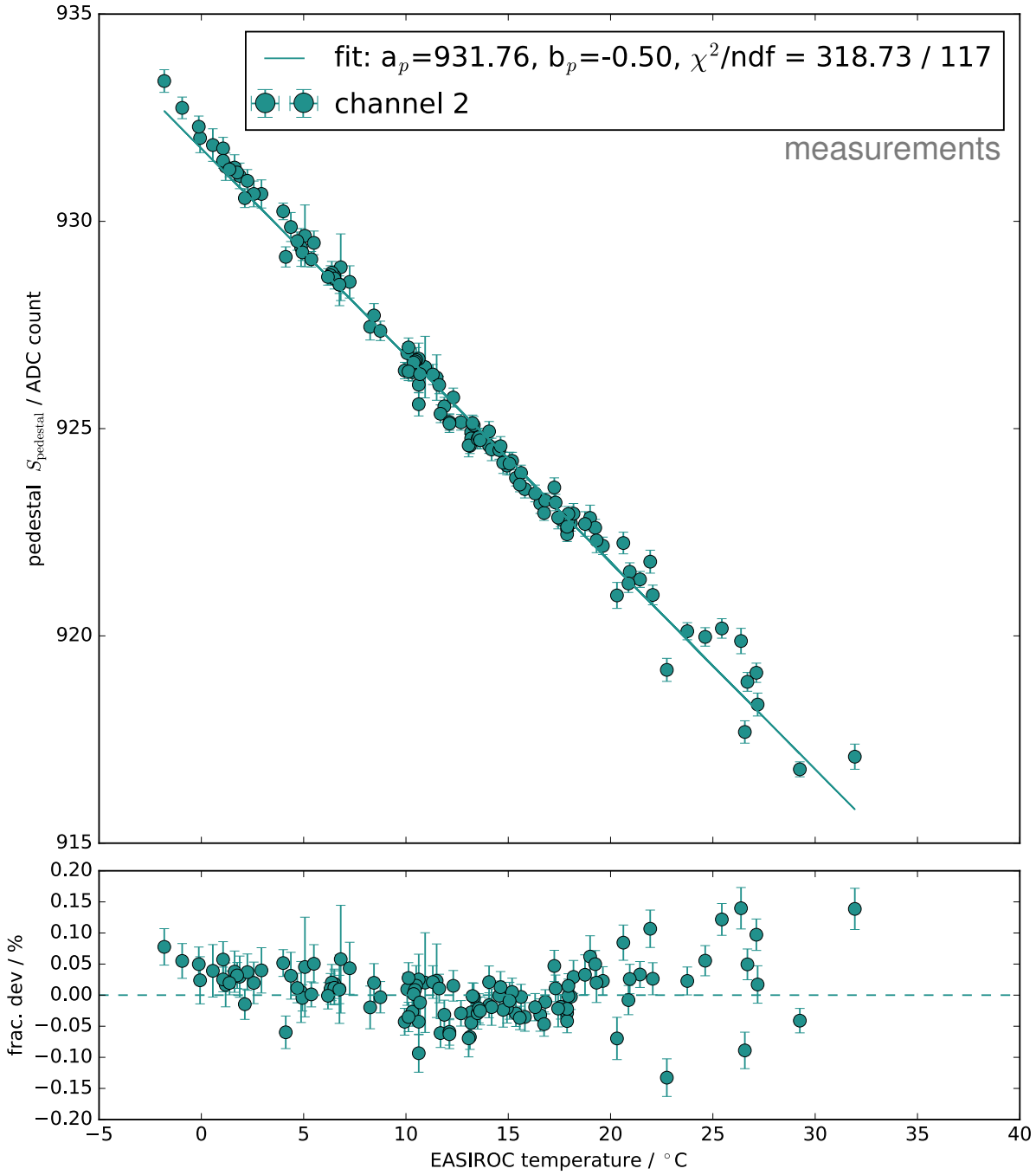

Figure 9.5.: Pedestal peak position $S_{\text{adc, pedestal}}$ as a function of the EASIROC temperature for unit channel 2. The temperature compensation is active. The position is determined by a fit of a Gaussian function to the signal spectrum. The uncertainty of each data point refers to the uncertainty on the fit. For each data point, the MIP spectrum includes events measured over one hour. The hardware trigger criterion is at least one stack where the signal in both units of the stack exceeds a 2.5 p.e.-threshold. A linear function is fitted to the data points. The change of the pedestal position is $< \Delta S_{\text{adc, pedestal}}/\Delta T_{\text{EASIROC}} >= -0.48\,\text{ADC count/K}$ or $1\%/20\,\text{K}$.

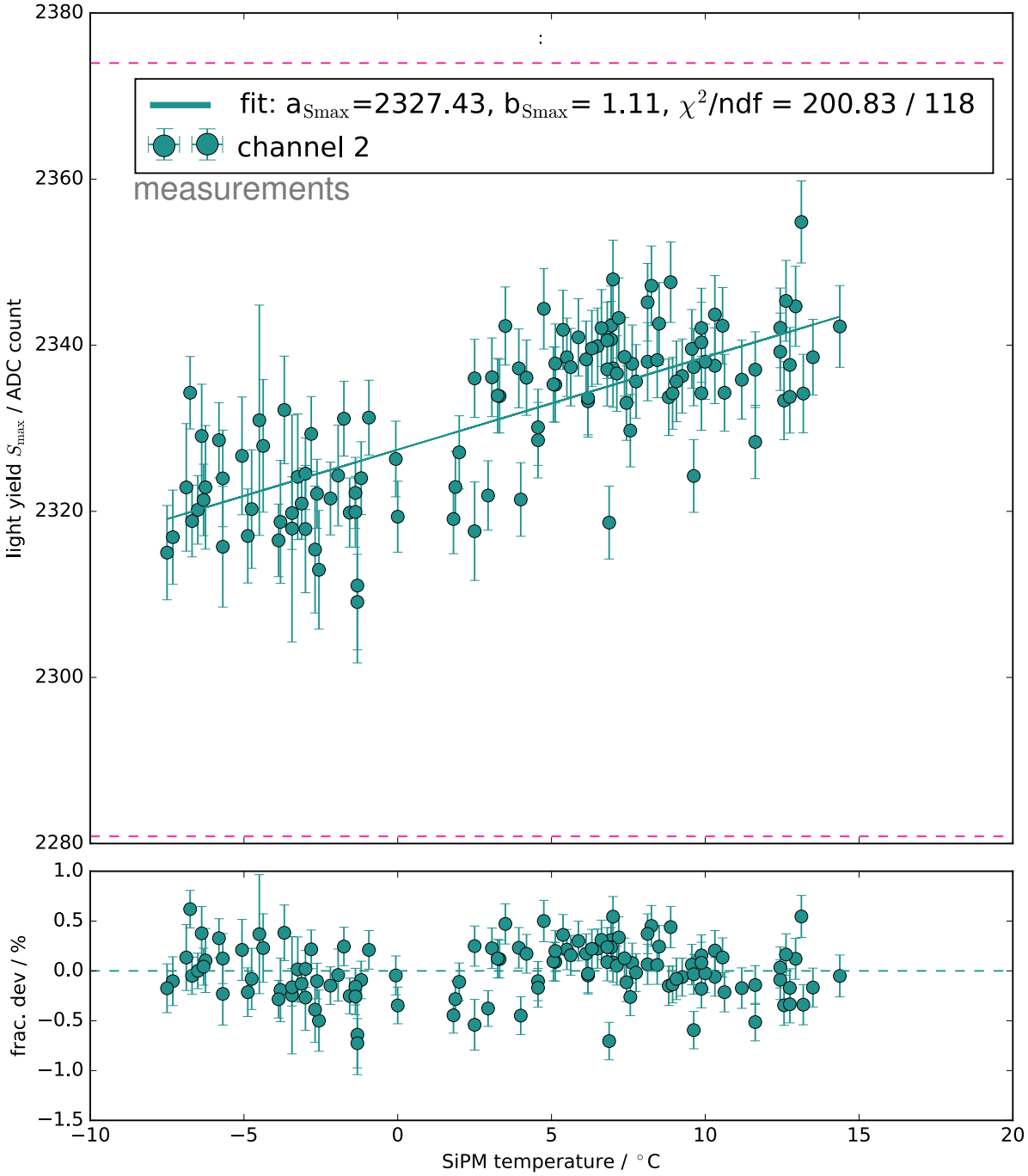

Figure 9.6.: MIP peak position $S_{\text{adc, max}}$ as a function of the SiPM temperature for unit channel 2. The temperature compensation is active. The position is determined by a fit of a log-normal function to the signal spectrum. The uncertainty of each data point refers to a propagation of the uncertainties on the fit parameters. For each data point, the MIP spectrum includes events measured over one hour. The hardware trigger criterion is at least one stack where the signal in both units of the stack exceeds a 2.5 p.e.-threshold. A linear function is fitted to the data points. The change of the position of the maximum is $< \Delta S_{\text{adc, max}}/\Delta T_{\text{SiPM}} >= 0.48\,\text{ADC count}\,/\,\text{K}$ or $0.2\%/10\,\text{K}$. By the two vertical dashed lines, a deviation by ±2% over a temperature range of $(0 \pm 20)\,^{\circ}\text{C}$ is indicated.

comparison is shown in appendix A in figure 5. The uncertainty on the data points is determined by the uncertainties on the fit for the log-normal distribution parameters m and s (cf. equation 8.19). They are further propagated to an uncertainty on the mode of the distribution referring to the maximum. The further units depict a comparable behavior and are presented in appendix A. The data are fitted by a linear function $S_{\text{adc, max}}(T_{\text{SiPM}}) = a_{S_{\text{max}}}(T_{\text{SiPM}} = 0\ ^\circ\text{C}) + b_{S_{\text{max}}} \cdot T_{\text{SiPM}}$. With a χ^2 / ndf = 200.83 / 118, the fit depicts a deviation by 5σ from the expected value but is for a parametrization of the data still reasonable.
Now, the signal in ADC count of each unit measured at any temperature can be converted into a signal in units of MIP. For each unit, an individual conversion function is defined. Exemplary for unit channel 2, it can be described by the following function

$$S_{\text{MIP}} = \frac{S_{\text{adc}} - S_{\text{adc, pedestal}}(T_{\text{EASIROC}})}{c_{\text{MIP}}} \tag{9.5}$$

$$= \frac{S_{\text{adc}} - S_{\text{adc, pedestal}}(T_{\text{EASIROC}})}{S_{\text{adc, max}}(T_{\text{SiPM}}) - S_{\text{adc, pedestal}}(T_{\text{EASIROC}})} \tag{9.6}$$

$$= \frac{S_{\text{adc}} - (931.55 + 0.48 \cdot T_{\text{EASIROC}} / ^\circ\text{C})}{(2325.11 + 0.48 \cdot T_{\text{SiPM}} / ^\circ\text{C}) - (931.55 + 0.48 \cdot T_{\text{EASIROC}} / ^\circ\text{C})} \quad . \tag{9.7}$$

The identical slope of 0.48 for $S_{\text{adc, max}}(T_{\text{SiPM}})$ and for $S_{\text{adc, pedestal}}(T_{\text{EASIROC}})$ is only coincidental. To estimate the uncertainty introduced by this method, the MIP peak position in units of MIP for each measurement is determined by the fit parameters of the average description of the data. Naturally, the MIP peak position using the actual parameters of the fit would result in a signal of $S_{\text{adc, max}} = 1\,\text{MIP}$. In figure 9.7, the calculated MIP peak positions are shown as a function of temperature. As expected, they scatter around the signal yield at the MIP peak position of 1.000 MIP. The standard deviation of 0.005 MIP is small. The conversion works well. A stable configuration of the setup is important for the monitoring. Exemplary for unit channel 2, the average light yield in photon equivalent is shown as a function of the measurement day and night in figure 9.8. The start of a day is defined by the time of the sun rise. The start of the night by the the time of the sun set. Each data point refers to the average light yield and its standard deviation. Included are the actual parameters determined by the charge spectrum, not the averaged values. Measurements at night and day are well in agreement within the uncertainties. The colors of the markers denote the average SiPM temperature. A change in the light yield sets in at measurement day 15. It refers to a change in the module setup. Between the days 15 to 25, the vertical distance between both modules was successively increased. By the larger distance between both modules, the median acceptance angle decreased. This results in a corresponding decrease of the signal yield corresponding to equation 8.13.

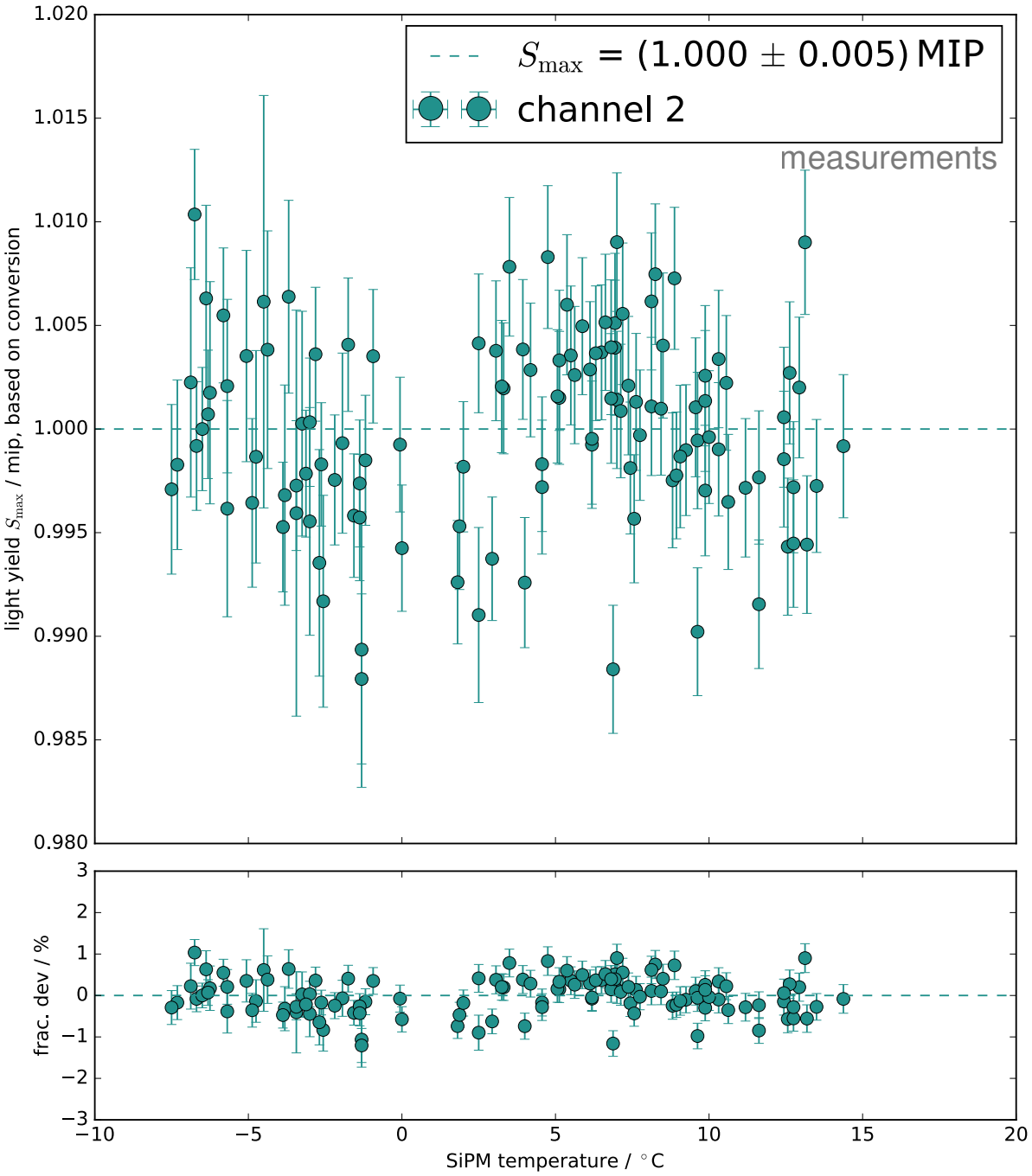

Figure 9.7.: Exemplary MIP peak position in units of MIP as a function of the SiPM temperature for channel 2. The temperature compensation is active. Each data point is determined by the fit parameters describing the average evolution of the signal spectrum characteristics with temperature.

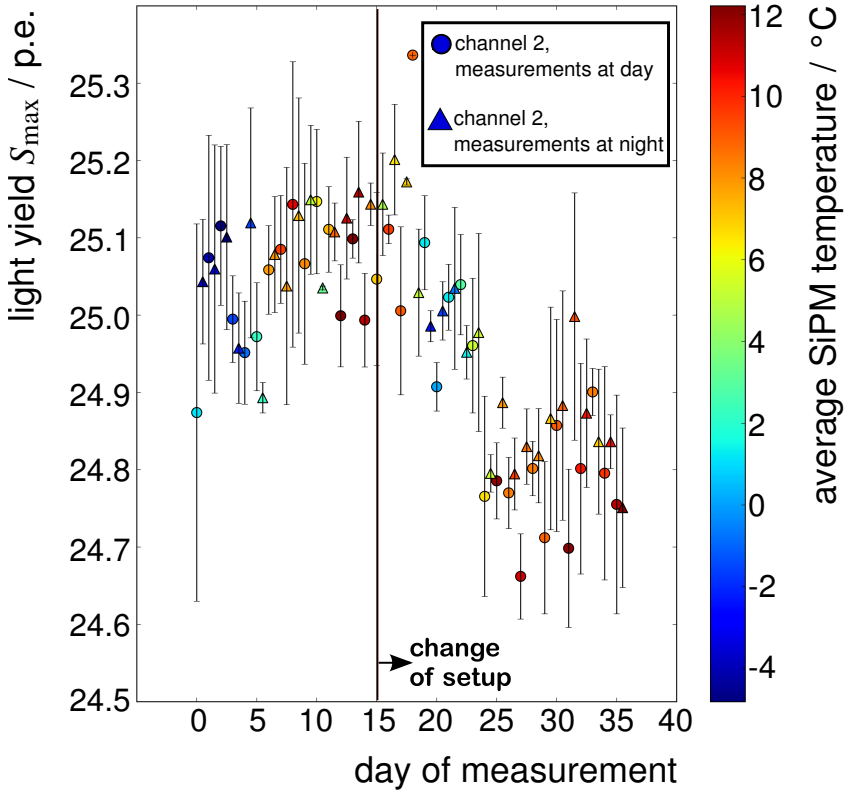

Figure 9.8.: Shown is the average light yield of unit channel 2 in p.e. as a function of the measurement day (circles) and night (triangles). The start of a day is defined by the time of the sun rise. The start of the night by the the time of the sun set. Each data point refers to the average light yield and its standard deviation. The colors of the markers denote the average SiPM temperature.

Trigger rate scan

As already mentioned in chapter 8, the signal rate as a function of the preset threshold can be used for the determination of an optimal trigger threshold for the chosen setup. Furthermore, differences in the gain and in the crosstalk probability become visible. The individual bias voltages for each SiPM given by Hamamatsu are used. The trigger rate in Hz as a function of the effective trigger threshold in units of V is shown in figure 9.9 for all channels of the MiniAMD demonstrator. The demonstrator is located on the roof of the physics department. The presented fast trigger rate scan is performed at an average temperature of (5.41 ± 0.15) °C measured at the SiPMs. Each data point refers to the average rate taken over a measurement time of 2.68 s. The rate scan ranges from a discriminator threshold[3] of -0.10 to 0.43 V in steps of roughly 0.05 V. For thresholds below 0 V the contribution of the baseline is visible. The steps of the darknoise correspond to the individual number of photon equivalent. Darknoise events dominate up to 0.26 V or 2.5 p.e. As discussed in chapter 8, SiPM 0 depicts an increased darknoise rate but behaves as expected for signals corresponding to particle passages. For larger thresholds the constant signal of atmospheric muons is apparent in all channels. The muon rate is superimposed by a background rate. This is indicated by a higher average trigger rate of around 40 Hz at an effective threshold of 0.3 V compared to an expected atmospheric muon rate of 10 Hz per unit (cf. equation 8.7). Compared to the measurements in the lab presented in chapter 8, the trigger rate is reduced. The rate is in-

[3] For the interpretation of the discriminator threshold please refer to section 8.1.1. The trigger rate scan initially ranges from 1000 to 600 DAC count in steps of 5 DAC count.

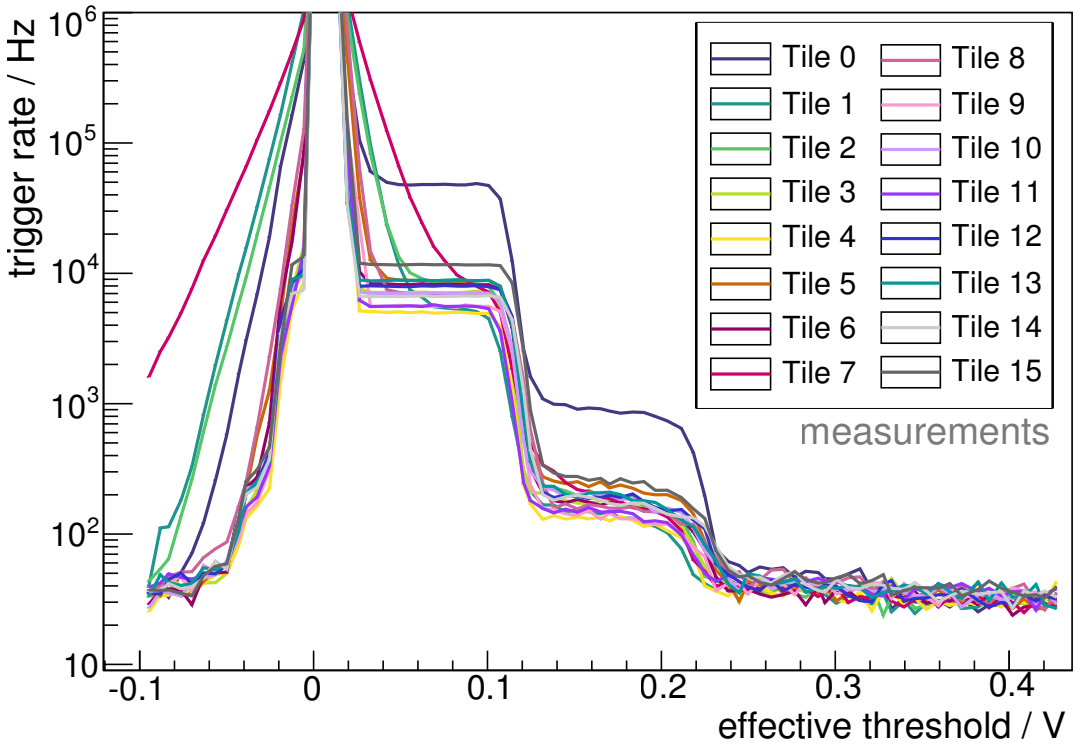

Figure 9.9.: Trigger rate scan as a function of effective threshold in V of the individual units of both MiniAMD modules. For each data point, the average over a measurement time of 2.68 s is shown. A step size of roughly 0.05 V from −0.10 to 0.43 V is chosen.

fluenced by the thermal noise which is less present at the low temperatures (60 Hz → 40 Hz for 25 °C → 5 °C). At an effective threshold of 0.7 V, the darknoise is strongly reduced and both measurements depict a comparable rate of 30 Hz. Additionally, the presence of an electronic noise component is indicated. Several SiPMs, e.g. SiPM 7, depict such an increased rate that no sharp step form is recognizable at a threshold of 0.08 V or 0.5 p.e. The influence of the electronic noise varies over time. However, at a threshold of 0.26 V or 2.5 p.e. the influence is negligible for all performed rate scans. The trigger rate corresponding to a threshold of 0.5 p.e. and 1.5 p.e. is dominated by the thermal noise of the SiPMs. It is thus expected (cf. chapter 4) that both rates strongly depend on the temperature at the SiPM. The underlying atmospheric muon flux is of minor importance but may also vary due to atmospheric conditions, such as the air temperature or pressure. The thermal noise rate is expected to increase with temperature. An exponential function $f_{1\text{ p.e.}} = a_{1\text{ p.e.}}(T_{\text{SiPM}} = 0\ ^\circ\text{C}) + \exp(b_{1\text{ p.e.}} \cdot T_{\text{SiPM}}) \cdot c_{1\text{ p.e.}}$ can be used to describe the trigger rate as a function of the SiPM temperature. Each data point refers to the average trigger rate in the region of the 1 p.e. plateau of a performed threshold scan. Its uncertainty refers to the corresponding standard deviation. Exemplary, the trigger rate at a threshold of 0.5 p.e. as a function of temperature is shown for unit channel 10 in figure 9.10. All further units depict a comparable behavior. The parameter $b_{1\text{ p.e.}} = 0.11$ of the exponential fit describes an expected doubling of the trigger rate per 8 K [114].

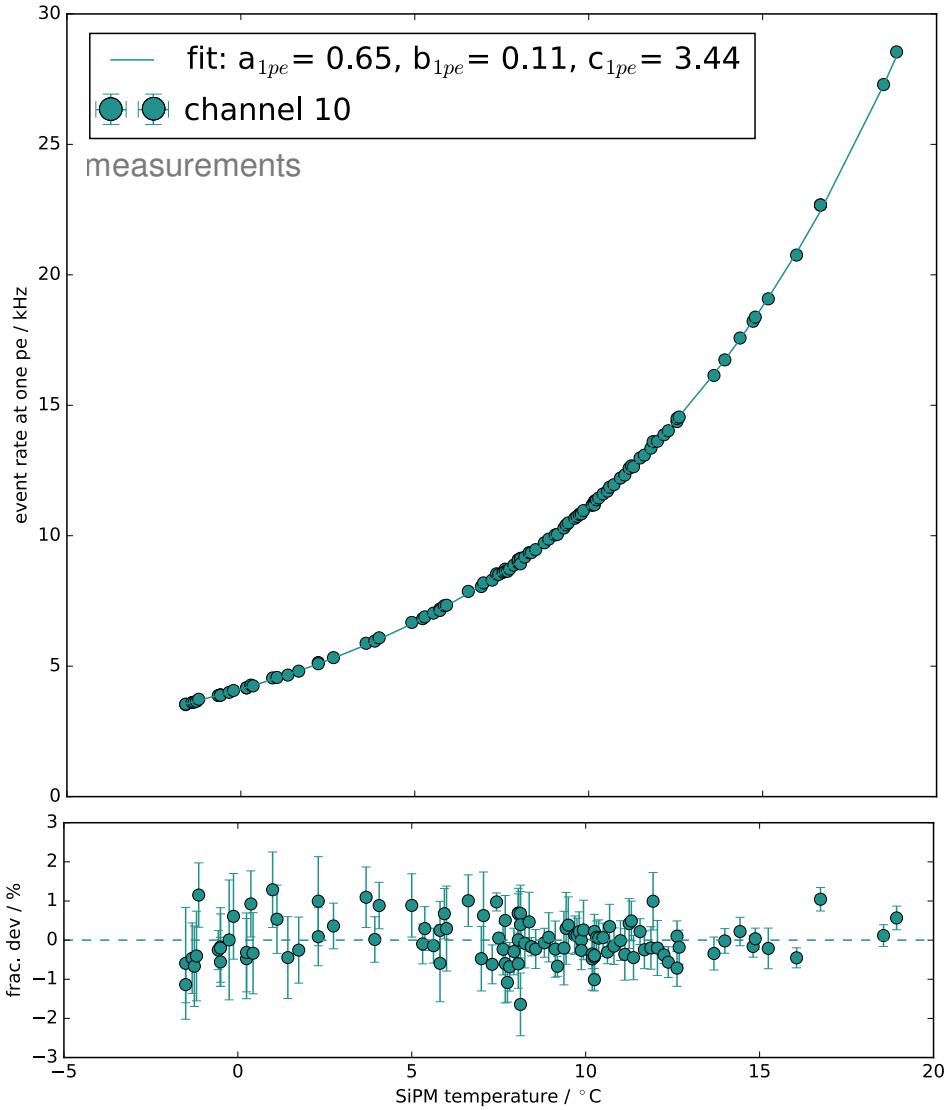

Figure 9.10.: Trigger rate at a threshold of 0.5 p.e. as a function of the SiPM temperature for unit channel 10.

9.3. Air shower array on the physics department building

To allow for a more detailed study of the response of the demonstrator on cosmic ray candidates, MiniAMD is measured in coincidence with a small-scale air shower array. The layout and the performance of this experiment are studied in detail to confirm a stable examination environment for the MiniAMD detector.
The response of the air shower experiment is not yet completely calibrated and is currently validated. Six identical detector stations are placed on the roof of the physics department building. Each station consists of a barrel with a diameter and height of roughly 22 cm containing about eight liters of liquid scintillator, read out by one silicon photomultiplier. To reduce the background of ambient light, the barrel is placed upside-down in a second enlarged barrel. The outer barrel is additionally protected against light leakage with a layer of adhesive aluminum tape at its outside. The SiPM is operated by frontend electronics which provide the needed operating voltage including a voltage regulation according to temperature to allow for a stable gain. Furthermore, it provides

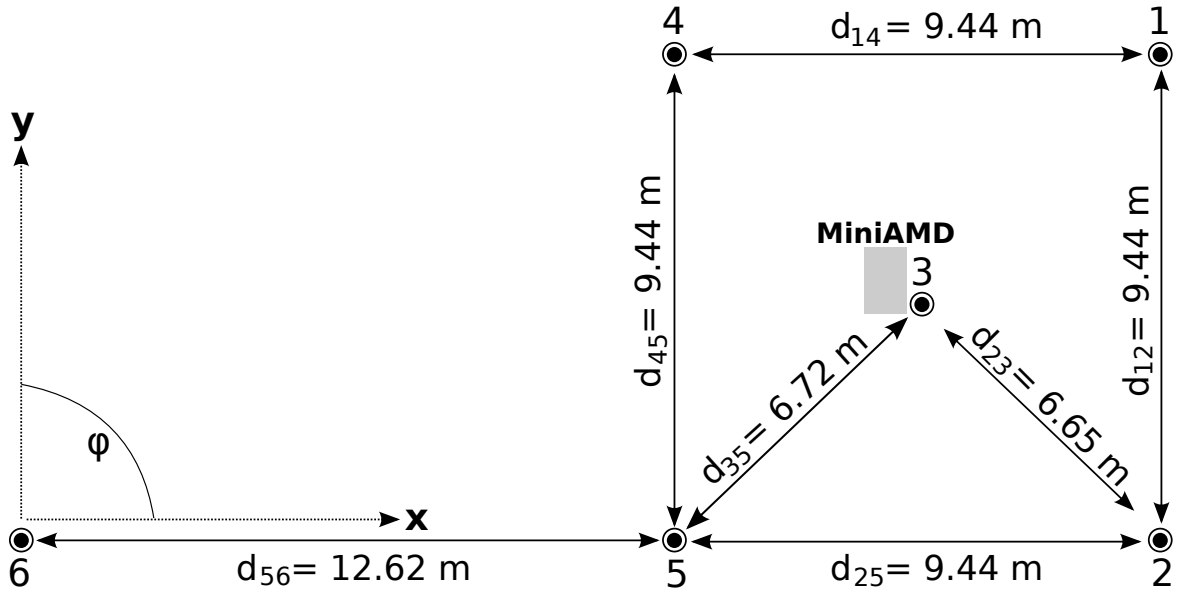

Figure 9.11.: Layout of the air shower array located on the roof of the physics department in Aachen. It consists of six stations detecting air shower particles via a liquid scintillator with SiPM readout. Indicated are the dimensions of the array and the definition of the chosen coordinate system used for the analysis. The MiniAMD detector is located in the triangle of stations 3, 4 and 5.

the amplification of the SiPM signal and two output channels. Both channels are guided to the readout electronics further described in the next section. A simultaneous trigger of several stations enables a reconstruction of the air shower arrival direction. An increasing number of stations being hit indicates an increased air shower energy. As the barrels have a cylindrical, extended form, they are also sensitive to inclined air showers.
The array layout is presented in figure 9.11. A photo is presented in figure 9.12. Five stations are forming a dense cluster while a sixth station is located further apart. Each station is connected to the readout electronics by cables of the same length of 30 m to simplify the timing and synchronization between stations. The readout electronics is located in a room next to the array. The array is described in detail in [197].

9.3.1. Readout electronics

The readout electronics is based on NIM trigger logic and on the digitization of the signals by DRS4 (Domino Ring Sampler) evaluation boards[4] [198, 199].
As discussed, each detector station has two output channels. The signals of both channels have opposite signs. Channel A is defined as the negative signal and is used to form an event trigger. Channel B has a positive sign and is used for the event digitization if an event trigger is received. Channel B provides a signal twice as large as channel A. The electronics setup processing of both signals is sketched in the following. Channel A of each detector station is compared to a discriminator with adjustable threshold. If the signal exceeds this *channel threshold*, a NIM pulse is forwarded to a combined FAN-IN module for all channels. The module provides a logic gate output referring to the *station multiplicity* n_{mult} (the number of stations triggered). A NIM pulse is defined as a

[4] comparable to the functionality of an oscilloscope

Figure 9.12.: Photo of the air shower array located on the roof of the physics department in Aachen. It consists of six stations. Each station consists of a barrel protected against light leakage with a layer of adhesive aluminum tape at its outside. The MiniAMD detector is located under a black pond liner in the middle of the array.

negative rectangular pulse with a standardized pulse height of $V_{\mathrm{nim}} = -0.8\,\mathrm{V}$. The output of the FAN-IN module is the sum of all NIM pulses arrived, divided by a factor of eight:

$$V_{\mathrm{multi}} = \frac{\sum V_{\mathrm{nim}}}{8} = \frac{n_{\mathrm{mult}}}{8} V_{\mathrm{nim}} \quad . \tag{9.8}$$

The output V_{multi} is compared to a further discriminator with adjustable threshold allowing the setting of a requirement on the station multiplicity.
Three stations are connected to one DRS4 evaluation board. Channel 4 is occupied as receiving the event trigger. For each triggered event, each DRS4 board provides three waveforms, each having a length of 200 ns in 1024 samples. All waveforms including timing information are sent to the PC and the data recorded are stored in ROOT [182] files.
The stored data is preprocessed before being analyzed. To allow for a precise determination of the pulse height and a time marker for each station enabling a reconstruction of the arrival direction, the baseline for each station has to be determined. As the baseline varies with time, this process is performed for each event and for each station separately.
Assuming a random fluctuation around the baseline at each time bin not included in the signal region, an average of the first 300 points in a trace is defined as the baseline value. Once the baseline is determined, the pulse height is calculated by the height of the waveform maximum reduced by the value of the baseline. To allow for a stable timing, that is important for the determination of the arrival direction, the time marker for each trigger is defined as the time bin at which the signal is reaching 50% of the pulse height. In figure 9.13, an exemplary waveform of one station is shown. Depicted by a frame is the region by which the baseline is determined and as triangle the trigger time marker at 50% of the maximum pulse height over baseline.

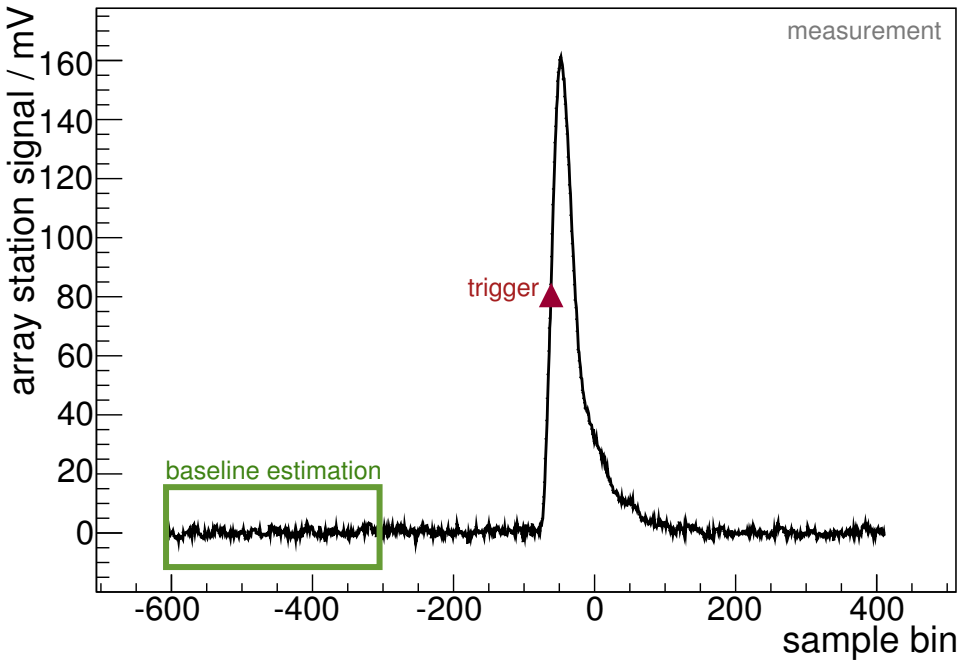

Figure 9.13.: Exemplary waveform of a station triggered by an air shower candidate. Shown is the signal height in mV as a function of sample bins. The triangle marks the time of trigger and is defined at 50% of the maximum pulse height over baseline. The baseline is determined by the average of the first 300 sample bins depicted by the frame. A reference time for the first time bin allows the conversion of the sampling bin to a UNIX timestamp.

9.3.2. Standalone performance of the air shower array

Data taken for this thesis are based on a required two-station-coincidence of the air shower array with a fixed channel threshold of 30 mV of each station. As shown in [197], the threshold setting allows for a significant suppression of random noise and results in a single detector trigger rate of 10 Hz. The rate is well compatible with the expectation for the atmospheric muon flux.
Before discussing the data with MiniAMD in coincidence, the standalone performance of the array is discussed in this section.
First, the event rate as a function of UNIX time in seconds for eight days is shown in figure 9.14. Each data point corresponds to the average rate detected over one hour and the corresponding standard deviation. On average, the array receives a trigger around every 30 seconds resulting in an event rate of around 0.033 Hz. Additionally, vertical lines indicate midnight between two consecutive days. A performed Fourier analysis shows no evidence of a day-night effect. In figure 9.15, the event rate as a function of the cumulative station multiplicity is shown. As expected, the rate is steeply falling with the amount of stations triggered, while the event rate for two station triggers is slightly larger than expected if assuming an exponential function. The random trigger coincidence rate of two or more stations is low ($\mathcal{O}(10^{-4}\,\mathrm{Hz})$). Therefore, a change in the particle density distribution may be indicated. For higher energetic air showers or showers with a core position close to the array, the amount of particles arriving simultaneously at ground, so the particle density, is increasing. For these showers not only more stations will be triggered, but also more particles will deposit energy in one station resulting in an increased average signal in each station. This is depicted in figure 9.16. The average signal contained in the events is rising with the station multiplicity. The maximum signal height reachable is around 900 mV at which a station saturates. For events with six stations an accumulation of events becomes visible, understandable as pile-up,

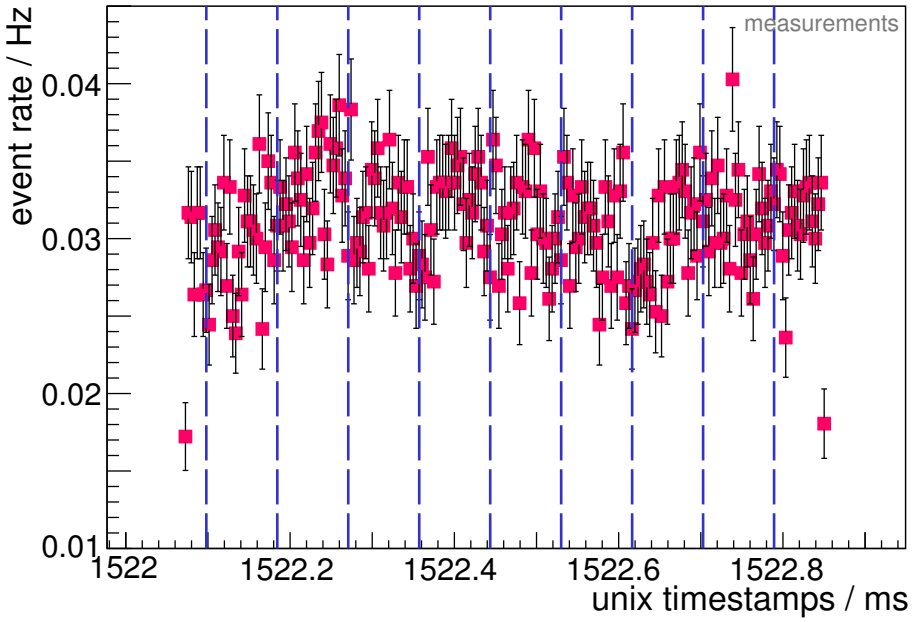

Figure 9.14.: Event rate as a function of UNIX time in seconds. For the hardware trigger at least a two-fold coincidence of the air shower array is required. Vertical dashed lines indicate midnight between two consecutive days.

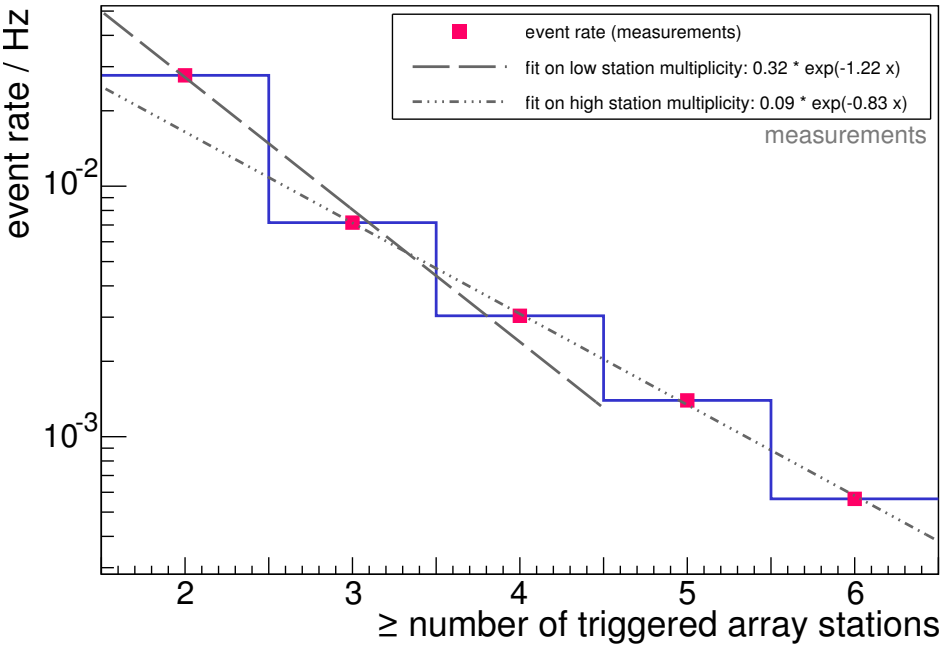

Figure 9.15.: Event rate as a function of cumulative station multiplicity of the air shower array. The hardware trigger required a two-fold coincidence of the air shower array.

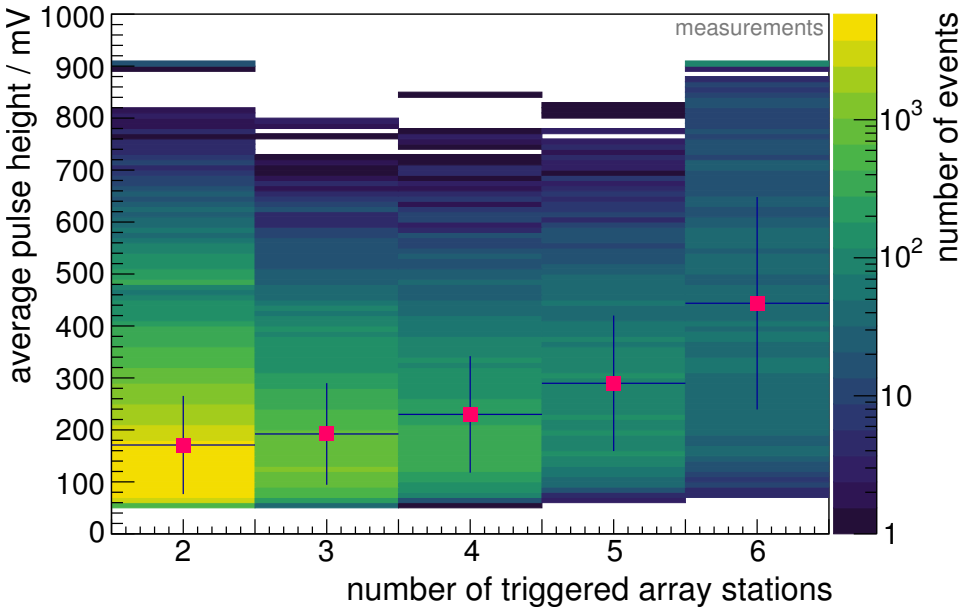

Figure 9.16.: Average detector signal height for one station as a function of station multiplicity of the air shower array. The signal height is a measure of the deposited energy in the stations. The hardware trigger required a two-fold coincidence of the air shower array.

as no more stations can be triggered. Furthermore, several events are detected in which all stations are saturated indicating energetic air showers with high particle density.
Thus, the increase of the average signal in the stations and of the number of stations measuring simultaneously a signal above threshold is a measure for the particles and energy contained in the air shower candidates.

Furthermore, the array enables the reconstruction of the shower arrival direction, based on the timing of the stations. The chronological order in which the stations have received a signal can be used to determine the zenith angle θ and the azimuthal angle ϕ of an event. The zenith is thereby defined as 0° for events arriving vertically with respect to the extended array and as 90° arriving horizontally to it. The azimuthal angle is defined in the coordinate system as depicted in figure 9.11. The calculation of the arrival direction is described in more detail in [197]. For the reconstruction of the arrival direction at least three stations have to be hit. This results in $\mathcal{O}(30\%)$ of all showers registered. If exactly three stations registered a signal, the arrival direction can be calculated via the time stamps at which the stations have triggered. If more stations are triggered, an improved reconstruction algorithm can be utilized taking the shower front into account. Therefore, a flat shower front is assumed as a first order approximation. The reconstruction by both algorithms is not successful for all showers with three or more triggered stations. The reconstruction efficiency is in the order of $\mathcal{O}(80\%)$. This allows for an event rate of around 0.007 Hz for reconstructable events. The reconstruction of the arrival directions is subject to the uncertainty on the timing determination, deviations in particle arrival times in an air shower, and also possible false trigger stations due to thermal or electric noise but also atmospheric muons, even if unlikely. A detailed investigation on the uncertainty on the reconstructed arrival direction is still on-going [201].
Based on the successfully reconstructed events, the zenith distribution and a polar plot representation of zenith and azimuthal angle are shown in 9.17. The zenith distribution is presented as a function of θ instead of the more common function of $\cos(\theta)$ to allow for a comparison to other experiments. The maximum of the distribution is at $\theta \approx 20^\circ$. The value is well compatible with

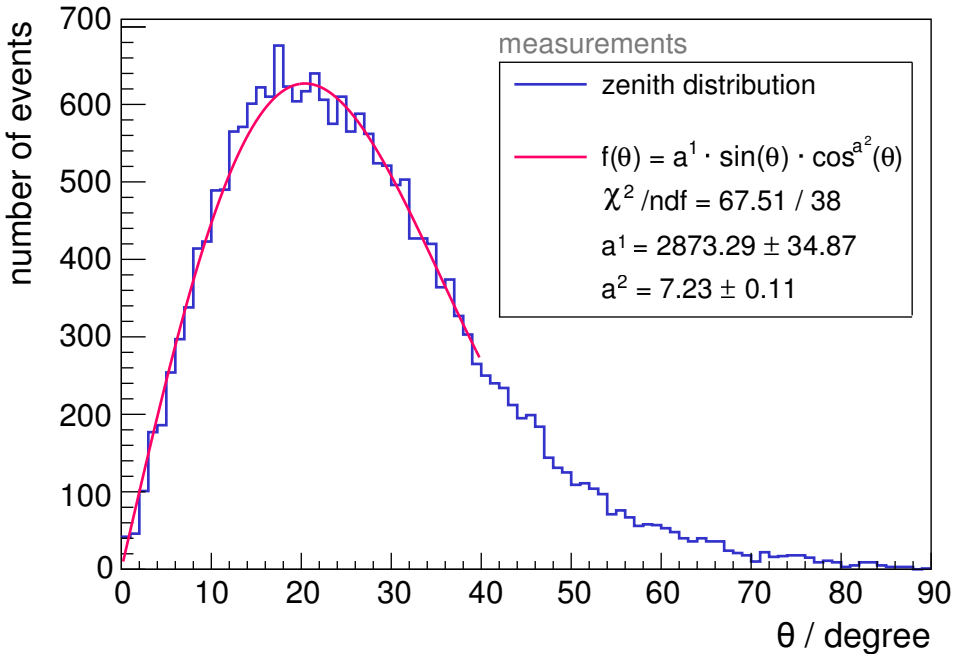

(a) Event rate as a function of the zenith angle in degree. The distribution peaks at 20°. The red line refers to the function 9.9 introduced by the LORA experiment [200].

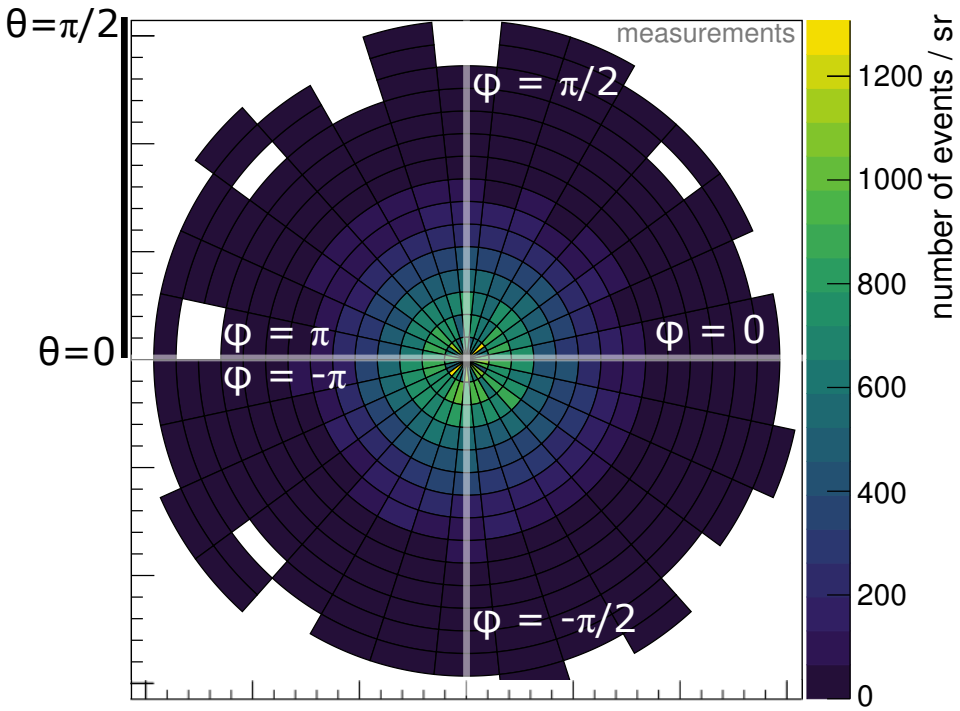

(b) Polar plot representation of the zenith (radial coordinate) and azimuth (angular coordinate) distribution. The bin content is normalized to the solid angle (cf. equation 9.10) covered by the corresponding angular bin.

Figure 9.17.: Angular distribution of events detected by the air shower array.

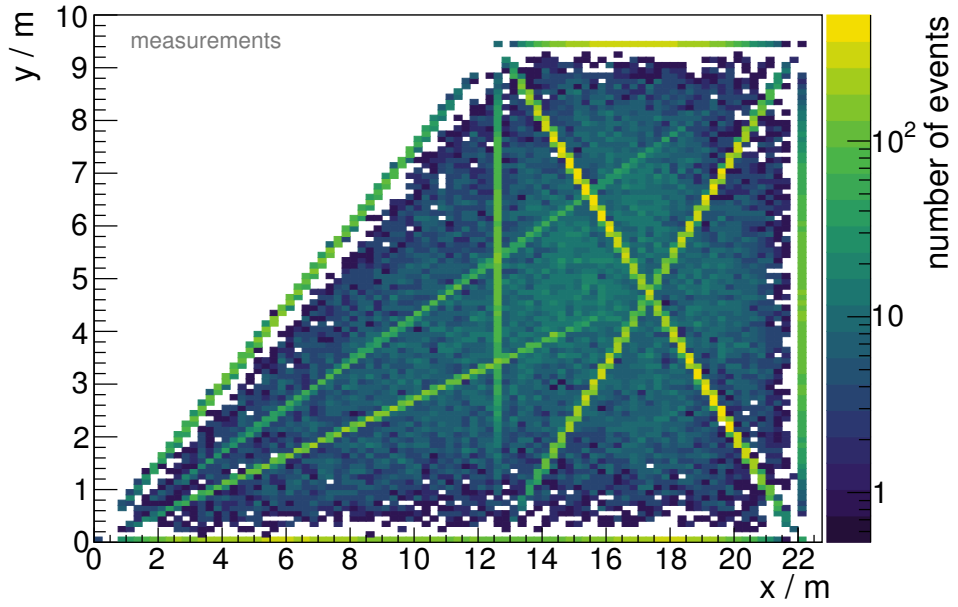

Figure 9.18.: Center of gravity of detected events in the x-y coordinate system of the air shower array as depicted in figure 9.11. Presented is the distribution of the shower core position of events detected by at least two stations of the air shower array.

the results determined by small-scale, calibrated arrays as EAS-TOP [202, 203] or LORA [200] with $\theta \approx 19°$. The distribution around the peak region (from 0° to 40°) was investigated by the following function introduced by the LORA experiment

$$f(\theta) = a_1 \sin(\theta)\cos(\theta)^{a_2} \quad . \tag{9.9}$$

The χ^2/ndf of 67.51/38 indicates a relatively large deviation by 3.4σ from the expected value. However, the result is already impressive for an uncalibrated and small-scale array. An asymmetric tail to larger zenith angles proves that the array is capable to detect also inclined air showers due to the extended form of the detector stations. The expected angular distribution is thereby a combination of

- the isotropic distribution of cosmic ray air showers,
- the solid angle acceptance of the array which is increasing with zenith angle $\propto \sin\theta$, and
- the attenuation of the showers (mainly the electromagnetic shower component) in the increasing amount of traversed atmosphere for large zenith angles.

As at the highest angles the atmospheric absorption dominates, the number of observed events is expected to be strongly suppressed. At the lowest zenith angles, the solid angle Ω is strongly reduced. The bin content of the polar representation is thus normalized to the solid angle of the corresponding angular bin. It can be calculated by

$$\Omega(\theta_1, \theta_2) = \int_0^{2\pi} \int_{\theta_1}^{\theta_2} \sin(\theta')\mathrm{d}\theta'\mathrm{d}\phi' = 2\pi(\cos(\theta_1) - \cos(\theta_2)) \quad . \tag{9.10}$$

As the array only provides a relatively small covered area and few detector stations, the determination of the position of the shower core is highly limited. As a first estimate the center of gravity (cog) may be calculated. The x-coordinate can be determined according to

$$\mathrm{cog}_x = \frac{\sum_{i=2}^{6} s_i \cdot x_i}{\sum_{i=2}^{6} x_i} \quad , \tag{9.11}$$

while s_i is the detected signal in a detector station i and x_i the x-coordinate of the position of the detector in the chosen coordinate system as depicted in figure 9.11. The y-coordinate can be equally determined. The center of gravity of all events is shown in figure 9.18. The structure is introduced by events with only two triggered stations. However, the center of gravity is well distributed within the array. A location of the MiniAMD demonstrator in the dense cluster is preferred.

These studies demonstrate that the air shower array, despite its small size, is very well suited for initial investigations of the MiniAMD demonstrator.

9.4. Measurements with MiniAMD on the roof of the physics department

The primary objective of the MiniAMD detector is the detection of important parameters of extensive air showers such as the particle density reaching the ground.
To allow for a more detailed study of the response of the demonstrator on cosmic ray candidates, MiniAMD is operated in self-triggering mode as well as in coincidence with the air shower array. Both measurement studies will be described and compared in the following. The detector is located

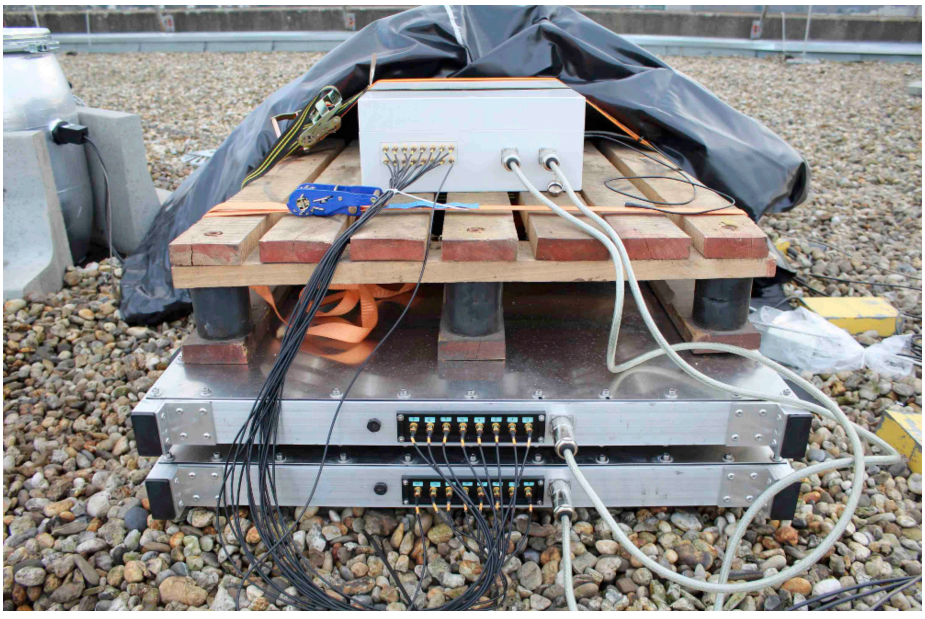

Figure 9.19.: Photo of the MiniAMD demonstrator located on the roof of the physics department. Two modules are located on top of each other. They are aligned such that a unit in the upper module is aligned to a counterpart in the lower module, forming a stack of units. On top of the demonstrator the electronics box is located. On the left side, a detector station of the air shower array, which is located on the roof and used as external trigger of the MiniAMD demonstrator, is visible.

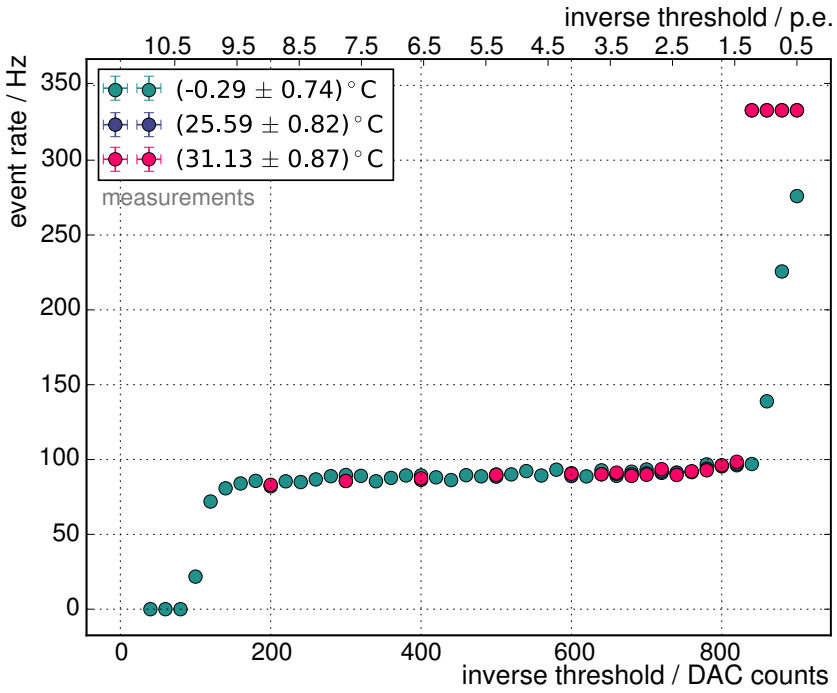

Figure 9.20.: The event rate of the MiniAMD demonstrator in self-triggering mode as a function of the discriminator threshold and of the p.e. value (top of figure). The hardware trigger criterion is at least one stack where the signal in both units of the stack exceeds a 2.5 p.e.-threshold. Shown is the trigger rate for three temperatures. Circular markers refer to a temperature of −0.29 °C, 25.59 °C, and 31.13 °C. Poisson statistics is used to determine the uncertainty on each data point.

in the triangle formed by the array stations 3 to 5, next to station 3 (cf. figure 9.11 and figure 9.12). The light demonstrator is stabilized by a palette and tension belts against wind. It is additionally covered by a pond liner against rain even if the modules are designed to be water-tight. A photo of the setup is presented in figure 9.19.

Hardware trigger conditions of MiniAMD

The conditions requested for a trigger of the MiniAMD detector system can be modified by the user while executing the measurement procedure from the shell or by the config file. At the time of this thesis several trigger conditions are available whereby the imposed threshold is the same for all connected units. First, a multiplicity trigger can be imposed, which asks for a certain amount of units or of stacks to be triggered. Secondly, a mask can be set to ask for explicit stacks or units. For example, these four triggers are used in the scope of the measurement with MiniAMD:

- Multiplicity trigger of at least one stack with a threshold trigger of 2.5 p.e.
- Multiplicity trigger of at least one stack with a threshold trigger of 3.5 p.e.
- Multiplicity trigger of at least one unit in the upper module and at least one unit in the lower module with a threshold trigger of 3.5 p.e.
- A single unit trigger out of the 16 units connected with a threshold trigger of 2.5 p.e.

Most important for the choice of the trigger threshold is the suppression of the darknoise component. At a threshold of 2.5 p.e., the darknoise rate is in the same order of the signal component for

a temperature of 26 °C (cf. figure 8.2 on page 108).
In self-triggering mode, each trigger generates an *ADC event* and a *discri event* if requested by the user. Both event types are explained below. The following data are stored in each ADC event: the event time, the event number, the amount of ADC count for high- and low-gain seen by the photosensor of the corresponding unit, and a flag if the unit has exceeded the imposed threshold. The discri event contains a timeline of the discriminator states of all units. For each timebin of 10 ns, the FPGA examines if a unit exceeded the threshold. If so, the binary status refers to state "1", otherwise it is set to "0". A detailed discussion of the potential of the discriminator status for future analyses is presented in section 9.5. An overview over both event types and the MiniAMD trigger chain is given in figure 9.21 on page 165.

Shown in figure 9.20 is the rate of events with at least one triggered stack as a function of the discriminator threshold. Measurements at three different temperatures are presented, for −0.29 °C, for 25.59 °C, and for 31.13 °C. Poisson statistics is used to determine the uncertainty of each data point. An increased temperature results in an increased false trigger rate by darknoise events for thresholds below 2 p.e. At a threshold of 2.5 p.e. for all presented temperatures, a stable plateau with an average trigger rate of around 100 Hz is reached[5]. The rate is slightly larger than the expected trigger rate for atmospheric muons for a stack but is still compatible if assuming a contribution of noise and background events. Therefore, this is the preferred trigger threshold. For the calculation of the expected trigger rate, the vertical muon flux of $70\,\mathrm{m^{-2}s^{-1}sr^{-1}}$ is multiplied with the weighted acceptance of the setup (cf. equation 8.5 and equation 8.7 on page 107). The weighted acceptance takes into account the anisotropic distribution of the incident muon flux $\frac{\mathrm{d}N}{\mathrm{d}cos(\theta)} \propto \cos(\theta)^n$, whereby the exponent can be determined empirically to $n \approx 2$. Additionally, the reduction of the effective area with increasing zenith angle is taken into account. The weighted acceptance of a stack with a vertical distance between both units of 10 cm is determined by a MC simulation to $\Gamma = 0.112 \pm 0.002\,\mathrm{m^2\,sr}$. This results in an expected trigger rate of a stack of 8 Hz. As for atmospheric muons, each stack acts like an independent detector, an absolute muon rate of 64 Hz is expected, compared to 100 Hz determined by measurements. It is expected that, besides muons, also electrons are detected by a stack. This is already indicated in figure 7.15b on page 102 in chapter 7. The measured spectrum of a two-fold coincidence can be explained by simulations of particle passages of muons and electrons. A combined, simulated rate is determined to be 11 Hz. The muon rate alone can be confirmed to be in the order of 8 Hz per detector unit.

9.4.1. Setup of MiniAMD in coincidence with the air shower array

All presented events for *coincident measurements* have the following trigger criteria if not otherwise stated. The trigger decision is sketched in figure 9.21. For MiniAMD, the signal in both units of at least one stack has to exceed a threshold of 2.5 p.e. (720 DAC count). Additionally, an external trigger by the air shower array has to be received. This trigger is provided if at least two stations of the air shower array have exceeded a threshold of 30 mV. If an air shower trigger occurs, all stations of the array are read out and their waveforms are stored in ROOT files. If MiniAMD has seen an event in coincidence, all units are read out. The data are stored in an ADC event. When no external trigger arrives within 640 ns after a MiniAMD trigger, the event is canceled. Furthermore, the discriminator status is stored in a discri event if an external trigger has been received. This event is stored regardless of the MiniAMD state. The trigger of the array is thereby formed by the readout electronics located in the room next to the roof as described in section 9.3. The trigger is then fed back to the MiniAMD demonstrator. The cables from the stations to the electronics and from the

[5] An average self-triggering rate of 99.96 ± 2.81 Hz is found for a long-term measurement over a temperature range from −5 °C to 15 °C. For around 30 days, every five hours MiniAMD was operated for one hour in self-triggering mode.

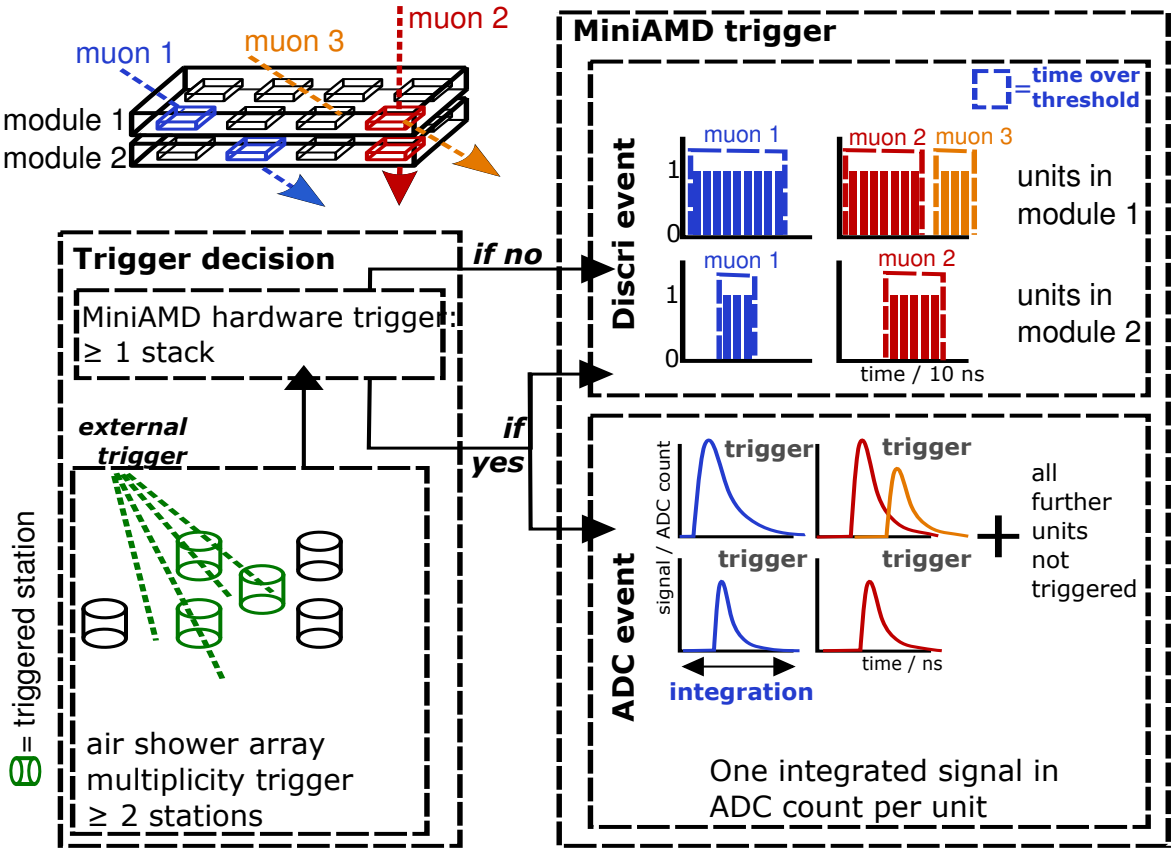

Figure 9.21.: Trigger chain of the MiniAMD detector. The default trigger criterion is an event in both units of at least one stack. A common discriminator threshold of 2.5 p.e. is imposed. However, also other trigger configurations can be chosen by the user. In self-triggering mode, each trigger generates an ADC and a discri event if requested. In coincidence with the air shower array, an additional external trigger has to be received within 640 ns after the trigger based on MiniAMD alone (see trigger decision in the box on the left). If a trigger is detected, an ADC and a discri event are generated. Otherwise, only the discri event is stored. An exemplary coincident event including three muons is presented. Each passing muon is color-coded (muon 1 = blue, muon 2 = red, muon 3 = orange). Two stacks, so 4 units, are triggered. The discri event is presented in the upper right box. It refers to the timeline of the binary discriminator states of all units. A unit over threshold corresponds to state "1". The total time over threshold is indicated by the envelope over all bins. The ADC event is presented in the lower right box. It contains the integrated signal of each unit for the low- and high-gain channel and a flag if the unit has exceeded the imposed threshold.

electronics to MiniAMD have each a length of around 30 m. The cable lengths introduce a signal delay of 60 m = 300 ns. The delay is confirmed by a simultaneous readout of the instantaneous signal seen by MiniAMD and the delayed signal arriving from the array by an oscilloscope and by investigation of the discri events in section 9.5.

First, the MiniAMD response to air shower candidates is presented without taking the response of the air shower array into account. However, as already described, these events are also triggered by at least two air shower array stations. They are compared to measurements with MiniAMD operated in self-triggering mode. Secondly, further information provided by the array are used to study the response depending on air shower characteristics such as the arrival direction distribution.

An exemplary coincident event, at which all six air shower stations and all 16 MiniAMD units were

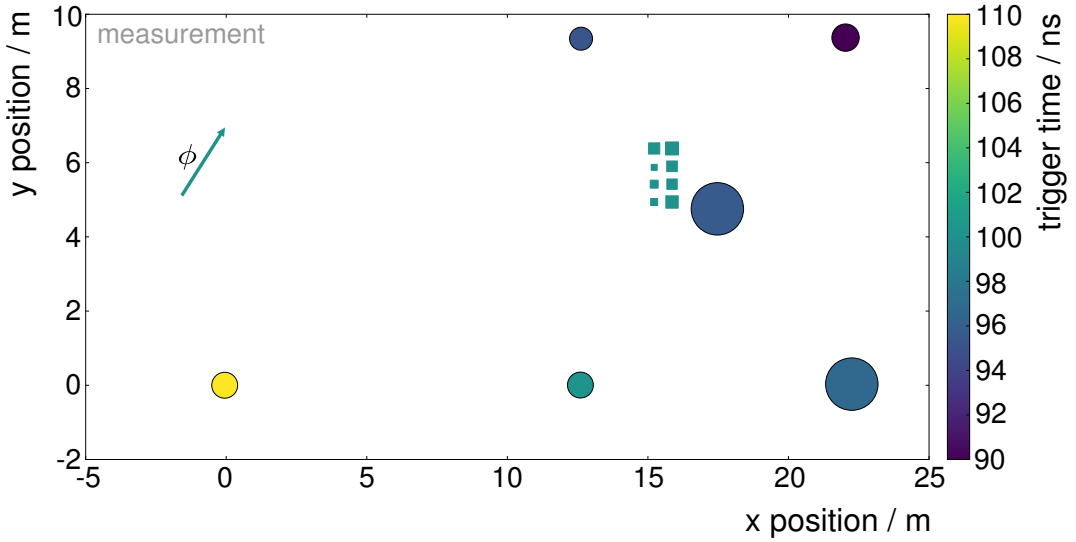

Figure 9.22.: Display of an exemplary event. Six air shower array stations are triggered. They are represented by circular markers. The size of the markers corresponds to the detected pulse height. The color refers to the arrival time at each station. By eight rectangles, the signal registered by MiniAMD is represented. The size of each rectangle depicts the average signal detected by a stack. All units except of unit 13 triggered at the same time. The direction corresponding to the azimuthal angle $\phi = 47°$, determined by the air shower array, is indicated by an arrow.

triggered, is presented in figure 9.22. Both experiments store their data on independent readout systems. Their UNIX timestamps have to be synchronized to allow for the study of coincident events. The deviation between both system clocks is slowly increasing, thus a matching algorithm is performed for each run. An overview about the algorithm is given in detail in appendix B. The array itself has a trigger rate of 0.033 Hz. Roughly every second event is also registered by the MiniAMD array. Atmospheric conditions alter the expected signal rate. The ratio of both event rates is expected to be stable. The ratio of the event rate for the array alone compared to the coincident rate as a function of the ambient temperature is shown in figure 9.23. The latter is estimated by the average temperature detected at the MiniAMD SiPMs. This is only one important quantity to describe the atmospheric conditions. The ratio is reasonably stable with an average value of 0.44 over a temperature range of 20 °C. Each data point corresponds to the average ratio for one measurement run, normally including one day and night of data. The uncertainty refers to the standard deviation. The combined measurement time is 13 days.

9.4.2. Comparison of MiniAMD data taken in self-triggering mode and in coincidence with the air shower array

Cosmic ray induced air showers consist of three main components: the electromagnetic, the muonic, and the hadronic component. The first two are of particular interest for the MiniAMD demonstrator. As both modules are located on top of each other, it is likely that particles of the electromagnetic component arriving ground may enter the upper MiniAMD module. This may lead to an increased signal in the units of the upper module if the particles get absorbed before entering the lower module. Alternatively, the muonic and the more energetic electromagnetic component won't get absorbed and will result in the same signal in both modules. Furthermore, the particles may produce secondaries while traversing the upper module resulting in an increased signal in the lower module. Therefore, the comparison of the response of both modules to the same events is discussed in

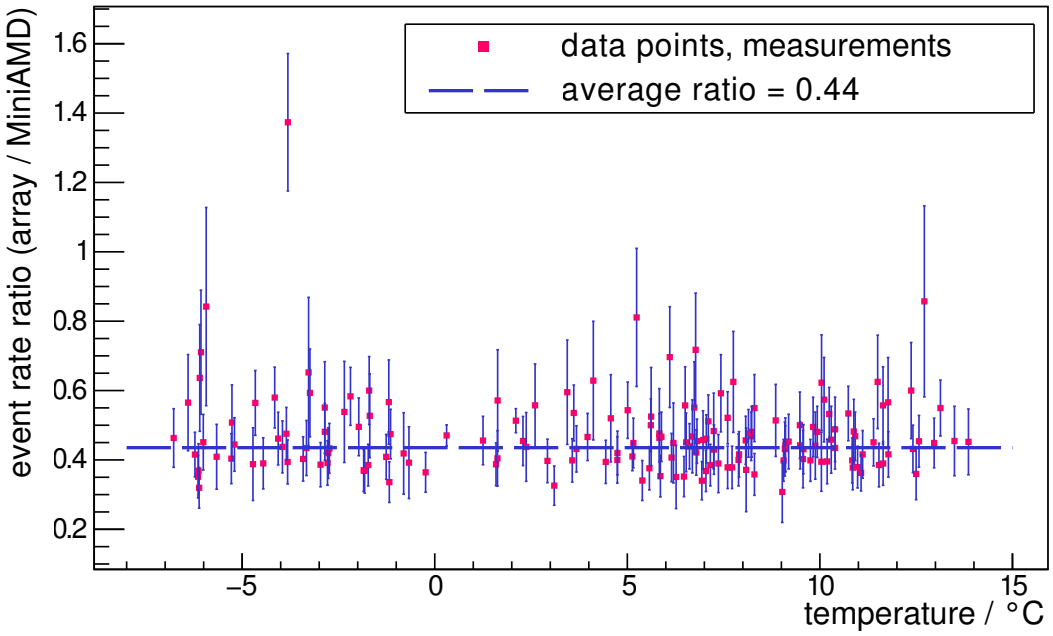

Figure 9.23.: Event rate ratio as a function of the average temperature detected at the SiPMs of the MiniAMD detector. The ratio is defined by the event rate of the air shower array only to the rate of coincidence events of the array and the MiniAMD detector. A two-fold coincidence of the air shower array is required. No temperature effect is visible. 44% of all array events are also detected by the MiniAMD detector.

the following. In figure 9.24, the number of triggered events as a function of unit id and the signal distribution of all units in both modules are shown as a function of signal in units of MIP. They are shown for MiniAMD in self-triggering mode in figure 9.24a and 9.24c, respectively; and for coincidence measurements in figure 9.24b and 9.24d, respectively. All distributions indicate a comparable response of all units. The self-triggered event rate of each unit lies within 4% deviation to the average trigger rate of roughly 12.7 Hz (cf. figure 9.24a). The average value is, as discussed, compatible with the expected atmospheric muon rate of 10 Hz for a single unit (cf. equation 8.7) but indicates a slight contribution of passage of further particle types or a possible contribution of noise events. Poisson statistics is used to determine the uncertainty on each data point. Measured in coincidence, the average rate is strongly reduced to 0.008 Hz (cf. figure 9.24b). By the requirement of a three-fold coincidence (at least two triggered air shower array stations and one triggered stack in MiniAMD), an increased particle density is needed. This is only fulfilled for air shower events with a shower core next to the array or with a reasonable energy. An estimation of the corresponding energy thresholds for both setups is calculated later in this section. However, a comparison between both modules indicates a strong correlation between event rates of units corresponding to a stack. As already mentioned, the MiniAMD demonstrator is covered by a liner during the measurements on the roof. To protect the liner against wind, lead blocks are used to weigh down the liner. The lead blocks are located on the roof surrounding the demonstrator. Due to harsh wind, two additional blocks, one made of lead (on unit ids 0 and 8), the other of concrete (on unit ids 3/11 and unit ids 4/12), are temporarily located on top of the MiniAMD demonstrator. The blocks cover around half of each detector unit for vertical particles. As expected, a more pronounced shielding is visible for the block made of lead. During the time period the lead block is located on the detector, the event rate was reduced by 10% compared to the maximum achieved event rate. The shielding by concrete reduces the rate by 5%. The shielding is visible for both units of a stack indicating the absorption of

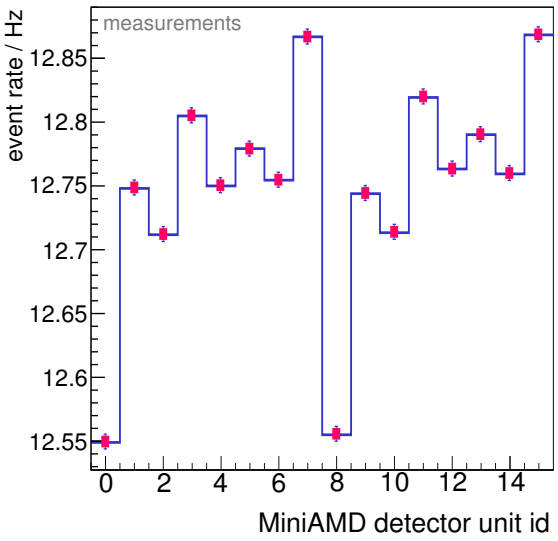

(a) Number of triggered events by MiniAMD in self-triggering mode as a function of the unit id. The average rate is 12.7 Hz.

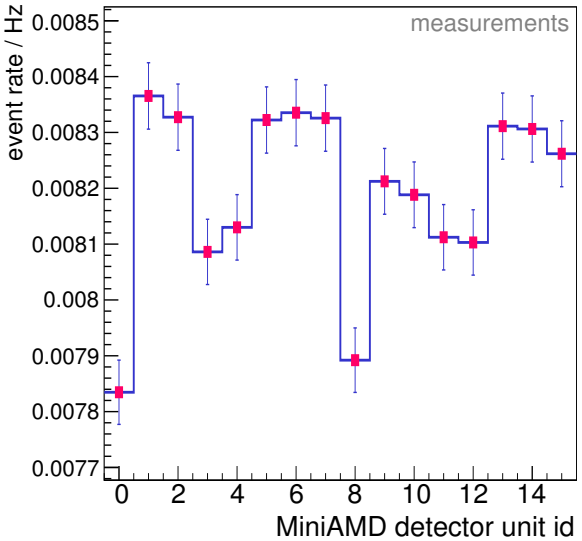

(b) Number of coincident triggered events as a function of the unit id. The average rate is 0.008 Hz.

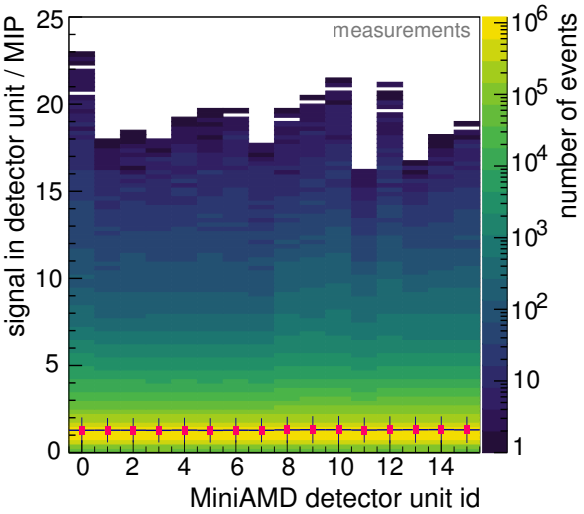

(c) Signal distribution in units of MIP as a function of unit id. MiniAMD was operated in self-triggering mode. All units show a comparable response indicated in the distribution and in the averaged profile.

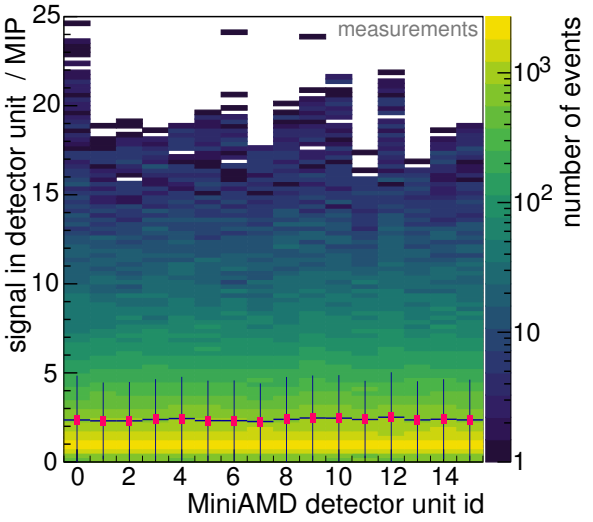

(d) Signal distribution in units of MIP as a function of unit id. MiniAMD was operated in coincidence with the array. All units show a comparable response indicated in the distribution and in the averaged profile.

Figure 9.24.: Comparison of the response of the units in both MiniAMD modules. The MiniAMD detector is operated in self-triggering mode (left) and in coincidence with the air shower array (right). If the signal in both units of at least one stack exceeds a threshold of 2.5 p.e. (and received an external trigger), all units are read out. The signal or trigger of all units above threshold are included in the distribution. Units with ids from 0 to 7 are located in the upper MiniAMD module while units with ids from 8 to 15 are located in the lower module.

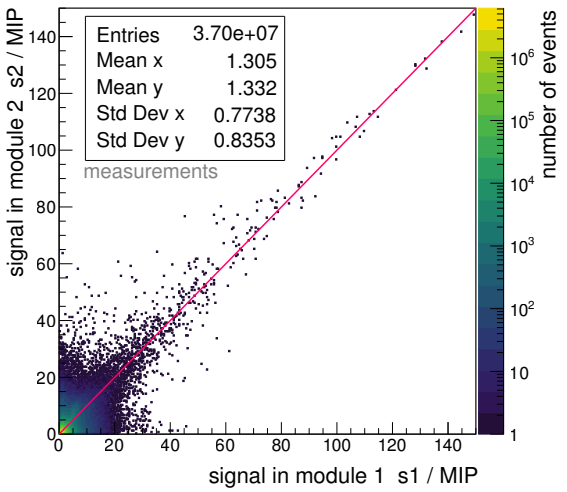

(a) MiniAMD in self-triggering mode. Signal in units of MIP measured in module 1 compared to the signal in units of MIP measured in module 2 for the same events.

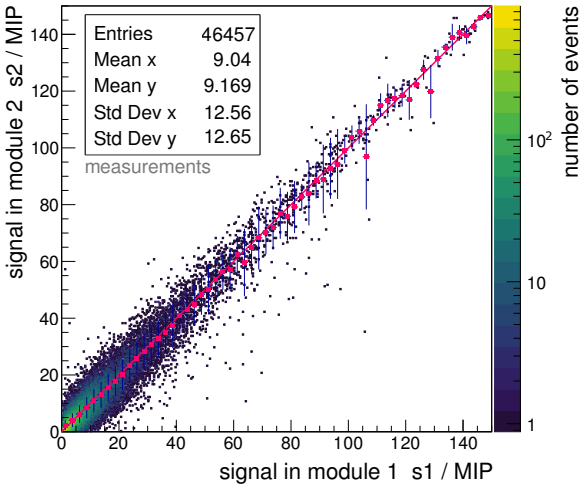

(b) MiniAMD in coincidence with the air shower array. Signal in units of MIP measured in module 1 compared to the signal in units of MIP measured in module 2 for the same events.

Figure 9.25.: Comparison of the signal measured in the upper module (module 1) and the lower module (module 2) for the same events. The signal is defined as the sum of all detector units which have exceeded the threshold, further detector units are not included.

particles, like muons, which would normally have passed both units. How the number of triggered events and the signal spectrum is influenced by different shielding setups is discussed in appendix D.
In comparison, the signal as a function of the unit id (cf. figure 9.24b) does not indicate any influence by the shielding. The distribution depicts an average signal yield of 1 MIP, as expected. The uncertainty bars of the profile are thereby referring to the rms of the event distribution for each unit id. The maximum signal detected is 25 p.e. No tendency of a detection of a larger signal in one of the modules is visible.

Comparison of signals in both MiniAMD modules

A more detailed comparison can be performed by studying the measured signal in the upper module (module 1) and the lower module (module 2) for the same events. The signal is thereby defined as the sum of the signals (in units of MIP) of all detector units which have exceeded the threshold. All further units are not included. The setup is studied for MiniAMD in self-triggering mode (cf. figure 9.25a) and in coincidence with the array (cf. figure 9.25b), respectively. The data set of the self-triggering mode is strongly dominated by low-signal events as single atmospheric muons (cf. figure 9.25a). Only a small fraction of events has higher signal yields. The distribution is broad in the low-signal regime with high fluctuations of the signals registered in both modules. In comparison, the coincident data set indicates an increased and more homogenous average signal yield as expected for air shower candidates with multiple particles arriving the detector (cf. figure 9.25b). For this data set, also a one-dimensional profile is presented, which corresponds to the average of the distribution along the y-axis for each x-axis bin. A correlation factor equal to one can be confirmed over the complete signal yield range. However, for both scenarios the largest signal detected corresponds to an energy deposition of 150 MIP in each module over integration time of the EASIROC. Furthermore, the spread of both distributions becomes narrower with larger signals

in both modules. However, the signals are symmetrically distributed along the linear correlation with a correlation factor equal to one for the complete signal range. Thus, a significantly stronger contribution of the electromagnetic component to signals measured by one module is excluded for both scenarios. This indicates that the electromagnetic component contributes in equal parts to both modules. Two possible explanations are conceivable. The electromagnetic component is not measured at all by the modules, or the particles are not absorbed in the upper module and deposit a comparable amount of energy in the scintillator units in the lower module. In principle, electrons are capable to reach the lower module. As presented in figure 7.13 on page 100, the average kinetic energy for atmospheric electrons is in the order of 20 MeV. The energy loss of electrons can be estimated based on

$$-\frac{\mathrm{d}E}{\mathrm{d}x} = \frac{E \cdot \rho}{X_0} \quad , \tag{9.12}$$

with E being the kinetic energy, x being the pathlength through a material with radiation length X_0 and density ρ. For the MiniAMD demonstrator, a vertical electron has to traverse in total 1.5 cm aluminum and two scintillator tiles with a total thickness of 1 cm. The radiation length and the density of the materials (aluminium and polyvinyltoluene) are taken from [204]. The energy loss in the aluminum is $-5.8\,\mathrm{MeV/cm}$ and in the scintillator $-1.25\,\mathrm{MeV/cm}$. This results in a minimum energy for an electron to traverse both tiles in a stack of roughly 10 MeV. This estimate confirms the possibility for electrons to be detected in both modules. For a more detailed study, a measurement of the modules in an electron beam could be performed.
In the scope of this thesis, it is assumed that both modules detect the same signal. Therefore, the *average signal*

$$\langle s \rangle = \frac{s_1 + s_2}{2} \tag{9.13}$$

of both modules should be used. s_1 and s_2 are the registered signals in the respective module in units of MIP. The full relative difference $\Delta s/\langle s \rangle = (s_1 - s_2)/\langle s \rangle$ as a function of the average signal $\langle s \rangle$ is presented in figure 9.26a and 9.26b for MiniAMD in self-triggering and in coincident mode, respectively. As for the direct comparison of the signals in both modules (cf. figures 9.25a and 9.25b), for low average signals a broad distribution is determined which becomes narrow with increasing signal yield. For the self-triggering mode, many events depict a large deviation close to ±2. These events may result from clipping single atmospheric muons. Those traversed the complete height of one unit but had only a small pathlength in a unit located in the other module. Furthermore, coincident events of a particle passage and a darknoise event are possible. These events are strongly reduced for the air shower candidates triggered by the array (cf. figure 9.26b). Additionally, two envelopes are depicted. They are referring to the expected maximum deviation if a Poissonian distribution[6] of the signal in both modules is assumed. They are determined by a toy Monte Carlo simulation. Therefore, the signals $s_{1,2}$ in both modules are drawn independently from a Poissonian distribution with the average signal $\langle s \rangle$ as expectation. The envelope in pink refers to the maximum deviation in the corresponding relative signal while the average signal is kept fixed to the expectation. This scenario is based on the assumption that the signals in both modules are strongly correlated but vary due to the event-to-event fluctuations of the light yield. It predicts a narrowing comparable to the presented data. For the blue envelope, not only the relative but also the average signal is calculated according to the drawn signals taking the uncertainty on the total number of particles into account. This scenario is based on the assumption that the signals in both modules are not correlated. Thereby, the low-signal distribution can be well described, while for larger signals the envelope is too broad. This is expected as for large particle densities, the relative deviations introduced by detection efficiency and area coverage are smaller. Even if a

[6] A Poissonian distribution is only a rough estimate of the underlying uncertainty.

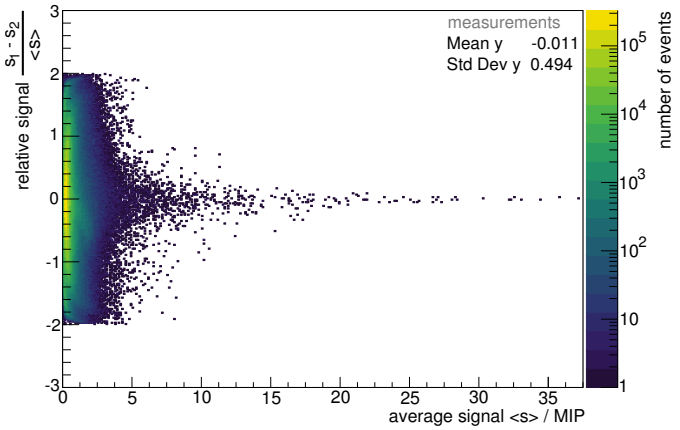

(a) MiniAMD in self-triggering mode. Relative signal as a function of the average signal measured in both modules in units of MIP.

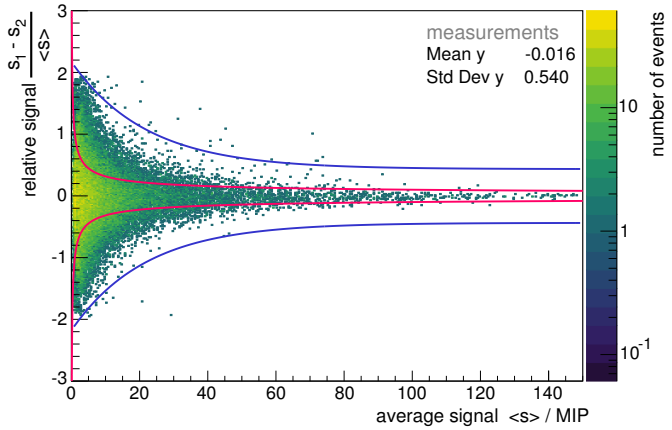

(b) MiniAMD in coincidence with the air shower array. Relative signal as a function of the average signal measured in both modules in units of MIP.

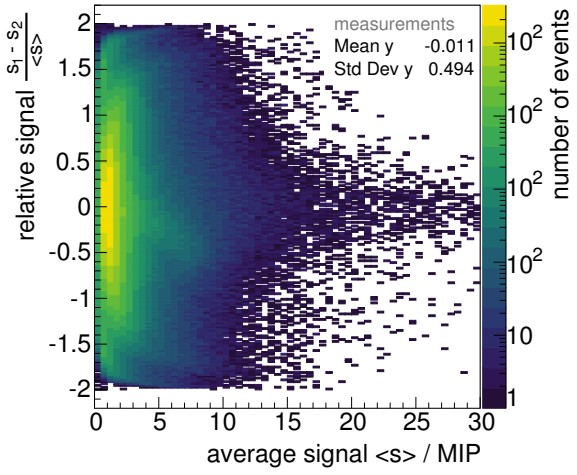

(c) MiniAMD in self-triggering mode. Zoom in the distribution of the relative signal as a function of the average signal measured in both modules in units of MIP. Standard configuration with module 1 located on module 2.

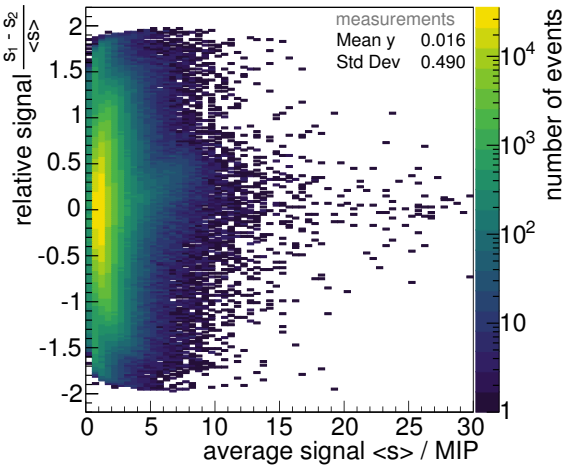

(d) MiniAMD in self-triggering mode. Zoom in the distribution of the relative signal as a function of the average signal measured in both modules in units of MIP. Switched module configuration with module 2 located on module 1.

Figure 9.26.: Comparison of the relative signal in MIP measured in the upper module (module 1) and the lower module (module 2) for the same events as a function of the average signal. The relative signal of both modules depicts a broad distribution for low-signal events narrowing with increasing average signal.

rough estimate, the study illustrates, that the measured distribution for averages signal larger than 20 p.e. can be well explained by the same signal detected by two different detectors. However, the average relative signal of both distributions is negative, indicating a slight tendency to larger signals in module 2 for both scenarios. To study this effect, the position of both modules was switched for a short time. While the default configuration was operated in self-triggering mode over a complete time of 100 hours, the switched setup was operated for 10 hours. Both configurations are presented in figure 9.26c and 9.26d, respectively, for the same signal regime. The average relative signal for the switched configuration is now positive indicating a slight tendency for larger signals in module 1, now the lower module. This is also confirmed for the data set of coincident events. To reduce the influence by the ambient temperature and the statistics, both configurations were also compared for the same amount of data taken at comparable temperatures. These studies confirm also a small increase for the lower module. The reason is that several particles undergo interactions in the material of the upper module, initiating small showers of secondaries. Those are registered as larger signal yield in the lower module.

Multiplicity as particle density estimator

The MiniAMD detector allows for two estimators for the particle density. The particle density is thereby a function of the shower energy and an important air shower quantity. Further influences are the distance to the shower core, the primary particle type, and intrinsic shower-to-shower fluctuations. First, the number of units or of stacks triggered per event, also referred to as *multiplicity*, is studied as possible estimator. It is expected that an increased particle density will trigger more detector units. Secondly, the overall signal registered in the detector is investigated.

CORSIKA simulation predictions

As the air shower array is not calibrated, the energy of the shower candidate is unknown. CORSIKA simulations are used to roughly verify a proper performance of the demonstrator. The corresponding simulations were already introduced in section 7.3.3. The shower core positions are homogeneously distributed on a circular area. In the circle center, the MiniAMD demonstrator is located. Additionally, the air shower array stations are assumed as circular detectors. For each event, all (anti-)muons and electrons/positrons of the shower, which reach the active area of the units, are registered as a hit with a signal yield of 1 MIP. These simulations provide an estimate of the expected particle density distribution, but also of the expected unit multiplicity distribution. To enable a comparison to the measured distribution, the simulated distribution of counts is translated in a distribution of the event rate.

Based on this consideration, a decreasing event rate is expected for higher unit / stack multiplicity if the MiniAMD detector response is correlated to the particle density. The event rate is presented as a function of the cumulative multiplicity for both, number of triggered units and stacks, in figure 9.27. The distributions for data sets of MiniAMD operated in self-triggering mode and in coincidence with the air shower array are compared. For both a decrease with increasing multiplicity can be found. However, for MiniAMD in self-triggering mode a strong increase for low numbers of units /stacks is apparent. Small particle densities, as single atmospheric muons, are dominating. For larger number of triggered units / stacks, both distributions converge. Both measured distributions agree well with those determined by CORSIKA simulations. The simulated event rate prediction for both experiments operated in coincidence is slightly higher than the measured rate. This indicates a lower trigger efficiency for the setup than assumed in the simulations.

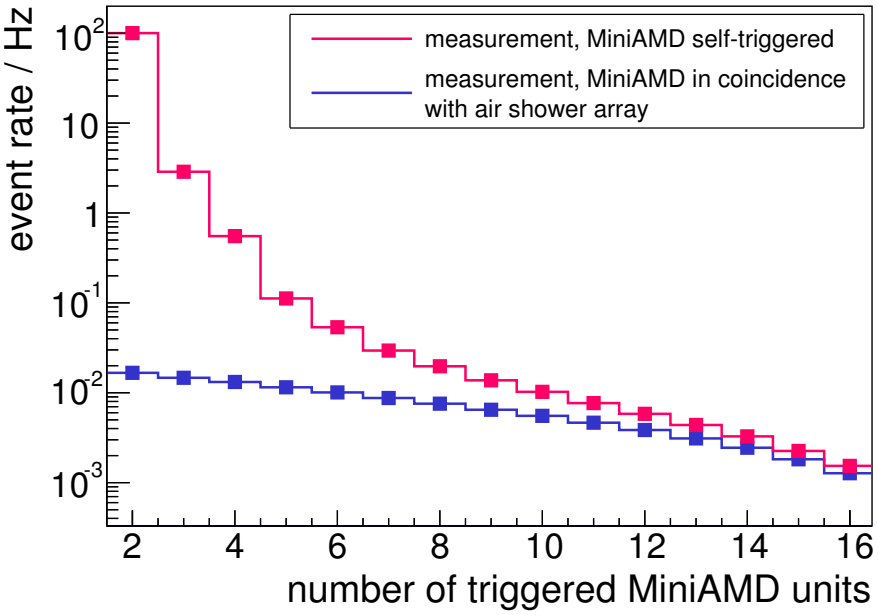

(a) Event rate as a function of cumulative unit multiplicity.

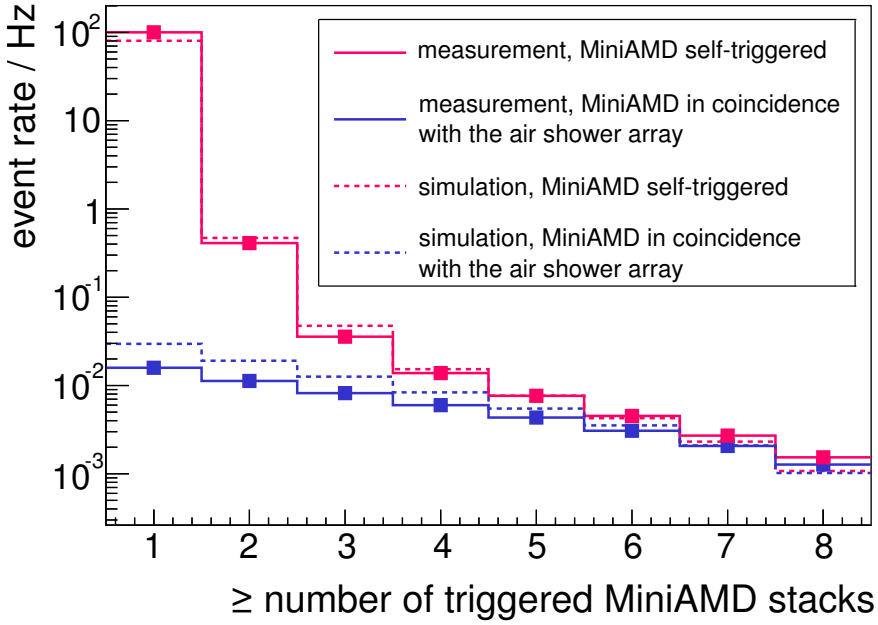

(b) Event rate as a function of cumulative stack multiplicity.

Figure 9.27.: Event rate in Hz as a function of cumulative unit and stack multiplicity of the MiniAMD demonstrator. Data sets of MiniAMD operated in self-triggering mode and in coincidence with the air shower array are compared. The first requires one triggered stack. The latter an additional, external trigger by the air shower array. Poisson statistics is used to determine the uncertainty of each data point.

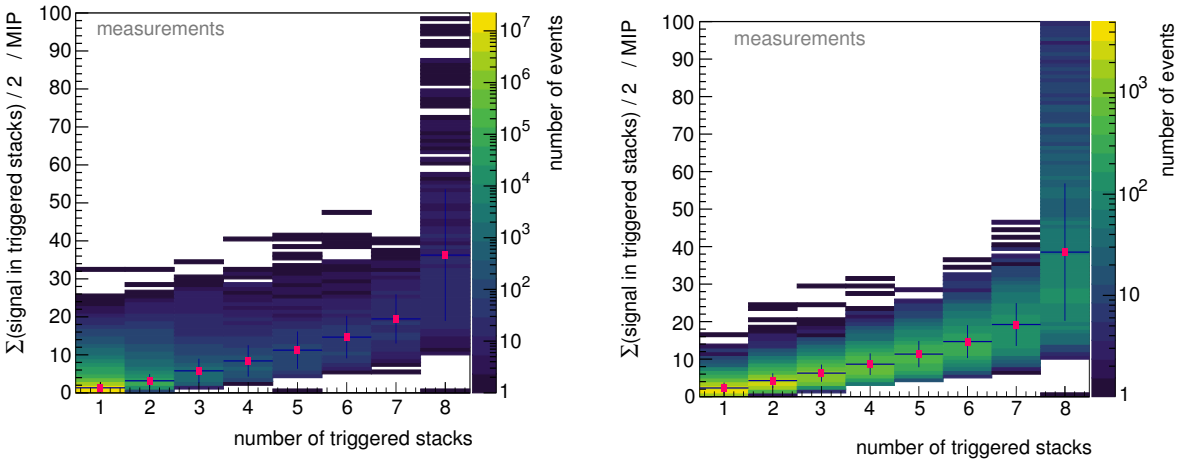

(a) MiniAMD in self-triggering mode. The lowest stack multiplicity is dominating with an average signal of 1 MIP.

(b) MiniAMD in coincidence with the air shower array. The events are more homogeneously distributed along the stack multiplicity.

Figure 9.28.: Average signal in MIP as a function of the number of triggered stacks. The average is calculated for the signal in MIP of all units which have exceeded the threshold. The profile corresponds to the mean signal of all events for the corresponding stack multiplicity. The uncertainties refer to the rms of the underlying distribution. The signal is increasing with an increased number of triggered stacks. A pile-up effect is visible for the maximum stack multiplicity.

Average signal as particle density estimator

Assuming the detected signal $\langle s \rangle$ and the multiplicity as estimator for the particle density, a correlation between both observables is expected. In figure 9.28, the average signal is presented as a function of the number of triggered stacks. The profile refers to the mean of all events included in the underlying histogram bin for each multiplicity. The uncertainty bars are referring to the rms of the distribution. As expected the signal is increasing with an increased number of triggered stacks. The correlation confirms both observables as possible measure for the particle density contained in the air shower candidates. The broad signal distribution at the maximum stack multiplicity results from the pile-up of all events which would have triggered more stacks if available. For MiniAMD in self-triggering mode, triggers of single stacks by individual muons are dominant. For MiniAMD operated in coincidence, a large fraction of the events is still included in the lowest stack multiplicity bin. A more homogenous distribution to higher multiplicities is depicted. Furthermore, the distribution of measured signals for each multiplicity bin is narrower for lower numbers of triggered stacks than in the self-triggering mode. However, the profiles of both configurations indicate a comparable performance in average.
As last step, the event rate as a function of the *particle density* is discussed. The particle density is defined, in the scope of this thesis, as the average signal $\langle s \rangle$ divided by the MiniAMD area of $1\,\mathrm{m}^2$. It is given in units of $\mathrm{MIP}/\mathrm{m}^2$. As the particle density is a function of the shower energy, a strong decrease for higher particle densities is expected which is predicted by the cosmic ray spectrum. Several distributions are shown in figure 9.29. First, a data set measured by MiniAMD in self-triggering mode is presented. It depicts a higher event rate for low densities (smaller than $20\,\mathrm{MIP}/\mathrm{m}^2$). Secondly, the distribution of data taken in coincidence with the array is shown. The distribution is less steep in the mentioned density regime and the large deviation is expected due to the stricter trigger criterion for the coincident setup. Both distributions converge for large densities and depict the

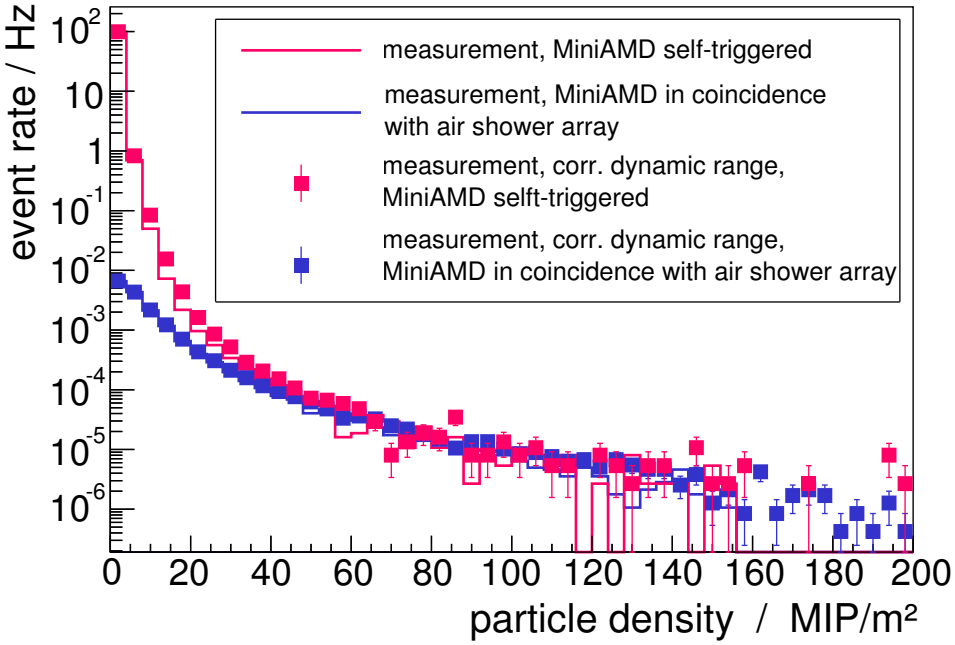

(a) The measured density distribution is compared to the distribution of the same data corrected for the non-linearity of the SiPM dynamic range. The correction allows signal yields larger than the former maximum of 150 MIP per event.

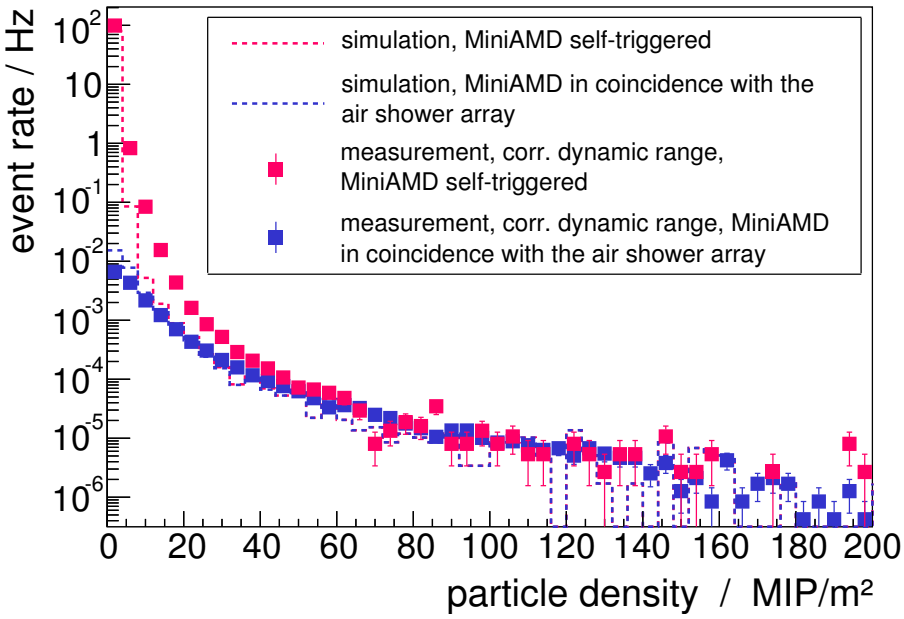

(b) The measured density distribution, corrected for the non-linearity of the SiPM dynamic range, is compared to the simulated particle density. The density is determined by CORSIKA air showers. The distribution measured in coincidence can be well described. The self-triggered distribution is underestimated by the simulation in the low particle density regime.

Figure 9.29.: The average signal $\langle s \rangle$ detected by the MiniAMD detector per MiniAMD area is expected to be an estimator for the particle density. The event rate as a function of the estimated particle density in units of MIP/m^2 is presented. A comparison of MiniAMD operated in coincidence with the array and in self-triggering mode depicts an increase event rate for low densities for the latter. Both distributions converge for large densities. Additionally, a simulated density profile is shown.

expected decrease in the event rate for increasing particle densities. The measurement indicates that MiniAMD is able to detect air shower candidates without the need of an external experiment. Additionally, a simulated density profile, obtained by CORSIKA simulations, is depicted. It is compared to the measured density distribution corrected for the influence of the non-linear dynamic range of SiPMs.

Influence by the non-linear dynamic range of SiPMs

The highest signals measured in one MiniAMD unit are in the order of 25 MIP per event. Each MIP corresponds to an average signal of (23.67± 2.47) p.e. detected by each of the eight SiPMs. The detected number of photons is in the order of 25 MIP × 23.67 p.e./MIP ≈ 600 p.e. However, the registered signal of a SiPM in p.e. is not directly proportional to the impinging photons (cf. chapter 4). The applied SiPM type has a total number of cells of 667. The registered amount of photons is thus in the regime of the dynamic range, which is strongly impaired by saturation effects. In principle, based on the knowledge of the SiPM behavior a recovery of these signals is possible [205]. Based on the simple approach presented in equation 4.7 on page 50, a number of photons corrected for the dynamic range is calculated for each unit of an event. The corrected signal distribution is presented in figure 9.29a. It allows for signal yields larger than the former maximum of 150 MIP per event detected so far and indicates the need of the consideration of the dynamic range.

The measured and corrected density distributions for both operation scenarios agree well with the simulated density profile despite the simple approach that each particle passage corresponds to a signal of 1 MIP. The comparison is depicted in figure 9.29b. The small deviations in the low density regime of the coincident data set are likely introduced by a trigger inefficiency while requesting an external trigger by the array. For the low density regime of the self-triggered distribution, measurements depict a significantly stronger contribution than predicted by the simulations. Additionally, a larger absolute trigger rate is found for the measurements. This may indicate background events initiated by SiPM darknoise or passages of particles not originating from cosmic ray induced air showers.
The average signal $\langle s \rangle$ distribution is shown in figure 9.30. The distribution includes data measured by MiniAMD in coincidence with the air shower array. It is presented with an equal bin width in logarithmic scale. Therefore, the number of events in a bin N is normalized to the average signal in the corresponding bin

$$\frac{\mathrm{d}N}{\mathrm{d}s} = \frac{\mathrm{d}N}{\mathrm{d}\log_{10}(s)} \frac{\mathrm{d}\log_{10}(s)}{\mathrm{d}s} = \frac{\mathrm{d}N}{\mathrm{d}\log_{10}(s)} \frac{1}{s\ln(10)} \quad . \tag{9.14}$$

The signal is expected to be also a function of the cosmic ray energy. Thus, it should follow the cosmic ray energy spectrum as a first approximation. Fitting a power law

$$f(\langle s \rangle) = a_1 \cdot \langle s \rangle^{a_2} \tag{9.15}$$

to the signal distribution for $\langle s \rangle$ larger than 15 MIP, indicates a slope with a value of $a_2 = -2.52 \pm 0.02$. This is, in first order, compatible with the expected spectral index of -2.7.

Energy threshold

Each cosmic ray experiment has its own lower energy threshold for the measurement of air shower candidates.
The minimum energy is influenced by several geometrical detector properties as the spacing between detector stations, the size and volume of the detector stations, its solid angle Ω, and effective

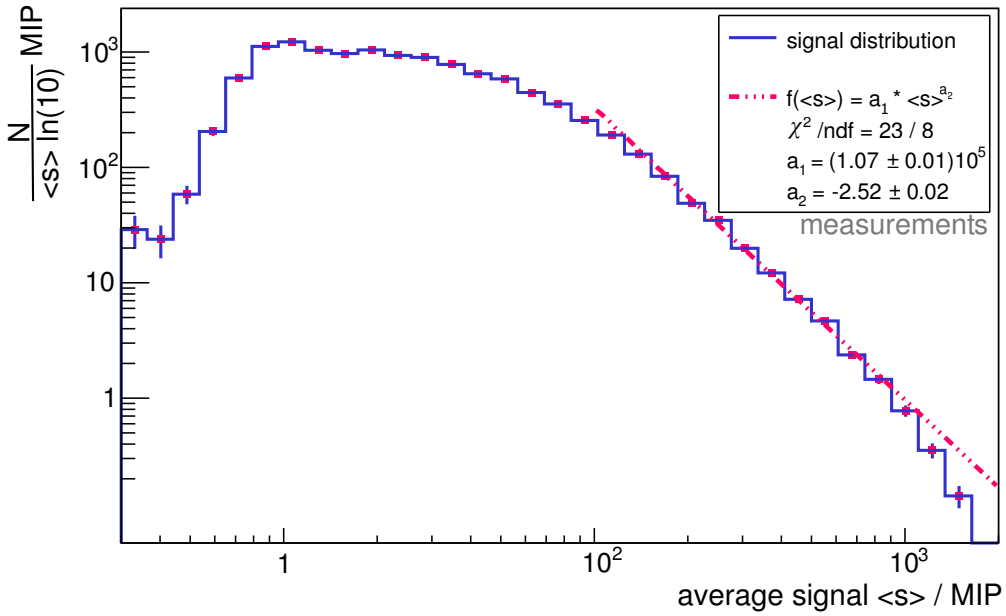

Figure 9.30.: The average signal $\langle s \rangle$ detected by the MiniAMD detector is expected to be a function of the cosmic ray energy. The number of events N, measured in coincidence with the air shower array, is shown as a function of the average signal detected $\langle s \rangle$. The number of events is normalized to the average signal $\langle s \rangle$ of the corresponding bin (cf. equation 9.14). In addition, a power law fit (cf. equation 9.15) is depicted. See text for discussion.

area A_{eff}. It depends further on characteristics as the chosen minimal trigger criterion or the bandwidth and capability of the electronics. A proper determination to allow for comparisons to other experiments has to be based on extensive MC simulations or detailed measurements.
The presented CORSIKA simulations are used to determine an estimate for the lower energy threshold for two setups. First, the air shower array is investigated. The measured event rate with a hardware trigger criterion of two stations is 0.033 Hz. In simulations, the minimal energy threshold is varied until the simulated event rate matches the measured event rate. The same trigger criterion is imposed. The corresponding lower energy threshold is around 50 TeV.
The same procedure is applied to the simulated events for the MiniAMD detector. The measured event rate with a hardware trigger criterion of 2 stacks and a threshold at 2.5 p.e. is 0.51 Hz. Triggering two stacks would require at least two muons at the same time. A coincident trigger due to atmospheric muons only is highly unlikely, so that an event with two stacks in coincident can be assumed to be an air shower candidate. For this setup, the lower energy threshold is around 100 GeV.

9.4.3. Studies of MiniAMD based on array reconstruction

The array allows for a reconstruction of the shower arrival direction due to an excellent timing resolution. For the MiniAMD detector, only the timeline of the discriminator states indicates a rough time distribution but with timebins of 10 ns. Therefore, a shower direction cannot be determined by MiniAMD in self-triggering mode. In figure 9.31, the azimuthal and zenith angular distributions are compared for events detected in coincidence with the array and for events which have not triggered MiniAMD. The average ratio of the event rate of coincident events compared to all events registered by the array in the same time period is 44%. Whereas a fraction of 85% of all events,

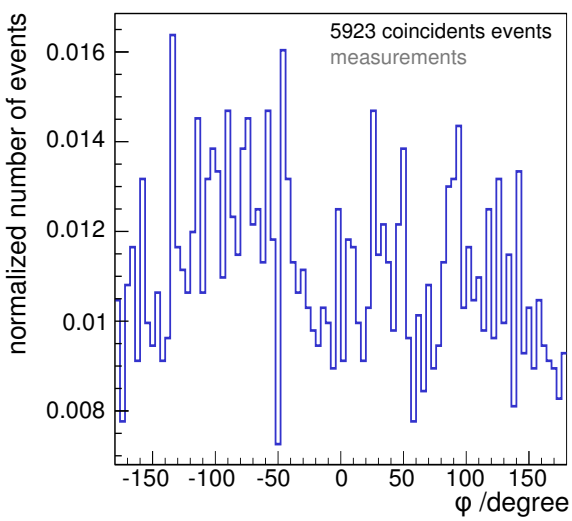

(a) Azimuth distribution for coincident events of MiniAMD and the air shower array.

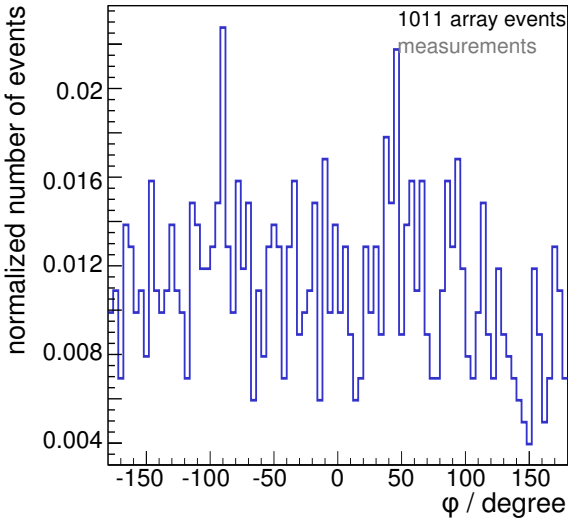

(b) Azimuth distribution for events detected by the air shower array, but vetoed by MiniAMD.

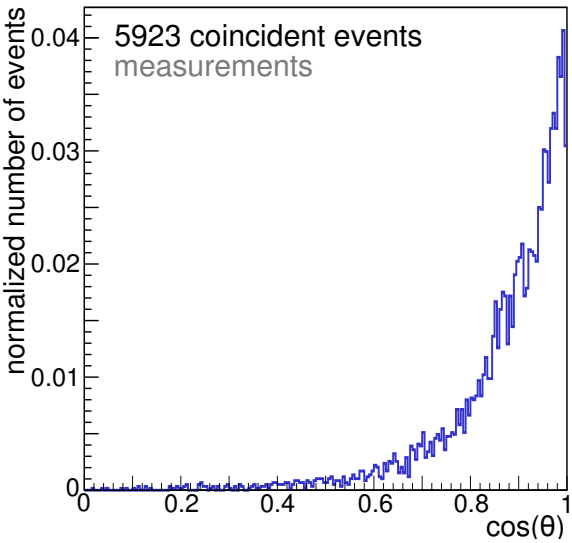

(c) Zenith distribution for coincident events of MiniAMD and the air shower array.

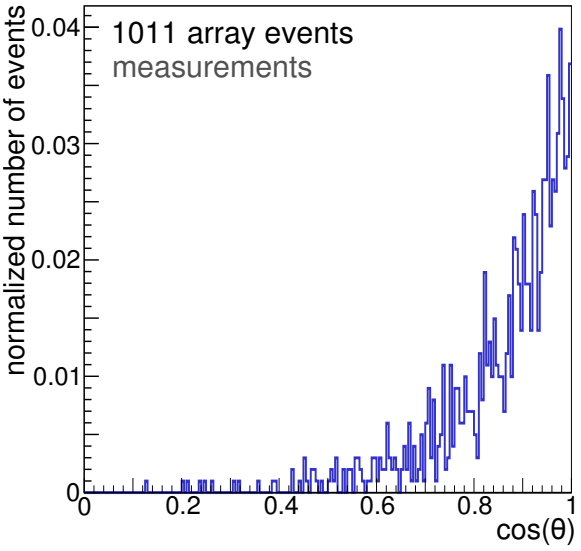

(d) Zenith distribution for events detected by the air shower array, but vetoed by MiniAMD.

Figure 9.31.: Comparison of the angular distribution of events detected in coincidence by the air shower array and MiniAMD (left) and of events detected by the air shower array only (right). Only events in time periods in which both experiments were active are studied. Shown is the event rate as a function of the zenith angle $\cos(\theta)$ (bottom) and azimuthal angle ϕ (top) in degree.

for which the geometry was reconstructed by the array, is also registered by MiniAMD. As for the reconstruction algorithm more than 2 array stations have to be triggered, the particle density and thus the probability for a coincident measurement is increased compared to the average ratio. Both angular distributions depict a comparable behavior. A significantly larger event loss is not visible in any angular range. A Kolmogorov-Smirnov test confirms that the shape of both distributions is well compatible. They can be understood as sub-samples of the angular distribution of the independent array data presented in the previous section 9.3. Both experiments indicate the station multiplicity and the average signal as important observables for the particle density. As confirmation, the ob-

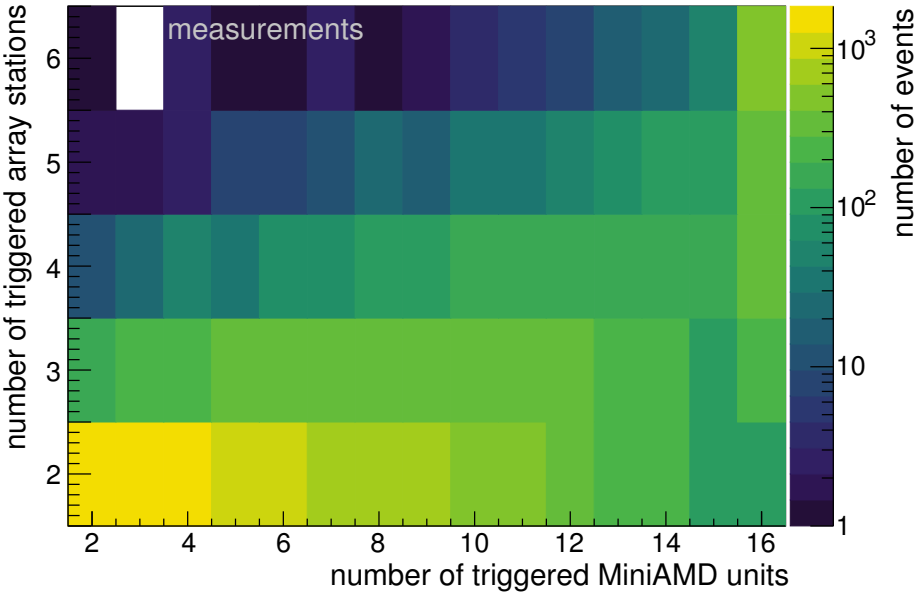

(a) Correlation of the number of triggered units in the MiniAMD demonstrator and the number of triggered stations of the air shower array.

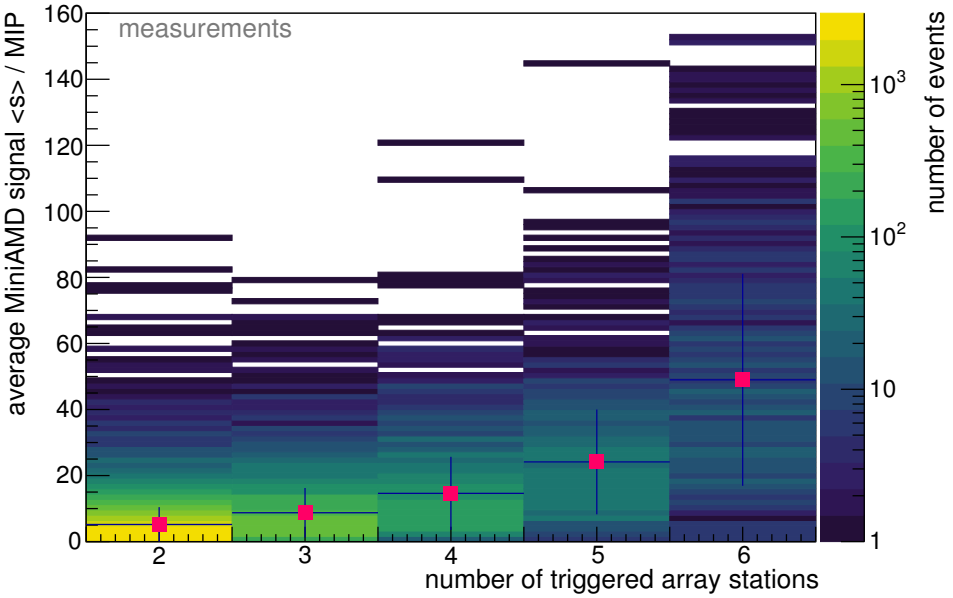

(b) Correlation of the average signal $\langle s \rangle$ registered in the MiniAMD demonstrator and the number of triggered stations of the air shower array. The signal detected by MiniAMD is defined as the combined signal of all units above threshold divided by two.

Figure 9.32.: Correlation of important characteristics of MiniAMD and the air shower array. An increase of the average signal for a larger number of stations is apparent. An increased energy deposit is thus indicated in both detectors. A correlation of station and unit multiplicity is apparent indicating that both observables are rising with increasing particle density on ground.

servables are compared to each other. A correlation with positive correlation coefficient is expected if the same air shower candidates are investigated. The correlation will be limited as the particle density distribution is not homogenous within the shower footprint but is steeply falling with the distance to the shower core. Furthermore, intrinsic fluctuations within the shower and detection efficiencies of both experiments will influence the result.
First, the number of triggered air shower stations as a function of the triggered MiniAMD units is presented in figure 9.32a. On average, the graph shows a rising unit multiplicity with increasing multiplicity of the array. The distribution is dominated by events including two MiniAMD units and two array stations. In figure 9.32b, the average signal $\langle s \rangle$ detected in the MiniAMD is compared to the number of triggered array stations for all coincident events. The profile depicts the mean of the underlying distribution in each station multiplicity bin. The uncertainty on each profile point corresponds to the corresponding rms. The signal in MiniAMD is increasing with increasing number of stations. The signal distribution for the maximum station multiplicity is broadened due to a pile-up effect. In figure 9.33a, the correlation of the average signals detected by both experiments in coincident events is presented. The average signals measured by MiniAMD and by the array, respectively, show a less significant correlation. A broad distribution is apparent for the low-signal regime. For events with a large signal a more pronounced correlation becomes visible. To reduce the amount of background events, the number of array stations needed is increased to three stations. The MiniAMD trigger still corresponds to at least one stack, where the signal in both units of the stack exceeds a 2.5 p.e.-threshold, and a trigger of the array in coincidence. The signal distribution of the reduced setup is presented in figure 9.33b. Additionally, a profile depicts the mean of the underlying distribution in each station multiplicity bin. The uncertainty on each profile point corresponds to the corresponding rms. A strongly improved correlation can be identified. The event rate as a function of the station multiplicity is presented in figure 9.34a. In the top figure, the rate is presented for coincident events. The event rate is exponentially decreasing with station multiplicity. In the bottom figure, the rate is presented for events only detected by the air shower array. The distribution is highly dominated by the lowest station multiplicity of two triggered array stations. Around 92% of all events is included in this bin and around 98% in the first two bins, respectively. These events correspond to low particle densities as indicated by CORSIKA simulation studies. For larger station multiplicities, trigger efficiency effects are dominating as sources of the event loss.
The average signal seen by the air shower array as a function of the station multiplicity is presented in figure 9.34b. Again coincident events are compared to events which are vetoed by MiniAMD. Both distributions indicate a comparable increase with station multiplicity. A slight, systematic tendency to lower average signals is indicated for the vetoed events for small station multiplicities. For larger station multiplicities, they are compatible within the uncertainty bars.

As a summary, both experiments react, as expected, comparable to the same air shower candidates. This proves the ability of MiniAMD not only to detect but also to study important air shower characteristics.

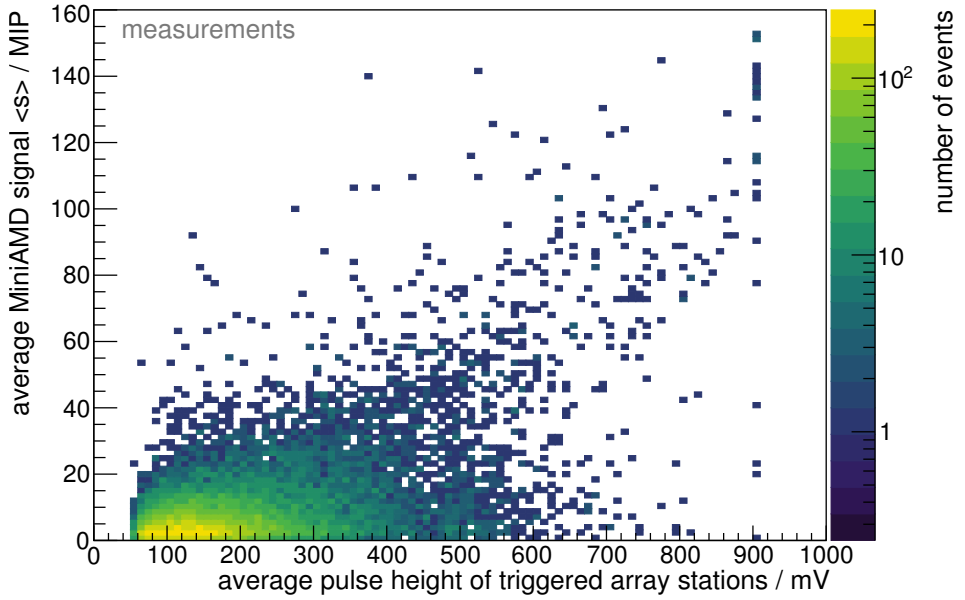

(a) Data set including events at which at least two array stations and at least one MiniAMD stack are triggered.

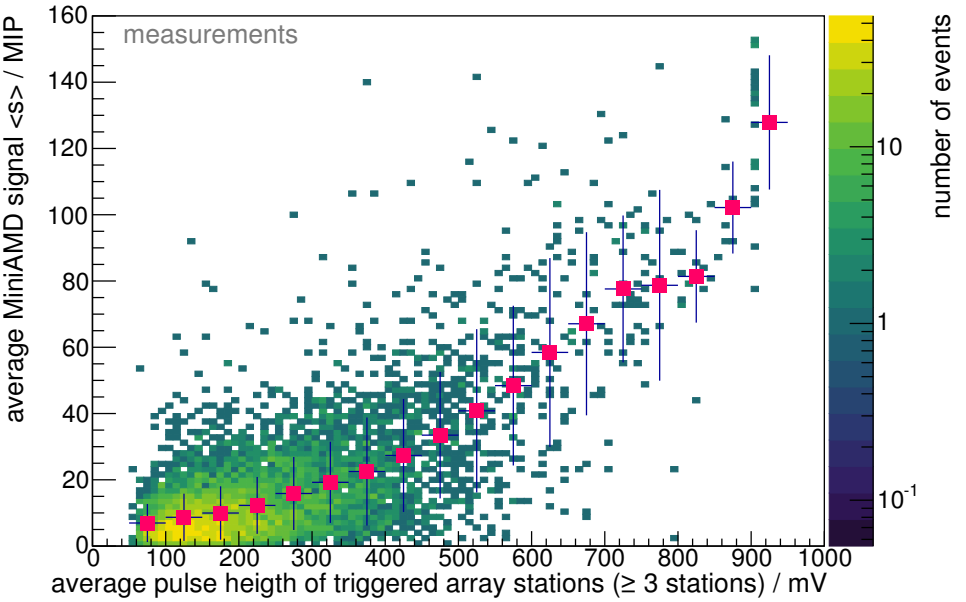

(b) Data set including only events at which at least three array stations and at least one MiniAMD stack are triggered.

Figure 9.33.: Correlation of the average signal measured by the MiniAMD demonstrator in units of MIP and the average pulse height measured by triggered stations of the air shower array in mV.

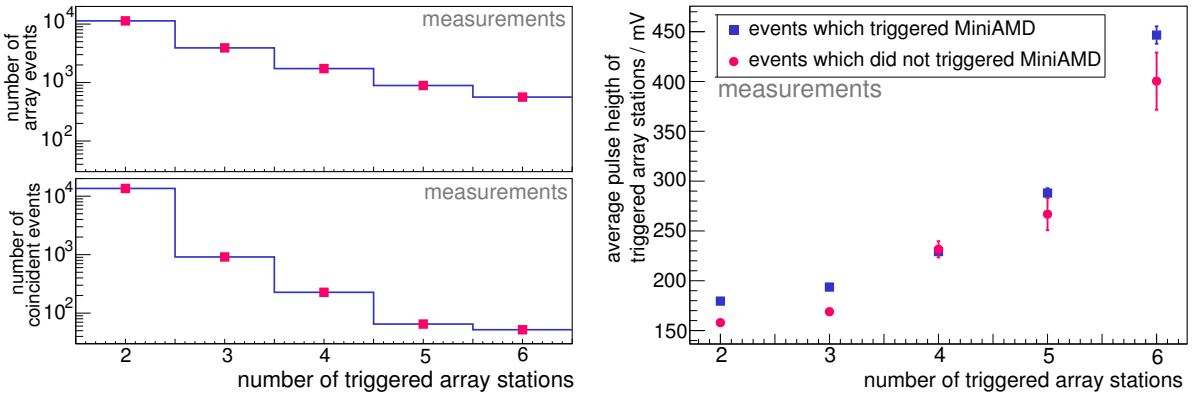

(a) Event rate as a function of station multiplicity for coincident events (top) and air shower array only events (bottom).

(b) Average signal height measured by array stations for coincident events with MiniAMD and for events which are vetoed by MiniAMD.

Figure 9.34.: Comparison of the event rate as a function of the station multiplicity and as a function of the average signal seen by the air shower array for events which are also detected by MiniAMD and for events which are only registered by the air shower array. Only events in time periods in which both experiments were active are studied.

9.5. Discriminator status

Besides the signal in ADC count of each unit (*ADC event*), the time trace of the binary status of the discriminators (*discri event*) can be used to study the events registered by the MiniAMD detector. The first is referred to as *integration method*, the latter as *counting method*. An active discriminator status corresponds to a signal larger than the imposed threshold. The status becomes inactive while the signal falls again below the threshold. The time a discriminator is active is referred to as *time over threshold* t_{th}. A counting of particle passages is possible if the particle density is small and a distinction between signals of individual particles is feasible.
A discri event consists of the timeline of the discriminator status of all MiniAMD units in 10 ns timebins. In each discri event, 128 timebins are included. Further stored information are the event time and number.
Three different configurations can be requested by enabling the corresponding configuration bits of the readout:

1. Discriminator events are generated and stored even if the buffers of the corresponding ADC event is full.

2. Discriminator events are synchronized with respect to the ADC events. As option, triggers are only processed and stored when an event of both types can be generated.

3. Discriminator events are synchronized with respect to received external triggers. As option, the discri events are automatically stored if an external trigger has been received. This is regardless of the actual MiniAMD state. Thus, empty discri events will be included in the data stream. The event number will refer to all external triggers received. A small probability of a mismatching of the discri events to the ADC event is identified. A fraction of 3% of all events were not stored in the discriminator trace. The reason is an overflow in the discri event buffer.

In this section, discri events registered by the MiniAMD detector, which is operated in coincidence with the air shower array, are discussed. Thus, the third configuration is chosen. The timestamp of

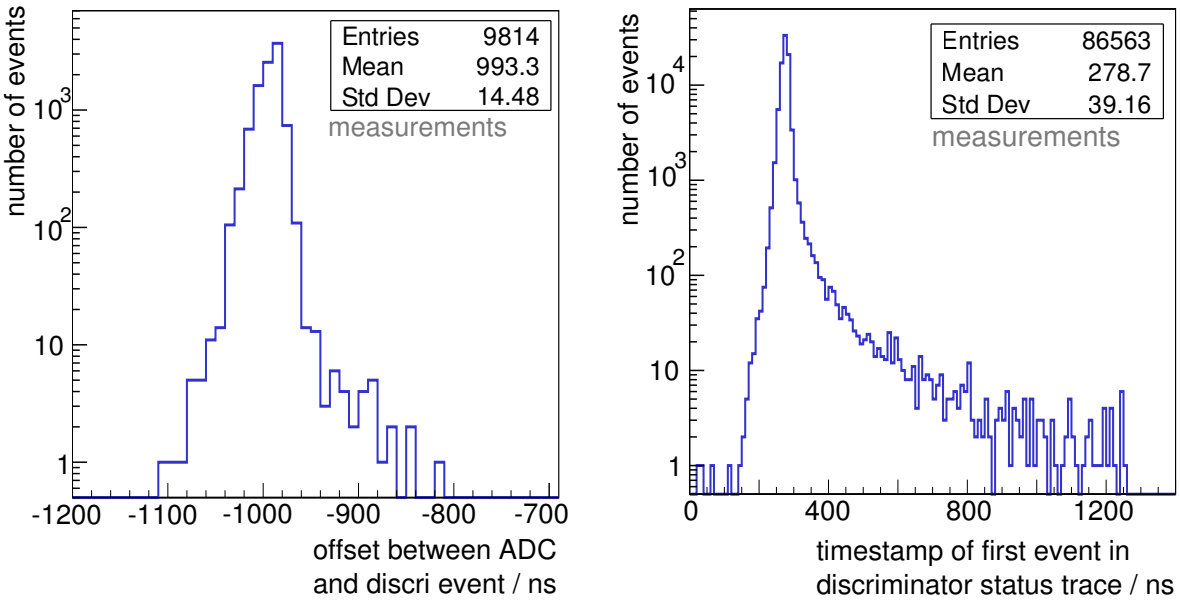

(a) Time offset between ADC and discri event. An offset by 1 μs is expected. The offset is based on the delay by the cable length and the trigger decision. The delay by cable is around 300 ns. The trigger decision is based on the time up to timebin 64 referring to a time of 640 ns.

(b) Timestamp at which the threshold was exceeded for the first time in the discriminator trace. Events of all units are included. A sharp peak at 300 ns can be confirmed. The time refers to the delay of the air shower array trigger due to cables.

Figure 9.35.: Comparison of timestamps referring to matching ADC and discri event registered by the MiniAMD detector. The detector was operated in coincidence with the air shower array.

the ADC event is defined by the signal of a detector unit above threshold. To determine if an event has fulfilled the trigger requirements, the first 64 time bins of the discriminator trace are taken into account while later time bins are not included in this decision. A further delay of 300 ns is expected due to the long cables used to form an external trigger by the array and to feed the signal to the MiniAMD detector. This results in an expected offset between the timestamp of the registered ADC and discri event of 64 timebins + 300 ns = (640 + 300) ns $\approx 1\,\mu$s. This is confirmed by comparisons of the timestamps for coincident ADC and discri events as shown in figure 9.35a. Additionally, in figure 9.35b is the distribution of the timestamp at which the threshold was exceeded for the first time in the discriminator trace. In the data set, all units of the MiniAMD detector are included. The tail to delayed timestamps indicates the temporal extension of air showers over several $\mathcal{O}(10\,\text{ns})$. A deviation in the first timestamp between individual units is not found. Besides the start of an event, the time over threshold t_{th} is of particular interest. It increases with deposited energy and the number of particles arriving.

Presented in figure 9.36, is the comparison of the number of events as a function of the time over threshold t_{th} for three configurations. In pink, measurements performed with the muon tomograph as external detector are presented. The setup and further analyses within this context are discussed in section 8.4. The data set includes only single particles which are triggered by MiniAMD. An external trigger in coincidence was requested. A sharp peak around $t_{\text{th}} = 80\,\text{ns}$ is apparent.
The maximum of the muon tomograph distribution is normalized to the maximum of the one obtained by the MiniAMD demonstrator operated in coincidence with the air shower array. Here, the trigger criterion for MiniAMD is at least one triggered stack with a discriminator threshold of 2.5 p.e. The time over threshold for all units of the events are included in the data set. Three components are apparent. The single particle component around $t_{\text{th}} = 80\,\text{ns}$, a longer time com-

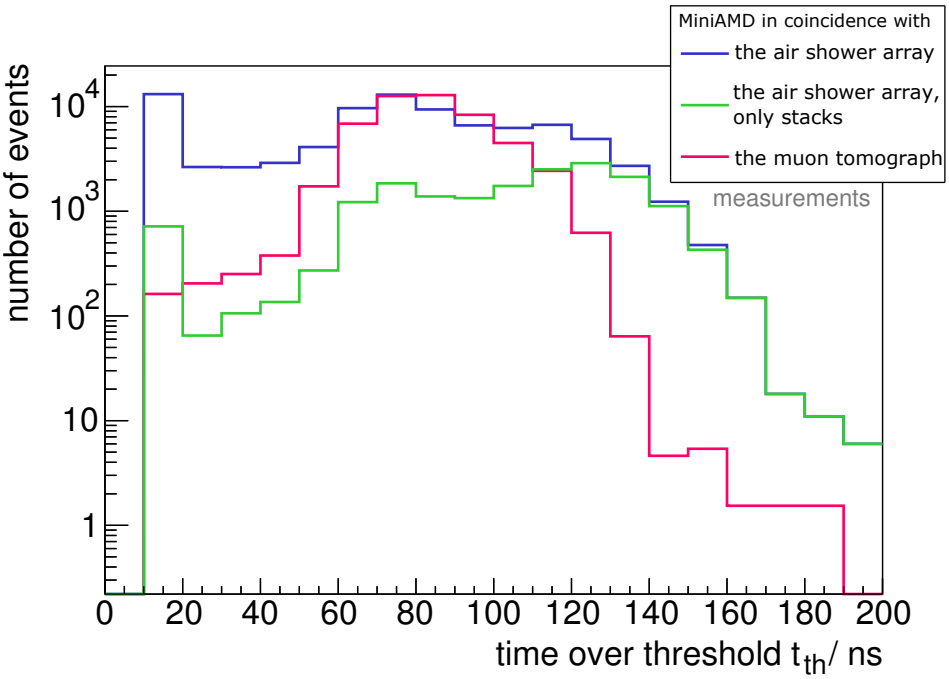

Figure 9.36.: Comparison of the number of events as a function of the time over threshold t_{th} for three configurations. In blue, the number of events is shown for the MiniAMD demonstrator operated in coincidence with the air shower array. In green, the same data set is shown, but only units, included in a triggered stack, are taken into account. In pink, measurements performed within the muon tomograph are presented. They are normalized to the maximum of the blue histogram. Three components are visible: Low-signal component, single atmospheric muons and air shower candidates. See text for more information.

ponent corresponding to air shower candidates and a low-signal component with a shorter time over threshold. The latter is assumed to be clipping muons or low energetic background particles which deposit only a small amount of energy. Of those, only clipping muons are also visible in the measurements in coincidence with the muon tomograph. As the overall amount of brief events is strongly reduced by an order of magnitude compared to measurements with the air shower array, a strong contribution of a further low-signal component is indicated. Furthermore, a significant increase of the 10 ns bin is apparent. It is assumed to refer to darknoise events. The threshold of 2.5 p.e. is chosen at the lower limit in terms of purity with a signal to noise ratio of roughly 1. Besides choosing a stricter threshold, also including the information on the time over threshold can be used to increase the purity of the data set. This has to be studied in more detail in future analyses. In green, the same data set is shown, but only units included in a triggered stack are taken into account. Thereby, a large amount of background events can be suppressed but also atmospheric muons are lost. The large time component of air shower candidates is unchanged. To study the potential of the discriminator state for future analyses, the signal in MIP generated by the ADC event is compared to the number of active discriminators in figure 9.37. The signal of the ADC event corresponds to the sum of the signal in MIP registered in all units above threshold. Figure 9.37a and 9.37b depict only events for which the first registered active state of the discriminators is taken into account. Thus, the maximum achievable number of active discriminators refers to events at which all 16 units were above threshold. A clear correlation between the signal in MIP and the discriminator status is visible. However, the correlation is not linear as indicated by the profile in figure 9.37a. The data points of the profile refer to the average of all events included in

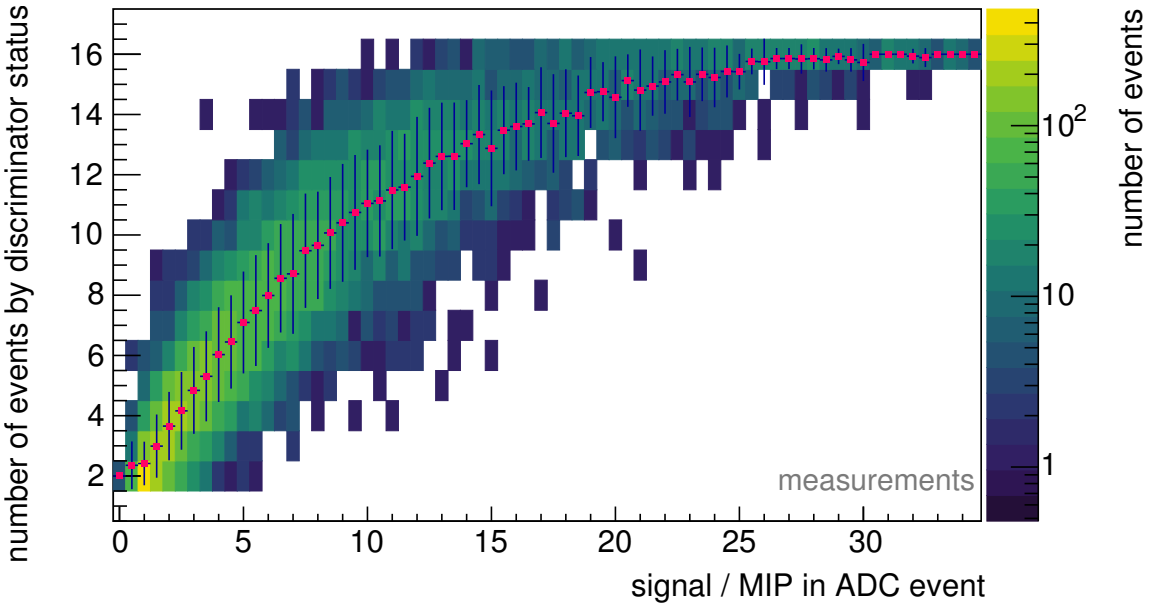

(a) Zoom on the correlation between the number of active discriminators and the signal in MIP. The correlation is visible up to the maximum achievable 16 discriminators above threshold. For the data set, only the first discriminator status is taken into account. The data points of the profile refer to the average of all events included in the underlying 2D histogram. The uncertainty bars correspond to the rms of the event distribution.

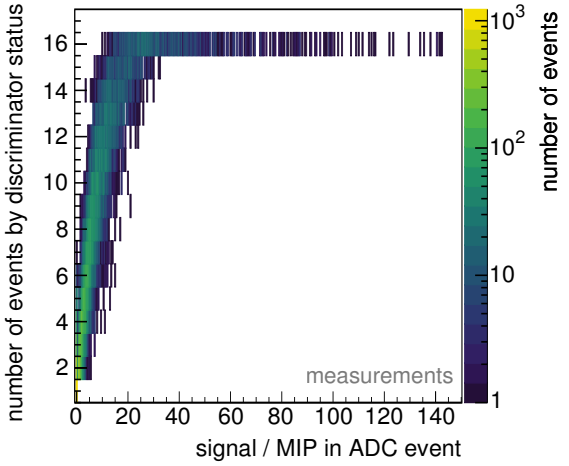

(b) For the data set, only the first discriminator status is taken into account. Additionally, discri events which have not passed the trigger criterion of one triggered stack are included with a signal of zero MIP.

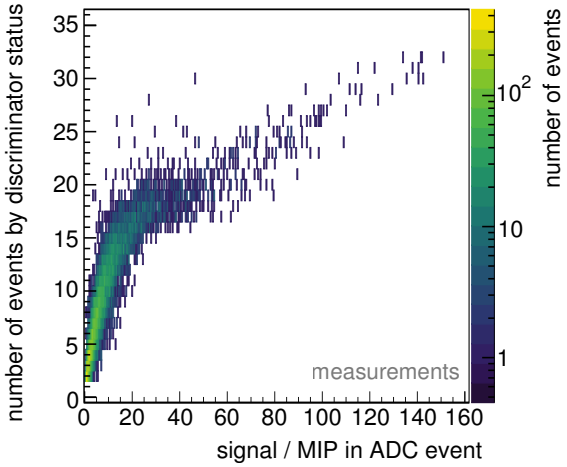

(c) The sum of all active discriminators in the timeline of an event is shown as a function of the signal yield in MIP.

Figure 9.37.: Correlation of number of events determined by the discriminator status and by the ADC event. The latter corresponds to the sum of the signal in MIP registered in all units above threshold. The data were taken in coincidence with the air shower array. The hardware trigger criterion is one triggered stack with a discriminator threshold of 2.5 p.e. in the MiniAMD detector and an external trigger received from the array.

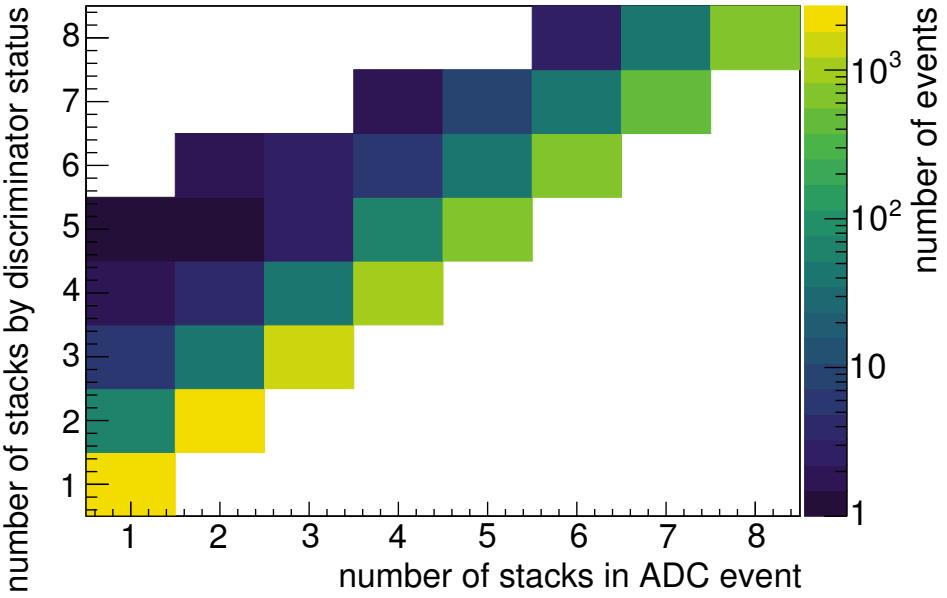

Figure 9.38.: Comparison of number of stacks registered in the discri and in the ADC event.

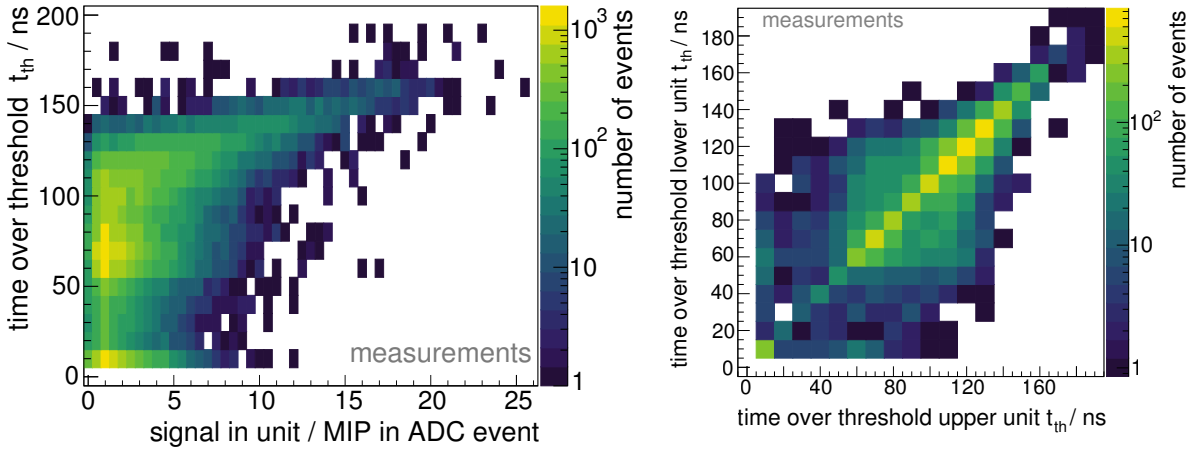

(a) Correlation of the time over threshold and the signal in MIP for the matching discri and ADC event of individual units.

(b) Correlation of the time over threshold for the upper and the lower unit in a triggered stack.

Figure 9.39.: The time over threshold as important quantity for future cosmic ray air shower analyses.

the underlying 2D histogram. The uncertainty bars correspond to the rms of the event distribution. First, the signal in MIP is reduced compared to the discriminator state. Low-signal particle and MIP particle passages result in the same discriminator state if exceeding the threshold. For increased signal yields, at a signal yield of roughly 8 MIP, the discriminator state starts to underestimate the amount of traversing particles. Individual particle passages cannot be identified anymore. In figure 9.37b, all discri events are presented which would have been registered if a more relaxed trigger criterion of at least one unit instead of a complete stack over threshold had been required. As no coincident ADC event was generated, these events lie within the zero signal bin region. The more relaxed criterion would have increased the number of coincidence events by 12%. Up to five units were triggered without producing a stack trigger. Figure 9.37c takes the complete timeline into account allowing several active states of a detector unit. A plateau for signal yields between 25 and

45 MIP is followed by a slow increase for an increasing signal registered in the ADC event. The rise is introduced by air shower candidates initiating not only a higher particle density but also a larger temporal extension.
As the timeline is larger than the integration time of the ADC event, the discri events include particle passages not accessible for the ADC event. This is depicted in figure 9.38. A strong linear correlation with a factor equal to one between both event types is indicated. A small fraction of events ($\mathcal{O}(10\%)$) registers an increased number of triggered stacks for the counting method. No event with an increased number of stack in the ADC event is found. This proves a good functional matching of both event types.
For a larger particle density, the counting of active discriminator states is not efficient. However, the time over threshold is also increasing with signal yield and can be utilized for future analyses. In figure 9.39a, the time over threshold distribution is shown as a function of the signal in MIP detected in the corresponding unit. At larger signal yield, several particles may traverse a unit. Those don't arrive simultaneously at the unit and the resulting photon distribution at the SiPM will be extended. In figure 9.39b, a comparison of the time over threshold measured by the upper and the lower unit in a triggered stack are presented. A linear correlation with a correlation factor equal to one is determined. Large deviations within the time response indicate clipping muons which deposit less energy in only one unit or coincident events of a MIP particle and a background event.

The presented studies of the discriminator status confirm that MiniAMD allows not only information on the integrated charge, but also for additional information based on the time over threshold of the discriminator. Both observables depend on the deposited energy and thus on the number of impinging particles. A combined analysis may improve the ability to study particles.

9.6. Conclusions - MiniAMD as universal charged particle detector

Important performance parameters of the MiniAMD prototype are summarized in the following.

1. The MiniAMD detector is well understood and characterized. It allows for a continous monitoring of important operation parameters.

2. The signal yield of the MiniAMD detector can be best estimated by the average signal of both modules $\langle s \rangle = (s_1 + s_2)/2$.

3. The lower module indicates a slightly increased signal yield, probably due to secondaries produced in the traversed material.

4. The event rate registered by individual units is 12.7 Hz while MiniAMD is operated in self-triggering mode. This is well comparable to the expected atmospheric muon rate.

5. The average signal is increasing with the number of triggered units or stacks. The event rate is decreasing. All three observables, the average signal and both multiplicity types, are confirmed to be estimators of the particle density.

6. The average signal can be described as a function of the cosmic ray energy.

7. The MiniAMD detector is sufficiently detecting air shower candidates, with and without operated in coincidence with an external experiment.

Besides the ability to detect cosmic ray air showers and atmospheric muons, the presented studies demonstrate that MiniAMD is a perfect device to study charged particles in general. It is highly

sensitive to particle passages for a wide range of impinging particles. Both modules can be independently operated and positioned. Besides its standalone performance, it can be used as trigger or veto device for an external detector.
An exemplary application is the current test stand in Aachen for the Surface Scintillator Detector (SSD) of the AugerPrime upgrade of the Pierre Auger Observatory. For information on the ongoing upgrade, please see section 3.4. In total, 135 SSDs will be manufactured and assembled in the mechanical workshop of the Physics Institute III A of the RWTH Aachen University. A procedure, that utilizes MiniAMD, has been developed to validate the performance of each SSD detector individually before shipment. The procedure is presented in [206] and is based on the detection of atmospheric muons. The SSD is located between the two MiniAMD modules with both modules having a fixed vertical distance of 1 m to each other. By requesting a single stack of MiniAMD as trigger for the SSD, mainly vertical muons are registered. Both halves of the SSD are tested individually. The detected signal yield should be comparable between both halves of an individual SSD and comparable to the average signal yield of all tested SSD modules.
For a future application of the MiniAMD among its successful use as trigger and test device, the installation of a lab course experiment is a promising candidate. With both modules being robust, but lightweight, students can easily study characteristics of atmospheric muons or shielding effects with absorber introduced between both modules.

Chapter 10

Reconstruction of number of muons in air showers

The main aim of the AugerPrime upgrade (cf. chapter 3.4) of the Pierre Auger Observatory (cf. chapter 3) is an improved determination of the chemical composition of ultra-high energy cosmic rays (UHECR). The construction of an additional scintillator detector on top of each of the existing water-Cherenkov (WCD) detector stations of the surface detector (SD, cf. chapter 3.1) will make a decisive contribution. Thereby, an improved distinction between the muonic and the electromagnetic component of an air shower will be enabled. In [207], a first simple algorithm is presented which is based on the different response of the individual detectors to the same air shower particles. It aims to obtain a parameter correlated with the number of muons which reaches the ground. This so-called *matrix formalism* has a minimal dependence on hadronic interaction models. A short introduction of the algorithm will be given in the beginning of this chapter. In the following, the algorithm is adapted to give a first impression of the performance of a large-scale detector with SiPM readout for the reconstruction of the number of muons. The concept of this *Aachen Muon Detector* (AMD, cf. section 6.4) comprises the detector units (cf. chapter 6) presented in this thesis. It was originally designed as an alternative proposal for the AugerPrime upgrade. For this study, the scintillator-based detector is located underneath the WCD stations. The WCD station acts as a shielding of the electromagnetic component. Systematic uncertainties and existing biases will not be discussed in this chapter. The study is intended to give a general overview of the reconstruction capability of the detector concept presented. An analysis on the determination power of the primary particle type will not be given. The structure of the analysis will follow the analysis presented in [207] with minor modifications.

10.1. Matrix formalism

As a first approach, the *matrix formalism* is chosen for the investigation of simulated detector data in this thesis. The algorithm is based on the total signal of each WCD and scintillator detector station, e.g. the sum of the observed light yield at the SiPM of each detector unit of a scintillator detector station[1]. Therefore, it does not benefit from the multi-channel design of the scintillator detector. A future analysis may aim at a multi-variate approach which should be optimized for the chosen photosensors, electronics, and layout. This will enhance the presented performance.

[1] A discussion of the total signal of each detector type and its corresponding physical unit is discussed later in this section.

However, the matrix formalism allows to study the ability of an exemplary detector layout on the reconstruction of the number of muons as mass-sensitive observable. A direct relation between detector observables at ground to physical parameters as the particle fluxes of the electromagnetic[2] and muonic[3] component is enabled. The formalism was originally developed for the analysis of a double layered WCD station [208]. The algorithm is based on the idea that the electromagnetic (em) and the muonic (μ) component will result in different signal yields in an extended detector. It has been successfully adapted by simulations for the reconstruction of the muonic signal contribution in air showers detected by two detector stations: The *surface detector stations* (SSD) and the *water-Cherenkov detector* stations of the AugerPrime upgrade. Both stations are located at the same position on top of each other. The same part of the shower is simultaneously studied, but yields different responses in the complementary detectors. The detailed analysis is presented in the doctoral thesis of David Schmidt [207]. To allow an adaption to the detector presented in this thesis, a comparable setup is chosen. Main difference is that the detector is located underneath and not above a WCD station. The signal of the scintillator detector under study is referred to as S_{scin}, the signal of the WCD station as S_{wcd}. These are the detector observables which are directly accessible in a real experiment.
The complete signal in each detector station is a combination of the signal introduced by the individual components.

$$S_{\mathrm{em}} = S^{\mathrm{em}}_{\mathrm{scin}} + S^{\mathrm{em}}_{\mathrm{wcd}} \tag{10.1}$$

$$S_{\mu} = S^{\mu}_{\mathrm{scin}} + S^{\mu}_{\mathrm{wcd}} \quad , \tag{10.2}$$

whereby S_{em} is referring to the electromagnetic component and S_{μ} to the muonic component. The contribution of the individual components, $S^{\mathrm{em}/\mu}_{\mathrm{scin}}$ and $S^{\mathrm{em}/\mu}_{\mathrm{wcd}}$, are not directly accessible in a real experiment.
They have to be derived by the inversion of a matrix which relates the physical (S_{em} and S_{μ}) and the detector (S_{scin} and S_{wcd}) observables

$$\begin{pmatrix} S_{\mathrm{scin}} \\ S_{\mathrm{wcd}} \end{pmatrix} = \begin{pmatrix} a & b \\ 1-a & 1-b \end{pmatrix} \begin{pmatrix} S_{\mathrm{em}} \\ S_{\mu} \end{pmatrix} \tag{10.3}$$

where

$$a = \frac{S^{\mathrm{em}}_{\mathrm{scin}}}{S^{\mathrm{em}}_{\mathrm{scin}} + S^{\mathrm{em}}_{\mathrm{wcd}}} \Bigg\} \text{Fraction of total electromagnetic signal measured by scintillator} \tag{10.4}$$

$$b = \frac{S^{\mu}_{\mathrm{scin}}}{S^{\mu}_{\mathrm{scin}} + S^{\mu}_{\mathrm{wcd}}} \Bigg\} \text{Fraction of total muonic signal measured by scintillator} \quad . \tag{10.5}$$

By means of inversion, the physical signals can be independently expressed as a linear combination of the real detector observables. The electromagnetic and muonic signal measured by the water-Cherenkov detector can be expressed as

$$S^{\mathrm{em}}_{\mathrm{wcd}} = \frac{1-a}{a-b}\left(-(b-1)S_{\mathrm{scin}} - bS_{\mathrm{wcd}}\right) \tag{10.6}$$

$$\boxed{S^{\mu}_{\mathrm{wcd}} = \frac{1-b}{a-b}\left((a-1)S_{\mathrm{scin}} + aS_{\mathrm{wcd}}\right)} \tag{10.7}$$

[2] electrons, positrons and photons
[3] muons and anti-muons

and for the scintillator-based detector as

$$S^{\mathrm{em}}_{\mathrm{scin}} = \frac{a}{a-b}\ (-(b-1)S_{\mathrm{scin}} - bS_{\mathrm{wcd}}) \tag{10.8}$$

$$S^{\mu}_{\mathrm{scin}} = \frac{b}{a-b}\ ((a-1)S_{\mathrm{scin}} + aS_{\mathrm{wcd}}) \quad . \tag{10.9}$$

In the following, the reconstruction capability of the muonic component in the WCD stations, S^{μ}_{wcd} (cf. equation 10.7), by a combined measurement of the SD and the scintillator-based detector is examined as an example.

10.1.1. Particle number conversion into signal

The signals of the WCD station and the scintillator-based detector are both depending on the path length of the particles through the detector. Thus, the signal of the WCD station is given in units of *vertical equivalent muons* (VEM). For the scintillator-based detector, the signal is given in units of *vertical minimum ionizing particles* (VMIP). It is expected that the signal of an individual particle in the scintillator increases with $\propto \cos(\theta)$, as discussed for example in figure 8.23. For a single particle event, θ refers to the zenith angle of the individual particle. For an air shower, the dependency can be approximated by θ referring to the shower zenith angle.
Both signals are assumed to be proportional to the real energy deposit by particles within the detector material. For the WCD station one VEM corresponds approximately to an energy deposit[4] of 240 MeV, while one VMIP corresponds to approximately 1 MeV energy deposit in the scintillator detector (cf. section 6.3).

10.2. Simulation setup

The performance of the detector for high-energy cosmic rays is studied by means of air shower simulations, performed by the CORSIKA framework [186]. A *fixed library* is used to quantify the response at station-level. Therefore, individual air showers for two energies (10^{19} eV and $10^{19.8}$ eV), one reference zenith angle ($\theta = 38\,^{\circ}$) and one hadronic interactions model (Epos-LHC [209]) were produced for two types of primaries (proton and iron or p and Fe). For the lower energy 200 individual showers, for the higher energy 100 showers were each distributed randomly on a simulated detector array. The showers are reused to increase the statistics. The lower energy showers are placed twice randomly on a simulated detector array, the higher energy showers are placed four times. The studied detector array layout corresponds to the regular SD array of the Pierre Auger Observatory. Additionally, 24 artificial stations are included in the array at a 1000 m distance to the shower core. This dense station ring will be explained in more detail in section 10.3.3. Instead of studying the WCD stations only, the described scintillator detector is also included at the WCD position. Both detectors at the same position are referred to as a *detector pair* in the following.

When simulating extensive air showers of high energy, a large number of particles needs to be tracked during the shower development in the atmosphere. To reduce the needed computing resources, a *thinning* procedure[5] is applied within CORSIKA [186, 210].

[4] assuming a WCD attenuation coefficient of $\approx 120\,\mathrm{g/cm^2}$ of 240 MeV for vertical particles and a muon energy loss of $2\,\mathrm{MeV/(g/cm^2)}$

[5] The procedure is applied to all secondary particles with energies E below a certain fraction of the primary energy E_0. This fraction is defined as the thinning level $\epsilon_{\mathrm{thin}} = E/E_0$ and can be modified by the user. If an interaction takes places, in which thinning becomes active, only one particle is selected at random. All further secondary particles produced in the interaction are discarded. This randomly chosen particle has a survival probability of p_i and is considered as

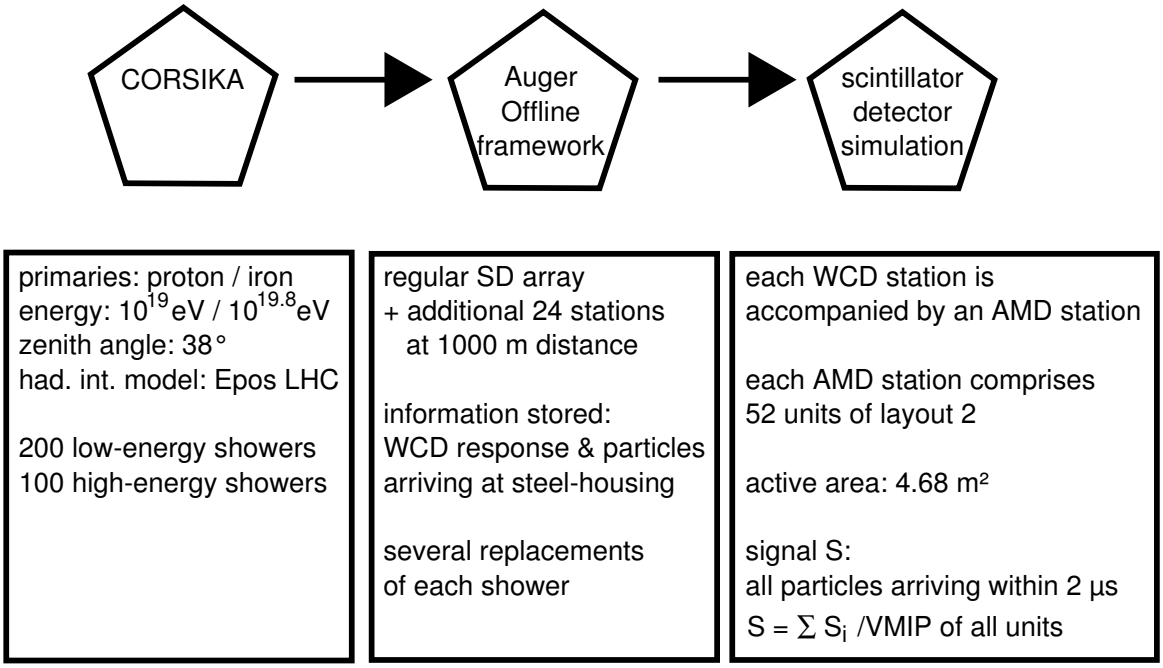

Figure 10.1.: Sketch of the simulation procedure. First, CORSIKA showers are simulated for two energies (10^{19} eV and $10^{19.8}$ eV), one reference zenith angle ($\theta = 38°$), one hadronic interaction model (Epos-LHC) and two types of primaries (proton and iron or p and Fe). These showers are randomly placed onto the regular SD array with additional 24 stations in a dense ring at the reference distance to the shower core of 1000 m. The WCD station response is stored. Additionally, all particles leaving the WCD station bottom are registered. These particles are injected in the scintillator detector simulation framework. Thereby, each WCD station is accompanied by one AMD detector. The particles have a starting position on top of the steel-housing. The light yields of the 52 scintillator detector units of each AMD station are stored and converted into a total signal S in VMIP. See text for more information.

At detector level, the air shower particles have to be resampled to attain the correct average amount of particles which would have reached the detector for an unthinned shower. Therefore, a resampling method is applied within the Offline framework [211] of the Pierre Auger Observatory. A detailed description of the method is given in [212]. Most important for the work in this thesis is thereby the definition of a *resampling area*. Only in these regions of the array the unthinning procedure is performed. In a standard setup, these would correspond to the active area of the WCD stations. As the scintillator-based detector is underneath the WCD detector, the resampling area has been enlarged within the *CachedShowerGenerator* module of the Offline framework by the author of this thesis. By a further modification of the framework within the *G4TankSimulatorOG* module, it was enabled that all information about the particles leaving the WCD station bottom is stored. The information comprise their position, direction, energy, and particle type. These particles are then inserted into the detector simulation framework developed in the scope of this thesis (cf. chapter 7). The particle start position is located at the top of the steel-housing of the scintillator detector. For the WCD stations, no modification of the Offline framework is needed. The framework allows access to the information on the reconstructed response of the WCD stations. Also, the initial par-

representative for the further development of the air shower. To account for energy conservation, a weight $w_i = 1/p_i$ is allocated to the particle.

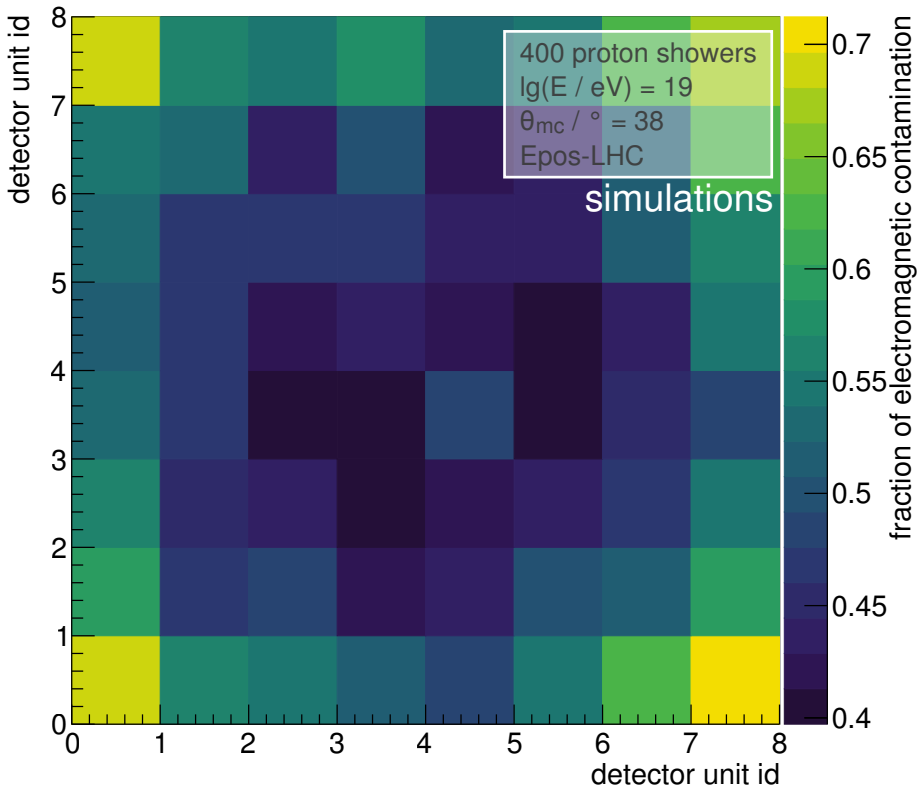

Figure 10.2.: Share of the electromagnetic component in the total signal yield as a function of the detector unit id of the scintillator detector located underneath a WCD station. The WCD radius corresponds to the width of roughly 6 detector units. The distribution includes 400 proton showers with an energy of 10^{19} eV and an incident angle of 38°. All showers were simulated with CORSIKA and the hadronic interaction model Epos-LHC.

ticles injected in the stations can be investigated. An overview of the simulation procedure is given in figure 10.1.

10.2.1. Scintillator detector

The water of the WCD station will provide shielding of the electromagnetic component for the scintillator detector with an attenuation coefficient of $\approx 120\,\mathrm{g/cm^2}$ for vertical particles. The following steel-housing provides an additional shielding by $\approx 10\,\mathrm{g/cm^2}$ for vertical particles. However, for inclined showers particles will enter the WCD station from the side and the slant depth of the absorber, which some particles traverse, will be reduced. Consequently, the electromagnetic contamination will be strongly enhanced. Besides the shielding of the electromagnetic component, also muons will be attenuated in the absorbers. Assuming a muon energy loss of $2\,\mathrm{MeV/(g/cm^2)}$, the minimum kinetic energy for a vertical muon to reach the active area of the scintillator detector is roughly 260 MeV. As indicated in figure 7.13, most of the muons have a larger kinetic energy and will thus be able to reach the scintillator detector. Also indicated in the figure are the energy thresholds applied by CORSIKA for each particle type.

As the matrix formalism is based on the total signal of the scintillator detector, a detector lay-

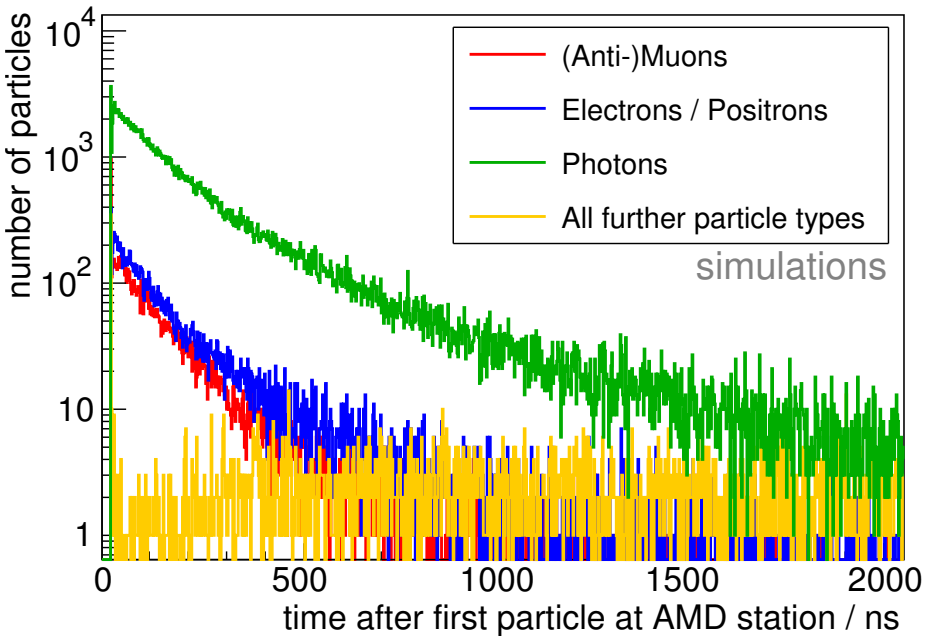

Figure 10.3.: Arrival time of the particles reaching the active area of the scintillator detector. The arrival times are given relative to the timestamp of the first particle arriving at the station. The highest particle rate is within the first 100 ns. The majority of the muons arrives within the first 1000 ns. The distributions include 400 proton showers with an energy of 10^{19} eV and an incident angle of 38°. All showers were simulated with CORSIKA and the hadronic interaction model Epos-LHC.

out is selected that exhibits a distribution of electromagnetic contamination as uniform as possible. It is comparable to the AMD layout presented in section 6.4 and in figure 6.8. It comprises a steel-housing in which trays of detector units of layout 2 are located. Eight trays are carrying eight units each. However, the further presented layout was designed for the routing of clear waveguides as used for units of layout 1. For units of layout 2, a spacing of 1 cm between detector units in a tray and a tray width of 32 cm are chosen. Thereby, the same active area but a more compact layout is achieved. The outer dimensions of the active scintillator detector area is reduced[6] to $2.5 \times 2.5\,\mathrm{m}^2$. The radius of the WCD station is 1.8 m. In figure 10.2, the share of the electromagnetic component in the total signal is presented as a function of the detector unit id. The distribution includes proton showers with an energy of 10^{19} eV and an incident angle of 38°. These showers were simulated with CORSIKA and the hadronic interaction model Epos-LHC. Even for the compact layout, the three units in each corner of the scintillator detector depict an enhanced contribution of the electromagnetic component. Therefore for the simple analysis ansatz presented, only the 52 central units of the 64 total units are taken into account. This corresponds to an active area of $A_{\mathrm{scin}} = 4.68\,\mathrm{m}^2$. The electromagnetic contamination is increasing from 0.4 to 0.6 from the inner to the outermost units. The average share of the electromagnetic component is 0.48 ± 0.01.
Even if not utilized in the scope of this thesis, the different response of the detector units in the corner allows for additional information on the shower and should be included in future analysis. In principle, the matrix method can be applied to the AMD detector itself. The units in the corner and the units completely covered by the WCD would yield different responses to the same air shower. This is one of the advantages of a multi-channel detector.

[6] compared to $3 \times 3\,\mathrm{m}^2$ in section 6.4

No proper SiPM and electronics simulation will be applied for the presented study. The total signal of the scintillator detector is the sum of all photons registered at the SiPM within the first 2 μs after the first particle arrived at the corresponding station. The time window roughly refers to the maximum reasonable integration window as would be used in the electronics. As depicted in figure 10.3, the majority of the muons arrives within the requested time window (within the first 500 ns with its peak at 50 ns). This is the same for electrons/positrons. Photons and further particle types arrive also later at the scintillator. The distributions in the figure include information of all particles reaching the active area of the scintillator detector stations of the regular array for proton showers with an energy of 10^{19} eV and an incident angle of 38 °. Photons with an energy > 100 keV are the most abundant particles in the shower reaching the scintillator detector station, followed by muons and electrons. However, only a few percent of the photons will result in a detectable signal in the scintillator material, since their energy is small.

10.3. Station-level evaluation

The matrix parameters refer to the fraction of the electromagnetic and of the muonic component detected by the scintillator detector and the WCD. For their determination within the scope of this thesis, the average response of both detectors (WCD and AMD) to 400 proton showers are studied.

10.3.1. Matrix parameters

First, the average signal yield for a passage of an (anti-) muon, electrons/positron or photon is determined for each detector individually. Then, for each detector pair in each shower, the muonic signal yields S^{μ}_{scin} and S^{μ}_{wcd} are calculated. They are approximated by the amount of muons traversing the active area of the corresponding detector multiplied by the average signal yield per muon without taking fluctuations into account. The electromagnetic signal yields $S^{\text{em}}_{\text{scin}}$ and $S^{\text{em}}_{\text{wcd}}$ correspond to the the signals introduced by photons and electrons/positrons. Again, both components are multiplied by the average signal yield per particle passage without taking fluctuations into account. For both detectors, the total signal (for example $S_{\text{wcd}} = S^{\mu}_{\text{wcd}} + S^{\text{em}}_{\text{wcd}}$) can be well reproduced by this estimation. The distributions of both parameters a and b (cf. equations 10.4 and 10.5) for stations, located at a distance to the shower core at 1000 m, are presented in figure 10.4a and 10.4b, respectively.
The matrix parameter b is symmetrically distributed with an average value of $b = 0.32$. The distribution has a width of 0.09. The value is well compatible to a pure geometry-based calculation for $b(\theta = 0)$, comparing only the effective areas

$$b(\theta = 0) = \frac{A_{\text{scin}}}{A_{\text{scin}} + A_{\text{wcd}}} \tag{10.10}$$

$$= \frac{4.68\,\text{m}^2}{4.68\,\text{m}^2 + 10\,\text{m}^2} \tag{10.11}$$

$$\approx 0.32 \quad . \tag{10.12}$$

The matrix parameter a depicts an asymmetry to higher values of a. This can be understood as the deviation in the electromagnetic contamination in different parts of the detector as discussed in figure 10.2. The average value of $a = 0.16$ is used for the following analysis. The distribution has a width of 0.06. The distributions of parameter a and b as a function of distance to the shower core are depicted in figure 10.4c and 10.4d, respectively. At distances close to the shower core, the distributions are symmetrical. For larger distances, asymmetries are observed as the particle density

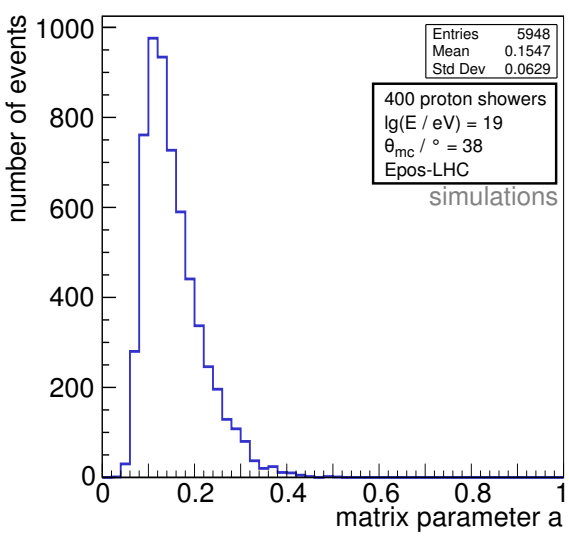

(a) Distribution of the matrix parameter a for stations at a reference distance to shower core of 1000 m.

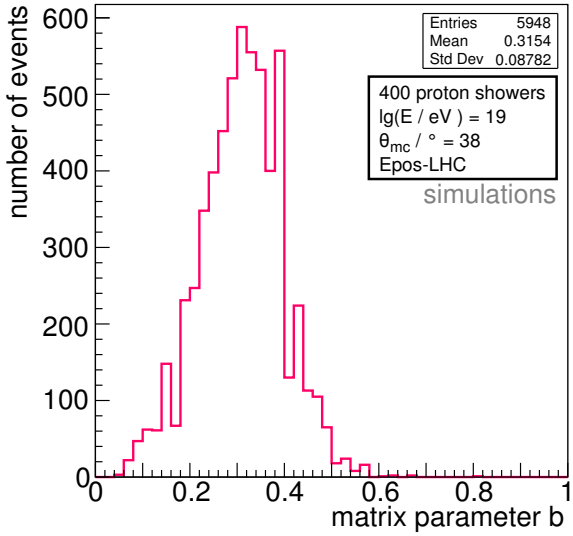

(b) Distribution of the matrix parameter b for stations at a reference distance to shower core of 1000 m.

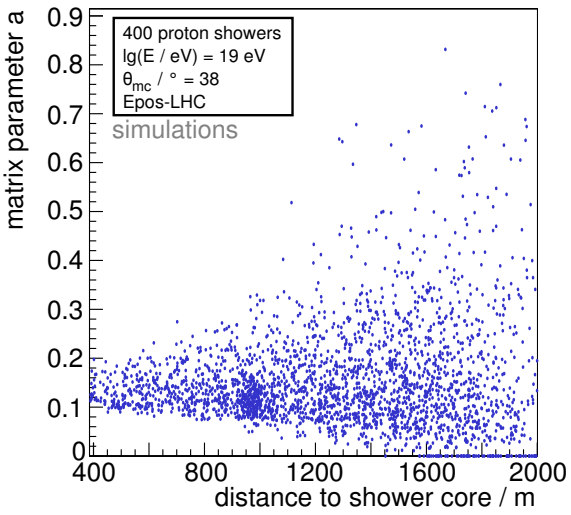

(c) Evolution of the matrix parameter a as a function of distance from the shower axis. At a distance of 1500 m, first stations exhibit zero values.

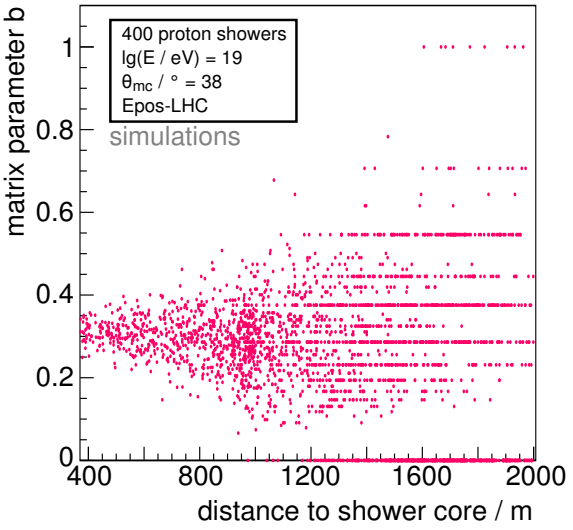

(d) Evolution of the matrix parameter b as a function of distance from the shower axis. At a distance of 1000 m, first stations exhibit zero values.

Figure 10.4.: Determination of the matrix parameters a and b by the average response of both detectors in individual detector pairs. The distributions include 400 proton showers with an energy of 10^{19} eV and an incident angle of 38°. All showers were simulated with CORSIKA and the hadronic interaction model Epos-LHC. See text for more information.

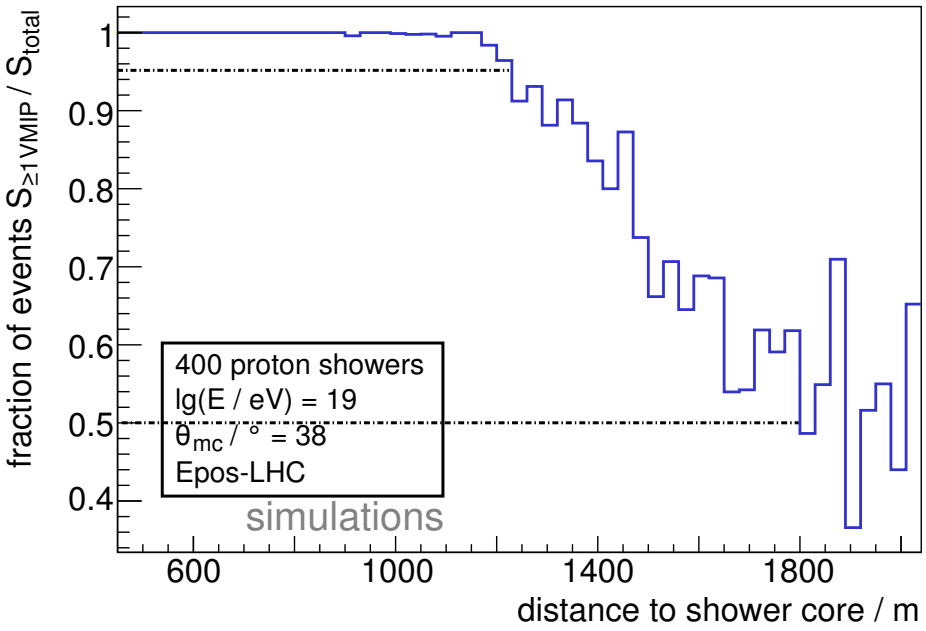

Figure 10.5.: Fraction of scintillator detector stations with a signal yield $S_{\mathrm{scin}} \geq 1\,\mathrm{VMIP}$ as a function of the distance to shower core. At a distance of 1200 m, 95% of all stations exhibit the requested signal yield. At a distance of 1800 m, the fraction is reduced to 50%. The distributions include 400 proton showers with an energy of 10^{19} eV and an incident angle of 38°. All showers were simulated with CORSIKA and the hadronic interaction model Epos-LHC.

is strongly decreasing and fluctuations within the signal yield are dominating[7]. For example, individual scintillator stations do not register any signal, resulting into zero values of both parameters. The missing signal in the scintillator is mainly driven by the reduced area of the scintillator detector and, consequently, by the limited coverage of the WCD station area. These distances will also correspond to the distances at which a reduced trigger probability of a stand-alone scintillator detector is expected. There are also detector pairs where muon trajectories only intersect the scintillator detector and not the WCD station. These stations are represented by a parameter b equal 1. They are located at a large distance to the shower core and are subject to the fluctuations introduced by the low particle density.

10.3.2. Trigger probability

Assuming the most simple trigger criterion of the total signal $S_{\mathrm{scin}} \geq 1\,\mathrm{VMIP}$, the trigger probability of the scintillator detector will decrease with increasing distance to the shower core as the particle density is reduced. This quantity is important if the detector is operated independently of the existing WCD station and no external trigger is applied. The trigger probability is approximated by the fraction of stations with a signal greater than 1 VMIP $S_{\geq 1\,\mathrm{VMIP}}$ to the total amount of stations S_{total}. The fraction is shown as a function of the lateral distance in figure 10.5 for proton showers with an energy of 10^{19} eV, an inclination angle of 38° and simulated with the hadronic interaction model Epos-LHC. At a distance of 1000 m first stations are affected. At a distance of 1200 m and of 1800 m the fraction drops to 95% and to 50%, respectively. In table 10.1, showers with proton and iron as primaries are summarized for two different primary energies of 10^{19} eV and $10^{19.8}$ eV.

[7] The discrete structures for matrix parameter b result from the small number of muons in a station, whereby the signal per muon is assumed to be a constant value in this estimation.

primary type	primary energy / eV	r / m at which $\frac{S_{\geq 1\,\mathrm{VMIP}}}{S_{\mathrm{all}}} =$	
		0.95	0.5
proton	10^{19}	1200	1800
	$10^{19.8}$	1800	2400
iron	10^{19}	1400	1900
	$10^{19.8}$	1800	2500

Table 10.1.: Summary of the distance above which the fraction of stations with a signal greater than 1 VMIP $S_{\geq 1\,\mathrm{VMIP}}$ drops to 95% or 50% compared to all stations.

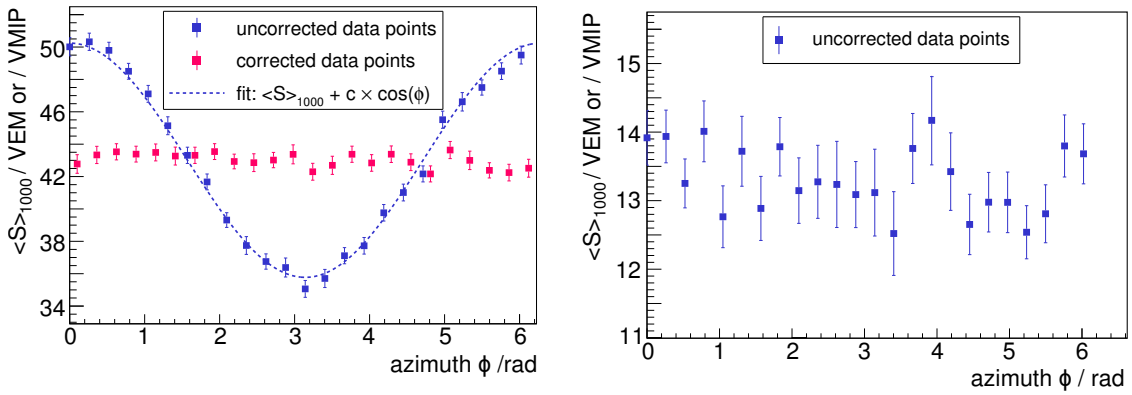

(a) A cosine function is fitted on the signal of the WCD stations in the dense ring. By applying the correction, they are distributed around the average value of the signals. The corrected data points can be used to determine the uncertainty on the MC WCD signal at 1000 m.

(b) The signal of the scintillator detector is dominated by the muonic component and depicts no significant azimuth dependency. No correction is applied.

Figure 10.6.: MC signal of the WCD and scintillator detector stations of the dense ring at a distance to shower core 1000 m as a function of their azimuthal position in respect to the shower azimuth is presented. The distributions include 400 proton showers with an energy of 10^{19} eV and an incident angle of 38°. All showers were simulated with CORSIKA and the hadronic interaction model Epos-LHC.

Compared to proton showers with the same energy, the distances at which the fraction of stations drops below 95% and 50% are larger for iron showers. This is expected as a larger number of muons is produced in iron showers. The same applies to showers with higher energies. Therefore, a stand-alone operation of the scintillator detector is feasible for high energy showers, but challenging for showers with low energies.

10.3.3. Ability of the reconstruction of the muonic signals in WCD stations at 1000 m

First, the matrix formalism is applied to individual pairs of WCD and scintillator detector at a reference distance of 1000 m. Therefore, an additional dense ring of 24 stations at a distance to the shower core of $r = 1000$ m is introduced in the simulation of the regular SD array grid to increase statistics. This distance refers to the estimator of the shower size, $S(1000)$ (refer to section 3.1

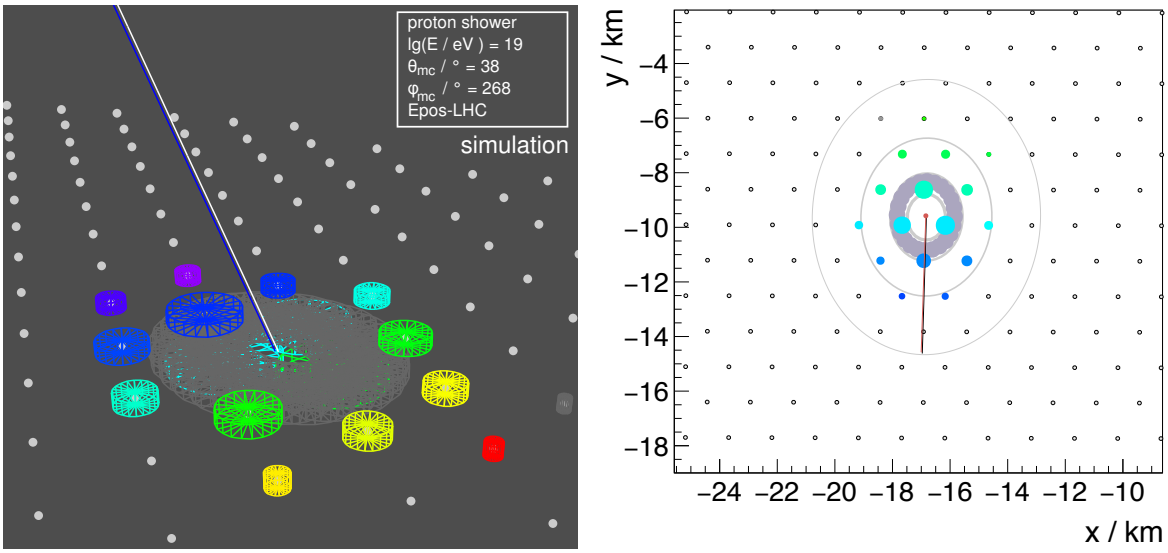

(a) A 3D model of the signal distribution on ground. The color code refers to the arrival time distribution (blue - early / red -late). The blue and white line represents the MC and reconstructed arrival direction, respectively.

(b) Bird's eye view of the signal distribution on ground. The color code refers to the arrival time distribution (blue - early / green -late). The red and black lines represent the MC and reconstructed arrival directions, respectively. The footprint on ground is elliptical as showers with an inclination angle of $\theta = 38\,^\circ$ are studied.

Figure 10.7.: Shown is a simulated shower with an energy of $E = 10^{19}\,\mathrm{eV}$, an inclination angle of $\theta = 38\,^\circ$ and an azimuth angle of $\phi = 268\,^\circ$ located on the surface detector grid of the Pierre Auger Observatory. The 24 artificial stations located on the dense ring are represented by grey circles. In both figures, the individual stations of the dense ring are difficult to identify because they stand unusually close to each other compared to the grid distance of the regular SD array. The regular stations have a color code corresponding to the shower front arrival time. The circle size corresponds to the amount of signal detected in the WCD station. The SD array allows for the excellent reconstruction of the shower arrival direction, also indicated in both figures.

for more information). The stations are arranged in a circle around the shower axis in the shower detector plane (cf. figure 3.8) with an equal distance between stations.

The ring at a distance of $r = 1000\,\mathrm{m}$ can be used to estimate the mean value and the uncertainty on the scintillator and WCD detector signals. In the scope of this study, these signals refer to the Monte Carlo (MC) signals. For both detectors the fraction of the total detected signal, which is derived exclusively from muon passages, is known in simulations. This fraction defines the MC muonic signal. Deviations in the signal correspond to the fluctuations in the number of muons and to the fluctuations of the energy deposit at each muon passage. For a reference zenith angle of $38\,^\circ$, it is expected that the MC signal of each WCD station has to be first corrected for its dependency on the azimuth angle. Depending on the position of the station with respect to the azimuth angle ϕ, a different amount of atmosphere is traversed, which would artificially increase the uncertainty on the registered signal. Exemplary in figure 10.6a, the MC WCD station signal as a function of its azimuthal position is presented. A cosine function of the form $\langle S_{1000}\rangle + c \times \cos(\phi)$ is fitted to the simulated data points. The signal in each station is then corrected for the bias (cf. figure 10.6). Now, the variance of the corrected signals of all stations in the ring is calculated. The uncertainty is then defined by $\sigma_S = \text{variance}/\sqrt{\langle S\rangle}$ with $\langle S\rangle$ being the average signal in all 24 stations.

For the scintillator detector, no correction is applied as the atmospheric absorption is less apparent

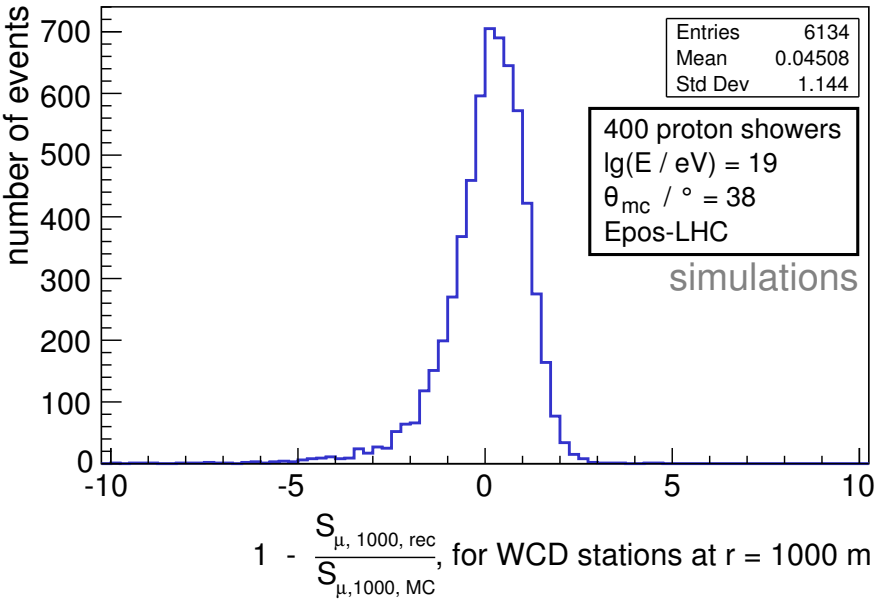

(a) Ability of the reconstruction of the muonic signal in individual WCD stations for proton primaries. The matrix formalism allows for a good reconstruction performance in average with a small bias of 0.05 but with a rather large resolution of 114%.

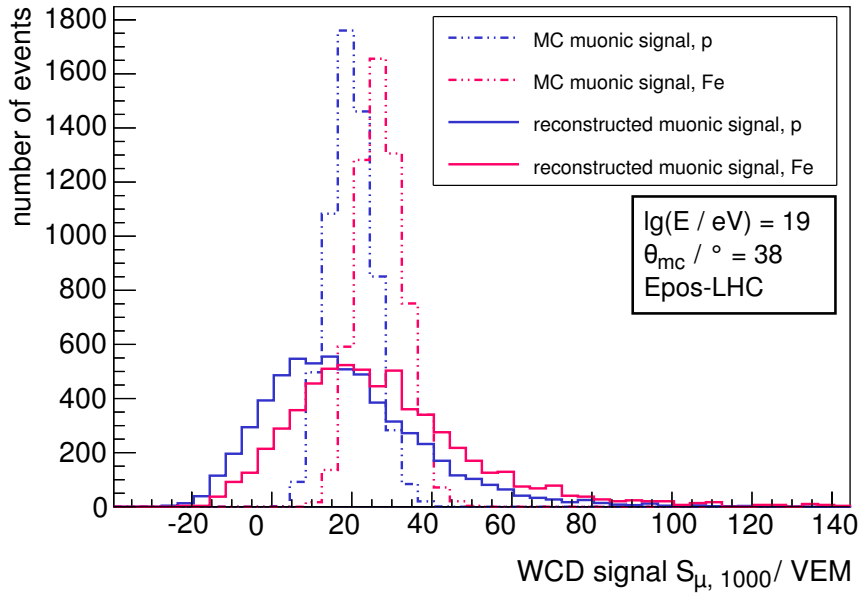

(b) Shown are MC and reconstructed muonic signals for the WCD stations located at a distance to shower core of 1000 m for both types of primaries. The MC and reconstructed distributions are represented by solids and dashed lines, respectively. The calculation of the figure of merit for the discrimination of proton and iron primaries is based on the mean and the width of the individual WCD distributions.

Figure 10.8.: Reconstruction of the muonic signal for individual WCD stations in simulated air showers. Presented are proton and iron showers with a primary energy of 10^{19} eV and an incidence angle of 38 °. All showers were simulated with CORSIKA and the hadronic interaction model Epos-LHC.

for the muonic signal. The signal does not depict a dependency on the azimuthal position of the station, as is shown in figure 10.6b. The same showers are used to determine the MC signals of the individual detectors.
An example of a single-event view as provided by the *EventBrowser* of the Offline framework is presented in figure 10.7a as a 3D model and in 10.7b from a bird's-eye view. Shown is a shower with an energy of $E = 10^{19}$ eV, an inclination angle of $\theta = 38\,^{\circ}$ and an azimuth angle of $\phi = 268\,^{\circ}$. The 24 additional stations located on the dense ring are represented by grey circles. The regular stations have a color code corresponding to the shower front arrival time. For all stations, the area of the circle refers to the amount of signal detected at each station. As expected, the steeply falling particle density with increasing distance to the shower core becomes visible. Additionally, the MC and the reconstructed arrival direction are indicated by a blue and white line (cf. figure 10.7a) or a red and a black line (cf. figure 10.7b), respectively.
In a real detector setup, the MC muonic signal is not accessible. Therefore, for each detector pair at a distance to shower core of 1000 m, the reconstructed muonic signal in the WCD station is determined according to equation 10.7. The reconstructed muonic signal in the WCD station is compared to the MC signal, calculated by the average MC muonic signal registered in all WCD detector stations at a distance of 1000 m. For all shower configurations, the same matrix parameters a and b as calculated in section 10.3.1 are applied. The deviation between MC and reconstructed muonic signals is presented in figure 10.8a for 400 proton showers with an energy of 10^{19} eV. It is expressed by

$$1 - \frac{S_{\mu,\,1000,\,\mathrm{rec}}}{S_{\mu,\,1000,\,\mathrm{MC}}} \tag{10.13}$$

with an ideal reconstruction exhibiting an average value of zero. On average, the matrix allows for good reconstruction at station-level. A small bias is apparent with an average shifted to 0.05. However, shower-to-shower and detector fluctuations result into a rather poor resolution of 114% corresponding to the width of the distribution. In table 10.2, the deviation from the MC muonic signal in the WCD stations for both energies and primary types are summarized. For all studies, the average muonic signal can be reproduced well. The resolution is improving, as expected, for iron showers at the same energy and for proton and iron showers with a higher energy for a given distance to shower core. Comparable biases and resolutions are achieved for the study of a combination of SSD and WCD [207].
The *figure of merit* (MF) is now used to quantify the ability to discriminate between proton and iron primaries at station-level. It is defined as

$$\mathrm{MF} = \frac{|\langle S_{\mu,\mathrm{p}}\rangle - \langle S_{\mu,\mathrm{Fe}}\rangle|}{\sqrt{\sigma^2_{S_{\mu,\mathrm{p}}} + \sigma^2_{S_{\mu,\mathrm{Fe}}}}} \quad . \tag{10.14}$$

Therefore, the distributions of the MC and reconstructed muonic signal in the WCD stations for both primaries are considered. It is expected that the reconstructed MF is significantly smaller than the MC MF as a perfect reconstruction of the pure muonic or electromagnetic signal cannot be achieved by real detector setup. They are presented in figure 10.8b. The mean of each distribution is defined as $\langle S_{\mu,\mathrm{p\,/\,Fe}}\rangle$, the width as the uncertainty $\sigma_{S_{\mu,\mathrm{p\,/\,Fe}}}$. The distributions indicate also negative reconstructed signals introduced by large fluctuations within the detector signals. Even if corresponding to an unphysical result, they are considered as part of the distribution and are included in the calculation of the mean and the width. The figure of merit based on the MC signals is considered as best achievable discrimination power. For an energy of 10^{19} eV, the MC MF states a value of 0.92. Merit factors above 1 allow for a good discrimination. As expected, the MF for the reconstructed muonic signal is reduced due to the poor resolution. Nevertheless, a MF of 0.28 can be achieved for low energies and the most simple ansatz. For larger energies, the figure of merit is increasing for both,

primary type	primary energy / eV	figure of merit MC	figure of merit reconstructed	$1-\frac{S_{\mu,\mathrm{rec}}}{S_{\mu,\mathrm{MC}}}$ for WCD at 1000 m	
				μ	σ
proton	10^{19}	0.92 ± 0.12	0.28 ± 0.16	0.05	1.14
iron				-0.03	0.90
proton	$10^{19.8}$	1.65 ± 0.09	0.44 ± 0.15	-0.03	0.51
iron				0.00	0.37

Table 10.2.: Summary of the reconstruction ability of the muonic signal in WCD stations. Therefore, the signals of individual WCD and scintillator detector pairs at a distance to shower core of 1000 m are analyzed by the matrix formalism. Compared are the figures of merit as an estimator of the discrimination power between proton and iron induced showers. The MC signals are based on the contribution of muons to the total detected signal of a station which is known in simulation, but not accessible in a real setup. The reconstructed signals based on the matrix formalism are subject to detector uncertainties and exhibit a lower figure of merit. Additionally, the bias and resolution of the ratio of the reconstructed to the MC muonic signal of the WCD is listed.

MC and reconstruction. While the MC MF is improved to 1.65, the reconstruction allows for a MF of 0.44. The study of the SSD with the WCD stations states slightly higher MF for the higher energy bin. This may result from the different location of the scintillator detector (underneath the WCD detector), but this effect has to be studied in detail in a future analysis. In table 10.2, all calculated figures of merit are summarized. The given uncertainties are calculated by the statistical method introduced in the following section.

10.3.4. Uncertainty estimator of the figure of merit

For the calculation of the uncertainty on the figure of merit the *bootstrap* method, as introduced in [213, 214, 215], is applied. The statistical method is considered as *resampling* approach. It allows for an estimate on the uncertainty of an observable which is determined by a single data set with n events. Now, this data set is considered as empirical distribution function. A bootstrapped sample is randomly select from the original sample. This sample has the same number of events as the original distribution. Therefore, the events are selected with replacement and certain events might get used multiple times, while other are not introduced in the bootstrapped sample. This corresponds to the repeated extraction of random numbers from the distribution function. The procedure is repeated for $R = 10000$ times to allow for a reasonable statistics. In the scope of this thesis, the MC and reconstructed muonic signals for proton and iron showers are used as original dataset. For each repetition, the figure of merit is calculated. The width σ_b of the thus derived MF distribution is used as an estimate of the standard deviation of the MF of the original data set with n events. An exemplary bootstrapped distribution is presented in figure 10.9. It is based on the MC muonic signals in all WCD stations located in the dense ring. The MC MF is calculated to 0.92 ± 0.12.

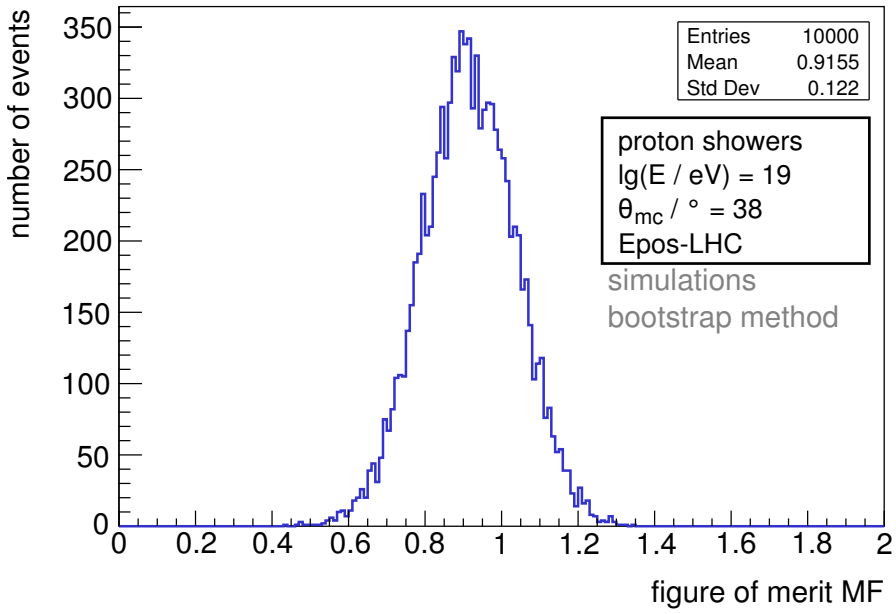

Figure 10.9.: An exemplary distribution of the figure of merit for the discrimination of proton and iron showers. The distribution is based on 10000 bootstrapped samples. The width σ_b of the distribution is an indicator for the uncertainty on the MF of the original MC data sample under study. See text for explanation of the method. The original distribution includes 200 proton and iron showers each with an energy of 10^{19} eV and an incident angle of 38°. All showers were simulated with CORSIKA and the hadronic interaction model Epos-LHC.

10.4. Event-level evaluation

As a next step, a muon number estimator is determined while taking all stations of an event into account and determining the muonic signal at a reference distance based on the matrix formalism. The particle distribution on ground is dependent on the distance to the shower axis r. While measuring with a detector array, each signal measured in a station is a sample of the shower footprint. The measured signal as a function of r can be modeled by a *lateral distribution function* (LDF) as presented in chapter 3.1 in equation 3.3 for the surface detector. Based on the presented air shower and corresponding detector simulations, a first parametrization for a LDF of the scintillator-based detector can be performed. The fitting procedure comprises two stages, the *global fit* and the *single event fit*. First, a global fit is performed for each primary type, primary energy and detector individually. It comprises the signals detected by all stations of the regular array in average. It allows for an initial guess of the scaling parameters γ and β of the LDF. Additionally, while studying many events, the uncertainties can be considered as Gaussian. In order to reduce possible biases of the fits, only a limited distance range is studied. For stations with a distance larger than 2000 m, no significant contribution to the signal can be found. As discussed in section 10.3.2, the trigger probability of the scintillator detector is already strongly reduced and is considered as possible bias of the LDF. Stations next to the shower core are the most important as they carry most of the information. However, stations closer to the core than about 200 m are not expected to add further information to the LDF fit. The core resolution introduces a systematic signal uncertainty, which is of the order of the statistical uncertainty σ_S of the signal.
As the scintillator-detector array geometry is identical to that of the SD, the values of r_{opt} of 1000 m and r_1 of 700 m were adopted from the SD LDF (cf. equation 3.3). The S_{1000} parameter is fixed

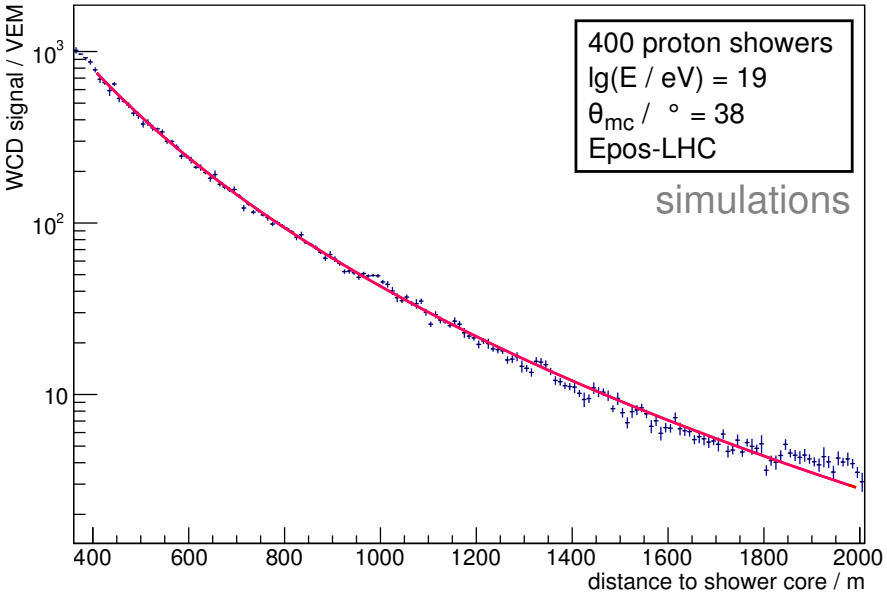

(a) Signal of the WCD stations as a function of the distance to shower core. A global LDF fit to the distribution is performed. The corresponding fit parameters are $S_{1000} = (42.83 \pm 0.59)\,\mathrm{VEM}$, $\beta = -1.37 \pm 0.18$, $\gamma = -2.44 \pm 0.05$ with a $\chi^2/\mathrm{ndf} = 448.3/157$.

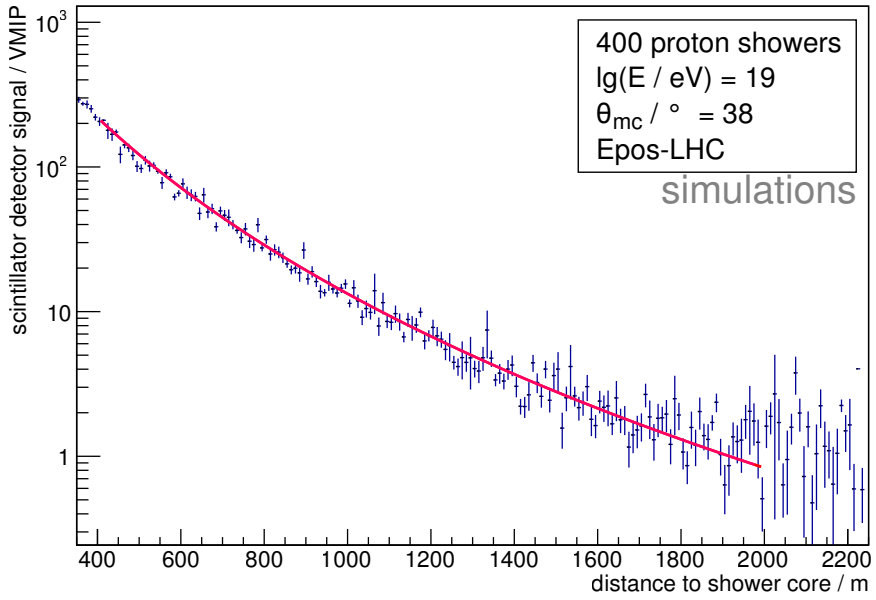

(b) Signal of the scintillator stations as a function of the distance to shower core. A global LDF fit to the distribution is performed. The corresponding fit parameters are $S_{1000} = (13.31 \pm 0.78)\,\mathrm{VMIP}$, $\beta = -0.74 \pm 0.14$, $\gamma = -4.13 \pm 0.07$ with a $\chi^2/\mathrm{ndf} = 341.8/157$.

Figure 10.10.: Fits on the lateral distribution of the WCD and scintillator detector signal as a function of the distance to shower core. The distributions include 400 proton showers with an energy of $10^{19}\,\mathrm{eV}$ and an incident angle of 38°.

to the average signal in the corresponding detector for the stations located in the dense ring. The distribution is fitted by a LDF with β and γ being the only free parameters. The existing WCD parametrization is used for the initial guesses of both fit parameters. Exemplary, two global fits are presented in figure 10.10 for the same proton showers with an energy of 10^{19} eV for the signals of the WCD and scintillator stations as a function of the distance to shower core.
Based on this global fit, an individual LDF is fitted individually to the WCD and scintillator detector for each event. For this analysis, an increased event statistics is used compared to the analysis on individual pairs of WCD and scintillator detector. For each energy and primary, 800 events are investigated. Only stations with a signal greater than 1 VEM or VMIP are included in the fitting procedure, as the proper inclusion of low-signal stations still needs to be investigated for the scintillator detector. The single fit has only S_{1000} as free parameter. The scaling parameters β and γ are kept fixed at their global fit values. An exemplary event is presented in figure 10.11. The iron shower has an energy of 10^{19} eV and an incidence angle of 38 °. For both detectors, fits on the lateral distributions are presented by solid lines. Poisson statistics is assumed for the uncertainty on the single station signal. The dashed lines depict the individual signal S_{1000}. This parameter is further used for the reconstruction of the muonic signal in the WCD station according to equation 10.7. The signal at 1000 m is considered as a first guess, the optimal distance for the matrix formalism application still needs to be validated. As for the station-level evaluation, the reconstructed muonic WCD signal is compared to the MC value. Additionally, the figure of merit is calculated. A summary of this study is given in table 10.3. The uncertainty on the figure of merit is calculated by the presented bootstrap method. As expected, the simultaneous consideration of all stations in an event improves the resolution of the reconstruction efficiency and, consequently, the figure of merit for showers with an energy of 10^{19} eV improves. A MF of 0.64 for the reconstructed signal is calculated compared to a MF of 1.68 for the MC muonic signals. For larger energies, the figure of merit is increasing for both, MC and reconstruction. While the MC MF is improved to 2, the reconstruction allows for a MF of 0.83. The reconstructed MF for the higher energy showers is considered to be already sufficient to significantly improve the discrimination between proton and iron primaries. The study of the SSD detector depicts an improved discrimination ability of the SSD at the event-level basis [207].
Additionally, the reconstruction of the number of muons depicts a slight deviation from the expected MC muonic signal for all energies and primaries. The deviation from the MC muonic signal is also present in the SSD study and is subject of current investigations.

In summary, the so far calculated figures of merit allow for a first overview on the reconstruction ability of the number of muons by a combination with the SD array of the Pierre Auger Observatory and a large-scale version of the presented scintillator detector in this thesis. As these factors are based on a fixed energy, they only give a limited interpretation on the reconstruction ability. In particular, the bias by fluctuations due to the low particle density for large distances from shower core needs further investigations. However, the figures of merit presented indicate a promising performance of the setup. It is expected that a dedicated and more complex analysis taking advantages from the multi-channel approach of the presented detector will improve the reconstruction efficiency of the number of muons. If an improved reconstruction is achieved, the setup allows for an improvement of the determination of the UHECR mass composition. However, an event-by-event determination will be challenging and need further investigations and keen knowledge about the combined setup.

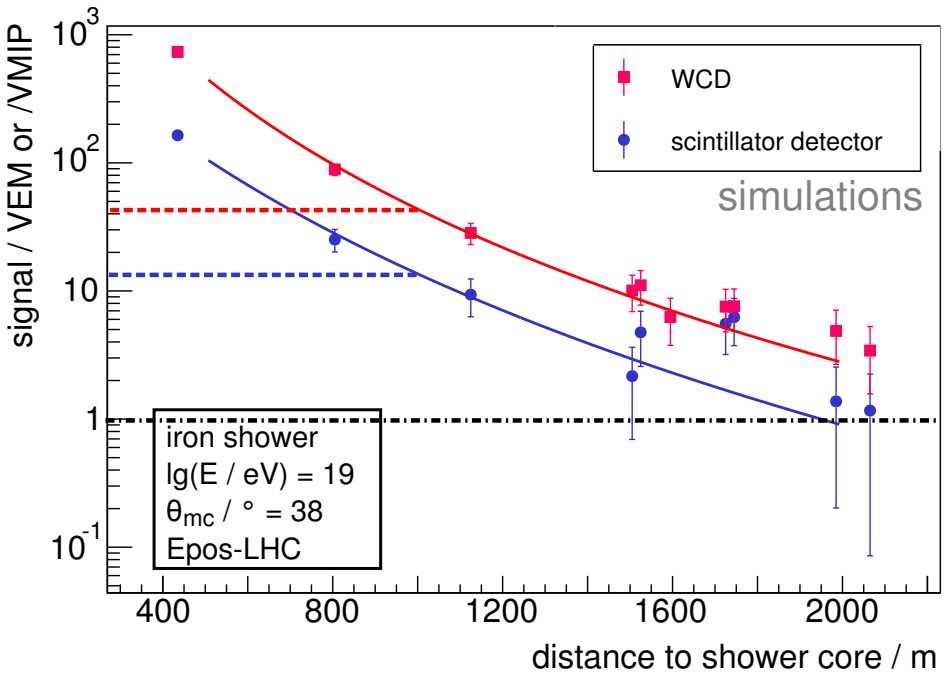

Figure 10.11.: Signal of the WCD and scintillator detector stations as a function of the distance to shower core. A single iron shower with an energy of 10^{19} eV and an incidence angle of 38° is shown. For both detectors, fits on the lateral distributions are presented by solid lines. The dashed lines depict the individual signal S_{1000} at a distance of 1000 m to the shower core. Additionally, a horizontal line at a signal of 1 VEM or VMIP indicates the requested trigger threshold.

primary type	**primary energy / eV**	**figure of merit MC**	**figure of merit reconstructed**	$1-\frac{S_{\mu,\mathrm{rec}}}{S_{\mu,\mathrm{MC}}}$ **for WCD at** 1000 m	
				μ	σ
proton	10^{19}	1.72 ± 0.09	0.64 ± 0.07	-0.09	0.23
iron				-0.34	0.17
proton	$10^{19.8}$	2.01 ± 0.08	0.83 ± 0.08	0.15	0.14
iron				-0.1	0.21

Table 10.3.: Summary of the reconstruction ability of the average muonic signal in the WCD stations at a reference distance of 1000 m, S_{1000}. Therefore, LDF fits on the WCD and scintillator station signal as a function of the distance to shower core are performed. Compared are the figures of merit as an estimator of the discrimination power between proton and iron induced showers. The MC signals are based on the contribution of muons to the total detected signal of a station which is known in simulation, but not accessible in a real setup. The reconstructed signals based on the matrix formalism are subject to detector uncertainties and exhibit a lower figure of merit.

Chapter 11

Conclusions

The largest observatory for extensive air showers induced by ultra-high energy cosmic rays is the Pierre Auger Observatory in Argentina. Currently, a major upgrade of the experiment is performed, called AugerPrime. The upgrade aims to answer important open questions of the research field like the origin of the flux suppression or an estimate of the proton flux contribution at highest energies. A key element of the upgrade is the establishment of an additional detector, called SSD, to improve the measurement of the muonic component in air showers. By a combined analysis of the newly installed detector and the already existing surface detector stations, an improved discrimination between different types of primaries on an event-per-event basis is enabled.

The Aachen Muon Detector (AMD) has been first introduced as a proposal for the upgrade. The concept of the detector will not be pursued further in the scope of the Pierre Auger Observatory. But the developed centerpiece, a so-called detector unit, allows for an excellent study of (atmospheric) muons and further charged particles, as well as cosmic ray candidates. The detector unit comprises a scintillator tile, a wavelength-shifting fibre and a single photosensor, a silicon photomultiplier (SiPM), per tile. In the scope of this thesis, a unit layout has been developed which allows for a high muon trigger efficiency and excellent light yield of 30 photon-equivalents per passage of a vertical minimum ionizing particle. Coincident measurements with an external detector, a muon tomograph, enabled a detailed investigation of the homogeneity. The layout depicts inhomogeneities of the light yield in the region of the point of contact of the SiPM and the scintillator tile, but a uniformly high trigger efficiency. All measurements of the detector unit performance are confirmed by a simulation framework, which has been developed in the scope of this thesis. While combining multiple detector units, a highly flexible and efficient detector module is achieved. A demonstrator based on this multi-channel approach, called MiniAMD, has been designed, constructed and tested. It consists of two individual modules, each comprising eight detector units. Operating both modules on top of each other, efficient trigger settings of units of the top and bottom module can be chosen to investigate atmospheric muons. With its high trigger efficiency, MiniAMD is thus a perfect candidate as trigger device for further detectors under study. It is, for example, used in the test stand of the assembled SSDs in the mechanical workshop of the Physics institute III A at the RWTH Aachen University. Furthermore, the ability of MiniAMD to detect air shower candidates is confirmed by coincident measurements with an external, small-scale detector array.

Based on this promising performance properties of the MiniAMD demonstrator, the Aachen Muon Detector concept is taken up again. It comprises 64 detector units located in a steel-housing which can be placed underneath the existing surface detector stations of the Pierre Auger Observatory. A preliminary analysis is performed, as a proof of concept, on the responses of both detectors to air shower simulations with an energy of 10^{19} eV or $10^{19.8}$ eV, a reference zenith angle of 38 °, with proton or iron primaries. Thereby, the ability of the reconstruction of the muonic signal is investigated. The study indicates that the fluctuations in the low particle density underneath the surface detector are a challenge and limit the discrimination power. At an energy of $10^{19.8}$ eV and for proton primaries, a resolution in the reconstructed muonic signal of individual surface detector stations at a distance to shower core of 1000 m is in the order of 50%. The determined resolution is comparable to that of the SSD detector, but indicates a slightly stronger dependence on particle density fluctuations. Nevertheless, the installation of the detector concept would contribute to improve the distinction between proton and iron showers.

Appendix

A. Monitoring of important characteristics of the MiniAMD demonstrator

This section allows for an overview of important characteristics of all units implemented in the MiniAMD demonstrator as a function of the temperature. The data is taken during measurements of the demonstrator at the roof of the physics department as presented in chapter 9. Units with channel [0-7] are located in module 1, units with channel [8-15] in module 2. Each data point corresponds to a MIP charge spectrum measurement of one hour. Two different temperatures have to be considered. The gain G depends on the SiPM temperature T_{SiPM}, while the baseline is more influenced by the temperature at the EASIROC T_{EASIROC}. By linear fits on the data, a general conversion of the signal in ADC count in units of MIP or in units of photon equivalents (p.e.) can be achieved depending on the temperature.

Gain stability

All units demonstrate a small change in the gain by temperature although a temperature compensation has been applied. The measurements of all units is presented in figure 1 for units located in module 1 and in figure 3 for units in module 2. The linear fit allows for a good description of the data indicated by the corresponding residuals (cf. figure 2 for module 1 and figure 4 for module 2). As the gain is slightly overcorrected for all units, for further measurements a reduced correction factor is strongly recommended ($60\,\mathrm{mV/K} \rightarrow 57\,\mathrm{mV/K}$).

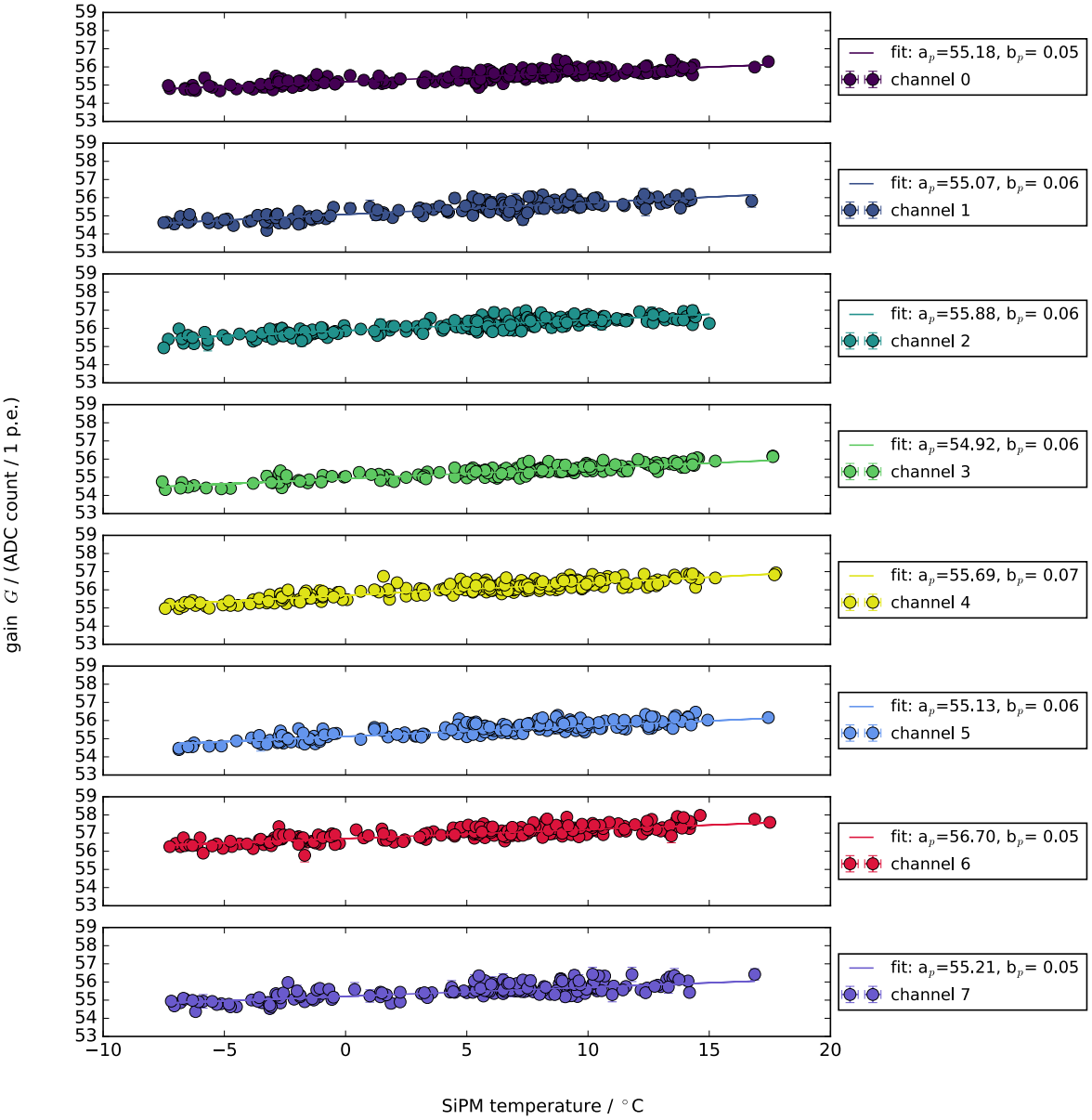

Figure 1.: Gain as a function of the SiPM temperature for all units located in module 1. For each unit, a linear function is fitted on the data points. The average change of the gain is $< \Delta G/\Delta T_{\mathrm{SiPM}} >= 0.06\,\mathrm{ADC\,count/K}$ or $1\%/10\,\mathrm{K}$.

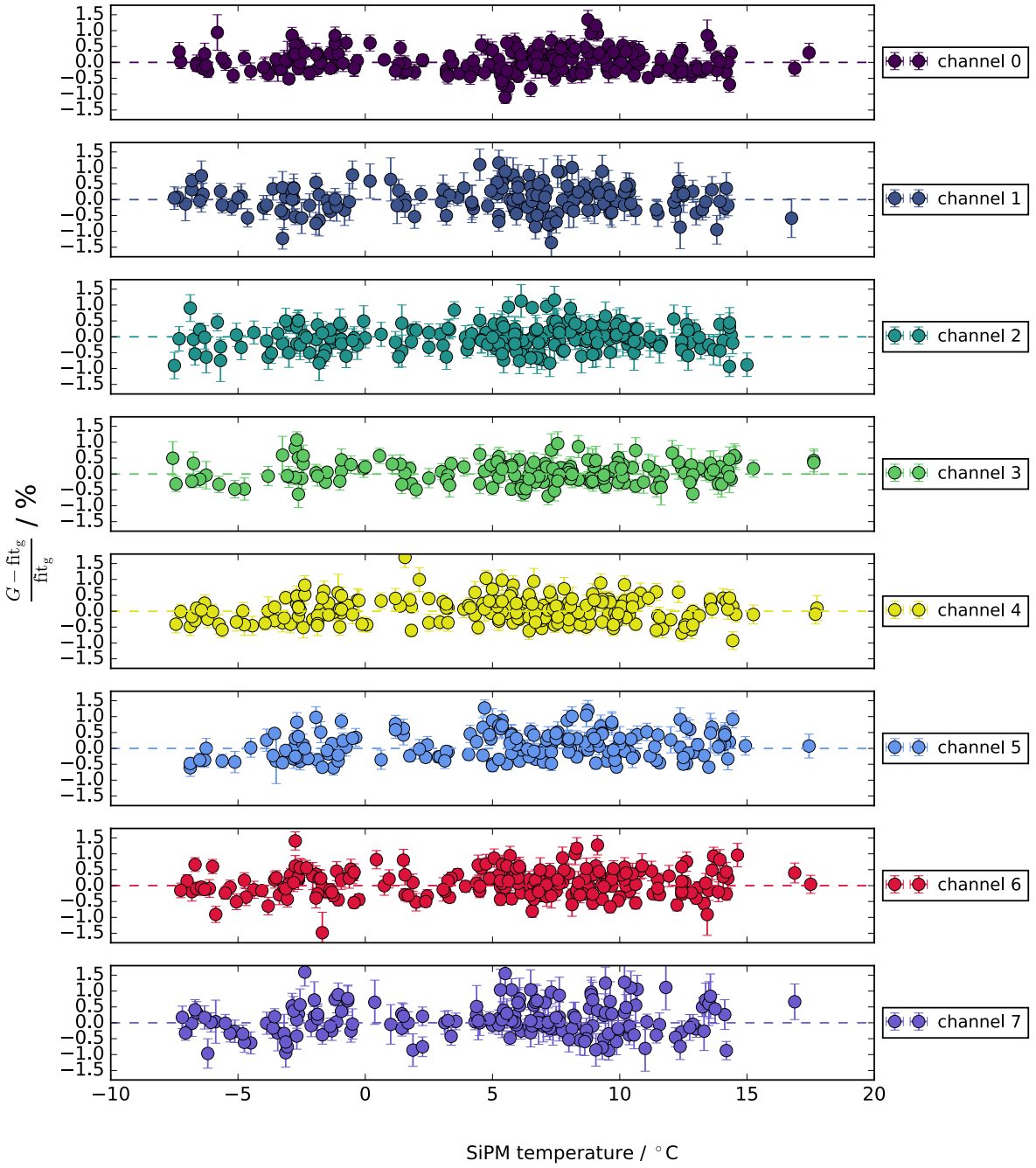

Figure 2.: Residuals $(G-\mathrm{fit_g})/\mathrm{fit_g}$ as a function of the SiPM temperature for all units located in module 1. The fit describes the development of the data well.

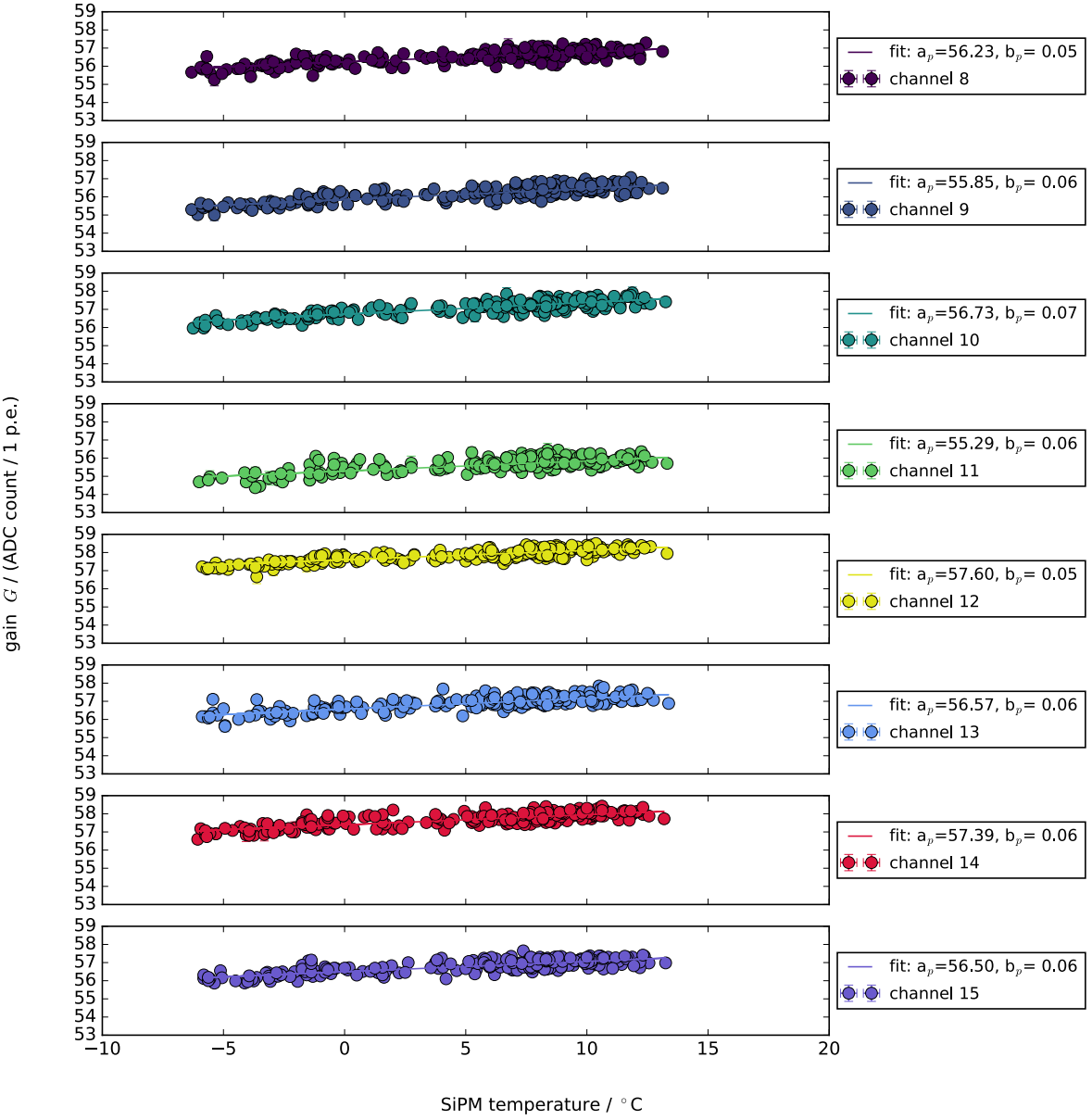

Figure 3.: Gain as a function of the SiPM temperature for all units located in module 2. For each unit, a linear function is fitted on the data points. The average change of the gain is $< \Delta G/\Delta T_{\text{SiPM}} >= 0.06\,\text{ADC count/K}$ or $1\%/10\,\text{K}$.

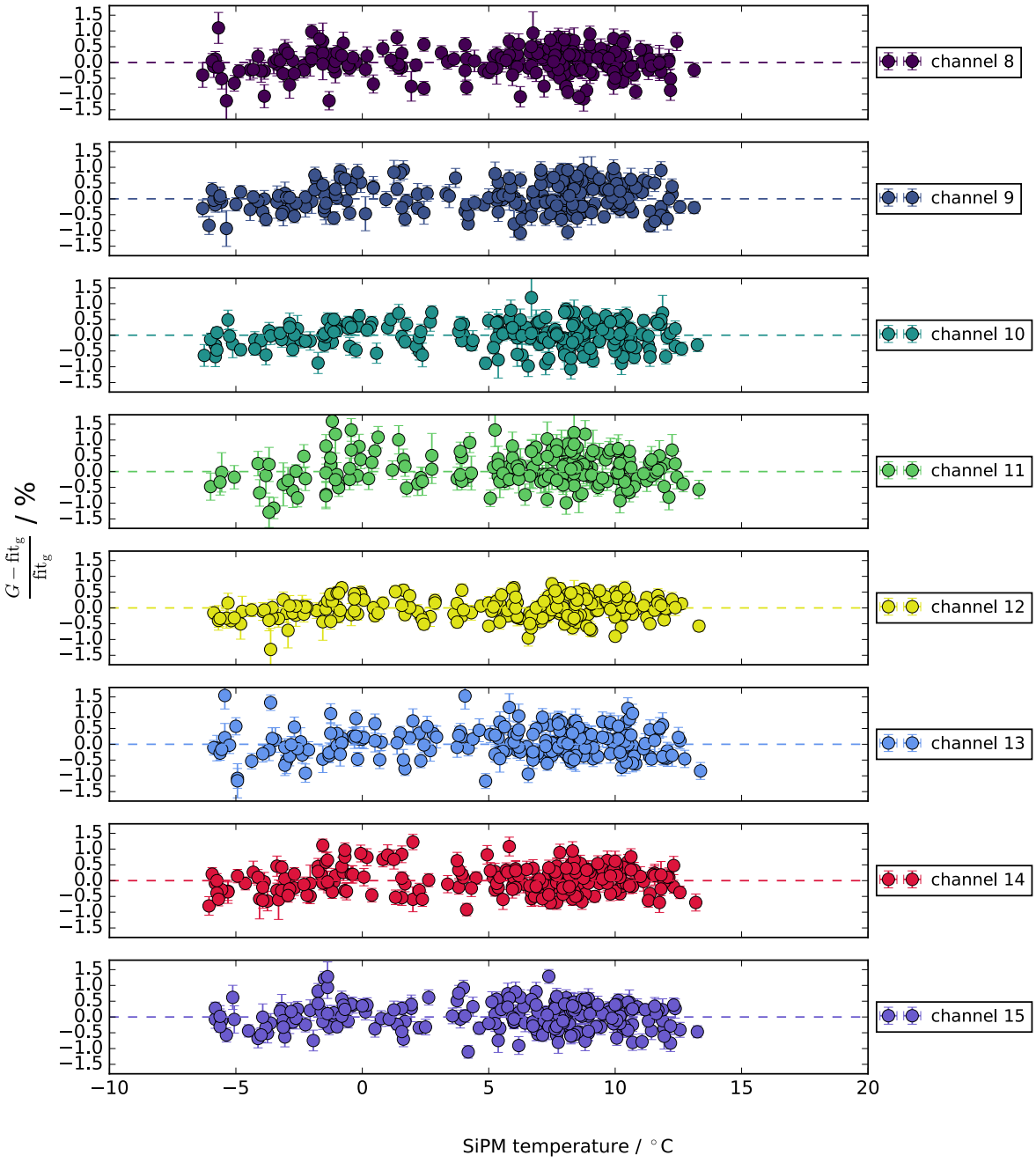

Figure 4.: Residuals $(G-\mathrm{fit_g})/\mathrm{fit_g}$ as a function of the SiPM temperature for all units located in module 2. The fit describes the development of the data well.

MIP peak stability

For each unit, the pedestal and the MIP peak position as a function of temperature is determined. A linear function is fitted to the corresponding data. Thereby, a conversion from the individual unit signal in ADC count to a signal in MIP for all temperatures can be achieved. The pedestal peak position depends on the temperature at the EASIROC. For each charge spectrum measurement, a Gaussian distribution is fitted on the pedestal peak. The mean of the Gaussian refers to the peak position. The uncertainty is given by the error on the mean provided by the ROOT framework. Figure 6 and figure 8 show the evolution of the position as a function of the EASIROC temperature for module 1 and module 2, respectively. The position is decreasing with temperature by a factor of roughly 0.5% /10K for all units. The linear fit $\text{fit}_\text{p} = a_\text{p} + b_\text{p} \cdot T_\text{EASIROC}$ is well describing the data except of the low and high temperature regime. The residuals determined for each data point in respect to the fit are presented in figure 7 and in figure 9 for module 1 and module 2, respectively.

In contrast, the MIP peak position is increasing with the temperature at the SiPM. The position is influenced by the gain which is, as discussed, not completely stable over a large temperature range. The position is once determined by the mode of a log-normal distribution (refer to equations 8.18 and 8.19) and by the mean of a Gaussian distribution. The comparison of the peak position is shown in figure 5. The color scale refers to the SiPM temperature. A strong correlation of both identification methods is determined. As the log-normal distribution is describing the spectrum better, this method is preferred.
In figure 10 and figure 12, the light yield in unit of ADC count is shown as a function of the SiPM temperature. Each data point refers to the mode of the log-normal distribution and the corresponding uncertainty is propagated by the error given on the fit parameters. The average evolution of the data can be well described by a linear fit $\text{fit}_{S_\text{max}} = a_{S_\text{max}} + b_{S_\text{max}} T_\text{SiPM}$. The residuals are presented in figure 11 and figure 13 for units in module 1 and 2, respectively.

By those studies, two individual conversion functions for all temperatures is achieved for all units. The first function converts the signal in ADC count S_adc to the signal in photon equivalent $S_\text{p.e.}$, the second converts the signal to the signal in MIP S_MIP

$$S_\text{p.e.} = \frac{S_\text{adc} - S_\text{adc, pedestal}(T_\text{EASIROC})}{G(T_\text{SiPM})} \tag{1}$$

$$S_\text{MIP} = \frac{S_\text{adc} - S_\text{adc, pedestal}(T_\text{EASIROC})}{S_\text{adc, max}(T_\text{SiPM}) - S_\text{adc, pedestal}(T_\text{EASIROC})} \quad . \tag{2}$$

The results for the signal in photon equivalent for all units is presented in figure 14 and in figure 16 for units located in module 1 and 2, respectively. Each data point corresponds to the signal yield calculated by its corresponding conversion function. The uncertainty is determined by Gaussian error propagation. The depicted signal yield is stable over a large temperature range of 20 °C. The light signal deviates within 2% of the average value $< S_\text{adc, max} >$. The residuals of all units are depicted in figure 15 and 17 for module 1 and 2, respectively. The light signal in p.e. is already corrected for the deviations in the gain of each SiPM, but still differs between units due to their individual light yield. A comparison of all units demonstrates an average light yield of (24.46 ± 2.27) p.e. with a maximum deviation between all units of 44% and to the average of 19%.

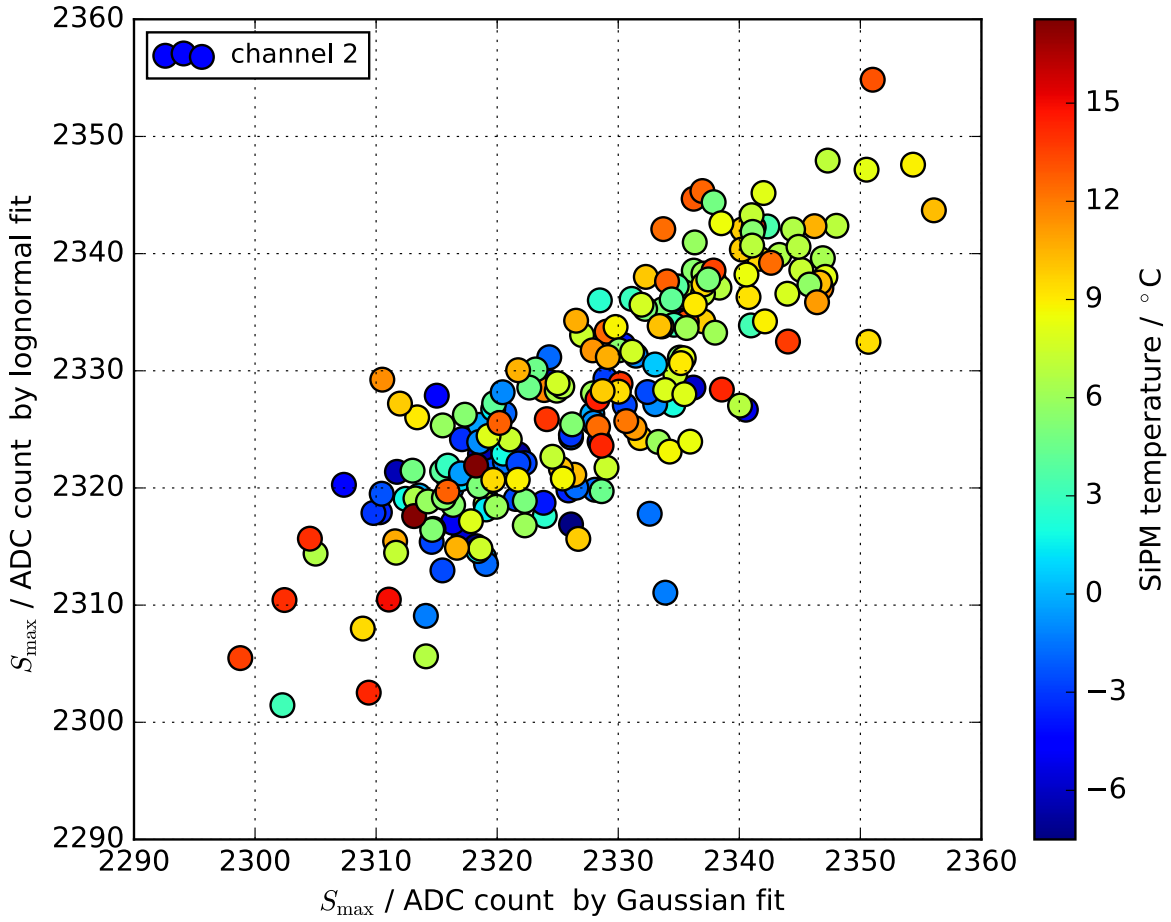

Figure 5.: Comparison of the MIP peak position $S_{\text{adc, max}}$ determined by a lognormal and by a Gaussian function. Both fits result in a well comparable position within 1% for all SiPM temperatures.

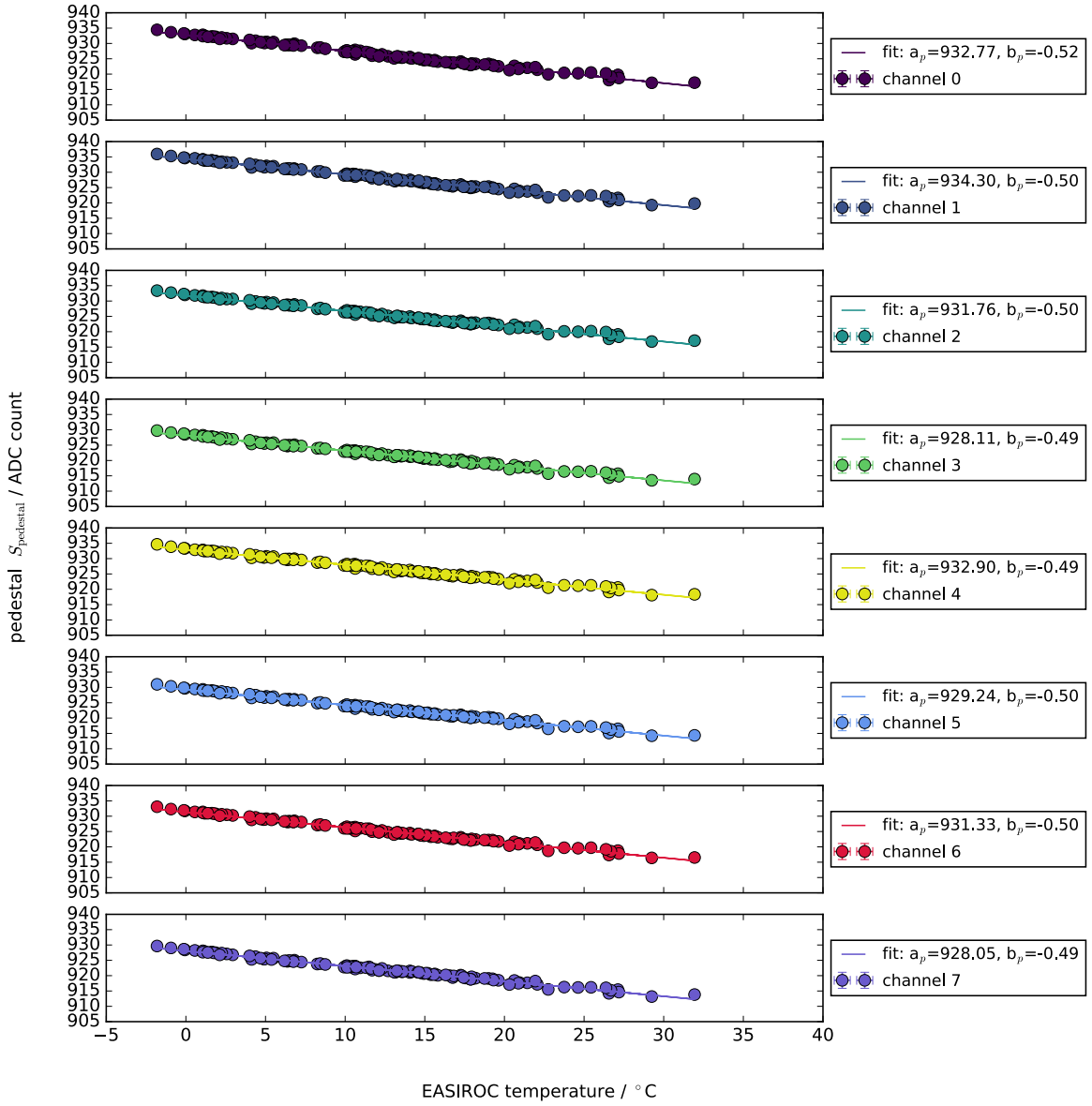

Figure 6.: Pedestal peak position $S_{\text{adc, pedestal}}$ as a function of the EASIROC temperature for all units located in module 1. For each unit, a linear function is fitted on the data points. The average change of the pedestal position is $< \Delta S_{\text{adc, pedestal}} / \Delta T_{\text{EASIROC}} >= -0.48\,\text{ADC count/K}$ or $0.5\%/10\,\text{K}$.

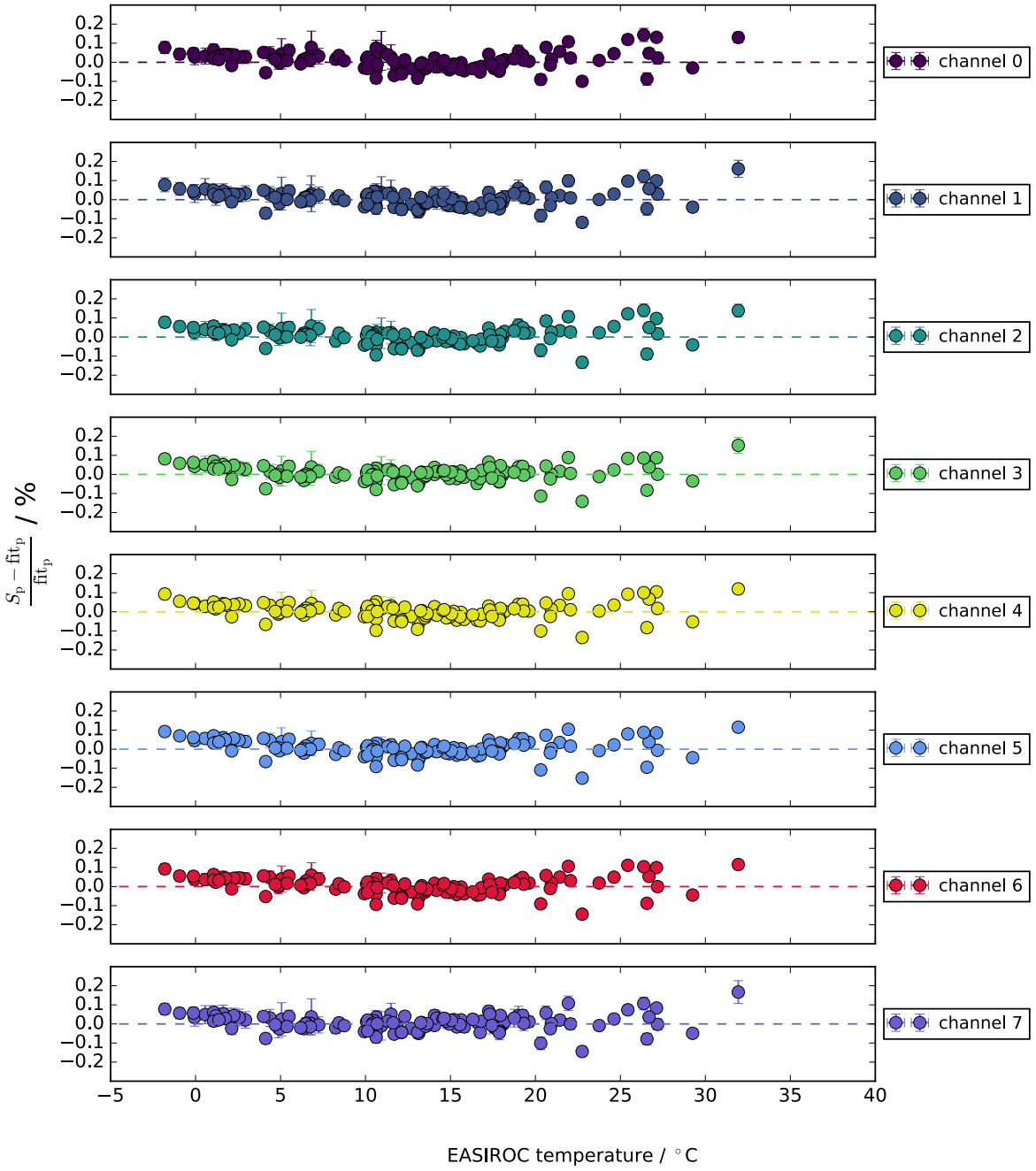

Figure 7.: Residuals $(S_{\text{adc, pedestal}} - \text{fit}_p)/\text{fit}_p$ as a function of the EASIROC temperature for all units located in module 1. The fit describes the development well in the medium temperature regime. At low and high temperatures the data demonstrates larger values than predicted by the fit.

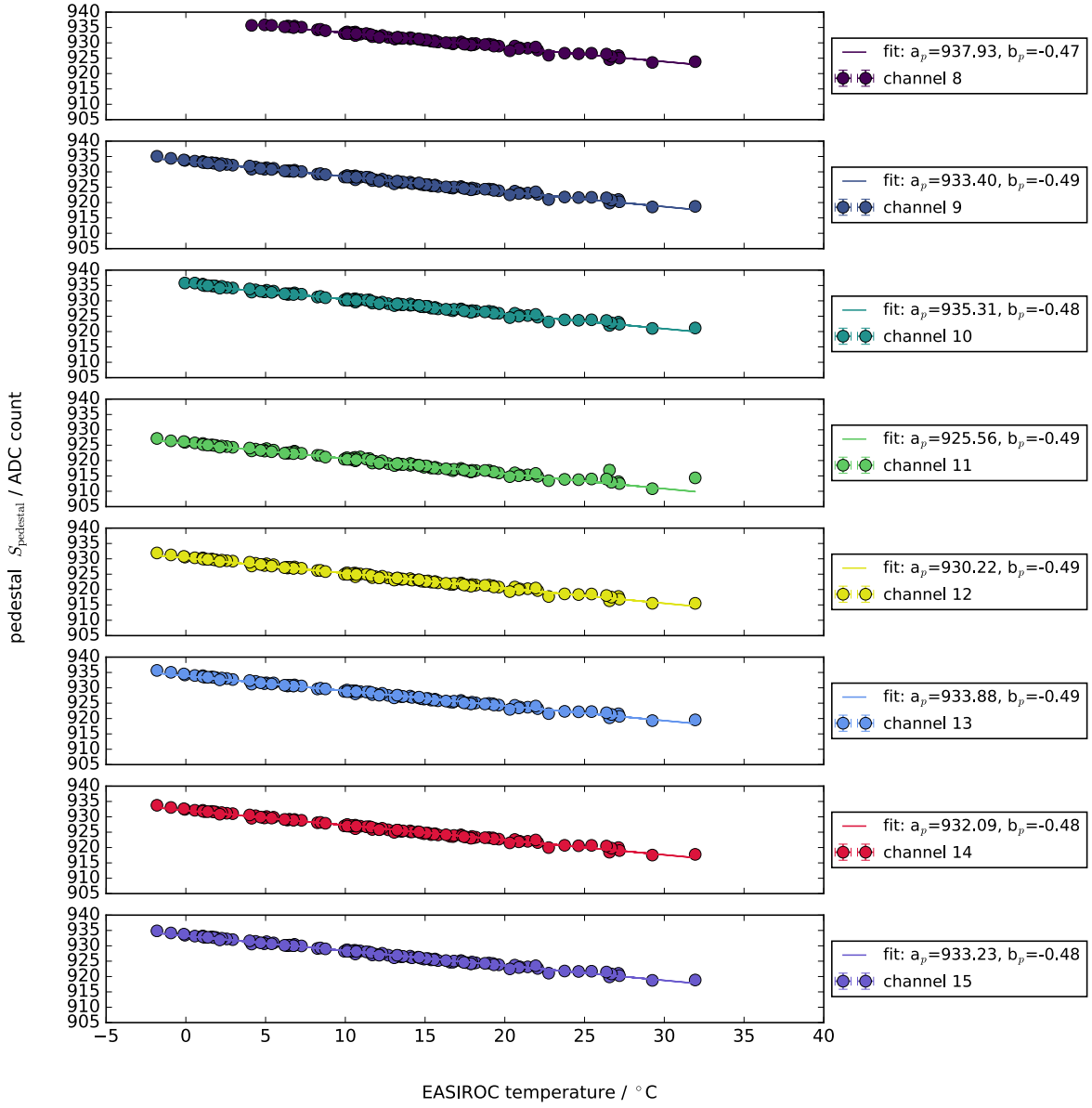

Figure 8.: Pedestal peak position $S_{\text{adc, pedestal}}$ as a function of the EASIROC temperature for all units located in module 2. For each unit, a linear function is fitted on the data points. The average change of the pedestal position is $< \Delta S_{\text{adc, pedestal}} / \Delta T_{\text{EASIROC}} >= -0.48\,\text{ADC count/K}$ or $0.5\%/10\,\text{K}$.

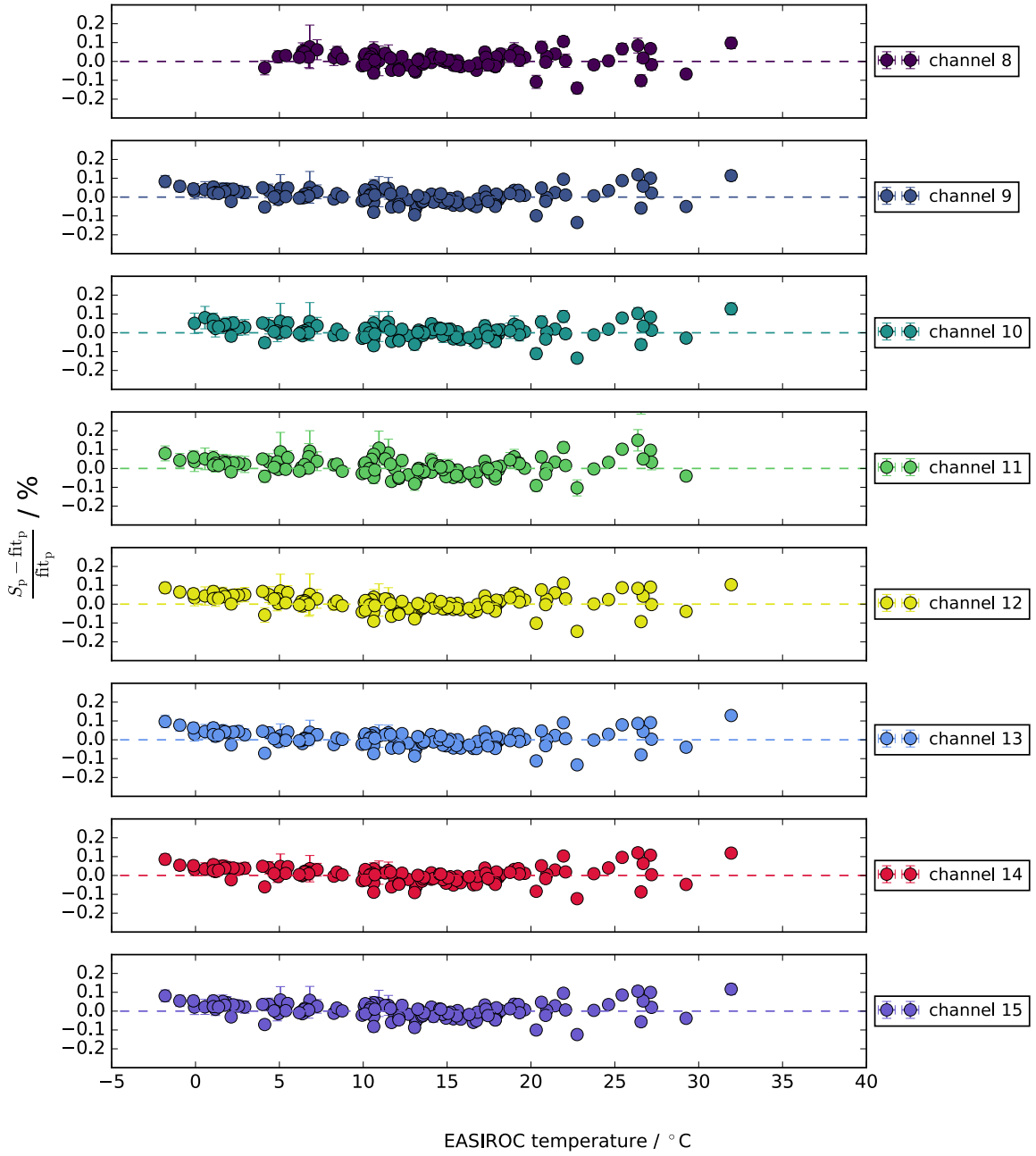

Figure 9.: Residuals $(S_{\mathrm{adc,\ pedestal}} - \mathrm{fit_p})/\mathrm{fit_p}$ as a function of the EASIROC temperature for all units located in module 2. The fit describes the development well in the medium temperature regime. At low and high temperatures the data demonstrates larger values than predicted by the fit.

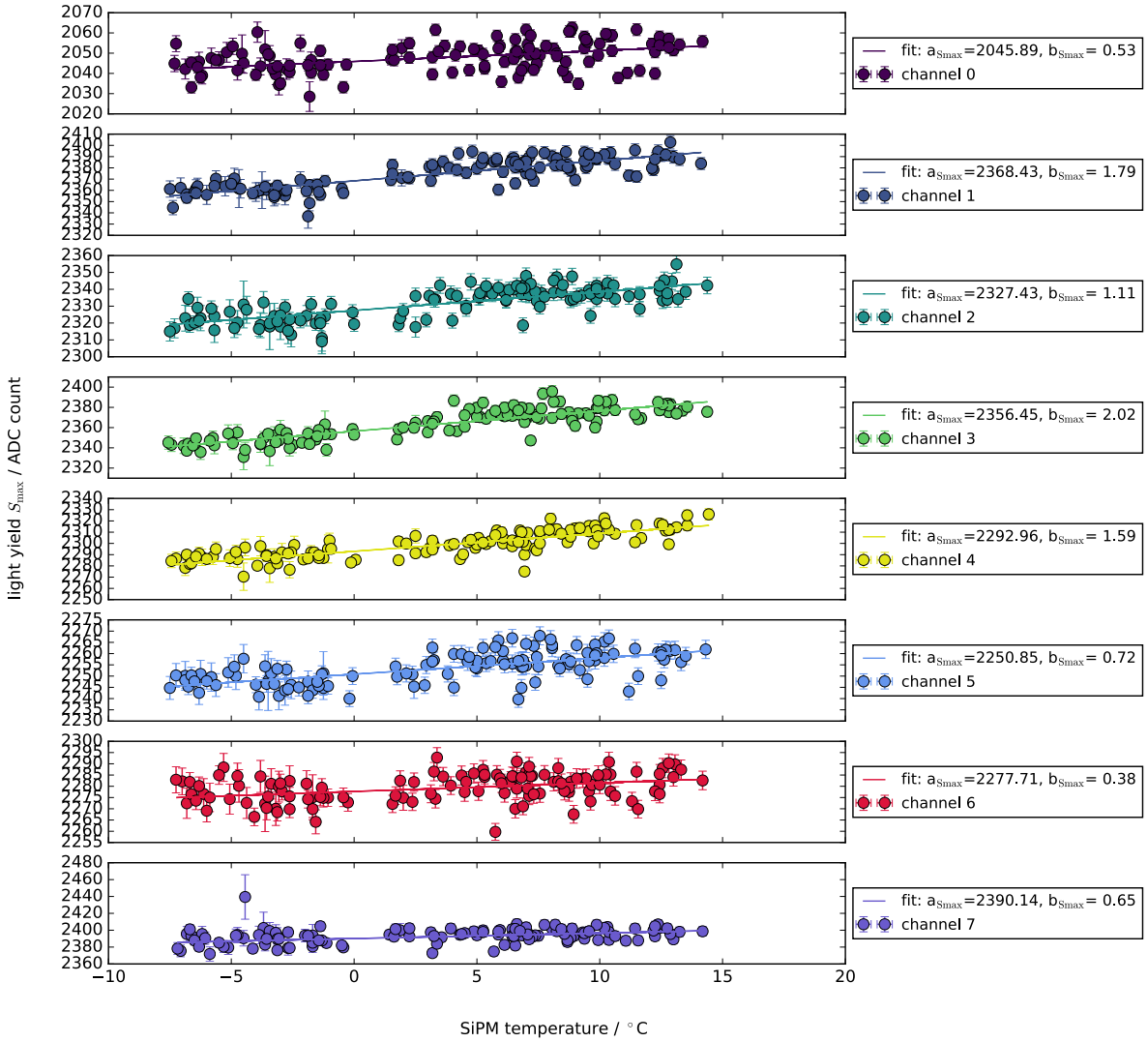

Figure 10.: MIP peak position $S_{\text{adc, max}}$ in ADC count as a function of the SiPM temperature for all units located in module 1. For each unit, the MIP peak position is determined by the mode of a log-normal fitted on the corresponding charge spectrum.

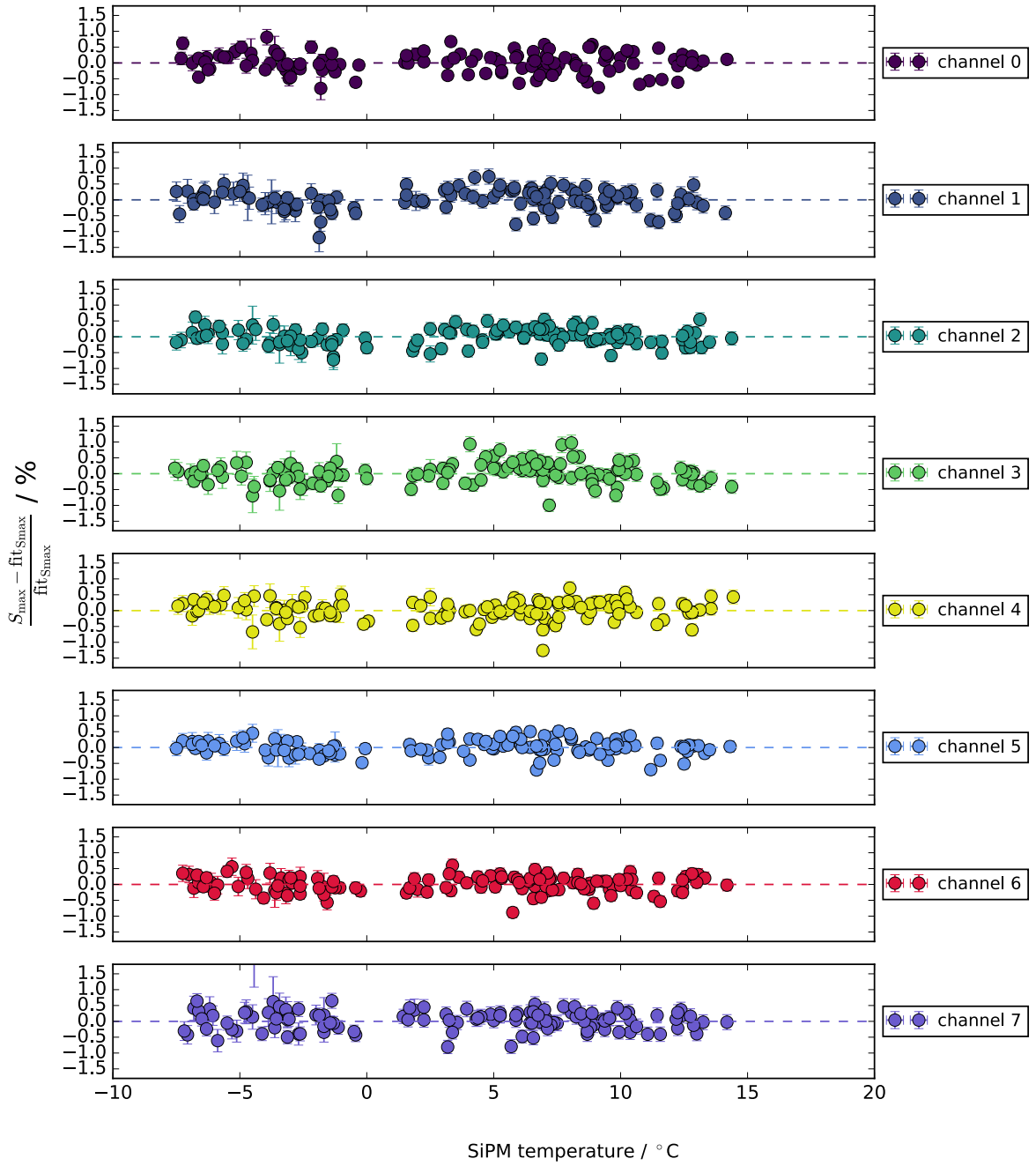

Figure 11.: Residuals $(S_{adc,\ max} - < S_{adc,\ max} >) / < S_{adc,\ max} >$ as a function of the SiPM temperature for all units located in module 1. The data are well described by the linear function.

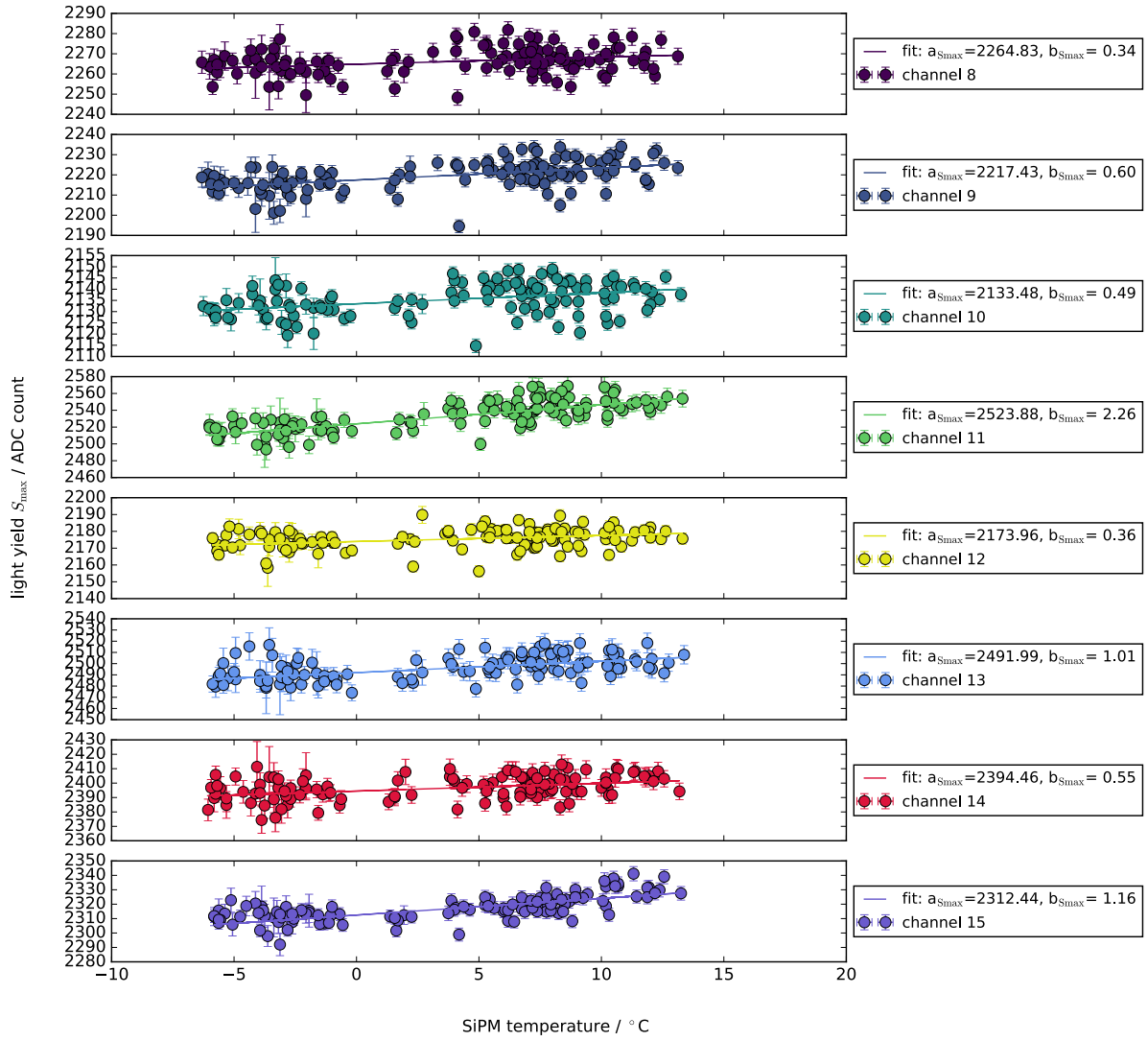

Figure 12.: MIP peak position $S_{\text{adc, max}}$ in ADC count as a function of the SiPM temperature for all units located in module 2. For each unit, the MIP peak position is determined by the mode of a log-normal fitted on the corresponding charge spectrum.

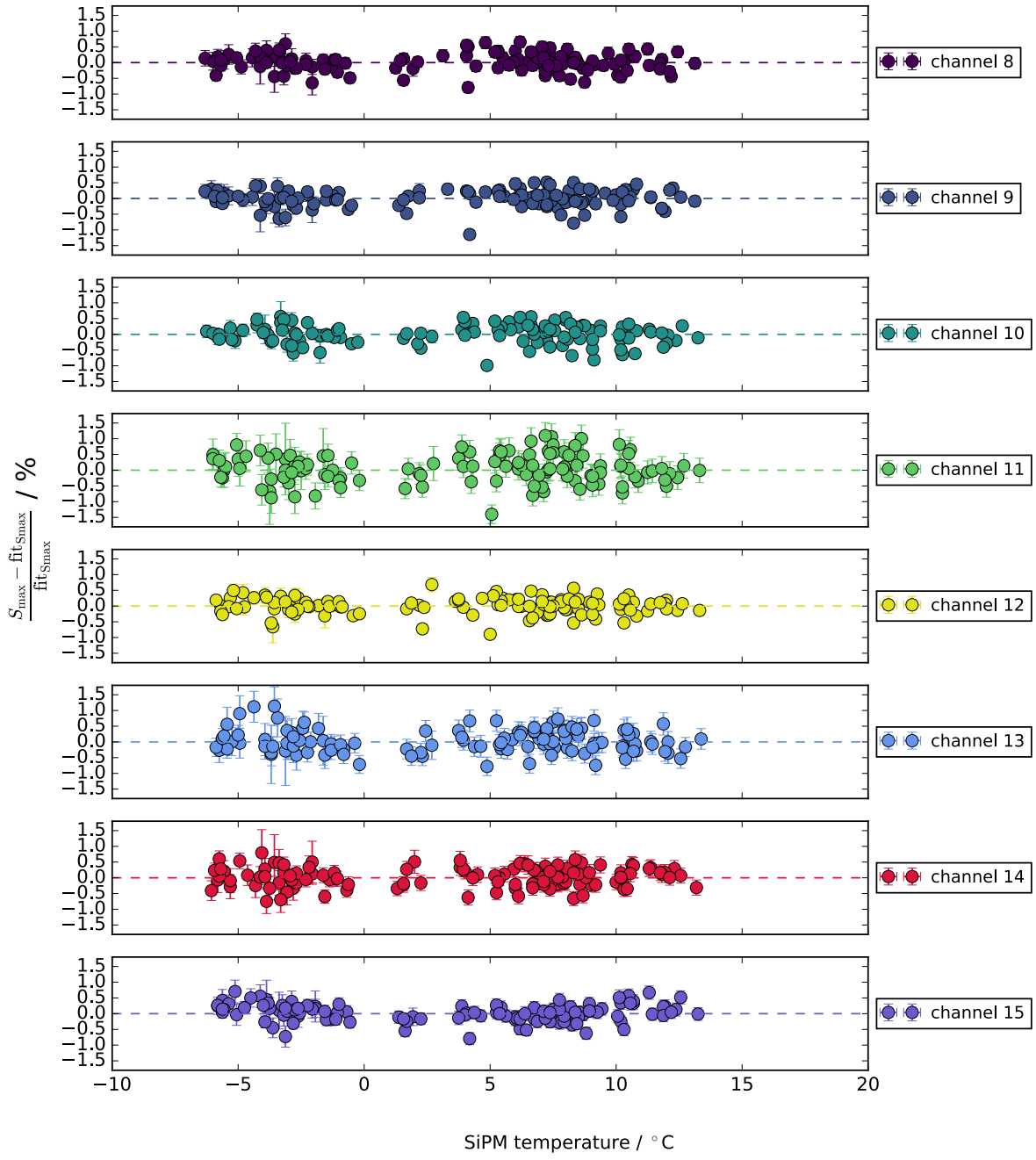

Figure 13.: Residuals $(S_{adc,\ max} - < S_{adc,\ max} >) / < S_{adc,\ max} >$ as a function of the SiPM temperature for all units located in module 2. The data are well described by the linear function.

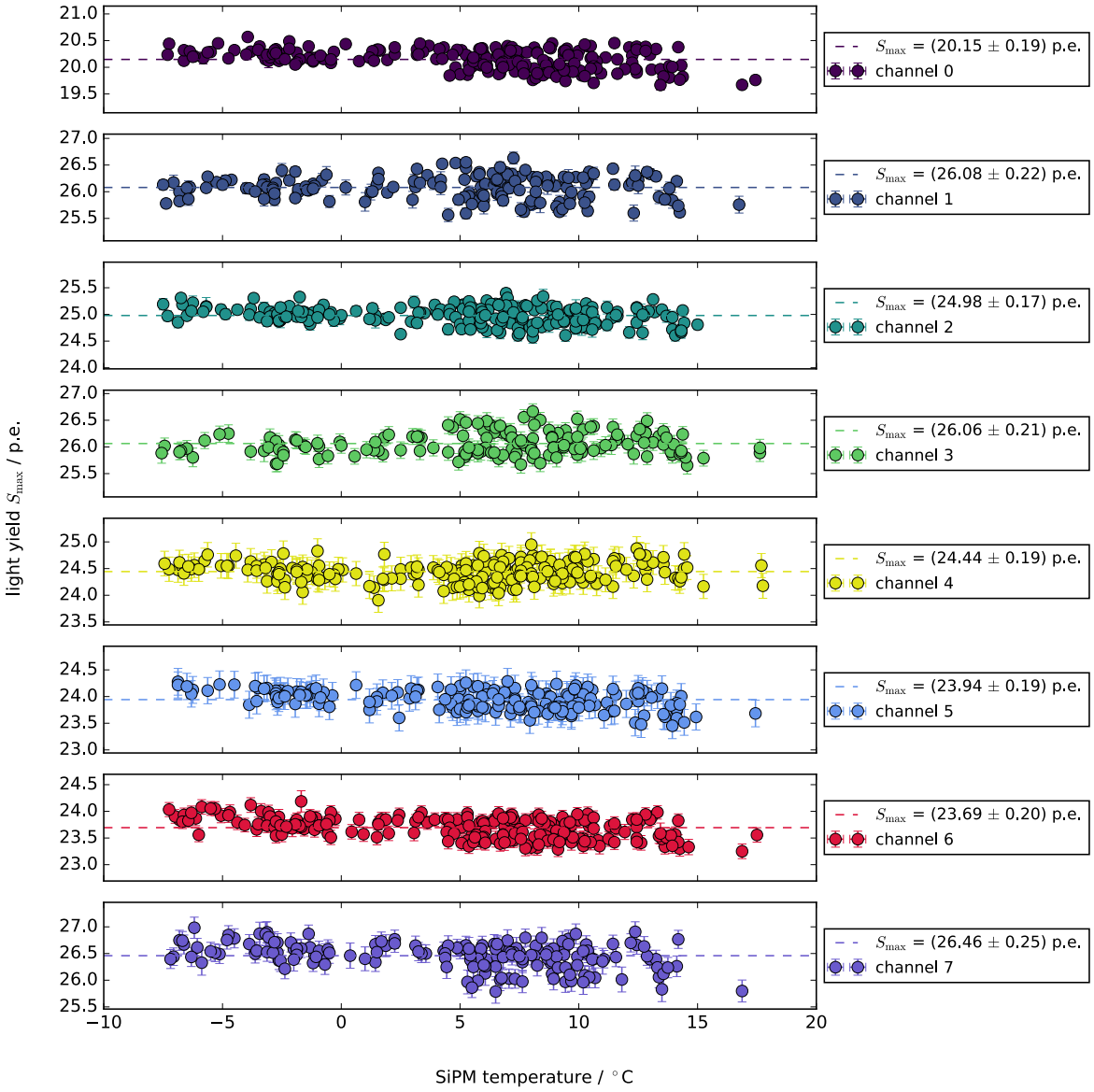

Figure 14.: MIP peak position $S_{\text{adc, max}}$ in p.e. as a function of the SiPM temperature for all units located in module 1. For each unit, the average of the data and its standard deviation is given. The light yields deviate by a maximum of 30%.

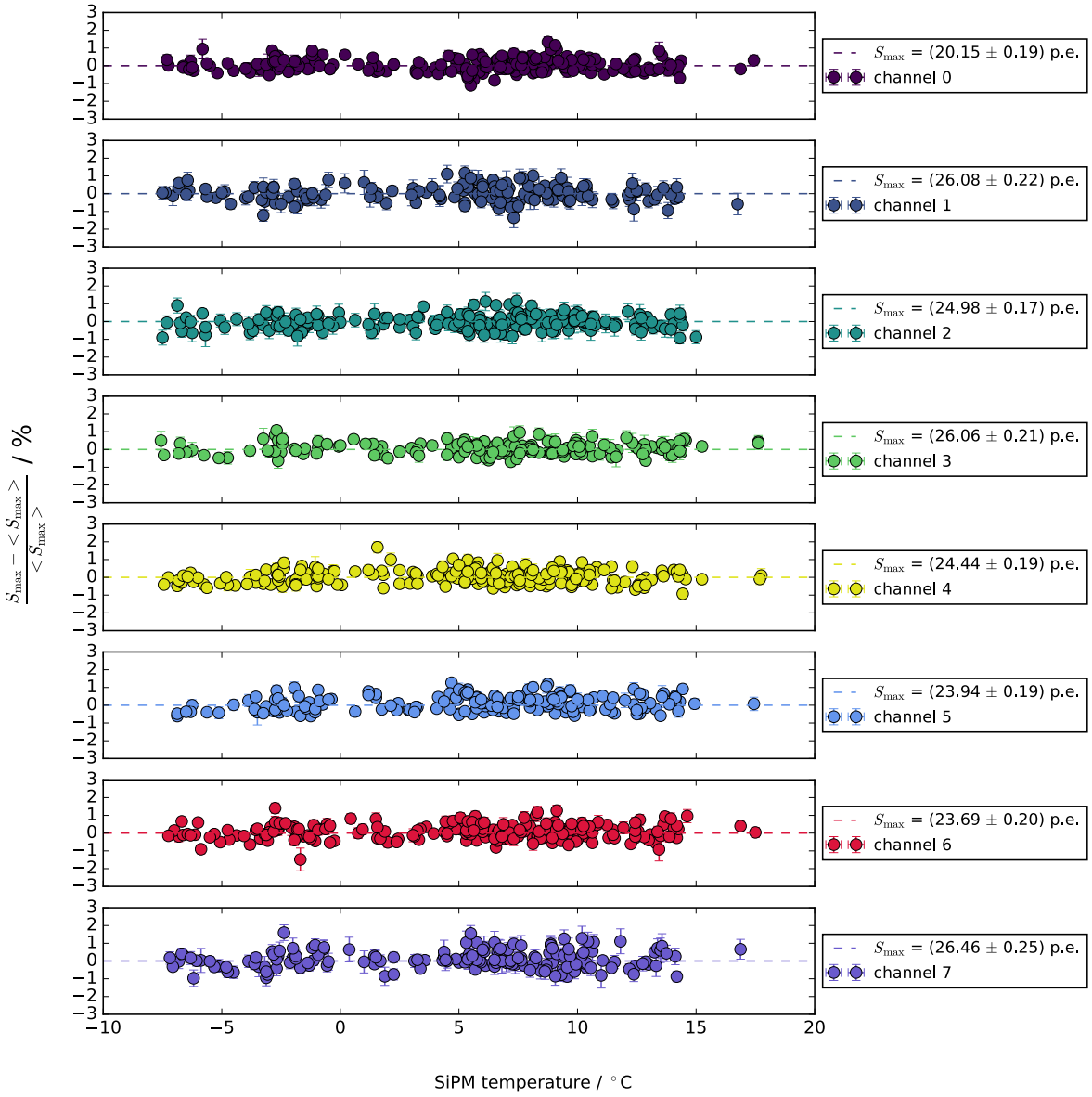

Figure 15.: Residuals $(S_{\text{adc, max}} - < S_{\text{adc, max}} >) / < S_{\text{adc, max}} >$ as a function of the SiPM temperature for all units located in module 1. The light yield deviates within 2% of the average.

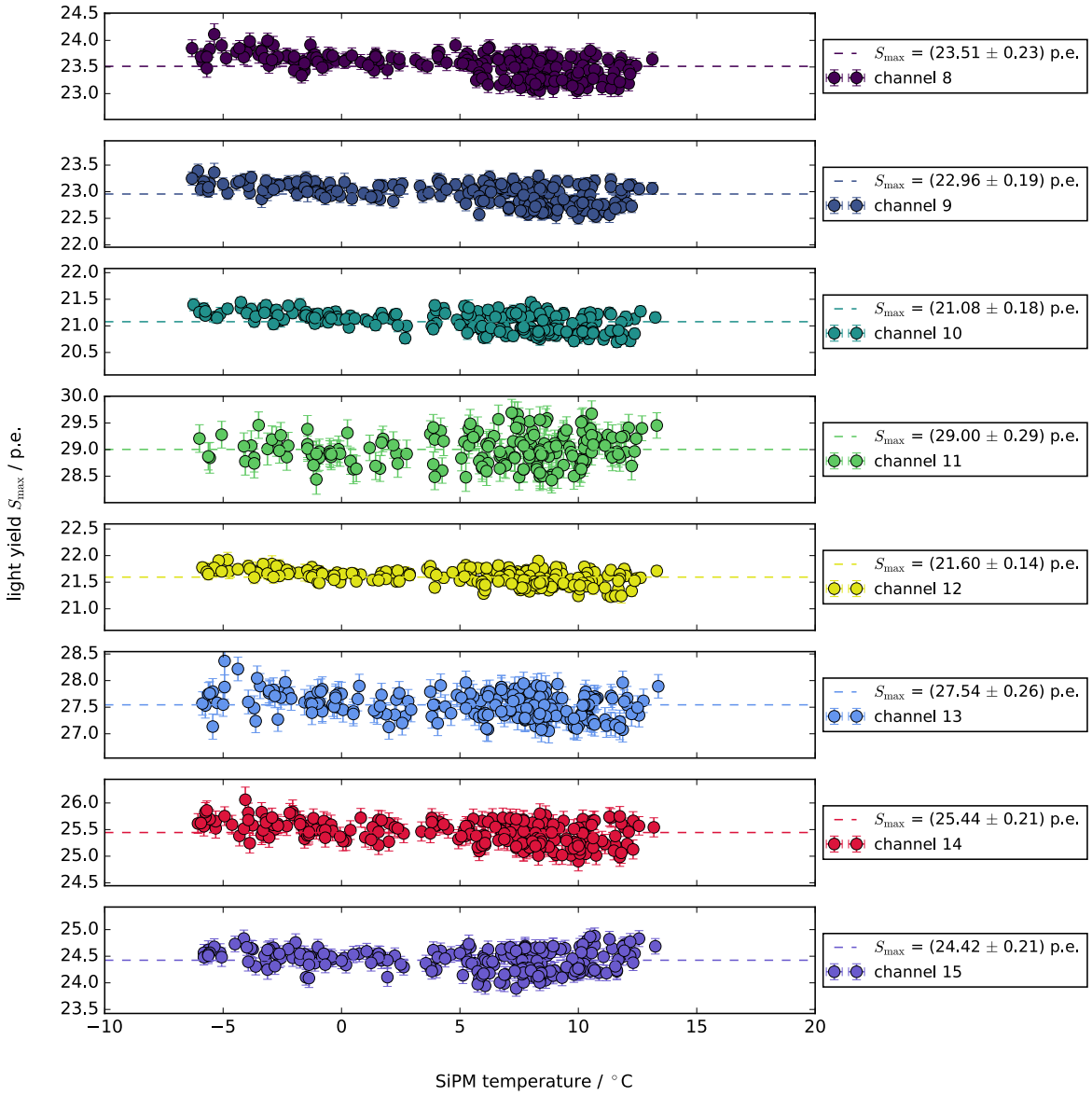

Figure 16.: MIP peak position $S_{\text{adc, max}}$ in p.e. as a function of the SiPM temperature for all units located in module 2. For each unit, the average of the data and its standard deviation is given. The light yields deviate by a maximum of 38%.

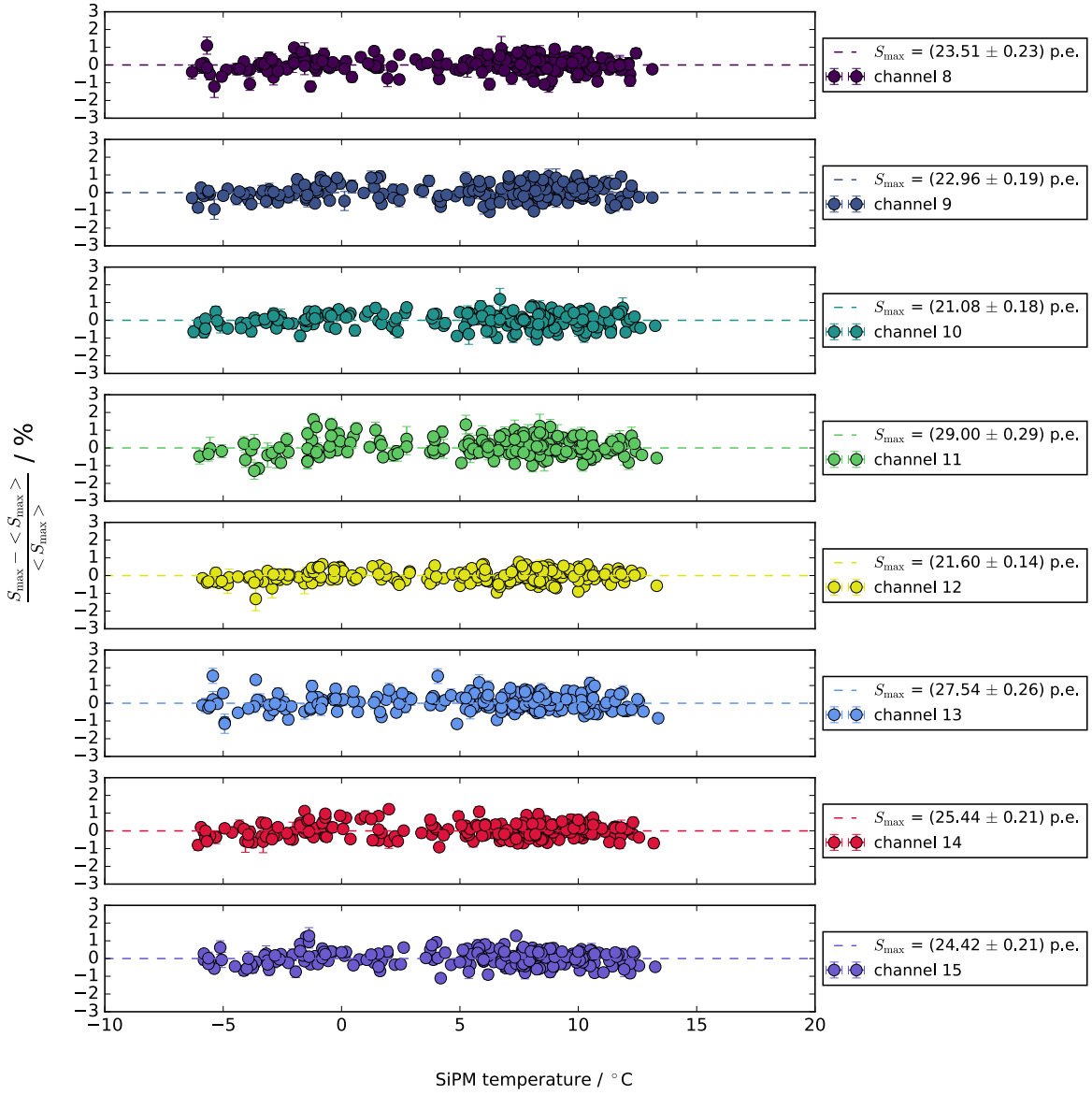

Figure 17.: Residuals $(S_{\text{adc, max}} - < S_{\text{adc, max}} >) / < S_{\text{adc, max}} >$ as a function of the SiPM temperature for all units located in module 2. The light yield deviates within 2% of the average.

Event rate at 0.5 and 1.5 p.e.

The trigger rate corresponding to a threshold of 0.5 p.e. and 1.5 p.e. is dominated by the thermal noise of the SiPMs. It is thus expected (cf. chapter 4) that both rates strongly depend on the temperature at the SiPM. The underlying atmospheric muon flux is of minor importance but may also variate due to atmospheric conditions as the air temperature or pressure. The thermal noise rate is expected to increase with ambient temperature. An exponential function can be used to describe the trigger rate as a function of the SiPM temperature. Each data point refers to the average trigger rate in the region of the 1 p.e. plateau of a performed threshold scan. Its uncertainty refers to the corresponding standard deviation. Exemplary, the trigger rate at a threshold of 0.5 p.e. as a function of temperature is shown for unit channel 10 in figure 9.10. All further units depict a comparable behavior. They are presented in figure 18 and in figure 19 for units located in module 1 and 2, respectively. The exponential fit $\mathrm{fit}_{1\,\mathrm{p.e.}} = a_{1\,\mathrm{p.e.}}(T_{\mathrm{SiPM}} = 0\,^{\circ}\mathrm{C}) + \exp(b_{1\,\mathrm{p.e.}} \cdot T_{\mathrm{SiPM}}) \cdot c_{1\,\mathrm{p.e.}}$ describes an expected doubling of the trigger rate per 8 K [114].

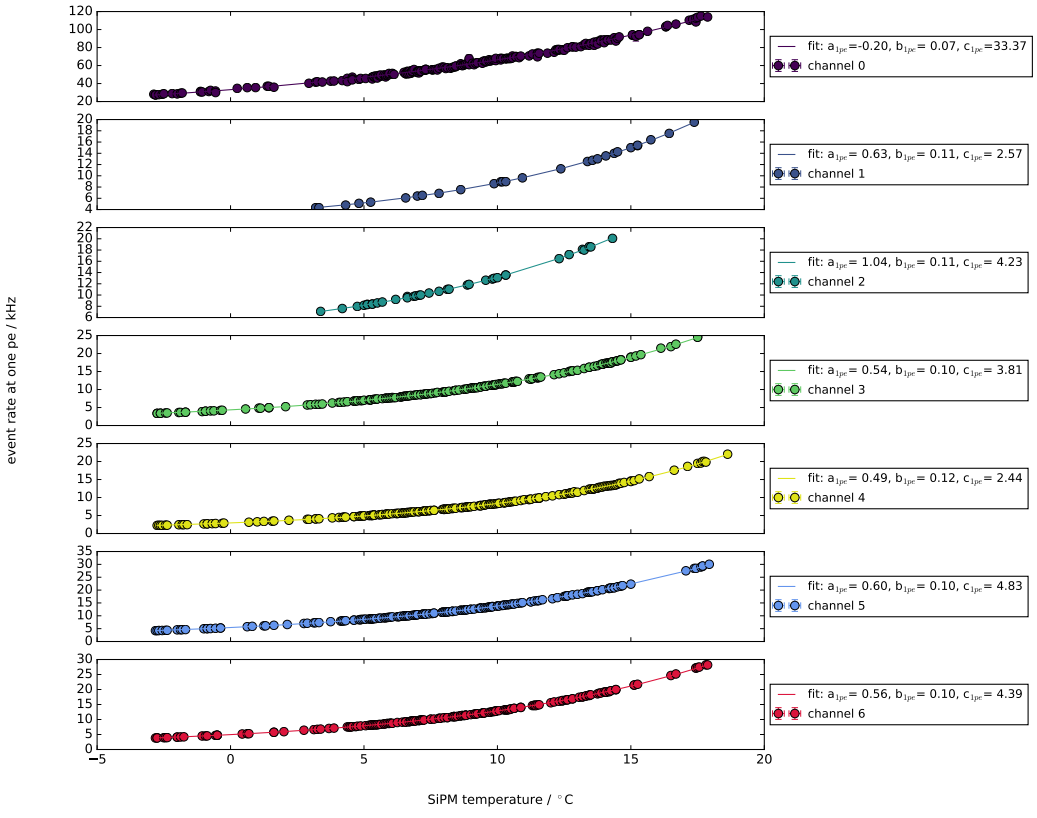

Figure 18.: For each unit of module 1, the event rate at a discriminator threshold corresponding to 0.5 p.e. is shown as a function of the SiPM temperature. A quadratic function is fitted on the data. Channel 0 corresponds to a SiPM with strongly increased thermal noise compared to all other SiPMs. For channel 1 and 2, only limited amount of data is available as the channels are subject to pick up noise.

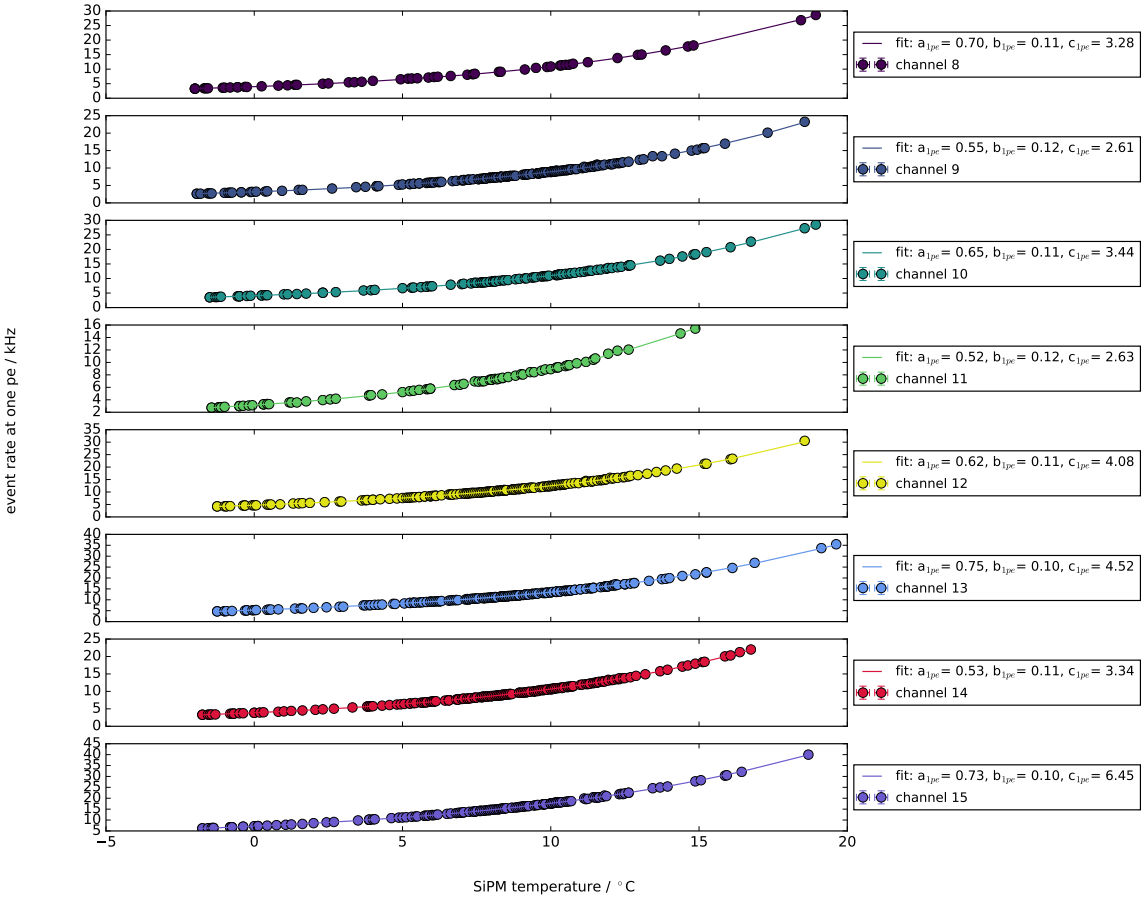

Figure 19.: For each unit of module 2, the event rate at a discriminator threshold corresponding to 0.5 p.e. is shown as a function of the SiPM temperature. A quadratic function is fitted on the data.

B. Synchronization of data streams between the air shower array and MiniAMD

As presented in chapter 9, the response of the detector demonstrator MiniAMD to air shower candidates is investigated while being operated in coincidence with a small-scale air shower array. Both experiments store their data on independent readout systems. Their unix timestamps have to be synchronized to allow for the study of coincident events. The deviation between both system clocks is slowly increasing, thus a matching algorithm is performed for each run. Furthermore, times in which one of both experiments is not active has to be excluded. For MiniAMD, measurements are performed to monitor important characteristics as the SiPM gain. Those introduce time periods in which no coincident data with the array are available (refer to appendix C for a discussion of the up-time of the detector). The air shower array shows short dead time periods about one minute in which data stored in the buffer is written to a ROOT file. During these periods, a hardware trigger may be registered by MiniAMD but the corresponding event has not been stored in the data stream of the air shower array.

For the synchronization of the data, a minimization of the average time difference between events of the array and the events registered at MiniAMD is performed, following equation 3.

$$\overline{\Delta t} = \frac{1}{n_{\text{miniamd}}} \sum_{i=0,1,2,.....}^{n_{\text{miniamd}}} \left| \Delta t_{\text{array, i}} - \Delta t_{\text{miniamd, i}} \right| \tag{3}$$

The index i refers to the event number index stored for the MiniAMD demonstrator. The index is thereby not referring to the amount of events successfully triggered by MiniAMD but the amount of requested triggers by the air shower array. The time difference between two consecutive events in MiniAMD $\Delta t_{\text{miniamd, i}}$ is compared to the time difference between the events of the air shower array $\Delta t_{\text{array, i}}$. An example of the synchronization procedure is presented in figure 20. In figure 20a, the average time difference is presented as a function of the starting index. A successful matching refers to $\overline{\Delta t} < 1\,\text{s}$. In figure 20b, an exemplary data stream for both detectors is presented. The MiniAMD timestamps (bottom) have been synchronized to the air shower array timestamps (middle). Only part of the events is detected in coincidence. Between the two lower figures, the event index, as registered by MiniAMD, is depicted. It is rising with each event detected by the array regardless of the MiniAMD trigger state. Thereby, the matching is enabled. For comparison, the top figure depicts the amount of array stations triggered. As indicated, most of the events are registered by two stations only.

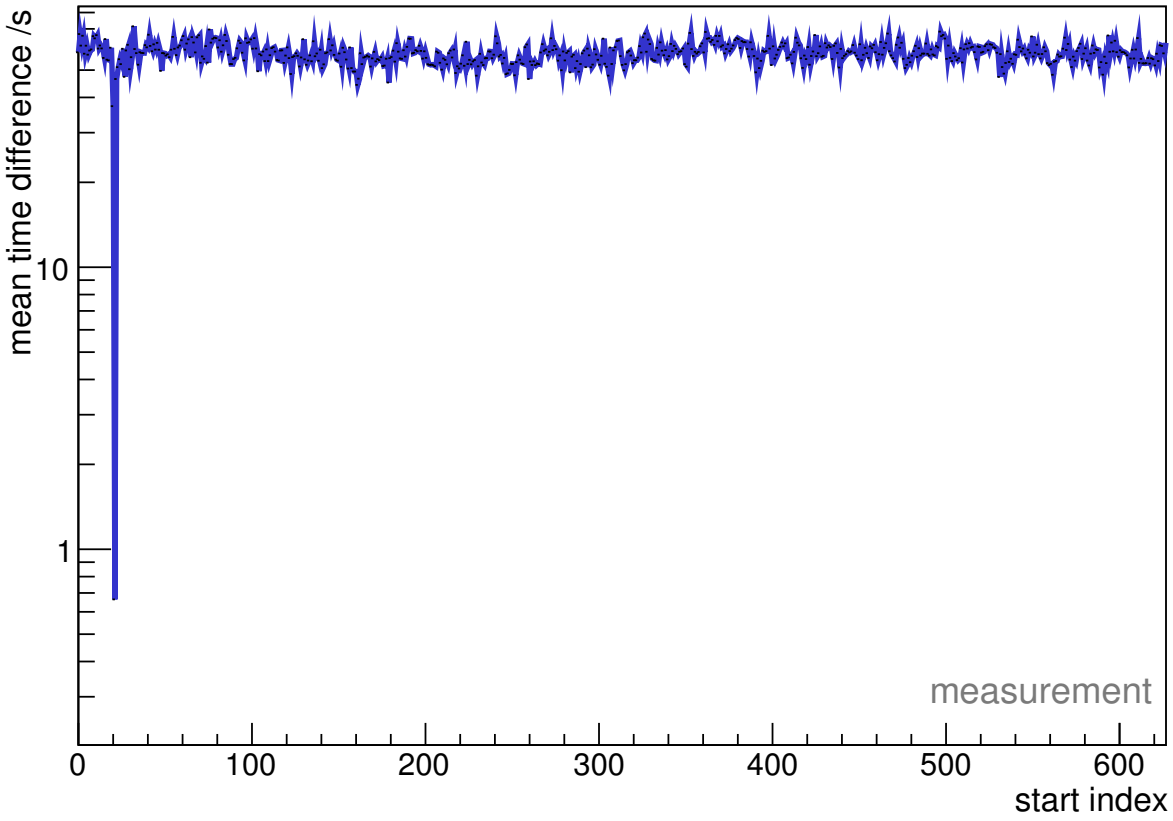

(a) Average time difference $\overline{\Delta t}$ in seconds as a function of the starting index in the array dataset. A clear minimum can be found at which the time difference is ≤ 1 s. Here, the data streams are synchronized.

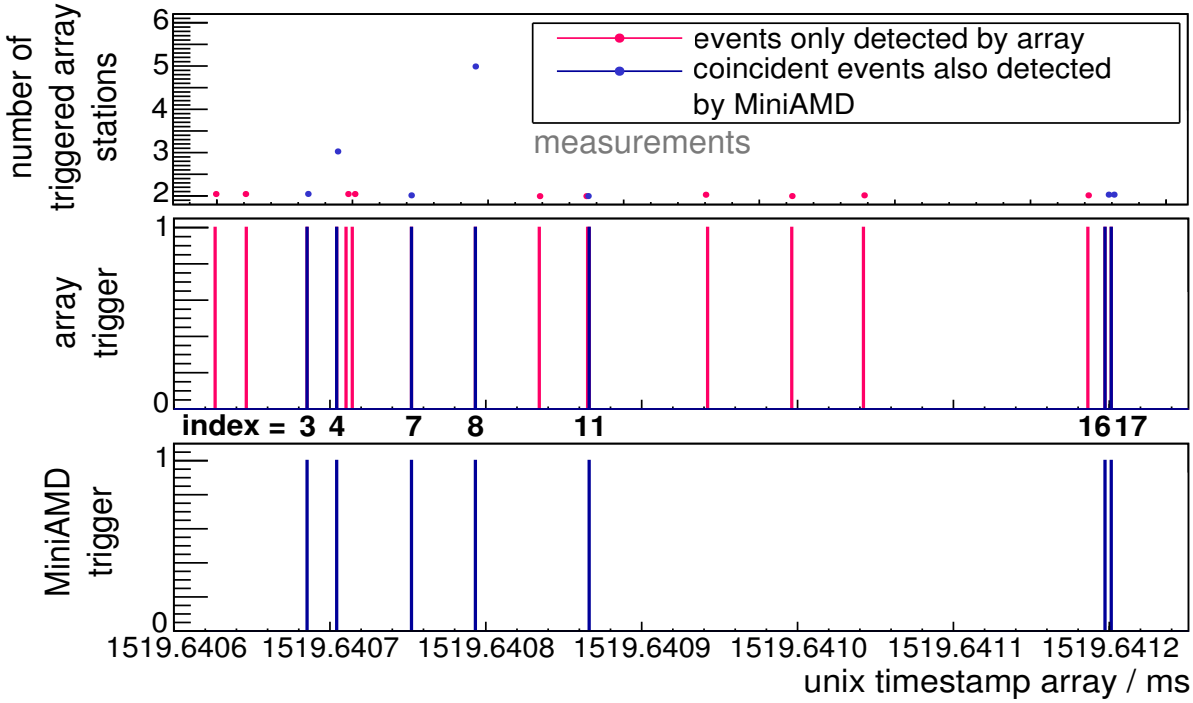

(b) Time traces of the array (middle) and of MiniAMD (bottom) as a function of the unix time of the array readout system. The MiniAMD timestamps have been shifted according to the matching algorithm. Coincident events are shown in blue, events of the array not detected by MiniAMD are depicted in red. Additionally, the number of array stations trigger is depicted (top).

Figure 20.: Matching algorithm of the events detected by the air shower array and MiniAMD.

C. Up-time of the detector

For the comparison of the spectra for different scenarios, not only the chosen trigger conditions as the threshold in DAC counts and the required multiplicity are crucial, but also the measurement time has a high impact.
As the electronics has only a limited readout frequency and bandwidth, measurements with low trigger requirements may result in a higher trigger frequency as manageable and therefore also in an event loss. Furthermore, each verification of the temperature results in an artificial dead time of approximately 1.5 seconds, at the time of this thesis. During the verification process, the buffer may overflow and data will be lost. Afterwards, a voltage adaption according to an occurring temperature change may follow. During the adaption process, the response of the sensor and the threshold setting are changing, the data are not read out and won't be accessible. The timespan between consecutive verifications has to be chosen such that the tracking of the temperature is reliable without introducing too much dead time of the system. Chosen timespans range between 30 seconds and 2 minutes resulting in a dead time between $1-5\%$. As the measurements have been performed during the development of a demonstrator detector, a stable readout and gain is the focus by the electronics. A less time consuming voltage adaption may be established in future works.
However, the user may decide to study the response of the detector with a user-defined dead time forced between consecutive registered events (refer to appendix E). As discussed in chapter 7, the shaping of the EASIROC slow shaper introduces an undershoot after registering an event. If a subsequent event arises during this time, the response on this event may be loared according to the undershoot. To avoid the displacement of the signal a minimum time of up to $2.5\,\mu$s without an event can be demanded before the next trigger is registered. The requirement introduces thus an artificial dead time of the system.

All these factors are reducing the up-time of the detector compared to the measurement time indicated by the system. Therefore, the data stored during self-triggering mode carry an event number which is referring to the actual amount of trigger seen by the system and not to the trigger stored in the data file. Thereby, a rough estimate of the system up-time is accessible. However, triggers not recorded due to the voltage adaption process after a temperature verification can naturally not be added to the event number and are missing. For a system triggered by an external experiment, the event number is referring to the amount of trigger requests by the external experiment as explained in chapter 9.5 and appendix B.

D. Study of different shielding scenarios between modules

The detector demonstrator MiniAMD is presented in chapter 9. The average trigger rate of the individual detector units depicts a significant decrease of the rate if a shielding is present (refer to figure 9.9). Two shielding configurations have been tested at the roof.

1. Module 1 is directly located on top of module 2. The distance between both units in a stack is about 10 cm. Different positions of two bricks (one made of concrete and one made of lead) are compared.

2. Module 1 is located on module 2 at the roof but with layers of high- and low-Z materials. The structure is designed as a sandwich (acrylic layer with a thickness of 12 mm, lead layer with a thickness of 2 mm, PVC plate with a thickness of f 2 mm and a layer of lead with a thickness of 2 mm). Distance between both units in a stack is increased to 30 cm.

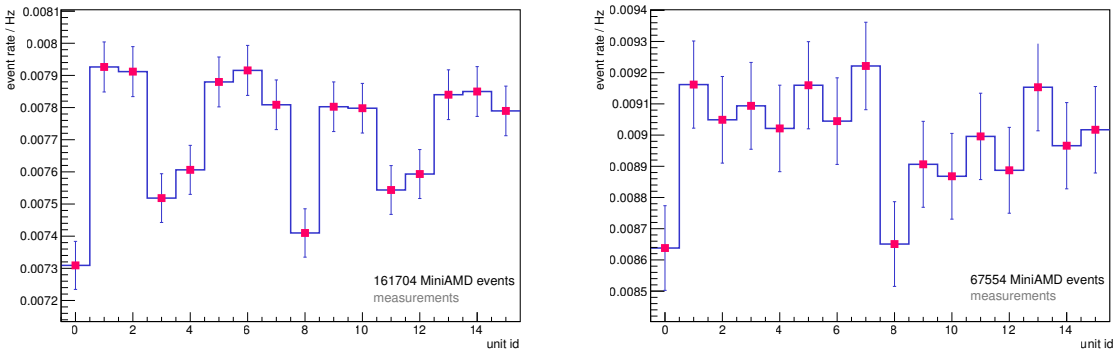

(a) Unit 0 and 8 are covered by a lead brick, while units 3, 4, 11 and 12 are covered by a brick made of concrete.

(b) Unit 0 and 8 are covered by a lead brick.

Figure 21.: Comparisons of event rate of all units depending on shielding by a brick made of lead and of concrete. Tiles with ids from 0 to 7 are located in the upper MiniAMD module while units with ids from 8 to 15 are located in the lower module. A random stack, for which both units have a signal exceeding a trigger threshold of 2.5 p.e., is requested for a trigger.

The first scenario studies the additional shielding introduced by two bricks for several positions on the MiniAMD detector. For the measurement, MiniAMD module 1 is located on module 2. Unit ids ranging from 0 to 7 correspond to units in the upper module (module 1) while unit ids ranging from 8 to 15 correspond to units in the lower module (module 2). For an event trigger, a random stack, for which both units have a signal exceeding a trigger threshold of 2.5 p.e., is requested. Both bricks (lead and concrete) are covering around half of a unit for vertical particles. The event rate as a function of the unit id is presented in figure 21 for two scenarios. For both, a more pronounced shielding is visible for the units covered by the lead brick. A shielding by lead reduces the event rate by 7%, while the shielding by concrete reduces the rate by 3.5%. The shielding is visible for both units of a stack with comparable effect of the shielding. This indicates that most events corresponds to punch-through particles if no shielding is apparent.

To study this effect further, an additional shielding is introduced between both modules of the MiniAMD demonstrator. It corresponds to scenario 2. It comprises acrylic and lead as shielding materials. A layer made of acrylic decelerates the electromagnetic component of the air shower crossing the upper module. If the electrons/positrons are such decelerated that they get absorbed in a following lead layer, it results in a decreased event rate in the lower module. If the deceleration is not sufficient and the electrons carry still enough energy to produce Bremsstrahlung, the opposite effect is expected with increased event rate in the lower module.

The measurement is presented in figure 22. The additional shielding results in an increased event rate (cf. figure 22a) and average detected signal in the lower module (cf. figure 22c). The profile of the average detected signal refers to the mean of all events included in the underlying histogram bin for each unit id. The uncertainty bars are referring to the rms of the distribution. This strongly indicates that high energetic particles leaving the upper module produce Bremsstrahlung in the material. The correlation plot of the detected signals in module 1 and 2 shows a clear deviation of the linear correlation as seen in the unshielded arrangement. An increased signal is apparent in the lower module (module 2) for the same events over the complete signal range (cf. figure 22b).

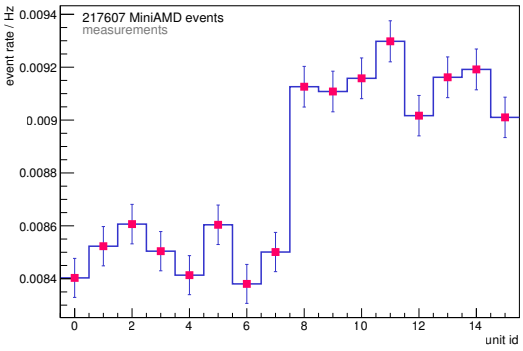

(a) Event rate as a function of the unit id. The event rate of the units of the lower module is strongly enhanced by the shielding sandwich.

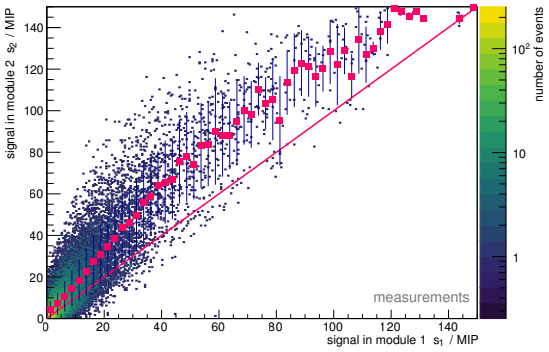

(b) Correlation of the measured signal in units of MIPs of module 1 and module 2 for the same events. The average signal of the lower module is strongly enhanced by the shielding sandwich.

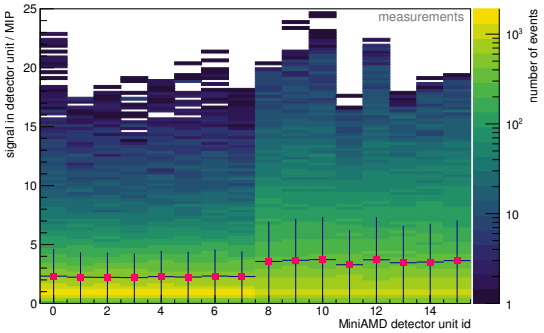

(c) Distribution of the detected signal as a function of the unit id. The average signal of the lower module is strongly enhanced by the shielding sandwich.

Figure 22.: An additional shielding is introduced between both modules of the MiniAMD demonstrator. The shielding consist of several layers (acrylic with a thickness of 12 mm, lead with a thickness of 2 mm, a PVC plate with a thickness of f 2 mm and a layer of lead with a thickness of 2 mm). Units with ids from 0 to 7 are located in the upper MiniAMD module while units with ids from 8 to 15 are located in the lower module.

E. Events with a signal yield smaller than required discriminator threshold

Within the scope of this thesis, several charge spectra indicate an unexpected shoulder left of the first peak over threshold (exemplary, cf. figure 8.14). These events, with signal yields smaller than the requested trigger threshold, originate from an undershoot present in the shaped signal of the slow shaper of the EASIROC as shown in chapter 7. To avoid those events, a hold-off time can be required. Thereby, a previous time window without any trigger is needed to allow for an event to be registered. In figure 23, two charge spectra as a function of ADC count are shown for the same unit of layout 2 operated with and without a required hold-off time of 1 μs. Both spectra are normalized to the same measurement time and have a discriminator threshold corresponding to 0.5 p.e. By the additionally required dead time before each trigger, the left shoulder of the 1 p.e. peak can be strongly reduced without influencing the actual charge spectrum.

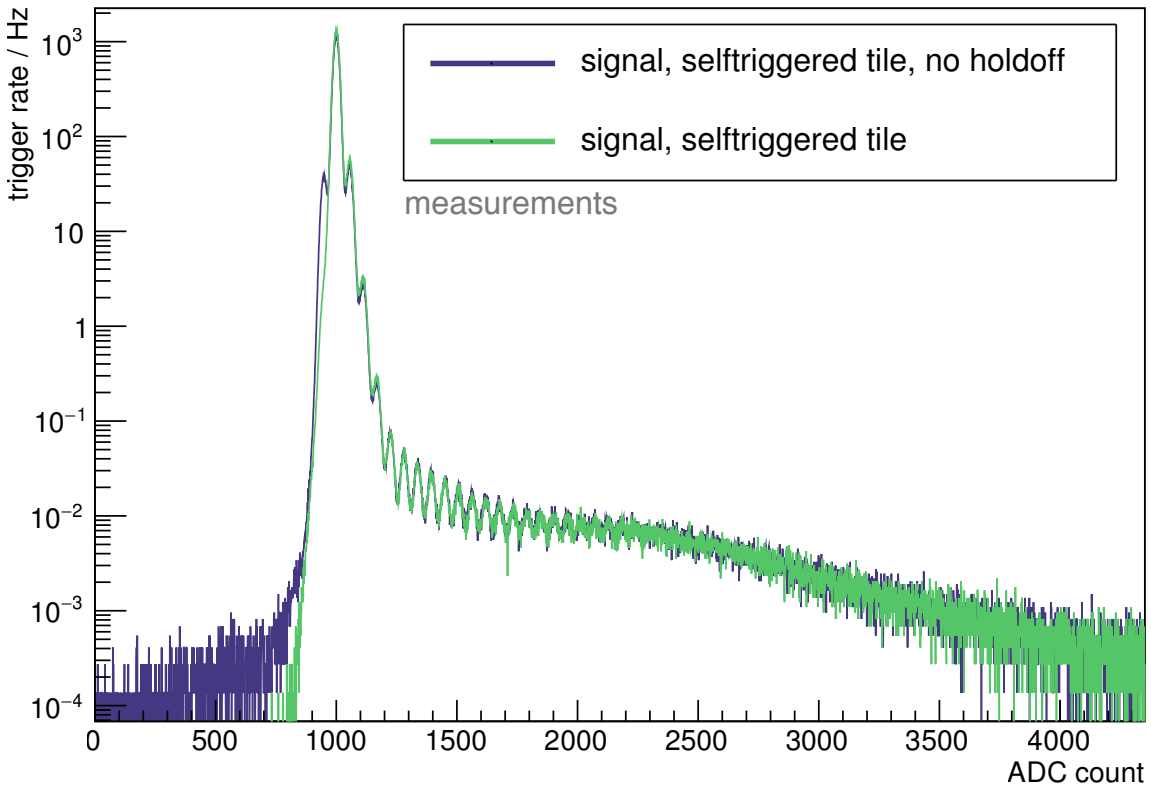

Figure 23.: Comparison of charge spectra as a function of ADC count for the same unit of layout 2 with and without a required hold-off time. Both spectra are normalized to the same measurement time. An unexpected shoulder to the left of the first peak above the threshold is visible for a tile without hold-off. The shoulder disappears when a hold-off time is required. Due to the hold-off time of $1\,\mu s$, an event is only accepted if no further event has been registered in the requested time window before. Thereby, an additional dead time is introduced, but prevents the event to be registered in the undershoot of the signal of a previous event. The undershoot originates from the slow shaper of the EASIROC and leads to signal yields smaller than the required threshold.

F. Implementation of material properties in Geant4

In this appendix, the elements and materials are listed, which have been used in the Geant4 [140] simulations in the scope of this thesis. Additionally, the properties of the elements and materials as given by the manufacturers are summarized. Furthermore, the physics processes, which have been considered in the simulations, will be listed.

Optical physics processes included in the Geant4 physics list

- Generation of photons in scintillator
  - Scintillation
  - Cherenkov radiation
- Wavelength shifting of photon in WLS fibre via absorption and re-emission of photons
- Attenuation effects
  - Absorption
  - Rayleigh scattering
- Optical processes at boundaries
  - Reflection
  - Refraction

Elements for the definition of Geant4 materials

Element	Atomic number Z	Standard atomic weight A/g/mol
Hydrogen (H)	1	1.00794
Carbon (C)	6	12.0107
Nitrogen (N)	7	14.0067
Oxygen (O)	8	15.9994
Fluorine (F)	9	18.998
Aluminum (Al)	13	26.9815
Titanium (Ti)	22	47.867
Lead (Pb)	82	207.2

G. Datasheet values

G.1. Scintillator EJ-212

EJ-212 [159] is a plastic scintillator specially designed to be used as thin sheets (thickness $\leq 5\,\text{mm}$). It is also best utilized in sizes up to 100 cm long.

Properties	Value	Unit
Light output	65	% Antracene
Scintillation efficiency	10000	photons / 1MeV e^-
Wavelength of maximum emission	423	nm
Light attenuation length	250	cm
Rise time	0.9	ns
Decay time	2.4	ns
Pulse width (FWHM)	2.7	ns
No. of H atoms per cc	5.17 x 10^{22}	
No. of C atoms per cc	4.69 x 10^{22}	
No. of electrons per cc	3.33 x 10^{23}	
Density	1.023	g/cc
Polymer base	Polyvinyltoluene	
Refractive index	1.58	
Softening point	75	°C
Vapor pressure	vacuum-compatible	
Coefficient of linear expansion	7.8 x 10^{-5} below 67 °C	
Light output vs. temperature	At 60 °C, the light output is reduced to 95 % of the light output at 20 °C. No change from 20 °C to -60 °C	
Temperature range	-20 to 60	°C

G.2. Optical cement EJ-500

EJ-500 [163] is a clear and colorless epoxy cement. It is ideal for optically bonding plastic scintillators and acrylic light guides. EJ-500 is fully cured at room temperature (20 °C) with a working life of 60 minutes. The mixed cement takes 3-4 hours to set and 24 hours to harden. However, it takes several days to achieve complete cure.

Properties	Value	Unit
Mixed viscosity	800	cps
Bond strength	1800	psi
Dielectric strength	420	volts/mil
Specific gravity, cured	1.17	
Service temperature	-65 to 105	°C
Optical transmission	nearly 100 above 400 nm	%

G.3. Wrapping materials as applied in Geant4

The applied wrapping materials for the scintillator tile are first presented in chapter 5.2.2. Here the parameters assumed for the Geant4 simulations are presented.

Parameters	Aluminum	Teflon	Tyvek
Chemical composition	Al	C_2F_4	C_2H_4
Density / g/cm^3	2.70	2.2	0.36
Refractive index n		1.365	1.5
Specular-lobe reflection	95 %	0 %	85 %
Diffuse reflection	5 %	100 %	15 %
Reflectivity		99 %	
Attenuation length μ_{att} **/ mm**		0.01	0.01
Surface roughness factor $\sigma/°$	5	5	5

G.4. Wavelength shifting fibres

The wavelength shifting fibres are of type BCF-92 [161] from Saint Gobain. The fibre has a diameter of 1 mm. The core contains a combination of fluorescent dopants selected to produce the desired scintillation, optical and radiation-resistance characteristics. The claddings are based on PMMA.

	Properties	Values
Core	Material	Polystyrene
	Refractive index	1.60
	Density / g/cm^3	1.05
	No. of H atoms per cc	4.82 x 10^{22}
	No. of C atoms per cc	4.85 x 10^{22}
	No. of electrons per cc	3.4 x 10^{23}
Inner cladding	Material	Acrylic
	Refractive index	1.49
	Thickness, round fibre	3 % of fibre diameter
	Thickness, square fibre	4 % of fibre size
Outer cladding	Material	Fluor-acrylic
	Refractive index	1.42
	Thickness, round fibre	1% of fibre diameter
	Thickness, square fibre	2% of fibre size
General	Numerical aperture	0.74
	Trapping efficiency, round fibre	5.6% minimum
	Trapping efficiency, square fibre	7.3%
	Wavelength of maximum absorption	405 nm
	Wavelength of maximum emission	492 nm

G.5. Optical fibre / Light guide

Edmund Optics offers ESKA acrylic fibre optics developed and manufactured by Mitsubishi [162]. The core of the fibre is made of acrylic polymer PMMA (polymethyl-methacrylate). It is sheathed with a special thin layer of fluorine polymer which has a lower refractive index than the fibre core. These fibres are designed to provide higher transmission in the wavelength regime of interest. They can be used for a wide range of applications, from general industrial light guides to short distance data transmission. The fibre is flexible, but is not designed to bear loads. An unjacketed version is used in this thesis.

Properties	Values	Unit
Acceptance angle	61	°
Minimum bend radius	25	mm
Material	Acrylic	
Attenuation	0.15	dB/m
Numerical aperture NA	0.51	
Operating temperature	-55 to + 70	$^{\circ}C$
Outer diameter	1.0	mm
Core diameter	980.00	μm
Fibre diameter	1000.00	μm
Refractive index core n_{core}	1.492	
Refractive index cladding n_{cladding}	1.402	

G.6. Silicon photomultiplier

Silicon photomultipliers (SiPMs) are compiled of several thousands of Geigermode avalanche photodiode as cells. Important SiPM characteristics are introduced in chapter 4. They are operated at a voltage V_{bias} which is higher than their breakdown voltage V_{break} which refers to the minimum needed voltage to induce an avalanche in a cell. The gain of a SiPM is in the order of 10^6 and is temperature depending. To achieve a stable gain the operating voltage has to be adjusted according to temperature. The photon detection efficiency (PDE) describes the SiPM capability to detect a photon. The main contribution to the darknoise of a SiPM is thermal noise caused by thermal excitations in a cell. It is referred to as uncorrelated noise while optical crosstalk and afterpulsing are summarized as correlated noise as they are only induced by a cell breakdown. Optical crosstalk is defined as photons emitted during a cell avalanche triggering neighboring cells. Afterpulsing are induced by additional, delayed avalanches in the same cell. In the original cell breakdown a charge carrier is trapped by impurities in the silicon lattice structure which is released after a short timespan.
Geometrical characteristics of the used silicon photomultiplier types S12571-050P and S13360-1350PE [105] are summarized in table 1.

Electrical and optical characteristics (measured at temperature of 25 °C) are presented in table 2.

	S12571-050P	S13360-1350PE
Effective photosensitive area / mm^2	1 x 1	1.3 x 1.3
Cell pitch / μm	50	50
Number of cells	400	667
Geometrical fill factor / %	62	74
Package	surface mount type	
Window material	epoxy resin	
Window refractive index	1.55	
Operating temperature / °C	0 to +40	-20 to +60

Table 1.: Geometrical characteristics of the used SiPM types.

Parameter	Symbol	Unit	**SiPM type S12571-050P**	**SiPM type S13360-1350PE**
Spectral response range	λ	nm	320 to 900	320 to 900
Peak sensitivity wavelength	λ_p	nm	450	450
Maximum photon detection efficiency^{*4}	PDE	%	35	40
Dark count^{*5}	typ	kcps	100	90
	max	kcps	200	270
Time resolution (FWHM)^{*6}		ps	250	not stated
Terminal capacitance		pF	35	60
Gain			1.2 x 10^6	1.7 x 10^6
Gain temperature coefficient		/°C	2.7 x 10^4	not stated
Breakdown voltage	V_{break}	V	65 ± 10	53 ± 5
Recommended operating voltage	V_{bias}	V	$V_{break} + 2.6$	$V_{break} + 3.0$
Crosstalk probability		%	$\mathcal{O}(25)$	$\mathcal{O}(3)$
Temperature coefficient of recommended operating voltage	$\Delta T(V_{break})$	mV/°C	60	54

^{*4}: Photon detection efficiency does not include crosstalk or afterpulsing.

^{*5}: Threshold = 0.5 p.e.

^{*6}: Single photon level.

Note: The above characteristics are measured at the recommended operating voltage.

Table 2.: Electrical and optical characteristics of the used SiPM types.

G.7. G4SiPM - properties defining a SiPM model

The following list of properties is used to define a SiPM model in the Geant4 simulation package G4SiPM [123]. The list taken from [54]. The properties can be modified by the user by a SiPM properties file which should be defined for each SiPM type under study. The list includes geometrical, operational and performance properties. Performance properties as the photon detection efficiency depend on the operating point which is defined by an ambient temperature T_{op} and its corresponding overvoltage V_{ov}. Not all properties may be known by the user for each available SiPM type. Therefore, if properties are not explicitly given be the user, default ones are used. They are assumed to be comparable for different SiPM models.

Property	Symbol	Unit
Geometrical and package properties		
Number of cells	n_{cell}	
Cell pitch	d_{cell}	μm
Fill factor	ϵ_{geom}	%
Coating thickness	d_{coat}	mm
Coating refractive index	n_{coat}	
Operational parameters		
Ambient temperature	T	°C
Bias voltage	v_{bias}	V
Relative fluctuation of the gain	σ_{pe}	%
Dead time	τ_{dead}	ns
Operating point		
Temperature	T_{op}	°C
Over-voltage	V_{ov}	V
Performance properties for operating points		
Breakdown voltage	V_{break}	V
Spectral photon detection efficiency	PDE (λ)	%
Thermal noise rate	f_{th}	kHz
Probability of fast afterpulsing	$p_{\text{ap,f}}$	%
Probability of slow afterpulsing	$p_{\text{ap,s}}$	%
Time constant of fast afterpulsing	$\tau_{\text{ap,f}}$	ns
Time constant of slow afterpulsing	$\tau_{\text{ap,s}}$	ns
Probability of optical crosstalk	p_{ct}	%
Recovery time constant	τ_{rec}	ns

H. Statistical distribution

The probability of finding one random trigger in a time interval T for a single detector is

$$p(T) = 1 - e^{-rT} \quad . \tag{4}$$

If now two detectors are operated in coincidence, each detector has a rate of random triggers r_i with $i = 1, 2$ and there is a probability p_2 to get a coincidence event in a gate width w T. Any infinitesimally small interval of time $\mathrm{d}t$ is equally likely to contain an event. The probability of finding an event in $\mathrm{d}t$ is given by $r_i\,\mathrm{d}t$. Thus, the probability to get a random coincidence in an infinitesimal time interval $\mathrm{d}t$ can be calculated according to

$$p_2 = R\,\mathrm{d}t = r_1\,\mathrm{d}t \times p(w;2) + r_2\,\mathrm{d}t \times p(w;1) \quad . \tag{5}$$

The factor $r_i \, \mathrm{d}t \times p(w; j)$ describes the probability of the gate being opened by a trigger of detector i times the probability of detector j to receive a trigger within the gate width w. If assuming that for both detectors $r_i w \ll 1$, the probability $p(w, i)$ can be expanded to first order $p(w; i) \approx r_i w$. Thereby, a rate R of random coincidences for two detectors can be expressed as

$$R \, \mathrm{d}t = 2 \cdot r_1 r_2 w \mathrm{d}t \tag{6}$$

$$\Rightarrow R = 2 \cdot r_1 r_2 w \quad . \tag{7}$$

This rate of random coincidences can be extended to more than two detectors, leading to a rate of $R = 3 \cdot r_1 r_2 r_3 w^2$ for a three-fold coincidence and so forth.
The rate of random coincidences for m detectors can thus be described by

$$R_m = m \cdot w^{m-1} \prod_{i=1}^{m} r_i \quad . \tag{8}$$

Characterization studies of optical components

The presented simulation framework in chapter 7 allows to study the expected performance of optical components standalone or in combination. The combination of a scintillator tile, a wavelength shifting (WLS) fibre, which is optionally coupled to an optical waveguide, and a silicon photomultiplier (SiPM) is thereby referred as a *unit* in this chapter. These simulations predict an excellent performance of the chosen unit design. However, simulations may not contain all characteristics of a real setup. Thus, the framework has been validated with respect to studies of complete units and individual optical detector components to prove the reliability of the simulation framework in terms of the expected light yield. Furthermore, these studies are designated to improve and to understand the small light yield of around 8 p.e. (photon equivalent) of previous assembled units (called layout 1) compared to simulations (around $30-35$ p.e.). These units of layout 1 are presented in chapter 6 and in the work of Lukas Middendorf [165]. They are based on the transmission of photons via the WLS fibre and an optical waveguide to the SiPM.

First, several characteristics of the WLS fibres are studied indicating a worse performance than predicted by simulations and by the according datasheet of the manufacturer. A probable reason may be an increased light loss along the fibres due to defects at the outer cladding of the fibres. Secondly, the optical coupling of the WLS fibres with optical waveguides is presented. Simulations predict a smooth transition of light between both fibres at a perfect optical coupling but a critical source of light loss if a small air gap is present. Measurements of the optical coupling indicate the latter scenario. Further on, several modifications of the design are investigated by means of a *test unit*. For example, the influence of the wrapping material around the scintillator tile is studied. The light yield detected by the photosensor reflects thereby the predictions of the simulated setup.
An overview of these measurements is given in figure 6.1.

I. Characterization of the WLS fibre and its coupling to an optical waveguide

The performance of wavelength shifting fibres is crucial for the light yield achieved with the complete unit. Therefore, different characteristics of the WLS fibre and the transmission efficiency by its coupling to an optical waveguide are studied and compared, if possible, to simulations performed by the framework introduced in chapter 7.
For these measurements, single WLS fibres are illuminated in different setups by a constant flux of an LED. The resulting light yield is detected by a pin photodiode or by a spectrum analyzer. Therefore, in the first instance the measurement equipment is briefly introduced before the performed studies are discussed.
The author of this work would like to point out that all presented studies are performed to determine the optimal choice of the materials or of the configurations of the unit layout. The goal is to achieve the best available light yield without claiming exact predictions about their performance as a single optical element or in an assembled setup. For such a prediction more intense studies would be needed which take care of the possible large systematics present in the current setups. Especially, the quality of fibres used in such investigations needs to be determined and monitored. During the work with WLS and optical fibres, it is found that an accidental damaging of the fibre ends can introduce an intensity loss by up to 50% especially for the multicladding WLS fibres used in this thesis. A more regular use of the fibres is less crucial but depicts compared to a freshly polished fibre[1] also an intensity loss of up to 20% over time.

[1] For the treatment of the WLS fibre and optical waveguide ends, please refer to section 5.2.3.2.

I.1. Equipment

LED

An UV-blue LED with a sharp emission spectrum $380-430\,\text{nm}$ and a peak wavelength of $405\,\text{nm}$ is used to illuminate the WLS fibre from the side. The LED is chosen to offer a high intensity, small incident angle of around 30° and a wavelength regime comparable to that of a plastic scintillator. The LED shows an increasing intensity until a thermal equilibrium (saturation state) is reached after roughly half an hour operation time.

Spectrum analyzer

For a few applications a spectrum analyzer (Ocean Optics USB650 UV-VIS Red Tide) is used to measure the wavelength spectrum of the incident light [216]. The spectrum analyzer detects photons in a wavelength regime of $200-880\,\text{nm}$ by a system consisting of mirrors and a grating guiding different wavelengths to different parts of a linear silicon CCD array. It has a sensitivity of 75 photons/count at $400\,\text{nm}$ and an optical resolution of $\sim 2.0\,\text{nm}$ FWHM. It offers a calibrated spectrum. The integration time, so the time of data taking, can be varied. An integration time is chosen at which no saturation of the CCD takes place. For each measurement the darknoise spectrum has to be determined and subtracted from the signal spectrum. Connected to a computer via the USB port, the analyzer has been read out by a software designed by Carsten Heidemann [217].

Pin photodiode

A silicon based pin photodiode, as already introduced in chapter 4, is used as photodetector whereby the measured current is proportional to the light intensity. In general, a pin photodiode can be operated in biased mode or in photovoltaic mode, where no bias voltage is applied. The photovoltaic mode is preferred when a photodiode is used in low light level applications, as thermal noise generated by the pin diode shunt resistor is the only source of detector noise. However, as a pin diode is not fully depleted without a bias voltage, the signal height may be reduced.
A Si-photodiode from Hamamatsu (type S2281-01) with BNC connector is used [218]. The diode has a sensitive area of $100\,\text{mm}^2$, a peak sensitivity between $600-800\,\text{nm}$ and can be operated with a reverse voltage of up to $5\,\text{V}$. The measured current of the diode operated at this maximum voltage is only slightly increased by 0.3% compared to the unbiased diode. This means that no significantly larger signal can be achieved by increasing the voltage and the diode is operated without reverse voltage for the following measurements.

Sourcemeter

Up to two pin photodiodes can be readout simultaneously by a dual-channel sourcemeter (Keithley 2614B) [219]. In principle, a sourcemeter allows not only for the measurement of the current of each photosensor but would also allow for the setting of the bias voltage if applied. The sourcemeter is connected to a PC to allow for an automatized data taking. 10 data points of the applied voltage and measured current for both channels are stored per measuring run. A stable data taking requires a warm up phase of two hours before the actual measurement.

Integration sphere

Two integrating spheres from Thorlabs (Model IS200) are used, one with three, the other with four ports [220]. An integrating sphere allows for a homogenous and stable light detection as

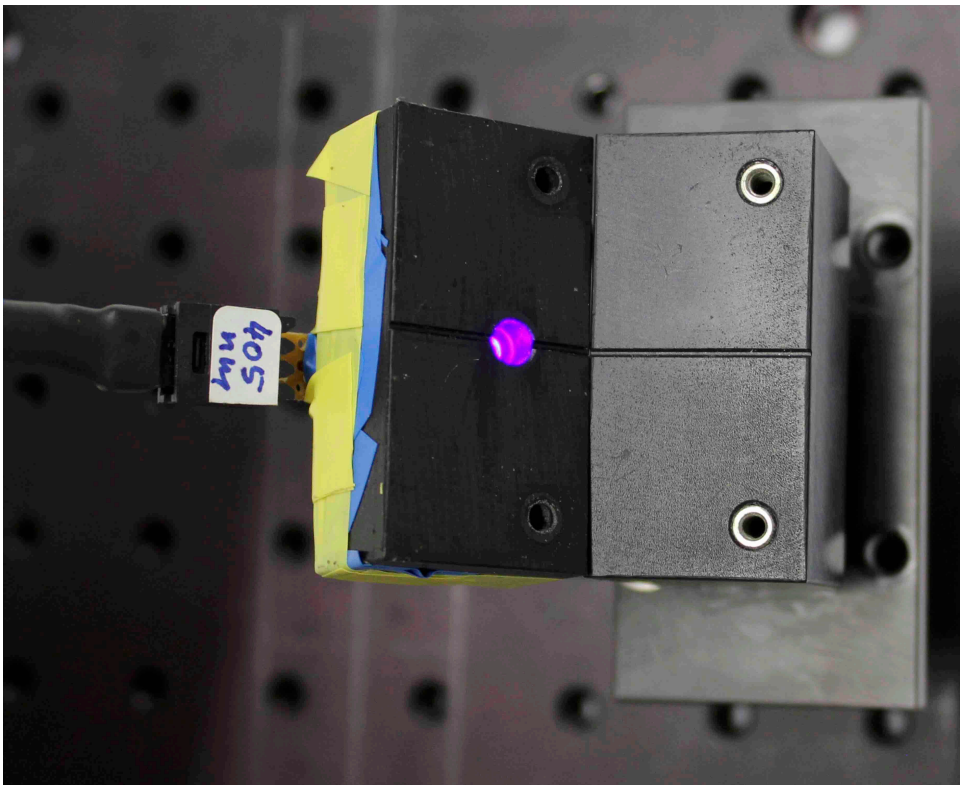

Figure 24.: Photo of the LED mount for studies of single WLS fibres. The mount comprises a groove in which a fibre can be located. The position of the fibre is fixed if the mount is closed and locked with screws. An LED is embedded in the top part of the mount behind a thin collimator to focus the light into the fibre core. The UV-blue LED has a peak wavelength of emission at 405 nm.

the incoming light is evenly spread by multiple reflections over the entire sphere surface. Each port offers an easy coupling of different optical components as optical fibres into the sphere or pin photodiodes as readout sensors. Thereby, the entering fibre and the readout sensors have to be installed in ports perpendicular to each other. The sphere is manufactured from PTFE based bulk material that has high reflectivity in the $250-2500$ nm wavelength range ($\sim 99\%$ from 350 to 1500 nm, $> 95\%$ for other wavelengths). Drawback of the use of an integrating sphere is a high light loss due to the amount of reflections. Only 1% of the incoming light can be detected at the ports. Also, the sphere is sensitive to the complete part of fibre located inside. Along the fibre, photons continuously leave the claddings which would be also detected by the photosensor. Therefore, the fibre placement should be kept the same for relative measurements between fibres.

LED mount

Each change in the position of the LED, the illuminated WLS fibre or the position of the pin diode would result in a change of the measured current. To reduce possible systematics the following setup has been used: A mount including a fixed installed LED is used to illuminate a WLS fibre through a thin collimator with a radius of 0.4 mm. The fibre is placed inside a groove and can be fixed via two locking screws. The light of the LED is shielded by the surrounding material of the mount. Thereby, the light is not only fed into the fibre core at a well defined position but scattered light is also prevented to enter further optical components included in the setup or to be directly detected by the pin photodiode. A photo of the LED mount flipped open is presented in figure 24.

I.2. WLS fibre spectrum

The maximum intensity of the WLS fibre (BCF-92 from Saint Gobain [161]) emission spectrum is expected to be reduced with increasing fibre length as more photons are attenuated on their way along the fibre. If this attenuation is wavelength-dependent, also the complete shape of the spectrum may change. The attenuation length of the WLS fibre is stated as $\lambda_{\text{att}} \geq 3.5\,\text{m}$. No dependency of the attenuation length on the wavelength is stated in the datasheet of the BC-92 WLS fibre and is thus not implemented in the Monte Carlo (MC) simulation, but may be present in measurements. However, the SiPM has a wavelength-depending photon detection efficiency. A possible deviation in the total light yield due to a different SiPM response has to be studied. Thereby, photons emitted in a scintillator tile can be collected over the complete WLS fibre length and the overall emission spectrum will be a convolution of all spectra of all possible pathlengths.

Measurement setup

Therefore, the emission spectrum of a WLS fibre as a function of wavelength is determined for different fibre lengths by a calibrated spectrum analyzer and is compared to simulated spectra. The following setup is used and is depicted in figure 25. The fibre is illuminated by the UV-blue LED with a peak wavelength of 405 nm which is installed in the LED mount. For all studied fibres the LED position is 1 cm away from one open fibre end. The other open fibre end is guided into an integration sphere such that around 1 cm of the fibre is located inside the sphere. In one port of the integration sphere, the spectrum analyzer is installed to detect the emission spectrum in a wavelength regime of $200 - 880\,\text{nm}$. In a second port, a pin photodiode is located and read out via a sourcemeter to allow for a second determination of the integrated intensity. Each fibre length is measured 10 times with unpolished and polished ends. Between each signal measurement, a noise measurement is performed.
For the spectrum analyzer, the darknoise spectra before and after each signal measurement are averaged and subtracted from the signal spectrum. For the pin photodiode, all values of the current corresponding to darknoise measurements are investigated for a potential deviation over time due to a temperature change. However, only a random distribution within 5% of the first data point has been found indicating a stable measurement procedure.

Simulation setup

The corresponding fibre lengths are simulated by WLS fibres in air with two open, so uncovered, ends. Photons are detected by a photosensor at one end. The photosensor is made out of air and is assumed to be a perfect sensitive detector. A small air gap of 0.001 mm between the sensor and the open fibre end is needed as photons being reflected back into the fibre at the surface to air would be otherwise also registered in the sensor[2]. To mimic the setup, a roughened surface of the WLS fibre by $5\,^\circ$ is assumed. The angle is determined by the standard deviation of the Gaussian distribution (around zero) of the angle between the microscopic and the overall mean optical surface of a material. This angle describing the WLS fibre surface roughness has been studied in [221]. The WLS fibre is illuminated at the same position as for the measurements. Therefore, for each simulation 10k photons are isotropically emitted inside a thin slice of 1 mm in the fibre core. The wavelength distribution of the photons follows the emission spectrum of the LED. Each simulated data point

[2] which is due to the basic configuration of Geant4 and cannot be avoided.

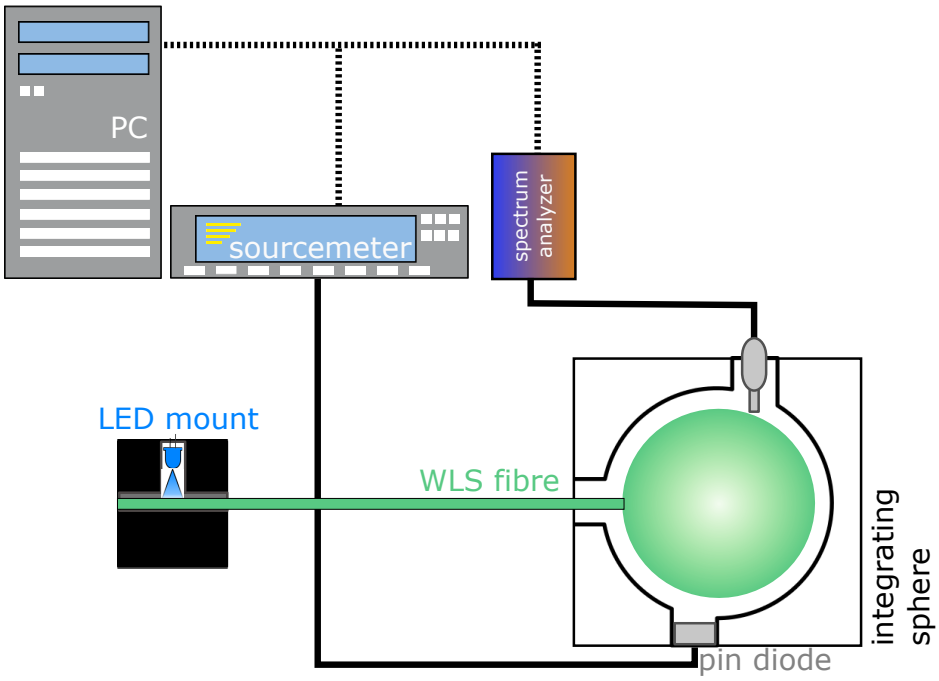

Figure 25.: Shown is the setup for the measurement of the WLS fibre emission spectrum. The WLS fibre is fixed in the LED mount at one end of the fibre. The other end is guided into an integration sphere. The emission spectrum is measured by a spectrum analyzer. The integrated intensity is also determined by a pin diode in a second port of the sphere. The diode is read out by a sourcemeter.

includes 1000 simulations of 10k photons emitted in the fibre.

Emission spectrum as a function of wavelength

In the datasheet of the BCF-92 type of Saint Gobain, the emission spectrum is given for an unspecified WLS fibre length with a peak emission of 492 nm. In figure 26, this spectrum is compared to the measured and the simulated spectrum of a WLS fibre of length 6 cm. The amplitude is shown in relative units as a function of the wavelength. The measured and the simulated spectra correspond to the average of all measurement cycles or simulations. Poisson statistics has been used to determine the uncertainty of each bin. The measured spectrum of the shortest WLS fibre looks well compatible to the spectrum given in the datasheet and by simulations. However, the measurements indicate a slightly broadened spectrum, while for simulations the spectrum is slightly narrower than the spectrum given in the datasheet. Those tendencies can be confirmed for studies of longer fibres which depict also increasing deviations between measurements and simulations with increased fibre length.
In figure 27a, the measured emission spectra for different fibre lengths with polished ends are presented in units of amplitude normalized to the maximum amplitude of the shortest fibre. The spectra shown refer to the measured signal subtracted by the corresponding average darknoise spectrum. No uncertainties are given to allow for an improved visibility. The data indicate a shift in the spectrum amplitude but also in the maximum wavelength of emission due to the wavelength-dependent attenuation. In comparison, simulations do also predict a decrease of the maximal amplitude but take a different evolution of the attenuation into account. They predict a less steep intensity loss

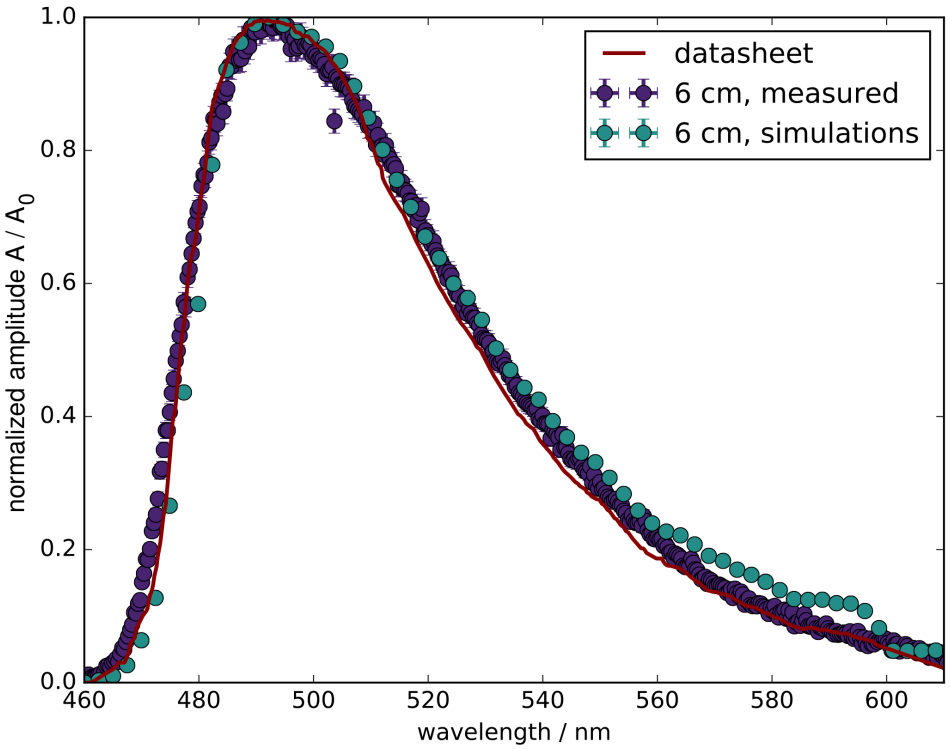

Figure 26.: Comparison of the emission spectrum of a BCF-92 WLS fibre as a function of wavelength. Presented are three different spectra, the spectrum given in the datasheet, the spectrum measured by a 600 mm long fibre illuminated by an LED and read out by a spectrum analyzer, and the spectrum determined by a simulation of the setup. They are all given in relative units, normalized to their maximum amplitude. The shapes of the spectra are well in agreement but indicate a tendency to a broader spectrum for measurements and a narrower spectrum for simulations.

and slightly narrower spectrum with nearly constant position of the maximum of the spectrum for long fibres. The simulated spectra are presented in figure 27b without uncertainties to improve the visibility of the plot. All simulations depict a steep decrease of the simulated spectrum around 600 nm which is introduced by the simulated LED spectrum allowing only a narrow wavelength regime.

For both, measurements with the spectrum analyzer and simulations, each individual as well as the average spectrum is used to determine the total number of photons detected. Thereby, the intensity I of each spectrum is defined by the integration over the wavelength regime $460-610$ nm. Simultaneously, the intensity is measured by a pin photodiode. The diode is used to verify the intensity calculated by the spectrum of the spectrum analyzer, as those may significantly dependent on the correct subtraction of the corresponding darknoise spectrum. The relative intensity is expressed by I/I_0, while I_0 is the intensity for the minimal fibre length measured (here 6 cm). The data points represent the average weighted mean and its external uncertainty for all spectra studied.
The relative intensity as a function of fibre length is further presented for WLS fibres with and without polished fibre ends in figure 28a. Unpolished ends are still cut with a sharp scalpel but without any further finish and depict a less uniform surface. This rougher surface may not only change the angular distribution of the emitted light but may also enhance the backscattering of photons into the fibre at the surface to air. The former would lead to a comparable intensity in an integrating sphere and cannot be studied with this setup. As presented in figure 28a, the relative intensity is decreasing with fibre length for both kinds of finish. However, the measurements performed with

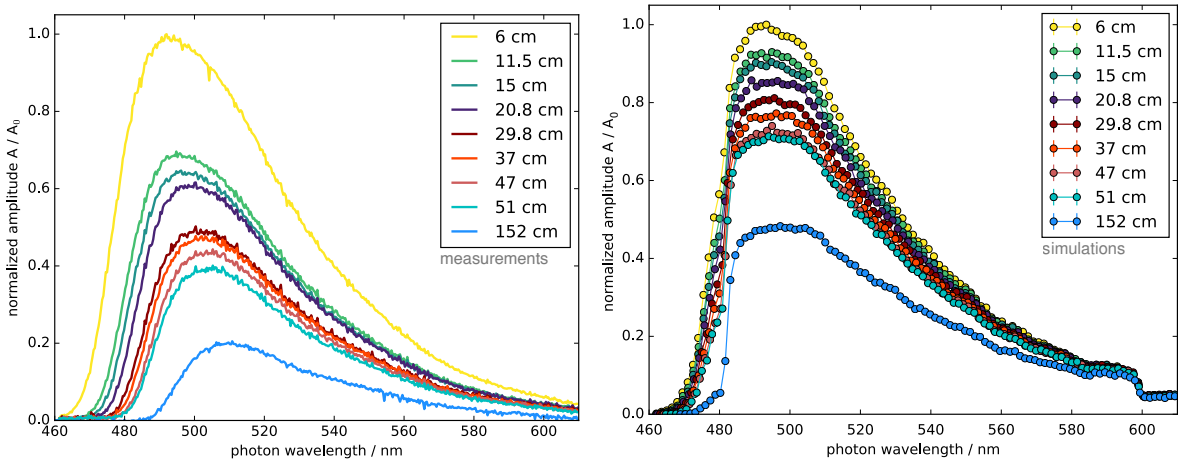

(a) Measurements demonstrate a wavelength-dependent attenuation and a strong intensity loss for long fibres.

(b) Simulations predict no wavelength dependency and a significantly reduced light loss.

Figure 27.: Comparison of the measured WLS fibre emission spectra to the spectra determined by simulations. The relative amplitude to the spectrum of the shortest fibre is given as a function of wavelength for different WLS fibre lengths. The UV-blue LED is fixed by a mount at one fibre end, while the other end is located in an integrating sphere and is read out by a spectrum analyzer.

unpolished ends depict a systematically reduced intensity of up to 40% compared to the measurements with polished ends. The shape of the spectrum is not influenced by the polishment. These measurements emphasize the need of a proper treatment of WLS fibre ends to allow for the best achievable light yield (refer to section 5.2.3.2). Furthermore, measurements for both detectors are shown and demonstrate a comparable intensity loss. Thus, the subtraction of the darknoise from the signal spectrum of the spectrum analyzer is sufficient and allows for a further study of the signal. The relative measurements are further compared to the simulations for fibres of the same length in figure 28b. The intensity is determined by the integration of the simulated spectrum in the same wavelength regime as defined by the spectrum analyzer. The result of the simulation of the shortest measured fibre length is normalized to the first data point of the measurement. Especially, the strong decrease in the detected light intensity for short fibre lengths cannot be reproduced by the simulation. But also the further intensity loss is steeper for the presented measurements. The attenuation is expected to follow an exponential decrease $I(l) = I_0 \cdot exp\left(-\frac{l}{\lambda_{att}}\right)$ for long fibre lengths l. The corresponding fits on the intensity decrease for fibre lengths $> 298\,\text{mm}$ depicts an attenuation length $\lambda_{att} = (3.4 \pm 0.2)\,\text{m}$ for simulated fibres which is well in the order of the stated value in the datasheet of $\lambda_{att} \geq 3.5\,\text{m}$. The measurements correspond to a significantly shorter attenuation length of only $\lambda_{att} = (1.5 \pm 0.4)\,\text{m}$. A potential source of light loss are defects along the fibre in the outer cladding, provoking more photons to leave the fibre on their way than expected. The simulations include a roughened surface taken a generally increased loss into account. However, based on the measurements an overestimation of the amount of simulated photons detected by a photosensor for a long WLS fibre is expected. This also applies for a completely assembled unit with a fibre inside a scintillator tile. For a correct implementation of the investigated behavior in the MC simulation, more studies would be needed as the overall state[3] of each fibre is crucial for the light yield.

[3] polishment of fibre ends, defects along the fibre, how often a fibre has been worked with

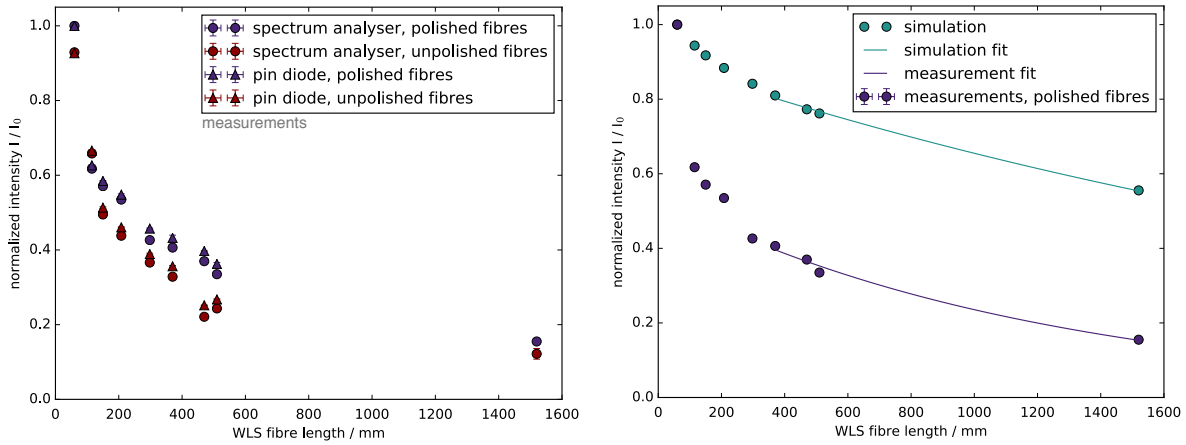

(a) Measurements of polished and unpolished fibres emphasize the need of proper polishment of the fibre ends. Both photodetectors show comparable results for the relative intensity loss.

(b) Comparison of measurements and simulations indicates an insufficient implementation of the wavelength-dependent attenuation in the simulation framework and additional light loss not accounted for along the fibres.

Figure 28.: Relative intensity measurements as a function of fibre lengths. Compared are measurements with polished and unpolished ends for two photosensors which are a pin diode and a spectrum analyzer simultaneously measuring the light emitted by an open fibre end in an integration sphere. The measurements of fibres with polished ends performed with the spectrum analyzer are compared to spectra predicted by simulations. A reduced attenuation length of $\lambda_{\text{att}} = 1.5\,\text{m}$ can be found for the measurements compared to an attenuation length of 3.4 m for simulations.

Besides the clear indication of an additional light loss along the fibre, a wavelength-depending attenuation is apparent. To study the shift of the wavelength of maximum emission of each spectrum (simulated or measured) is determined. Therefore, each spectrum is fitted in the peak region by a Gaussian fit. An exemplary fit on the signal for the shortest measured fibre length is shown in figure 29a. The wavelength of maximum emission is defined as the mean of the Gaussian distribution with an uncertainty given for the fitted value by ROOT. In the example, the peak wavelength is determined as $(493.14 \pm 0.30)\,\text{nm}$ which is slightly larger than the datasheet value of 492 nm. For all further spectra a comparable uncertainty on the position of the peak is found. In figure 29b, a nearly stable wavelength of maximum emission is predicted by simulations for all fibre lengths with a slight decrease of 5 nm. The measurements depict a stronger shift of the wavelength from 493 nm to 510 nm for a fibre length from 6 cm to 150 cm.

To calculate an estimate how much simulations and measurements differ, a multiplication of each spectrum with the photon detection efficiency (PDE) is performed. Therefore, each average spectrum is interpolated and normalized to one. The PDE as a function of wavelength of the SiPM type S13360-1350PE given by Hamamatsu in the datasheet is also interpolated and normalized. By the following integration of the product, an efficiency to detect photons can be estimated. As the PDE is not flat in the according wavelength regime, the shift in the peak wavelength and the change in the measured spectrum shape are relevant. However, the clear deviation in the overall intensity will still dominate the determined efficiency. Shown in figure 30 is this detection efficiency for each fibre length for simulations and measurements relative to the efficiency of the shortest measured wavelength. By performing an interpolation of the data and assuming a uniform distribution of photons along a fibre of length $600 - 1500\,\text{mm}$, an overall decrease of detected photons in a real setup can be roughly estimated to a factor of 2. The factor is expected to be reduced for newly assembled units as a frequent reuse of fibres is the most important sources of the loss of light.

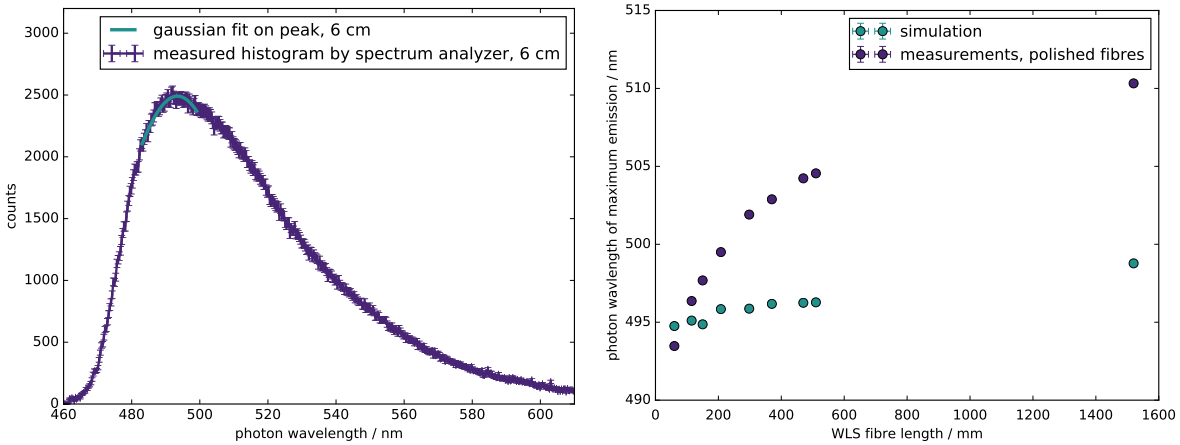

(a) Fit of a Gaussian distribution at the peak of a measured emission spectrum of a WLS fibre with 6 cm length. The wavelength corresponding to the maximum amplitude is defined as wavelength of maximum emission.

(b) Comparison of the measured and simulated evolution of the wavelength of maximum emission as a function of fibre length.

Figure 29.: For each spectrum, the wavelength of maximum emission is determined by a fit of a Gaussian distribution to the peak region. These wavelengths are shown as a function of the WLS fibre length for measured and simulated data. The measurements indicate a continuous shift in the peak position of ~ 20 nm for the 1500 mm long fibre compared to the shortest fibre measured. Simulations predict a stable peak wavelength around 495 nm with a slight increase of 5 nm.

I.3. Reflective end of WLS fibre

As a small-sized SiPM type has been chosen, only one end of the fibre will guide the light onto the photosensor. The other end has to be mirrored. Most of the photons being re-emitted by the wavelength-shifting process in the direction of the fibre end inside the tile would be otherwise lost. However, the light yield is only increased if the back-scattered photons are still contained in the WLS fibre after leaving the reflected surface and if they are not absorbed along their way through the WLS fibre to the SiPM. As these processes at optical boundaries depend on the roughness and shape of the surface, as well as the amount of air / adhesive between WLS fibre and reflective material, simulations provide only rough predictions of a real setup. To validate the simulated results, a study of different materials has been performed proving highly specular reflective foils as optimal material.

Measurement setup

The setup used is presented in figure 31. It is based on the illumination of a WLS fibre of type BCF-92 from the side by a UV-blue LED. The fibre has a length of 29.8 cm and has polished ends. The LED is located in the middle of the fibre in the fixed mount to keep the position of fibre and LED constant for all measurements. One end of the fibre is covered by a (reflective) material. The photons leaving the other end are detected by a pin photodiode. The materials studied are:

- Air as natural reflective surface.
- Water / optical gel to mimic an optical surface at which nearly all light is leaving the fibre.
- Highly reflective (ESR) foil as specular reflective material as used in unit layout 2 (99% reflectivity, cf. chapter 6, [153]).

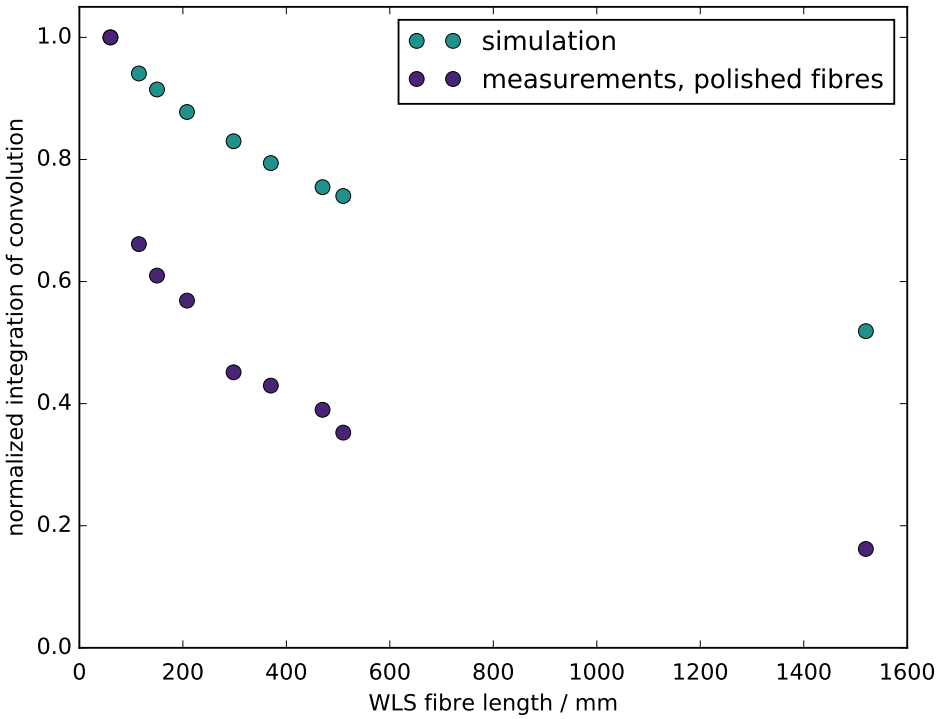

Figure 30.: Each average emission spectrum of the WLS fibre, simulated and measured, is interpolated and normalized to one. A multiplication with a normalized photon detection efficiency of the SiPM type S13360-1350PE by Hamamatsu is performed. The product is integrated and the resulting detection efficiency is shown as a function of fibre length relative to the efficiency of the shortest fibre. A strongly reduced detection efficiency is presented for a real setup compared to predictions of the simulation.

- PTFE tape and Tyvek as diffuse reflective material [152, 154, 222].
- Chrome spray as used in the unit layout 1 (cf. chapter 6, [223]).

A specular reflective material is preferred due to the maximum acceptance angle of the WLS fibre. In theory, all photons will be reflected back into the WLS fibre by an ideal specular reflector with 100% reflectivity for an ideal optical coupling. A diffuse reflector randomizes the angular distribution and many photons will not fulfill the requirements of the maximum acceptance angle of the fibre and will be lost.
For the most extreme case, one can assume that all photons are only being reflected once by each reflector and no further process will take place. If the angle of the photon after reflection is larger than the maximum acceptance angle of the WLS fibre, the photon is considered to be lost. This angles is stated as 35.7° in the datasheet. For this case, the amount of surviving photons of an ideal diffusive reflector compared to an ideal specular reflector can be estimated according to

$$\frac{1}{2\pi}\int_{\theta=0^\circ}^{37.5^\circ}\int_{\phi=0}^{2\pi}\sin(\theta')\mathrm{d}\theta'\mathrm{d}\phi' = 2\pi\cdot 0.2\frac{1}{2\pi} = 0.2 \quad . \tag{9}$$

Corresponding to this calculated lower limit, a diffusive reflector would achieve only 20% of the photons reflected back into the fibre by the specular reflector.

As the response of the pin diode is temperature dependent and ambient light would be captured by the WLS fibre, all measurements are performed in a temperature stabilized and dark laboratory. At low illumination levels, the statistical uncertainty will be dominated by the fluctuations on

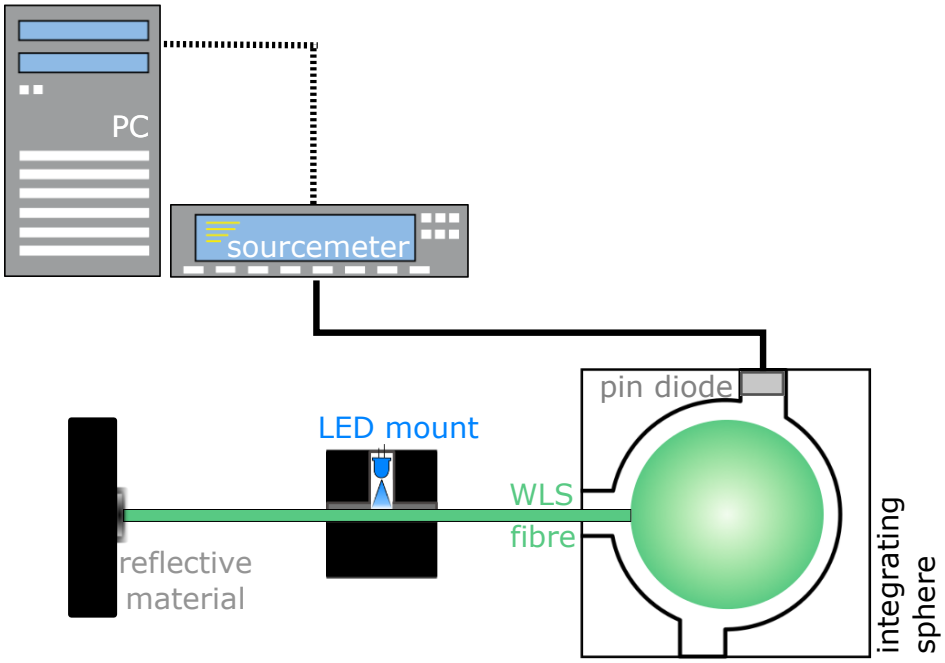

Figure 31.: Shown is a sketch of the measurement setup studying the reflective cover material. The WLS fibre is fixed in the LED mount. The mount is located in the middle of the WLS fibre. It comprises a groove in which a fibre can be located and fixed if the mount is closed and locked with screws. The integrated intensity is determined by a pin diode read out by a sourcemeter.

the measured photodiode current. Therefore, the measured current of the diode is averaged over 10 data points for each measurement. However, the setup is more likely to be dominated by systematic uncertainties as the coupling between the optical surfaces of the fibre and of the reflective material or the position of the WLS fibre in respect to the photodiode. Thus, all measurements of one material are performed 10 times to achieve an estimate of the uncertainties included in the setup. Thereby, the fibre end is always measured with and without the reflective material under study. A continuous measurement of the fibre with no additional reflective material applied is important as polished fibre ends may suffer from many measurement cycles or the light yield may change according to temperature. As in theory, the light yield for a fibre with an open end to air will always be the same in a fixed setup, the relative determination can compensate for such effects.

The light yield as a function of the studied materials are shown in figure 32. The data points refer to the weighted average value of all measurements of the corresponding material and its external uncertainty relatively to measurements of a fibre without any material (optical boundary to air). All measurements show a significantly increased light yield for a highly specular reflective (ESR) foil (65% improvement), a medium increase for diffusive reflectors (40% improvement) and nearly no improvement for an applied chrome spray at the fibre end (5% improvement). An optical coupling to a second fibre, another WLS fibre of type BCF-92, introduces an increase of 5%. This indicates a non-ideal transmission at the optical boundary. The coupling between optical fibres will be discussed later in this chapter.

Simulation setup

The presented measurements are compared to simulations. The simulated data points are slightly shifted to allow for a better visibility (cf. figure 32). The simulations comprise a WLS fibre of the same length in air with a slightly roughened surface. For each simulation, 10k photons are isotropically emitted inside a slice of the fibre core located in the middle of the fibre length. The wavelength distribution of these photons corresponds to the LED emission spectrum used in the setup. The reflective materials are first simulated based on predefined properties of optical surfaces from Look-Up Tables (LUT) in Geant4. Therefore, the fibre end is covered by an element consisting of the applied material as Teflon, Tyvek or ESR foil. The materials are defined with properties corresponding to the datasheets of the applied material by the *G4Material* class. The optical boundary of each element to the surface of the fibre is defined as a *G4LogicalBorderSurface* with the predefined option *groundteflonair*, *groundtyvekair* and *polishedvm2000air*, respectively. These optical boundaries take automatically a small air gap between the fibre and the material into account. To implement the already defined properties of the cover material also for the optical boundary processes, they have to be additionally handed over to the boundary object.
Simulations of the fibre end covered by reflective materials predict also the ESR foil as best choice. However, an increased light yield by 20% compared to measurements indicates a non-ideal coupling of foil and fibre end in the real setup. A possible explanation for this deviation would be surfaces tilted against each other or an increased roughness of the fibre surface than implemented. These effects will reduce the reflectivity only for specular reflective materials and not for diffusive materials. For the latter, simulated and measured improvements of the light yield are well in agreement. However, the light yield increase of the chrome spray is clearly overestimated by simulations which indicates a wrong assumption of the optical properties of the reflector.

Alternatively, the open fibre end can be defined with a certain specular reflectivity. Thereby, a reflectivity of the fibre end of 100% means that all photons will be reflected back inside the fibre without any losses and for a reflectivity of 0% all photons having a contact to the fibre end surface will be absorbed. No multiple scattering or a smearing of the reflectivity angle between the fibre surface and the reflective cover will be taken into account. In figure 33, the expected linear increase of the light yield with increasing reflectivity can be confirmed. This simulation process is much faster than for a simulation including a proper described optical boundary. As the highly reflective foil will be used for units of layout 2, the corresponding simulation of these units will be performed assuming a reflective fibre end with a fixed reflectivity of 65% based on the presented measurements.

I.4. Coupling to an optical fibre

The angular distribution of photons at the optical surface of the open fibre end is crucial to investigate sources of light losses for example during a coupling of the WLS with an optical fibre. Besides geometrical effects as the numerical aperture of both fibre types, the existence of air at the optical boundary will change the optical coupling.
A measured angular distribution of photons leaving a WLS fibre is performed in [221]. The measurement is shown in figure 34 (violet). Most photons are leaving the fibre under $30-45\,^{\circ}$ in respect to the surface normal. Assuming now a fibre coupling of a WLS fibre type BCF-92 and a ESKA optical waveguide with a small air gap between both fibres, photons are leaving the WLS fibre under large angles up to a maximum exiting angle of $90\,^{\circ}$. However, only photons with an incident angle of $61\,^{\circ}$ are contained afterwards in the optical waveguide. A vertical line in figure 34 marks the maximum angle accepted by the optical fibre. The shaded area under the violet curve depicts the amount of photons lost due to the smaller numerical aperture of the optical fibre. In-

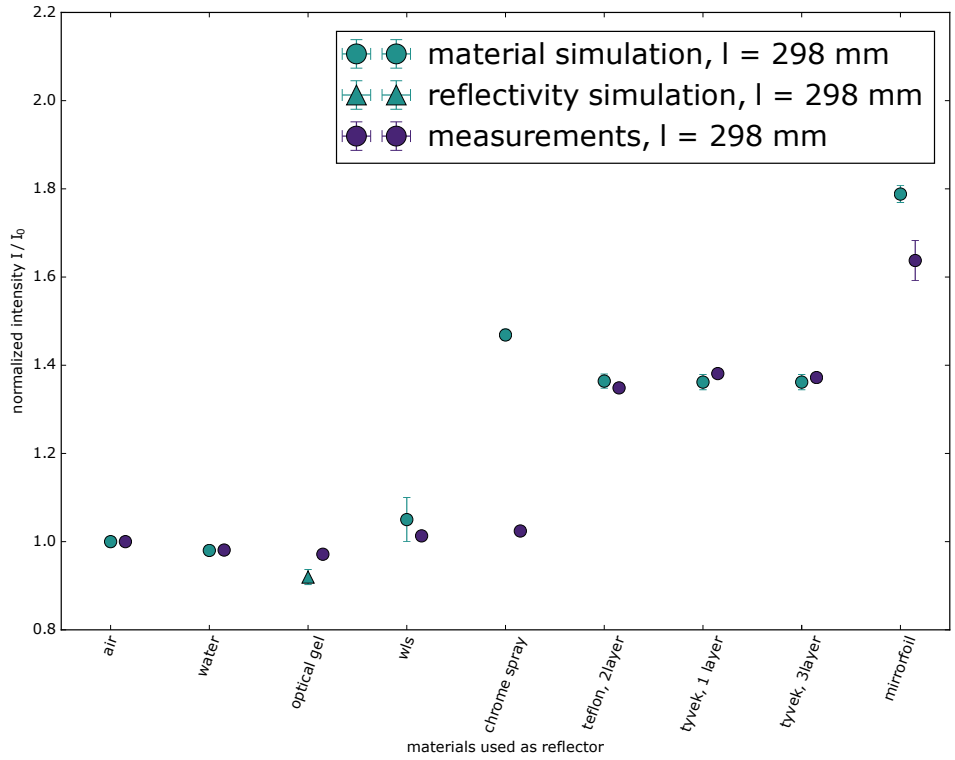

Figure 32.: Study of the light yield for different reflective materials used as cover of a WLS fibre of type BCF-92 of Saint Gobain. The relative improvement in the light yield is shown in respect to the fibre without cover (surface to air). For each data point 10 measurements have been performed for each replacement of the fibre. Shown is the average value of the relative change in the light yield while the uncertainty is determined by the uncertainties of each measurement repetition. Measurements are compared to simulations of the corresponding material (circles) or a fixed reflectivity (triangles, cf. figure 33). Both point out that the highly specular reflective foil is the optimal material. See text for more information.

tegrating both, the complete distribution and the shaded area only, results in approximately 10% of the photons which cannot be contained in the optical fibre. This has to be compared to a direct coupling to a SiPM, which offers a high and stable angular photon detection efficiency up to 75° [54]. If assuming that all photons are lost above this critical angle, only 1% of the photons is not reaching the active area of the SiPM. Thus, a WLS fibre can be efficiently readout directly coupled to the photosensor.
Additionally shown by the green curve, is an estimated angular distribution of photons inside the WLS fibre. The amount of photons can be estimated by a recalculation of the measured angular distribution of WLS fibres in air to the distribution in the WLS fibre core according to Snell's law. Most of the photons propagate inside the WLS fibre with an angle of 20° which is supported by simulations [221]. Naturally, this calculation does not include photons which have not left the WLS fibre at the optical boundary to the ambient air but have been reflected back into the WLS fibre according to the Fresnel equations (cf. chapter 5.2.3.2). Also depicted by a green vertical line and shaded area are the corresponding maximum acceptance angle of the optical fibre and the photons which will be not contained after entering the waveguide. In chapter 5.2.3, a multi-layer approach is discussed introducing an air gap between the WLS fibre and an optical waveguide. Based on Fresnel equations 5.19, the approach results in the loss of half of the light if a uniform angular distribution is assumed.

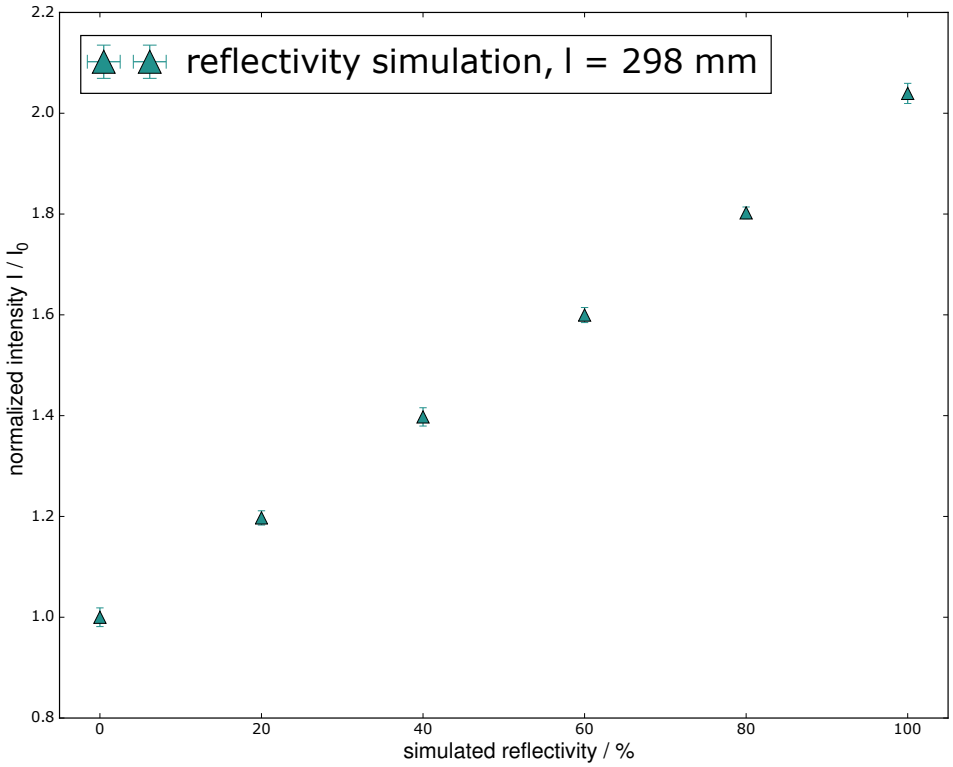

Figure 33.: Study of the simulated light yield by a defined reflectivity coefficient for the fibre end surface. A WLS fibre of type BCF-92 of Saint Gobain with a fibre length of 298 mm has been simulated. As expected, the increase is linear with increasing reflectivity. To reproduce the measured increase of photons being reflected back by the highly reflective foil a reflectivity of the fibre end of 65% can be used to simplify the simulation process.

Measurement setup

To study the optical coupling between a WLS fibre of type BCF-92 of Saint Gobain and an optical waveguide in more detail, the following setup has been used. A sketch of the setup is shown in figure 35a. A photo of the setup can be found in figure 35b. It comprises two main parts, the illumination of the WLS fibre by the UV-blue LED at a fixed position as well as the coupling to the optical waveguide and the readout of signal. The fibre with a length of 20 cm is glued within a groove into an acrylic tile. One WLS fibre end sticks out of the material and is guided through a mount screwed onto the tile. This setup corresponds to the unit layout 1 presented in chapter 6. The surfaces of the WLS fibre and the optical waveguide are placed directly bordering without any additional optical coupling via optical gel or adhesive. The optical waveguide is fixated by a duct, which can be moved by a xy-table. The opposite end of the waveguide is located in an integration sphere. A pin photodiode located in one port perpendicular of the fibre entrance is measuring the amount of photons transmitted. The complete setup comprising the waveguide mount and its readout is located on another x-table. Thereby, the position of the fibre can be adjusted without changing the position of waveguide inside the sphere to avoid systematic uncertainties introduced by a repositioning.

With the presented setup, four different fibre types are investigated and compared to the light yield of the WLS fibre without any coupling. All studied types have a length of 15 cm. A continuous review of the light yield of the single WLS fibre is performed for each measurement cycle of the four different fibre types to verify the actual light yield provided by the WLS fibre. All transmission

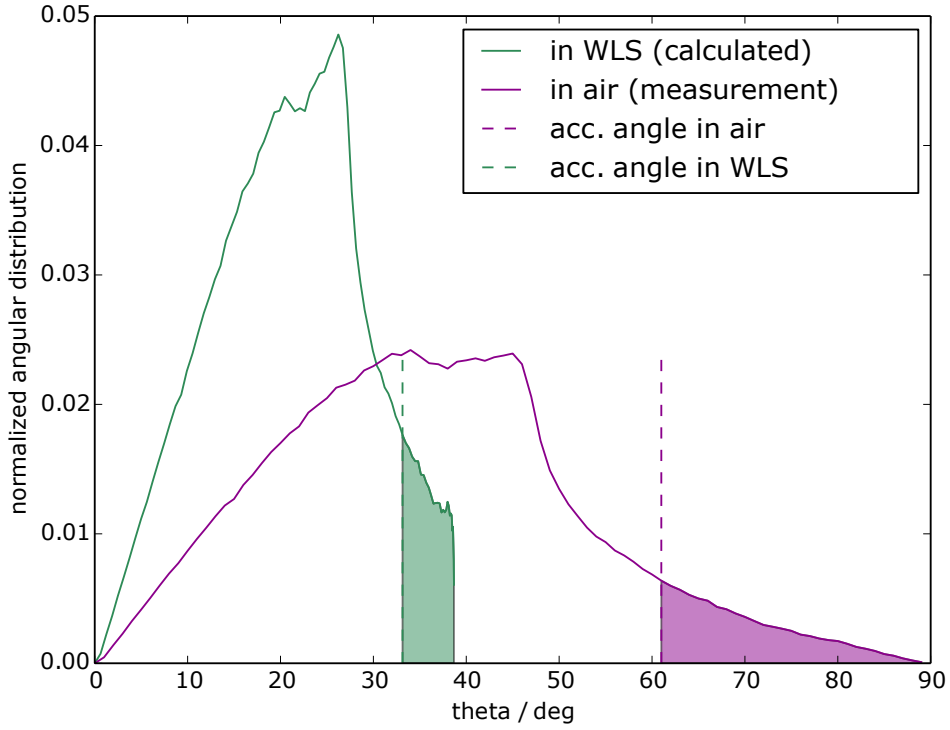

Figure 34.: Angular distribution of light exiting a WLS fibre into air before (green) and after leaving (violet) the WLS fibre. The violet curve is based on studies in [221]. The green curve can be calculated based on the former distribution and applying Snell's law. Not included in the green curve are photons which could have left the fibre by a transition into a different material than air. The shaded areas mark the amount of light that is not induced in the transparent fibre due to the acceptance angle of 61°. The loss is in the order of 10%. Plot has first been presented in [183].

efficiencies are calculated in relative terms to those measurements. This enables a compensation for changes in the detected photodiode current due to temperature deviations or wear marks of the fibre end surfaces after several measurement cycles. Always the same WLS fibre and acrylic tile are used and their position is unchanged. The four fibre types studied are:

1. A jacketed optical waveguide of type Super ESKA [224].
2. An optical waveguide of type BCF-98 by Saint Gobain [185].
3. The optical waveguide used in the unit layout 1, a ESKA acrylic fibre produced by Mitsubishi [162].
4. A second WLS fibre of type BCF-92 by Saint Gobain [161].

In figure 36, the four fibre are shown next to the arylic test tile. The mount of the WLS fibre is shown disassembled on top of the photo. For the measurements, the mount is screwed onto the tile. The drilling holes are visible in the material. For units of layout 1, the coupling of WLS and optical fibre takes place inside the mount in a narrow duct which can be firmly screwed to fixate the coupling position. For this measurement setup, the coupling takes place outside of the mount.

Each fibre type is repositioned 10 times. For each repositioning 10 data points are taken by the sourcemeter used to read out the photodiode. The relative intensity loss by a coupling to the different fibre types is shown in relation to the single WLS fibre without coupling in figure 37. Each data point refers to the weighted mean and its external uncertainty. The uncertainty is a

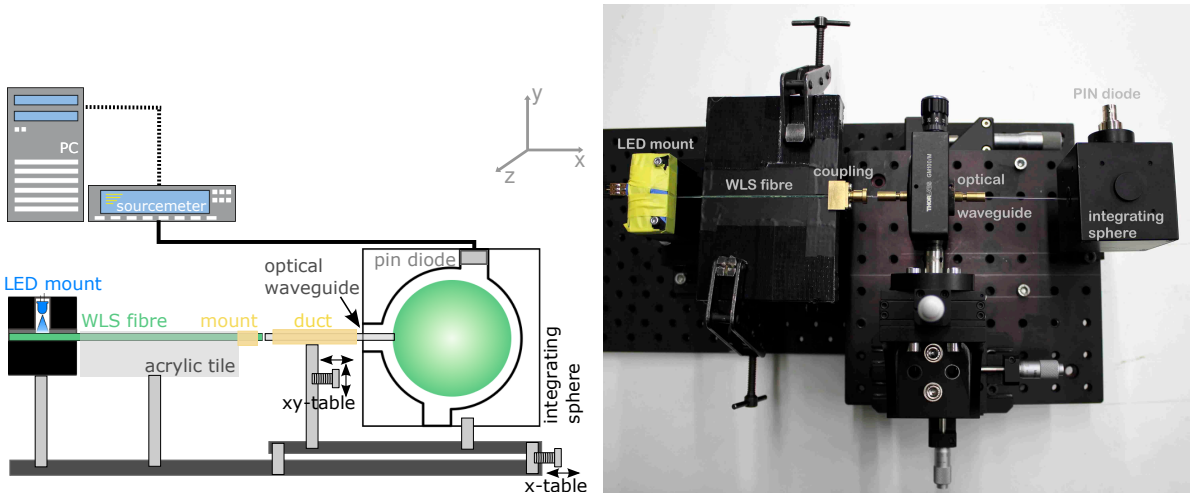

(a) Sketch of the setup from the side.

(b) Photo of the setup from above.

Figure 35.: Setup for the measurement of the optical coupling between WLS fibre and optical waveguide. On the left, the illumination of the WLS fibre takes place. Shown are from left to right, the LED mount, at which the WLS fibre is illuminated from the side at a fixed position, an acrylic tile with a groove, in which a 20 cm WLS fibre is glued, and the mount for the mechanical coupling of the WLS fibre and an optical waveguide. The optical waveguide is fixated in a duct which can be fine positioned by a xy-table. The other open end of the optical waveguide is located inside an integration sphere. A pin photodiode reads out the light emitted by the waveguide. The setup for the waveguide readout is firmly installed on a second platform controllable by another x-table.

combination of the uncertainty on the photodiode current determination and the repositioning of the coupling. It is shown that a coupling to an additional waveguide is a significant source of light loss, way larger than the 10% predicted by pure geometrical calculations. For the fibre of type ESKA used in unit layout 1, only 30% of the photons are transmitted to the photosensor. As an optical waveguide has a negligible attenuation for the waveguide length, the light loss is due to the optical coupling itself. The further waveguide types predict an even lower efficiency. For the jacketed fibre this is expected as the jacketing is influencing the outermost cladding. The BCF-98 optical waveguide should have the same properties as the installed fibre in unit layout 1, but presents a reduced efficiency. This may be an aging effect as an old fibre has been used which has been e.g. exposed to day light for a long time. However, also the overall state of the fibre as the grade of polishment of the fibre end can have an influence.
Interesting is, that the coupling to another WLS fibre of type BCF-92 is improving the transmission efficiency to 45%. As a WLS fibre has a strongly reduced attenuation length, it is expected that the amount of photons is reduced compared to an optical waveguide. A possible explanation for the detected increase could be, that the fibre has a larger maximum angle of acceptance compared to an optical waveguide. Additionally, the overall fibre state has to be taken into account. Furthermore, the pin diode detects all photons emitted along the fibre end located inside the integration sphere. All fibres are located with roughly 1 cm inside the sphere. The amount of emitted photons along this short part is reduced for an optical waveguide compared to WLS fibres. This can be shown by placing the fibres directly at the edge of the sphere. The light intensity is reduced by 7% for a WLS fibre compared to a protruding fibre. This is reduced to 2% for the optical waveguide. But as the exact positioning of the fibres at the sphere edge is less reliable, the presented setup with a protruding fibre has been chosen. However, important is that all fibre types depict a large light

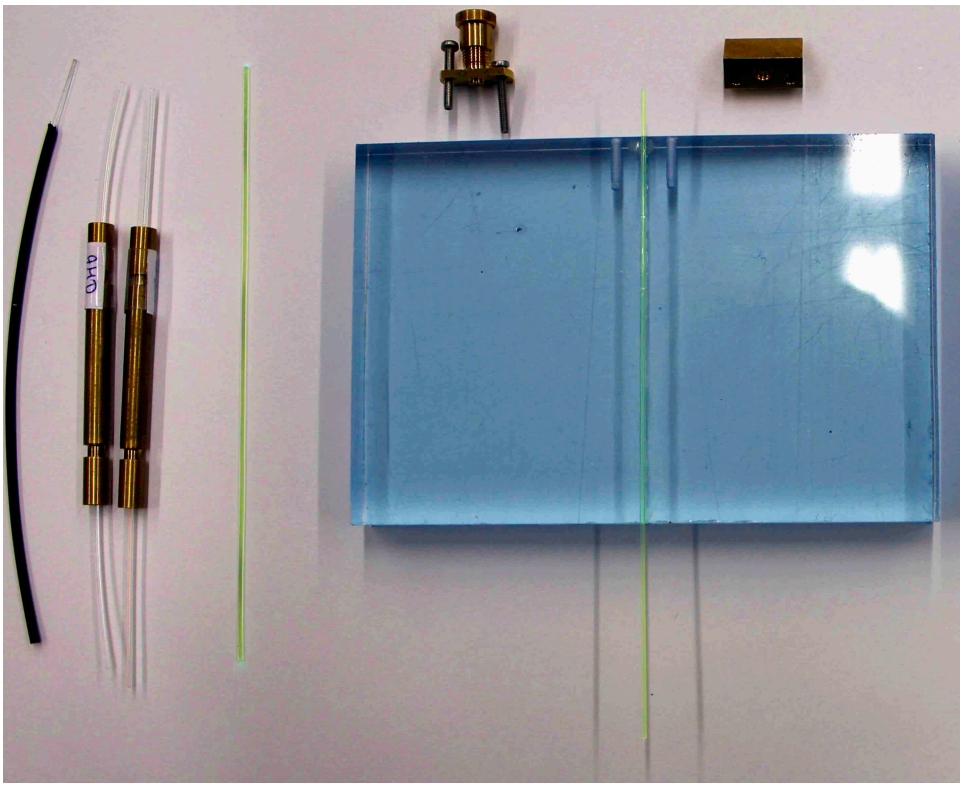

Figure 36.: Shown from left to right are the four studied fibre types, the acrylic tile in which the 20 cm WLS fibre is glued in and the disassembled mechanical coupling. The four fibre types are a jacketed Super ESKA, BCF-98 and ESKA fibre as optical waveguides as well as a BCF-92 WLS fibre. Two fibre types are located in the duct which is used to hold the waveguide in place.

loss of 50-80% due to the coupling. Furthermore, the strong influence by systematic uncertainties is clarified.

Now, an intended air gap is introduced by a fine placing of the platform at which the waveguide and its readout is installed. The combined movement avoids the uncertainty introduced by a different amount of fibre located inside the integrating sphere as discussed. A photo of the coupling is shown in figure 38. The optical waveguide (right) is installed in a duct. The WLS fibre (left) depicts some wear marks, probably introduced by the previous installation of the mechanical mount. The coupling seems to be well aligned by eye and no large air gap can be identified. But it is apparent that the region of the coupling is highly illuminated in the photo as photons are scattered at the optical boundary and reach in larger number the camera sensor.

To find the optimal position of the fibre alignment and to study the influence of a misalignment, the position of the fibre in z-direction is changed. The definition of the coordinate system is illustrated in figure 35 and 38. The surfaces of both fibres are parallel orientated to each other. Starting at a positioning by eye, the intensity is constantly measured after a replacement of the fibre in steps of few $\mathcal{O}(10-100\,\mu\text{m})$ in both z-directions. The displacement takes place until both surfaces no longer have any contact with each other. A symmetric light loss around the real center of the fibre is shown in figure 39 as a function of the shift in z-direction. Each data point corresponds to a single measurement. The uncertainties shown are the standard deviation of the 10 current values of the photodiode measured by the sourcemeter. The intensity is given normalized to the maximum intensity determined. As expected, no photon current is measured at a displacement around 1 mm which corresponds to the fibre diameter. The zero position in z-direction refers to the position at

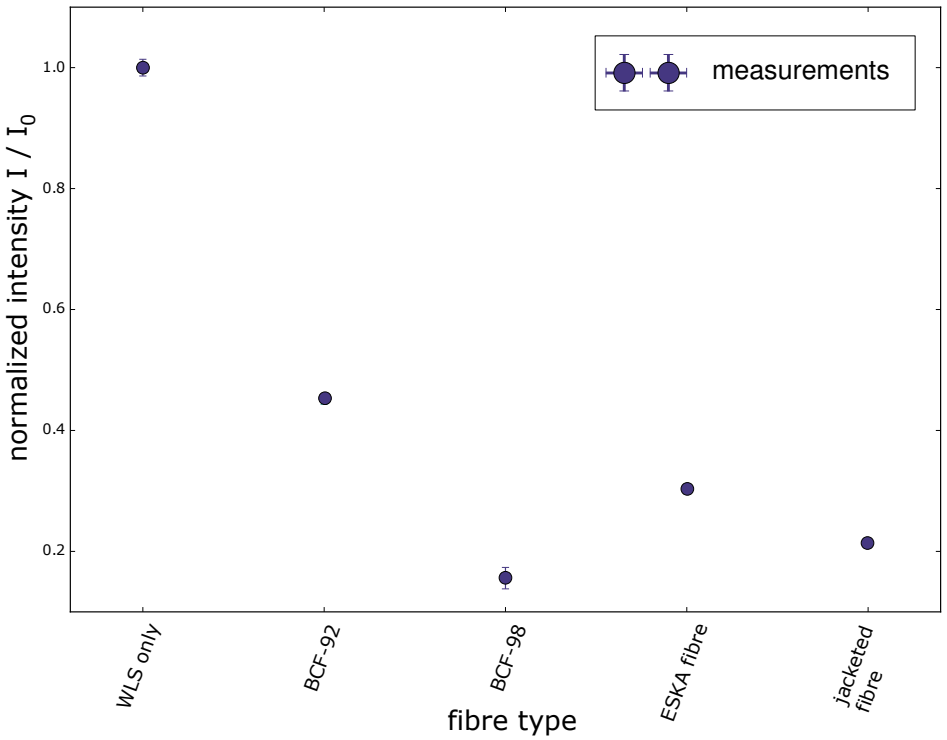

Figure 37.: Relative intensity measured at the photodiode for the coupling of the WLS fibre to four different waveguides in respect to the intensity measured at the WLS fibre without any coupling. All four fibre types demonstrate that at the optical interconnection more than half of the photons are lost. For the optical waveguide under study, called the AMD fibre, the intensity loss can be found to 70%.

which the author thought the fibres are aligned introducing a change of 10% in intensity for roughly 0.2 mm offset. This emphasizes the need of a correct alignment of fibres.

Starting from the optimal alignment of both fibres, an intended air gap is introduced between those. The determined decrease is shown relative to the intensity at the starting position in figure 40 as a function of the air gap size. Each data point corresponds to a single measurement. The uncertainties shown are the standard deviation of the 10 current values of the photodiode measured by the sourcemeter. An exponential decrease can be found. For an air gap of 1 mm the intensity is reduced to only 50%.

Simulation setup

For comparison, the setup is simulated for different distances between a WLS fibre and an optical waveguide / another WLS fibre. All fibres are simulated with a length of 15 cm and a roughened surface. The air gap ranges from several micrometer to several millimeter. The WLS fibre is illuminated at the same point of the fibre as for the measurements. As reference the intensity detected after an ideal coupling to an optical waveguide without any air gap is used. Already a small air gap of few μm introduces an intensity loss which is strongly decreasing until a stable intensity loss is reached for a 2 mm air gap. The exponential decrease is in excellent agreement with the presented measurements and can explain the intensity loss at an optical coupling by an air gap in between both fibres. A small shift between both curves can be determined which may corresponds to the fact, that for a measurement an ideal coupling is never achieved. However, to reproduce the transmission efficiency of only 30% determined by measurement, an air gap of 0.8 mm would be needed. This

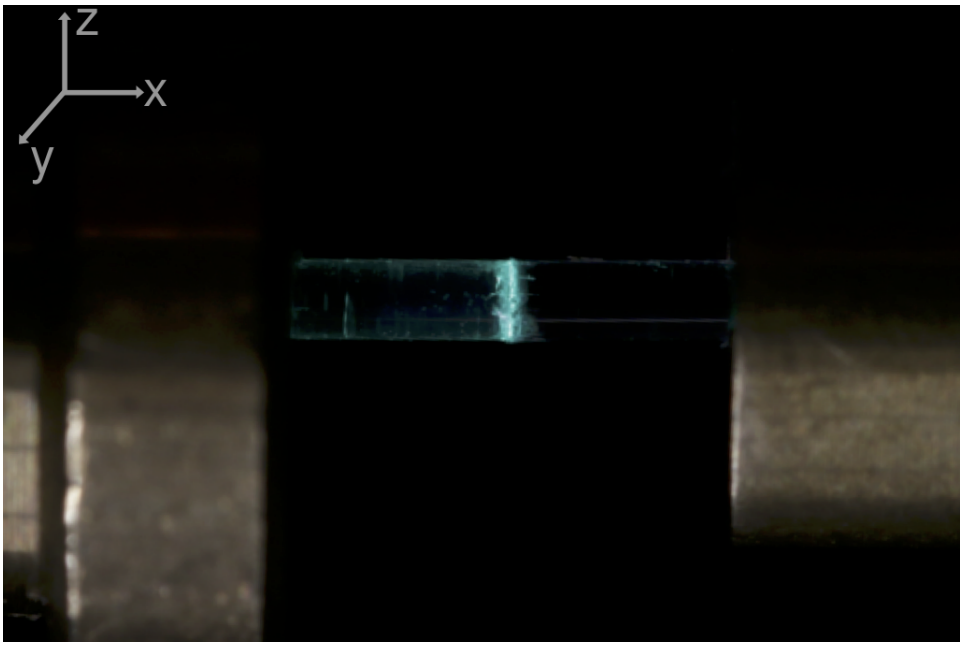

Figure 38.: To study the influence of an air gap in between the WLS fibre and the waveguide, the latter is moved away from the WLS fibre. Shown, is a photo of the best achievable coupling used as reference. It can be seen that for the WLS fibre end (on the left) already some marks are apparent due to the previous installation of the mechanical mount at the acrylic tile. The fibres seem to be well aligned and no significant air gap is visible. From an optical point of view, however, many photons seem to leave the coupling area and cause a strong illumination of this area.

air gap would be already visible by eye in figure 38. To be even more consistent with the measured value, thus an additional source of intensity loss as a rougher surface of the fibre end or a tilting angle between both surfaces is needed based on the simulations. However, the simple multi-layer calculation presented in chapter 5.2.3 indicated a larger amount of light loss than simulated and in the same order as derived by the measurements. The coupling to a WLS fibre indicates a stronger loss already for the smallest gaps while the intensity loss is converging for larger gaps. This is a contrary trend as depicted by the measurements in figure 37 and needs a further investigation in the future.

I.5. Summary of presented studies

The presented studies of single WLS fibres demonstrated the following important characteristics for their expected performance in a combined setup with a scintillator tile:

- The wavelength of maximum emission of the WLS fibre emission spectrum is increasing as a function of the fibre length. This behaviour is not properly implemented in the MC simulation. As the photon detection efficiency of the SiPM is decreasing in the corresponding wavelength regime, the MC simulation overestimates the number of photons detected by the SiPM.

- The number of surviving photons as a function of WLS fibre length is significantly reduced for measurements compared to the results of simulations. The MC simulation overestimates the number of photons detected by the SiPM by a factor of $\lesssim 2$. The factor will be reduced for newly assembled units as frequent reuse of fibres causes the greatest loss of light.

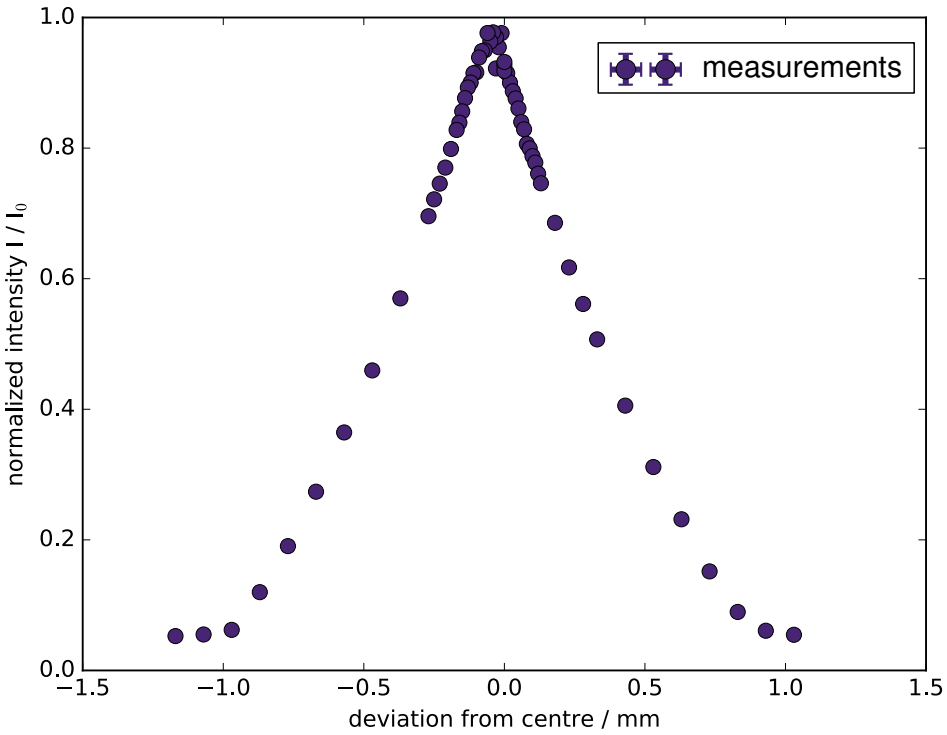

Figure 39.: The influence of a misalignment between WLS fibre and optical waveguide is studied by a deliberated shift while both surfaces always face each other. A symmetrical reduction of intensity is apparent for a shift in both direction of the center. The maximum intensity loss is at a shift of 1 mm corresponding to the fibre diameter. The zero position refers to the position at which the author of this thesis aligned the fibres by eye. An uncertainty on this positioning of around 10% is indicated. Each data point depicts a single measurement corresponding to the average and the uncertainty determined by the standard deviation of the 10 photodiode current values measured by the sourcemeter. The intensity is given normalized to the maximum intensity determined.

- The coupling of a WLS fibre to an optical waveguide is a large source of light loss. Only $\approx 30\%$ of photons are transmitted. Thus, the sole use of one WLS fibre in the setup is strongly recommenced. A narrow air gap and a misalignment of fibres are reasonable factors, but further attenuation factors are necessary to explain the total light loss.

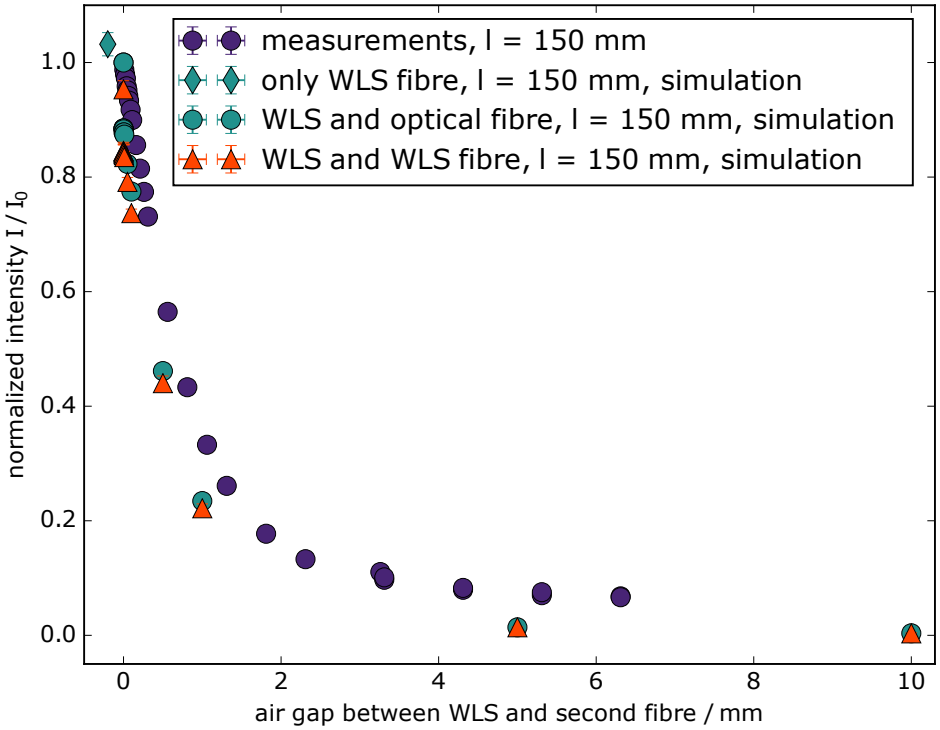

Figure 40.: Measured relative intensity loss due to a small air gap between a WLS fibre and an optical waveguide as a function of the size of the air gap (blue circles). A strong decrease is shown for already small air gap changes. The intensity loss can be explained by photons leaving the fibre under large angles with directions located outside of the waveguide re-entering area. In comparison, MC simulations for an optical waveguide (green circles) and a WLS fibre (triangles) are shown. Those confirm an air gap as source of significant light loss. However, an additional source is needed to explain the intrinsic light loss of 70% between a WLS fibre measured with and without coupled to an optical waveguide.

J. Modifications of individual scintillator units

Several details of the centre piece of the detector, the *unit*, are studied by means of a *test tile* comprising changing components. The knowledge, gained from these measurements, is integrated in the design of the unit (called *layout 2*, cf. section 6).
Always the same test tile is used which also avoids fluctuations in the signal due to intrinsic deviations of the light yield of each individual scintillator tile. The test tile is measured in coincidence with two units of *layout 1* (cf. section 6 and the work of Lukas Middendorf [165]) in a stack. These units will be referred as *trigger units* in the rest of this section. By the stack, a pure atmospheric muon sample can be achieved.

The MIP (minimum ionizing particle) peak corresponding to the maximum of the charge distribution of atmospheric muons is then used in units of photon equivalents (p.e.) to determine the signal yield achieved by the test tile. An exemplary spectrum can be found in figure 44 in this section. The spectrum is discussed in detail in section 8.1.3.
The test tile includes a WLS fibre located in a sigma-shaped groove. The WLS fibre is sticking out of the tile by 5 cm to allow a fine positioning of the SiPM via a xy-table. The position of the fibre in respect to the SiPM is verified by a macro photo with a camera. For few measurements the WLS is coupled to an optical waveguide which is then located on the SiPM at a carrier board. An example

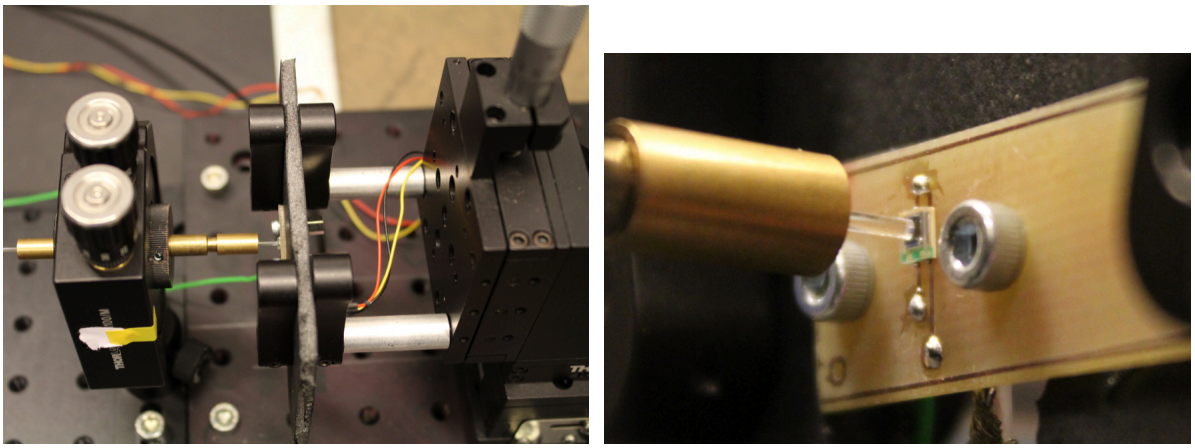

(a) The fibre is located in a duct which is hold in place by a mount. The SiPM on the carrier board is placed in front of the fibre end by means of a xy-table.

(b) Macro photo of the coupling. The fibre is placed in the centre of the SiPM.

Figure 41.: Verification of the position of a SiPM on a xy-table in respect to a optical fibre which is coupled to the WLS fibre sticking out of the scintillator tile under study. The SiPM is located on a carrier board.

of the coupling of the SiPM to a waveguide is depicted in 41. The waveguide is located in a duct with collets. The duct is hold in place by a mount. The duct is only needed for the optical waveguide coupling. Otherwise, the WLS fibre is directly placed in front of the SiPM to avoid wear marks on the WLS fibre especially at the polished surfaces while insertion into the duct.

For the test tile a state-of-the-art SiPM type S13360-1350PE by Hamamatsu [105] is used. Each trigger unit comprises a WLS fibre which is coupled to an optical waveguide of 30 cm and is read out by SiPMs of type S12571-050P.

All measurements have been performed with the same EASIROC evaluation board, but with the corresponding SiPM carrier board and power supply unit for each SiPM type (cf. section 6). The default overvoltages 2.5 V (layout 1) and 3 V (layout 2) stated in the datasheets [111] have been applied.

As shaping parameters a 125 ns nominal peaking time[4] and the highest possible gain[5] has been applied. While main operation parameters as the discriminator threshold or the baseline of the EASIROC are temperature depending, the temperature at which the measurements are performed are indicated. They are mostly stable for each measurement procedure. For all measurements the temperature ranged within $26-28$ °C. A compensation of the temperature-depending change of the breakdown voltage is applied to keep the SiPM gain constant as described in section 4. The configuration scripts and measurement programs for studies of scintillator units by the presented readout electronics have been modified but are based on programs developed by Lukas Middendorf and which are presented in his doctoral thesis [165].

First, the influence of the reflective material used for mirroring of the fibre end inside the tile is investigated for a setup of a WLS fibre inside a tile. The result is compared to the study of WLS fibres illuminated by a LED (cf. section I.3). These measurements confirm a highly reflective foil as optimal material. Secondly, the influence of different reflective materials used as wrapping of the tiles is investigated. The wrapping is needed to guide photons leaving otherwise the scintilla-

[4] corresponding to a shaping setting of 5
[5] corresponding to a feedback setting of 1

tor back into the tile to increase the chance for them being captured by the WLS fibre. Thereby, a diffusive material as Tyvek or PTFE tape is found as best performing wrapping. At least, the optical coupling to a transparent waveguide found as potential source of light loss (cf. section I.4) is studied in terms of a complete unit. The signal yield is as expected significantly decreased by such a coupling. Also a direct coupling of a SiPM to a WLS fibre, directly at tile edge, shows a non-perfect coupling, but is found as the best available option.

J.1. Reflective end of WLS fibre located in a tile

The potential of reflective materials at one fibre end to increase significantly the light yield of a WLS fibre has been presented in figure 32. The studied short WLS fibres are illuminated by a LED at a fixed position. Inside a scintillator tile, the fibre implemented captures photons along its entire length of 1 m if a muon deposit energy in the scintillator material. The resulting light yield will thus be a convolution of a wide range of photon pathlengths inside the fibre. Therefore, two materials have been studied in the test tile. Thereby, the WLS fibre is not glued into the groove of the tile to allow an easy exchange but is perfectly hold in place in the sigma-shaped groove due to friction. The two materials studied are:

1. Chrome spray as used in unit layout 1.
    - Measured twice with two layers of spray.
    - Measured twice with three layers of spray. The third layer is applied over the previous two layers.
    - Measured once with four layers of spray. The fourth layer is applied over the previous three layers.
2. Highly reflective foil (99% reflectivity) as used in unit layout 2.
    - Three times a piece of foil is glued onto the fibre end. Between each revision, the fibre end is cut and polished.

For each measurement, the SiPM is repositioned five times in front of the WLS fibre. The MIP peak position is determined in units of p.e. by fits on the signal charge spectrum. The spectrum comprises events, in which the test tile is read out while the trigger tiles have seen a signal larger than the discriminator threshold of 2.5 p.e. regardless of the trigger state of the test tile. The overall signal yield is calculated by a weighted mean of all measurements, whereby the uncertainty of each measurement is determined by the uncertainty of the fit results. Besides uncertainties introduced by the repetition of mirroring and repositioning, an additional uncertainty is included by the wrapping of the tile. This has to be redone for each mirroring cycle to allow for a modification of the WLS fibre end. The average temperature during the measurements of the SiPM of the test tile is $(27.16 \pm 0.38)\,^{\circ}\mathrm{C}$. As expected due to the measurements of a WLS fibre illuminated by an LED, the mirroring of the WLS fibre by the chrome spray has only a small effect compared to an open fibre end. As the fibre is not glued into the groove, the open end has a surface to air. Within the uncertainties the light yield of the open end and the chrome spray are consistent with each other and with the previous studies. The highly specular reflective foil glued onto the fibre end is recommended, but improves the light yield only by 15% compared to an increase by 70% for the previous study. Possible explanations are a non-parallel alignment of the mirror foil and the stronger attenuation due to an increased fibre length. Assuming a nominal attenuation length of $\lambda_{\mathrm{att}} = 3.5\,\mathrm{m}$, the reduced light intensity for $l = [0.80, 1.80]\,\mathrm{m}$ additional pathlength can be calculated by $I(l)/I_0 = \exp(-l/\lambda_{\mathrm{att}}) = [0.79, 0.59]$. The reflectivity of the complete setup is thus $[56, 41]\%$ compared to a shorter WLS fibre with a length of 15 cm but which is still not compatible with the determined

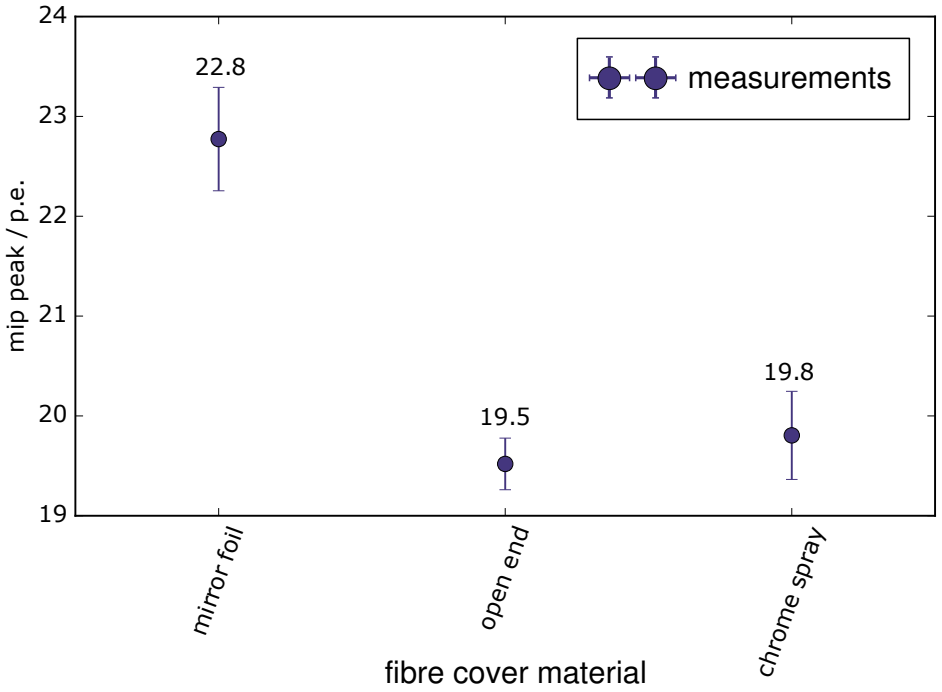

Figure 42.: Study of the influence on the light yield of different reflective materials used for mirroring of the fibre end. The fibre is located inside a test tile. The largest light yield is achieved for a highly specular reflective foil glued onto the fibre end. The light yield is increased by 15%, compared to a WLS fibre with surface to air and a WLS fibre mirrored by chrome spray as implemented in units of layout 1. The average temperature during the measurements is (27.16 ± 0.38) °C for the SiPM of the test tile.

efficiency. However, the previous studies of artificially illuminated WLS fibres indicate an even stronger attenuation, especially compared to short WLS fibre lengths. The derived intensity dropped by a factor of 3 from a WLS fibre length of 15 cm to 150 cm. The corresponding overall efficiency is in an acceptable range compared to the mirrored fibre in the scintillator tile. Furthermore, the WLS fibre is bent inside the sigma-shaped groove provoking a stronger light loss in the rounded corners compared to straight fibres for the measurements of a single WLS fibre.

J.2. Wrapping type

Besides the mirror coating of the fibre end inside the tile, also the wrapping of the complete scintillator tile with a reflective material is important. The minimal signal yield is expected for a unit without any additional wrapping, where photons are only guided back into the scintillator material by reflections at the surface to air. As already presented in chapter 5, the use of reflective material as wrapping of scintillator tiles can significantly increase the signal yield. Based on the studies presented in table 5.1, the best reflectivity is expected for a wrapping by PTFE tape also known under the trademark Teflon, followed by Tyvek paper and aluminum foil. The wrapping by highly reflective ESR foil is not studied as it is too expensive to apply. In figure 43, the signal yields of the studied materials are compared to a unit without wrapping. The signal yield is defined by the position of the MIP peak maximum in units of p.e. The tile is rewrapped five times by two layers of aluminum foil as well as 10 times by a Tyvek sheet and 3 times by a PTFE tape. For wrappings by Tyvek or PTFE tape, two additional layers of aluminum foil are added as external protection. They allow not only for an improved reflectivity and stability, but also for a shielding against ambient

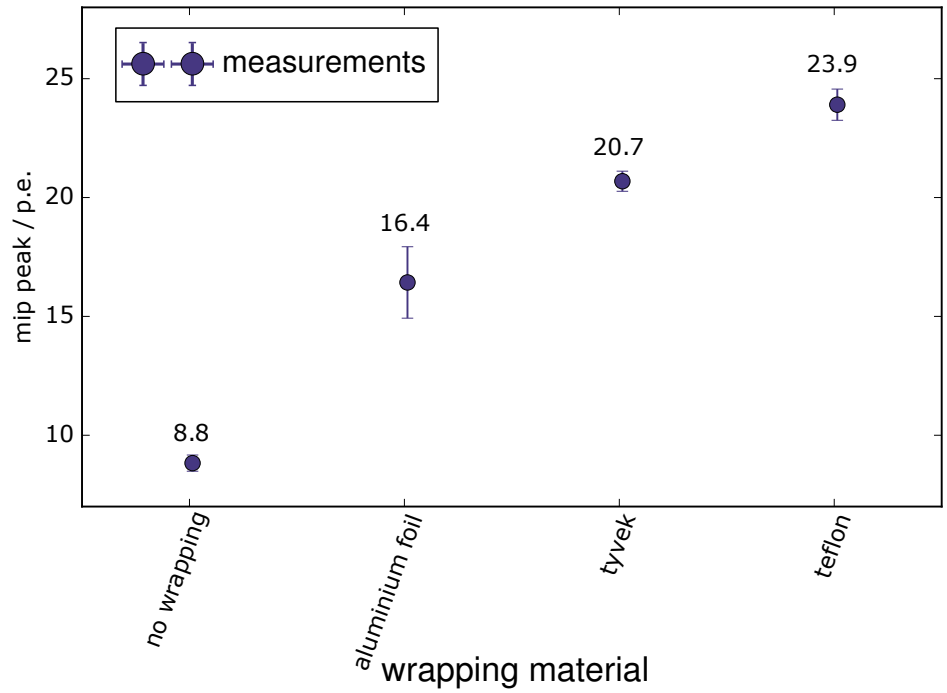

Figure 43.: Study of the influence of different wrapping materials on the light yield achieved by the test tile. The largest light yield is determined for diffusive materials. Compared to a tile without any additional material, so with only reflections at the surface to air, the light yield is increased by a factor of 2.5. The average temperature during the measurements is $(26.23 \pm 0.16)\,^{\circ}\mathrm{C}$ for the SiPM at the test tile.

light. Important is, that the edges and corners of the tile are completely covered. For each wrapping cycle, the SiPM is repositioned five times to investigate the uncertainty on the coupling efficiency between WLS fibre and SiPM. The fibre end inside the tile is mirrored by a reflective foil. The fibre is glued inside the groove along its entire length. The data points correspond to the weighted mean and the error bars to its external error. The average temperature during the measurements is $(26.23 \pm 0.16)\,^{\circ}\mathrm{C}$ of the SiPM at the test tile. The wrapping based on PTFE tape is the most efficient in terms of light yield (a factor of 2.5 higher compared to unwrapped tile and 1.15 compared to a Tyvek wrapping). However, the procedure needs two persons and more time as the tape has to be carefully applied in windings. Therefore, a wrapping with one layer of Tyvek and two additional aluminum layers is preferred.

J.3. Optical waveguide

A coupling to an optical waveguide is implemented in units of layout 1 to reduce the transmission loss by the relatively small attenuation length of the WLS fibre over long distances. The coupling is identified as potential source of light loss. The previous studies for artificially illuminated WLS fibres coupled to various types of optical waveguides are summarized in figure 37. For units of layout 1, a mechanical coupling is implemented by a mount comprising a narrow duct with the size of a fibre and a collet chuck to hold both, the WLS fibre and the optical waveguide, in place (cf. figure 6.1). Thereby, both fibres are located surface to surface, without any additional optical pad or gel. To investigate the influence of such a coupling, a unit of layout 1 is studied with and without an additional coupling to a waveguide of length 15 cm. The unit is measured in coincidence with the two trigger units in the stack. Thereby, the light is not guided onto the corresponding SiPM

type of layout 1 but to the actual type S13360-1350PE to allow for a better comparison to the light yield achieved by the test tile. For the measurement without the waveguide, the mechanical mount has been removed to have direct access to the WLS fibre. The average temperature during the measurements is (26.51 ± 0.18) °C.
Three configurations are studied whereby all tiles have been wrapped by Tyvek and two additional aluminum layers:

1. Test tile with a WLS fibre end mirrored by a highly reflective foil. The WLS fibre sticks out of the tile and is directly coupled to a SiPM of type S13360-1350PE.

2. Unit of layout 1 with a WLS fibre end mirrored by chrome spray.
   - The WLS fibre is coupled to an optical waveguide using the mechanical mount. The optical waveguide is readout by the same SiPM.
   - The WLS fibre is directly coupled to the same SiPM.

In figure 44, the three charge spectra are depicted as a function of the charge given in ADC count of the high gain of the slow shaper. For all three configurations, the MIP peak is clearly visible with an excellent single p.e. resolution. The bump at the end of the charge spectrum is a saturation feature of the EASIROC for the high gain as all higher energetic events are accumulated. A calibration between high and low gain allows for a significantly increased dynamic range and the effect vanishs. The calibration is introduced in chapter 8. The MIP peak in the charge spectrum of the unit of layout 1 with and without optical coupling corresponds to 7.5 p.e. and 21.2 p.e., respectively. The increase light yield by a factor of 2.8 is well in comparison to the test unit and verifies the optical coupling as largest source of light loss of unit layout 1. Therefore, the direct coupling of the WLS fibre to a SiPM is strongly preferred.
Actually, an improved light yield of unit 2 by 15% is expected due to a different mirroring of the WLS fibre in the tile by reflective foil compared to a non-efficient chrome spray for layout 1. For the measurement of the unit of layout 2, only a small increase in the light yield of 5% can be identified. However, the comparison of the performance of several units presented in table 8.2 will identify a large spread within the overall light yield of up to 30% which can well explain the results.

J.4. WLS fibre glued inside groove

As a last step, the influence of the coupling between the WLS fibre and the SIPM, directly located at the scintillator edge, is studied as well as the need of a glued fibre inside the groove. For the coupling to a WLS fibre, the SiPM circuit board has to be screwed onto the tile. This cannot be done unlimited firmly, as this may cause cracks in the material. Thus, air gaps and slightly tilted surfaces are a potential light loss for this coupling procedure. The use of optical pads or gels to improve the optical coupling are not considered as the complete setup may be subject to thermal expansions if measured within a large temperature range. The efficiency of the coupling may strongly variate over time if the pad or the gel is squeezed or kept relaxed during the extension. Thus, it is expected, that the SiPM circuit board screwed at the tile results in a reduced light yield compared to the one achieved by the placement by the xy-table. The xy-table placement enables a clear view on the interconnection and the possibility to put pressure on the contact surface between fibre and SiPM to avoid an air gap in-between.
For the measurement, the WLS fibre end is cut at the tile edge and then mechanically polished to achieve a homogenous surface. The light yield after the modification is given as the MIP peak position in units of p.e. The measurement is presented in figure 45 compared to the light yield achieved by the former coupling with the fibre sticking out. For both studies, the SiPM has been

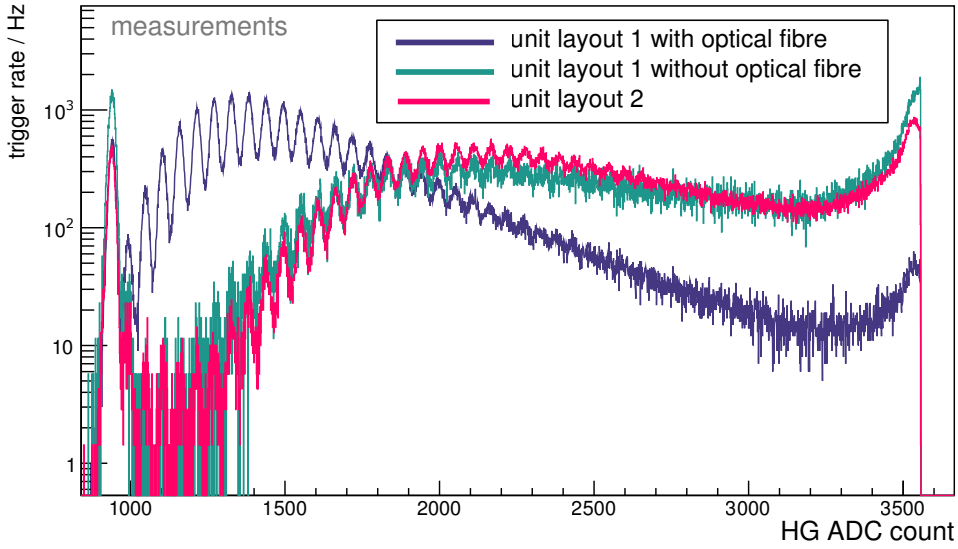

Figure 44.: Comparison of a unit layout 1 with and without the optical coupling to a transparent waveguide to the signal yield of the test tile. Shown are the charge spectra as a function of ADC count for the high gain of the EASIROC slow shapers. The outer tiles of the stack have been used as trigger with a discriminator threshold of 2.5 p.e. If a trigger is received, the middle tile under investigation is read out regardless of its own trigger status. Thus, the spectrum contains besides the MIP peak, the pedestal peak corresponding to electronic noise visible at a HG ADC count of roughly 925 and few dark noise events.

repositioned several times and the average including its standard deviation is shown. The signal of a SiPM located at the tile edge is, as discussed, slightly reduced by 6% but still provides an excellent light yield. Furthermore, it indicates a more stable connection, if repositioned, compared to the freely movable fibre and is therefore strongly recommended.
For these measurements, the WLS fibre ends have to be glued inside the groove to ensure a stable position in respect to the photosensor. This gluing procedure of the fibre needs a lot of time to avoid air inclusions in the optical adhesive. It has been shown during the test measurements, that the position of the WLS fibre in the groove is already stable due to friction by its sigma shape. This can be also confirmed after heavily shaking of the tile. For units of layout 1, the WLS fibre has been glued into the groove along its entire length. Therefore, it is investigated if the light yield changes for a fibre entirely glued inside the groove or only at its end. Optical adhesive has thereby both advantages and disadvantages for the trapping efficiency of photons inside the tile. It allows a smoother transition between the refractive indices of scintillator material and WLS fibre compared to air and allows more photons to enter the fibre. But the same smooth transition allows photons in the round corners of the tile to leave the fibre more easily. As both processes may cancel out, a faster production time might be achieved without loss of light. In figure 45, the light yield collected of the same WLS fibre for passages of atmospheric muons is shown first with only the fibre ends and then for the entire fibre glued into the groove. No significant deviation can be found. The slight tendency visible indicates a less efficient light yield for the fibre glued over its entire length. Therefore, for the further production the WLS fibre is only glued into the groove at its end.

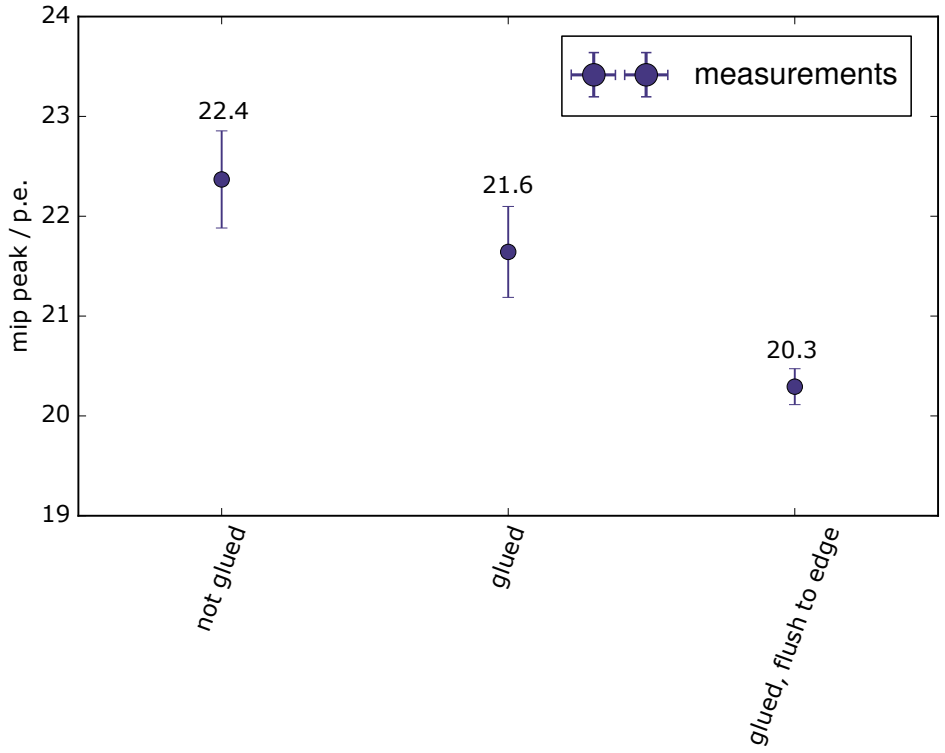

Figure 45.: Study of the influence on the light yield of the test tile by the coupling of the SiPM to a WLS fibre directly at the scintillator tile edge. The WLS fibre is once glued over its entire length into the milled groove in the tile and once only its end are fixated. The light yield is compared to a SiPM coupled to a WLS fibre still sticking out of the tile. Each data point corresponds to the average value and the standard deviations determined by several replacements of the SiPM. Within the uncertainties no deviation between the two different states of the WLS fibre gluing so that for a faster production only the fibre ends are glued into the groove. A reduction of the light yield by 6% can be found for the direct coupling from SiPM to a WLS fibre.

References

[1] K.-H. Kampert and A. A. Watson. „Extensive air showers and ultra high-energy cosmic rays: a historical review“. In: *European Physical Journal H* 37 (Aug. 2012), pp. 359–412. DOI: 10.1140/epjh/e2012-30013-x. arXiv: 1207.4827.

[2] A. Letessier-Selvon and T. Stanev. „Ultrahigh energy cosmic rays“. In: *Reviews of Modern Physics* 83 (July 2011), pp. 907–942. DOI: 10.1103/RevModPhys.83.907. arXiv: 1103.0031 [astro-ph.HE].

[3] M. Nagano and A. A. Watson. „Observations and implications of the ultrahigh-energy cosmic rays“. In: *Reviews of Modern Physics* 72 (July 2000), pp. 689–732. DOI: 10.1103/RevModPhys.72.689.

[4] J. J. Beatty and S. Westerhoff. „The Highest-Energy Cosmic Rays“. In: *Annual Review of Nuclear and Particle Science* 59 (Nov. 2009), pp. 319–345. DOI: 10.1146/annurev.nucl.58.110707.171154.

[5] J. Blümer, R. Engel, and J. R. Hörandel. „Cosmic Rays from the Knee to the Highest Energies“. In: *Prog. Part. Nucl. Phys.* 63 (2009), pp. 293–338. DOI: 10.1016/j.ppnp.2009.05.002. arXiv: 0904.0725 [astro-ph.HE].

[6] R. Engel, D. Heck, and T. Pierog. „Extensive air showers and hadronic interactions at high energy“. In: *Ann. Rev. Nucl. Part. Sci.* 61 (2011), pp. 467–489. DOI: 10.1146/annurev.nucl.012809.104544.

[7] A. Aab et al. „The Pierre Auger Cosmic Ray Observatory“. In: *Nucl. Instrum. Meth.* A798 (2015), pp. 172–213. DOI: 10.1016/j.nima.2015.06.058. arXiv: 1502.01323 [astro-ph.IM].

[8] P. Billoir. *Phenomenology of Ultra-High-Energy Atmospheric Showers*. In: Physics and Astrophysics of Ultra-High-Energy-Cosmic Rays, edited by M. Lemoine and G. Sigl. Berlin, Heidelberg: Springer, 2001.

[9] M. Stephan. „Measurement of the Light Flux of Stars and the Night-Sky with Silicon Photomultipliers“. PhD thesis. RWTH Aachen University, 2014.

[10] S. Cecchini and M. Spurio. „Atmospheric muons: experimental aspects“. In: *Geoscientific Instrumentation, Methods and Data Systems Discussions* 2 (Aug. 2012), pp. 603–641. DOI: 10.5194/gid-2-603-2012. arXiv: 1208.1171 [astro-ph.EP].

[11] K. Olive and P. D. Group. „Review of Particle Physics“. In: *Chinese Physics C* 38.9 (2014), p. 090001. URL: http://stacks.iop.org/1674-1137/38/i=9/a=090001.

[12] W. Heitler. *Quantum theory of radiation*. 1954.

[13] J. Matthews. „A Heitler model of extensive air showers“. In: *Astroparticle Physics* 22 (Jan. 2005), pp. 387–397. DOI: 10.1016/j.astropartphys.2004.09.003.

[14] S. Tavernier. *Interactions of Particles in Matter*. In: Experimental Techniques in Nuclear and Particle Physics. Berlin, Heidelberg: Springer, 2009. ISBN: 9783642008290. URL: https://doi.org/10.1007/978-3-642-00829-0_2.

[15] T. Stanev. *High Energy Cosmic Rays*. Berlin, Heidelberg: Springer, 2010. DOI: 10.1007/978-3-540-85148-6.

[16] A. Aab et al. „The Pierre Auger Observatory Upgrade - Preliminary Design Report“. In: *arxiv preprint* (2016). arXiv: 1604.03637 [astro-ph.IM].

[17] A. Aab et al. „Muons in air showers at the Pierre Auger Observatory: Mean number in highly inclined events“. In: *Phys. Rev.* D91.3 (2015), p. 032003. DOI: 10.1103/PhysRevD.91.059901,10.1103/PhysRevD.91.032003. arXiv: 1408.1421 [astro-ph.HE].

[18] P. Blasi. „The Origin of Galactic Cosmic Rays“. In: *Astron. Astrophys. Rev.* 21 (2013), p. 70. DOI: 10.1007/s00159-013-0070-7. arXiv: 1311.7346 [astro-ph.HE].

[19] A. Aab et al. „Depth of maximum of air-shower profiles at the Pierre Auger Observatory. I. Measurements at energies above $10^{17.8}$ eV“. In: *Phys. Rev.* D90.12 (2014), p. 122005. DOI: 10.1103/PhysRevD.90.122005. arXiv: 1409.4809 [astro-ph.HE].

[20] J. A. Simpson. „Elemental and isotopic composition of the galactic cosmic rays“. In: *Ann. Rev. Nucl. Part. Sci.* 33 (1983), pp. 323–382. DOI: 10.1146/annurev.ns.33.120183.001543.

[21] W. D. Apel et al. „Kneelike structure in the spectrum of the heavy component of cosmic rays observed with KASCADE-Grande“. In: *Phys. Rev. Lett.* 107 (2011), p. 171104. DOI: 10.1103/PhysRevLett.107.171104. arXiv: 1107.5885 [astro-ph.HE].

[22] A. Aab et al. „The Pierre Auger Observatory: Contributions to the 35th International Cosmic Ray Conference (ICRC 2017)“. In: *Proceedings, 35th International Cosmic Ray Conference (ICRC 2017): Bexco, Busan, Korea, July 12-20, 2017*. 2017. arXiv: 1708.06592 [astro-ph.HE]. URL: https://inspirehep.net/record/1617990/files/arXiv:1708.06592.pdf.

[23] J. R. Hörandel. „Models of the knee in the energy spectrum of cosmic rays“. In: *Astropart. Phys.* 21 (2004), pp. 241–265. DOI: 10.1016/j.astropartphys.2004.01.004. arXiv: astro-ph/0402356 [astro-ph].

[24] T. Antoni et al. „KASCADE measurements of energy spectra for elemental groups of cosmic rays: Results and open problems“. In: *Astropart. Phys.* 24 (2005), pp. 1–25. DOI: 10.1016/j.astropartphys.2005.04.001. arXiv: astro-ph/0505413 [astro-ph].

[25] W. D. Apel et al. „KASCADE-Grande measurements of energy spectra for elemental groups of cosmic rays“. In: *Astropart. Phys.* 47 (2013), pp. 54–66. DOI: 10.1016/j.astropartphys.2013.06.004. arXiv: 1306.6283 [astro-ph.HE].

[26] W. D. Apel et al. „The KASCADE-Grande experiment“. In: *Nucl. Instrum. Meth.* A620 (2010), pp. 202–216. DOI: 10.1016/j.nima.2010.03.147.

[27] A. Aab et al. „Evidence for a mixed mass composition at the ‘ankle’ in the cosmic-ray spectrum“. In: *Phys. Lett.* B762 (2016), pp. 288–295. DOI: 10.1016/j.physletb.2016.09.039. arXiv: 1609.08567 [astro-ph.HE].

[28] H. Kawai et al. „Telescope array experiment“. In: *Nucl. Phys. Proc. Suppl.* 175-176 (2008), pp. 221–226. DOI: 10.1016/j.nuclphysbps.2007.11.002.

[29] P. Bhattacharjee and G. Sigl. „Origin and propagation of extremely high-energy cosmic rays“. In: *Phys. Rept.* 327 (2000), pp. 109–247. DOI: 10.1016/S0370-1573(99)00101-5. arXiv: astro-ph/9811011 [astro-ph].

[30] D. Walz. „Constraining models of the extragalactic cosmic-ray origin with the Pierre Auger Observatory“. PhD thesis. RWTH Aachen University, 2016.

[31] K. Greisen. „End to the Cosmic-Ray Spectrum?“ In: *Phys. Rev. Lett.* 16 (17 Apr. 1966), pp. 748–750. DOI: 10.1103/PhysRevLett.16.748. URL: https://link.aps.org/doi/10.1103/PhysRevLett.16.748.

[32] G. T. Zatsepin and V. A. Kuzmin. „Upper limit of the spectrum of cosmic rays“. In: *JETP Lett.* 4 (1966). [Pisma Zh. Eksp. Teor. Fiz.4,114(1966)], pp. 78–80.

[33] E. Fermi. „On the origin of the cosmic radiation“. In: *Phys. Rev.* 75 (1949), pp. 1169–1174. DOI: 10.1103/PhysRev.75.1169.

[34] T. Winchen. „The principal axes of the directional energy distribution of cosmic rays measured with the Pierre Auger Observatory“. PhD Thesis. RWTH Aachen University, 2013.

[35] K. V. Ptitsyna and S. V. Troitsky. „Physical conditions in potential accelerators of ultra- high-energy cosmic rays: updated Hillas plot and radiation-loss constraints“. In: *Phys. Usp.* 53 (2010), pp. 691–701. DOI: 10.3367/UFNe.0180.201007c.0723. arXiv: 0808.0367 [astro-ph].

[36] J. Tueller et al. „Swift BAT Survey of AGN“. In: *Astrophys. J.* 681 (2008), p. 113. DOI: 10.1086/588458. arXiv: 0711.4130 [astro-ph].

[37] A. Aab et al. „Searches for Anisotropies in the Arrival Directions of the Highest Energy Cosmic Rays Detected by the Pierre Auger Observatory“. In: *Astrophys. J.* 804.1 (2015), p. 15. DOI: 10.1088/0004-637X/804/1/15. arXiv: 1411.6111 [astro-ph.HE].

[38] A. Aab et al. „Observation of a Large-scale Anisotropy in the Arrival Directions of Cosmic Rays above 8×10^{18} eV“. In: *Science* 357.6537 (2017), pp. 1266–1270. DOI: 10.1126/science.aan4338. arXiv: 1709.07321 [astro-ph.HE].

[39] A. Aab et al. „Large Scale Distribution of Ultra High Energy Cosmic Rays Detected at the Pierre Auger Observatory With Zenith Angles up to 80°“. In: *Astrophys. J.* 802.2 (2015), p. 111. DOI: 10.1088/0004-637X/802/2/111. arXiv: 1411.6953 [astro-ph.HE].

[40] R. Jansson and G. R. Farrar. „A New Model of the Galactic Magnetic Field“. In: *Astrophys. J.* 757, 14 (Sept. 2012), p. 14. DOI: 10.1088/0004-637X/757/1/14. arXiv: 1204.3662.

[41] M. Unger. „Highlights from the Pierre Auger Observatory“. In: *Proceedings, 35th International Cosmic Ray Conference (ICRC 2017): Bexco, Busan, Korea, July 12-20, 2017* (2017), p. 1102. arXiv: 1710.09478 [astro-ph.HE].

[42] C. Bonifazi. „The angular resolution of the Pierre Auger Observatory“. In: *Nucl. Phys. Proc. Suppl.* 190 (2009), pp. 20–25. DOI: 10.1016/j.nuclphysbps.2009.03.063. arXiv: 0901.3138 [astro-ph.HE].

[43] P. Abreu et al. „The Pierre Auger Observatory V: Enhancements“. In: *Proceedings, 32nd International Cosmic Ray Conference (ICRC 2011): Beijing, China, August 11-18, 2011*. 2011. arXiv: 1107.4807 [astro-ph.IM]. URL: https://inspirehep.net/record/919727/files/arXiv:1107.4807.pdf.

[44] B. Fick et al. „The Central Laser Facility at the Pierre Auger Observatory“. In: *JINST* 1.11 (2006), P11003–P11003. DOI: 10.1088/1748-0221/1/11/P11003.

[45] P. Abreu et al. „Techniques for Measuring Aerosol Attenuation using the Central Laser Facility at the Pierre Auger Observatory“. In: *JINST* 8 (2013), P04009. DOI: 10.1088/1748-0221/8/04/P04009. arXiv: 1303.5576 [astro-ph.IM].

[46] J. Abraham et al. „A study of the effect of molecular and aerosol conditions in the atmosphere on air fluorescence measurements at the Pierre Auger Observatory“. In: *Astroparticle Physics* 33.2 (2010), pp. 108–129. ISSN: 0927-6505. DOI: https://doi.org/10.1016/j.astropartphys.2009.12.005. URL: http://www.sciencedirect.com/science/article/pii/S0927650509001935.

[47] P. Abreu et al. „Description of Atmospheric Conditions at the Pierre Auger Observatory using the Global Data Assimilation System (GDAS)“. In: *Astropart. Phys.* 35 (2012), pp. 591–607. DOI: 10.1016/j.astropartphys.2011.12.002. arXiv: 1201.2276 [astro-ph.HE].

[48] B. Keilhauer and M. Will. „Description of Atmospheric Conditions at the Pierre Auger Observatory Using Meteorological Measurements and Models“. In: *Eur. Phys. J. Plus* 127 (2012), p. 96. DOI: 10.1140/epjp/i2012-12096-8. arXiv: 1208.5417 [astro-ph.IM].

[49] J. Chirinos. „Cloud Monitoring at the Pierre Auger Observatory“. In: *Proceedings, 33rd International Cosmic Ray Conference (ICRC 2013): Rio de Janeiro, Brazil, July 2-9, 2013*, p. 0994. URL: http://www.cbpf.br/~icrc2013/papers/icrc2013-0994.pdf.

[50] P. Abreu et al. „Identifying Clouds over the Pierre Auger Observatory using Infrared Satellite Data“. In: *Astropart. Phys.* 50-52 (2013), pp. 92–101. DOI: 10.1016/j.astropartphys.2013.09.004. arXiv: 1310.1641 [astro-ph.IM].

[51] M. Monasor et al. „The impact of the air-fluorescence yield on the reconstructed shower parameters of ultra-high energy cosmic rays“. In: *Astropart. Phys.* 34 (2011), pp. 467–475. DOI: 10.1016/j.astropartphys.2010.10.009. arXiv: 1010.3793 [astro-ph.IM].

[52] V. Rizi et al. „Atmospheric monitoring with LIDARs at the Pierre Auger Observatory“. In: *Eur. Phys. J. Plus* 127 (2012), p. 92. DOI: 10.1140/epjp/i2012-12092-0.

[53] S. Y. BenZvi et al. „The Lidar System of the Pierre Auger Observatory“. In: *Nucl. Instrum. Meth.* A574 (2007), pp. 171–184. DOI: 10.1016/j.nima.2007.01.094. arXiv: astro-ph/0609063 [astro-ph].

[54] T. Niggemann. „The silicon photomultiplier telescope FAMOUS for the detection of fluorescence light“. PhD thesis. RWTH Aachen University, 2016.

[55] I. Allekotte et al. „The Surface Detector System of the Pierre Auger Observatory“. In: *Nucl. Instrum. Meth.* A586 (2008), pp. 409–420. DOI: 10.1016/j.nima.2007.12.016. arXiv: 0712.2832 [astro-ph].

[56] J. Abraham et al. „Trigger and aperture of the surface detector array of the Pierre Auger Observatory“. In: *Nucl. Instrum. Meth.* A613 (2010), pp. 29–39. DOI: 10.1016/j.nima.2009.11.018. arXiv: 1111.6764 [astro-ph.IM].

[57] A. Castellina. „The dynamic range of the AugerPrime Surface Detector: technical solution and physics reach“. In: *The Pierre Auger Observatory: Contributions to the 35th International Cosmic Ray Conference (ICRC 2017)*. 2017, pp. 161–168. URL: https://inspirehep.net/record/1618432/files/1617990_161-168.pdf.

[58] A. Aab et al. „Reconstruction of inclined air showers detected with the Pierre Auger Observatory“. In: *JCAP* 1408.08 (2014), p. 019. DOI: 10.1088/1475-7516/2014/08/019. arXiv: 1407.3214 [astro-ph.HE].

[59] K. Kamata and J. Nishimura. „The Lateral and the Angular Structure Functions of Electron Showers“. In: *Progress of Theoretical Physics Supplement*. Vol. 6. Jan. 1958, pp. 93–155.

[60] K. Greisen. „Cosmic ray showers“. In: *Ann. Rev. Nucl. Part. Sci.* 10 (1960), pp. 63–108. DOI: 10.1146/annurev.ns.10.120160.000431.

[61] D. B. et al. „Measurement of the Lateral Distribution Function of UHECR Air Showers with the Pierre Auger Observatory“. In: *Proceedings, 29th International Cosmic Ray Conference (ICRC 2005) - by Forschungszentrum Karlsruhe, Institute for Nuclear Physics, and University Karlsruhe, Institute for Experimental Nuclear Physics: Pune, India, August 3-11, 2005*. Aug. 2005.

[62] P. L. Ghia. „Statistical and systematic uncertainties in the event reconstruction and S(1000) determination by the Pierre Auger surface detector“. In: *Proceedings, 29th International Cosmic Ray Conference (ICRC 2005) - by Forschungszentrum Karlsruhe, Institute for Nuclear Physics, and University Karlsruhe, Institute for Experimental Nuclear Physics: Pune, India, August 3-11, 2005*. 2005. arXiv: astro-ph/0507029 [astro-ph]. URL: http://lss.fnal.gov/cgi-bin/find_paper.pl?conf-05-270-E-TD.

[63] D. Newton, J. Knapp, and A. A. Watson. „The Optimum Distance at which to Determine the Size of a Giant Air Shower“. In: *Astropart. Phys.* 26 (2007), pp. 414–419. DOI: 10.1016/j.astropartphys.2006.08.003. arXiv: astro-ph/0608118 [astro-ph].

[64] I. Valino. „The flux of ultra-high energy cosmic rays after ten years of operation of the Pierre Auger Observatory“. In: *Proceedings, 34th International Cosmic Ray Conference (ICRC 2015): The Hague, The Netherlands, July 30-August 6, 2015* (2016), p. 271.

[65] J. Hersil et al. „Observations of Extensive Air Showers near the Maximum of Their Longitudinal Development“. In: *Phys. Rev. Lett.* 6 (1961), pp. 22–23. DOI: 10.1103/PhysRevLett.6.22.

[66] A. Schulz. „Measurement of the energy spectrum and mass composition of ultra-high energy cosmic rays“. PhD thesis. Karlsruher Institut für Technologie (KIT), 2016.

[67] V. Verzi. „The Energy Scale of the Pierre Auger Observatory“. In: *Proceedings, 33rd International Cosmic Ray Conference (ICRC 2013): Rio de Janeiro, Brazil, July 2-9, 2013*, p. 0928. URL: http://www.cbpf.br/~icrc2013/papers/icrc2013-0928.pdf.

[68] A. Aab et al. „The Pierre Auger Observatory: Contributions to the 33rd International Cosmic Ray Conference (ICRC 2013)“. In: *Proceedings, 33rd International Cosmic Ray Conference (ICRC 2013): Rio de Janeiro, Brazil, July 2-9, 2013*. 2013. arXiv: 1307.5059 [astro-ph.HE]. URL: http://lss.fnal.gov/archive/2013/conf/fermilab-conf-13-285-ad-ae-cd-td.pdf.

[69] C. Meurer and N. Scharf. „HEAT - a low energy enhancement of the Pierre Auger Observatory“. In: *Astrophys. Space Sci. Trans.* 7 (2011), pp. 183–186. DOI: 10.5194/astra-7-183-2011. arXiv: 1106.1329 [astro-ph.IM].

[70] J. Abraham et al. „The Fluorescence Detector of the Pierre Auger Observatory“. In: *Nucl. Instrum. Meth.* A620 (2010), pp. 227–251. DOI: 10.1016/j.nima.2010.04.023. arXiv: 0907.4282 [astro-ph.IM].

[71] T. H.-J. Mathes. „The HEAT telescopes of the Pierre Auger Observatory: Status and first data“. In: *Proceedings, 32nd International Cosmic Ray Conference (ICRC 2011): Beijing, China, August 11-18, 2011*. Vol. 3. 2011, p. 153. DOI: 10.7529/ICRC2011/V03/0761. URL: https://inspirehep.net/record/924989/files/924989.pdf.

[72] F. Arqueros, J. R. Hörandel, and B. Keilhauer. „Air Fluorescence Relevant for Cosmic-Ray Detection - Summary of the 5th Fluorescence Workshop, El Escorial 2007“. In: *Nucl. Instrum. Meth.* A597 (2008), pp. 1–22. DOI: 10.1016/j.nima.2008.08.056. arXiv: 0807.3760 [astro-ph].

[73] M. Ave et al. „Measurement of the pressure dependence of air fluorescence emission induced by electrons“. In: *Astropart. Phys.* 28 (2007), pp. 41–57. DOI: 10.1016/j.astropartphys.2007.04.006. arXiv: astro-ph/0703132 [ASTRO-PH].

[74] M. Ave et al. „Precise measurement of the absolute fluorescence yield of the 337 nm band in atmospheric gases“. In: *Astropart. Phys.* 42 (2013), pp. 90–102. DOI: 10.1016/j.astropartphys.2012.12.006. arXiv: 1210.6734 [astro-ph.IM].

[75] J. Rosado, F. Blanco, and F. Arqueros. „On the absolute value of the air-fluorescence yield“. In: *Astropart. Phys.* 55 (2014), pp. 51–62. DOI: 10.1016/j.astropartphys.2014.02.003. arXiv: 1401.4310 [astro-ph.IM].

[76] M. Ave. „Energy Dependence of Air Fluorescence Yield measured by AIRFLY“. In: *arxiv preprint* (2007). arXiv: 0711.4518 [astro-ph].

[77] M. L. de Oliveira et al., the Pierre Auger collaboration. „Manufacturing the Schmidt corrector lens for the Pierre Auger Observatory“. In: *Nucl. Instrum. Meth.* A522 (2004), pp. 360–370. DOI: 10.1016/j.nima.2003.11.409.

[78] HZC Photonics Technology Co., Ltd. *Photomultipler tubes product specifications XP3062*. 2018. URL: http://www.hzcphotonics.com/products/XP3062.pdf.

[79] H. Gemmeke et al. „Design of the trigger system for the AUGER fluorescence detector“. In: *IEEE Trans. Nucl. Sci.* 47 (2000), pp. 371–375. DOI: 10.1109/23.846184.

[80] A. Schmidt et al. „Third Level Trigger for the Fluorescence Telescopes of the Pierre Auger Observatory“. In: *Nucl. Instrum. Meth.* A601 (2009), pp. 347–353. DOI: 10.1016/j.nima.2009.01.002. arXiv: 0807.4421 [astro-ph].

[81] M. Giller et al. „Energy spectra of electrons in the extensive air showers of ultra-high energy“. In: *J. Phys.* G30 (2004), pp. 97–105. DOI: 10.1088/0954-3899/30/2/009.

[82] F. Nerling et al. „Universality of electron distributions in high-energy air showers: Description of Cherenkov light production“. In: *Astropart. Phys.* 24 (2006), pp. 421–437. DOI: 10.1016/j.astropartphys.2005.09.002. arXiv: astro-ph/0506729 [astro-ph].

[83] J. Pekala et al. „Atmospheric multiple scattering of fluorescence and Cherenkov light emitted by extensive air showers“. In: *Nucl. Instrum. Meth.* A605 (2009), pp. 388–398. DOI: 10.1016/j.nima.2009.03.244. arXiv: 0904.3230 [astro-ph.HE].

[84] T. K. Gaisser and A. M. Hillas. „Reliability of the method of constant intensity cuts for reconstructing the average development of vertical showers“. In: *Proceedings, 15th International Cosmic Ray Conference (ICRC 1977): Plovdiv, Bulgaria, August 13-26, 1977, Conference Papers. Volume* 8 (1977), pp. 353–357.

[85] C. Song et al. „Energy estimation of UHE cosmic rays using the atmospheric fluorescence technique“. In: *Astroparticle Physics* 14.1 (2000), pp. 7–13. ISSN: 0927-6505. DOI: https://doi.org/10.1016/S0927-6505(00)00101-8. URL: http://www.sciencedirect.com/science/article/pii/S0927650500001018.

[86] M. Risse and D. Heck. „Energy release in air showers“. In: *Astropart. Phys.* 20 (2004), p. 661. DOI: 10.1016/j.astropartphys.2003.10.006. arXiv: astro-ph/0308158 [astro-ph].

[87] M. J. Tueros. „Estimate of the non-calorimetric energy of showers observed with the fluorescence and surface detectors of the Pierre Auger Observatory“. In: *Proceedings, 33rd International Cosmic Ray Conference (ICRC 2013): Rio de Janeiro, Brazil, July 2-9, 2013*, p. 0705. URL: http://www.cbpf.br/~icrc2013/papers/icrc2013-0705.pdf.

[88] F. G. Schröder. „Radio detection of Cosmic-Ray Air Showers and High-Energy Neutrinos“. In: *Prog. Part. Nucl. Phys.* 93 (2017), pp. 1–68. DOI: 10.1016/j.ppnp.2016.12.002. arXiv: 1607.08781 [astro-ph.IM].

[89] A. Aab et al. „Energy Estimation of Cosmic Rays with the Engineering Radio Array of the Pierre Auger Observatory“. In: *Phys. Rev.* D93.12 (2016), p. 122005. DOI: 10.1103/PhysRevD.93.122005. arXiv: 1508.04267 [astro-ph.HE].

[90] Ch. Glaser. „Absolute Energy Calibration of the Pierre Auger Observatory using Radio Emission of Extensive Air Showers“. PhD thesis. RWTH Aachen University, 2016.

[91] T. Huege et al. „Radio detection of cosmic rays in the Pierre Auger Observatory“. In: *Nucl. Instrum. Meth.* A617 (2010), pp. 484–487. DOI: 10.1016/j.nima.2009.10.012. arXiv: 0906.4970 [astro-ph.IM].

[92] C. Glaser. „Results and Perspectives of the Auger Engineering Radio Array“. In: *EPJ Web Conf.* 135 (2017), p. 01006. DOI: 10.1051/epjconf/201713501006. arXiv: 1609.01513 [astro-ph.HE].

[93] P. Abreu et al. „Antennas for the Detection of Radio Emission Pulses from Cosmic-Ray“. In: *JINST* 7 (2012), P10011. DOI: 10.1088/1748-0221/7/10/P10011. arXiv: 1209.3840 [astro-ph.IM].

[94] B. Daniel et al. „The AMIGA enhancement of the Pierre Auger Observatory“. In: *J. Phys. Conf. Ser.* 632.1 (2015), p. 012088. DOI: 10.1088/1742-6596/632/1/012088.

[95] I. Mariş. „The AMIGA infill detector of the pierre auger observatory: Performance and first data“. In: *Proceedings, 32nd International Cosmic Ray Conference (ICRC 2011): Beijing, China, August 11-18, 2011*. Vol. 1. Jan. 2011, pp. 267–270.

[96] F. Sánchez. „The AMIGA detector of the Pierre Auger Observatory: overview“. In: *Proceedings, 32nd International Cosmic Ray Conference (ICRC 2011): Beijing, China, August 11-18, 2011*. Vol. 3. 2011, pp. 149–152. DOI: 10.7529/ICRC2011/V03/0742. URL: https://inspirehep.net/record/924988/files/924988.pdf.

[97] B. Wundheiler. „The AMIGA Muon Counters of the Pierre Auger Observatory: Performance and Studies of the Lateral Distribution Function“. In: *Proceedings, 34th International Cosmic Ray Conference (ICRC 2015): The Hague, The Netherlands, July 30-August 6, 2015*. 2016, p. 324.

[98] D. Impiombato et al. „Characterization and performance of the ASIC (CITIROC) front-end of the ASTRI camera“. In: *Nucl. Instrum. Meth.* A794 (2015), pp. 185–192. DOI: 10.1016/j.nima.2015.05.028. arXiv: 1506.00264 [physics.ins-det].

[99] J. Fleury et al. „Petiroc and Citiroc: front-end ASICs for SiPM read-out and ToF applications“. In: *JINST* 9 (2014), p. C01049. DOI: 10.1088/1748-0221/9/01/C01049.

[100] D. Beznosko et al. „FNAL-NICADD extruded scintillator“. In: *Proceedings, 2004 IEEE Nuclear Science Symposium and Medical Imaging Conference (NSS/MIC 2004): Rome, Italy, October 16-22, 2004*. 2. 2004, pp. 790–793. DOI: 10.1109/NSSMIC.2004.1462328. URL: http://lss.fnal.gov/cgi-bin/find_paper.pl?conf-04-216.

[101] R. Foord et al. „The Use of Photomultiplier Tubes for Photon Counting“. In: *Appl. Opt.* 8.10 (Oct. 1969), pp. 1975–1989. DOI: 10.1364/AO.8.001975. URL: http://ao.osa.org/abstract.cfm?URI=ao-8-10-1975.

[102] A. Wright. *The Photomultiplier Handbook*. OUP Oxford, 2017. ISBN: 9780192528087. URL: https://books.google.de/books?id=ujooDwAAQBAJ.

[103] Hamamatsu Photonics K.K. *PMT Handbook Chapter 12*. 2018. URL: https://www.hamamatsu.com/resources/pdf/etd/PMT_handbook_v3aE-Chapter12.pdf.

[104] Hamamatsu Photonics K.K. *PMT Handbook Chapter 2*. 2018. URL: https://www.hamamatsu.com/resources/pdf/etd/PMT_handbook_v3aE-Chapter2.pdf.

[105] Hamamatsu Photonics K.K. *Hamamatsu Website*. 2018. URL: http://www.hamamatsu.com.

[106] Y. Fukuda et al. „The Super-Kamiokande detector". In: *Nucl. Instrum. Meth.* A501 (2003), pp. 418–462. DOI: 10.1016/S0168-9002(03)00425-X.

[107] F. An et al. „Neutrino Physics with JUNO". In: *J. Phys.* G43.3 (2016), p. 030401. DOI: 10.1088/0954-3899/43/3/030401. arXiv: 1507.05613 [physics.ins-det].

[108] D. Renker and E. Lorenz. „Advances in solid state photon detectors". In: *JINST* 4 (2009), P04004. DOI: 10.1088/1748-0221/4/04/P04004.

[109] P. Buzhan et al. „Silicon photomultiplier and its possible applications". In: *Nucl. Instrum. Meth.* A504 (2003), pp. 48–52. DOI: 10.1016/S0168-9002(03)00749-6.

[110] N. Otte. „The Silicon Photomultiplier: A New Device for High Energy Physics, Astroparticle Physics, Industrial and Medical Applications". In: *eConf* C0604032 (2006), p. 0018.

[111] *MPPC*. Hamamatsu Photonics K.K. 2019. URL: https://www.hamamatsu.com/resources/pdf/ssd/mppc_kapd9005e.pdf.

[112] Z. Li et al. „A novel analog power supply for gain control of the Multi-Pixel Photon Counter (MPPC)". In: *Nucl. Instrum. Meth.* A850 (2017), pp. 35–41. DOI: 10.1016/j.nima.2017.01.029. arXiv: 1606.03727 [astro-ph.IM].

[113] T. Bretz et al. „Dynamic range measurement and calibration of SiPMs". In: *JINST* 11.03 (2016), P03009. DOI: 10.1088/1748-0221/11/03/P03009.

[114] J. Schumacher. „Exploring silicon photomultipliers for the Upgrade of the Pierre Auger Observatory". PhD Thesis. RWTH Aachen University, 2018.

[115] S. S. Majos et al. „Noise and radiation damage in silicon photomultipliers exposed to electromagnetic and hadronic radiation". In: *Nucl. Instrum. Meth.* A602 (2009), pp. 506–510. DOI: 10.1016/j.nima.2009.01.176.

[116] Y. Qiang et al. „Radiation Hardness Tests of SiPMs for the JLab Hall D Barrel Calorimeter". In: *Nucl. Instrum. Meth.* A698 (2013), pp. 234–241. DOI: 10.1016/j.nima.2012.10.015. arXiv: 1207.3743 [physics.ins-det].

[117] D. Neise et al. „FACT – Status and experience from five years of operation of the first G-APD Cherenkov Telescope". In: *Nucl. Instrum. Meth.* A876 (2017), pp. 17–20. DOI: 10.1016/j.nima.2016.12.053.

[118] S. M. Sze and K. K. Ng. *Physics of semiconductor devices*. New York: John Wiley & Sons, 2006.

[119] K. K. Ng. *Complete Guide to Semiconductor devices*. 2nd ed. New York: John Wiley & Sons, 2002.

[120] Horst Zimmermann. *Integrated Silicon Optoelectronics*. Berlin, Heidelberg: Springer, 2010.

[121] S. Cova et al. „Avalanche photodiodes and quenching circuits for single-photon detection". In: *Appl. Opt.* 35.12 (1996), p. 1956. DOI: 10.1364/ao.35.001956.

[122] F. Scheuch et al. „Electrical characterization and simulation of SiPMs". In: *Nucl. Instrum. Meth.* A787 (2015). New Developments in Photodetection NDIP14, pp. 340–343. ISSN: 0168-9002. DOI: https://doi.org/10.1016/j.nima.2015.01.066. URL: http://www.sciencedirect.com/science/article/pii/S0168900215000984.

[123] T. Niggemann et al. „G4SiPM: A novel silicon photomultiplier simulation package for Geant4“. In: *Nucl. Instrum. Meth.* A787 (2015), pp. 344–347. DOI: 10.1016/j.nima.2015.01.067.

[124] M. Lauscher. „Characterisation Studies of Silicon Photomultipliers for the Detection of Fluorescence Light from Extensive Air Showers“. Master's Thesis. RWTH Aachen University, 2012.

[125] P. Buzhan et al. „An advanced study of silicon photomultiplier“. In: *ICFA Instrum. Bull.* 23 (2001), pp. 28–41.

[126] W. G. Oldham, R. Samuelson, and P. Antognetti. „Triggering phenomena in avalanche diodes“. In: *IEEE Trans. Electron Devices* 19.9 (1972), pp. 1056–1060. DOI: 10.1109/t-ed.1972.17544.

[127] D. Wilson. „Angular Dependence of the Relative Photon Detection Efficiency of Silicon Photomultipliers“. Bachelor's Thesis. RWTH Aachen University, 2012.

[128] M. Nemallapudi et al. „SiPM angular response and enhanced light extraction“. In: *2013 IEEE Nuclear Science Symposium and Medical Imaging Conference* (2013), pp. 1–5. DOI: 0.1109/nssmic.2013.6829586.

[129] M. L. Cutler. „Reflection of light from multi-layer films“. Bachelor's Thesis. Massachusetts Institute of Technology, 1939.

[130] SensL Technologies Ltd. *SensL Website*. 2018. URL: http://www.sensl.com.

[131] G. Bonanno et al. „Precision measurements of Photon Detection Efficiency for SiPM detectors“. In: *Nucl. Instrum. Meth.* A610 no. 1 (2009), pp. 93–97.

[132] G. Zappalà et al. „Set-up and methods for SiPM Photo-Detection Efficiency measurements“. In: *Journal of Instrumentation* 11.08 (2016), P08014. URL: http://stacks.iop.org/1748-0221/11/i=08/a=P08014.

[133] A. N. Otte et al. „A measurement of the photon detection efficiency of silicon photomultipliers“. In: *Nucl. Instrum. Meth.* A567 (2006), pp. 360–363. DOI: 10.1016/j.nima.2006.05.145.

[134] Y. Musienko, S. Reucroft, and J. Swain. „The gain, photon detection efficiency and excess noise factor of multi-pixel Geiger-mode avalanche photodiodes“. In: *Nucl. Instrum. Meth.* A567 (Nov. 2006), pp. 57–61. DOI: 10.1016/j.nima.2006.05.214.

[135] R. Newman. „Visible light from a silicon p-n junction“. In: *Phys. Rev.* 100 (June 1995), pp. 700–703.

[136] A. L. Lacaita et al. „On the bremsstrahlung origin of hot-carrier-induced photons in silicon devices“. In: *IEEE Trans. Electron Dev.* 40 (Mar. 1993), pp. 577–582.

[137] A. G. Chynowth and K. G. McKay. „Photon emission from avalanche breakdown in silicon“. In: *Phys. Rev.* 102 (Jan. 1956), pp. 369–376.

[138] R. Mirzoyan, R. Kosyra, and H.-G. Moser. „Light emission in Si avalanches“. In: *Nucl. Instrum. Meth.* A610.1 (2009). New Developments In Photodetection NDIP08, pp. 98–100. ISSN: 0168-9002. DOI: https://doi.org/10.1016/j.nima.2009.05.081. URL: http://www.sciencedirect.com/science/article/pii/S0168900209010377.

[139] P. Eckert et al. „Characterisation Studies of Silicon Photomultipliers“. In: *Nucl. Instrum. Meth.* A620 (2010), pp. 217–226. DOI: 10.1016/j.nima.2010.03.169. arXiv: 1003.6071 [physics.ins-det].

[140] S. Agostinelli et al. „GEANT4: A Simulation toolkit“. In: *Nucl. Instrum. Meth.* A506 (2003), pp. 250–303. DOI: 10.1016/S0168-9002(03)01368-8.

[141] T. Niggemann. *G4SiPM repository*. 2018. URL: https://github.com/ntim/g4sipm.

[142] H. Kolanoski and N. Wermes. *Teilchendetektoren: Grundlagen und Anwendungen*. Berlin, Heidelberg: Springer, 2016. ISBN: 9783662453506. URL: https://books.google.de/books?id=L5uFCwAAQBAJ.

[143] G. F. Knoll. *Radiation detection and measurement; 4th ed.* New York: John Wiley & Sons, 2010. URL: https://cds.cern.ch/record/1300754.

[144] L. Landau. „On the energy loss of fast particles by ionization". In: *J. Phys.(USSR)* 8 (1944), pp. 201–205.

[145] S. R. Cherry, J. A. Sorenson, and M. E. Phelps. „Chapter 7 - Radiation Detectors". In: *Physics in Nuclear Medicine (Fourth Edition)*. Ed. by S. R. Cherry, J. A. Sorenson, and M. E. Phelps. Fourth Edition. Philadelphia: W.B. Saunders, 2012, pp. 87–106. ISBN: 978-1-4160-5198-5. DOI: https://doi.org/10.1016/B978-1-4160-5198-5.00007-1. URL: https://www.sciencedirect.com/science/article/pii/B9781416051985000071.

[146] F. Sauli, ed. *Instrumentation in high-energy physics*. Singapore, Singapore: World Scientific (1992) 585 p. (Advanced series on directions in high energy physics, 9), 1992.

[147] In: *The Theory and Practice of Scintillation Counting*. Ed. by J. BIRKS. International Series of Monographs in Electronics and Instrumentation. Pergamon, 1964. ISBN: 978-0-08-010472-0. DOI: https://doi.org/10.1016/B978-0-08-010472-0.50003-3.

[148] F. D. Brooks. „DEVELOPMENT OF ORGANIC SCINTILLATORS". In: *Nucl. Instrum. Meth.* 162 (1979), pp. 477–505. DOI: 10.1016/0029-554X(79)90729-8.

[149] Saint Gobain. *BC-620 Reflector Paint for Plastic Scintillators*. 2018. URL: https://www.crystals.saint-gobain.com/sites/imdf.crystals.com/files/documents/sgc-bc620-data-sheet_69725.pdf.

[150] Eljen Technology. *EJ-510 Reflector Paint for Plastic Scintillators*. 2018. URL: http://www.eljentechnology.com/products/accessories/ej-510-ej-520.

[151] S. Weingarten. „Prototypdetektoren für das geplante Upgradeprojekt Muon Track Fast Tag am CMS-Experiment". Master's thesis. RWTH Aachen University, 2013.

[152] Saint Gobain. *BC-642 PTFE Reflector Tape*. 2018. URL: https://www.crystals.saint-gobain.com/products/assembly-materials.

[153] 3M Optical Systems. *Enhanced Specular Reflector*. 2018. URL: http://multimedia.3m.com/mws/media/374730O/vikuiti-tm-esr-sales-literature.pdf?fn=ESR%20ss2.pdf.

[154] M. Janecek and W. W. Moses. „Optical Reflectance Measurements for Commonly Used Reflectors". In: *Nuclear Science, IEEE Transactions on* 55 (Sept. 2008), pp. 2432–2437.

[155] Kuraray Co., Ltd. *Plastic Scintillating Fibers*. 2018. URL: http://kuraraypsf.jp/pdf/all.pdf.

[156] Saint-Gobain Crystals. *Scintillating Optical Fibres. data sheet*. 2018. URL: http://www.%20crystals.saint-gobain.com/uploadedFiles/SG-Crystals/Documents/SGC%%2020Fibers%20Brochure.pdf.

[157] O. Ziemann et al. *POF Handbook - Optical Short Range Transmission Systems*. Springer, 2nd edition, 2008.

[158] C. P. Achenbach. „Active optical fibres in modern particle physics experiments". In: *arxiv preprint* (2004). arXiv: nucl-ex/0404008 [nucl-ex].

[159] Eljen Technology. *EJ-212 Plastic Scintillator. data sheet*. 2018. URL: http://www.eljentechnology.com/index.php/products/plastic-scintillators/64-ej-212.

[160] Eljen Technology. *EJ-212 Plastic Scintillator. data sheet*. 2018. URL: http://www.eljentechnology.com/index.php/products/plastic-scintillators/64-ej-200.

[161] Saint Gobain. *BCF-92 Plastic Scintillating Fibers*. 2018. URL: https://www.crystals.saint-gobain.com/products/scintillating-fiber.

[162] ESKA acrylic fiber optics offered by Edmund Optics, developed and manufactured by Mitsubishi. *Optical Grade Plastic Light Guide*. 2018. URL: https://www.edmundoptics.com/p/1000mum-with-1-fiber-optical-grade-plastic-light-guide/69/.

[163] Eljen Technology. *EJ-500 optical cement. data sheet*. 2018. URL: https://eljentechnology.com/images/products/data_sheets/EJ-500.pdf.

[164] R. Meißner. „Development and Characterisation of a Scintillator Based Muon Detector with SiPM Readout for Air Shower Experiments“. Master's Thesis. RWTH Aachen University, 2015.

[165] L. Middendorf. „Data Acquisition for an SiPM based muon detector“. PhD Thesis. RWTH Aachen University, 2018.

[166] Finetech GmbH&Co.KG. *Modular Hot Air SMD Rework Station*. 2019. URL: https://www.finetech.de/products/finetech-product-overview/smd-hot-air-rework-station-fineplacer-pico-rs/.

[167] *EASIROC - Software & Test Board User Guide*. Omega - Orsay Micro Electronics Group Associated, Institut National de Physique Nucléaire et de Physique des Particules. 2012.

[168] *EASIROC - Datasheet*. Omega - Orsay Micro Electronics Group Associated, Institut National de Physique Nucléaire et de Physique des Particules. 2011.

[169] D. E. Groom, N. V. Mokhov, and S. I. Striganov. „Muon stopping power and range tables 10-MeV to 100-TeV“. In: *Atom. Data Nucl. Data Tabl.* 78 (2001), pp. 183–356. DOI: 10.1006/adnd.2001.0861.

[170] M. N. Polyanskiy. *Refractive index database*. https://refractiveindex.info. Accessed on 2019-01-25.

[171] T. Hebbeker et al. *Muon measurement using scintillator tiles with SiPM readout*. Internal Note of the Pierre Auger Collaboration GAP2013-057. 2013.

[172] C. Peters et al. „The muon detector prototype AMD for the determination of the muon content in UHECRs“. In: *Proceedings of Science PoS(ICRC2015)596*. 2015. URL: https://pos.sissa.it/archive/conferences/236/596/ICRC2015_596.pdf.

[173] J. Kemp et al. „The application of SiPMs in the fluorescence telescope FAMOUS and the Aachen Muon Detector“. In: *Proceedings of Science PoS(ICRC2017)466*. 2017. URL: https://pos.sissa.it/301/466.

[174] C. Peters et al. „Prospects of Silicon Photomultipliers for Ground-Based Cosmic Ray Experiments“. In: *Proceedings of 2016 International Conference on Ultra-High Energy Cosmic Rays (UHECR2016)*. DOI: 10.7566/JPSCP.19.011030. eprint: https://journals.jps.jp/doi/pdf/10.7566/JPSCP.19.011030. URL: https://journals.jps.jp/doi/abs/10.7566/JPSCP.19.011030.

[175] Geant4 collaboration. *Geant4 Book For Application Developers*. 2018. URL: http://geant4.web.cern.ch/geant4/UserDocumentation/UsersGuides/ForApplicationDeveloper/html/index.html.

[176] J. Allison et al. „Recent developments in GEANT4“. In: *Nucl. Instrum. Meth.* A835 (2016), pp. 186–225. DOI: 10.1016/j.nima.2016.06.125.

[177] The Geant4 Collaboration. *Geant4 User Documentation*. 2018.

[178] NIST Office of Reference Materials. *NIST catalogue - materials*. 2018. URL: https://www.nist.gov/srm.

[179] E. Dietz-Laursonn. *GODDeSS Source Code Repository*. 2018. URL: https://forge.%20physik.rwth-aachen.de/projects/goddess.

[180] E. Dietz-Laursonn et al. „GODDeSS: a Geant4 extension for easy modelling of optical detector components“. In: *Journal of Instrumentation* 12.04 (2017), P04026.

[181] E. Dietz-Laursonn. „Optical Set-Up for Automatised SiPM Characterisation“. PhD Thesis. RWTH Aachen University, 2016.

[182] R. Brun and F. Rademakers. „ROOT: An object oriented data analysis framework“. In: *Nucl. Instrum. Meth.* A389 (1997), pp. 81–86. DOI: 10.1016/S0168-9002(97)00048-X.

[183] D. Keßler. „Coupling of optical fibers for the Aachen Muon Detector“. Bachelor's Thesis. RWTH Aachen University, 2016.

[184] M. Wirtz. „Simulation studies of a novel scintillator detector with SiPM readout for muons of cosmic ray air showers“. Bachelor's Thesis. RWTH Aachen University, 2014.

[185] Saint Gobain. *BCF-98 Clear Waveguide*. 2018. URL: https://www.crystals.saint-gobain.com/products/scintillating-fiber.

[186] D. Heck et al. „CORSIKA: A Monte Carlo code to simulate extensive air showers“. In: *FZKA-6019* (1998).

[187] H. Anderhub et al. „FACT - The first Cherenkov telescope using a G-APD camera for TeV gamma-ray astronomy“. In: *Nucl. Instrum. Meth.* A639 (May 2011), pp. 58–61.

[188] H. Anderhub et al. „Design and Operation of FACT – The First G-APD Cherenkov Telescope“. In: *JINST* 8 (2013), P06008. DOI: 10.1088/1748-0221/8/06/P06008. arXiv: 1304.1710 [astro-ph.IM].

[189] A. Biland et al. „Calibration and performance of the photon sensor response of FACT – The First G-APD Cherenkov telescope“. In: *JINST* 9.10 (2014), P10012. DOI: 10.1088/1748-0221/9/10/P10012. arXiv: 1403.5747 [astro-ph.IM].

[190] J. Kónya and N. M. Nagy. „Chapter 13 - Environmental Radioactivity“. In: *Nuclear and Radiochemistry*. Ed. by J. Kónya and N. M. Nagy. Oxford: Elsevier, 2012, pp. 375–394. ISBN: 978-0-12-391430-9. DOI: https://doi.org/10.1016/B978-0-12-391430-9.00013-5. URL: http://www.sciencedirect.com/science/article/pii/B9780123914309000135.

[191] Bundesamt für Strahlenschutz. *Local gamma dose rate*. 2019. URL: https://odlinfo.bfs.de/DE/index.html.

[192] W. D. Apel et al. „Muon tracking in KASCADE-Grande: Lateral distributions of EAS muon densities“. In: *Proc. of the 21st European Cosmic Ray Symp., Kosice, SK, September 9-12, 2008 Kosice* (2009).

[193] P. Doll et al. „Muon tracking detector for the air shower experiment KASCADE“. In: *Nucl. Instrum. Meth.* A488.3 (2002), pp. 517–535. ISSN: 0168-9002. DOI: https://doi.org/10.1016/S0168-9002(02)00560-0. URL: http://www.sciencedirect.com/science/article/pii/S0168900202005600.

[194] A. Streich. „Scintillator Surface Detector for the Upgrade of the Pierre Auger Observatory“. Auger internal note GAP-2017-045. Master's Thesis. Karlsruher Institut für Technologie, 2017.

[195] Pico Technology. *PicoScope type 6403. data sheet*. 2018. URL: https://www.picotech.com/oscilloscope/6000/picoscope-6000-specifications.

[196] T. Bretz et al. „An integrated general purpose SiPM based optical module with a high dynamic range“. In: *JINST* 13.06 (2018), P06001. DOI: 10.1088/1748-0221/13/6/P06001, 10.1088/1748-0221/13/06/P06001. arXiv: 1803.04841 [physics.ins-det].

[197] S. Weingarten. „Szintillationsdetektoren mit Silizium-Photomultipliern“. Phd thesis. RWTH Aachen University, 2018.

[198] S. Ritt, R. Dinapoli, and U. Hartmann. „Application of the DRS chip for fast waveform digitizing“. In: *Nucl. Instrum. Meth.* A623 (2010), pp. 486–488. DOI: 10.1016/j.nima.2010.03.045.

[199] Paul Scherrer Institut. *DRS4 Evaluation Board. User's Manual*. 2018. URL: https://www.psi.ch/drs/DocumentationEN/manual_rev50.pdf.

[200] S. Thoudam et al. „LORA: A scintillator array for LOFAR to measure extensive air showers“. In: *Nucl. Instrum. Meth.* A767 (2014), pp. 339–346. ISSN: 0168-9002. DOI: https://doi.org/10.1016/j.nima.2014.08.021. URL: http://www.sciencedirect.com/science/article/pii/S0168900214009413.

[201] F. Tischbein. „Measurement of cosmic air showers - a laboratory class experiment“. Bachelor's Thesis. RWTH Aachen University, 2018.

[202] M. Aglietta et al. „UHE cosmic ray event reconstruction by the electromagnetic detector of EAS-TOP“. In: *Nucl. Instrum. Meth.* A336.1 (1993), pp. 310–321. ISSN: 0168-9002. DOI: https://doi.org/10.1016/0168-9002(93)91115-4. URL: http://www.sciencedirect.com/science/article/pii/0168900293911154.

[203] M. Aglietta et al. „Results on high-energy cosmic rays by EAS-TOP at Gran Sasso“. In: *Il Nuovo Cimento C* 20 (Jan. 1997), pp. 985–1007.

[204] The Particle Data Group. *Atomic and Nuclear Properties of Materials*. 2019. URL: http://pdg.lbl.gov/2014/AtomicNuclearProperties/.

[205] T. Bretz et al. „SiPMs - A revolution for high dynamic range applications“. In: *Proceedings of Science PoS(ICRC2017)472*. 2017. URL: https://pos.sissa.it/301/472/pdf.

[206] J. Kemp. „doctoral thesis, to be published“. PhD Thesis. RWTH Aachen University.

[207] D. Schmidt. „Sensitivity of AugerPrime to the masses of ultra-high-energy cosmic rays“. PhD Thesis. Karlsruher Institut für Technologie (KIT) and the Universidad Nacional de San Martín (UNSAM), 2018.

[208] A. Letessier-Selvon et al. „Layered water Cherenkov detector for the study of ultra high energy cosmic rays“. In: *Nucl. Instrum. Meth.* A767 (2014), pp. 41–49. ISSN: 0168-9002. DOI: https://doi.org/10.1016/j.nima.2014.08.029. URL: http://www.sciencedirect.com/science/article/pii/S0168900214009589.

[209] T. Pierog et al. „EPOS LHC: Test of collective hadronization with data measured at the CERN Large Hadron Collider“. In: *Phys. Rev.* C92.3 (2015), p. 034906. DOI: 10.1103/PhysRevC.92.034906. arXiv: 1306.0121 [hep-ph].

[210] A. M. Hillas. „Two interesting techniques for Monte-Carlo simulation of very high energy hadron cascades“. In: *Proceedings, 15th International Cosmic Ray Conference (ICRC 1977): Plovdiv, Bulgaria, August 13-26, 1977, Conference Papers. Volume* 8 (1981), pp. 193–196.

[211] S. Argiro et al. „The Offline Software Framework of the Pierre Auger Observatory“. In: *Nucl. Instrum. Meth.* A580 (2007), pp. 1485–1496. DOI: 10.1016/j.nima.2007.07.010. arXiv: 0707.1652 [astro-ph].

[212] P. Billoir. „A sampling procedure to regenerate particles in a ground detector from a ‘thinned’ air shower simulation output“. In: *Astroparticle Physics* 30.5 (2008), pp. 270–285. ISSN: 0927-6505. DOI: https://doi.org/10.1016/j.astropartphys.2008.10.002. URL: http://www.sciencedirect.com/science/article/pii/S0927650508001394.

[213] T. Hesterberg. „What Teachers Should Know about the Bootstrap: Resampling in the Undergraduate Statistics Curriculum“. In: *arxiv preprint* (2014). arXiv: 1411.5279 [stat.OT].

[214] K. Singh and M. Xie. „Bootstrap : A Statistical Method“. In: 2008.

[215] B. Efron. „Bootstrap methods: Another look at the Jackknife“. In: *Ann. Statist.* 7 (1979), pp. 1–26.

[216] *USB-650 Red Tide Spectrometers*. Datasheet. Ocean Optics, Inc. June 2018. URL: https://oceanoptics.com/product/usb-650-red-tide-spectrometers/.

[217] E. Dietz-Laursonn. „Detailed Studies of Light Transport in Optical Components of Particle Detectors“. PhD Thesis. RWTH Aachen University, 2016.

[218] *Si photodiodes with BNC connector, S2281 series*. Datasheet. Hamamatsu Photonics K.K. June 2018. URL: http://www.hamamatsu.com/resources/pdf/ssd/s2281_series_kspd1044e.pdf.

[219] *Series 2600B, SourceMeter SMU Instruments*. Datasheet. Keithley. June 2018. URL: https://www.tek.com/keithley-source-measure-units/smu-2600b-series-sourcemeter.

[220] *Integrating Spheres*. Datasheet. Thorlabs. June 2018. URL: https://www.thorlabs.com/newgrouppage9.cfm?objectgroup_id=1658&pn=IS200.

[221] S. Nieswand. „Measurement of exit characteristics of light from optical multimode plastic fibres“. Master’s thesis. RWTH Aachen University, 2016.

[222] C. Silva et al. „Reflectance of Polytetrafluoroethylene (PTFE) for Xenon Scintillation Light“. In: *Journal of Applied Physics* 107 (Apr. 2010), pp. 064902–064902.

[223] Dupli-Color. *DUPLI-COLOR Silver Chrome Effect Spray*. 2018. URL: https://www.motipdupli.com/en/INT/lang/products/dupli-color/decoration/effect/ipg-1080/tm-1080.html.

[224] Super ESKA, developed and manufactured by Mitsubishi. *Super ESKA Polyethylene Jacketed Optical Fiber Cord*. 2018. URL: http://i-fiberoptics.com/pdf/sh4001.pdf.

Declaration of pre-released partial results

The following publications contain pre-released partial results of this work and are cited with shortened author lists. The reference number is given in the brackets. It is identical to the reference number stated in the bibliography. The author of this thesis is author or coauthor of the publications:

[171] T. Hebbeker et al. “Muon measurement using scintillator tiles with SiPM readout". Internal Note of the Pierre Auger Collaboration GAP2013-057. 2013

[172] C. Peters et al. “The muon detector prototype AMD for the determination of the muon content in UHECRs". In: Proceedings of Science PoS(ICRC2015)596. 2015. https://pos.sissa.it/archive/conferences/236/596/ICRC2015_596.pdf

[173] J. Kemp et al. “The application of SiPMs in the fluorescence telescope FAMOUS and the Aachen Muon Detector". In: Proceedings of Science PoS(ICRC2017)466. 2017. https://pos.sissa.it/301/466

[174] C. Peters et al. “Prospects of Silicon Photomultipliers for Ground-Based Cosmic Ray Experiments". In: Proceedings of 2016 International Conference on Ultra-High Energy Cosmic Rays (UHECR2016). https://journals.jps.jp/doi/abs/10.7566/JPSCP.19.011030

The hardware development and extensive characterization studies of the readout electronics have been performed by Rebecca Meißner and Lukas Middendorf. Their work is essential for the presented measurements in this thesis. Additionally, a detailed description of the electronics and basic principles of several measurements are presented. Results and images are cited where applicable:

[164] R. Meißner. “Development and Characterisation of a Scintillator Based Muon Detector with SiPM Readout for Air Shower Experiments". Master’s Thesis. RWTH Aachen University, 2015

[165] L. Middendorf. “Data Acquisition for an SiPM based muon detector". PhD Thesis. RWTH Aachen University, 2018

Additionally, first studies of sub-parts of the work, presented in this thesis, have been pre-released in several theses. These studies comprise simulations performed by the presented detector simulation framework and measurements:

[183] D. Keßler. “Coupling of optical fibers for the Aachen Muon Detector". Bachelor’s Thesis. RWTH Aachen University, 2016

[184] M. Wirtz. “Simulation studies of a novel scintillator detector with SiPM readout for muons of cosmic ray air showers". Bachelor’s Thesis. RWTH Aachen University, 2014

[54] T. Niggemann. “The silicon photomultiplier telescope FAMOUS for the detection of fluorescence light". PhD thesis. RWTH Aachen University, 2016.

Acknowledgments - Danksagungen

Mein herzlicher Dank gilt Prof. Thomas Hebbeker für die tolle Chance, einen eigenen Detektorprotoypen von Beginn an zu begleiten, mich maßgeblich an ihm zu beteiligen, und dennoch die Arbeit in einer großen, internationalen Kollaboration kennenzulernen. Sein Wissen und seine langjährige Erfahrung waren von unschätzbarem Wert für mich und meine Arbeit. PD Dr. Oliver Pooth danke ich aufrichtig für die Bereitschaft als Berichter tätig zu sein.
Für die tolle Arbeitsatmosphäre möchte ich mich bei allen Mitgliedern des Instituts, besonders bei den Hallenbewohnern & friends, bedanken. Sie haben mein Promotionsstudium unglaublich bereichert und zu einer wundervollen Erfahrung gemacht. Namentlich möchte ich gerne Dr. Karl, Julian Kemp, Lukas Middendorf, Paulo Ferreira, Johannes Schumacher, Tim Niggemann, Markus Lauscher, Matthias Plum, Thomas Bretz, Martin Urban, Christian Hofer und Simon Weingarten hervorheben. Sie haben mich maßgeblich bei der Entwicklung von MiniAMD und den dazugehörigen Messungen unterstützt. Mein aufrichtiger Dank geht dabei vor allem an Julian Kemp, der immer ein offenes Ohr für mich hatte und sich vor allem in der Schlussphase stets Zeit für eine Diskussion genommen hat. Der MiniAMD-Support Hotline, Lukas Middendorf, danke ich dafür, dass er während unserer vielen gemeinsam Stunden im Labor nie die Geduld mit mir verloren und mich unermüdlich in die Geheimnisse der MiniAMD-Elektronik eingeweiht hat. Jonas Kasper, Ronja Hetzel und Erik Dietz-Laursonn danke ich für den tollen Support bei den vielen Geant4-Fragen. Das hervorragende Arbeitsumfeld wurde auch durch die vielen Menschen im Physikalischen Institut III ermöglicht, die die Infrastruktur im Institut gewährleisten. Seien es die guten IT-Geister, Thomas Kreß und Andreas Nowack, oder die Verwaltung, Melanie Roder, Iris Rodewick und Markus Merschmeyer. Ohne euch wäre das Institutsleben nicht das Gleiche! Ein großer Dank geht auch an alle Mitarbeiter der Mechanik- und Elektronikwerkstatt des III. Physikalischen Instituts A. Ihre Hilfe war unerlässlich für die Konstruktion, das Fertigen und den Zusammenbau der Kachelprototypen und MiniAMD. Eine große Freude war auch die Zusammenarbeit mit KollegInnen am KIT. Darko Veberic, Alexander Streich und David Schmidt haben mich bei Messungen und Simulationen gerne unterstützt. Anne Zilles und Daniela Mockler haben dafür gesorgt, dass ein Besuch in Karlsruhe immer etwas besonderes war. Zudem möchte ich gerne allen kritischen Korrekturlesern danken, die sich durch die Massen an Text gearbeitet haben, die ich fabriziert habe. Zu aller Letzt möchte ich meiner Familie, Antje Berger und Florian Scheuch danken. Sie haben mir jederzeit zur Seite gestanden und mich, wenn immer nötig, ermutigt meine Arbeit fortzusetzen.
Diese Arbeit wurde vom evangelischen Studienwerk Villigst, vom Bundesministerium für Wissenschaft und Forschung (BMBF) und der RWTH Aachen University finanziert und unterstützt. Die in der Arbeit präsentierten Simulationen wurden mit Rechenressourcen durchgeführt, die von der RWTH Aachen University unter dem Projekt rwth0210 zur Verfügung gestellt wurden.